# Rotational and Structural Analyses of Astrochemically Relevant Molecules

By

Houston Hartwell Smith

A dissertation submitted in partial fulfillment of the requirements for the degree of

Doctor of Philosophy

(Physical Chemistry)

at the

UNIVERSITY OF WISCONSIN – MADISON

2023

Date of final oral examination: July 19, 2023

The dissertation is approved by the following members of the Final Oral Committee:

Robert McMahon, Professor, Chemistry
Claude Woods, Emeritus Professor, Chemistry
Etienne Garand, Professor, Chemistry
Susanna L. Widicus Weaver, Professor, Chemistry and Astronomy

**To my family that made this possible.**

# Rotational And Structural Analyses of Astrochemically Relevant Molecules

Houston Hartwell Smith

Under the supervision of Professor Robert J. McMahon and Professor R. Claude Woods at the University of Wisconsin – Madison

Abstract: Rotational spectroscopy is an extremely powerful technique that allows for identification of molecules in different gaseous environments given their rotational spectrum has been measured, assigned, and least-squares fit to a proper Hamiltonian. Rotational spectroscopy is unique in that structural isomers, conformers, isotopologues, and vibrational states of a molecule all have a different rotational spectrum enabling their positive identification in a gas sample. Given the specificity of the technique and ubiquity of radio frequencies in the interstellar medium (ISM), the majority of the near 300 molecules detected in the ISM have come from radioastronomy. This thesis comprises the spectral assignment of five molecules with a unifying theme of providing new or updated spectroscopic constants for the search of these molecules in the ISM. Additionally, several molecules (1-cyanocyclobutene, 2-cyanopyrimidine, and cyanopyrazine) have their two lowest-energy vibrationally excited states Coriolis coupled to each other. This thesis uses a two-state, Coriolis coupled Hamiltonian to adequately address the measured rotational spectra, which are greatly affected by this coupling, and this results in an extremely precise determination of the energy separation between the vibrationally excited states. Two other molecules (ketene and methacrylonitrile) utilized the spectroscopic constants of different isotopologues along with high-level theoretical corrections to achieve highly precise and accurate semi-experimental equilibrium structures ($r_e^{SE}$) with general precision to the ten-thousandth of an Angstrom and hundredths of a degree for bond distances and angles, respectively.

**Acknowledgements**

The journey to pursue my PhD in chemistry started long before attending the University of Wisconsin – Madison in the Fall of 2018. I trace it back to 8th grade where two teachers, Ms. Gordon and Ms. Kelly, sparked my interests in physical science and math. Their encouragement to continue to ask probing questions on whatever material we were discussing helped begin to mold me into the scientist I am today. I am grateful they took the time to answer the numerous questions I asked instead of dismissing them, because I don't know how that would have affected my interests in becoming a scientist. The next major influence was a history teacher in high school, Mr. Bissell, whom I actually had for three years for various classes. To date, I think he has been my favorite and most impactful instructor because of the way he taught his classroom. He not only taught us about countless different history lessons, but with each class, he encouraged you to share your independent thoughts on that specific topic. He would allow the lecture to evolve throughout the class period with the discussion of his students, but he was able to simultaneously keep the discussion on topic without dominating the conversation. I continue to admire his ability to encourage students' participation in the class, while covering all the teaching objectives necessary. His ability to make me feel respected as an individual for my thoughts was truly inspirational, and throughout my time as a teaching assistant at the University of Wisconsin – Madison, I tried to adopt a lot of his teaching ideology.

Upon attending Emory University in the Fall of 2014, I quickly began research with Dr. Susanna Widicus Weaver as a first-year undergraduate. At that time, I had no idea chemistry and astronomy could be combined into astrochemistry, and the experience opened my eyes to a whole new field. Her openness to take in new undergraduate students is quite unusual in the field, due to the time required to get the new students up to speed on the research being performed in her lab.

She allowed me to be a part of her research and began my journey of learning about rotational spectroscopy and astrochemistry. The four years I spent in her lab are very memorable, because I have gained life-long friends that were graduate students at the time, and she provided an amazing environment for me to continue to develop my skills as a scientist. She also encouraged me to apply to graduate schools and is a contributing reason as to why I attended the University of Wisconsin – Madison to obtain my PhD in chemistry.

Once at the University of Wisconsin – Madison, it did not take me long to find my home in the McMahon | Woods group continuing my passion for astrochemistry. A unique aspect of the group is that, in practicality, each graduate student has three advisors within the group: Bob, Claude, and Brian. Each person has played a crucial role in mentoring me throughout my time in the group. I am grateful for the conversations I have had with Bob about the overarching goals of the group and all the help and feedback about manuscripts for publication. He was instrumental in streamlining the submission process and was a wonderful mentor. I have spent more time individually with Claude, especially in recent years, and his passion for chemistry and knowledge has been extremely impactful in my life. Our conversations about science and his methodical approach to problems are something I will always remember and try to embody as a scientist. Brian's role in the group is hard to explain to anyone outside the group, but the quickest way is to describe him as the life-blood of the group. He is a mentor to all graduate students all while performing his teaching responsibilities to an exceptionally high level. His positive outlook and productivity were and are awe inspiring to me, and I continue to strive to reach a percentage of his efficiency. He has always been someone I can rely on, and for that, I am grateful. During my time here, I have seen the McMahon | Woods group have a significant turnover with several graduate students receiving their PhDs and moving on and new graduate students joining the group. I am

thankful that every group member throughout my time I consider a friend, and I will always remember the office conversations and Fridays at the Library. I am happy to see the members that have graduated starting new chapters in their life, and I look forward to the day all the current members graduate and get to begin theirs. I want to highlight one previous graduate student, Maria Zdanovskaia, for her unbelievable contribution to our research group. She always set a lofty goal as to the productivity a graduate student could obtain all while never refusing to answer any questions I had. Along with Brian, she was the most crucial person helping with the daily activities of being a rotational spectroscopist. Since her graduation, I have tried to fill the shoes she left, but they were quite large. My productivity would certainly have been diminished without her help, and for that I am forever grateful.

Now on to the most influential people in my life: my family. The older I become, the more I understand that I have a profound bond with my parents and grandparents, and I continue to be grateful for it. This has been a journey we have been on together and is not something I have undertaken alone. The concluding accomplishment, my PhD, is thus an accomplishment I share with you all because you have all played vital parts in my achievement. My mom has been the most instrumental with the continued belief and support throughout my academic time. I am unsure if I would have been able to complete my thesis without your vocal support and frequent visits. In addition to my father's support, the reignition of our love for motorsports has played a crucial role in improving my mental health. I always look forward to our conversations, and I always know you will be in my corner. I also can't forget to thank my grandparents for our weekly chats every Sunday evening, because you both helped me stay grounded and feel close to my family even with so much distance between us. I am excited to start my new chapter after graduate school, but I do hope it is closer to Georgia.

## Table of Contents

## List of Tables

## List of Schemes

## List of Figures

### Chapter 2: Synthesis, Purification, and Rotational Spectroscopy of 1-Cyanocyclobutene ($C_5H_5N$)

**Chapter 1: Thesis Overview**

Rotational spectroscopy is the unifying aspect of all the chapters in this thesis, particularly its implementation to facilitate the search for astrochemically relevant molecules *via* radioastronomy, to determine a highly precise and accurate semi-experimental equilibrium structure ($r_e^{SE}$), and least-squares analysis of Coriolis-coupled excited states. The pure laboratory rotational spectra of astrochemically relevant molecules are highly desirable because observational spectra are usually due to a complex mixture of various molecules. This mixture makes it quite difficult to assign molecular transitions for an unknown molecular species. Laboratory rotational spectroscopists acquire spectra of molecules that are believed to be present in various space environments and fully assign molecular transitions *via* a least-squares fit to the rotational Hamiltonian of the molecule. Once this process is complete, radioastronomers can be confident that if a series of molecular transitions are present in their observational spectra, that molecule is present in that environment. Radioastronomers can be confident in this assignment, since the rotational spectrum of any molecule is unique; a rotational spectrum is specific to the conformation, vibration, and isotopologue of that molecule. Furthermore, radioastronomy is a primary tool to observe various gaseous space environments because background radiation and collisions between molecules result in photon emission between rotational energy levels. A rich chemical diversity has been observed in the interstellar medium (ISM) and circumstellar shells, with about 300 molecules detected to date.[19,20] Among these molecules, the cyano moiety is quite prevalent, due to its typically large permanent dipole moment and due to the relative abundance of carbon and nitrogen in the ISM. The McMahon | Woods research group has been interested in expanding two areas of organic nitriles: aryl nitriles/isonitriles[21-27] and nitrile-containing isomers of pyridine.[28-32] Chapter 2 focuses on one of the nitrile-containing isomers of pyridine, 1-

cyanocyclobutene[32], while Chapters 3 and 4 focus on 2-cyanopyrimidine and cyanopyrazine, respectively. Radioastronomers have searched for pyridine, pyrimidine, and pyridazine in the ISM, but they have been unsuccessful to date.[33] Pyrazine has no permanent dipole moment, so it cannot be detected by radioastronomy.

Pyridine is a common component of various biotic molecules[34], *e.g.*, vitamins and co-enzymes, so its presence in the ISM would be evidence of a prebiotic molecule being present in these environments. The detection of an isomer of pyridine, *e.g.*, 1-cyanocyclobutene, could act as a tracer for and suggest the presence of pyridine. The cyano substituent of 1-cyanocyclobutene increases the permanent dipole moment in comparison to that of pyridine, thus favoring the likelihood of 1-cyanocyclobutene detection if these isomers are present at similar abundances. Before our work, there had not been a measured rotational spectrum of 1-cyanocyclobutene, and thus, the molecule could not have been sought by radioastronomers. The lack of analysis is likely due, at least in part, to the fact that 1-cyanocyclobutene is not commercially available. For our study, it was synthesized by Dr. Sam Kougias, a graduate student in our research group (now graduated). We observed, assigned, and least-squares fit the rotational spectrum from 130 GHz to 360 GHz for the vibrational ground state and two lowest-energy vibrationally excited states of 1-cyanocyclobutene. The completion of the ground-state least-squares fit now allows radioastronomers to search for rotational transitions of 1-cyanocyclobutene in the ISM. The least-squares fit for the rotational transitions for each vibrational state in the Coriolis-coupled dyad of the two lowest-energy vibrationally excited states of 1-cyanocycylobutene allowed for the determination of a precise energy separation with ~0.000004 $cm^{-1}$ precision. Without this least-squares fit, no rotational transitions from either vibrational state could be predicted and assigned in any observational data, because the Coriolis coupling shifts rotational transitions sometimes

GHz from their original predictions. This work was published in the Journal of Physical Chemistry A, and a reprint of that article is located in Appendix C.

Chapters 3 and 4 cover similar projects where the rotational spectra were measured from 130 GHz to 500 GHz for both 2-cyanopyrimidine and cyanopyrazine. These works were published in the Journal of Molecular Spectroscopy, and a reprint of these articles are located in Appendix C. These chapters have similar motivation to Chapter 2 regarding the vibrational ground state of each molecule, because – being derivatives – these molecules could act as tracer molecules for pyrimidine and pyrazine in various interstellar environments. The rotational transitions for the ground state of each molecule were measured, assigned, and least-squares fit to a partial-octic distorted-rotor Hamiltonian. The overall uncertainties of these least-squares fits are below the 50 kHz measurement uncertainty of our spectrometer. Most of the least-squares fitting of 2-cyanopyrimidine was performed by me, while the majority for cyanopyrazine was performed by Dr. Brian Esselman. Neither molecule had previously had its rotational spectrum published, so our work allows radioastronomers to search for the heterocyclic aromatic molecules in the ISM. The two lowest-energy vibrationally excited states of each molecule are also Coriolis coupled, and we were able to complete a detailed least-squares fit analysis for each dyad, resulting in a similar precision in the energy separation between vibrational states of each molecule. In addition to the completion of these two Coriolis-coupled dyad least-squares fit, our research group has now completed a variety of Coriolis-coupled dyad least-squares fits for aromatic molecules,[21-24,27] which has allowed us to explore any trends observed. Analysis of additional Coriolis-coupled dyads will allow more detailed comparisons to be made and could give insight into the vibrational motions and bonding of aromatic molecules. Extensive work was performed by Dr. Andrew Owen, a former graduate student, to theoretically predict vibrational coupling parameters, which

was presented in his thesis.[35] More insight into the differences between the theoretical predictions and experimental values for various coupling parameters can be gained as our group increases the number of vibrationally-coupled excited state that have been successfully least-squares fit.

A semi-experimental ($r_e^{SE}$) equilibrium structure and high-level theoretical structures of ketene ($H_2CCO$) are presented in Chapter 5. This work was published in the Journal of Chemical Physics, and a reprint of that article is located in Appendix C. The previous literature on the rotational and vibrational spectroscopy of ketene is plentiful, with the first reports dating back over 70 and 85 years, respectively. During this time, various structures of ketene were reported with improving precision as more isotopologues were measured, computational chemistry advanced, and experimental techniques and technologies improved. The first structures of ketene were substitution structures ($r_s$) based off of Kraitchman's seminal paper.[36] The first complete substitution structure, where every atom was isotopically substituted once, was completed in 1990 by Brown *et al*.[3] Fundamentally, a substitution structure does not represent the equilibrium structure of a molecule, because it does not take vibration-rotation interactions or electron-mass distribution into account. For a direct comparison to theoretical equilibrium structures ($r_e$), a technique, the semi-experimental equilibrium structure ($r_e^{SE}$), was pioneered by Pulay, Meyer, and Boggs.[37] This approach relies on making computational corrections to ground-state rotational constants ($B_0$) to obtain equilibrium constants ($B_e$) and using these in a non-linear least-squares fit to optimize structural parameters of a molecule. Different computational theories have been utilized since its inception for these corrections, *e.g.*, Density Functional Theory (DFT) or Coupled Cluster theory (CC). In the last 20 years, it has been shown that computational corrections calculated by Coupled Cluster theory result in the most accurate molecular structures.[38,39] In our work, five isotopologues, [2-$^2$H, 1-$^{13}$C]-ketene, [2-$^2$H, 2-$^{13}$C]-ketene, [2-$^2$H, $^{18}$O]-ketene, [2-$^2$H,

$^{17}$O]-ketene, and [2,2-$^{2}$H, $^{17}$O]-ketene, were newly measured, and the rotational spectra of previously known isotopologues were also extended to 750 GHz. The least-squares fitting of the rotational constants from 16 isotopologues, along with computational corrections from coupled cluster calculations with single, double, and perturbative triple excitations [CCSD(T)/cc-pCVTZ] resulted in the most precise and accurate structure of ketene to date. The resultant $r_e^{SE}$ structural parameters were compared to the best theoretical estimate (BTE), described in Chapter 5, and all BTE values showed agreement with the respective $r_e^{SE}$ structural parameters within their 2σ uncertainties. The discrepancies between the BTE structure and the $r_e^{SE}$ structure for each structural parameter are 0.0003 Å, 0.0000 Å, and 0.0004 Å, for $r_{C–C}$, $r_{C–H}$, and $r_{C–O}$, respectively, and 0.009° for $\theta_{C–C–H}$. The precision from the $r_e^{SE}$ structural parameters is astonishing, with heavy-atom bond lengths determined to ten thousandths of an Angstrom and the bond angle determined to thousandths of a degree. For perspective, the precision of the bond lengths is only an order of magnitude larger than the radius of a carbon nucleus, 2.47 fm.[40] The presented $r_e^{SE}$ helps to set the precedent on how precise a semi-experimental equilibrium structure can be with high level theoretical corrections and could act as a benchmark for newer theoretical structure calculations.

Chapter 6 details a semi-experimental equilibrium structure ($r_e^{SE}$) of methacrylonitrile ($C_4H_5N$), along with an extension of its measured rotational spectrum to 500 GHz. A total of 34 isotopologues of methacrylonitrile were observed, measured, and least-squares fit to determine precise spectroscopic constants. These 34 isotopologues comprise the protic, heavy-atom substituted isotopologues of the protic, every combination of deuterium substitution, and the heavy-atom substitutions of the perdeuterio isotopologue. Due to the presence of a methyl functional group, the main isotopologue was least-squares fit with the XIAM[41] program to account for the internal rotation splitting of rotational transitions. All other isotopologues were treated as

simple distorted rotors, because the isotopologues that would have visible internal rotation splitting (heavy-atom substituted isotopologues of the protic, [1-$^2H_{cis}$], [1-$^2H_{trans}$], and [1,1-$^2H$]) were in low abundance, so only unsplit rotational transitions were observed. Due to the inability to precisely determine the rotational constants for two heavy-atom substituted isotopologues of the perdeuterio, 32 isotopologues were utilized in the least-squares fit of the structure determination. Methacrylonitrile is the first $r_e^{SE}$ structure determination from our group where a structural parameter was held constant at the calculated BTE value, due to the inability to determine the parameter with a high level of precision and the resulting effects to other structural parameters. This issue was attributed to three atoms lying extremely close to a principal axis, and to the inability of the 32 isotopologues to significantly rotate the principal axes away from these three atoms. The near-axis problem has been discussed previously,[42-45] but no universal solution is available. The solution in this work – holding the $\theta_{C2\text{-}C4\text{-}N}$ fixed to the BTE value – is an empirical solution to the near-axis problem, and the resulting $r_e^{SE}$ is of similar precision to our previously determined semi-experimental equilibrium structure determinations.[46-53] The 2σ uncertainties of the $r_e^{SE}$ parameters are ≤ 0.0008 Å and ≤ 0.053° for the bond distances and angles, respectively. In total, 12 of the 16 $r_e^{SE}$ structural parameters agree with the BTE values to within their respective 2σ uncertainties. The specific parameters that are not in agreement between the BTE and $r_e^{SE}$ values and the overall attempt to determine a highly precise and accurate $r_e^{SE}$ structure given this near-axis problem are discussed.

Additionally, I travelled to the Canadian Light Source (CLS) synchrotron in December 2021 with Professor Claude Woods and Sam Wood, a current graduate student, to record the Fourier-transformed infrared spectra of $HN_3$ and $DN_3$. Both $HN_3$ and $DN_3$ were separately synthesized in a custom-built apparatus, which will be discussed in detail in Sam Wood's thesis,

on-site at the CLS. Further studies were performed by on-site research scientists during January and February 2022. The total data collection at CLS resulted in the infrared spectrum of $HN_3$ and $DN_3$ being measured from 30 $cm^{-1}$ to 5000 $cm^{-1}$ with a precise resolution of ~0.0009 $cm^{-1}$ with varying pressures between 1 and 100 mTorr. The resulting data has allowed Professor Claude Woods to thoroughly examine and assign vibrational transitions for over a dozen and over twenty vibrational states of $HN_3$ and $DN_3$, respectively. Professor Claude Woods presented the results and current progress of this analysis for $DN_3$ in two presentations at the International Symposium on Molecular Spectroscopy (ISMS) in 2022 and 2023.[54,55] The data collected at the CLS along with previously collected millimeter-wave spectra could allow for a global treatment of the vibrational coupling for a majority of these vibrational states, which would be the first of its kind and would set a precedent for the most complex vibrational coupling to be fully treated.

## References


1. B. Bak; E. S. Knudsen; E. Madsen; J. Rastrup-Andersen, "Preliminary Analysis of the Microwave Spectrum of Ketene," *Phys. Rev.* **79**, 190-190 (1950).
2. A. P. Cox; L. F. Thomas; J. Sheridan, "Internuclear distances in keten from spectroscopic measurements," *Spectrochim. Acta* **15**, 542-543 (1959).
3. R. D. Brown; P. D. Godfrey; D. McNaughton; A. P. Pierlot; W. H. Taylor, "Microwave spectrum of ketene," *J. Mol. Spectrosc.* **140**, 340-352 (1990).
4. A. Guarnieri; A. Huckauf, "The Rotational Spectrum of ($^{17}$O)Ketene," *Z. Naturforsch., A: Phys. Sci.* **56**, 440-446 (2001).
5. A. Guarnieri, "The Millimeterwave Spectrum of Four Rare Ketene Isotopomers," *Z. Naturforsch., A: Phys. Sci.* **60**, 619-628 (2005).
6. L. Nemes; Akad. Nauk SSSR, Sib. Otd., Inst. Opt. Atmos., 1974, p 2
7. L. Nemes, "Rotation-vibration analysis of the Coriolis-coupled $\nu_5$, $\nu_6$, $\nu_8$, and $\nu_9$ bands of $H_2CCO$," *J. Mol. Spectrosc.* **72**, 102-123 (1978).
8. F. Winther; F. Hegelund; L. Nemes, "The infrared spectrum of dideuteroketene below 620 $cm^{-1}$," *J. Mol. Spectrosc.* **117**, 388-402 (1986).
9. J. L. Duncan; A. M. Ferguson; J. Harper; K. H. Tonge; F. Hegelund, "High-resolution infrared rovibrational studies of the $A_1$ species fundamentals of isotopic ketenes," *J. Mol. Spectrosc.* **122**, 72-93 (1987).
10. J. L. Duncan; A. M. Ferguson, "High resolution infrared analyses of fundamentals and overtones in isotopic ketenes," *Spectrochim. Acta A Mol. Biomol. Spectrosc.* **43**, 1081-1086 (1987).
11. F. Hegelund; J. Kauppinen; F. Winther, "The high resolution infrared spectrum of the $\nu_9$, $\nu_6$ and $\nu_5$ bands in ketene-$d_2$," *Mol. Phys.* **61**, 261-273 (1987).
12. J. W. C. Johns; L. Nemes; K. M. T. Yamada; T. Y. Wang; J. Doménech; J. Santos; P. Cancio; D. Bermejo; J. Ortigoso; R. Escribano, "The ground state constants of ketene," *J. Mol. Spectrosc.* **156**, 501-503 (1992).
13. R. Escribano; J. L. Doménech; P. Cancio; J. Ortigoso; J. Santos; D. Bermejo, "The $\nu_1$ band of ketene," *J. Chem. Phys.* **101**, 937-949 (1994).
14. M. C. Campiña; E. Domingo; M. P. Fernández-Liencres; R. Escribano; L. Nemes, "Analysis of the high resolution spectra of the $\nu_5$ and $\nu_6$ bands of ketene," *An. Quim., Int. Ed.* **94**, 23-26 (1998).
15. M. Gruebele; J. W. C. Johns; L. Nemes, "Observation of the $\nu_6 + \nu_9$ Band of Ketene via Resonant Coriolis Interaction with $\nu_8$," *J. Mol. Spectrosc.* **198**, 376-380 (1999).
16. L. Nemes; D. Luckhaus; M. Quack; J. W. C. Johns, "Deperturbation of the low-frequency infrared modes of ketene ($CH_2CO$) " *J. Mol. Struct.* **517-518**, 217-226 (2000).
17. H. R. Johnson; M. W. P. Strandberg, "The Microwave Spectrum of Ketene," *J. Chem. Phys.* **20**, 687-695 (1952).
18. A. Guarnieri; A. Huckauf, "The Rotational Spectrum of Ketene Isotopomers with $^{18}$O and $^{13}$C Revisited," *Z. Naturforsch., A: Phys. Sci.* **58**, 275-279 (2003).
19. H. S. P. Müller; S. Thorwirth; D. A. Roth; G. Winnewisser, "The Cologne Database for Molecular Spectroscopy, CDMS," *Astron. Astrophys.* **370**, L49-L52 (2001).
20. H. S. P. Müller; F. Schlöder; J. Stutzki; G. Winnewisser, "The Cologne Database for Molecular Spectroscopy, CDMS: a Useful Tool for Astronomers and Spectroscopists," *J. Mol. Struct.* **742**, 215-227 (2005).
21. M. A. Zdanovskaia; B. J. Esselman; H. S. Lau; D. M. Bates; R. C. Woods; R. J. McMahon; Z. Kisiel, "The 103 – 360 GHz Rotational Spectrum of Benzonitrile, the First Interstellar Benzene Derivative Detected by Radioastronomy," *J. Mol. Spectrosc.* **351**, 39-48 (2018).
22. M. A. Zdanovskaia; B. J. Esselman; R. C. Woods; R. J. McMahon, "The 130 - 370 GHz Rotational Spectrum of Phenyl Isocyanide ($C_6H_5NC$)," *J. Chem. Phys.* **151**, 024301 (2019).

23. P. M. Dorman; B. J. Esselman; J. E. Park; R. C. Woods; R. J. McMahon, "Millimeter-Wave Spectrum of 4-Cyanopyridine in its Ground State and Lowest-Energy Vibrationally Excited States, $\nu_{20}$ and $\nu_{30}$," *J. Mol. Spectrosc.* **369**, 111274 (2020).
24. P. M. Dorman; B. J. Esselman; R. C. Woods; R. J. McMahon, "An Analysis of the Rotational Ground State and Lowest-energy Vibrationally Excited Dyad of 3-Cyanopyridine: Low Symmetry Reveals Rich Complexity of Perturbations, Couplings, and Interstate Transitions," *J. Mol. Spectrosc.* **373**, 111373 (2020).
25. B. J. Esselman; M. A. Zdanovskaia; H. H. Smith; R. C. Woods; R. J. McMahon, "The 130–500 GHz rotational spectroscopy of cyanopyrazine ($C_4H_3N_2$-CN)," *J. Mol. Spectrosc.* **389**, 111703 (2022).
26. H. H. Smith; B. J. Esselman; M. A. Zdanovskaia; R. C. Woods; R. J. McMahon, "The 130–500 GHz rotational spectrum of 2-cyanopyrimidine," *J. Mol. Spectrosc.* **391**, 111737 (2023).
27. M. A. Zdanovskaia; M.-A. Martin-Drumel; Z. Kisiel; O. Pirali; B. J. Esselman; R. C. Woods; R. J. McMahon, "The eight lowest-energy vibrational states of benzonitrile: analysis of Coriolis and Darling-Dennison couplings by millimeter-wave and far-infrared spectroscopy," *J. Mol. Spectrosc.* **383**, 111568 (2022).
28. S. M. Kougias; S. N. Knezz; A. N. Owen; R. A. Sanchez; G. E. Hyland; D. J. Lee; A. R. Patel; B. J. Esselman; R. C. Woods; R. J. McMahon, "Synthesis and Characterization of Cyanobutadiene Isomers—Molecules of Astrochemical Significance," *J. Org. Chem.* **85**, 5787-5798 (2020).
29. M. A. Zdanovskaia; P. M. Dorman; V. L. Orr; A. N. Owen; S. M. Kougias; B. J. Esselman; R. C. Woods; R. J. McMahon, "Rotational Spectra of Three Cyanobutadiene Isomers ($C_5H_5N$) of Relevance to Astrochemistry and Other Harsh Reaction Environments," *J. Am. Chem. Soc.* **143**, 9551-9564 (2021).
30. M. A. Zdanovskaia; B. J. Esselman; S. M. Kougias; A. R. Patel; R. C. Woods; R. J. McMahon, "The 130–360 GHz rotational spectrum of syn-2-cyano-1,3-butadiene ($C_5H_5N$) – a molecule of astrochemical relevance," *Mol. Phys.* **119**, e1964629 (2021).
31. B. J. Esselman; S. M. Kougias; M. A. Zdanovskaia; R. C. Woods; R. J. McMahon, "Synthesis, Purification, and Rotational Spectroscopy of (Cyanomethylene)Cyclopropane—An Isomer of Pyridine," *J. Phys. Chem. A* **125**, 5601-5614 (2021).
32. H. H. Smith; S. M. Kougias; B. J. Esselman; R. C. Woods; R. J. McMahon, "Synthesis, Purification, and Rotational Spectroscopy of 1-Cyanocyclobutene ($C_5H_5N$)," *J. Phys. Chem. A* **126**, 1980-1993 (2022).
33. S. B. Charnley; Y.-J. Kuan; H.-C. Huang; O. Botta; H. M. Butner; N. Cox; D. Despois; P. Ehrenfreund; Z. Kisiel; Y.-Y. Lee; A. J. Markwick; Z. Peeters; S. D. Rodgers, "Astronomical Searches for Nitrogen Heterocycles," *Adv. Space Res.* **36**, 137-145 (2005).
34. T. Tahir; M. Ashfaq; M. Saleem; M. Rafiq; M. I. Shahzad; K. Kotwica-Mojzych; M. Mojzych, "Pyridine Scaffolds, Phenols and Derivatives of Azo Moiety: Current Therapeutic Perspectives," *Molecules* **26**, 4872 (2021).
35. A. N. Owen, "Computational Methods Applied to the Study of the Structure, Spectra, and Reactivity of Small Organic Molecules," University of Wisconsin − Madison, ProQuest; 2022.
36. J. Kraitchman, "Determination of Molecular Structure from Microwave Spectroscopic Data," *Am. J. Phys.* **21**, 17-24 (1953).
37. P. Pulay; W. Meyer; J. E. Boggs, "Cubic force constants and equilibrium geometry of methane from Hartree–Fock and correlated wavefunctions," *J. Chem. Phys.* **68**, 5077-5085 (1978).
38. J. Gauss; J. F. Stanton, "Equilibrium structure of LiCCH," *Int. J. Quantum Chem.* **77**, 305-310 (2000).
39. K. L. Bak; J. Gauss; P. Jørgensen; J. Olsen; T. Helgaker; J. F. Stanton, "The Accurate Determination of Molecular Equilibrium Structures," *J. Chem. Phys.* **114**, 6548-6556 (2001).
40. I. Angeli; K. P. Marinova, "Table of experimental nuclear ground state charge radii: An update," *At. Data Nucl. Data Tables* **99**, 69-95 (2013).

41. H. Hartwig; H. Dreizler In *Z NATURFORSCH A*, 1996; Vol. 51, p 923
42. L. Pierce, "Note on the use of ground-state rotational constants in the determination of molecular structures," *J. Mol. Spectrosc.* **3**, 575-580 (1959).
43. B. P. Stoicheff, "The variation of carbon-carbon bond lengths with environment as determined by spectroscopic studies of simple polyatomic molecules," *Tetrahedron* **17**, 135-145 (1962).
44. H. D. Rudolph, "Contribution to the systematics of r0-derived molecular structure determinations from rotational parameters," *Struct. Chem.* **2**, 581-588 (1991).
45. H. D. Rudolph, "Accurate molecular structure from microwave rotational spectroscopy," *Advances in Molecular Structure Research* **1**, 63-114 (1995).
46. Z. N. Heim; B. K. Amberger; B. J. Esselman; J. F. Stanton; R. C. Woods; R. J. McMahon, "Molecular Structure Determination: Equilibrium Structure of Pyrimidine (*m*-$C_4H_4N_2$) from Rotational Spectroscopy ($r_e^{SE}$) and High-Level Ab Initio Calculation ($r_e$) Agree Within the Uncertainty of Experimental Measurement," *J. Chem. Phys.* **152**, 104303 (2020).
47. B. J. Esselman; M. A. Zdanovskaia; A. N. Owen; J. F. Stanton; R. C. Woods; R. J. McMahon, "Precise equilibrium structure of thiazole (*c*-$C_3H_3NS$) from twenty-four isotopologues," *J. Chem. Phys.* **155**, 054302 (2021).
48. V. L. Orr; Y. Ichikawa; A. R. Patel; S. M. Kougias; K. Kobayashi; J. F. Stanton; B. J. Esselman; R. C. Woods; R. J. McMahon, "Precise equilibrium structure determination of thiophene (*c*-$C_4H_4S$) by rotational spectroscopy—Structure of a five-membered heterocycle containing a third-row atom," *J. Chem. Phys.* **154**, 244310 (2021).
49. A. N. Owen; M. A. Zdanovskaia; B. J. Esselman; J. F. Stanton; R. C. Woods; R. J. McMahon, "Semi-Experimental Equilibrium ($r_e^{SE}$) and Theoretical Structures of Pyridazine (*o*-$C_4H_4N_2$)," *J. Phys. Chem. A* **125**, 7976-7987 (2021).
50. H. A. Bunn; B. J. Esselman; P. R. Franke; S. M. Kougias; R. J. McMahon; J. F. Stanton; S. L. Widicus Weaver; R. C. Woods, "Millimeter/Submillimeter-wave Spectroscopy and the Semi-experimental Equilibrium ($r_e^{SE}$) Structure of 1*H*-1,2,4-Triazole (*c*-$C_2H_3N_3$)," *J. Phys. Chem. A* **126**, 8196-8210 (2022).
51. A. N. Owen; N. P. Sahoo; B. J. Esselman; J. F. Stanton; R. C. Woods; R. J. McMahon, "Semi-experimental equilibrium ($r_e^{SE}$) and theoretical structures of hydrazoic acid ($HN_3$)," *J. Chem. Phys.* **157**, 034303 (2022).
52. M. A. Zdanovskaia; B. J. Esselman; S. M. Kougias; B. K. Amberger; J. F. Stanton; R. C. Woods; R. J. McMahon, "Precise equilibrium structures of 1*H*- and 2*H*-1,2,3-triazoles ($C_2H_3N_3$) by millimeter-wave spectroscopy," *J. Chem. Phys.* **157**, 084305 (2022).
53. H. H. Smith; B. J. Esselman; S. A. Wood; J. F. Stanton; R. C. Woods; R. J. McMahon, "Improved semi-experimental equilibrium structure and high-level theoretical structures of ketene," *J. Chem. Phys.* **158**, 244304 (2023).
54. R. C. Woods; B. K. Amberger; B. Billinghurst; B. J. Esselman; P. Kania; Z. Kisiel; R. J. McMahon; V. L. Orr; A. N. Owen; H. H. Smith; S. Urban; K. Vavra; S. A. Wood, "Combined Millimeter Wave and FTIR Spectra of $DN_3$," *International Symposium on Molecular Spectroscopy* (2022).
55. R. C. Woods; B. K. Amberger; B. Billinghurst; B. J. Esselman; P. Kania; Z. Kisiel; R. J. McMahon; V. L. Orr; A. N. Owen; H. H. Smith; S. Urban; K. Vavra; S. A. Wood, "Analysis of Combined Millimeter-wave and Fourier Transform Infrared Spectra of $DN_3$: Extension of the Analysis to Eight New Vibrational States," *International Symposium on Molecular Spectroscopy* (2023).

**Synthesis, Purification, and Rotational Spectroscopy of 1-Cyanocyclobutene ($C_5H_5N$)**

Houston H. Smith, Samuel M. Kougias, Brian J. Esselman, R. Claude Woods,* Robert J. McMahon*

Department of Chemistry, University of Wisconsin–Madison, 1101 University Avenue, Madison, Wisconsin 53706-1322, United States

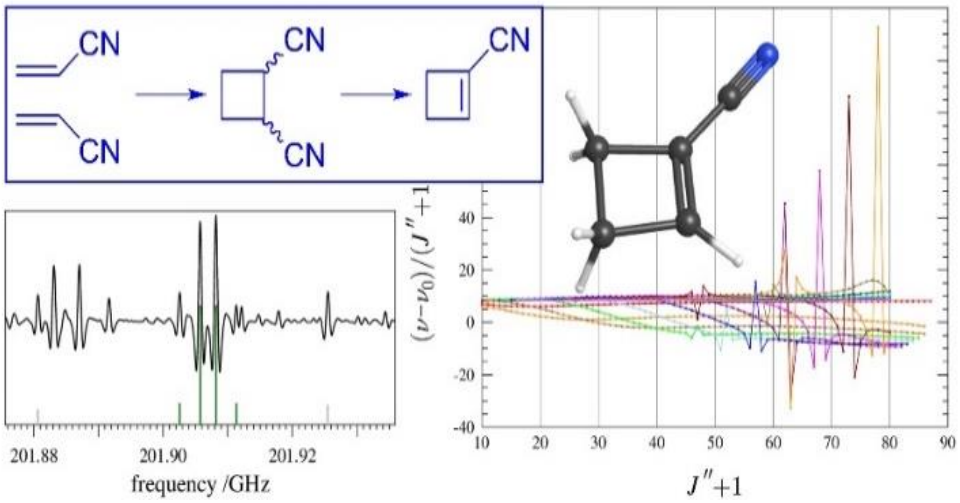


**ABSTRACT:**

The rotational spectrum of 1-cyanocyclobutene from 130 to 360 GHz has been observed, assigned, and least-squares fit for the ground state and the two lowest-energy vibrationally excited states. Synthesis by UV photochemical dimerization of acrylonitrile and subsequent base-catalyzed dehydrocyanation affords a highly pure sample, yielding several thousand observable rotational transitions for this small organic nitrile. Over 2500 *a*-type, R-branch transitions of the ground state were least-squares fit to low-error with partial-octic A- and S-reduced Hamiltonians, providing precise determinations of the corresponding spectroscopic constants. In both reductions, computed spectroscopic constants are in close agreement with their experimentally determined counterparts. Two vibrationally excited states ($\nu_{27}$ and $\nu_{17}$) form a Coriolis-coupled dyad,

displaying many *a*-type and *b*-type local resonances and related nominal interstate transitions. Somewhat unexpectedly, despite the very small permanent *b*-axis dipole moment, a number of *b*-type transitions could be observed for the $\nu_{17}$ state; this is explained in terms of state mixing by the Coriolis perturbations. Over 2200 transitions for each of these states were least-squares fit to a low-error, two-state, partial-octic, A-reduced Hamiltonian with nine Coriolis-coupling terms ($G_a$, $G_a^J$, $G_a^K$, $G_a^{JJ}$, $F_{bc}$, $F_{bc}^K$, $G_b$, $G_b^J$, and $F_{ac}$). The availability of so many observed rotational transitions, including resonant transitions and nominal interstate transitions, enabled a very accurate and precise determination of the energy difference ($\Delta E_{27,17}$ = 14.0588093 (43) $cm^{-1}$) between $\nu_{27}$ and $\nu_{17}$. The spectroscopic constants presented herein provide a starting point for future astronomical searches for 1-cyanocyclobutene.

## INTRODUCTION

The interstellar medium (ISM) and circumstellar shells are known to contain complex and diverse chemical environments, with almost 250 molecules currently detected, including many new detections in the last few years.[1-2] Organic nitriles comprise an important subset of interstellar molecules because of their chemical relationship to molecules of prebiotic relevance, *e.g.*, pyridine. The cyano moiety is prevalent among organic species detected in the ISM because their typically large permanent dipole moments lead to a higher likelihood that molecules containing this functional group may be detected *via* radioastronomy, relative to other functionalities. The assignment of laboratory rotational spectra of organic nitriles is highly desirable to facilitate the detection of new molecules in the ISM. We have been interested in expanding two areas of organic nitrile assignments: aryl nitriles/isonitriles[3-6] and nitrile-containing isomers of pyridine.[7-10] The aryl nitriles/isonitriles are of interest as possible tracer molecules for molecular species, *e.g.*, benzene, pyridine, pyrimidine, pyrazine, and pyridazine. While pyridine, pyrimidine, and

pyridazine have permanent dipole moments, they have been sought unsuccessfully in the ISM,[11] The addition of the cyano substituent could be beneficial by significantly increasing the dipole moment, allowing the substituted species to serve as a tracer molecule for the parent species. Benzene and pyrazine do not have a permanent dipole; while the former has been detected by infrared spectroscopy, tracer molecules are necessary for their existence in the ISM to be inferred by radioastronomy. The recent detections of benzonitrile,[12] 1- and 2-cyanoaphthalene[13], and 1-cyano-1,3-cyclopentadiene[14] signify great advances utilizing this technique and strongly encourage further studies of the laboratory rotational spectra of nitrile-containing tracer molecules.

Nitrogen-containing isomers of pyridine ($C_5H_5N$) provide similar motivation as tracers of pyridine's presence in various environments. Importantly, the detection, or lack thereof, of particular $C_5H_5N$ isomers could help elucidate the reaction chemistry of small organic nitriles and/or pathways for formation of aromatic molecules such as pyridine. We recently investigated seven structural isomers of pyridine (including the present case) that are shown in Figure 2.1, several of which are proposed to be a part of complex, astrochemically relevant processes.[15-17] Two derivatives, *E*- and *Z*-1-cyano-1,3-butadiene (***E*-1**, ***Z*-1**) have recently been detected *via* laboratory rotational spectroscopy in various chemical environments.[18-19] Another 1,3-butadiene derivative, 2-cyano-1,3-butadiene (**3**), has been generated by UV irradiation of cyanoacetylene and ethylene.[20] In terms of potential relevance to astrochemistry, 1-cyanocyclobutene (**5**) has been generated by photolysis of 2-cyano-1,3-butadiene,[21] and the reverse transformation can be achieved by thermolysis.[22-23] Due to their proposed importance and recent detection in reactive environments, the astronomical search for these isomers seems warranted.

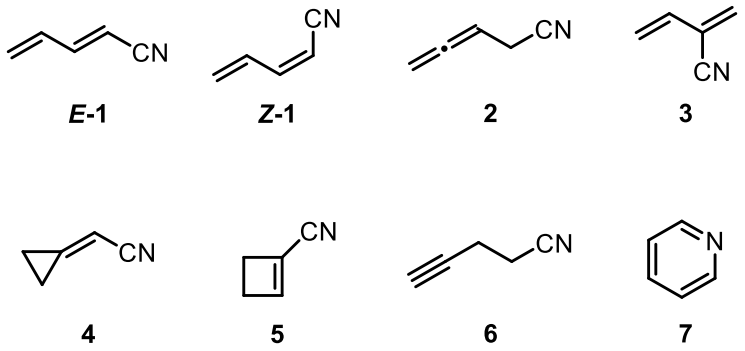


**Figure 2.1.** $C_5H_5N$ isomers that have been studied by rotational spectroscopy: (*E*)-1-cyano-1,3-butadiene (***E*-1**), (*Z*)-1-cyano-1,3-butadiene (***Z*-1**), 4-cyano-1,2-butadiene (**2**), 2-cyano-1,3-butadiene (**3**), (cyanomethylene)cyclopropane (**4**), 1-cyanocyclobutene (**5**), 4-cyano-1-butyne (**6**), and pyridine (**7**).

1-Cyanocyclobutene (**5**), the pyridine isomer presented in this work, has a planar, four-membered ring. The π bond within the ring enforces the planarity of the ring by greatly restricting the ability of the carbon atoms to move out-of-plane. Structurally similar, four-membered ring molecules with π-conjugated substituents have been studied by rotational spectroscopy, *e.g.*, β-propiolactone (**10**)[24-26] and diketene (**11**) (Figure 2.2).[27] Each of these species, like cyanocyclobutene, has a planar ring due to the presence of $sp^2$-hybridized carbon atoms in the ring or conjugation between ring atoms and substituents. Unlike the molecules mentioned above, rotational or vibrational spectra of 1-cyanocyclobutene (**5**) have not been reported in the literature. Cyanocyclobutane (**8**), due to its fully saturated ring, exhibits two non-planar conformers (−CN equatorial or axial), which have been well-studied by rotational and vibrational spectroscopy.[28-32] While the fully unsaturated cyanocyclobutadiene (**9**) has been generated and characterized under matrix-isolation conditions,[33] it has not been analyzed *via* gas-phase spectroscopy. Exploration of the spectroscopy and structures of these similar compounds allows meaningful comparisons to be made of these strained four-membered ring systems.

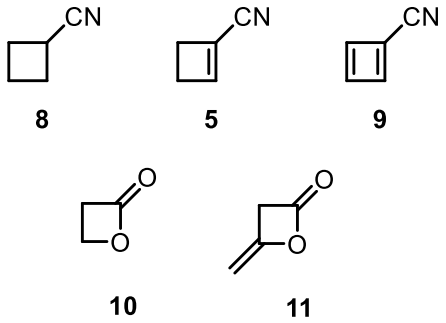


**Figure 2.2.** Structurally similar four-membered ring species: cyanocyclobutane (**8**), 1-cyanocyclobutene (**5**), cyano-1,3-cyclobutadiene (**9**), β-propiolactone (**10**), and diketene (**11**).

## EXPERIMENTAL AND THEORETICAL METHODS

### Synthesis

1-Cyanocyclobutene (**5**) has been prepared *via* a number of synthetic methods: photo-induced 4π electrocyclization from 2-cyano-1,3-butadiene (**3**),[21] ring expansion from 1-cyano-bicyclo[1.1.0]butane,[34] base-catalyzed elimination from 1-chloro-2-cyanocyclobutane[22, 35] or 1,2-dicyanocyclobutane,[22, 35] dehydration of 1-cyclobutene-1-carboxamide,[36] or photocatalyzed [2+2] cycloaddition of ethylene and cyanoacetylene.[37] To prepare a sample for analysis *via* rotational spectroscopy, the base-catalyzed elimination of 1,2-dicyanocyclobutane described by Gale and Cherkofsky[22] was utilized. By this route, 1-cyanocyclobutene (**5)** could be selectively obtained on multi-gram scale in a two-step synthesis starting from acrylonitrile and isolated from the 1,2-dicyanocyclobutanes by distillation. As shown in Scheme 2.1, acrylonitrile (**12**) was photo-dimerized to generate 1,2-dicyanocyclobutane (**13**) *via* a [2+2] cycloaddition in 66% yield using $Mo(CO)_6$ as a photosensitizer.[38] Depending on the reaction conditions, this dimerization can produce predominantly the *trans* stereoisomers of 1,2-dicyanocyclobutane[39] or a mixture (58:42) of *trans* and *cis* (1,2-dicyanocyclobutane) isomers.[40] As evidenced by the $^1$H NMR data provided in the Supporting Information, our reaction yielded an approximately a 1:1 mixture of the *trans* and *cis* diastereomers. Dehydrocyanation of the mixture of 1,2-dicyanocyclobutane isomers (**13**)

by passing through a heated quartz tube packed with Ascarite afforded the desired compound, 1-cyanocyclobutene (**5**) in 11% yield.

**Scheme 2.1. Syntheses of 1,2-Dicyanocyclobutane (13) and 1-Cyanocyclobutene (5).**

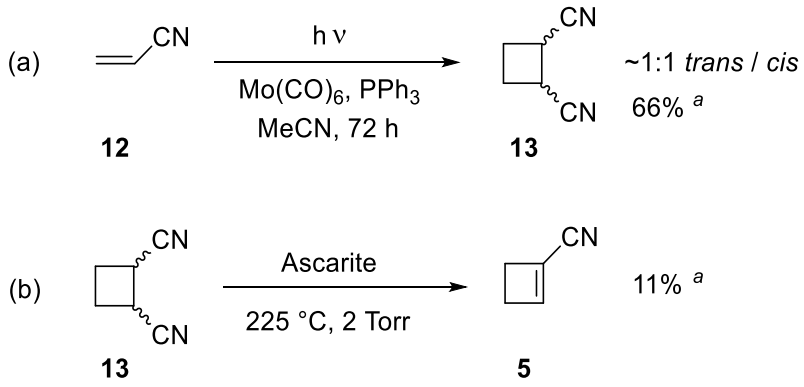


[a] Isolated yield

## Spectroscopy

Using a millimeter-wave spectrometer that has been previously described,[4, 41] the rotational spectrum of 1-cyanocyclobutene was collected from 130 to 230 GHz and from 235 to 360 GHz, in a continuous flow at room temperature, with a sample pressure of 4 mTorr. The separate spectral segments were combined into a single broadband spectrum using Kisiel's Assignment and Analysis of Broadband Spectra (AABS) software.[42-43] Pickett's SPFIT/SPCAT[44] was used for least-squares fits and spectral predictions, along with the PIFORM, PLANM, and AC programs for analysis.[45-46] A uniform frequency measurement uncertainty of 50 kHz was assumed for all measurements.

### Computational Analysis

Electronic structure calculations were carried out with Gaussian 16[47] using the WebMO[48] interface to obtain predicted values for various spectroscopic constants. Optimized geometries at the B3LYP/6-311+G(2d,p) and the MP2/6-311+G(2d,p) levels were obtained using "verytight" convergence criteria and an "ultrafine" integration grid, and subsequent anharmonic vibrational frequency calculations were carried out. Although the B3LYP predictions of the spectroscopic constants were adequate to begin the analysis, they did not have the expected agreement with the experimental spectroscopic constants. Thus, MP2 calculations were performed, and these had slightly closer agreement with the experimental constants. All computational output files can be found in the Supporting Information.

## RESULTS AND DISCUSSION

### Ground Vibrational State

1-Cyanocyclobutene (Figure 2.3) is a highly prolate, asymmetric top molecule ($\kappa = -0.94$) with a strong dipole moment along its *a*-principal axis ($\mu_a$ = 4.2 D, MP2) and much weaker *b*-component ($\mu_b$ = 0.07 D, MP2). The experimental spectrum from 130 – 360 GHz is dominated by ${}^{a}R_{0,1}$ transitions that appear in clearly observable bands sharing a single *J* value (Figure 2.4). In this frequency range, the (+) and (−) symmetry ${}^{a}R_{0,1}$ transitions are degenerate for the initial series, $K_a = 0^+$ and $K_a = 1^-$ but lose degeneracy at higher $K_a$. The (+) and (−) symmetry transitions become degenerate at different *J* values depending on the particular band. As the $K_a$ quantum number increases, transitions of the two symmetries attain $K_a$ degeneracy. The transitions in the series shown in Figure 2.4 become prolate ($K_a$) degenerate at $K_a$ = 10. This series continues to even lower frequency as the $K_a$ value increases until the transitions become too weak to be observed.

These bands are separated by approximately $B_0 + C_0$ (~ 4.5 GHz). Transitions for the singly substituted heavy isotopologues, $^{13}C$ and $^{15}N$, could not be detected at their natural abundance. We attribute this to the spectral density arising from the ground and vibrationally excited states of the main isotopologue. Thus, the work presented herein addresses only the analysis of the ground vibrational state and first two vibrationally excited states of the normal species.

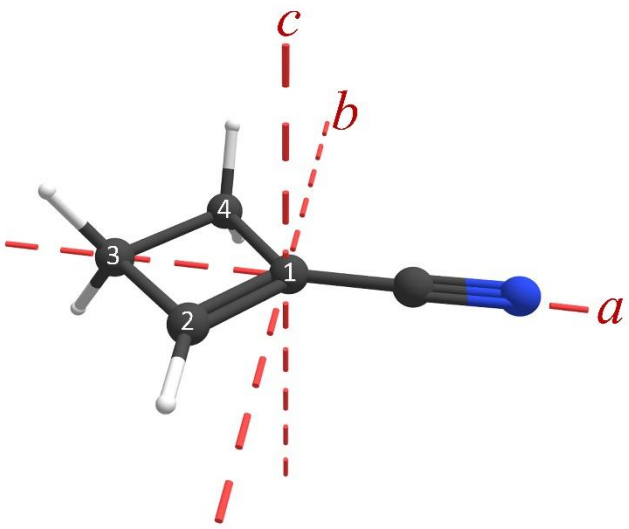


**Figure 2.3.** 1-Cyanocyclobutene (**5**, $C_s$, $C_5H_5N$) structure with principal inertial axes ($\mu_a$ = 4.2 D, $\mu_b$ = 0.07 D, MP2/6-311+G(2d,p)).

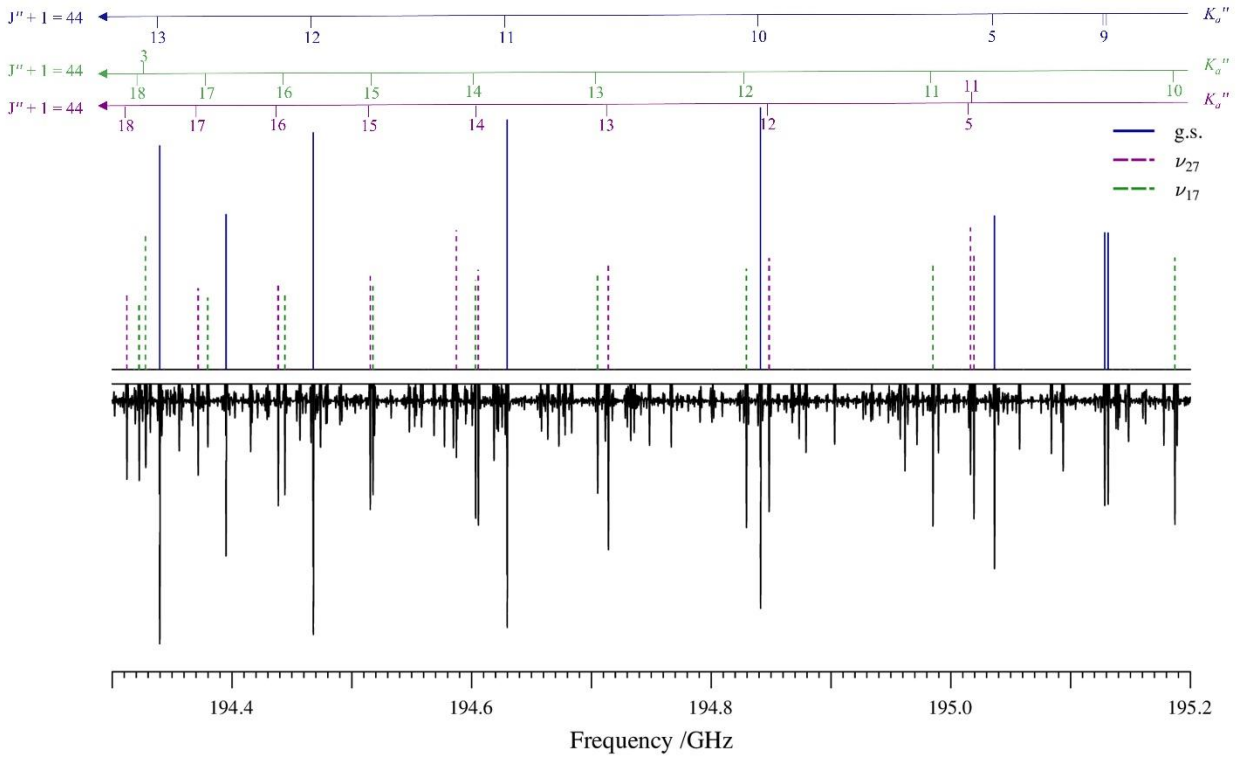


**Figure 2.4.** Predicted (top) and experimental (bottom) rotational spectra of 1-cyanocyclobutene (**5**) from 194.3 to 195.2 GHz. Ground-state transitions for the $J'' + 1 = 44$ band appear in dark blue, $\nu_{27}$ in purple, and $\nu_{17}$ in green. The complete frequency spectrum from 130 to 360 GHz was obtained automatically over approximately six days given these experimental parameters: 0.6 MHz/sec sweep rate, 10 ms time constant, and 50 kHz AM and 500 kHz FM modulation in a tone burst design.

Over 2500 transitions, represented in Figure 2.5, were measured and least-squares fit to partial-octic, distorted-rotor Hamiltonians in the $I^r$ representation for both the A ($\sigma_{fit} = 0.024$ MHz) and S reductions ($\sigma_{fit} = 0.024$ MHz). The resulting values of the spectroscopic constants are shown in Table 2.1, along with their computational counterparts. The computed rotational constants (MP2/6-311+G(2d,p)) are within 1% of the experimental values. Even with this relatively small difference, the predicted sum of $B_0 + C_0$ is approximately 37 MHz too small, which results in ${}^aR_{0,1}$ band locations off by 1.3 – 4.1 GHz with $J'' + 1$ ranging from 32 to 87. While line assignments inside these obvious bands are initially challenging from computational predictions, the R-branch $K_a = 0$ series, which are ouside of these bands and have spacing that mainly depends on $C_0$, were

the first targets for assignment. This series was readily identified *via* a Loomis-Wood plot and subsequent assignment and least-squares fitting was straightforward. The computed quartic centifugal distortion constants agree quite well with the experimental values, the largest discrepancies being in $\delta_J$ (5%) and in $d_2$ (6%) for the A- and S-reductions, respectively. Likewise, there is satisfactory agreement between the computed and experimental sextic distortion constants, with the largest discrepancies being in $\phi_J$ (32%) and in $h_3$ (9%) for the A and S reductions, respectively. The transitions included in the final data set were insufficient to satisfactorily determine the sextic constants $\Phi_K$, $H_\mathrm{k}$, or $h_1$. These constants were held at their computed values, in a manner similar to previous works where there were only *a*-type transitions across a similar range of *J* and *K* values.[4-5] Even with the inability to determine a complete set of sextic distortion constants, three octic centrifugal distortion constants, $L_{JJK}$, $L_{JK}$, and $L_{KKJ}$, were satisfactorily determined and their inclusion improved the $\sigma_{\mathrm{fit}}$. Presently, no commonly available computational software is able to predict octic centrifugal distortion constants, so the octic constants that were not determined were held at zero in the least-squares fit. This likely affects the reported octic distortion constants and somewhat reduces their physical meaningfulness compared to the well-determined quartic and sextic distortion constants.

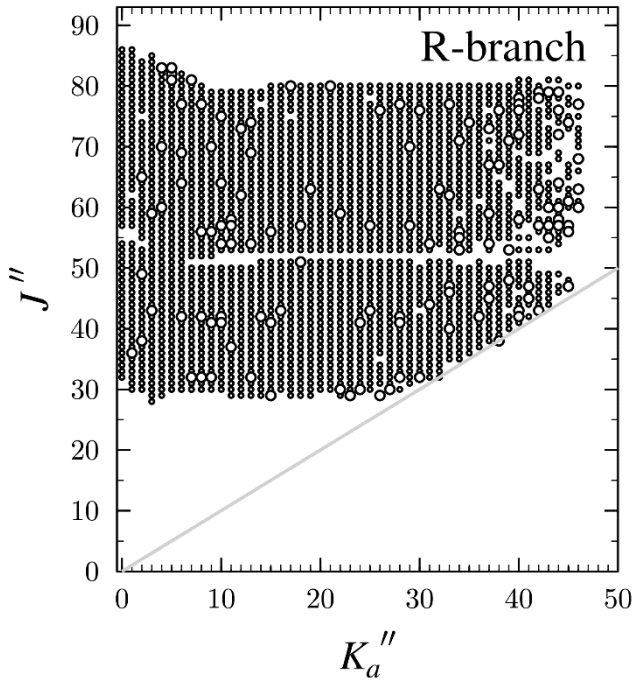


**Figure 2.5.** Data distribution plots for the least-squares fit of spectroscopic data for the vibrational ground state of 1-cyanocyclobutene (**5**). R-branch transitions are represented by black circles. The size of the symbol is proportional to the value of $|(f_{obs.} - f_{calc.})/\delta f|$, where $\delta f$ is the frequency measurement uncertainty, and all values are smaller than 3.

**Table 2.1. Spectroscopic Constants for the Ground Vibrational State of 1-Cyanocyclobutene (S- and A-reduced Hamiltonian, $I^r$ representation).**

| S Reduction, $I^r$ representation | | | A Reduction, $I^r$ representation | | |
|---|---|---|---|---|---|
| | Experimental | MP2 [a] | | Experimental | MP2 [a] |
| $A_0$ (MHz) | 12492.5719 (78) | 12418 | $A_0$ (MHz) | 12492.5807 (81) | 12418 |
| $B_0$ (MHz) | 2364.413212 (66) | 2344 | $B_0$ (MHz) | 2364.41929 (11) | 2344 |
| $C_0$ (MHz) | 2038.935375 (72) | 2022 | $C_0$ (MHz) | 2038.929419 (99) | 2022 |
| $D_J$ (kHz) | 0.112235 (11) | 0.108 | $\Delta_J$ (kHz) | 0.135307 (18) | 0.129 |
| $D_{JK}$ (kHz) | 5.513431 (92) | 5.39 | $\Delta_{JK}$ (kHz) | 5.37497 (12) | 5.26 |
| $D_K$ (kHz) | 3.046 (74) | 3.18 | $\Delta_K$ (kHz) | 3.252 (75) | 3.28 |
| $d_1$ (kHz) | −0.0204606 (23) | −0.0194 | $\delta_J$ (kHz) | 0.020490 (11) | 0.0194 |
| $d_2$ (kHz) | −0.0115338 (69) | −0.0108 | $\delta_K$ (kHz) | 2.9188 (18) | 2.80 |
| $H_J$ (Hz) | −0.00004395 (77) | −0.0000441 | $\Phi_J$ (Hz) | 0.0000146 (19) | 0.0000103 |
| $H_{JK}$ (Hz) | 0.011349 (15) | 0.0109 | $\Phi_{JK}$ (Hz) | 0.01604 (32) | 0.0155 |
| $H_{KJ}$ (Hz) | −0.070845 (85) | −0.0718 | $\Phi_{KJ}$ (Hz) | −0.0875 (11) | −0.0880 |
| $H_K$ (Hz) | [0.0710] | 0.071 | $\Phi_K$ (Hz) | [0.0825] | 0.0825 |
| $h_1$ (Hz) | [−0.000000621] | −0.000000621 | $\phi_J$ (Hz) | 0.00000622 (99) | 0.00000417 |
| $h_2$ (Hz) | 0.00002895 (78) | 0.0000272 | $\phi_{JK}$ (Hz) | 0.00802 (20) | 0.00774 |
| $h_3$ (Hz) | 0.00000527 (33) | 0.00000479 | $\phi_K$ (Hz) | 0.163 (14) | 0.165 |
| $L_{JJK}$ (μHz) | −0.0000326 (12) | | $L_{JJK}$ (μHz) | −0.0000387 (12) | |
| $L_{JK}$ (μHz) | 0.0004759 (53) | | $L_{JK}$ (μHz) | 0.000300 (16) | |
| $L_{KKJ}$ (μHz) | −0.005681 (28) | | $L_{KKJ}$ (μHz) | −0.005089 (57) | |
| $\Delta_i$ (uÅ$^2$) [b,c] | −6.334144 (27) | | $\Delta_i$ (uÅ$^2$) [b,c] | −6.332842 (31) | |
| $N_{\text{lines}}$ [d] | 2529 | | $N_{\text{lines}}$ [d] | 2529 | |
| $\sigma_{fit}$ (MHz) | 0.024 | | $\sigma_{fit}$ (MHz) | 0.024 | |

[a] Evaluated with the 6-311+G(2d,p) basis set. [b] Inertial defect, $\Delta_i = I_c - I_a - I_b$. [c] Calculated using PLANM from the $B_0$ constants. [d] Number of fitted transition frequencies

**Fundamental Vibrational States $\nu_{27}$ and $\nu_{17}$**

The vibrational energy manifold of 1-cyanocyclobutene below 550 $cm^{-1}$ (Figure 2.6) consists of the ground state and three sets of vibrationally excited states. The first set is a Coriolis-coupled dyad of the two lowest-energy vibrationally excited states ($\nu_{27}$ and $\nu_{17}$). The next-lowest energy set of vibrational states consists of a likely Coriolis-, Fermi-, and Darling-Dennison-coupled tetrad of the corresponding two-quanta vibrational states ($2\nu_{27}$, $\nu_{27}+\nu_{17}$ and $2\nu_{17}$) and fundamental $\nu_{26}$. Near 500 $cm^{-1}$, the three-quanta states of $\nu_{27}$ and $\nu_{17}$ form a complex polyad with $\nu_{27}+\nu_{26}$, $\nu_{17}+\nu_{26,}$ $\nu_{25}$, and $\nu_{16}$. While all of these states are sufficiently intense to be observed in the current spectral data, this work strictly focuses on the Coriolis-coupled dyad of $\nu_{27}$ and $\nu_{17}$ at *ca.* 165 $cm^{-1}$. The lowest-energy fundamental state, $\nu_{27}$ (A", 159 $cm^{-1}$), is an out-of-plane bend of the cyano

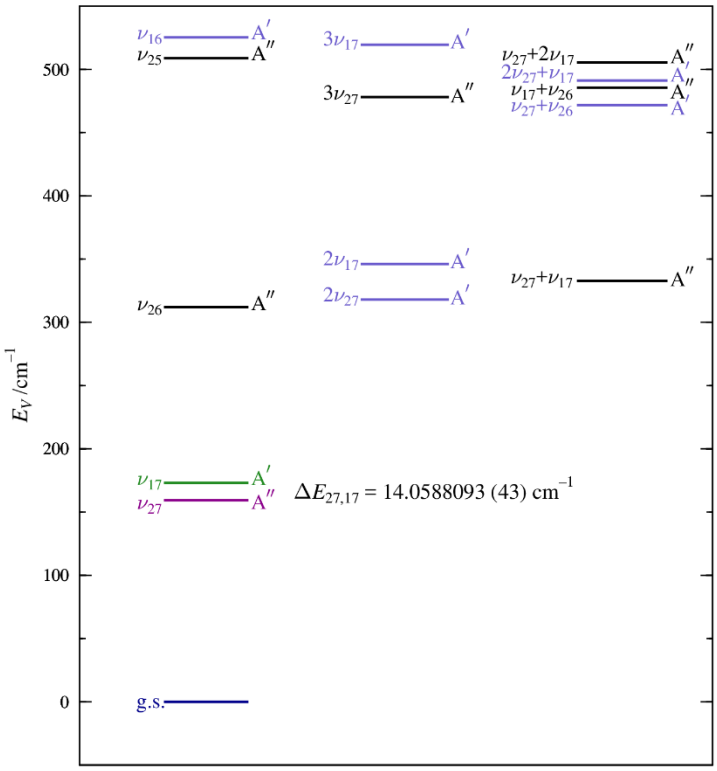


**Figure 2.6.** Vibrational energy levels of 1-cyanocyclobutene (**5**) below 550 cm$^{-1}$ from computed fundamental frequencies (MP2/6-311+G(2d,p)). The value of $\Delta E_{27,17}$ results from the experimental perturbation analysis of $\nu_{27}$ and $\nu_{17}$ in this work.

substituent, with a simultaneous distortion of the cyclobutene ring by a large motion of the C(3)$H_2$ group with respect to C(1). The second-lowest energy fundamental state, $\nu_{17}$ (A', 173 cm$^{-1}$), is an in-plane bend of the cyano substituent, combined with some in-plane distortion of the cyclobutene ring. The two lowest-energy vibrational states are expected to have strong interactions, due to the small predicted energy separation (14 cm$^{-1}$) and the combination of relatively large $A_v$ rotational constants, Coriolis $\zeta$ values, and $J$ values observed in this frequency range. As expected, a single-state model could not adequately predict or fit the transitions observed for either vibrationally excited state. Therefore, a two-state, partial-octic, A-reduced Hamiltonian was employed to model $\nu_{27}$ and $\nu_{17}$ in a manner similar to our previous work on (cyanomethylene)cyclopropane.[10] The least-squares fit incorporated at least 2200 transitions for each vibrationally excited state and had a low statistical error ($\sigma_{fit}$ = 0.031 MHz). The wide range of $J$ (28 to 87) and $K_a$ (0 to 46 and 43

for $\nu_{27}$ and $\nu_{17}$, respectively) quantum numbers recorded is illustrated in the data set distribution plot (Figure 2.7). This distribution of least-squares fit transitions is only slightly diminished in comparison to the vibrational ground state, due to the low energy (and thus high population) of these vibrationally excited states.

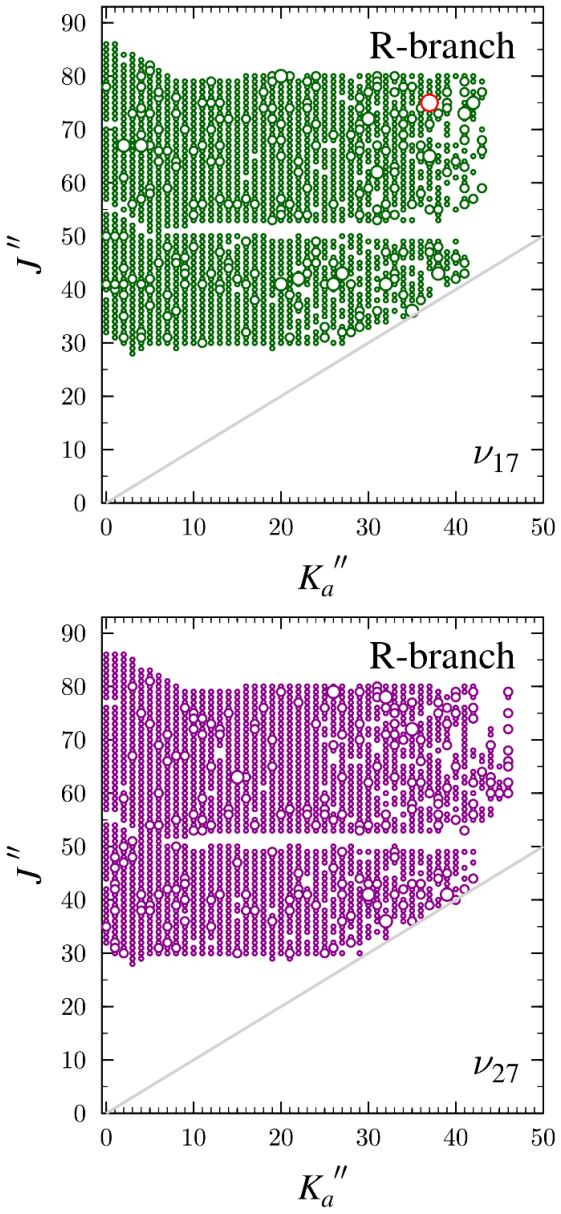


**Figure 2.7.** Data distribution plot for data in the two-state fit of $\nu_{27}$ and $\nu_{17}$ of 1-cyanocyclobutene (**5**). The size of the plotted symbol is proportional to the value of $|(f_{obs.} - f_{calc.})/\delta f|$, where $\delta f$ is frequency measurement uncertainty, and values greater than or equal to 3 are marked in red. Colored circles denote millimeter-wave data.

The spectroscopic constants resulting from the final least-squares fit (Table 2.2) include a precise determination of the rotational constants for each vibrational state. The rotational constants are well determined for each state, and the largest experimental uncertainty appears in the values of the $A_v$ constants, whose relative statistically uncertainty are only 0.003% of their values. The near-absence of *b*-type transitions (*vide infra*), due to the very small $\mu_b$ value, contributes to this diminished precision of $A_v$, as in the ground state. As has been shown for similar cases,[3-5, 49] the Coriolis-coupled dyad increases the uncertainty in the $A_v$ rotational constants somewhat, due to the high correlation between $A_v$ and the *a*-type Coriolis parameters. A full set of quartic distortion constants and a few ($\Phi_J$, $\Phi_{JK}$, and $\Phi_{KJ}$) sextic distortion constants were determined for each vibrational state. All distortion constants that could not be determined in the fit were held constant at their corresponding ground-state values. There are no clear signs of Coriolis coupling being absorbed by the quartic distortion constants, and all are within expected deviations from the ground state (< 10%, except $\Delta_K$ at 15% for $\nu_{27}$).

**Table 2.2. Spectroscopic Constants for Vibrationally Excited States $\nu_{27}$ and $\nu_{17}$ of 1-Cyanocyclobutene (5) (A-reduced Hamiltonian, $I^r$ representation).**

| | Ground State | $\nu_{27}$ (A", 159 $cm^{-1}$) [a,b] | $\nu_{17}$ (A', 173 $cm^{-1}$) [a,b] |
|---|---|---|---|
| $A_0$ (MHz) | 12492.5807 (81) | 12576.09 (31) | 12402.39 (31) |
| $B_0$ (MHz) | 2364.41929 (11) | 2367.99024 (40) | 2370.86901 (39) |
| $C_0$ (MHz) | 2038.929419 (99) | 2043.148392 (65) | 2041.224377 (62) |
| $\Delta_J$ (kHz) | 0.135307 (18) | 0.138684 (12) | 0.139633 (12) |
| $\Delta_{JK}$ (kHz) | 5.37497 (12) | 5.53104 (59) | 5.16909 (58) |
| $\Delta_K$ (kHz) | 3.252 (75) | 3.744 (25) | 3.233 (29) |
| $\delta_J$ (kHz) | 0.020490 (11) | 0.0205743 (24) | 0.0219861 (20) |
| $\delta_K$ (kHz) | 2.9188 (18) | 2.92104 (42) | 2.99398 (54) |
| $\Phi_J$ (Hz) | 0.0000146 (19) | 0.00002013 (98) | 0.0000183 (10) |
| $\Phi_{JK}$ (Hz) | 0.01604 (32) | 0.016545 (44) | 0.015331 (43) |
| $\Phi_{KJ}$ (Hz) | −0.0875 (11) | −0.10018 (25) | −0.06685 (23) |
| $\Phi_K$ (Hz) | [0.0825] | [0.0825] | [0.0825] |
| $\phi_J$ (Hz) | 0.00000622 (99) | [0.00000622] | [0.00000622] |
| $\phi_{JK}$ (Hz) | 0.00802 (20) | [0.00802] | [0.00802] |
| $\phi_K$ (Hz) | 0.163 (14) | [0.163] | [0.163] |
| $\Delta E$ | | 421472.50 (13) MHz / 14.0588093 (43) $cm^{-1}$ | |
| $G_a$ (MHz) | | 19993.0 (33) | |
| $G_a^J$ (MHz) | | −0.016787 (14) | |
| $G_a^K$ (MHz) | | −0.2226 (14) | |
| $G_a^{JJ}$ (MHz) | | 0.00000003739 (26) | |
| $F_{bc}$ (MHz) | | −0.1191 (29) | |
| $F_{bc}^K$ (MHz) | | −0.00010156 (99) | |
| $G_b$ (MHz) | | 97.09 (85) | |
| $G_b^J$ (MHz) | | −0.780 (57) | |
| $F_{ac}$ (MHz) | | −0.0004476 (74) | |
| $\Delta_i$ (u$Å^2$) [c,d] | −6.332842 (31) | −6.25371 (99) | −6.3242 (10) |
| $N_{lines}$ [e] | 2529 | 2300 | 2233 |
| $\sigma_{fit}$ (MHz) | 0.024 | 0.030 | 0.032 |

[a] Fundamental frequencies calculated using MP2/6-311+G(2d,p). [b] Octic centrifugal distortion constants not shown were held constant at their ground state values. [c] Inertial defect, $\Delta_i = I_c - I_a - I_b$. [d] Calculated using PLANM from the $B_0$ constants. [e] Number of fitted transition frequencies.

**Coriolis-Coupling Analysis**

The least-squares fit determines a precise energy separation ($\Delta E_{27,17}$ = 421472.50 (13) MHz; 14.0588093 (43) $cm^{-1}$) between $\nu_{27}$ and $\nu_{17}$. The computed energy difference (13.8 $cm^{-1}$; MP2) agrees very well with the experimentally determined value. The B3LYP computed value (17.9 $cm^{-1}$) is slightly overpredicted (*ca.* 5 $cm^{-1}$), as was the case in several similar works involving coupled dyads.[3-6,9] The high precision of the experimental value of $\Delta E_{27,17}$ arises because the data set includes all of the following: i) numerous rotational transitions involved in global interactions between the two fundamentals, ii) rotational transitions involved in local resonances occurring from energy-level crossings, and iii) (formally forbidden) interstate transitions that involve changes in both rotational and vibrational quantum numbers. The symmetries of the two fundamentals, $\nu_{27}$ (A", 159 $cm^{-1}$) and $\nu_{17}$ (A', 173 $cm^{-1}$), allow for both *a*- and *b*-type Coriolis coupling between the states. The final least-squares fit required incorporation of nine Coriolis-coupling terms ($G_a$, $G_a^J$, $G_a^K$, $G_a^{JJ}$, $F_{bc}$, $F_{bc}^K$, $G_b$, $G_b^J$, $F_{ac}$) to quantitatively account for both of these types of coupling across the observed spectrum.

The initial fitting process of the first several $K_a$ series for each vibrational state was accomplished by varying the energy separation and the $G_a$ value to account for, and adequately predict, the global undulation that is present for each series. This global undulation in Figure 2.8 appears to be small relative to the magnitude of the local resonances at higher $J$ and $K_a$. Figures 9 and 10, however, better illustrate the substantial impact of the global undulation on several $K_a$ series. The undulation is observed at low $J$ for low $K_a$ series and progresses higher in $J$ as $K_a$ increases until approximately $K_a$ = 20 for $\nu_{27}$ (lower for $\nu_{17}$) where the position of the global undulation has increased to $J$ values beyond the range investigated in this experiment. The values of $J$ for a particular $K_a$ at which the global undulation is most apparent are always those which

correspond to the changeover from oblate asymmetric top behavior at low *J* to prolate-like at high *J*. During fitting, if any local resonances were predicted in the $K_a$ series, transitions involved in the resonance, along with several transitions at lower and higher *J* values, were omitted from the fit until the global undulation was treated well. Once the global perturbation was well predicted, the local resonances could be more readily assigned. As more transitions were incorporated into the least-squares fit, additional coupling terms were needed to account for the complex interactions between the two fundamental states. During the fitting process, all centrifugal distortion constants were monitored for signs of absorbed Coriolis perturbation or unfavorable correlations between distortion and coupling constants. This iterative process allowed for a fully predictive fit to be achieved, which in turn makes it possible to perform a final frequency sweep measuring and recording every visible transition for each fundamental. Lastly, the nominal interstate transitions were measured and included in the least-squares fit in all cases where confident assignments could be made (*vide infra*).

Figure 2.8 illustrates the regularity of the *a*-type local resonances, which begin at $K_a = 4^-$ at $J = 48$ and subsequently increase in *J* by five until the end of the measured frequency range. As the local resonances progress to higher *J*, their magnitude increases with the largest resonance occurring at $K_a = 10^-$. This most displaced transition at $J = 78$ is approximately 9 GHz away from its unperturbed predicted position. A significant number of resonances (~ 40) were observed, with the majority being *a*-type resonances. The *a*-type resonances were also significantly larger in magnitude than *b*-type resonances, as can be seen in Figures 2.9 and 2.10.

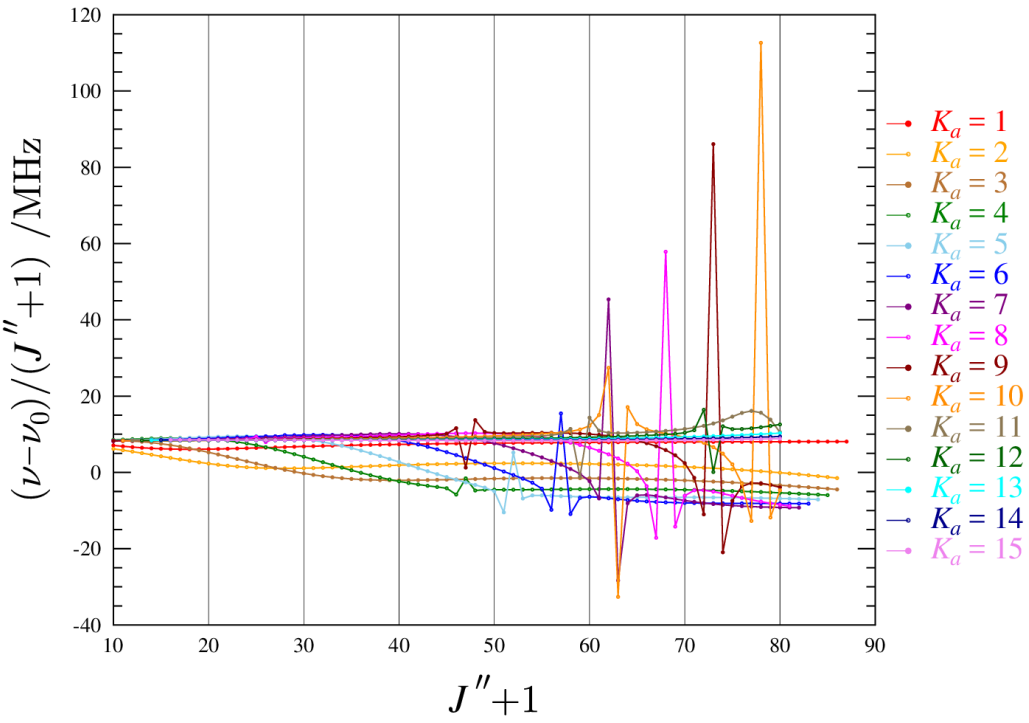


**Figure 2.8.** Superimposed resonance plots of $\nu_{27}$ for $^{a}R_{0,1}$ $K_a^-$ series from 1 to 15 for 1-cyanocyclobutene (**5**). Measured transitions are omitted for clarity, but they are indistinguishable from the plotted values on this scale. The plotted values are frequency differences between excited-state transitions and their ground-state counterparts, scaled by ($J''$ + 1).

A few *a*-type resonances are shown in Figure 2.9a; the $K_a = 1^-$ series of $\nu_{17}$ has two *a*-type resonances, at $J = 37$ and 47, with $\Delta K_a = 4$ and 2 selection rules, respectively. The paired resonance at $J = 37$ is in Figure 2.9c with the $K_a = 5^+$ ($\Delta K_a = 4$) series of $\nu_{27}$ and is obscured by the global undulation. The magnitude of the resonance and $J$ value are exactly the same in the two series, although the different scale factors in the plots make this more difficult to see in the figure. The second paired local resonance at $J = 47$ is shown in Figure 2.9b with the $K_a = 3^+$ ($\Delta K_a = 2$) series of $\nu_{27}$, and in this case the symmetry is more visually obvious. Figure 2.9d containing the $K_a = 3^-$ series of $\nu_{17}$ is included because it shows another paired resonance for the $K_a = 5^+$ series of $\nu_{27}$ at $J = 58$. The $K_a = 3^-$ series of $\nu_{17}$ has a second resonance at $J = 43$, which is paired with the $K_a = 7^+$ series of $\nu_{27}$ (not shown). An example of a *b*-type local resonance at $J = 72,73$ is shown in

Figure 2.10, between the $K_a = 9^+$ series of $\nu_{17}$ and the $K_a = 12^+$ series of $\nu_{27}$ ($\Delta K_a = 3$). The $\Delta K_a$ selection rule is always even for *a*-type and odd for *b*-type resonances; in addition, there is a change in symmetry for *a*-type and no change in symmetry for *b*-type coupling.

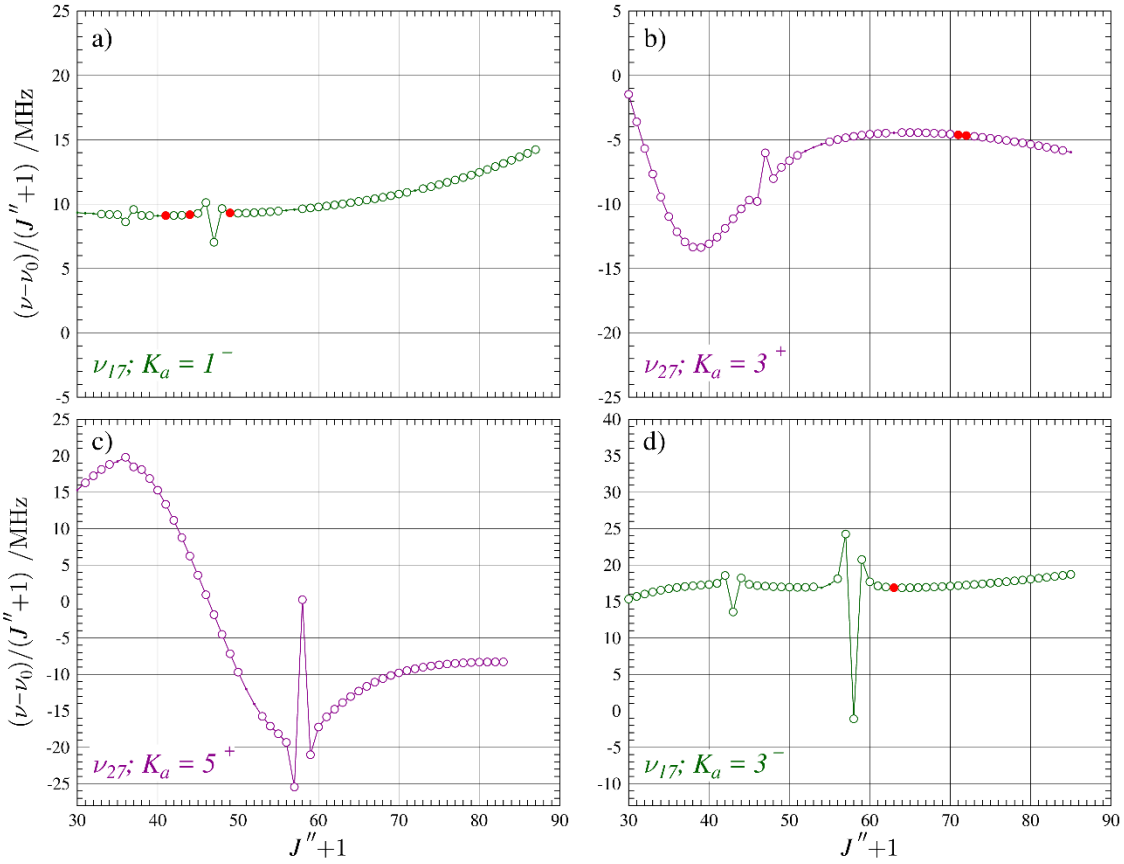


**Figure 2.9.** Resonance plots for 1-cyanocyclobutene (**5**) showing the $K_a = 1^-$ and $3^-$series for $\nu_{17}$ and $K_a = 3^+$ and $5^+$ series for $\nu_{27}$. These are examples of resonances conforming to the $\Delta K_a = 2$ or 4 selection rules for *a*-type resonances. The plotted values are frequency differences between excited-state transitions and their ground-state counterparts, scaled by ($J''$+1) in order to make the plots more horizontal. Measured transitions are represented by circles: $\nu_{27}$ (purple), $\nu_{17}$ (green). The measured transitions with $|(f_{obs.} - f_{calc.})/\delta f| > 3$ are marked in red. Predictions from the final coupled fit are represented by a solid, colored line.

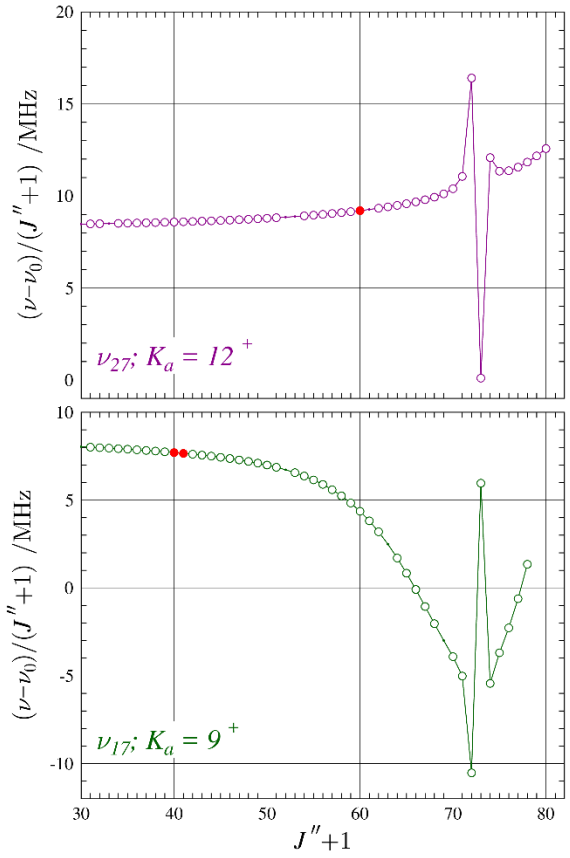


**Figure 2.10.** Resonance plots for 1-cyanocyclobutene (**5**) showing the $K_a = 9^+$ series for $\nu_{17}$ and $K_a = 12^+$ series for $\nu_{27}$. These two resonances conform to the $\Delta K_a = 3$ selection rule for *b*-type resonances. The plotted values are frequency differences between excited-state transitions and their ground-state counterparts, scaled by $(J''+1)$ in order to make the plots more horizontal. Measured transitions are represented by circles: $\nu_{27}$ (purple), $\nu_{17}$ (green). The measured transitions with $|(f_{obs.} - f_{calc.})/\delta f| > 3$ are marked in red. Predictions from the final coupled fit are represented by a solid, colored line.

An additional indication of unaddressed Coriolis coupling would be if the vibration-rotation interaction constants for $\nu_{27}$ and $\nu_{17}$ exhibit large, equal and opposite values. The $B_0 - B_v$ and $C_0 - C_v$ values presented in Table 2.3 are relatively small in magnitude, exhibit the same sign, and show excellent agreement between experiment and theory. These observations support the interpretation that these values are physically meaningful and that their corresponding rotational constants are well determined and likely free of residual Coriolis-coupling effects. The experimental and computational $A_0 - A_v$ values are in quite poor agreement and are much larger in

magnitude than the $B_0 - B_v$ or $C_0 - C_v$ values for each vibrational state. It is unclear to what extent these large values of $A_0 - A_v$ and the disagreement between their theoretical and experimental values are caused by residual unaddressed Coriolis coupling or by poorly estimated $A_0 - A_v$ values. A similar observation was made for the $A_0 - A_v$ values in the analogous Coriolis-coupled dyad of (cyanomethylene)cyclopropane.[10] While the discrepancy is larger for 1-cyanocyclobutene (**5**), for both molecules, the computed values for these interactions are of opposite sign than the fitted ones. Given the close agreement in the averages of these values, at least some untreated coupling must be manifest in either or both the experimental and theoretical values. The very large data sets and the overall quality of the least-squares fits, however, make it possible that $A_{27}$ and $A_{17}$ are close to their true values, despite the discrepancy with the theoretical calculations.

**Table 2.3. Vibration-rotation interaction and Coriolis-coupling constants of 1-cyanocyclobutene (5).**

| | Experimental | B3LYP [a] | MP2 [a] |
|---|---|---|---|
| $A_0 - A_{27}$ (MHz) | −83.41 (31) | 17.8 | 17.4 |
| $B_0 - B_{27}$ (MHz) | −3.57095 (41) | −3.42 | −3.25 |
| $C_0 - C_{27}$ (MHz) | −4.21897 (12) | −4.07 | −3.94 |
| $A_0 - A_{17}$ (MHz) | 90.19 (31) | −11.1 | −7.26 |
| $B_0 - B_{17}$ (MHz) | −6.44972 (41) | −6.11 | −6.29 |
| $C_0 - C_{17}$ (MHz) | −2.29495 (12) | −2.14 | −2.26 |
| $\frac{(A_0-A_{27})+(A_0-A_{17})}{2}$ (MHz) | 3.38 (22) | 3.36 | 5.05 |
| $\frac{(B_0-B_{27})+(B_0-B_{17})}{2}$ (MHz) | −5.01033 (29) | −4.77 | −4.77 |
| $\frac{(C_0-C_{27})+(C_0-C_{17})}{2}$ (MHz) | −3.256965 (83) | −3.10 | −3.10 |
| $\zeta^a_{27,17}$ | 0.807 | 0.751 | 0.744 |
| $\zeta^b_{27,17}$ | 0.021 | 0.027 | 0.0227 |

[a] Evaluated with the 6-311+G(2d,p) basis set.

The lowest-order spectroscopic Coriolis coupling parameters, $G_a$ and $G_b$ can be predicted, given the Coriolis constant ζ, by eq. (1).

$$G_x = \frac{\omega_{27} + \omega_{17}}{\sqrt{\omega_{27} \times \omega_{17}}} \zeta^x_{27,17} B^x_e \approx 2\zeta^x_{27,17} B^x_e \quad (1)$$

The experimental ζ values in Table 2.3 were calculated from eq. (1) using harmonic frequencies computed by MP2, the experimentally determined $G_x$, and rotational constants corrected by half the sum of the corresponding MP2 vibration-rotation interaction constants for all vibrations. The experimental value of $\zeta^a_{27,17}$ is slightly greater than the computational predictions, while the experimental value of $\zeta^b_{27,17}$ is smaller by a similar magnitude.

The observed resonances are a result of state mixing between $\nu_{27}$ and $\nu_{17}$. This state mixing can result in interstate transitions, where simultaneous changes in rotational and vibrational quantum numbers occur. The energy separation in the Coriolis-coupled dyad, $\nu_{27}$ and $\nu_{17}$, (14.0588093 (43) $cm^{-1}$) is small enough to cause intense local resonances and state mixing, and this allowed a significant number (57) of nominal interstate transitions to be assigned. These transitions were assigned by comparison of the experimental and predicted frequencies, as well as by comparison of the observed average frequencies, which should ideally be exactly the same for matched sets of corresponding inter- and intrastate transitions. Two nominal interstate transitions, along with their corresponding intrastate transitions, are shown in Figure 2.11. Each measured transition includes its *obs.* – *calc.* value in parentheses. The average frequencies of the inter- and intrastate transitions shown in Figure 2.11 differ by only 62 kHz, illustrating the accuracy of the measurements and the correctness of the assignments. The corresponding intrastate resonances ($J''$ + 1 = 73) from the $K_a = 9^-$ series of $\nu_{27}$ and the $K_a = 5^+$ series of $\nu_{17}$ are displayed in Figure 2.11 to illustrate the resonances and observable interstate transitions occur at the same $J$ values, as a result of significant state mixing. For example, the smallest energy separation, $\Delta E$ = 8984 MHz,

occurs between $73_{9,65}$ for $\nu_{27}$ and $73_{5,68}$ for $\nu_{17}$, which corresponds to the intrastate transitions most shifted in frequency for each vibrational state.

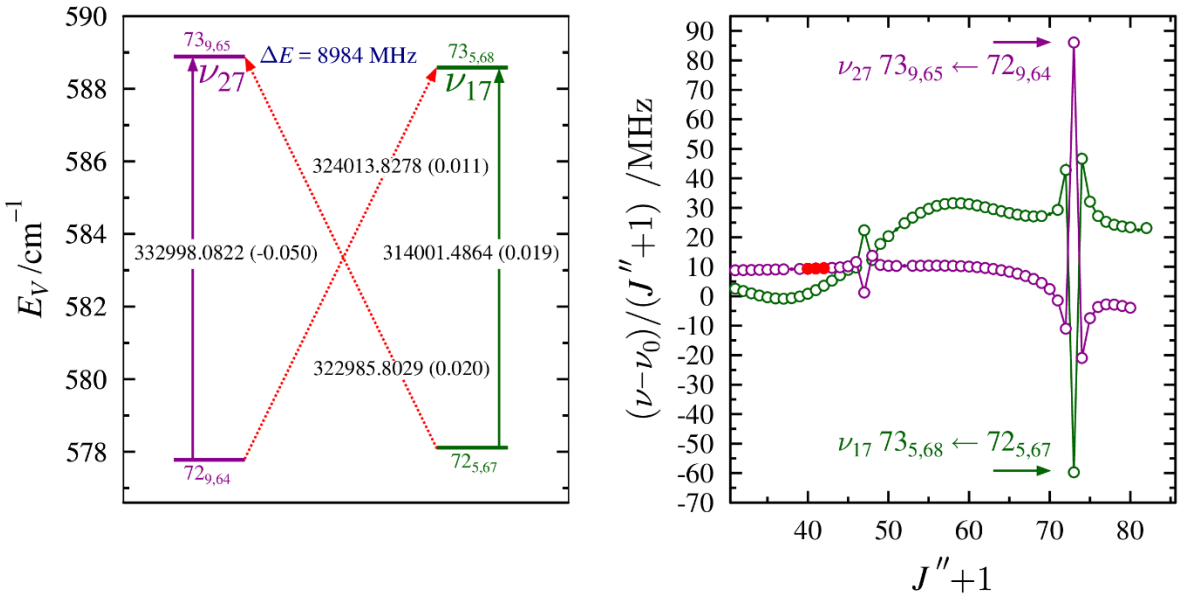


**Figure 2.11.** Energy diagram (left) depicting a representative matched pair of nominal interstate transitions between the $\nu_{27}$ (purple) and $\nu_{17}$ (green) vibrational states of 1-cyanocyclobutene (**5**). Standard $^aR_{0,1}$ transitions within vibrational states are denoted by vertical arrows. The diagonal, dashed arrows indicate nominal interstate transitions that are formally forbidden, but enabled as a result of rotational energy level mixing. Values printed on each of the arrows are the corresponding transition frequency (in MHz) with its *obs.* – *calc.* value in parentheses. The marked energy separation is between the two strongly interacting rotational energy levels. Resonance plots (right) of the $K_a$ series of $\nu_{27}$ and $\nu_{17}$ that contain the corresponding resonant transitions labeled with their quantum numbers and marked by colored arrows.

A rarely reported type of intensity enhancement by state mixing has been found in this spectrum. 1-Cyanocyclobutene has a quite small *b*-type dipole moment ($\mu_a$ = 4.2 D, $\mu_b$ = 0.07 D, MP2), which prevented observation of any *b*-type transitions in the ground state or in $\nu_{27}$. Due to the Coriolis-coupling between $\nu_{27}$ and $\nu_{17}$, however, indirect state mixing enhances the intensity of approximately 35 *b*-type transitions for $\nu_{17}$ sufficiently that they become measurable and are included in the least-squares fit of the coupled dyad. As exemplified in the Loomis-Wood plot in Figure 2.12, many of these intense *b*-type transitions occur near the *J*-levels where degeneracy of

the ${}^{a}R_{0,1}$ $K_a^+$ and $K_a^-$ series is established, and also near, but not necessarily exactly coincident with, $J$ values where local resonances are observed between the two vibrational states. In most $K_a^+/K_a^-$ series for $\nu_{17}$, the rigid-rotor asymmetry splitting results in only the expected doublet at low $J$ values. In the case of the $K_a^+/K_a^-$ = 1 and 2 series shown, however, the two transitions involving the $J$ = 48 level both exhibit the formation of a quartet that includes observably intense *b*-type transitions. At lower $J$-levels, the *b*-type transitions disappear, and the series progresses with the expected doublet pattern. Due to strong, local perturbation, transitions in the $J'' + 1 = 50 – 53$ range are non-degenerate, but do not exhibit a clear doublet structure. The $K_a^+/K_a^-$ = 1 and 2 series become degenerate after the resonances at $J'' + 1 = 57$. These *b*-type transitions are allowed, to a negligible extent, due to the small *b*-type dipole moment component. They are much more intense, however, due to intensity borrowing from *a*-type transitions with the same $J$ values. Although the closest relevant resonance with $\nu_{27}$ is at $J$ = 51, this is still a $J$ region of significant state mixing with $\nu_{27}$, which has the effect of perturbing the energy levels of $\nu_{17}$. The perturbation causes two of the $\nu_{17}$ energy levels to cross at or near the $J$ value where the observed *b*-type transitions are most intense. In some of the observed cases, the mixing is sufficiently strong that SPFIT and SPCAT reverse the label of the mixed energy levels, resulting in an apparent exchange of the *a*-type and *b*-type identification of the transitions in the quartet. An example of that can be seen in the $J$ = 48 to 49 transitions in Figure 2.12, where SPFIT and SPCAT misidentified the *a*- and *b*-type transitions. As a result, this frequency segment in the Loomis-Wood plot has been manually shifted by ~ 3 MHz to visually align all (lower frequency) *a*-type transitions for clarity. In an extreme case of intensity borrowing, $J'' + 1 = 81$ for $K_a^+/K_a^-$ = 5 and 6 transitions, almost all of the intensity is transferred from the *a*-type to *b*-type transitions. In all cases, SPCAT does accurately reproduce the observed pattern of the quartet, including the relative intensities. A

summary listing of all *b*-type transitions included in the least-squares fit is provided in the Supporting Information.

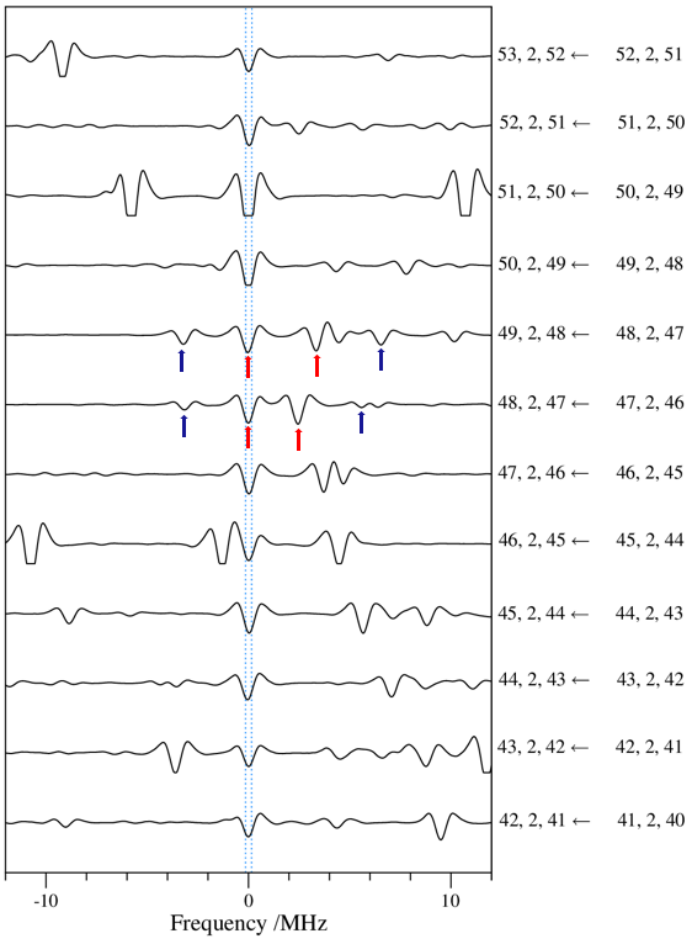


**Figure 2.12.** Loomis-Wood plot centered on $K_a = 2^-$ series for $\nu_{17}$ ranging in $J'' + 1 = 42$ to 53. The $K_a = 1^+$ can be seen higher in frequency below $J'' + 1 = 47$ in a typical doublet pattern progressing further away in frequency as $J'' + 1$ decreases. A quartet of *a*-type (red) and *b*-type (blue) transitions is then observed for $J'' + 1 = 48$ and 49. The Loomis-Wood frequency segment corresponding to $J'' + 1 = 49$ was shifted lower in frequency by 3 MHz for this figure due to the SPCAT misassignment of the *a*- and *b*-type transitions.

There are several important clues to the quantum mechanical origin of the intensity enhancement of the nominally *b*-type transitions. First, this quartet phenomenon requires having both *a*- and *b*-type Coriolis coupling between $\nu_{27}$ and $\nu_{17}$, which is easily confirmed by setting the *b*-type Coriolis parameters to zero in SPCAT, in which case the predicted intensities of the lines

in question are not greater than they are in the ground state spectrum, *i.e*., negligible. Second, unlike the local resonances observed between states, the enhancement effect is not present in the spectra of both vibrational levels; it is present only in $\nu_{17}$ (to be explained below). Finally, the frequency splittings of the quartets and the intensities of the "*b*-type" peaks are both highly dependent upon the energy-level splittings of the two near-degenerate rotational levels in $\nu_{17}$ and on the distance of these two levels from the Coriolis-connected rotational levels in $\nu_{27}$, although not in a simply recognizable way. All these observations can be clearly understood by consideration of the diagonalization of the two-state Hamiltonian matrix for the *J* involved, focusing on the three or four vib-rotational levels of most interest. Figure 2.13 shows an example of four vib-rotational levels, where the $48_{1,47}$ and $48_{2,47}$ energy levels for $\nu_{17}$ are connected to the $48_{5,44}$ and $48_{4,44}$ energy levels, respectively for $\nu_{27}$ through *a*-type Coriolis coupling. These $\nu_{17}$ energy levels are also connected to the other two rotational energy levels ($48_{1,47}$ to $48_{4,44}$ and $48_{2,47}$ to $48_{5,44}$) through *b*-type coupling (to a lesser extent). This double coupling in the matrix allows the $48_{1,47}$ and $48_{2,47}$ energy levels to indirectly mix with each other. The degree of this mixing is normally small, but it is greatly amplified when the two levels are very close to each other, *i.e*., near-degenerate, ultimately leading to the *b*-type transitions we have observed. In general, two connecting states in $\nu_{27}$, *e.g*., both $48_{5,44}$ and $48_{4,44}$ in the above instance, are not required for this effect, and cases of only one rotational energy level of $\nu_{27}$ interacting strongly with the two near-degenerate energy levels of $\nu_{17}$ are observed here. At first glance, one would suspect, from the symmetry of the interaction and the quantum number types involved, that the same phenomenon could be observed in $\nu_{27}$. It must be remembered, however, that because $\nu_{27}$ has the lower vibrational energy, its resonances must always have the higher $K_a$ value. The higher $K_a$ value implies a greater oblate asymmetry (lower $K_c$) at any particular *J* value, which in turn yields much

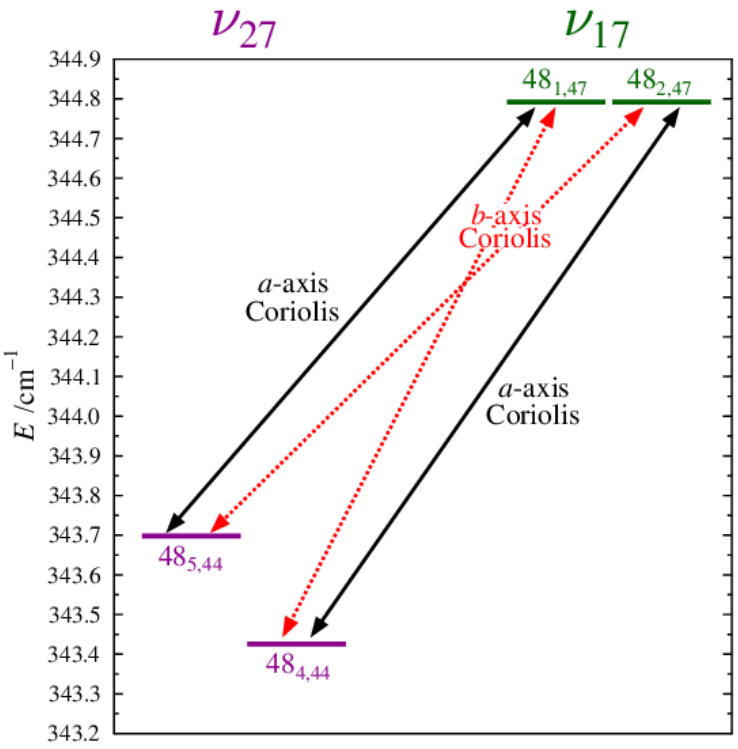


**Figure 2.13**. Four-state vib-rotational energy level diagram showing the states involved in creating an observable quartet in the $K_a^+/K_a^- = 1$ and 2 series. The red and black arrows indicate the *b*- and *a*-axis Coriolis interactions, respectively, that allow for state mixing between states.

larger asymmetry splittings. This renders the indirect mixing of the two rotational states in $\nu_{27}$ inconsequential. An interesting aspect of the "*b*-type" intensities predicted by SPCAT is that they do, in fact, depend on the value of $\mu_b$ to a noticeable extent (about 10% when going from 0 D to 0.07 D). This behavior is understood by considering that the intensities are proportional to the absolute square of a sum of (large) $\mu_a$ and (small) $\mu_b$ matrix elements. Thus, the cross term is more substantial than the square of the $\mu_b$ term (which leads to negligible intensity by itself) and does produce significant increases or decreases in predicted intensity. This example of a quantum interference effect may well be more important in other molecules with a somewhat larger $\mu_b$. Meanwhile, this phenomenon is not possible in a molecule where the second dipole component is *exactly* zero, since the molecular symmetry that causes it will also mean that only one type of

Coriolis coupling is allowed between any two vibrational states. Of course, if both dipole moment components are comparable in magnitude, the effects of the indirect coupling may not even be noticed.

Higher up the vibrational manifold, at approximately 330 $cm^{-1}$, the two-quanta vibrational states of $\nu_{27}$ (A″) and $\nu_{17}$ (A′) form a coupled tetrad with $\nu_{26}$. This tetrad is expected to be well-isolated from other vibrationally excited states and of sufficient intensity that the rotational spectra of all four states can be measured, assigned, and least-squares fit, using the spectral data we have already acquired. Despite the complicating interaction with $\nu_{26}$ (A″), this tetrad could be addressed using the same general methodology recently employed with benzonitrile, where the triad consisting of the overtones and simple combination of the two lowest-lying states were analyzed very successfully.[50] In that study, the harmonic and anharmonic vibrational constants for the states involved were well predicted by the *xguinea* routine of CFOUR, as was the Darling-Dennison coupling term connecting the two overtone states. Furthermore, it was found that the higher-order Coriolis coupling coefficients, *e.g.*, $G_a^J$ or $F_{bc}$, for the triad scaled rather closely as a factor of $\sqrt{2}$ from the corresponding ones of the dyad. Equivalent predictions and scaling for 1-cyanocyclobutene should greatly expedite assignment of the tetrad, and a successful fit would provide a further test of the accuracy of the predicted and scaled parameters. The $\nu_{26}$ fundamental should be coupled by anharmonic resonance to the combination state and by higher-order Coriolis interactions to all three triad states. Acquisition and analysis of the modestly strong $\nu_{17}$ band, its two hot bands, and possibly the weaker $\nu_{27}$ and $\nu_{26}$ bands, by high-resolution infrared spectroscopy, and a successful perturbation analysis of the tetrad, in addition to the results of this study, could potentially provide highly accurate absolute vibrational energies of the lowest six excited vibrational levels of 1-cyanocyclobutene.

## CONCLUSION

The ground-state spectroscopic constants of 1-cyanocyclobutene (**5**) from this work should provide an excellent foundation for predicting frequencies for an astronomical search, even for transitions well outside the range explored here. In the lower microwave region and for the lower *J* transitions most often used in radioastronomy, these predictions would require inclusion of the effects of nuclear hyperfine structure. The needed quadrupole coupling constants can be well estimated computationally, or they could be much better determined by measuring and analyzing a few resolved hyperfine multiplets for low *J* transitions occurring in the lower microwave region. Unlike several other $C_5H_5N$ isomers,[8] the ground state of 1-cyanocyclobutene (**5**) is well fit by a single-state Hamiltonian model, so the present centrifugal distortion analysis should provide accurate frequency estimates well above the current range. The accuracy is of course expected to degrade gradually as one encounters quantum number values further removed from those sampled in this study.

The experimentally well-determined higher-order Coriolis coupling parameters for interacting fundamental states in 1-cyanocyclobutene (**5**) contribute to a steadily growing list of organic molecules that have been analyzed in this level of detail. A similar statement can be made about the quartic centrifugal distortion constants for the two vibrationally excited states. Neither these higher-order Coriolis constants, nor the changes between the ground state and vibrationally excited-state centrifugal distortion constants, however, can be meaningfully estimated *via* any readily available computational software package. A practical computational approach to obtaining these constants thus remains a pressing challenge for theory. Not only would such computed values serve as a measure of quality for a least-squares fit, they would likely improve the initial predictions of excited-state rotational spectra and thereby facilitate the early stage of the

fitting process. Incorporation of these computed values in the least-squares fit for all constants that could not be adequately determined should also improve the accuracy of those constants that can be varied and fit.

**General Experimental Methods**

All commercial reagents were purchased from Sigma-Aldrich or Oakwood Chemical and used as received, unless otherwise noted. $^{1}$H NMR spectra (400 or 500 MHz) and $^{13}$C-NMR spectra (100 or 125 MHz) were obtained in $CDCl_3$ on a Bruker 400 MHz AVANCE III or Bruker 500 MHz DCH AVANCE III spectrometer; chemical shifts (δ) are reported as ppm downfield from internal standard $SiMe_4$ or referenced to residual solvent signals. Mass spectra were acquired using electrospray ionization (ESI) or the atmospheric solids analysis probe (ASAP) on a Thermo Scientific Q-Exactive Plus mass spectrometer. GC/MS analysis was performed on a Shimadzu GCMS-2010S instrument. IR spectra were obtained on a Bruker TENSOR Fourier transform infrared instrument as neat samples using an attenuated total reflectance accessory (Bruker PLATINUM ATR).

**Mixture of *trans*- and *cis*-1,2-Dicyanocyclobutane (13)**

***Note:*** *Exposure of the reaction mixture to short-wavelength UV-C (254 nm) is critical, and necessitates the use of a quartz reaction vessel or immersion probe.*

Photolyses were carried out in an immersion-type quartz photochemical reactor (Ace Glass # 7861-250) having an inner annular volume of 500 mL and equipped with a magnetic stirrer. Into the water-cooled quartz immersion probe was inserted a centrally positioned 450 W medium-pressure mercury arc lamp (Hanovia # 679A36, 122 mm arc length). The quartz lamp chamber was continuously purged with a slow, steady stream of dry $N_2$ to prevent ozone generation/damage

during lamp operation. Molybdenum hexacarbonyl ($Mo(CO)_6$, 5.43 g, 20.6 mmol), triphenylphosphine ($PPh_3$, 5.42 g, 20.7 mmol), hydroquinone (350 mg, 3.2 mmol), acrylonitrile (195 mL, 160 g, 3 mol), and acetonitrile (143 mL) were added to the annular reactor compartment and stirred until most of the solids were dissolved. The reaction mixture was purged under a steady stream of dry $N_2$ for 5 min. The reactor vessel was then maintained under a nitrogen atmosphere. With the immersion probe coolant flowing, the lamp was ignited, and the temperature of the stirred reaction was maintained at 55-60 ºC by the heat of the mercury lamp throughout the course of the photolysis. Any remaining undissolved reactants dissolved within minutes of igniting the lamp as the reaction temperature increased. The reaction progress was monitored *via* $^1$H-NMR over the 72-h photolysis. After the irradiation time had elapsed, the photolysis was halted, and the reaction vessel was cooled to room temperature. The amber-colored reactor contents were filtered through a coarse glass-fritted funnel and concentrated *in vacuo* to remove acetonitrile and acrylonitrile. The resulting deep-red oil was purified *via* short-path vacuum distillation to afford a mixture of 1,2-dicyanocyclobutane stereoisomers (**13**) as a viscous amber oil that solidified upon cooling to room temperature (14.6 g, 76%, bp = 110–125 ºC at 2 Torr). $^1$H-NMR ($CDCl_3$, 500 MHz): $\delta$ (ppm) 3.42 - 3.60 (m, 2H), 2.42 – 2.62 (m, 4H). *trans:* $^{13}C\{^1H\}$-NMR ($CDCl_3$, 125 MHz): $\delta$ (ppm) 118.6, 26.6, 24.8. *cis*: $^{13}C\{^1H\}$-NMR ($CDCl_3$, 125 MHz): $\delta$ (ppm) 118.3, 26.7, 24.8. IR (neat): ($cm^{-1}$) 2969 (m), 2242 (s), 1444 (m), 1244 (w), 1205 (m), 751 (w), 492 (w). HRMS (ASAP-MS) *m/z*: $[M+H]^+$ Calcd for $C_6H_7N_2$: 107.0604. Found: 107.0604.

**1-Cyanocyclobutene (5)**

A vertical quartz tube 50 cm long and 2.5 cm in diameter, packed 20 cm of its length with Ascarite (Aldrich, 20-30 mesh) was heated in a 40 cm long cylindrical tube furnace to 200 ºC for 2 h under a steady stream of dry $N_2$ to remove water or absorbed gases from the Ascarite bed. A stoppered

pressure-equalizing dropping funnel containing 1,2-dicyanocyclobutane (**13**, 9.95 g, 92 mmol) was connected to the top of the quartz reactor tube and the bottom was connected to a vacuum manifold thru a series of three dry ice/acetone cooled traps. The temperature of the tube furnace was set to 225 ºC, and the system was evacuated to a pressure of 500 mTorr. The dropping funnel at the top of the reactor was lightly heated with a heat gun until the 1,2-dicyanocyclobutane was thoroughly melted and degassed. The 1,2-dicyanocyclobutane melt was added dropwise to the heated reaction tube. The rate of addition was sufficient to maintain an internal pressure below 2 Torr. The complete dropwise delivery of molten **13** to the heated reactor bed was achieved over a course of 2 h. A total of 1.56 grams of hazy, colorless liquid was recovered from the traps after the addition of **13** was completed. The collected distillate was cooled to 0 ºC on ice and allowed to separate. The clear organic supernatant layer was separated and dried over granular anhydrous $Na_2SO_4$ to yield 1-cyanocyclobutene (**5**) as a colorless oil (834 mg, 11%). $^1$H-NMR ($CDCl_3$, 500 MHz): $\delta$ (ppm) 6.78 (t, $J$ = 1.4 Hz, 1H), 2.84 (dd, $J$ = 3.4 Hz, 2H), 2.63 (ddd, $J$ = 3.4 Hz, 3.2 Hz, 1.4 Hz, 2H) $^{13}$C{$^1$H}-NMR ($CDCl_3$, 125 MHz): $\delta$ (ppm) 153.0, 117.2, 113.9, 32.4, 30.3. IR (neat): ($cm^{-1}$) 2978 (w), 2937 (m), 2835 (w), 2218 (m), 1584 (w), 1425 (w), 1252 (m), 1213 (w), 1162 (w), 1073 (w), 936 (w), 910 (m), 867 (m), 757 (m), 684 (w), 584 (w), 516 (s). HRMS (ASAP-MS) *m/z*: $[M+H]^+$ Calcd for $C_5H_6N$: 80.0495. Found: 80.0494.

## ASSOCIATED CONTENT

### Supporting Information

The Supporting Information is available free of charge at https://pubs.acs.org/doi/10.1021/acs.jpca.2c00384.

Table of *b*-type transitions observed in $\nu_{17}$ paired with the corresponding *a*-type transitions; experimental IR, $^{1}$H NMR, $^{13}$C NMR, and mass spectra of all compounds (PDF)

Computational chemistry output files, least-squares fitting output files from SPFIT (ZIP)

## AUTHOR INFORMATION


### Corresponding Authors

**Robert J. McMahon** – *Department of Chemistry, University of Wisconsin–Madison, Madison, Wisconsin 53706, United States*; orcid.org/0000-0003-1377-5107; Email: robert.mcmahon@wisc.edu

**R. Claude Woods** – *Department of Chemistry, University of Wisconsin–Madison, Madison, Wisconsin 53706, United States*; orcid.org/0000-0003-0865-4693; Email: rcwoods@wisc.edu

### Authors

**Houston H. Smith** – *Department of Chemistry, University of Wisconsin–Madison, Madison, Wisconsin 53706, United States*; orcid.org/0000-0002-9385-8078

**Samuel M. Kougias** – *Department of Chemistry, University of Wisconsin–Madison, Madison, Wisconsin 53706, United States*; orcid.org/0000-0002-9877-0817

**Brian J. Esselman** – *Department of Chemistry, University of Wisconsin–Madison, Madison, Wisconsin 53706, United States*; orcid.org/0000-0002-9385-8078

Complete contact information is available at: https://pubs.acs.org/10.1021/jcpa.xxx


### Notes

The authors declare no competing financial interest.

**ACKNOWLEDGMENTS**

We gratefully acknowledge the National Science Foundation for support of this project (CHE-1954270). We thank Michael McCarthy for the loan of an amplification-multiplication chain and Aatmik R. Patel for stimulating discussions regarding the synthesis of 1-cyanocyclobutene precursors and the assessment of synthetic routes. We thank the following organizations and individuals for support of shared departmental facilities: Bruker AVANCE 400 NMR spectrometer (NSF CHE-1048642), Bruker AVANCE 500 NMR spectrometer (gift from Paul J. and Margaret M. Bender), and Thermo Scientific Q Exactive Plus mass spectrometer (NIH 1S10 OD020022-1).

## REFERENCES

(1) Müller, H. S. P.; Schlöder, F.; Stutzki, J.; Winnewisser, G., The Cologne Database for Molecular Spectroscopy, CDMS: a Useful Tool for Astronomers and Spectroscopists. *J. Mol. Struct.* **2005**, *742*, 215-227.

(2) Müller, H. S. P.; Thorwirth, S.; Roth, D. A.; Winnewisser, G., The Cologne Database for Molecular Spectroscopy, CDMS. *Astron. Astrophys.* **2001**, *370*, L49-L52.

(3) Zdanovskaia, M. A.; Esselman, B. J.; Lau, H. S.; Bates, D. M.; Woods, R. C.; McMahon, R. J.; Kisiel, Z., The 103 – 360 GHz Rotational Spectrum of Benzonitrile, the First Interstellar Benzene Derivative Detected by Radioastronomy. *J. Mol. Spectrosc.* **2018**, *351*, 39-48.

(4) Zdanovskaia, M. A.; Esselman, B. J.; Woods, R. C.; McMahon, R. J., The 130 - 370 GHz Rotational Spectrum of Phenyl Isocyanide ($C_6H_5NC$). *J. Chem. Phys.* **2019**, *151*, 024301.

(5) Dorman, P. M.; Esselman, B. J.; Park, J. E.; Woods, R. C.; McMahon, R. J., Millimeter-Wave Spectrum of 4-Cyanopyridine in its Ground State and Lowest-Energy Vibrationally Excited States, $\nu_{20}$ and $\nu_{30}$. *J. Mol. Spectrosc.* **2020**, *369*, 111274.

(6) Dorman, P. M.; Esselman, B. J.; Woods, R. C.; McMahon, R. J., An Analysis of the Rotational Ground State and Lowest-energy Vibrationally Excited Dyad of 3-Cyanopyridine: Low Symmetry Reveals Rich Complexity of Perturbations, Couplings, and Interstate Transitions. *J. Mol. Spectrosc.* **2020**, *373*, 111373.

(7) Kougias, S. M.; Knezz, S. N.; Owen, A. N.; Sanchez, R. A.; Hyland, G. E.; Lee, D. J.; Patel, A. R.; Esselman, B. J.; Woods, R. C.; McMahon, R. J., Synthesis and Characterization of Cyanobutadiene Isomers—Molecules of Astrochemical Significance. *J. Org. Chem.* **2020**, *85*, 5787-5798.

(8) Zdanovskaia, M. A.; Dorman, P. M.; Orr, V. L.; Owen, A. N.; Kougias, S. M.; Esselman, B. J.; Woods, R. C.; McMahon, R. J., Rotational Spectra of Three Cyanobutadiene Isomers ($C_5H_5N$) of Relevance to Astrochemistry and Other Harsh Reaction Environments. *J. Am. Chem. Soc.* **2021**, *143*, 9551-9564.

(9) Zdanovskaia, M. A.; Esselman, B. J.; Kougias, S. M.; Patel, A. R.; Woods, R. C.; McMahon, R. J., The 130–360 GHz rotational spectrum of syn-2-cyano-1,3-butadiene ($C_5H_5N$) – a molecule of astrochemical relevance. *Mol. Phys.* **2021**, *119*, e1964629.

(10) Esselman, B. J.; Kougias, S. M.; Zdanovskaia, M. A.; Woods, R. C.; McMahon, R. J., Synthesis, Purification, and Rotational Spectroscopy of (Cyanomethylene)Cyclopropane—An Isomer of Pyridine. *J. Phys. Chem. A* **2021**, *125*, 5601-5614.

(11) Charnley, S. B.; Kuan, Y.-J.; Huang, H.-C.; Botta, O.; Butner, H. M.; Cox, N.; Despois, D.; Ehrenfreund, P.; Kisiel, Z.; Lee, Y.-Y., et al., Astronomical Searches for Nitrogen Heterocycles. *Adv. Space Res.* **2005**, *36*, 137-145.

(12) McGuire, B. A.; Burkhardt, A. M.; Kalenskii, S. V.; Shingledecker, C. N.; Remijan, A. J.; Herbst, E.; McCarthy, M. C., Detection of the Aromatic Molecule Benzonitrile (*c*-$C_6H_5CN$) in the Interstellar Medium. *Science* **2018**, *359*, 202-205.

(13) McGuire, B. A.; Loomis, R. A.; Burkhardt, A. M.; Lee, K. L. K.; Shingledecker, C. N.; Charnley, S. B.; Cooke, I. R.; Cordiner, M. A.; Herbst, E.; Kalenskii, S., et al., Detection of Two

Interstellar Polycyclic Aromatic Hydrocarbons via Spectral Matched Filtering. *Science* **2021**, *371*, 1265-1269.

(14) McCarthy, M. C.; Lee, K. L. K.; Loomis, R. A.; Burkhardt, A. M.; Shingledecker, C. N.; Charnley, S. B.; Cordiner, M. A.; Herbst, E.; Kalenskii, S.; Willis, E. R., et al., Interstellar Detection of the Highly Polar Five-Membered Ring Cyanocyclopentadiene. *Nat. Astron.* **2021**, *5*, 176-180.

(15) Morales, S. B.; Bennett, C. J.; Le Picard, S. D.; Canosa, A.; Sims, I. R.; Sun, B. J.; Chen, P. H.; Chang, A. H. H.; Kislov, V. V.; Mebel, A. M., et al., A Crossed Molecular Beam, Low-Temperature Kinetics, and Theoretical Investigation of the Reaction of the Cyano Radical (CN) with 1,3-Butadiene ($C_4H_6$). A Route to Complex Nitrogen-Bearing Molecules in Low-Temperature Extraterrestrial Environments. *Astrophys. J.* **2011**, *742*, 26.

(16) Sun, B. J.; Huang, C. H.; Chen, S. Y.; Chen, S. H.; Kaiser, R. I.; Chang, A. H. H., Theoretical Study on Reaction Mechanism of Ground-State Cyano Radical with 1,3-Butadiene: Prospect of Pyridine Formation. *J. Phys. Chem. A* **2014**, *118*, 7715-7724.

(17) Jamal, A.; Mebel, A. M., Theoretical Investigation of the Mechanism and Product Branching Ratios of the Reactions of Cyano Radical with 1- and 2-Butyne and 1,2-Butadiene. *J. Phys. Chem. A* **2013**, *117*, 741-755.

(18) Mishra, P.; Fritz, S. M.; Herbers, S.; Mebel, A. M.; Zwier, T. S., Gas-phase Pyrolysis of *Trans* 3-Pentenenitrile: Competition Between Direct and Isomerization-Mediated Dissociation. *PCCP* **2021**, *23*, 6462-6471.

(19) McCarthy, M. C.; Lee, K. L. K.; Carroll, P. B.; Porterfield, J. P.; Changala, P. B.; Thorpe, J. H.; Stanton, J. F., Exhaustive Product Analysis of Three Benzene Discharges by Microwave Spectroscopy. *J. Phys. Chem. A* **2020**, *124*, 5170-5181.

(20) Guillemin, J. C.; Ferris, J. P., Photochemistry of Unsaturated Nitriles on Titan. *Eur. Space Agency, [Spec. Publ.] ESA SP* **1992**, *ESA SP-338*, 177-81.

(21) Gale, D. M., 1-Cyanobicyclo[1.1.0]butane and 1-cyanocyclobutene by photolysis of 2-cyano-1,3-butadiene. Patent number US3459647A, 1969.

(22) Gale, D. M.; Cherkofsky, S. C., Dehydrocyanation of Dinitriles. Preparation of 1-Cyclobutenecarbonitrile by Direct Dehydrocyanation of 1,2-Cyclobutanedicarbonitrile. *J. Org. Chem.* **1973**, *38*, 475-478.

(23) Sarner, S. F.; Gale, D. M.; Hall, H. K.; Richmond, A. B., Gas-phase Thermolysis Kinetics of Small Ring Nitriles. *J. Phys. Chem.* **1972**, *76*, 2817-2819.

(24) Kwak, N.; Simmons, J. W.; Goldstein, J. H., Microwave Spectrum of Propiolactone. *J. Chem. Phys* **1955**, *23*, 2450-2450.

(25) Boone, D. W.; Britt, C. O.; Boggs, J. E., Microwave Spectrum, Dipole Moment, and Ring-Puckering Vibration of β-Propiolactone. *J. Chem. Phys* **1965**, *43*, 1190-1194.

(26) Chen, Z.; van Wijngaarden, J., A Combined *Ab Initio*, Fourier Transform Microwave and Fourier Transform Infrared Spectroscopic Investigation of β-Propiolactone: The $\nu_8$ and $\nu_{12}$ bands. *J. Mol. Spectrosc.* **2009**, *257*, 164-169.

(27) Orr, V. L.; Esselman, B. J.; Dorman, P. M.; Amberger, B. K.; Guzei, I. A.; Woods, R. C.; McMahon, R. J., Millimeter-wave Spectroscopy, X-ray Crystal Structure, and Quantum Chemical Studies of Diketene – Resolving Ambiguities Concerning the Structure of the Ketene Dimer. *J. Phys. Chem. A* **2016**, *120*, 7753-7763.

(28) Durig, J. R.; Carreira, L. A.; Lafferty, W. J., Spectra and Structure of Small Ring Compounds. Microwave Spectrum of Cyanocyclobutane. *J. Mol. Spectrosc.* **1973**, *46*, 187-193.

(29) Fong, M. Y.; Harmony, M. D., Microwave Spectrum, Dipole Moment, Quadrupole Coupling Constants, and Conformation of Cyanocyclobutane. *J. Chem. Phys* **1973**, *58*, 4260-4264.

(30) Caminati, W.; Velino, B.; Della Valle, R. G., Rotational Spectra of Several Vibrational Excited States of Axial and Equatorial Cyanocyclobutane and Potential Energy Function of the Ring Puckering. *J. Mol. Spectrosc.* **1988**, *129*, 284-292.

(31) Durig, J. R.; Ganguly, A.; Klaassen, J. J.; Guirgis, G. A., The $r_0$ Structural Parameters, Conformational Stability, and Vibrational Assignment of Equatorial and Axial Cyanocyclobutane. *J. Mol. Struct.* **2009**, *923*, 28-38.

(32) Caminati, W.; Velino, B.; Dakkouri, M.; Schäfer, L.; Siam, K.; Ewbank, J. D., Reinvestigation of the Microwave Spectrum of Cyanocyclobutane: Assignment of the Axial Conformer. *J. Mol. Spectrosc.* **1987**, *123*, 469-475.

(33) Menke, J. L.; McMahon, R. J., Photochemistry of matrix-isolated 5-cyano-2H-pyran-2-one (δ-cyano-α-pyrone) and cyanocyclobuta-1,3-diene. *Can. J. Chem.* **2011**, *89*, 186-194.

(34) Miki, S.; Matsumura, S.-i.; Ohno, T.; Yoshida, Z.-i., Co(II)porphyrin Catalyzed Isomerization of Bicyclobutanecarbonitrile. *Tetrahedron Lett.* **1986**, *27*, 3669-3672.

(35) Gale, D. M., Mono- and Dichlorocyclobutanecarbonitriles by Cycloaddition of Vinyl Chloride and an Acrylonitrile. Patent number US3642859A, 1972.

(36) Tietz, R. F.; Kenyon, W. G., 1-Cyanocyclobutene Monomer and Polymer and Their Preparation. Patent number US3468861A, Sept. 23, 1969.

(37) Ferris, J. P.; Guillemin, J. C., Photochemical Cycloaddition Reactions of Cyanoacetylene and Dicyanoacetylene. *J. Org. Chem.* **1990**, *55*, 5601-5606.

(38) Hughes, W. B., Photodimerization of Acrylonitrile. Patent number US3623966A, 1971-11-30.

(39) Miyashita, A.; Ikezu, S.; Nohira, H., Stereospecific Photodimerization of Unsaturated Compounds Induced by Nickel Complexes. *Chem. Lett.* **1985**, *14*, 1235-1238.

(40) Hosaka, S.; Wakamatsu, S., Photodimerization of Acrylonitrile. *Tetrahedron Lett.* **1968**, *9*, 219-220.

(41) Esselman, B. J.; Amberger, B. K.; Shutter, J. D.; Daane, M. A.; Stanton, J. F.; Woods, R. C.; McMahon, R. J., Rotational Spectroscopy of Pyridazine and its Isotopologs from 235–360 GHz: Equilibrium Structure and Vibrational Satellites. *J. Chem. Phys.* **2013**, *139*, 224304.

(42) Kisiel, Z.; Pszczółkowski, L.; Drouin, B. J.; Brauer, C. S.; Yu, S.; Pearson, J. C.; Medvedev, I. R.; Fortman, S.; Neese, C., Broadband Rotational Spectroscopy of Acrylonitrile: Vibrational Energies from Perturbations. *J. Mol. Spectrosc.* **2012**, *280*, 134-144.

(43) Kisiel, Z.; Pszczółkowski, L.; Medvedev, I. R.; Winnewisser, M.; De Lucia, F. C.; Herbst, E., Rotational Spectrum of *Trans–Trans* Diethyl Ether in the Ground and Three Excited Vibrational States. *J. Mol. Spectrosc.* **2005**, *233*, 231-243.

(44) Pickett, H. M., The Fitting and Prediction of Vibration-rotation Spectra with Spin Interactions. *J. Mol. Spectrosc.* **1991**, *148*, 371-377.

(45) Kisiel, Z., PROSPE - Programs for ROtational SPEctroscopy; http://info.ifpan.edu.pl/~kisiel/prospe.htm (accessed 04-03-2021).

(46) Kisiel, Z., Assignment and Analysis of Complex Rotational Spectra. In *Spectroscopy from Space*, 1 ed.; Demaison, J.; Sarka, K.; Cohen, E. A., Eds. Springer Netherlands: Dordrecht, 2001; pp 91-106.

(47) Frisch, M. J.; Trucks, G. W.; Schlegel, H. B.; Scuseria, G. E.; Robb, M. A.; Cheeseman, J. R.; Scalmani, G.; Barone, V.; Petersson, G. A.; Nakatsuji, H., et al. *Gaussian 16 rev C.01*, Gaussian, Inc.: Wallingford, CT, USA, 2016.

(48) Schmidt, J. R.; Polik, W. F., WebMO Enterprise, version 20.0; WebMO LLC: Madison, WI, USA, 2020; http://www.webmo.net (accessed April, 2021).

(49) Kisiel, Z.; Kraśnicki, A., The Millimetre-Wave Rotational Spectrum of Phenylacetylene. *J. Mol. Spectrosc.* **2010**, *262*, 82-88.

(50) Zdanovskaia, M. A.; Martin-Drumel, M.-A.; Kisiel, Z.; Pirali, O.; Esselman, B. J.; Woods, R. C.; McMahon, R. J., The eight lowest-energy vibrational states of benzonitrile: analysis of Coriolis and Darling-Dennison couplings by millimeter-wave and far-infrared spectroscopy. *J. Mol. Spectrosc.* **2022**, *383*, 111568.

# The 130 − 500 GHz Rotational Spectrum of 2-Cyanopyrimidine

Houston H. Smith, Brian J. Esselman, Maria A. Zdanovskaia,

R. Claude Woods*, Robert J. McMahon*

*Department of Chemistry, University of Wisconsin–Madison, Madison, Wisconsin 53706, USA*

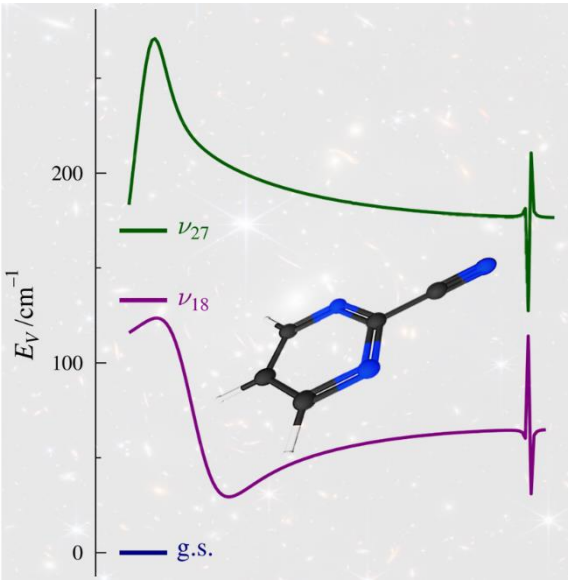


**Abstract**

The rotational spectrum of 2-cyanopyrimidine has been obtained from 130 GHz to 500 GHz. Over 7500 vibrational ground-state transitions have been assigned and least-squares fit to partial octic, A- and S-reduced Hamiltonians with low error ($\sigma_{fit}$ = 34 kHz). The two lowest-energy fundamental modes, the out-of-plane ($\nu_{18}$) and in-plane ($\nu_{27}$) nitrile bending modes, form a Coriolis-coupled dyad similar to the analogous fundamental states of other cyanoarenes. The coupled dyad was least-squares fit to a partial octic, A-reduced Hamiltonian ($\sigma_{fit}$ = 47 kHz) with over 6700 transitions for each vibrational state, including transitions that are perturbed or involved in resonances, as well as symmetry-allowed nominal interstate transitions resulting from Coriolis coupling. The spectroscopic information from these transitions enabled the determination of a highly precise energy separation ($\Delta E_{18,27}$ = 38.9673191 (77) cm$^{-1}$) and six Coriolis-coupling

coefficients ($G_a$, $G_a^J$, $G_a^K$, $G_a^{JJ}$, $F_{bc}$, and $F_{bc}^K$). The spectroscopic constants and transitions presented in this work provide the foundation for future radioastronomical searches for 2-cyanopyrimidine.

**Keywords**
rotational spectroscopy, vibrational spectroscopy, Coriolis coupling, interstellar molecule, astrochemistry

## Introduction

There has been long-standing interest in elucidating the molecular composition of various extraterrestrial environments, with particular attention on aromatic compounds. The detection of benzene *via* infrared spectroscopy in proto-planetary nebula CRL 618 [1] was a catalyst to search for other aromatic molecules; the search for aromatic heterocycles, however, has been unsuccessful [2-5]. Pyrimidine is of particular interest as an astronomical target because its core is present in various biological and prebiotic molecules. These include thymine, uracil, cytosine, thiamine (vitamin B1), and alloxan, as well as various synthetic drugs [6]. Therefore, detection of pyrimidine in an extraterrestrial environment would signify detection of a biologically relevant molecule in a harsh, possibly prebiotic environment. Despite multiple efforts, there have been no reported interstellar detections of this molecule [2,5,7]. Radioastronomy, which relies on the population of the species in the source observed and on the intrinsic intensity of its rotational transitions due to its dipole moment, is the preferred method of detection due to being reasonably unambiguous in molecular identification. The inability to detect nonpolar or weakly polar aromatic molecules has led to attempts to detect simple derivatives of those molecules with nitrile substituents, which tend to bestow a large dipole moment. The larger dipole moment leads to a greater chance of detection by radioastronomy, which is illustrated by the prevalence of nitrile-containing molecules detected in the interstellar medium (ISM) [8,9]. Such attempts to detect

nitrile-containing derivatives have been successful for benzonitrile [10] and cyanonaphthalenes [11], suggesting their parent molecules are also present in space. These astronomical detections rely on the availability of accurate spectroscopic constants determined from laboratory spectra. Given the success of nitrile-substituted detections, our group reported the rotational spectral analyses of several nitrile-containing heteroaromatic compounds (Fig. 3.1), including benzonitrile [12,13], 2-cyanopyridine [14], 3-cyanopyridine [15], 4-cyanopyridine [16], cyanopyrazine [17], and 2-cyanopyrimidine (presented in this work) in their ground and vibrationally excited states. In contrast to the situation with benzonitrile and the cyanopyridines, for which some spectroscopic data had been previously available [18-21], 2-cyanopyrimidine and cyanopyrazine did not have previously reported rotational spectra.

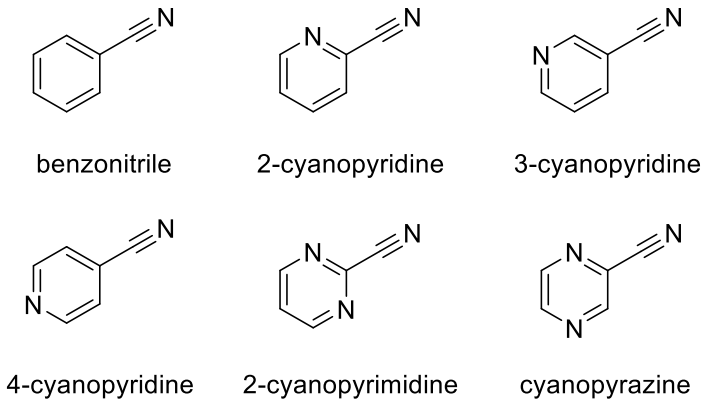


**Fig. 3.1.** Cyanoarenes derived from benzene, pyridine, pyrimidine, and pyrazine.

The two lowest-energy fundamental vibrational modes for molecules containing a vinyl nitrile moiety are typically the in-plane and out-of-plane bending modes of the nitrile, and these modes are often sufficiently close in energy that Coriolis coupling is observed in the millimeter-wave frequency transitions. Analysis of the rotational spectra for these vibrational modes for benzonitrile [12,13], 3-cyanopyridine [15], 4-cyanopyridine [16], cyanopyrazine [17], 1-cyanocyclobutene [22], (cyanomethylene)cyclopropane [23], and acrylonitrile [24] required the use of vibrationally coupled Hamiltonians to assign the observed rotational transitions and resulted

in the determination of a highly accurate and precise energy separation between the two fundamental states (Table 3.1). For each of the cyano-substituted aromatic compounds observed, the out-of-plane nitrile bending mode is lower in energy (Table 3.1). The coupling and state mixing result in rotational transitions influenced by Coriolis perturbation. This perturbation results in the appearance of local resonances, *i.e.*, transitions whose frequencies are drastically shifted from where they would be expected in the absence of perturbation, and formally forbidden, nominal interstate transitions. While band origins can be determined from high-resolution infrared spectroscopy, as has been done for benzonitrile [13] and acrylonitrile [24], it is the various coupling interactions affecting the rotational transition frequencies that enable the highly precise determination of the energy separation between vibrational states. This work presents the rotational spectroscopy and analysis of the ground and two lowest-energy vibrationally excited states of 2-cyanopyrimidine from 130 GHz to 500 GHz.

**Table 3.1**
Energy differences between out-of-plane and in-plane nitrile bending modes for molecules containing a vinyl nitrile moiety

| | out-of-plane | in-plane | $\Delta E_{\text{ip–oop}}$ ($\text{cm}^{-1}$) |
|---|---|---|---|
| benzonitrile [12,13] | $\nu_{22}$, $B_1$ | $\nu_{33}$, $B_2$ | 19.1081701(74) |
| 3-cyanopyridine [15] | $\nu_{30}$, A″ | $\nu_{21}$, A′ | 15.7524693 (37) |
| 4-cyanopyridine [16] | $\nu_{20}$, $B_1$ | $\nu_{30}$, $B_2$ | 18.806554 (11) |
| cyanopyrazine [17] | $\nu_{27}$, A″ | $\nu_{19}$, A′ | 24.8245962 (60) |
| 2-cyanopyrimidine (this work) | $\nu_{18}$, $B_1$ | $\nu_{27}$, $B_2$ | 38.9673191 (77) |
| 1-cyanocyclobutene [22] | $\nu_{27}$, A″ | $\nu_{17}$, A′ | 14.0588093 (43) |
| (cyanomethylene)cyclopropane [23] | $\nu_{27}$, A″ | $\nu_{17}$, A′ | −29.8975453 (33) |
| acrylonitrile [24,25] | $\nu_{15}$, A″ | $\nu_{11}$, A′ | −104.378277 (6) |

## Experimental Methods

A commercial sample of 2-cyanopyrimidine (Aldrich, 95% purity) was used without further purification. Using a millimeter-wave spectrometer that has been previously described [26,27], the rotational spectrum of 2-cyanopyrimidine was collected from 130 to 230 and from 235

to 360 GHz in a continuous flow at room temperature, with a sample pressure of 3 mTorr. Additional spectral data were obtained with a newly acquired amplification and multiplication chain that extended the frequency range to 500 GHz with a sample pressure of 4 mTorr. The separate spectral segments were combined into a single broadband spectrum using Kisiel's Assignment and Analysis of Broadband Spectra (AABS) software [24,28]. The complete spectrum from 130 to 500 GHz was obtained using automated data collection software over approximately nine days given these experimental parameters: 0.6 MHz/sec sweep rate, 10 ms time constant, and 50 kHz AM and 500 kHz FM modulation in a tone-burst design [29]. Pickett's SPFIT/SPCAT programs [30] were used for least-squares fits and spectral predictions, along with Kisiel's PIFORM, PLANM, and AC programs for analysis [31,32]. A uniform frequency measurement uncertainty of 0.050 MHz was assumed for all measurements.

**Computational Methods**

Electronic structure calculations were carried out with Gaussian 16 [33] using the WebMO interface [34] to obtain theoretical spectroscopic constants. Optimized geometries at the B3LYP/6-311+(2d,p) and MP2/6-311+(2d,p) levels were obtained using "verytight" convergence criteria and an "ultrafine" integration grid. Subsequent anharmonic vibrational frequency calculations were carried out to obtain vibration-rotation interaction constants and predictions of the centrifugal distortion constants. These methods have been effective to generate the necessary spectroscopic constants for adequate *a priori* predictions for other cyanoarenes [12,13,15-17]. From the optimized geometries, magnetic calculations were also performed to obtain theoretical nuclear quadrupole coupling constants. Computational output files can be found in the supplementary material

**2-Cyanopyrimidine Rotational Spectrum**

The rotational spectrum of 2-cyanopyrimidine was obtained from 130 GHz to 500 GHz. This frequency range satisfactorily covered the most intense rotational transitions, as judged by comparison to the predicted rotational populations in the 2-cyanopyrimidine spectrum at ambient temperature (Fig. 3.2). While the peak transition intensities occur near 220 GHz, there is still substantial intensity well beyond 400 GHz. As will be discussed below, this extension in the frequency range to 500 GHz was vital in the analysis of the Coriolis-coupled dyad of $\nu_{18}$ and $\nu_{27}$, because most resonances were observed between 375 GHz and 500 GHz, providing crucial coupling information.

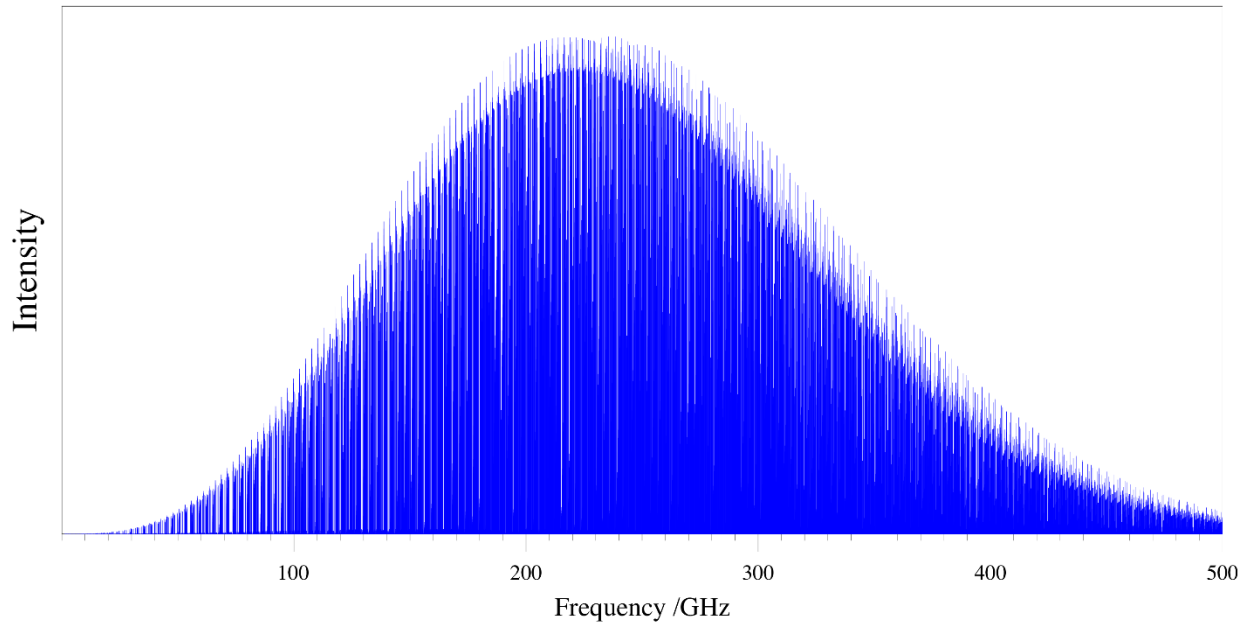


**Fig. 3.2.** Predicted rotational spectrum of the ground vibrational state of 2-cyanopyrimidine at 292 K.

**Ground-State Spectral Analysis**

The rotational spectrum of 2-cyanopyrimidine ($\mu$ = 6.5 D (B3LYP), $\kappa$ = −0.851) has not been previously reported. As a consequence of $C_{2v}$ symmetry and the nitrile substituent lying along the *a*-principal axis (Fig. 3.3), 2-cyanopyrimidine exhibits only *a*-type rotational transitions.

The rotational spectrum of this prolate, asymmetric top is thus dominated by $^{a}R_{0,1}$ ground-state and vibrationally excited-state transitions across the frequency range studied. Figure 3.4 shows a small subset of the spectrum from 198 GHz to 199 GHz along with predicted stick spectra for the ground state and the two lowest-energy vibrationally excited states, $\nu_{18}$ and $\nu_{27}$. It is apparent that the spectrum also includes unassigned transitions that are due to higher-energy vibrationally excited states, but they are not addressed in this work. Similar to other monosubstituted arenes, despite being a near-prolate top ($\kappa = -0.851$), the most prominent band structure for the ground state of 2-cyanopyrimidine follows the recognizable oblate-type band pattern at low $K_a$ [12,13,15-17,35]. Bands start at $K_a = 0$ and increase in $K_a$ as $J''$ decreases. The band in Fig. 3.4 begins with a $K_c$-degenerate pair of $^{a}R_{0,1}$ transitions, which lose degeneracy at higher $K_a$ values. The degenerate $^{a}R_{0,1}$ transitions have quantum numbers that follow either $K_a + K_c = J$ or $K_a + K_c = J + 1$, and $K_a$ series with these selection rules are subsequently referred to as $K_a^{+}$ and $K_a^{-}$, respectively.

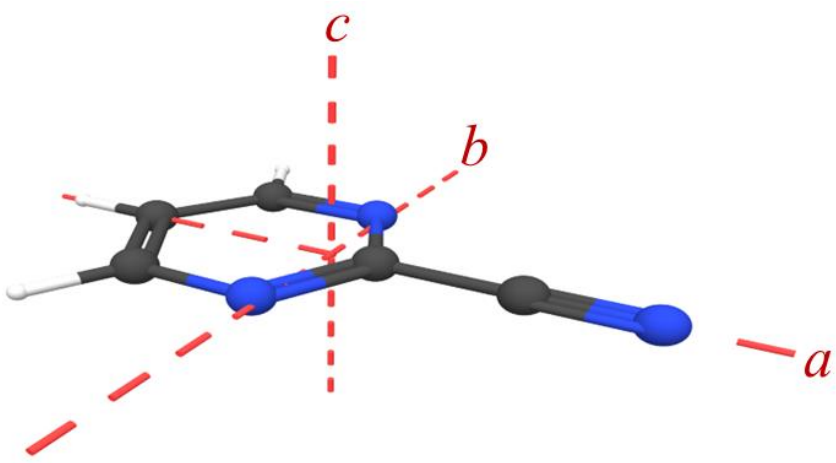


**Fig. 3.3**. 2-Cyanopyrimidine ($C_{2v}$, $\mu_a$ = 6.5 D, B3LYP) structure with principal inertial axes.

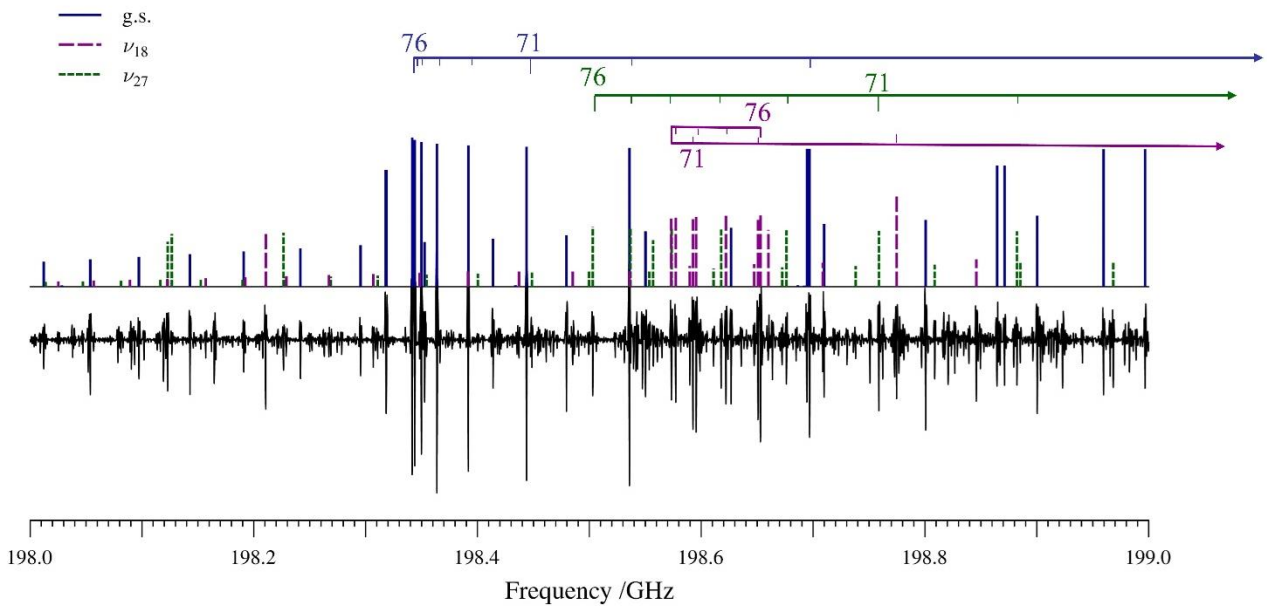


**Fig. 3.4.** Experimental rotational spectrum (bottom) of 2-cyanopyrimidine from 198 to 199 GHz and stick spectra (top) from experimental spectroscopic constants. The ground state (blue), $\nu_{18}$ (magenta), and $\nu_{27}$ (green) are labeled by the upper energy-level quantum number, $J'' + 1$.

The vibrational ground state of 2-cyanopyrimidine has been least-squares fit to partial octic A- and S-reduced, single-state Hamiltonians with low error ($\sigma_{fit}$ = 36 kHz). As shown in Fig. 3.5, the final transition data set (~7600 transitions) encompasses an extensive range of quantum numbers with $J'' + 1$ = 42 to 189 and $K_a$ = 0 to 63. The resulting spectroscopic constants are reported in Table 3.2 along with respective computed values (B3LYP and MP2). Though a partial octic Hamiltonian was utilized, no computational comparison is possible for the octic centrifugal distortion constants, because there is no readily available software to compute these values. As a result, octic terms that were undeterminable in the least-squares fit were set to a value of zero. There were an insufficient number of nuclear quadrupole coupling resolved transitions to obtain experimental nuclear quadrupole coupling constants, therefore these terms were not included in the Hamiltonian. Least-squares fitting files and computed nuclear quadrupole coupling constants can be found in the supplementary material.

**Table 3.2**

Experimental and computational spectroscopic constants for the ground vibrational state of 2-cyanopyrimidine (A- and S-reduced Hamiltonians, $I^r$ representation)

| | A Reduction, $I^r$ representation | | | | S Reduction, $I^r$ representation | | |
|---|---|---|---|---|---|---|---|
| | Experimental [a] | B3LYP [b] | MP2 [b] | | Experimental [a] | B3LYP [b] | MP2 [b] |
| $A_0$ (MHz) | 6043.4539 (12) | 6051 | 5986 | $A_0$ (MHz) | 6043.4535 (12) | 6051 | 5986 |
| $B_0$ (MHz) | 1651.140609 (36) | 1649 | 1635 | $B_0$ (MHz) | 1651.139276 (36) | 1649 | 1635 |
| $C_0$ (MHz) | 1296.639905 (39) | 1295 | 1284 | $C_0$ (MHz) | 1296.641199 (39) | 1295 | 1284 |
| $\Delta_J$ (kHz) | 0.0483056 (22) | 0.0464 | 0.0460 | $D_J$ (kHz) | 0.0354922 (20) | 0.0345 | 0.0338 |
| $\Delta_{JK}$ (kHz) | 1.037502 (25) | 0.976 | 1.01 | $D_{JK}$ (kHz) | 1.114400 (26) | 1.05 | 1.08 |
| $\Delta_K$ (kHz) | 0.3608 (18) | 0.389 | 0.351 | $D_K$ (kHz) | 0.3003 (18) | 0.330 | 0.290 |
| $\delta_J$ (kHz) | 0.01154427 (86) | 0.0111 | 0.0110 | $d_1$ (kHz) | −0.01154436 (86) | −0.0111 | −0.0110 |
| $\delta_K$ (kHz) | 0.660687 (56) | 0.621 | 0.635 | $d_2$ (kHz) | −0.00640999 (54) | −0.00594 | −0.00611 |
| $\Phi_J$ (Hz) | 0.000001716 (84) | 0.00000174 | 0.00000187 | $H_J$ (Hz) | −0.000012737 (77) | −0.0000117 | −0.0000129 |
| $\Phi_{JK}$ (Hz) | 0.0017323 (24) | 0.00149 | 0.00163 | $H_{JK}$ (Hz) | 0.0011987 (19) | 0.00103 | 0.00115 |
| $\Phi_{KJ}$ (Hz) | −0.008505 (15) | −0.00739 | −0.00819 | $H_{KJ}$ (Hz) | −0.006498 (16) | −0.00566 | −0.00634 |
| $\Phi_K$ (Hz) | 0.0107 (10) | 0.00653 | 0.00718 | $H_K$ (Hz) | 0.0116 (10) | 0.00528 | 0.00583 |
| $\phi_J$ (Hz) | 0.000001226 (19) | 0.000000881 | 0.000000922 | $h_1$ (Hz) | −0.000000239 (19) | −0.000000409 | −0.00000046 |
| $\phi_{JK}$ (Hz) | 0.0008021 (15) | 0.000751 | 0.000824 | $h_2$ (Hz) | 0.000007394 (15) | 0.00000674 | 0.00000740 |
| $\phi_K$ (Hz) | 0.008258 (34) | 0.00731 | 0.00779 | $h_3$ (Hz) | 0.0000014737 (48) | 0.00000129 | 0.00000139 |
| $L_J$ (mHz) | 0.0000000167 (12) | | | $L_J$ (mHz) | 0.0000000114 (12) | | |
| $L_{JJK}$ (mHz) | −0.000002409 (17) | | | $L_{JJK}$ (mHz) | −0.000002025 (17) | | |
| $L_{JK}$ (mHz) | 0.00001448 (22) | | | $L_{JK}$ (mHz) | 0.00001835 (22) | | |
| $L_{KKJ}$ (mHz) | −0.0001149 (31) | | | $L_{KKJ}$ (mHz) | −0.0001301 (31) | | |
| $L_K$ (mHz) | [0.] | | | $L_K$ (mHz) | [0.] | | |
| $\Delta_i$ (uÅ$^2$) [c,d] | 0.057658 (21) | | | $\Delta_i$ (uÅ$^2$) [c,d] | 0.057568 (21) | | |
| $N_{\text{lines}}$ [e] | 7591 | | | $N_{\text{lines}}$ [e] | 7591 | | |
| $\sigma_{\text{fit}}$ (MHz) | 0.036 | | | $\sigma_{\text{fit}}$ (MHz) | 0.036 | | |

[a] Off-diagonal octic centrifugal distortion terms (not shown in table) were held constant at a value of zero.
[b] Evaluated with the 6-311+G(2d,p) basis set.
[c] Inertial defect, $\Delta_i = I_c - I_a - I_b$.
[d] Calculated using PLANM from the $B_0$ constants.
[e] Number of fitted transition frequencies.

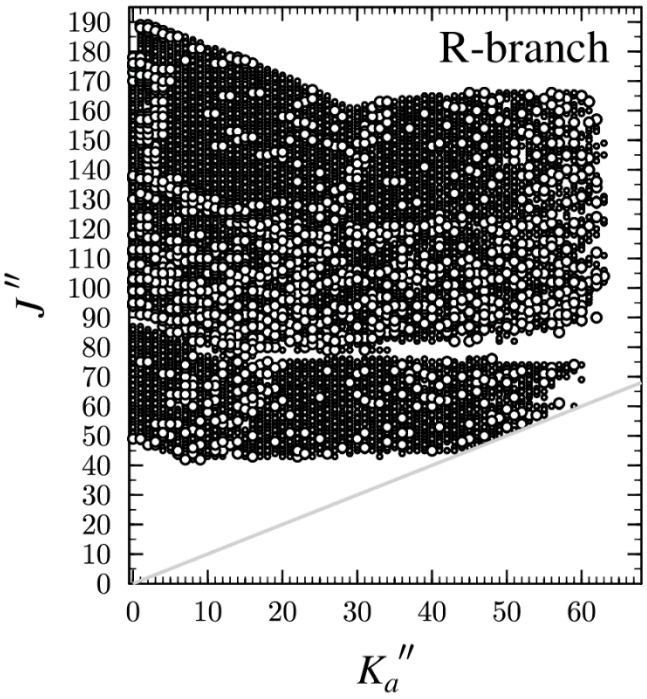


**Fig. 3.5.** Data distribution plot for the least-squares fit of spectroscopic data for the vibrational ground state of 2-cyanopyrimidine. The size of the outlined circle is proportional to the value of $|(f_{obs.} - f_{calc.})/\delta f|$, where $\delta f$ is the frequency measurement uncertainty.

The MP2-computed rotational constants are in satisfactory agreement with the experimental values (within ~1%), but the B3LYP-computed rotational constants are closer in agreement (within ~0.13%). This result is similar to the situation observed for cyanopyrazine [17]. The B3LYP-computed quartic centrifugal-distortion constants are also in good agreement with the experimental values (within 10%), with $\Delta_K$ and $D_K$ having the largest difference from experiment. The MP2 quartic centrifugal distortion constants are in slightly closer agreement with the experimental values (within 5%), with $\delta_J$ and $d_1$ having the largest discrepancies. There is poorer agreement for the sextic centrifugal distortion constants for both sets of computed values. With the exception of $\Phi_K$ and $\phi_J$, the B3LYP values are within ~15%, and the MP2 values are within 10%, excluding $H_K$, and $h_1$. The B3LYP values of $\Phi_K$ and $H_K$ are approximately half of their experimental values, and the MP2 values are only slightly closer. The values of $\phi_J$ and $h_1$ are the

smallest of the sextic centrifugal distortion constants, so it is not surprising that their predictions have large relative errors. The worst of these, the MP2 prediction of $h_1$, is approximately twice the size of the experimental value. Unlike the case of cyanopyrazine [17], however, no sign change in the value of $h_1$ was observed for 2-cyanopyrimidine. On average, the MP2 computed distortion constants are in closer agreement than the B3LYP values. Despite the discrepancies described for each set of computed values, they provide very good *a priori* predictions of the rotational spectrum and are important in assisting the early stage of least-squares fitting.

**Spectral Analysis of $\nu_{18}$ and $\nu_{27}$**

The two lowest-energy vibrationally excited states of 2-cyanopyrimidine are an isolated, Coriolis-coupled dyad, similar to those seen in other cyanoarenes [12,13,15-17]. The lower-energy vibration, $\nu_{18}$ ($B_1$, 132 $cm^{-1}$ B3LYP), is an out-of-plane bend of the nitrile group with respect to the aromatic ring, while $\nu_{27}$ ($B_2$, 175 $cm^{-1}$ B3LYP) involves an in-plane bend of the nitrile group. The vibrational manifold of 2-cyanopyrimidine below 600 $cm^{-1}$ is presented in Fig. 3.6, which depicts additional possible coupled states, especially above 450 $cm^{-1}$. This work focuses only on the coupled dyad of $\nu_{18}$ and $\nu_{27}$. The initial assignment of $\nu_{18}$ and $\nu_{27}$ was performed using a single-state, distorted-rotor Hamiltonian for each vibrational state. Computationally predicted rotational constants and ground-state distortion constants were used for initial predictions. This technique allowed for the assignment of three series corresponding to $K_a$ = 0, 1, and 2 for both states, but there was apparent perturbation in each least-squares fit that was untreated in a single-state model. Thus, a two-state model was adopted, initially using the $\Delta E_{18,27}$ and $G_a$ values predicted by B3LYP and the rotational constants $A_0$, $B_v$ and $C_v$ ($A_0$ is the experimental ground-state value and $B_v$ and $C_v$ are the experimental ground-state values corrected by the

respective B3LYP vibration-rotation interaction constants, $\alpha_B$ and $\alpha_C$, for each vibrational state). The vibration-rotation interaction constant, $\alpha_A$, was not used because it showed clear signs of absorbed perturbation (equal magnitude but opposite sign for each state; *vide infra*). Quartic, sextic, and octic distortion constants were set to their ground-state values, and in the initial least-squares fitting process, only $\Delta E$ and $C_v$ were allowed to vary. As transitions were added to the least-squares fit, additional rotational, centrifugal, and Coriolis-coupling coefficients were varied to model the experimental spectrum until all observed transitions for each vibrational state were assigned across the frequency region measured. The extent of the rotational transitions measured are shown in Fig. 3.7, and the spectroscopic constants determined in the least-squares fit are provided in Table 3.3.

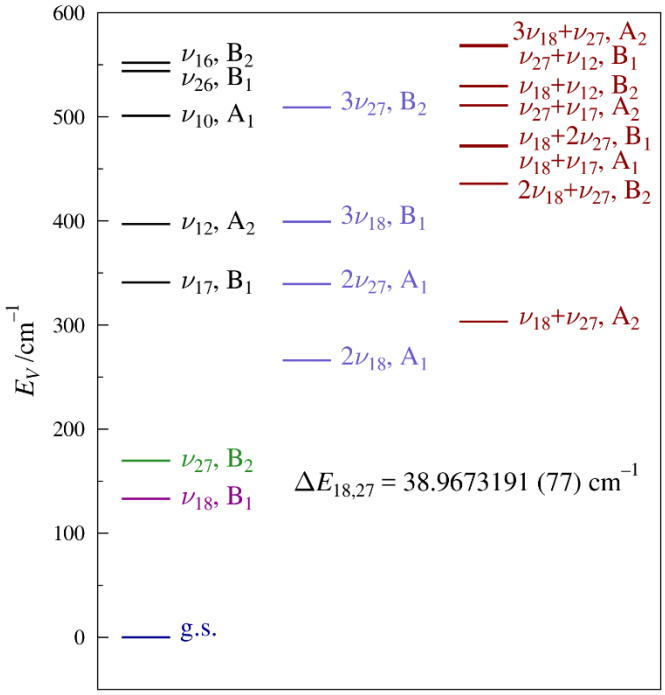


**Fig. 3.6.** Vibrational energy levels of 2-cyanopyrimidine below 600 cm$^{-1}$ from computed fundamental frequencies (B3LYP/6-311+G(2d,p)). The value of $\Delta E_{18,27}$ results from the experimental perturbation analysis of $\nu_{18}$ and $\nu_{27}$ in this work (*vide infra*).

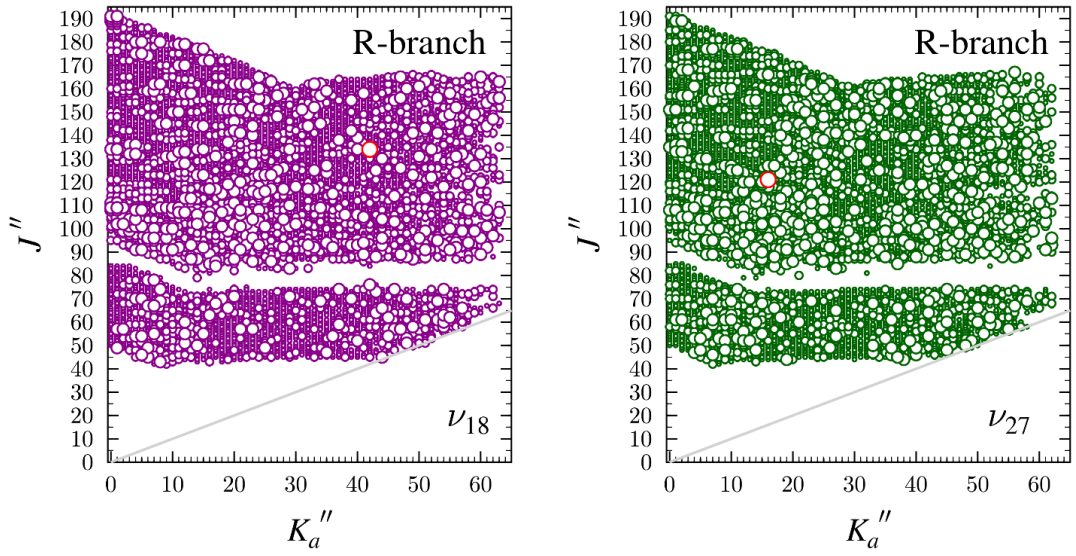


**Fig. 3.7** Data distribution plots for the least-squares fit of spectroscopic data for the lowest-energy fundamental states of 2-cyanopyrimidine, $\nu_{18}$ (magenta) and $\nu_{27}$ (green). The size of the symbol is proportional to the value of $|(f_{obs.} - f_{calc.})/\delta f|$, where $\delta f$ is the frequency measurement uncertainty, and values greater than 3 are depicted in red.

**Table 3.3**

Experimentally determined spectroscopic constants for the ground and vibrationally excited states $\nu_{18}$ and $\nu_{27}$ of 2-cyanopyrimidine (A-reduced Hamiltonian, $I^r$ representation).

| | ground state [a] | $\nu_{18}$ ($B_1$, 133 cm$^{-1}$) [a,b] | $\nu_{27}$ ($B_2$, 175 cm$^{-1}$) [a,b] |
|---|---|---|---|
| $A_v$ (MHz) | 6043.4539 (12) | 6051.08 (13) | 6032.06 (13) |
| $B_v$ (MHz) | 1651.140609 (36) | 1653.012774 (36) | 1654.267680 (36) |
| $C_v$ (MHz) | 1296.639905 (39) | 1298.754909 (32) | 1297.555132 (34) |
| $\Delta_J$ (MHz) | 0.0483056 (22) | 0.0492650 (13) | 0.0493417 (13) |
| $\Delta_{JK}$ (MHz) | 1.037502 (25) | 1.06773 (49) | 0.98437 (49) |
| $\Delta_K$ (MHz) | 0.3608 (18) | [0.3608] | 0.4143 (13) |
| $\delta_J$ (MHz) | 0.01154427 (86) | 0.01162990 (85) | 0.01194518 (88) |
| $\delta_K$ (MHz) | 0.660687 (56) | 0.663053 (60) | 0.662360 (57) |
| $\Phi_J$ (MHz) | 0.000001716 (84) | 0.000002372 (31) | 0.000002309 (31) |
| $\Phi_{JK}$ (MHz) | 0.0017323 (24) | 0.0017797 (84) | 0.0016502 (88) |
| $\Phi_{KJ}$ (MHz) | −0.008505 (15) | −0.008081 (11) | [−0.008506] |
| $\Phi_K$ (MHz) | 0.0107 (10) | [0.0107] | [0.0107] |
| $\phi_J$ (MHz) | 0.000001226 (19) | 0.000001384 (18) | 0.000001592 (18) |
| $\phi_{JK}$ (MHz) | 0.0008021 (15) | 0.0008179 (11) | 0.0007685 (11) |
| $\phi_K$ (MHz) | 0.008258 (34) | 0.008228 (26) | 0.008475 (27) |
| $\Delta E_{18,27}$ (MHz) | | 1168210.84 (23) | |
| $\Delta E_{18,27}$ (cm$^{-1}$) | | 38.9673191 (77) | |
| $G_a$ (MHz) | | 10666.3 (75) | |
| $G_a^J$ (MHz) | | −0.006165 (29) | |
| $G_a^K$ (MHz) | | −0.00466 (14) | |
| $G_a^{JJ}$ (MHz) | | 0.00000000635 (44) | |
| $F_{bc}$ (MHz) | | −0.3779 (26) | |
| $F_{bc}^k$ (kHz) | | −0.000006992 (97) | |
| $\Delta_i$ (uÅ$^2$) [c,d] | 0.057658 (21) | −0.1214 (19) | 0.1997 (19) |
| $N_{lines}$ [e] | 7591 | 7114 | 6712 |
| $\sigma_{fit}$ (MHz) | 0.036 | 0.046 | 0.048 |

[a] Octic centrifugal distortion constants are not shown and are held constant at their ground-state values in Table 3.2.
[b] Fundamental frequencies calculated using B3LYP/6-311+G(2d,p).
[c] Inertial defect, $\Delta_i = I_c - I_a - I_b$.
[d] Calculated using PLANM from the $B_v$ constants.
[e] Number of fitted transition frequencies.

The final least-squares fit is an exhaustive collection of transitions across the frequency region and totals over 7100 transitions for $\nu_{18}$ and 6700 for $\nu_{27}$. The totals are only slightly lower than that for the ground state (~7600), which is expected due to the somewhat lower intensity of vibrationally excited states. The observed transitions range from 42 to 192 in $J'' + 1$ for both states and $K_a = 0$ to 63 and 62 for $\nu_{18}$ and $\nu_{27}$, respectively. The data set includes transition frequencies that are shifted *via* global perturbations and intense resonances and included 17 transitions that are formally forbidden, coupling-allowed interstate transitions. To achieve a satisfactory fit, it was necessary to extend the frequency range beyond 360 GHz, because most resonances occur in this region. These highly perturbed resonant transitions are critical in determining accurate and precise Coriolis-coupling constants. The importance of data in the higher frequency region was noted in the earlier case of cyanopyrazine [17], and it is even more important for 2-cyanopyrimidine. Attempts to obtain a satisfactory least-squares fit using only data from the 130 GHz to 360 GHz frequency range were ultimately unsuccessful. Least-squares fitting of the final data set, including resonant transitions and symmetry-allowed interstate transitions, provides a precise energy separation between $\nu_{18}$ and $\nu_{27}$ ($\Delta E_{18,27}$ = 38.9673191 (77) $cm^{-1}$). Based on similar results in molecules where the band origins have been measured independently by high-resolution infrared spectroscopy [13], the accuracy is presumed to be comparable to the precision. This large energy separation required much higher values of $J$ and $K$ of $\nu_{18}$ before the energy levels are sufficiently close to create resonances than in some previous works with smaller energy separations between the coupled modes [12,13,15,16,35]. Along with a precise value of $\Delta E_{18,27}$, the least-squares fit nearly provides a complete set of quartic and sextic distortion constants, excluding $\Delta_K$ for $\nu_{18}$, $\Phi_{KJ}$ for $\nu_{27}$ and $\Phi_K$ for both $\nu_{18}$ and $\nu_{27}$. Unfortunately, $\Delta_K$ of $\nu_{18}$ could not be determined, which is attributed to the high correlation of $\Delta_K$ with $A_{18}$ and the limitation of being able to measure only

$^{a}R_{0,1}$ transitions. In addition, six Coriolis-coupling terms ($G_a$, $G_a^J$, $G_a^K$, $G_a^{JJ}$, $F_{bc}$, and $F_{bc}^K$) were determined. The inclusion of all of these coupling terms was needed to obtain a satisfactory least-squares fit with a total error lower than the measurement uncertainty of 50 kHz.

A measure of the quality of the least-squares fit comes from the comparison of the computed rotational constants to those experimentally determined to establish whether or not any of the computed constants show signs of untreated Coriolis coupling. The vibration-rotation interaction constants (Table 3.4) provide a straightforward comparison between the experimental and computed values, where unaddressed Coriolis coupling appears as large values with opposing sign between the two vibrational states. The MP2 values of $B_0 - B_\nu$ and $C_0 - C_\nu$ are in excellent agreement with the experimental values (within 6%), which provides confidence in the method to determine the vibration-rotation interactions. The corresponding B3LYP values are approximately as accurate as the MP2 values for $B_0 - B_\nu$ and $C_0 - C_\nu$ (within 7%). In contrast, both the B3LYP and MP2 values of $A_0 - A_\nu$ show poor agreement with the experimental values, each having similarly large discrepancies and much larger magnitudes than the experimental values (Table 3.4). The disagreement indicates the presence of untreated Coriolis coupling in both computational results or the experimental values. The fact that the experimental values are significantly smaller than either computed value suggests that the least-squares fit may be performing a better job of treating the Coriolis coupling. This situation, in which the experimental $A_0 - A_\nu$ values have different signs than the computed values, was also noted in previous works [17,22]. The average of the computed $A_0 - A_\nu$ values for $\nu_{18}$ and $\nu_{27}$ cancels out the unaddressed Coriolis effects, and these averages are in excellent agreement with the experimental average (Table 3.4). Unsurprisingly, the corresponding average values for the $B_\nu$ and $C_\nu$ values are also in excellent agreement between both theoretical treatments and experiment. The $\Delta E_{18,27}$ values for both

computational methods are in close agreement; the B3LYP value is approximately 4 $cm^{-1}$ too large and the MP2 value is approximately 2 $cm^{-1}$ too small. The experimental Coriolis $\zeta^{a}_{18,27}$ value is also in satisfactory agreement with both the MP2 and B3LYP values with the experimental value being slightly larger (7%). The agreement between experimental and computational Coriolis $\zeta^{a}_{18,27}$ values, along with a low $\sigma_{fit}$ value, indicate a satisfactory treatment of the Coriolis coupling that is present in the $\nu_{18}$-$\nu_{27}$ dyad of 2-cyanopyrimidine.

**Table 3.4**
Vibration-rotation interaction and Coriolis-coupling constants of the 2-cyanopyrimidine $\nu_{18}$-$\nu_{27}$ dyad.

| | Experimental | B3LYP [a] | MP2 [a] |
|---|---|---|---|
| $A_0 - A_{18}$ (MHz) | −7.62 (13) | 81.13 | 95.75 |
| $B_0 - B_{18}$ (MHz) | −1.872165 (51) | −1.84 | −1.77 |
| $C_0 - C_{18}$ (MHz) | −2.115004 (50) | −2.09 | −2.03 |
| $A_0 - A_{27}$ (MHz) | 11.39 (13) | −77.53 | −92.33 |
| $B_0 - B_{27}$ (MHz) | −3.127071 (51) | −2.96 | −3.08 |
| $C_0 - C_{27}$ (MHz) | −0.915227 (52) | −0.85 | −0.91 |
| $\frac{(A_0-A_{18})+(A_0-A_{27})}{2}$ (MHz) | 1.88 (09) | 1.80 | 1.71 |
| $\frac{(B_0-B_{18})+(B_0-B_{27})}{2}$ (MHz) | −2.499618 (36) | −2.40 | −2.43 |
| $\frac{(C_0-C_{18})+(C_0-C_{27})}{2}$ (MHz) | −1.515115 (36) | −1.47 | −1.47 |
| $\lvert\zeta^{a}_{18,27}\rvert$ | 0.873 | 0.809 | 0.810 |
| $\Delta E_{18,27}$ ($cm^{-1}$) | 38.9673191 (77) | 42.70 | 36.64 |

[a] Evaluated with the 6-311+G(2d,p) basis set.

The successful incorporation of many resonant and symmetry-allowed, nominal interstate transitions into the data set indicates an adequate treatment of the dyad by the Hamiltonian, since these transitions are highly dependent on $\Delta E_{18,27}$ and the Coriolis-coupling coefficients utilized in the least-squares fit. One example of the state mixing between vibrational states is shown in Fig. 3.8, where a sharp resonance occurs between the $K_a = 11^{-}$ series of $\nu_{18}$ and $K_a = 7^{+}$ series of $\nu_{27}$ ($\Delta K_a = 4$). The most perturbed transition, at $J'' + 1 = 176$, is ~500 MHz from its unperturbed

location. Each of these series also displays large undulations occurring from both global coupling perturbations. The progression of the global undulation, from low to high frequencies as $K_a$ increases, is displayed in Fig. 3.9. This plot highlights several of the resonances present for the $\nu_{18}$-$\nu_{27}$ dyad, and the most perturbed transition, located in $K_a = 43$, is ~ 1 GHz from its unperturbed location. Most resonances are above $J'' + 1 = 130$, reaffirming the utility of the extension of the frequency range to 500 GHz.

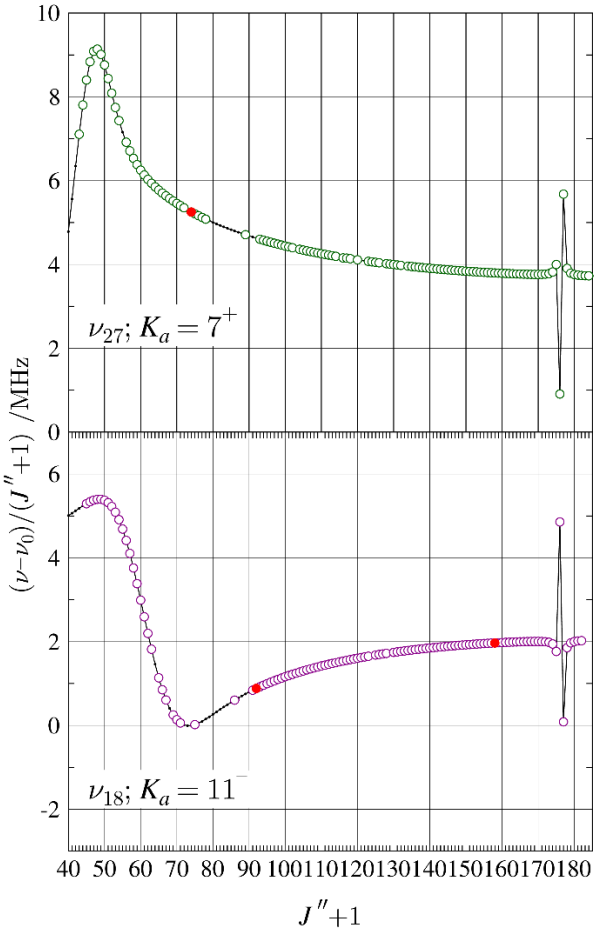


**Fig. 3.8.** Resonance plots for 2-cyanopyrimidine showing the $K_a = 11^-$ series for $\nu_{18}$ and $K_a = 7^+$ series for $\nu_{27}$. These two resonances conform to the $\Delta K_a = 4$ selection rule for *a*-type resonances. The plotted values are frequency differences between excited-state transitions and their ground-state counterparts, scaled by $(J'' + 1)$ in order to make the plots more horizontal. Measured transitions are represented by circles: $\nu_{18}$ (magenta), $\nu_{27}$ (green). Red circles indicate transitions whose *obs.* - *calc*. values are more than three times the experimental uncertainty. Predictions from the final coupled fit are represented by a solid, colored line.

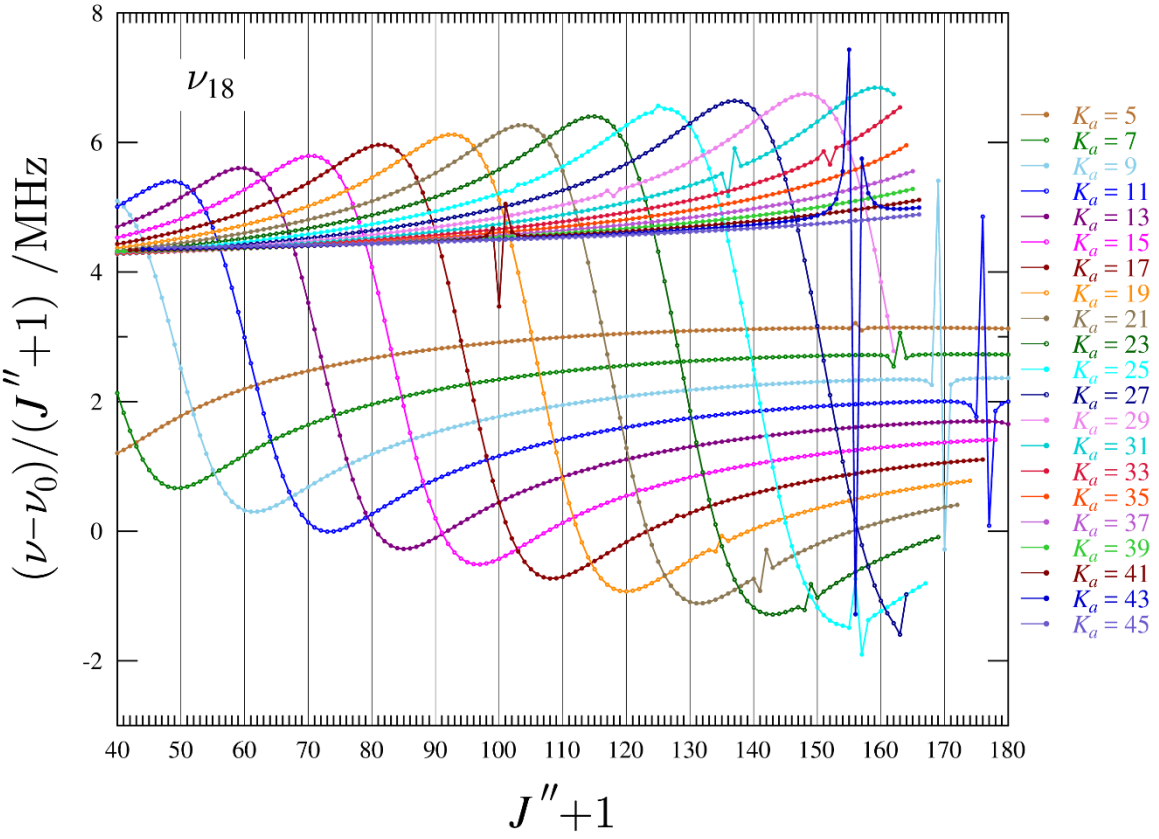


**Fig. 3.9.** Superimposed resonance plots of $\nu_{18}$ for ${}^{a}R_{0,1}$ odd-$K_a^-$ series from 5 to 45 for 2-cyanopyrimidine. Measured transitions are omitted for clarity, but they are indistinguishable from the plotted values on this scale. The plotted values are frequency differences between excited-state transitions and their ground-state counterparts, scaled by ($J''$ + 1).

A total of 17 independent nominal interstate transitions were measured and incorporated into the least-squares fit, and they were crucial in finalizing several Coriolis-coupling constants and confirming the assignment of some resonant transitions. These nominal interstate transitions occur when rotational energy levels from each vibrational state are close enough in energy that intense state-mixing occurs. In many cases, it is possible to measure corresponding intrastate and interstate transitions for each level to create a matched set of four transitions (Fig. 3.10). As these four transitions involve the same energy levels, the average of the interstate transitions must be the same as the intrastate transitions. This condition confirms the assignment of all transitions when

the difference between the sets of transitions is less than the measurement uncertainty of 50 kHz. The frequency difference between the transitions in Fig. 3.10 is only 36 kHz despite the higher *obs*. – *calc*. for individual transitions, *e.g.*, the intrastate transition of $\nu_{18}$, where it is one of two transitions in the fit that is greater than three times the measurement uncertainty and is shown in red in the resonance plot of Fig. 3.10 and in the data distribution plot (Fig. 3.7). The typical working procedure for least-squares fitting is to scrutinize transitions with greater than two times the measurement uncertainty with regards to including such transitions in the least-squares fit. This transition displays an abnormal line shape, which is likely due to another underlying transition distorting its true frequency. Although this would typically warrant the exclusion of this transition, the very limited number of these important resonant and nominal interstate transitions in the data set make even this imperfectly measured transition highly valuable for the coupling information it provides. As a result, it was retained in the final data set with explicably high error.

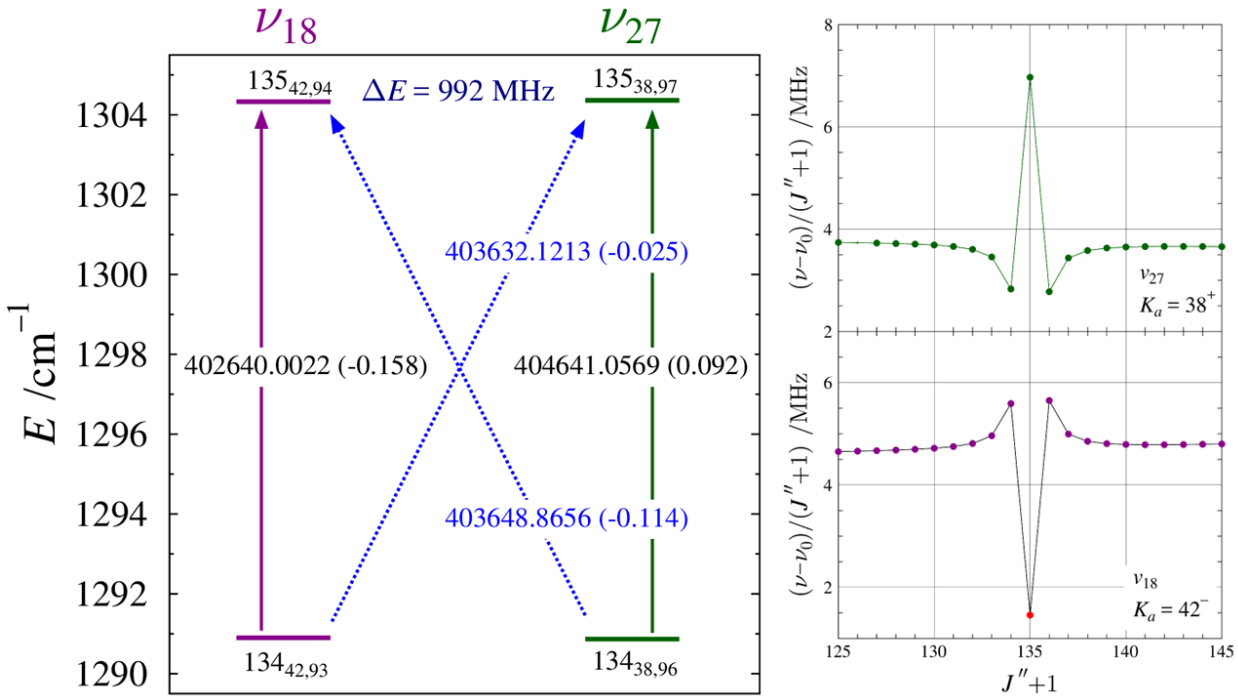


**Fig. 3.10.** Energy diagram (left) depicting a representative matched pair of nominal interstate transitions between the $\nu_{18}$ (magenta) and $\nu_{27}$ (green) vibrational states of 2-cyanopyrimidine. Standard $^qR_{0,1}$ transitions within vibrational states are denoted by vertical arrows. The diagonal, dashed arrows indicate nominal interstate transitions that are formally forbidden but enabled as a result of rotational energy level mixing. Values printed on each of the arrows are the corresponding transition frequency (in MHz) with its *obs.* – *calc.* value in parentheses. The marked energy separation is between the two strongly interacting rotational energy levels. Resonance plots (right) of the $K_a$ series of $\nu_{18}$ and $\nu_{27}$ show the corresponding resonant intrastate transitions.

Measurement of the precise and accurate value of the energy difference for the out-of-plane and in-plane nitrile bending modes for a variety C(sp$^2$)–CN-containing organic molecules, including the previously studied cyanoarenes, allows for an analysis of the structural factors that impact the vibrational mode energies. As shown in Fig 1, the structure of each of the cyanoarenes recently studied in our group [15-17] differs from benzonitrile [12,13] by N-atom substitution in the aromatic ring. Similar to benzonitrile, 3-cyanopyridine [15], and 4-cyanopyridine [16] have *ortho* C–H groups adjacent to the nitrile. Cyanopyrazine [17] has an *ortho* C–H group and a nitrogen atom. 2-Cyanopyrimidine from this work completes this series by providing analogous

data for a cyanoarene with two *ortho* nitrogen atoms. There is a monotonic increase in the $\Delta E_{\text{ip–oop}}$ values with increasing substitutions of *ortho* C–H groups with nitrogen atoms shown in Table 3.5. There is a smaller change to $\Delta E_{\text{ip–oop}}$ with meta substitution in the reverse direction, such that the effects of *ortho* and *meta* substitution are approximately +10 and −3 $cm^{-1}$, respectively.

**Table 3.5**
Experimental energy separations for selected organic species for the out-of-plane and in-plane nitrile bending modes

| | $\Delta E_{\text{ip–oop}}$ ($cm^{-1}$) | *ortho* N | *meta* N | *para* N |
|---|---|---|---|---|
| benzonitrile [12,13] | 19.1081701(74) | 0 | 0 | 0 |
| 3-cyanopyridine [15] | 15.7524693 (37) | 0 | 1 | 0 |
| 4-cyanopyridine [16] | 18.806554 (11) | 0 | 0 | 1 |
| cyanopyrazine [17] | 24.8245962 (60) | 1 | 1 | 0 |
| cyanopyrimidine (this work) | 38.9673191 (77) | 2 | 0 | 0 |

**Conclusion**

To expand the search for heterocyclic aromatic molecules in the interstellar medium, the current study provides the necessary laboratory data to conduct an astronomical search for 2-cyanopyrimidine. The larger dipole moment of 2-cyanopyrimidine (6.3 D) vs. pyrimidine (2.3 D) increases the possibility of detection in the ISM if these species were to have similar abundances. The combination of the spectroscopic constants provided here, along with computed (provided in Supplementary Material) or experimental nuclear quadrupole coupling constants, would reliably predict transition frequencies much lower or slightly higher in frequency than the frequency range of the current measurements (130-500 GHz). The least-squares fit of the Coriolis-coupled dyad of $\nu_{18}$ and $\nu_{27}$ allows for a precise determination of the energy separation of the fundamental modes, $\Delta E_{18,27}$, but high-resolution infrared spectroscopy is needed to determine the fundamental frequencies. This infrared study would be challenging, however, since $\nu_{18}$ and $\nu_{27}$ have quite low predicted intensities (0.1 and 0.6 km/mol (MP2), respectively). Of the cyanoarenes studied to date,

2-cyanopyrimidine exhibits the largest energy difference for the out-of-plane and in-plane nitrile bending modes ($\Delta E_{\text{ip–oop}}$ = 38.9673191 (77) $\text{cm}^{-1}$) of the studied cyanoarenes. This large energy separation notwithstanding, a two-state Hamiltonian is required to adequately address the transition frequencies observed for each vibrational state – even in the 130 – 360 GHz range. At the same time, highly-perturbed transition frequencies (resonances) above 360 GHz are required to adequately describe the Coriolis perturbation and obtain a satisfactory least-squares fit. This behavior demonstrates how broadly Coriolis perturbation can affect transition frequencies, even those that are not "highly" perturbed as resonances, and that the resonant transitions provide important constraints on the determination of the spectroscopic parameters that cannot be obtained from transition frequencies influenced by the global Coriolis interaction alone.

**Acknowledgments**

We gratefully acknowledge funding from the U.S. National Science Foundation for support of this project (CHE-1954270). We thank Michael McCarthy for the loan of an amplification-multiplication chain and the Harvey Spangler Award (to B.J.E) for support of the purchase of the corresponding zero-bias detector.

**ORCID**

Houston H. Smith: 0000-0002-3762-1842

Brian J. Esselman: 0000-0002-9385-8078

Maria A. Zdanovskaia: 0000-0001-5167-8573

R. Claude Woods: 0000-0003-0865-4693

Robert J. McMahon: 0000-0003-1377-5107

**Data availability**

Data are provided in the article and in the Supplementary Material.

**Supplementary material**

Computational chemistry output files, least-squares fitting output files from SPFIT.

Supplementary data associated with this article can be found, in the online version, at https://doi.org/10.1016/j.jms.2023.111737.

**References**


[1] J. Cernicharo, A.M. Heras, A.G.G.M. Tielens, J.R. Pardo, F. Herpin, M. Guélin, L.B.F.M. Waters, Infrared Space Observatory's Discovery of $C_4H_2$, $C_6H_2$, and Benzene in CRL 618, Astrophys. J. 546 (2001) L123-L126.

[2] T.J. Barnum, M.A. Siebert, K.L.K. Lee, R.A. Loomis, P.B. Changala, S.B. Charnley, M.L. Sita, C. Xue, A.J. Remijan, A.M. Burkhardt, B.A. McGuire, I.R. Cooke, A Search for Heterocycles in GOTHAM Observations of TMC-1, J. Phys. Chem. A (2022).

[3] M.L. Kutner, D.E. Machnik, K.D. Tucker, R.L. Dickman, Search for interstellar pyrrole and furan, Astrophys. J. 242 (1980) 541-544.

[4] Y.-J. Kuan, C.-H. Yan, S.B. Charnley, Z. Kisiel, P. Ehrenfreund, H.-C. Huang, A search for interstellar pyrimidine, Mon. Not. R. Astron. Soc. 345 (2003) 650-656.

[5] S.B. Charnley, Y.-J. Kuan, H.-C. Huang, O. Botta, H.M. Butner, N. Cox, D. Despois, P. Ehrenfreund, Z. Kisiel, Y.-Y. Lee, A.J. Markwick, Z. Peeters, S.D. Rodgers, Astronomical searches for nitrogen heterocycles, Adv. Space Res. 36 (2005) 137-145.

[6] J.B. N, Naganna M. Goudgaon, A comprehensive review on pyrimidine analogs-versatile scaffold with medicinal and biological potential, J. Mol. Struct. 1246 (2021) 131168.

[7] M.N. Simon, M. Simon, Search for Interstellar Acrylonitrile, Pyrimidine, and Pyridine, Astrophys. J. 184 (1973) 757-762.

[8] H.S.P. Müller, S. Thorwirth, D.A. Roth, G. Winnewisser, The Cologne Database for Molecular Spectroscopy, CDMS, Astron. Astrophys. 370 (2001) L49-L52.

[9] H.S.P. Müller, F. Schlöder, J. Stutzki, G. Winnewisser, The Cologne Database for Molecular Spectroscopy, CDMS: a Useful Tool for Astronomers and Spectroscopists, J. Mol. Struct. 742 (2005) 215-227.

[10] B.A. McGuire, A.M. Burkhardt, S.V. Kalenskii, C.N. Shingledecker, A.J. Remijan, E. Herbst, M.C. McCarthy, Detection of the Aromatic Molecule Benzonitrile (*c*-$C_6H_5CN$) in the Interstellar Medium, Science 359 (2018) 202-205.

[11] B.A. McGuire, A. Loomis Ryan, A.M. Burkhardt, K. Lee Kin Long, C.N. Shingledecker, S.B. Charnley, I.R. Cooke, M.A. Cordiner, E. Herbst, S. Kalenskii, M.A. Siebert, E.R. Willis, C. Xue, A.J. Remijan, M.C. McCarthy, Detection of two interstellar polycyclic aromatic hydrocarbons via spectral matched filtering, Science 371 (2021) 1265-1269.

[12] M.A. Zdanovskaia, B.J. Esselman, H.S. Lau, D.M. Bates, R.C. Woods, R.J. McMahon, Z. Kisiel, The 103–360 GHz rotational spectrum of benzonitrile, the first interstellar benzene derivative detected by radioastronomy, J. Mol. Spectrosc. 351 (2018) 39-48.

[13] M.A. Zdanovskaia, M.-A. Martin-Drumel, Z. Kisiel, O. Pirali, B.J. Esselman, R.C. Woods, R.J. McMahon, The eight lowest-energy vibrational states of benzonitrile: analysis of Coriolis and Darling-Dennison couplings by millimeter-wave and far-infrared spectroscopy, J. Mol. Spectrosc. 383 (2022) 111568.

[14] P.M. Dorman, B.J. Esselman, R.C. Woods, R.J. McMahon, The 130 to 500 GHz Rotational Spectroscopy of 2-cyanopyridine (*o*-$C_5H_4N$-CN), manuscript in preparation (2022).

[15] P.M. Dorman, B.J. Esselman, R.C. Woods, R.J. McMahon, An analysis of the rotational ground state and lowest-energy vibrationally excited dyad of 3-cyanopyridine: Low symmetry reveals rich complexity of perturbations, couplings, and interstate transitions, J. Mol. Spectrosc. 373 (2020) 111373.

[16] P.M. Dorman, B.J. Esselman, J.E. Park, R.C. Woods, R.J. McMahon, Millimeter-wave spectrum of 4-cyanopyridine in its ground state and lowest-energy vibrationally excited states, $\nu_{20}$ and $\nu_{30}$, J. Mol. Spectrosc. 369 (2020) 111274.

[17] B.J. Esselman, M.A. Zdanovskaia, H.H. Smith, R.C. Woods, R.J. McMahon, The 130-500 GHz Rotational Spectroscopy of Cyanopyrazine ($C_4H_3N_2$-CN), J. Mol. Spectrosc. 389 (2022) 111703.

[18] S. Doraiswamy, S.D. Sharma, Microwave spectrum of 2-cyanopyridine, Curr. Sci. 40 (1971) 398-399.

[19] R.G. Ford, The microwave spectra and dipole moments of the cyanopyridines, J. Mol. Spectrosc. 58 (1975) 178-184.

[20] N. Heineking, H. Dreizler, Nuclear Quadrupole Coupling Effects in the Rotational Spectrum of 4-Cyanopyridine, Zeitschrift für Naturforschung A 42 (1987) 83-86.

[21] N. Vogt, K.P.R. Nair, J.-U. Grabow, J. Demaison, Microwave rotational spectrum and ab initio computations on 4-cyanopyridine: molecular structure and hyperfine interactions, Mol. Phys. 116 (2018) 3530-3537.

[22] H.H. Smith, S.M. Kougias, B.J. Esselman, R.C. Woods, R.J. McMahon, Synthesis, Purification, and Rotational Spectroscopy of 1-Cyanocyclobutene ($C_5H_5N$), J. Phys. Chem. A 126 (2022) 1980-1993.

[23] B.J. Esselman, S.M. Kougias, M.A. Zdanovskaia, R.C. Woods, R.J. McMahon, Synthesis, Purification, and Rotational Spectroscopy of (Cyanomethylene)Cyclopropane—An Isomer of Pyridine, J. Phys. Chem. A 125 (2021) 5601-5614.

[24] Z. Kisiel, M.-A. Martin-Drumel, O. Pirali, Lowest vibrational states of acrylonitrile from microwave and synchrotron radiation spectra, J. Mol. Spectrosc. 315 (2015) 83-91.

[25] G. Cazzoli, Z. Kisiel, The rotational spectrum of acrylonitrile in excited states of the two low-frequency CCN bending vibrational modes, J. Mol. Spectrosc. 130 (1988) 303-315.

[26] B.K. Amberger, B.J. Esselman, J.F. Stanton, R.C. Woods, R.J. McMahon, Precise Equilibrium Structure Determination of Hydrazoic Acid ($HN_3$) by Millimeter-wave Spectroscopy, J. Chem. Phys. 143 (2015) 104310.

[27] B.J. Esselman, B.K. Amberger, J.D. Shutter, M.A. Daane, J.F. Stanton, R.C. Woods, R.J. McMahon, Rotational Spectroscopy of Pyridazine and its Isotopologs from 235-360 GHz: Equilibrium Structure and Vibrational Satellites, J. Chem. Phys. 139 (2013) 224304.

[28] Z. Kisiel, L. Pszczółkowski, I.R. Medvedev, M. Winnewisser, F.C. De Lucia, E. Herbst, Rotational spectrum of *trans–trans* diethyl ether in the ground and three excited vibrational states, J. Mol. Spectrosc. 233 (2005) 231-243.

[29] H.M. Pickett, Determination of collisional linewidths and shifts by a convolution method, Applied Optics 19 (1980) 2745-2749.

[30] H.M. Pickett, The fitting and prediction of vibration-rotation spectra with spin interactions, J. Mol. Spectrosc. 148 (1991) 371-377.

[31] Z. Kisiel, Assignment and Analysis of Complex Rotational Spectra. In: Spectroscopy from Space, J. Demaison, K. Sarka, E.A. Cohen, (Eds.), Springer Netherlands, Dordrecht, 2001; pp. 91-106.

[32] Z. Kisiel, PROSPE - Programs for ROtational SPEctroscopy. http://info.ifpan.edu.pl/~kisiel/prospe.htm

[33] M.J. Frisch, G.W. Trucks, H.B. Schlegel, G.E. Scuseria, M.A. Robb, J.R. Cheeseman, G. Scalmani, V. Barone, G.A. Petersson, H. Nakatsuji, X. Li, M. Caricato, A.V. Marenich, J. Bloino, B.G. Janesko, R. Gomperts, B. Mennucci, H.P. Hratchian, J.V. Ortiz, A.F. Izmaylov, J.L. Sonnenberg, Williams, F. Ding, F. Lipparini, F. Egidi, J. Goings, B. Peng, A. Petrone, T. Henderson, D. Ranasinghe, V.G. Zakrzewski, J. Gao, N. Rega, G. Zheng, W. Liang, M. Hada, M. Ehara, K. Toyota, R. Fukuda, J. Hasegawa, M. Ishida, T. Nakajima, Y. Honda, O. Kitao, H. Nakai, T. Vreven, K. Throssell, J.A. Montgomery Jr., J.E. Peralta, F. Ogliaro, M.J. Bearpark, J.J. Heyd, E.N. Brothers, K.N. Kudin, V.N. Staroverov, T.A. Keith, R. Kobayashi, J. Normand, K. Raghavachari, A.P. Rendell, J.C. Burant, S.S. Iyengar, J. Tomasi, M. Cossi, J.M. Millam, M. Klene, C. Adamo, R. Cammi, J.W. Ochterski, R.L. Martin, K. Morokuma, O. Farkas, J.B. Foresman, D.J. Fox, Gaussian 16 Rev. C.01. Wallingford, CT, 2016.

[34] J.R. Schmidt, W.F. Polik, WebMO Enterprise. 17.0.012e ed.; WebMO, LLC., Holland, MI, USA, 2017.

[35] M.A. Zdanovskaia, B.J. Esselman, R.C. Woods, R.J. McMahon, The 130–370 GHz rotational spectrum of phenyl isocyanide ($C_6H_5NC$), J. Chem. Phys. 151 (2019) 024301.

# The 130 to 500 GHz Rotational Spectroscopy of Cyanopyrazine (*p*-$C_4H_3N_2$-CN)

Brian J. Esselman, Maria A. Zdanovskaia, Houston H. Smith,

R. Claude Woods*, Robert J. McMahon*

*Department of Chemistry, University of Wisconsin–Madison, Madison, Wisconsin 53706, USA*

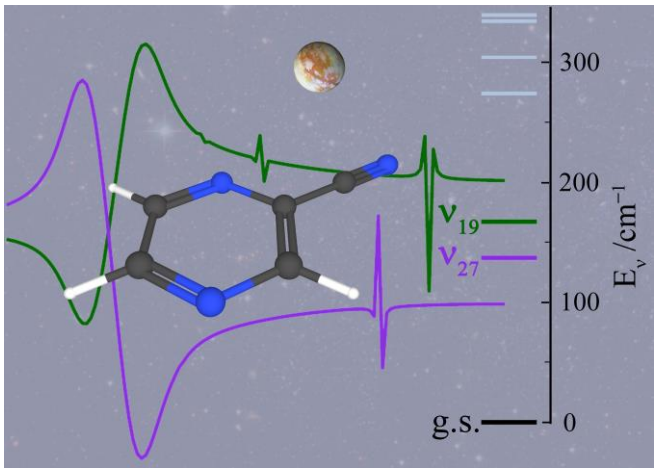


**Abstract:**

The rotational spectrum of cyanopyrazine (2-pyrazinecarbonitrile, *p*-$C_4H_3N_2$-CN) has been obtained from 130 to 500 GHz. Rotational transitions of cyanopyrazine have been measured, assigned, and least-squares fit for the first time. Over 7000 transitions of the ground vibrational state have been least-squares fit to partial octic, A- and S-reduced Hamiltonians with low statistical uncertainty ($\sigma_{fit}$ = 34 kHz). Similar to other cyanoarenes, the first two fundamental modes are the out-of-plane ($\nu_{27}$, A″) and in-plane ($\nu_{19}$, A′) nitrile bending modes, which form an *a*- and *b*-axis Coriolis-coupled dyad. Greater than 5800 transitions from each of these vibrational modes were fit to a partial octic, A-reduced Hamiltonian ($\sigma_{fit}$ = 38 kHz), and the analysis reveals the precise energy separation, $\Delta E_{27,19}$, between the coupled vibrational states, as well as values for eight *a*- and *b*-type Coriolis-coupling coefficients, $G_a$, $G_a^J$, $G_a^K$, $G_a^{JJ}$, $F_{bc}^K$, $G_b$, $G_b^J$, and $F_{ac}$. Cyanopyrazine is a strongly polar derivative of pyrazine, thus cyanopyrazine can serve as a potential tracer

molecule for its nonpolar parent compound in extraterrestrial environments. The transition frequencies and spectroscopic constants provided in this work, combined with theoretical or experimental nuclear quadrupole coupling constants, provide the foundation for future radioastronomical searches for cyanopyrazine.

**Keywords**

rotational spectroscopy, Coriolis coupling, interstellar molecule, astrochemistry

## Introduction

The feasibility of radioastronomical detection of a molecule depends upon its population in the source of interest and on the intrinsic intensity of its rotational transitions due to its dipole moment. The direct detections of benzene [1] and other nonpolar species [1, 2] in extraterrestrial environments rely upon infrared spectroscopy but can be supported or suggested by detection of their polar, substituted derivatives by radioastronomy. The recent radioastronomical detections of benzonitrile [3] and two cyanonaphthalenes [4] not only provide confirmation of these species in the interstellar medium (ISM), but also suggest the presence of their parent species, benzene and naphthalene. The presence of these nitrile-substituted aromatic molecules and the many other nitrile-containing organic species in the ISM [5-7] inspired the recent rotational spectral analyses of several nitrile-containing heteroaromatic compounds (Fig. 4.1) by our group, including benzonitrile [8, 9], 3-cyanopyridine [10], and 4-cyanopyridine [11] up to 360 GHz in their ground and vibrationally excited states. Similarly inspired, McNaughton *et al*. reported the 2 to 100 GHz spectroscopy of several polycyclic aromatic nitriles (1-cyanonaphthalene, 2-cyanonaphthalene, 9-cyanoanthracene, and 9-cyanophenanthrene) [12]. To facilitate astronomical searches for

additional cyanoarenes, we have measured the laboratory rotational spectra of cyanopyrazine (presented in this work), 2-cyanopyridine [13], and 2-cyanopyrimidine [14].

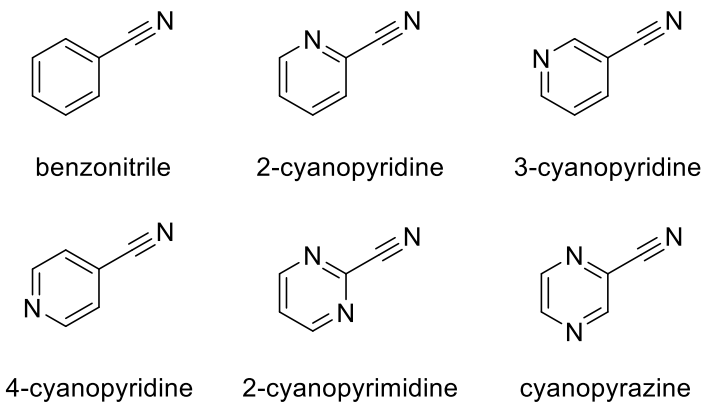


**Fig 4.1.** Cyanoarenes derived from benzene, pyridine, pyrimidine, and pyrazine.

Unlike its isomeric dinitrogen-containing benzene analogues, pyridazine ($\mu_a$ = 4.22 [15]) and pyrimidine ($\mu_a$ = 2.334 D [16]), pyrazine ($D_{2h}$, $\mu$ = 0) does not possess a permanent dipole moment due to the *para* substitution of its nitrogen atoms and cannot be the direct target of a radioastronomical search. While neither pyridazine nor pyrimidine has been detected in the ISM [17-20], and both molecules are part of a larger dilemma regarding the apparent absence of aromatic heterocycles in the list of organic molecules in the ISM, pyrazine represents an intriguing potential astrochemical species. It is nearly isoenergetic with pyrimidine, both of which are 19.7 kcal/mol more stable than pyridazine [21-23]. Due to its lack of a permanent dipole moment, tracer molecules are required to explore the potential contribution of pyrazine to interstellar organic chemistry. Substituted pyrazines have not garnered significant attention in the spectroscopy community. Transition frequencies and rotational constants have been provided for chloropyrazine [24, 25], but not for other substituted pyrazines. Given the prevalence of organic

nitriles in the ISM, cyanopyrazine is the ideal tracer molecule for pyrazine. Detection of any heterocycle or substituted heterocycle in the ISM would represent a dramatic breakthrough for the field [17-20], because derivatives of the parent aromatic compounds are ubiquitous in biologically relevant molecules. Alkylated pyrazines are found in various natural sources, including coffee beans, cocoa beans, and vegetables and are produced by insects, fungi, and bacteria [26].

The two lowest-energy vibrational modes of the cyanoarenes are typically the out-of-plane and in-plane nitrile bending modes, which are often sufficiently close in energy to observe Coriolis coupling between them at millimeter-wave frequencies. Analysis of the rotational spectra for these vibrational modes for benzonitrile [8, 9], 3-cyanopyridine [10], and 4-cyanopyridine [11] provided highly accurate and precise relative energy values, Table 4.1. The Coriolis coupling and resultant state mixing necessitate that transitions of the vibrational modes are least-squares fit as a Coriolis-coupled dyad. It is this interaction that results in numerous resonant transitions and coupling-allowed, nominal interstate transitions that provide the accurate and precise vibrational energy spacing. Only for benzonitrile have the precise band origins of each mode been measured by high-resolution, infrared spectroscopy [9]. Herein, we report the rotational spectroscopy and analysis of the ground and two lowest-energy fundamentals of cyanopyrazine from 130 to 500 GHz.

**Table 4.1**
Energy differences between out-of-plane and in-plane nitrile bending modes for cyanoarenes

| | out-of-plane | in-plane | $\Delta E$ ($cm^{-1}$) |
|---|---|---|---|
| benzonitrile [8, 9] | $\nu_{22}$, $B_1$ | $\nu_{33}$, $B_2$ | 19.1081701(74) |
| 3-cyanopyridine [10] | $\nu_{30}$, A″ | $\nu_{21}$, A′ | 15.7524693 (37) |
| 4-cyanopyridine [11] | $\nu_{20}$, $B_1$ | $\nu_{30}$, $B_2$ | 18.806554 (11) |

**Experimental Methods**

A commercial sample of cyanopyrazine was used without further purification for all spectroscopic measurements. The rotational spectrum was collected using a millimeter-wave spectrometer that has been previously described [27, 28] in the 130 to 230 and 235 to 360 GHz frequency ranges, in a continuous flow at room temperature, with sample pressures of 3 to 12 mTorr. Additional spectral data were obtained with a newly acquired amplification and multiplication chain that extended the frequency range up to 500 GHz. The separate spectral segments were combined into a single broadband spectrum using Kisiel's Assignment and Analysis of Broadband Spectra (AABS) software [29, 30]. The complete spectrum from 130 to 500 GHz was obtained automatically over approximately nine days given the following experimental parameters: 0.045 kHz frequency increment, 0.6 MHz/sec sweep rate, 10 ms time constant, and 50 kHz AM and 500 kHz FM modulation in a tone-burst design. Pickett's SPFIT/SPCAT [31] were used for least-squares fits and spectral predictions, along with Kisiel's PIFORM, PLANM, and AC programs for analysis [32]. A uniform frequency measurement uncertainty of 0.050 MHz was assumed for all measurements.

**Computational Methods and Results**

Electronic structure calculations were carried out with Gaussian 16 [33] using the WebMO interface [34] to obtain theoretical spectroscopic constants. Optimized geometries at the B3LYP/6-311+(2d,p) and MP2/6-311+(2d,p) levels of theory were obtained using "verytight" convergence criteria and an "ultrafine" integration grid, and subsequent anharmonic vibrational frequency calculations were carried out using 2$^{nd}$ order vibrational perturbation theory (VPT2). All computational output files can be found in the supplemental material.

**Cyanopyrazine Rotational Spectra**

The recently expanded frequency range of our instrument allowed us to measure the spectrum of cyanopyrazine up to 500 GHz, a frequency coverage beyond that used in previous works on cyanoarenes (up to 375 GHz) [8-11]. This is nearly an optimal range for cyanopyrazine at the ambient laboratory temperature (Fig. 4.2), as it covers the most intense transitions based upon the rotational populations. It was additionally advantageous to expand the frequency coverage for the least-squares fitting of $\nu_{27}$ and $\nu_{19}$, due to the $J'' + 1$ values of the most intense transitions of these vibrationally excited states (*vide infra*). The relatively low value of $C_0$ (~1276 MHz) for all cyanopyrazine vibrational states results in the $K_a = 0$ series transition near 130 GHz having a value of $J'' + 1 = 51$ and increasing to $J'' + 1 = 195$ just before 500 GHz. This range of $J'' + 1$ (and the resulting range of $K_a$) quantum numbers provides a wealth of spectroscopic information on the centrifugal distortion and necessitates a high-order Hamiltonian to adequately model the spectrum.

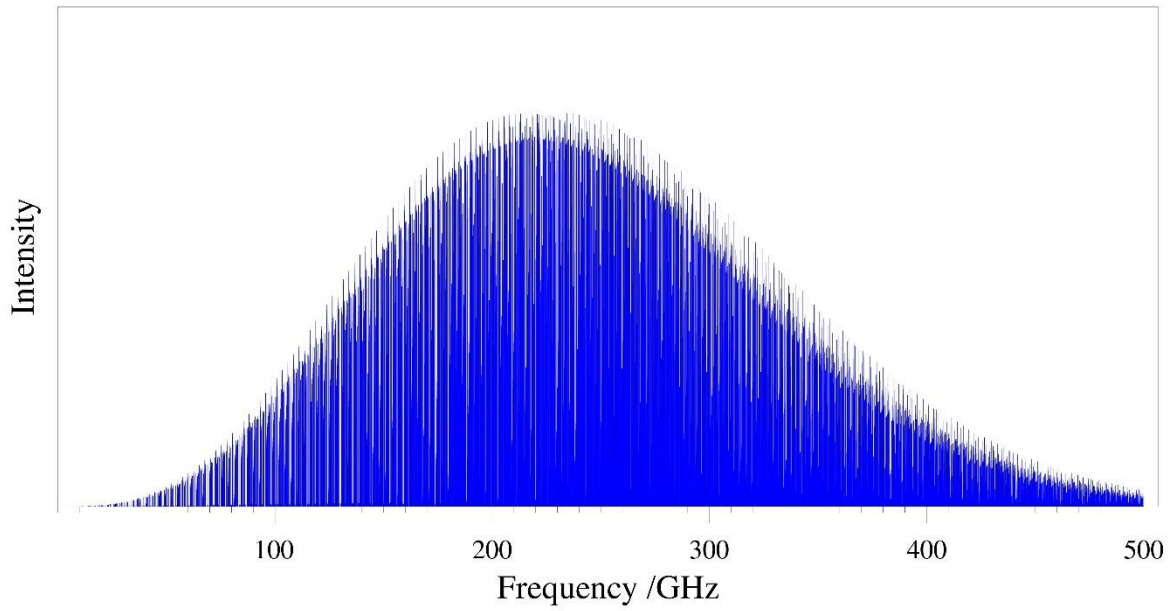


**Fig. 4.2.** Predicted spectrum from SPCAT of the ground vibrational state of cyanopyrazine up to 500 GHz at 292 K.

**Ground-State Spectral Analysis**

The ground-state spectrum of cyanopyrazine (B3LYP $\mu_a$ = 4.2 D , $\mu_b$ = 0.1 D, $\kappa$ = −0.854) has not been reported, despite this benzonitrile analog being commercially available. The strong electron-withdrawing effect of the nitrile group results in a dipole moment nearly coincidental with that substituent (Fig. 4.3) and the *a* principal axis. Due to the asymmetry of the ring caused by the nitrile substitution, there is also a slight *b*-axis dipole component. The large difference in the *a*- and *b*-axis dipole components results in *a*-type transitions that are roughly 2000 times more intense than the *b*-type transitions. As a result, the rotational spectrum of cyanopyrazine is dominated by intense $^{a}R_{0,1}$ transitions across the frequency range (Fig. 4.4). Despite being a prolate molecule, cyanopyrazine and other substituted arenes [8-11, 35] have prominent oblate-type bands, in which transitions in the bands begin at $K_a$ = 0 and increase in $K_a$ as frequency increases. Cyanopyrazine displays prolate-type bands at high $K_a$, though the spacing and intensity make them much less prominent. The much weaker Q-branch transitions could not be observed and assigned for cyanopyrazine owing to the spectral density created by excited vibrational states of cyanopyrazine. Thus, the final transition data set for the ground vibrational state contained only *a*-type, R-branch transitions. As shown in Fig. 4.5, these transitions cover a broad range of quantum numbers, including $J''$ + 1 = 42 to 189 and $K_a$ = 0 to 66. The spectral density and frequency range investigated allowed for the measurement, assignment, and least-squares fitting of 7078 independent transition frequencies to partial octic, A- and S-reduced Hamiltonians with low error ($\sigma_{fit}$ = 34 kHz). The resulting spectroscopic constants are reported in Table 4.2, along with their corresponding computed values. Though several octic terms are required in the A and S reduction least-squares fits, no readily available computational software is able to provide these values for

comparison. Thus, $L_K$ and the off-diagonal octic terms that could not be satisfactorily determined were held at values of zero in the least-squares fitting.

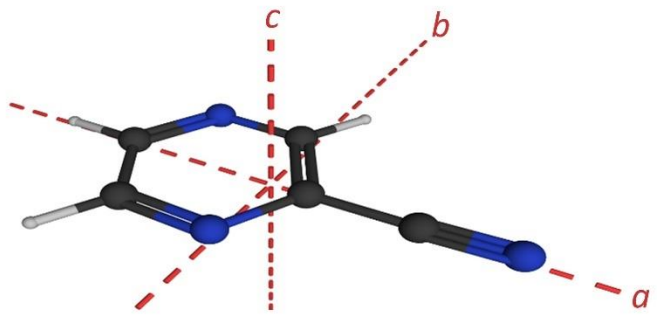


**Fig. 4.3.** Cyanopyrazine ($C_s$, $\mu_a$ = 4.2 D , $\mu_b$ = 0.1 D, B3LYP) structure with principal axes.

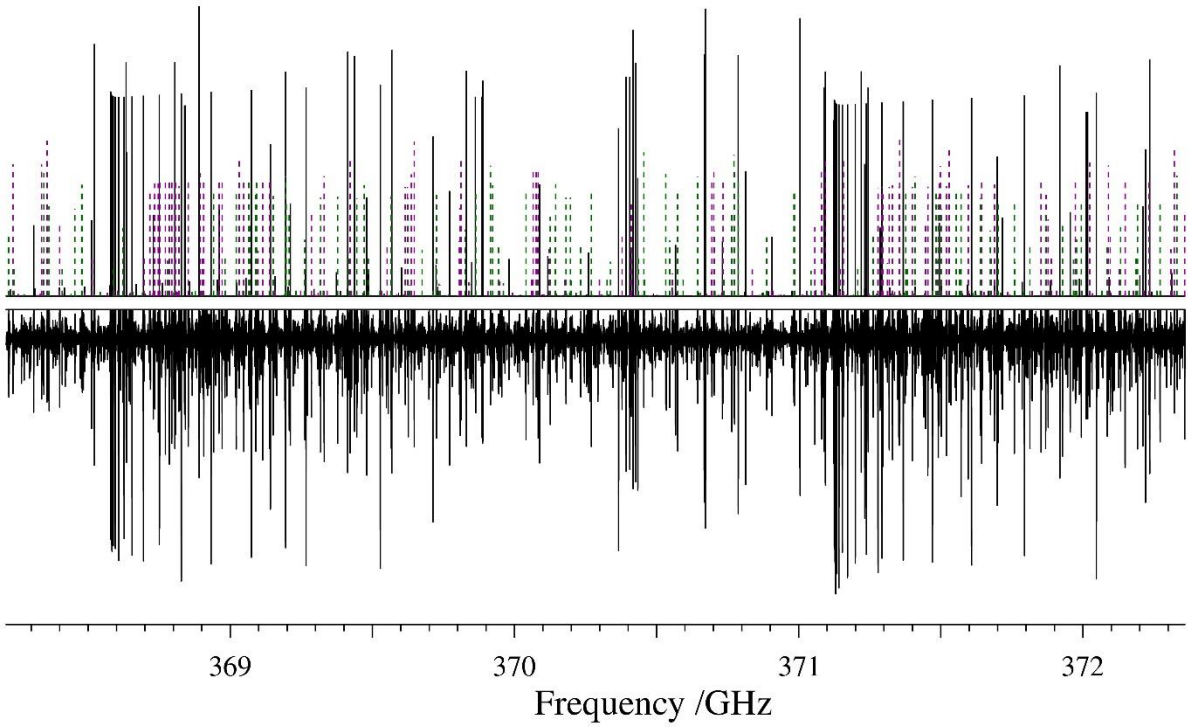


**Fig. 4.4.** Predicted (top) and experimental (bottom) rotational spectra of cyanopyrazine from 368.2 to 372.4 GHz. Ground-state cyanopyrazine with prominent transitions for the $J'' + 1 = 144$ and $J'' + 1 = 145$ bands appear in black. Transitions for $\nu_{27}$ are in purple and transitions for $\nu_{19}$ are in dark green. Unassigned transitions are attributable to other vibrationally excited states of cyanopyrazine.

**Table 4.2**

Experimental and computational spectroscopic constants for the ground vibrational state of cyanopyrazine (S- and A-reduced Hamiltonian, $I^r$ representation)

| S reduction, $I^r$ representation | | | | A reduction, $I^r$ representation | | | |
|---|---|---|---|---|---|---|---|
| | Experimental | B3LYP [a] | MP2 [a] | | Experimental | B3LYP [a] | MP2 [a] |
| $A_0$ (MHz) | 6003.12984 (58) | 6016.1 | 5950.4 | $A_0$ (MHz) | 6003.12822 (58) | 6016.1 | 5950.4 |
| $B_0$ (MHz) | 1621.517450 (24) | 1619.4 | 1605.5 | $B_0$ (MHz) | 1621.518806 (24) | 1619.4 | 1605.5 |
| $C_0$ (MHz) | 1276.428481 (25) | 1276.7 | 1264.1 | $C_0$ (MHz) | 1276.427155 (25) | 1276.7 | 1264.1 |
| $D_J$ (kHz) | 0.0359497 (18) | 0.0348 | 0.0345 | $\Delta_J$ (kHz) | 0.0492594 (19) | 0.0471 | 0.0472 |
| $D_{JK}$ (kHz) | 1.182301 (25) | 1.11 | 1.15 | $\Delta_{JK}$ (kHz) | 1.102415 (24) | 1.04 | 1.07 |
| $D_K$ (kHz) | 0.2897 (13) | 0.317 | 0.282 | $\Delta_K$ (kHz) | 0.3525 (13) | 0.379 | 0.345 |
| $d_1$ (kHz) | −0.01183021 (59) | −0.0112 | −0.0113 | $\delta_J$ (kHz) | 0.01182909 (60) | 0.0112 | 0.0113 |
| $d_2$ (kHz) | −0.00665773 (39) | −0.00616 | −0.00636 | $\delta_K$ (kHz) | 0.702668 (42) | 0.660 | 0.677 |
| $H_J$ (Hz) | −0.000014359 (71) | −0.0000123 | −0.0000135 | $\Phi_J$ (Hz) | 0.000001797 (74) | 0.00000275 | 0.00000306 |
| $H_{JK}$ (Hz) | 0.0013660 (16) | 0.00117 | 0.00129 | $\Phi_{JK}$ (Hz) | 0.0019713 (18) | 0.00170 | 0.00185 |
| $H_{KJ}$ (Hz) | −0.007530 (15) | −0.00646 | −0.00718 | $\Phi_{KJ}$ (Hz) | −0.009803 (15) | −0.00845 | −0.00932 |
| $H_K$ (Hz) | 0.01171 (81) | 0.00594 | 0.00652 | $\Phi_K$ (Hz) | 0.01097 (83) | 0.00738 | 0.00807 |
| $h_1$ (Hz) | 0.000000244 (14) | −0.000000153 | −0.000000148 | $\phi_J$ (Hz) | 0.000001844 (15) | 0.00000129 | 0.00000142 |
| $h_2$ (Hz) | 0.000008265 (11) | 0.00000756 | 0.00000829 | $\phi_{JK}$ (Hz) | 0.0009204 (11) | 0.000864 | 0.000945 |
| $h_3$ (Hz) | 0.0000016326 (42) | 0.00000145 | 0.00000156 | $\phi_K$ (Hz) | 0.009580 (31) | 0.00862 | 0.00925 |
| $L_J$ (mHz) | 0.0000000295 (10) | | | $L_J$ (mHz) | 0.0000000361 (10) | | |
| $L_{JJK}$ (mHz) | −0.000002512 (15) | | | $L_{JJK}$ (mHz) | −0.000002972 (15) | | |
| $L_{JK}$ (mHz) | 0.00002268 (18) | | | $L_{JK}$ (mHz) | 0.00001795 (19) | | |
| $L_{KKJ}$ (mHz) | −0.0001332 (26) | | | $L_{KKJ}$ (mHz) | −0.0001153 (26) | | |
| $L_K$ (mHz) | [0.] | | | $L_K$ (mHz) | [0.] | | |
| $\Delta_i$ (uÅ$^2$) [b, c] | 0.075770 (12) | | | $\Delta_i$ (uÅ$^2$) [b, c] | 0.076419 (12) | | |
| $N_{\text{lines}}$ [d] | 7078 | | | $N_{\text{lines}}$ [d] | 7078 | | |
| $\sigma_{\text{fit}}$ (MHz) | 0.034 | | | $\sigma_{\text{fit}}$ (MHz) | 0.034 | | |

[a] Evaluated with the 6-311+G(2d,p) basis set.

[b] Inertial defect, $\Delta_i = I_c - I_a - I_b$.

[c] Calculated using PLANM from the $B_0$ constants.

[d] Number of fitted transition frequencies.

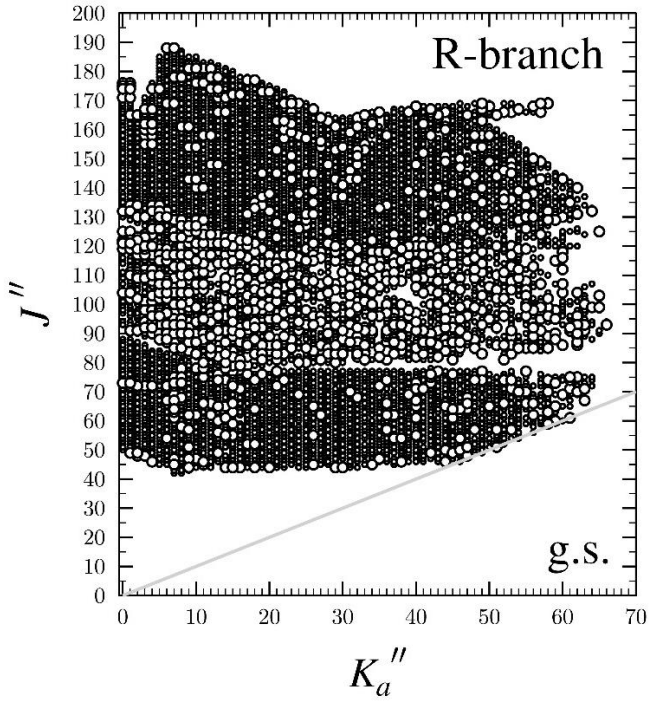


**Fig. 4.5.** Data distribution plot for the least-squares fit of spectroscopic data for the vibrational ground state of cyanopyrazine. The size of the symbol is proportional to the value of $|(f_{obs.} - f_{calc.})/\delta f|$, where $\delta f$ is the frequency measurement uncertainty, and all values are smaller than 3.

The B3LYP computed rotational constants are in excellent agreement with the experimental values, similar to that seen for 3- and 4-cyanopyridine [10, 11]. The largest discrepancy between the experimental and computed rotational constant values is for $A_0$, which is over-estimated by 13 MHz (0.21%). The B3LYP values of $B_0$ and $C_0$ are within 2.1 MHz and 0.3 MHz of their experimental values, respectively. All of the B3LYP quartic centrifugal distortion constants are in good agreement (within 10% of their experimental values) in both reductions. There is much poorer agreement between the computed sextic distortion constants and the experimental values, typically varying from 6 to 30%. Both $\Phi_J$ and $H_K$, however, differ by about 50% from their computed values, while $h_1$ is the wrong sign. At first glance, it appears that the MP2 computed values are worse than their B3LYP counterparts. Though the agreement of the

MP2 values is inferior for the rotational constants, the deviations from the experimental values all remain less than 1%. For nearly all of the remaining spectroscopic constants, the MP2 value is closer to the experimental value than the B3LYP-computed value. All of the MP2 quartic centrifugal distortion constants are within 5% of their experimental values, and all of them show better agreement than the B3LYP values. With regard to the sextic centrifugal distortion constants, the MP2 constant general agreement is between 0.2 and 6%. The exceptions are $\Phi_J$, $\Phi_K$, $\phi_J$, $H_K$, and $h_1$, with large discrepancies of 70%, −26%, −23%, −44%, and −160%, respectively. As with the B3LYP value of $h_1$, its MP2 value has the incorrect sign. Despite the issues with both sets of computed spectroscopic constants, both B3LYP and MP2 values provide *a priori* predictions of the rotational spectrum of cyanopyrazine sufficient to identify and assign its transitions in the experimental spectrum.

**Spectral Analysis of $\nu_{27}$ and $\nu_{19}$**

Similar to other cyanoarenes [8-11], the first two fundamental modes of cyanopyrazine are the out-of-plane and in-plane nitrile bending modes, $\nu_{27}$ and $\nu_{19}$, respectively. These two states form a Coriolis-coupled dyad, which is well separated in energy from the ground state and the next vibrationally excited state, $2\nu_{27}$. The previous low-resolution infrared (IR) spectroscopy of cyanopyrazine provides an assignment of most of the cyanopyrazine vibrational modes [36-39], though there is some ambiguity about the assignment of the modes at 160, 173, and 339 $cm^{-1}$, with both of the lower modes assigned A″ symmetry [38]. The two lowest-energy modes, $\nu_{27}$ (A″) and $\nu_{19}$ (A′), are predicted to have energies of 137 and 167 $cm^{-1}$ (B3LYP) or 136 and 162 $cm^{-1}$ (MP2). It is likely that the mode at 339 $cm^{-1}$, designated A′ in the solution phase IR and Raman vibrational study, is $\nu_{26}$ (A″), but it is not clear whether either of the modes observed at 160 and 173 $cm^{-1}$ are $\nu_{27}$ (A″) or $\nu_{19}$ (A′). As a result of that ambiguity, the vibrational state diagram shown Fig. 4.6. is

based upon the B3LYP fundamental frequencies. The initial predictions for these vibrational states were made based upon the experimental ground-state rotational constants, computational vibration-rotation interaction constants, and the ground-state centrifugal distortion constants. After initial measurement, assignment, and least-squares fitting of these fundamental states, it became clear that a single-state Hamiltonian was insufficient to model their rotational spectra. To address this problem, a Coriolis-coupled dyad Hamiltonian was employed similar to our previous works [8-11, 35, 40, 41]. The A″ and A′ symmetries of these states allows both *a*- and *b*-axis Coriolis coupling. Thus initially, computed $G_a$, $G_b$, and $\Delta E_{27,19}$ values were added to the least-squares fit. As transitions were added to the fit, these parameters were allowed to vary, and additional parameters were included until the available transitions could be modeled adequately. The breadth of transitions is shown in Fig. 4.7, and the resulting spectroscopic constants are provided in Table 4.3.

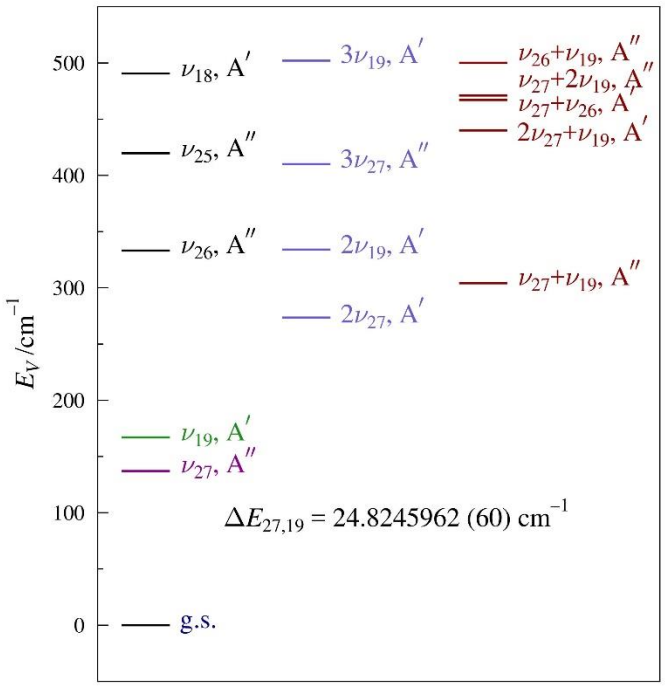


**Fig. 4.6.** Vibrational energy levels of cyanopyrazine below 500 cm$^{-1}$ from computed fundamental frequencies (B3LYP/6-311+G(2d,p)). The value of $\Delta E_{27,19}$ results from the experimental perturbation analysis of $\nu_{27}$ and $\nu_{17}$ in this work (*vide infra*).

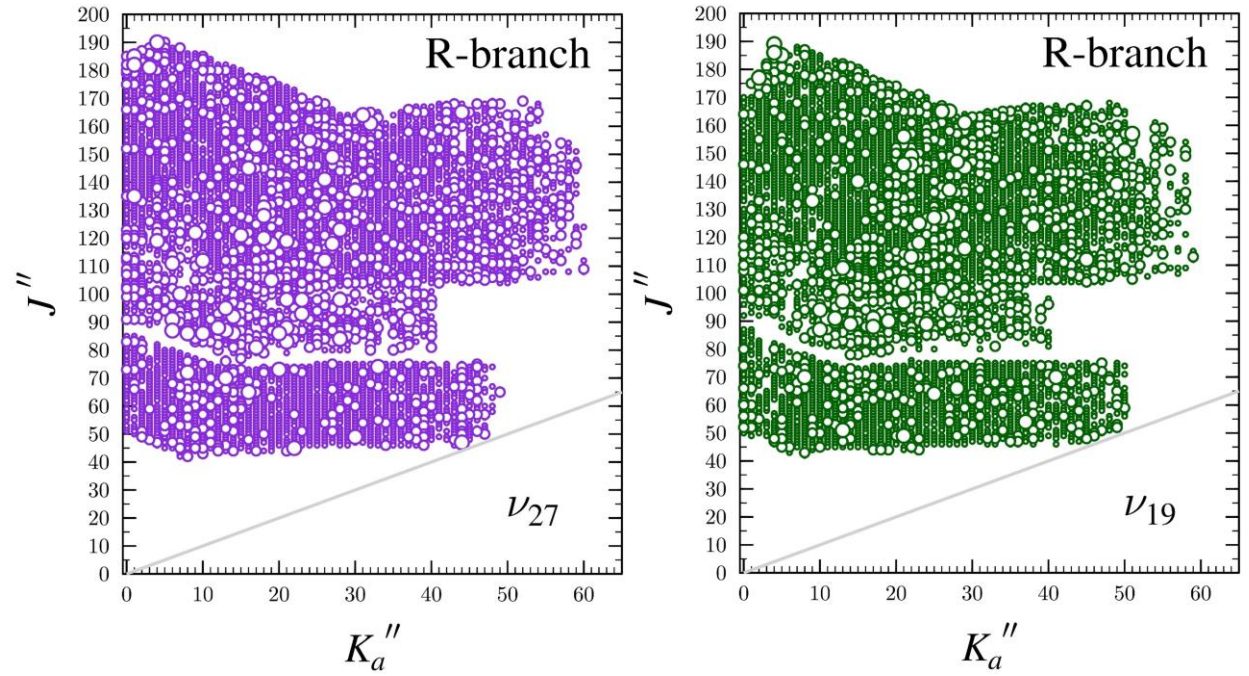


**Fig. 4.7** Data distribution plots for the least-squares fit of spectroscopic data for the lowest-energy fundamental states of cyanopyrazine, $\nu_{27}$ (purple) and $\nu_{19}$ (dark green). The size of the symbol is proportional to the value of $|(f_{obs.} - f_{calc.})/\delta f|$, where $\delta f$ is the frequency measurement uncertainty, and all values are smaller than 3.

**Table 4.3**

Experimentally determined parameters for the ground state and vibrationally excited states $\nu_{27}$ and $\nu_{19}$ of cyanopyrazine (A-reduced Hamiltonian, $I^r$ representation).

| | ground state [a] | $\nu_{27}$ (A″, 136 cm$^{-1}$) [a,b] | $\nu_{19}$ (A′, 162 cm$^{-1}$) [a,b] |
|---|---|---|---|
| $A_v$ (MHz) | 6003.12822 (58) | 6026.492 (18) | 5977.166 (18) |
| $B_v$ (MHz) | 1621.518806 (24) | 1623.29554 (16) | 1624.75111 (17) |
| $C_v$ (MHz) | 1276.427155 (25) | 1278.422236 (28) | 1277.400270 (27) |
| $\Delta_J$ (kHz) | 0.0492594 (19) | 0.05013381 (98) | 0.0504064 (10) |
| $\Delta_{JK}$ (kHz) | 1.102415 (24) | 1.12777 (17) | 1.05278 (17) |
| $\Delta_K$ (kHz) | 0.3525 (13) | 0.3421 (28) | 0.4081 (42) |
| $\delta_J$ (kHz) | 0.01182909 (60) | 0.01191174 (61) | 0.01227503 (66) |
| $\delta_K$ (kHz) | 0.702668 (42) | 0.704032 (38) | 0.706581 (29) |
| $\Phi_J$ (Hz) | 0.000001797 (74) | 0.000002534 (20) | 0.000002850 (20) |
| $\Phi_{JK}$ (Hz) | 0.0019713 (18) | 0.0020104 (37) | 0.0018932 (37) |
| $\Phi_{KJ}$ (Hz) | −0.009803 (15) | −0.0104488 (91) | −0.008731 (12) |
| $\Phi_K$ (Hz) | 0.01097 (83) | 0.00672 (61) | 0.00602 (53) |
| $\phi_J$ (Hz) | 0.000001844 (15) | 0.000002043 (12) | 0.000002359 (14) |
| $\phi_{JK}$ (Hz) | 0.0009204 (11) | [0.0009204] | [0.0009204] |
| $\phi_K$ (Hz) | 0.009580 (31) | [0.009580] | [0.009580] |
| $\Delta E_{27,19}$ (MHz) | | 744222.67 (18) | |
| $\Delta E_{27,19}$ (cm$^{-1}$) | | 24.8245962 (60) | |
| $G_a$ (MHz) | | 10789.33 (63) | |
| $G_a^J$ (MHz) | | −0.0052515 (62) | |
| $G_a^K$ (MHz) | | −0.029393 (77) | |
| $G_a^{JJ}$ (MHz) | | 0.00000000517 (11) | |
| $F_{bc}^K$ (MHz) | | −0.00001287 (20) | |
| $G_b$ (MHz) | | −134.02 (45) | |
| $G_b^J$ (MHz) | | 0.0000378 (12) | |
| $F_{ac}$ (MHz) | | −1.079 (12) | |
| $\Delta_i$ (uÅ$^2$) [c] | | 0.012604 (26) | 0.02917 (26) |
| $N_{\text{lines}}$ [e] | | 6257 | 5893 |
| $\sigma_{\text{fit}}$ (MHz) | | 0.038 | 0.037 |

[a] Octic centrifugal distortion constants not shown and held constant at their ground-state values in Table 4.2.
[b] Fundamental frequencies calculated using MP2/6-311+G(2d,p).
[c] Inertial defect, $\Delta_i = I_c - I_a - I_b$.
[d] Calculated using PLANM from the $B_0$ constants.
[e] Number of fitted transition frequencies.

The final least-squares fit of the Coriolis-coupled dyad ($\nu_{27}$ and $\nu_{19}$) contained over 12,000 transitions, including many transitions involving energy levels perturbed by the coupling, many intensely shifted resonant transitions created by nearly degenerate energy levels of $\nu_{27}$ and $\nu_{19}$, and 37 formally forbidden, coupling-allowed, nominal interstate transitions. Due to the intensity of the transitions for each vibrationally excited state, the numbers of transitions for each state in the final data set for $\nu_{27}$ and $\nu_{19}$ (6256 and 5871, respectively) are decreased only slightly from that of the ground state (7078). In the frequency range studied, the observed transitions range from 42 to 191 in $J'' + 1$ and from 0 to 60 in $K_a$. As many of the more intense resonant transitions and nominal interstate transitions occur beyond 360 GHz, obtaining a satisfactory least-squares fit necessitated extending the measured spectral range up to 500 GHz, which had not been necessary in previous works on analogous species [8-11]. The need for higher frequency can be attributed to the larger experimental energy difference between the coupled states, relative to the previously studied compounds (Table 4.1). In cyanopyrazine, the energy separation between $\nu_{27}$ and $\nu_{19}$ (24.8245962 (60) $cm^{-1}$) requires higher values of $J$ and $K$ for the energy levels of $\nu_{27}$ to approach those of $\nu_{19}$ closely enough to create resonances (*vide infra*). It is important to note that this energy difference varies substantially from the frequencies reported for the two lowest-energy fundamentals in the previously reported low-resolution IR and Raman spectroscopic data [38] of 173 and 160 $cm^{-1}$ casting doubt on the previous liquid-phase IR assignments. In addition to determining a highly accurate and precise $\Delta E_{27,19}$ value, the least-squares fit provides a nearly complete set of spectroscopic constants of a sextic centrifugally distorted, A-reduced Hamiltonian (excluding the off-diagonal terms $\phi_{JK}$ and $\phi_K$) and eight Coriolis-coupling coefficients ($G_a$, $G_a^J$, $G_a^K$, $G_a^{JJ}$, $F_{bc}^K$, $G_b$, $G_b^J$, and $F_{ac}$). Attempts to include $F_{bc}$ in the least-squares fit were made, but were not successful.

In view of that, we found it surprising that $F_{bc}^{K}$ was necessary to achieve a reasonable fit and could be well determined.

The computed spectroscopic constants $B_v$ and $C_v$ are in quite close agreement with their experimentally determined values (Table 4.4). At both the MP2 and B3LYP levels, the predicted vibration-rotation interaction constants ($B_0 - B_v$) differ by less than 10% from their experimental values, with the MP2 values in slightly closer agreement than the B3LYP values. The very close agreement seen for the $B_0 - B_v$ values provides evidence that the deperturbation of the constants in the computational results and the treatment of the Coriolis-coupling were both reasonably effective. For the $A_0 - A_v$ values, however, there is a very large discrepancy between the computed and experimental values. At both levels of theory, the magnitudes of the $A_0 - A_v$ values are computed to be five or six times larger than the experimental values. This is largely due to residual untreated Coriolis-coupling in the computed values, given the very large magnitudes of the values and the smaller magnitudes of the experimental $A_0 - A_v$ values in this and similar works. The B3LYP-predicted values are slightly closer to the experimental ones than the MP2 values, in this case. Given the fairly large experimental $A_0 - A_v$ values, it is possible that they also retain untreated Coriolis coupling, though to a much lesser extent than the computed values. The MP2 $\Delta E_{27,19}$ value of 26.4 $cm^{-1}$ is in excellent agreement with the very precise experimental value, while the B3LYP value is an overestimate by 6 $cm^{-1}$. The Coriolis $\zeta_{27,19}^{x}$ values show very good agreement between theory and experiment at the B3LYP and MP2 levels of theory, which, combined with the low $\sigma_{fit}$ value, indicates a satisfactory treatment of the *a*-axis and *b*-axis Coriolis coupling in the least-squares fit.

**Table 4.4.** Vibration-rotation interaction and Coriolis-coupling constants of cyanopyrazine.

| | Experimental | B3LYP [a] | MP2 [a] |
|---|---|---|---|
| $A_0 - A_{27}$ (MHz) | −23.364 (18) | 112.0 | 138.7 |
| $B_0 - B_{27}$ (MHz) | −1.77673 (17) | −1.71 | −1.66 |
| $C_0 - C_{27}$ (MHz) | −1.995081 (37) | −1.97 | −1.92 |
| $A_0 - A_{19}$ (MHz) | 25.962 (18) | −109.5 | −136.4 |
| $B_0 - B_{19}$ (MHz) | −3.23230 (17) | −3.07 | −3.18 |
| $C_0 - C_{19}$ (MHz) | −0.973115 (37) | −0.90 | −0.95 |
| $\frac{(A_0-A_{27})+(A_0-A_{19})}{2}$ (MHz) | 1.299 (13) | 1.29 | 1.14 |
| $\frac{(B_0-B_{27})+(B_0-B_{19})}{2}$ (MHz) | −2.50452 (12) | −2.39 | −2.42 |
| $\frac{(C_0-C_{27})+(C_0-C_{19})}{2}$ (MHz) | −1.484098 (26) | −1.43 | −1.44 |
| $\lvert\zeta^a_{27,19}\rvert$ | 0.899 | 0.804 | 0.808 |
| $\lvert\zeta^b_{27,19}\rvert$ | 0.0413 | 0.036 | 0.037 |
| $\Delta E_{27,19}$ (cm$^{-1}$) | 24.8245962 (60) | 30.6 | 26.4 |

[a] Evaluated with the 6-311+G(2d,p) basis set.

Further evidence of an adequate treatment of the dyad by the Hamiltonian model is the ability to include many resonant and nominal interstate transitions in the data set, whose prediction is heavily dependent on the $\Delta E_{27,19}$ value and Coriolis-coupling constants. Sharp *a*-type and *b*-type resonances are observed due to mixing of $\nu_{27}$ and $\nu_{19}$ energy levels that are nearly degenerate, as shown in Fig. 4.8. A "minus" superscript on the $K_a$ value indicates that $K_a + K_c = J + 1$, whereas a "plus" superscript indicates that $K_a + K_c = J$. At $J'' + 1 = 157$, there is an intense *a*-type resonance between $\nu_{27}$ and $\nu_{19}$ with a $\Delta K_a = 2$ selection rule. The resonant transitions are displaced from their unperturbed transition frequencies by about 1.5 GHz. There are additional small resonances in the $K_a = 16^-$ series of $\nu_{19}$ that correspond to resonances in different $\nu_{27}$ series. Each of these series displays the large undulations due to centrifugal distortion and Coriolis coupling between these states. Figure 4.9 shows how these resonances and undulations progress across the $K_a^+$ series of $\nu_{27}$. The undulations and resonances become more pronounced and move to progressively higher $J''+1$ values as a function of $K_a$. While it is generally possible to obtain quartic distortion

constants and preliminary values of the energy difference and Coriolis-coupling constants from the undulations, many local resonances are often needed to obtain precise determinations of these constants. The resonance progression plot shows that, for cyanopyrazine, most of the intense resonances occur after $J'' + 1 = 100$, reiterating the importance of obtaining the higher-frequency data (360 – 500 GHz) used in this work.

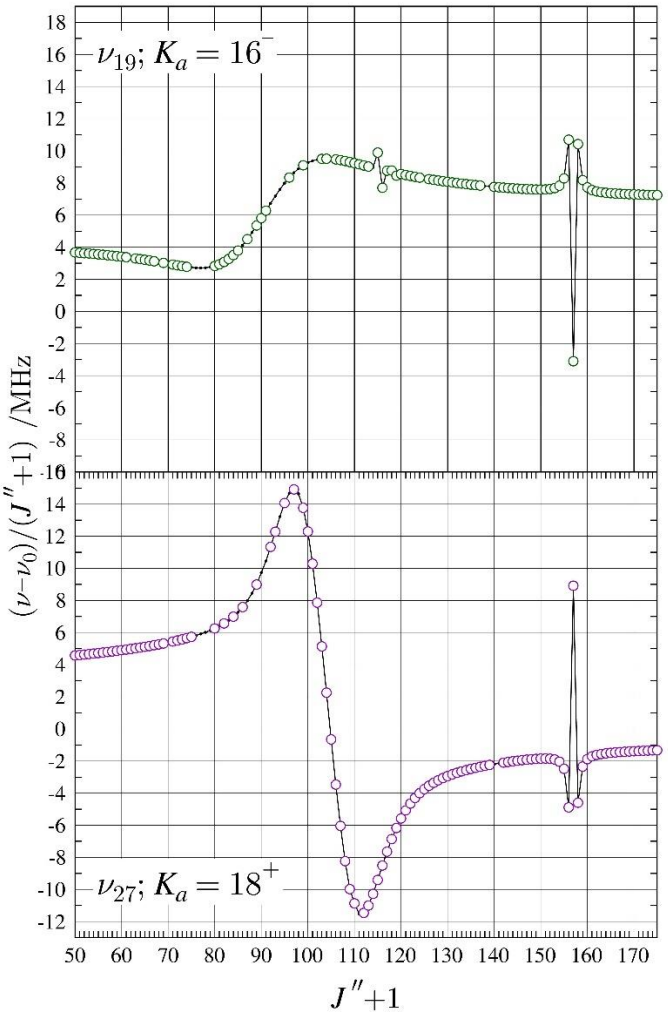


**Fig. 4.8.** Resonance plots for cyanopyrazine showing the $K_a$ = 16⁻ series for $\nu_{19}$ and $K_a$ = 18⁺ series for $\nu_{27}$. These two resonances conform to the $\Delta K_a = 2$ selection rule for *a*-type resonances. The plotted values are frequency differences between excited-state transitions and their ground-state counterparts, scaled by $(J''+1)$ in order to make the plots more horizontal. Measured transitions are represented by circles: $\nu_{27}$ (purple), $\nu_{17}$ (green). Predictions from the final coupled fit are represented by a solid, colored line.

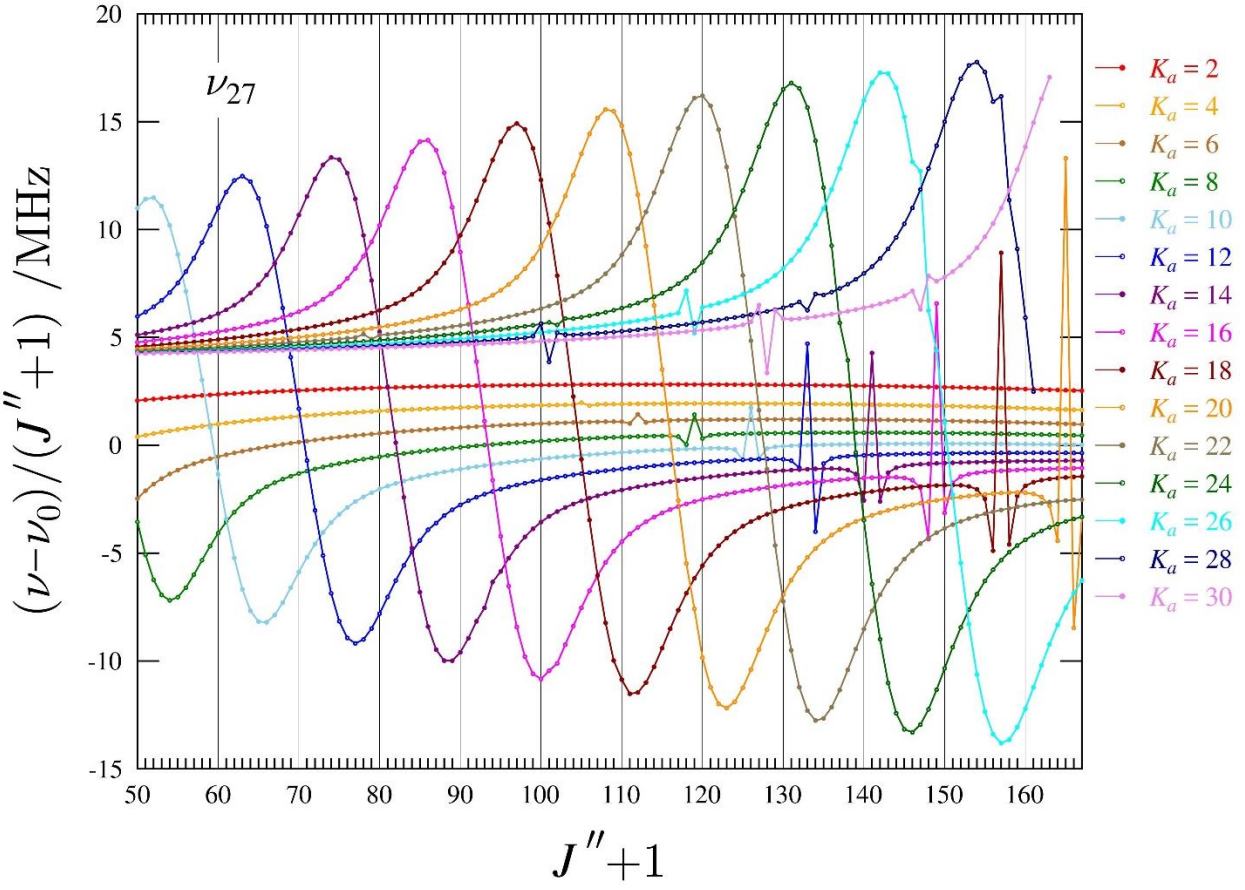


**Fig. 4.9.** Superimposed resonance plots of $\nu_{27}$ for ${}^{a}R_{0,1}$ even-$K_a^+$ series from 2 to 30 for cyanopyrazine. Measured transitions are omitted for clarity, but they are indistinguishable from the plotted values on this scale. The plotted values are frequency differences between excited-state transitions and their ground-state counterparts, scaled by ($J''$ + 1).

Two additional types of transitions are observed in the excited-state spectra of cyanopyrazine that are made possible by the coupling of the fundamental states: *b*-type transitions that are more intense than they would be due purely to the *b*-axis dipole moment and nominal interstate transitions. As observed with cyanocyclobutene [41], the state mixing of $\nu_{27}$ and $\nu_{19}$ allows intensity transfer from *a*-type transitions to *b*-type transitions. In this case, *b*-type transitions observed for each vibrationally excited state, unlike cyanocyclobutene where they were

only observed in $\nu_{17}$. The result is that there are many *b*-type, R-branch transitions assigned, measured, and least-squares fit for the dyad despite the very small $\mu_b$ (approximately 42 times smaller than $\mu_a$). Formally forbidden, nominal interstate rotational transitions are observable from the energy levels with the most intense state-mixing. They share at least one energy level with a transition involved in a resonance and borrow intensity from those resonant transitions. In some cases, the intensity borrowing is so profound that the intrastate resonant transitions have vanishingly small intensities and cannot be observed. In other cases, such as the one highlighted in Fig. 4.10, all four transitions (two intrastate resonant transitions and two interstate transitions) can be observed and included in the least-squares fit. Since the four transitions involve the same four energy levels, the average of the nominal interstate frequencies should be the same as that of the intrastate frequencies. For the particular set depicted in Fig. 4.10, the averages differ by only 25 kHz, giving confidence in their assignment and in the dyad least-squares fit overall. The inclusion of the many *b*-type transitions and the nominal interstate transitions provides a substantial constraint on the $\Delta E_{27,19}$ value and Coriolis-coupling constants. As a result, we are confident that the spectroscopic constants provided are well-determined and likely to be physically meaningful and predictive beyond the studied frequency range.

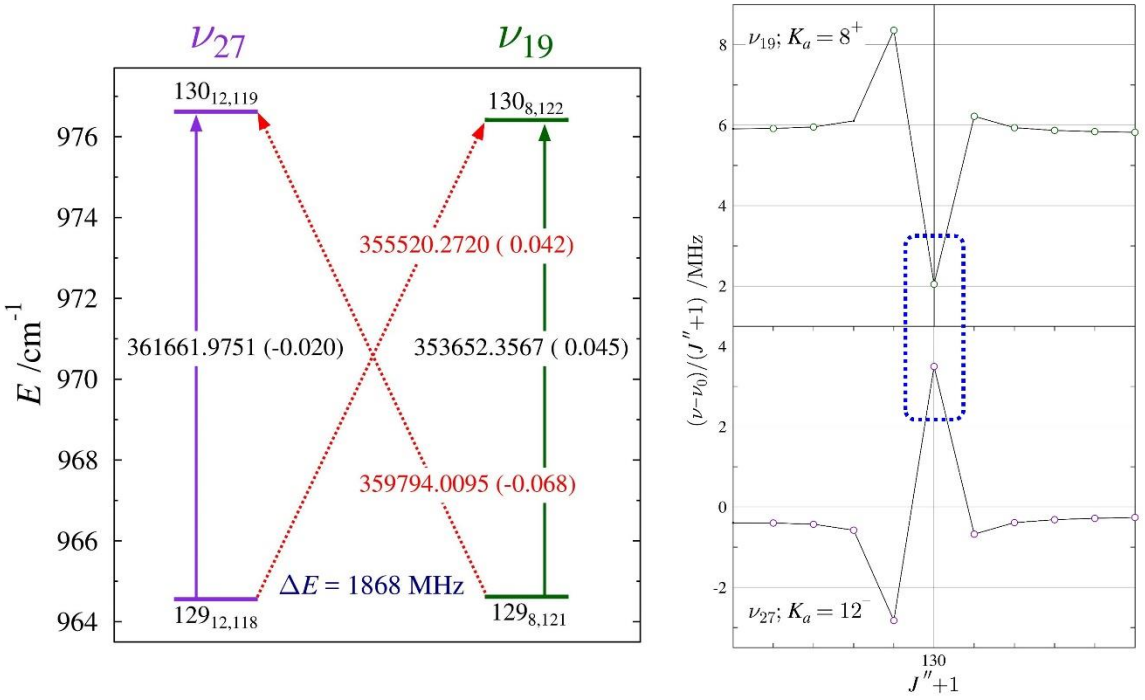


**Fig. 4.10.** Energy diagram (left) depicting a representative matched pair of nominal interstate transitions between the $\nu_{27}$ (purple) and $\nu_{19}$ (dark green) vibrational states of cyanopyrazine. Standard $^aR_{0,1}$ transitions within vibrational states are denoted by vertical arrows. The diagonal, dashed arrows indicate nominal interstate transitions that are formally forbidden, but enabled as a result of rotational energy level mixing. Values printed on each of the arrows are the corresponding transition frequency (in MHz) with its *obs.* – *calc.* value in parentheses. The marked energy separation is between the two strongly interacting rotational energy levels. Resonance plots (right) of the $K_a$ series of $\nu_{27}$ and $\nu_{19}$ that contain the corresponding resonant transitions identified with a blue box.

## Conclusion

The transition frequencies and spectroscopic constants for cyanopyrazine, presented in this work, provide the necessary laboratory data for future astronomical searches for this potential pyrazine tracer. Combined with computed or experimental nuclear quadrupole coupling constants the spectroscopic constants should reliably predict transition frequencies to much lower or slightly higher frequencies for the ground and two lowest-energy fundamentals. While this work provides the precise and accurate energy separation between vibrational modes $\nu_{27}$ and $\nu_{19}$, high-resolution

infrared spectroscopy or other spectroscopy that would provide a direct measurement of the frequency of either $\nu_{27}$ and $\nu_{19}$ is needed to determine both fundamental frequencies. This would be somewhat challenging due to the low predicted intensities of $\nu_{27}$ and $\nu_{19}$, 1.5 and 0.4 km/mol (MP2), respectively. Such an investigation would also resolve the ambiguity concerning the proper assignment of these two modes from the previous low-resolution infrared study. A high-resolution infrared study would further provide the necessary information to begin to address the complex set of interacting vibrationally excited states higher in energy than $\nu_{27}$ and $\nu_{19}$. The two-quanta states of $\nu_{27}$ and $\nu_{19}$ are expected to form a complicated tetrad of states with $\nu_{26}$ (0.8 km/mol, MP2), as shown in Fig. 4.6. Although the mm-wave intensities of these states are expected to strong enough to readily observe their spectra and many perturbation constants can be predicted by scaling the coupling constants between $\nu_{27}$ and $\nu_{19}$ by a factor of $\sqrt{2}$, achieving a satisfactory least-squares fit will still be a challenging endeavor.

**Acknowledgments**

We gratefully acknowledge funding from the U.S. National Science Foundation for support of this project (CHE-1664912 and CHE-1954270). We thank Michael McCarthy for the loan of an amplification-multiplication chain and the Harvey Spangler Award (to B.J.E.) for support of the purchase of the corresponding zero-bias detector.

**Declarations of Competing Interest: none**

**Supplementary material**

Supplementary data associated with this article can be found, in the online version, at https://doi.org/10.1016/j.jms.2022.111703.

**References**

[1] J. Cernicharo, A.M. Heras, A.G.G.M. Tielens, J.R. Pardo, F. Herpin, M. Guélin, L.B.F.M. Waters, Infrared Space Observatory's Discovery of $C_4H_2$, $C_6H_2$, and Benzene in CRL 618, Astrophys. J. 546(2) (2001) L123-L126.
[2] S.T. Ridgway, D.N.B. Hall, S.G. Kleinmann, D.A. Weinberger, R.S. Wojslaw, Circumstellar acetylene in the infrared spectrum of IRC +10° 216, Nature 264(5584) (1976) 345-346.
[3] B.A. McGuire, A.M. Burkhardt, S.V. Kalenskii, C.N. Shingledecker, A.J. Remijan, E. Herbst, M.C. McCarthy, Detection of the Aromatic Molecule Benzonitrile (*c*-$C_6H_5CN$) in the Interstellar Medium, Science 359(6372) (2018) 202-205.
[4] B.A. McGuire, A. Loomis Ryan, A.M. Burkhardt, K. Lee Kin Long, C.N. Shingledecker, S.B. Charnley, I.R. Cooke, M.A. Cordiner, E. Herbst, S. Kalenskii, M.A. Siebert, E.R. Willis, C. Xue, A.J. Remijan, M.C. McCarthy, Detection of two interstellar polycyclic aromatic hydrocarbons via spectral matched filtering, Science 371(6535) (2021) 1265-1269.
[5] M.C. McCarthy, B.A. McGuire, Aromatics and Cyclic Molecules in Molecular Clouds: A New Dimension of Interstellar Organic Chemistry, J. Phys. Chem. A 125(16) (2021) 3231-3243.
[6] H.S.P. Müller, F. Schlöder, J. Stutzki, G. Winnewisser, The Cologne Database for Molecular Spectroscopy, CDMS: a Useful Tool for Astronomers and Spectroscopists, J. Mol. Struct. 742(1–3) (2005) 215-227.
[7] H.S.P. Müller, S. Thorwirth, D.A. Roth, G. Winnewisser, The Cologne Database for Molecular Spectroscopy, CDMS, Astron. Astrophys. 370(3) (2001) L49-L52.
[8] M.A. Zdanovskaia, B.J. Esselman, H.S. Lau, D.M. Bates, R.C. Woods, R.J. McMahon, Z. Kisiel, The 103–360 GHz rotational spectrum of benzonitrile, the first interstellar benzene derivative detected by radioastronomy, J. Mol. Spectrosc. 351 (2018) 39-48.
[9] M.A. Zdanovskaia, M.-A. Martin-Drumel, Z. Kisiel, O. Pirali, B.J. Esselman, R.C. Woods, R.J. McMahon, The eight lowest-energy vibrational states of benzonitrile: analysis of Coriolis and Darling-Dennison couplings by millimeter-wave and far-infrared spectroscopy, J. Mol. Spectrosc. 383 (2022) 111568.
[10] P.M. Dorman, B.J. Esselman, R.C. Woods, R.J. McMahon, An analysis of the rotational ground state and lowest-energy vibrationally excited dyad of 3-cyanopyridine: Low symmetry reveals rich complexity of perturbations, couplings, and interstate transitions, J. Mol. Spectrosc. 373 (2020) 111373.
[11] P.M. Dorman, B.J. Esselman, J.E. Park, R.C. Woods, R.J. McMahon, Millimeter-wave spectrum of 4-cyanopyridine in its ground state and lowest-energy vibrationally excited states, $\nu_{20}$ and $\nu_{30}$, J. Mol. Spectrosc. 369 (2020) 111274.
[12] D. McNaughton, M.K. Jahn, M.J. Travers, D. Wachsmuth, P.D. Godfrey, J.-U. Grabow, Laboratory rotational spectroscopy of cyano substituted polycyclic aromatic hydrocarbons, Mon. Not. R. Astron. Soc. 476(4) (2018) 5268-5273.
[13] P.M. Dorman, B.J. Esselman, R.C. Woods, R.J. McMahon, Unpublished work, (2022).
[14] H.H. Smith, B.J. Esselman, R.C. Woods, R.J. McMahon, Unpublished work, (2022).
[15] W. Werner, H. Dreizler, H.D. Rudolph, Zum Mikrowellenspektrum des Pyridazins, Z. Naturforsch. A 22(4) (1967) 531-543.
[16] G.L. Blackman, R.D. Brown, F.R. Burden, The microwave spectrum, dipole moment, and nuclear quadrupole coupling constants of pyrimidine, J. Mol. Spectrosc. 35(3) (1970) 444-454.

[17] T.J. Barnum, M.A. Siebert, K.L.K. Lee, R.A. Loomis, P.B. Changala, S.B. Charnley, M.L. Sita, C. Xue, A.J. Remijan, A.M. Burkhardt, B.A. McGuire, I.R. Cooke, A Search for Heterocycles in GOTHAM Observations of TMC-1, J. Phys. Chem. A (2022).
[18] E.E. Etim, R.O.A. Adelagun, C. Andrew, O. Enock Oluwole, Optimizing the searches for interstellar heterocycles, Adv. Space Res. 68(8) (2021) 3508-3520.
[19] S.B. Charnley, Y.-J. Kuan, H.-C. Huang, O. Botta, H.M. Butner, N. Cox, D. Despois, P. Ehrenfreund, Z. Kisiel, Y.-Y. Lee, A.J. Markwick, Z. Peeters, S.D. Rodgers, Astronomical searches for nitrogen heterocycles, Adv. Space Res. 36(2) (2005) 137-145.
[20] Y.-J. Kuan, C.-H. Yan, S.B. Charnley, Z. Kisiel, P. Ehrenfreund, H.-C. Huang, A search for interstellar pyrimidine, Mon. Not. R. Astron. Soc. 345 (2003) 650-656.
[21] M. Nabavian, R. Sabbah, R. Chastel, M. Laffitte, Thermodynamique de composés azotés-II.—Étude thermochimique des acides aminobenzoïques, de la pyrimidine, de l'uracile et de la thymine, J. Chim. Phys. 74 (1977) 115-126.
[22] J. Tjebbes, The heats of combustion and formation of the three diazines and their resonance energies, Acta Chem. Scand. 16(4) (1962) 916-921.
[23] Z.N. Heim, B.K. Amberger, B.J. Esselman, J.F. Stanton, R.C. Woods, R.J. McMahon, Molecular structure determination: Equilibrium structure of pyrimidine (*m*-$C_4H_4N_2$) from rotational spectroscopy ($r_e^{SE}$) and high-level ab initio calculation ($r_e$) agree within the uncertainty of experimental measurement, J. Chem. Phys. 152(10) (2020) 104303.
[24] S. Akavipat, C.F. Su, R.L. Cook, Microwave spectra of chloropyrazine, J. Mol. Spectrosc. 111(1) (1985) 209-210.
[25] P.M. Higgins, B.J. Esselman, M.A. Zdanovskaia, R.C. Woods, R.J. McMahon, Millimeter-wave spectroscopy of the chlorine isotopologues of chloropyrazine and twenty-two of their vibrationally excited states, J. Mol. Spectrosc. 364 (2019) 111179.
[26] F.B. Mortzfeld, C. Hashem, K. Vranková, M. Winkler, F. Rudroff, Pyrazines: Synthesis and Industrial Application of these Valuable Flavor and Fragrance Compounds, Biotechnol. J. 15(11) (2020) 2000064.
[27] B.K. Amberger, B.J. Esselman, J.F. Stanton, R.C. Woods, R.J. McMahon, Precise Equilibrium Structure Determination of Hydrazoic Acid ($HN_3$) by Millimeter-wave Spectroscopy, J. Chem. Phys. 143(10) (2015) 104310.
[28] B.J. Esselman, B.K. Amberger, J.D. Shutter, M.A. Daane, J.F. Stanton, R.C. Woods, R.J. McMahon, Rotational Spectroscopy of Pyridazine and its Isotopologs from 235-360 GHz: Equilibrium Structure and Vibrational Satellites, J. Chem. Phys. 139 (2013) 224304.
[29] Z. Kisiel, L. Pszczółkowski, B.J. Drouin, C.S. Brauer, S. Yu, J.C. Pearson, I.R. Medvedev, S. Fortman, C. Neese, Broadband rotational spectroscopy of acrylonitrile: Vibrational energies from perturbations, J. Mol. Spectrosc. 280 (2012) 134-144.
[30] Z. Kisiel, L. Pszczółkowski, I.R. Medvedev, M. Winnewisser, F.C. De Lucia, E. Herbst, Rotational spectrum of *trans–trans* diethyl ether in the ground and three excited vibrational states, J. Mol. Spectrosc. 233(2) (2005) 231-243.
[31] H.M. Pickett, The fitting and prediction of vibration-rotation spectra with spin interactions, J. Mol. Spectrosc. 148(2) (1991) 371-377.
[32] Z. Kisiel, PROSPE - Programs for ROtational SPEctroscopy, 2020. http://info.ifpan.edu.pl/~kisiel/prospe.htm. (Accessed 07-11-2020.
[33] M.J. Frisch, G.W. Trucks, H.B. Schlegel, G.E. Scuseria, M.A. Robb, J.R. Cheeseman, G. Scalmani, V. Barone, G.A. Petersson, H. Nakatsuji, X. Li, M. Caricato, A.V. Marenich, J. Bloino,

B.G. Janesko, R. Gomperts, B. Mennucci, H.P. Hratchian, J.V. Ortiz, A.F. Izmaylov, J.L. Sonnenberg, D. Williams-Young, F. Ding, F. Lipparini, F. Egidi, J. Goings, B. Peng, A. Petrone, T. Henderson, D. Ranasinghe, V.G. Zakrzewski, J. Gao, N. Rega, G. Zheng, W. Liang, M. Hada, M. Ehara, K. Toyota, R. Fukuda, J. Hasegawa, M. Ishida, T. Nakajima, Y. Honda, O. Kitao, H. Nakai, T. Vreven, K. Throssell, J.A. Montgomery, Jr. , J.E. Peralta, F. Ogliaro, M.J. Bearpark, J.J. Heyd, E.N. Brothers, K.N. Kudin, V.N. Staroverov, T.A. Keith, R. Kobayashi, J. Normand, K. Raghavachari, A.P. Rendell, J.C. Burant, S.S. Iyengar, J. Tomasi, M. Cossi, J.M. Millam, M. Klene, C. Adamo, R. Cammi, J.W. Ochterski, R.L. Martin, K. Morokuma, O. Farkas, J.B. Foresman, D.J. Fox, Gaussian 16 rev C.01, Gaussian, Inc., Wallingford, CT, USA, 2016.

[34] J.R. Schmidt, W.F. Polik, WebMO Enterprise, version 19.0; WebMO LLC: Madison, WI, USA, 2019; http://www.webmo.net (accessed August, 2019).

[35] M.A. Zdanovskaia, B.J. Esselman, R.C. Woods, R.J. McMahon, The 130–370 GHz rotational spectrum of phenyl isocyanide ($C_6H_5NC$), J. Chem. Phys. 151(2) (2019) 024301.

[36] H. Shindo, Studies on the Infrared Spectra of Heterocyclic Compound. VIII. Infrared Spectra of Substituted Pyrazines and their *N*-Oxides, Chem. Pharm. Bull. 8(1) (1960) 33-45.

[37] J. Bus, T.J. Liefkens, W. Schwaiger, Infrared spectrometry of pyrazines, Recl. Trav. Chim. Pays-Bas 92(1) (1973) 123-6.

[38] M.J.M. Delgado, F. Márquez, M.I. Suero, J.I. Marcos, Vibrational spectra of pyrazincarbonitrile and [$^{15}$N]pyrazincarbonitrile, J. Raman Spectrosc. 20(2) (1989) 63-65.

[39] K.V. Shuvaev, T.S.M. Abedin, C.A. McClary, L.N. Dawe, J.L. Collins, L.K. Thompson, Ligand directed self-assemblyvs. metal ion coordination algorithm—when does the ligand or the metal take control?, Dalton Trans. (16) (2009) 2926-2939.

[40] B.J. Esselman, S.M. Kougias, M.A. Zdanovskaia, R.C. Woods, R.J. McMahon, Synthesis, Purification, and Rotational Spectroscopy of (Cyanomethylene)Cyclopropane—An Isomer of Pyridine, J. Phys. Chem. A 125(25) (2021) 5601-5614.

[41] H.H. Smith, S.M. Kougias, B.J. Esselman, R.C. Woods, R.J. McMahon, Synthesis, Purification, and Rotational Spectroscopy of 1-Cyanocyclobutene ($C_5H_5N$), J. Phys. Chem. A 126(12) (2022) 1980-1993.

# Improved Semi-experimental Equilibrium Structure and High-Level Theoretical Structures of Ketene

Houston H. Smith,[1] Brian J. Esselman,[1] Samuel A. Wood,[1]

John F. Stanton,[2,*] R. Claude Woods,[1,*] Robert J. McMahon[1,*]

[1] *Department of Chemistry, University of Wisconsin–Madison, Madison, Wisconsin 53706, USA*

[2] *Quantum Theory Project, Departments of Physics and Chemistry, University of Florida, Gainesville, Florida 32611, United States*

* corresponding authors
E-mail address: johnstanton@chem.ufl.edu (J.F. Stanton)
E-mail address: rcwoods@wisc.edu (R.C. Woods)
E-mail address: robert.mcmahon@wisc.edu (R.J. McMahon)

## Abstract

The millimeter-wave rotational spectrum of ketene ($H_2C=C=O$) has been collected and analyzed from 130 GHz to 750 GHz, providing highly precise spectroscopic constants from a sextic, S-reduced Hamiltonian in the $I^r$ representation. Chemical synthesis of deuteriated samples allowed spectroscopic measurements of five previously unstudied ketene isotopologues. Combined with previous work, these data provide a new, highly precise, and accurate semi-experimental ($r_e^{SE}$) structure for ketene from 32 independent moments of inertia. This $r_e^{SE}$ structure was determined with the experimental rotational constants of each available isotopologue, together with computed vibration-rotation interaction and electron-mass distribution corrections from coupled-cluster calculations with single, double, and perturbative triple excitations [CCSD(T)/cc-pCVTZ]. The $2\sigma$ uncertainties of the $r_e^{SE}$ parameters are $\leq 0.0007$ Å and 0.014° for the bond distances and angle, respectively. Only S-reduced spectroscopic constants were used in the structure determination, due to a breakdown in the A reduction of the Hamiltonian for the most prolate ketene species. All four $r_e^{SE}$ structural parameters agree with the "best

theoretical estimate" (BTE) values, which are derived from a high-level computed $r_e$ structure [CCSD(T)/cc-pCV6Z] with corrections for use of a finite basis set, the incomplete treatment of electron correlation, relativistic effects, and the diagonal Born-Oppenheimer breakdown. In each case, the computed value of the geometric parameter lies within the statistical experimental uncertainty ($2\sigma$) of the corresponding semi-experimental coordinate. The discrepancies between the BTE structure and the $r_e^{SE}$ structure are 0.0003 Å, 0.0000 Å, and 0.0004 Å, for $r_{C–C}$, $r_{C–H}$, and $r_{C–O}$, respectively, and 0.009° for $\theta_{C–C–H}$.

**Introduction**

Ketenes ($R_2C=C=O$) represent an important functional group in organic chemistry.[1,2] The reactivity of ketenes, albeit modulated by the nature of the substituents, is generally very high with respect to cycloaddition reactions and the addition of nucleophiles. As such, ketenes are precursors to the family of carboxylic acid derivatives, including anhydrides, carboxylic acids, esters, and amides (Scheme 5.1). It is the central relationship to these and other functional groups that places ketenes as important intermediates in diverse areas of science, including synthetic organic chemistry,[1-3] petroleum refining,[4] photolithography,[5] atmospheric chemistry,[6] combustion,[7] and astrochemistry.[8] The parent molecule of the family, ketene ($H_2C=C=O$), is a paradigm in terms of structure, bonding, and reactivity. It is a cornerstone of structural organic chemistry and has attracted substantial interest from both experimental and theoretical communities. In the current study, we describe the determination of a highly precise, gas-phase molecular structure for ketene using state-of-the-art methods for both experiment and theory.

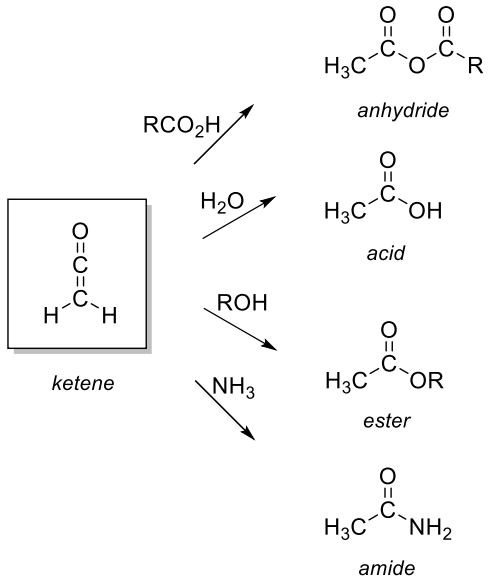


**Scheme 5.1.** Reactions of ketene with various nucleophiles

Ketene ($H_2C{=}C{=}O$, $C_{2v}$, ethenone) has been identified as an interstellar molecule, with its initial detection in Sgr B2 in 1977.[9] Its detection in that source was later confirmed,[10] and various subsequent studies detected ketene in other galactic[11-15] and extra-galactic[16] sources. Ketene has been generated from photolysis of interstellar ice analogues comprising of a wide variety of chemical compositions ($O_2 + C_2H_2$, $CO_2 + C_2H_4$, $CO + CH_4$).[8] The central, electrophilic carbon atom of ketene reacts with common interstellar molecules $H_2O$, $NH_3$, $CH_3OH$, and HCN to form acetic acid, acetamide, methyl acetate, and pyruvonitrile, respectively.[17-19] Some of these reaction products have potential prebiotic importance in the interstellar medium. Ketene can also be generated from the decomposition of two known interstellar molecules: acetic acid[20] and acetone.[21] Acylium cation ($H_3C{-}C{\equiv}O^+$, $C_{3v}$),[22] which has been recently detected in the ISM,[23] is a protonated form of ketene. Due to its prevalence and possible role in the chemical reactions of extraterrestrial environments, the observation of rotational transitions of ketene in its ground and vibrationally excited states is important to radioastronomers. Previously, the rotational spectra of various ketene

isotopologues have been observed and assigned up to a frequency of 350 GHz. In this work, we extended the frequency range to 750 GHz for fifteen ketene isotopologues, including all singly substituted heavy-atom isotopologues of ketene, ketene-$d_1$, and ketene-$d_2$. The doubling of the spectral range for ketene isotopologues, along with new isotopologue analyses, expands the capabilities for radioastronomers to search for ketene spectral lines in different extra-terrestrial environments.

The pure rotational spectra of ketene and its isotopologues have been studied extensively for over seventy years. The rotational spectrum of ketene and its two deuteriated isotopologues, [2-$^2$H]-ketene (HDC=C=O) and [2,2-$^2$H]-ketene ($D_2$C=C=O), were measured in the early 1950s.[24,25] Subsequently, heavy-atom substituted isotopologues [2-$^{13}$C]-ketene and [$^{18}$O]-ketene were measured in 1959 and 1963,[26,27] but the final single-substitution isotopologue, [1-$^{13}$C]-ketene, was not reported until 1990.[28] In 1966, the proton spin-rotation and deuterium nuclear quadrupole constants were determined for ketene, [2-$^2$H]-ketene, and [2,2-$^2$H]-ketene.[29] The frequency range was extended into the millimeter-wave region (up to 220 GHz) for [2-$^2$H]-ketene and [2,2-$^2$H]-ketene, permitting analysis of their centrifugal distortion in 1976.[30] More recent works have expanded the measured frequency range further to 350 GHz for various isotopologues, refined the least-squares fits, and measured the spectrum of new isotopologues [$^{17}$O]-ketene,[31] [1,2-$^{13}$C]-ketene,[32] [2,2-$^2$H, 1-$^{13}$C]-ketene,[32] [2,2-$^2$H, 2-$^{13}$C]-ketene,[32] and [2,2-$^2$H, $^{18}$O]-ketene.[32] For ketene, itself, Nemes *et al.* reported the measurement of 82 *a*-type, $\Delta K_a = 0$ transitions up to 800 GHz.[33] Figure 5.1 illustrates the eleven isotopologues for which rotational spectra have been previously reported (black) and the five isotopologues newly measured in this work (blue).

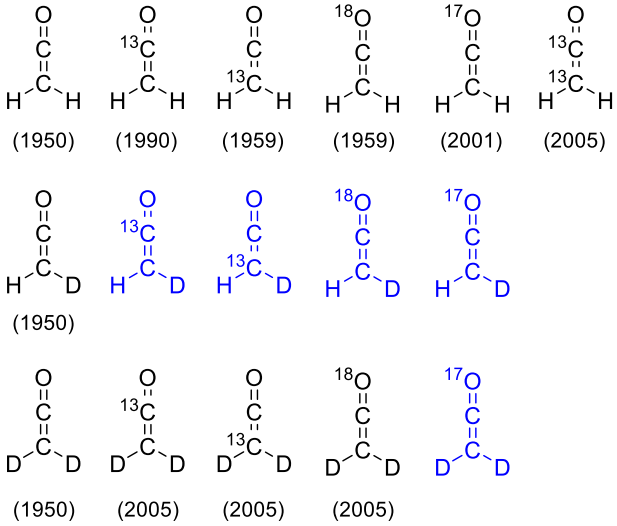


**FIG. 5.1.** Ketene isotopologues previously measured (black) and newly measured in this work (blue). Ketene, [2-$^{2}$H]-ketene, and [2,2-$^{2}$H]-ketene were measured by Bak *et al.*[24] [2-$^{13}$C]-ketene and [$^{18}$O]-ketene were measured by Cox *et al.*[26] [1-$^{13}$C]-ketene was measured by Brown *et al.*[28] [$^{17}$O]-ketene was measured by Guarnieri *et al.*[31] [1,2-$^{13}$C]-ketene, [2,2-$^{2}$H, 1-$^{13}$C]-ketene, [2,2-$^{2}$H, 2-$^{13}$C]-ketene, and [2,2-$^{2}$H, $^{18}$O]-ketene were measured by Guarnieri.[32] The date listed indicates the first literature report of that isotopologue.

The gas-phase infrared spectrum of ketene was recorded nearly eighty-five years ago.[34] The rotational structure in the infrared spectrum was first analyzed by Halverson and Williams,[35] followed by Harp and Rasmussen,[36] Drayton and Thompson,[37] Bak and Andersen,[38] and Butler *et al.*[39] Infrared spectra of [2-$^{2}$H]-ketene and [2,2-$^{2}$H]-ketene were reported in 1951[40] and the first vibration-rotation bands of ketene and [2,2-$^{2}$H]-ketene were observed by Arendale and Fletcher in 1956.[41,42] The first complete analysis of rotationally resolved infrared spectrum of the nine fundamental states present in ketene, [2-$^{2}$H]-ketene, and [2,2-$^{2}$H]-ketene was performed by Cox *et al.* in 1963.[43] Nemes explored the Coriolis coupling present in $\nu_5$, $\nu_6$, $\nu_8$, and $\nu_9$ of ketene in two separate works in 1974 and 1978.[44,45] A similar work was done on [2,2-$^{2}$H]-ketene by Winther *et al.*, where $\nu_5$, $\nu_6$, $\nu_8$, and $\nu_9$ were examined.[46] A high-resolution infrared analysis of the four $A_1$ vibrational states for ketene, [2-$^{2}$H]-ketene, and [2,2-$^{2}$H]-ketene was performed by Duncan[47] and

followed by the high-resolution infrared study of $\nu_5$, $\nu_6$, $\nu_7$, and $\nu_8$ fundamental states and two overtone states for ketene by Duncan and Ferguson.[48] The $\nu_9$, $\nu_6$, and $\nu_5$ bands in [2,2-$^2$H]-ketene were analyzed with high-resolution infrared spectroscopy by Hegelund *et al.*[49] Escribano *et al.*[50] examined the $\nu_1$ band of ketene in 1994, which is coupled to other vibrational modes. The fundamental states, $\nu_5$ and $\nu_6$, were reexamined by Campina *et al.*[51] in 1998 along with the observation of $\nu_6 + \nu_9$ in 1999 by Gruebele *et al.*[52] Johns *et al.*[53] were able to update the ground-state spectroscopic constants derived from millimeter-wave data along with the infrared data provided by Campina *et al.*[51] and Escribano *et al.*[50] Nemes *et al.*[54] revisited the non-linear least-squares fitting of $\nu_5$, $\nu_6$, and $\nu_9$ and were able to remove most of the Coriolis perturbation contributions to the $A_\nu$ rotational constants and derive new experimental Coriolis $\zeta$ constants. The vibrational energy manifold up to 3400 cm$^{-1}$ is presented in Fig. 5.2, using the experimental frequencies where available and supplementing with CCSD(T) values where they are not available.

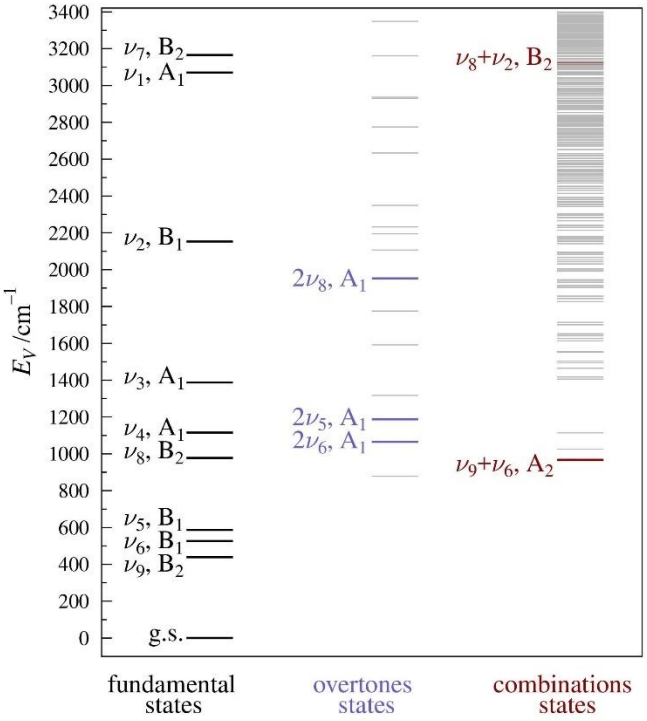


**FIG. 5.2.** Vibrational energy levels of ketene below 3400 cm$^{-1}$. Experimentally observed vibrational energy levels (black, purple, maroon) are each taken from the most recent literature report and labeled.[44-54] Unobserved vibrational energy levels (gray) are depicted using computed fundamental frequencies (CCSD(T)/cc-pVTZ). Overtone and combination states are provided up to five quanta.

The observation and assignment of various ketene isotopologues has been used for several structural determinations presented in Table 5.1.[28,55-58] The first zero-point average structure ($r_z$), accounting for harmonic vibrational corrections, centrifugal distortion, and electronic corrections, was determined in 1976.[55] A second $r_z$ structure was calculated in 1987,[56] after several works examining the vibrational spectra of ketene isotopologues facilitated a more physically realistic general harmonic force field to be applied to the structure calculation.[47,48,59] The additional measurement of [1-$^{13}$C]-ketene by Brown *et al.*[28] enabled the first complete substitution structure ($r_s$) determination, where every atom was isotopically substituted at least once in the structure determination. The first semi-experimental equilibrium structure ($r_e^{SE}$), using vibration-rotation interaction corrections calculated from an anharmonic force field, was calculated in 1995 with the

rotational constants of the six isotopologues available at that time.[57] The six isotopologues in this $r_e^{SE}$ structure provide twelve independent moments of inertia, which is more than sufficient to determine the four structural parameters of ketene. Guarnieri *et al.*[31,32,60] measured and assigned rotational transitions for five new isotopologues and determined an updated $r_e^{SE}$ from rotational constants of eleven isotopologues (twenty-two independent moments of inertia) using vibration-rotation corrections calculated at the MP2/cc-pVTZ level in 2010.[58] The two $r_e^{SE}$ structures are generally in good agreement, but disagree somewhat with respect to the $r_{C–H}$ value.

**Table 5.1.** Select previously reported structures of ketene.

| | Mallinson *et al.*[55] | Duncan *et al.*[56] | Brown *et al.*[28] | East *et al.*[57] | Guarnieri *et al.*[58] |
|---|---|---|---|---|---|
| | $r_z$ 1976 | $r_z$ 1987 | $r_s$ 1990 | $r_e^{SE}$ 1995 | $r_e^{SE}$ 2010 |
| $r_{C-C}$ | 1.317 1 (20) [a] | 1.3165 (15) [b] | 1.314 (72) [c] | 1.312 12 (60) [d] | 1.312 2 (12) [d] |
| $r_{C-H}$ | 1.079 7 (10) [a] | 1.080 02 (33) [b] | 1.082 5 (15) [c] | 1.075 76 (14) [d] | 1.076 3 (2) [d] |
| $r_{C-O}$ | 1.160 8 (20) [a] | 1.161 4 (14) [b] | 1.162 (72) [c] | 1.160 30 (58) [d] | 1.160 7 (12) [d] |
| $\theta_{C-C-H}$ | 119.02 (10) [a] | 119.011 (31) [b] | 118.72 (5) [c] | 119.110 (12) [d] | 119.115 (22) [d] |
| $N_{iso}$ [e] | 5 | 5 | 6 | 6 | 11 |

[a] Uncertainties as stated in Mallinson *et al.*[55]
[b] 3σ values
[c] Uncertainties estimated as recommended by Costain[61] and Harmony *et al.*[62]
[d] All statistical uncertainties adjusted from previous reports to be 2σ values
[e] Number of isotopologues used in the structure determination

The foundation for semi-experimental equilibrium ($r_e^{SE}$) structure determination was pioneered by Pulay, Meyer, and Boggs,[63] and accuracy of the structures obtained using this approach have been exemplified in various works.[64-67] The accuracy of semi-experimental structures using different computational methods was investigated in the 1990s and 2000s[68-74] and was comprehensively reviewed by Puzzarini[75] and Puzzarini and Stanton.[76] The coupled-cluster method for both geometry optimizations and anharmonic force-field calculations, along with sufficiently large basis sets for the molecule of interest, was shown to provide the most accurate structural parameters.[73,77] For larger molecules, where coupled-cluster methods are not feasible, structural parameters derived from density functional methods, *e.g.*, B3LYP/SNSD, display reasonable accuracy.[78] A number of our recent works have shown remarkable agreement of CCSD(T)/cc-pCV5Z or CCSD(T)/cc-pCV6Z $r_e$ structures with $r_e^{SE}$ structures determined using CCSD(T)/cc-pCVTZ vibration-rotation corrections.[79-86] Due to the small number of atoms in ketene, the coupled-cluster approach is utilized in this work to obtain an $r_e^{SE}$ structure at similar levels of precision and accuracy to those recent works.

**Experimental Methods**

The rotational spectra of synthesized samples of ketene and deuteriated ketene, described later, were continuously collected in segments from 130 – 230 GHz, 235 – 360 GHz, 350 – 500 GHz, and 500 – 750 GHz. The instrument covering the 130 – 360 GHz range has been described previously.[87-89] The 350 – 500 GHz and 500 – 750 GHz segments were obtained with a newly acquired amplification and multiplication chain, VDI Mini SGX (SGX-M), with external multipliers, WR4.3X2 and WR2.2X2 attached for 350 – 500 GHz and WR4.3X2 and WR1.5X3 attached for 500 – 750 GHz. These spectral segments were detected by VDI zero-bias detectors WR2.2ZBD and WR1.5ZBD, respectively. The complete spectrum from 130 to 750 GHz was

obtained using automated data collection software over approximately twelve days with these experimental parameters: 0.6 MHz/sec sweep rate, 10 ms time constant, and 50 kHz AM and 500 kHz FM modulation in a tone-burst design.[90] The frequency spectra were combined into a single spectral file using Assignment and Analysis of Broadband Spectra (AABS) software.[91,92] Pickett's SPFIT/SPCAT programs[93] were used for least-squares fits and spectral predictions, along with Kisiel's PIFORM, PLANM, and AC programs for analysis.[94,95] Additional short-frequency ranges of the spectrum were collected with an increased number of scans for low-abundance isotopologues. In our least-squares fits, we assume a uniform 50 kHz frequency measurement uncertainty for our measured transitions, 50 kHz for literature values that did not specify an uncertainty, and 25 kHz for transitions reported by Guarnieri *et al*.[31,32,60] Least-squares fitting output files are provided in the supplementary material.

In this study, we measured and assigned the rotational spectrum from 130 GHz to 750 GHz for the primary (Fig. 5.3) and deuterium-substituted ketene isotopologues, including their heavy-atom isotopologues, $^{13}$C and $^{18}$O. All $^{17}$O-substituted isotopologues, including new detection of [2-$^{2}$H, $^{17}$O]-ketene and [2,2-$^{2}$H, $^{17}$O]-ketene, were measured from 230 GHz to 500 GHz. The reduced frequency coverage is due to lower signal-to-noise ratios (*S*/*N*) for the hardware configurations outside that range. Transitions of [1,2-$^{13}$C]-ketene could not be measured or assigned due to the proximity of its transitions to those of [2-$^{13}$C]-ketene and the inherently lower *S*/*N* for an isotopologue approximately 0.0121% the intensity of the main isotopologue. Thus, we were unable to improve upon the spectroscopic constants presented by Guarnieri.[32] Due to the planarity condition, each isotopologue provides two independent moments of inertia. With 16 isotopologues used for the new structure determination, an $r_e^{SE}$ structure for ketene was obtained by using 32 independent moments of inertia.

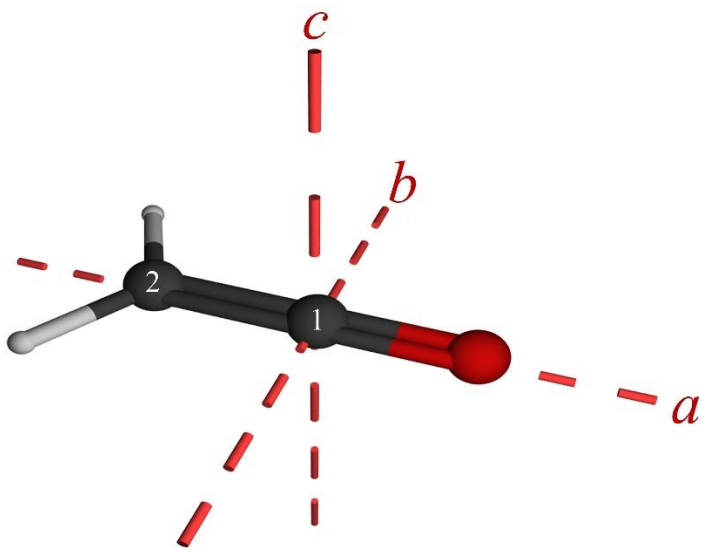


**FIG. 5.3.** Ketene structure with principal inertial axes and standard carbon atom numbering.

**Computational Methods**

Calculations were carried out using a development version of CFOUR.[96] The ketene structure was first optimized at the CCSD(T)/cc-pCVTZ level of theory. The optimized geometry and the same level of theory was subsequently used for an anharmonic, second-order vibrational perturbation theory (VPT2) calculation, wherein cubic force constants are evaluated using analytical second derivatives at displaced points.[97-99] Magnetic property calculations were performed for each isotopologue to obtain the electron-mass corrections to the corresponding rotational constants. The "best theoretical estimate" (BTE), as described previously, is based on a CCSD(T)/cc-pCV6Z optimized structure with four additional corrections[79-86] that address the following:

1. Residual basis set effects beyond cc-pCV6Z.
2. Residual electron correlation effects beyond the CCSD(T) treatment.
3. Effects of scalar (mass-velocity and Darwin) relativistic effects.
4. The fixed-nucleus approximation *via* the diagonal Born-Oppenheimer correction.

Equations used to calculate these corrections and the values of each of these corrections for ketene are provided in the supplementary material (**S7** – **S13** and **Table S-V**). One of the most important factors of the algorithm used to determine the BTE is the estimation of residual basis set effects, specifically estimated as the difference between the (directly computed) cc-pCV6Z geometry at the CCSD(T) level of theory and the estimate of the CCSD(T) geometry at the basis set limit. Following others,[100] the latter is estimated by assuming an exponential convergence pattern with respect to the highest angular momentum basis functions present in the basis. A complete explanation of the BTE calculation is provided in the Supplementary Material.

The *xrefit* module of CFOUR calculates the moments of inertia and semi-experimental equilibrium structure using the experimental, S-reduced rotational constants and computational electron-mass distribution and vibration-rotation corrections. X*refiteration*[82] was used to determine the suitability of the ketene isotopologues for the structure determination. The routine begins by determining a structure using a single isotopic substitution at each position and then sequentially adds the most uncertainty-minimizing isotopologue to the structural least-squares fit until all available isotopologues are incorporated.

Computational output files are provided in the Supplementary Material.

**Synthesis of Ketene Isotopologues**

Ketene was synthesized by pyrolysis of acetone (HPLC grade, Sigma-Aldrich) at atmospheric pressure using a lamp described by Williams and Hurd,[101] and collected in a −130 °C cold trap (Scheme 5.2a). After collection, the cold trap was isolated and placed under vacuum to remove volatile impurities; ketene was then transferred to a stainless-steel cold trap for spectroscopic investigation. A mixed deuterio/protio-solution of acetone-$d_x$ was produced by a procedure modified from Paulsen and Cooke,[102] using acetone, $D_2O$, and lithium deuteroxide

(LiOD). The reaction mixture was distilled, yielding approximately 50% deuterium-enriched acetone. Pyrolysis and purification of this mixture produced ketene, [2-$^2$H]-ketene, and [2,2-$^2$H]-ketene (Scheme 5.2b). An independent sample of [2,2-$^2$H]-ketene (Scheme 5.2c) with high deuterium incorporation was generated by pyrolysis of acetone-$d_6$ (99.5%, Oakwood Chemical).

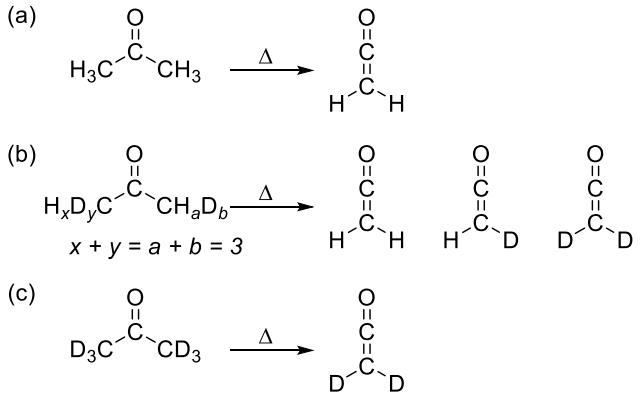


**Scheme 5.2.** Ketene isotopologue synthesis scheme: (a) ketene-$h_2$ by pyrolysis of acetone-$h_6$, (b) mixture of ketene isotopologues by pyrolysis of 50% deuterium-enriched acetone, (c) ketene-$d_2$ by pyrolysis of acetone-$d_6$.

**Analysis of Rotational Spectra**

The rotational spectrum of ketene is dominated by $^aR_{0,1}$ transitions, but a select few low-intensity $^aQ_{0,-1}$ transitions were observable in the lower frequency range. Ketene has an *a*-axis dipole, $\mu_a$ = 1.414 (10) D[25] and is extremely close to a prolate top ($\kappa$ = −0.997 for the main isotopologue, Eqn. 1), which can result in a breakdown of the A-reduction least-squares fit ($I^r$ representation) of the Hamiltonian.

$$\kappa = \left(\frac{2B-A-C}{A-C}\right) \quad (1)$$

The A-reduction breakdown for molecules that approach a spherical top, a prolate top (in the $I^{r/l}$ representation), or an oblate top (in the $III^{r/l}$ representation) have been discussed previously.[84,103-108] (The output files of least-squares fitting for each isotopologue to sextic, A- and S-reduction Hamiltonians in the $I^r$ representation are provided in the Supplementary Material.) For ketene, the

experimental and computed A-reduction spectroscopic constants do not appear to display the unreasonably large *K*-dependent centrifugal distortion constants that have been noted in other cases where the A reduction breaks down. There is, however, a significant difference between the A- and S-reduction determinable constants (Eqns. S1 – S6 in the Supplementary Material) from the least-squares fits in the A and S reductions. The $\kappa$ values for the ketene isotopologues vary from −0.9915 ([2,2-$^{2}$H]-ketene) to −0.9975 ([$^{18}$O]-ketene). The greatest discrepancies in the determinable constants occur for the $A_0$ constant of the isotopologues with the greatest $\kappa$ values, [$^{18}$O]-ketene and [$^{17}$O]-ketene. Fig. 5.4 presents the differences in the determinable constants (nominal $B''$ values) in the A and S reductions as a function of $\kappa$. While the trend does not show a clearly defined behavior, the variability in $A_0''$ increases as $\kappa$ approaches the prolate-top limit (−1.000). Additionally, in each case, the A-reduction fits have a larger statistical uncertainty than the S-reduction fits. Doose *et al.*[109] observed similar issues with [2,2-$^{2}$H]-ketene ($\kappa$ = −0.9915), including high uncertainties and high correlations for some parameters when only pure rotational transitions were used in the least-squares fit. For these reasons, only the S-reduction spectroscopic constants are presented in the main text of this work and used in the $r_e^{SE}$ structure determination. The S-reduction spectroscopic constants for all ketene isotopologues are presented in Table 5.2.

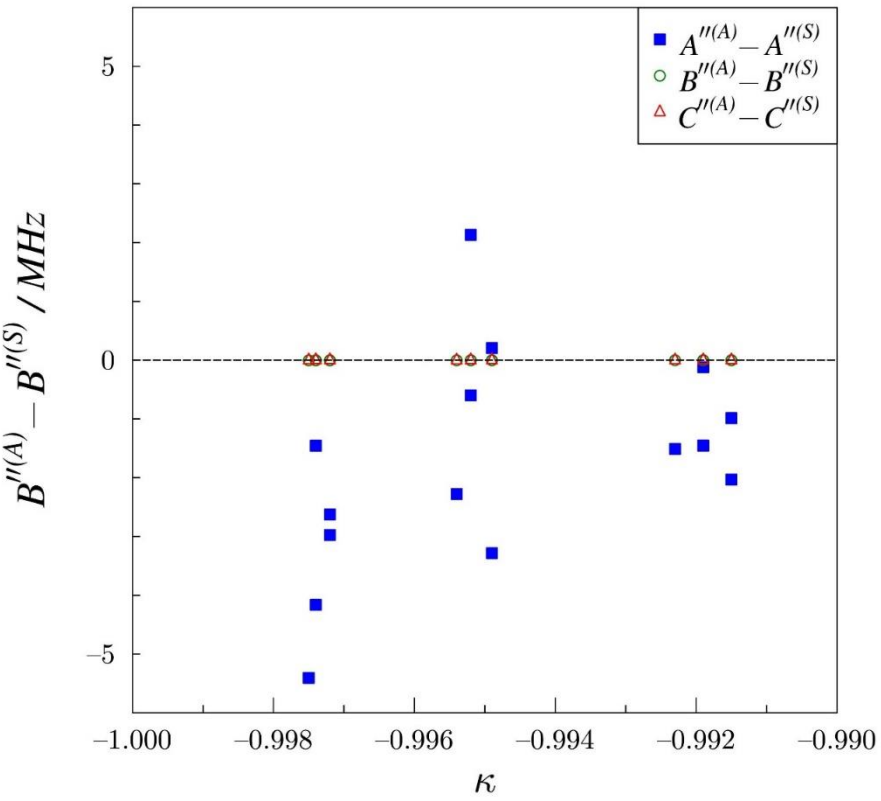


**FIG. 5.4.** Difference between the determinable constants ($A_0''$, $B_0''$, and $C_0''$) derived using the A- and the S-reduced Hamiltonians for ketene isotopologues as a function of $\kappa$. The symbols for the *b*- and *c*-axis differences are so close to zero that they are overlapped and difficult to distinguish on the plot. Note the increase in scatter and the deviation from zero as $\kappa$ approaches the prolate limit of −1.000.

**TABLE 5.2.** Experimental and computational spectroscopic constants for ketene (S-reduced Hamiltonian, $I^r$ representation) and experimental spectroscopic constants for several isotopologues in the ground vibrational state.

| | normal isotopologue | | | [1-$^{13}$C] | [2-$^{13}$C] | [$^{18}$O] |
|---|---|---|---|---|---|---|
| | Guarnieri *et al.* 2003 [a] | CCSD(T) [b] | Current Work | | | |
| $A_0$ (MHz) | 282032 (22) | 281680 | 282121.6 (18) | 282104.2 (25) | 282108.1 (26) | 282142.0 (40) |
| $B_0$ (MHz) | 10293.31963 (81) | 10234 | 10293.31894 (24) | 10293.62959 (44) | 9960.97788 (37) | 9761.23701 (38) |
| $C_0$ (MHz) | 9915.90393 (80) | 9861 | 9915.90304 (24) | 9916.21087 (44) | 9607.13942 (35) | 9421.12472 (37) |
| $D_J$ (kHz) | 3.2804 (18) | 3.15 | 3.28123 (30) | 3.27963 (49) | 3.09008 (35) | 2.94928 (14) |
| $D_{JK}$ (kHz) | 478.27 (11) | 477 | 477.384 (31) | 476.701 (43) | 451.182 (36) | 434.455 (47) |
| $D_K$ (kHz) | [22840] [c] | 20700 | [20700] [d] | [20700] [d] | [20700] [d] | [20700] [d] |
| $d_1$ (kHz) | −0.14757 (84) | −0.125 | −0.147726 (11) | −0.147875 (96) | −0.132961 (89) | −0.12548 (11) |
| $d_2$ (kHz) | −0.05621 (51) | −0.0433 | −0.055755 (57) | −0.05596 (11) | −0.04928 (11) | −0.04547 (17) |
| $H_J$ (Hz) | [−0.00204] [c] | −0.000466 | −0.00125 (13) | −0.00111 (21) | −0.00110 (14) | [−0.0003194] |
| $H_{JK}$ (Hz) | 2.27 (21) | 2.80 | 2.9142 (89) | 2.976 (13) | 2.5876 (91) | 2.495 (13) |
| $H_{KJ}$ (Hz) | −526.2 (45) | −711 | −647.7 (11) | −673.7 (15) | −603.0 (13) | −614.2 (17) |
| $H_K$ (Hz) | [5230] [c] | 5890 | [5890] [d] | [5930] [d] | [5850] [d] | [5850] [d] |
| $h_1$ (Hz) | | 0.0000264 | [0.0000264] [d] | [0.0000259] [d] | [0.0000237] [d] | [0.000025] [d] |
| $h_2$ (Hz) | | 0.000442 | [0.000442] [d] | [0.000444] [d] | [0.000369] [d] | [0.000339] [d] |
| $h_3$ (Hz) | | 0.0000724 | [0.0000724] [d] | [0.000073] [d] | [0.0000595] [d] | [0.0000544] [d] |
| $L_{JK}$ (mHz) | −21.3 (46) | | | | | |
| $L_{JKK}$ (mHz) | 3475 (59) | | | | | |
| $N_{lines}$ [e] | 156 | | 307 [f] | 209 | 230 | 189 |
| σ (MHz) | 0.040 | | 0.037 | 0.048 | 0.041 | 0.041 |

[a] Constants as reported in Ref. [60] [b] $B_0$ values obtained from Eqn. (2) using the computed values for $B_e$ [CCSD(T))/cc-pCV6Z], vibration–rotation interaction, and electron-mass distribution [both evaluated using CCSD(T)/cc-pCVTZ]. Distortion constants computed using CCSD(T)/cc-pCVTZ. [c] Constant held fixed to value in Ref. [53] as stated by Ref [60]. [d] Constant held fixed at the CCSD(T)/cc-pCVTZ value. [e] Number of independent transitions. [f] Transitions reported by Brown *et al.*[28], Johnson *et al.*[25], and Guarnieri *et al.*[60] are included in the least-squares fit. See Supplementary Material for transitions used from previous works for non-standard isotopologues.

**TABLE 5.2 (Continued).** Experimental and computational spectroscopic constants for ketene (S-reduced Hamiltonian, $I^r$ representation) and experimental spectroscopic constants for several isotopologues in the ground vibrational state.

| | [$^{17}$O] | [1,2-$^{13}$C] | [2-$^{2}$H] | [2-$^{2}$H, 1-$^{13}$C] | [2-$^{2}$H, 2-$^{13}$C] | [2-$^{2}$H, $^{18}$O] |
|---|---|---|---|---|---|---|
| $A_0$ (MHz) | 282175 (13) | 282031 (22) | 194292.2 (13) | 194256.1 (23) | 193984.2 (26) | 194243.2 (31) |
| $B_0$ (MHz) | 10013.4722 (14) | 9960.8650 (25) | 9647.06533 (21) | 9646.68707 (65) | 9373.43143 (63) | 9145.12930 (76) |
| $C_0$ (MHz) | 9655.9096 (13) | 9607.0550 (27) | 9174.64351 (20) | 9174.26089 (64) | 8926.17792 (60) | 8719.33331 (72) |
| $D_J$ (kHz) | 3.09997 (63) | 3.0881 (21) | 3.00461 (37) | 3.00529 (64) | 2.82755 (61) | 2.69945 (58) |
| $D_{JK}$ (kHz) | 454.371 (92) | 451.12 (11) | 328.426 (25) | 327.242 (41) | 315.948 (35) | 297.756 (44) |
| $D_K$ (kHz) | [20700] [d] | [22840] [c] | 17400 (674) | 15380 (1098) | 17090. (1276) | 16760. (1576) |
| $d_1$ (kHz) | −0.13467 (76) | −0.1331 (27) | −0.226195 (49) | −0.22686 (15) | −0.20328 (16) | −0.19148 (17) |
| $d_2$ (kHz) | −0.04845 (60) | −0.0509 (11) | −0.08410 (15) | −0.08375 (26) | −0.07565 (27) | −0.06877 (30) |
| $H_J$ (Hz) | [−0.00384] [d] | [−0.00204] [c] | −0.001380 (80) | −0.00104 (15) | −0.00103 (12) | [−0.0001117] [d] |
| $H_{JK}$ (Hz) | 2.561 (89) | 2.07 (23) | 2.2843 (67) | 2.316 (11) | 2.0655 (83) | 1.948 (11) |
| $H_{KJ}$ (Hz) | −635.8 (33) | −506.9 (42) | −254.39 (89) | −264.6 (15) | −240.3 (13) | −238.6 (15) |
| $H_K$ (Hz) | [5870] [d] | [5230] [c] | [4070] [d] | [3970] [d] | [4060] [d] | [4040] [d] |
| $h_1$ (Hz) | [0.0000258] [d] | | [0.000194] [d] | [0.000195] [d] | [0.000161] [d] | [0.000165] [d] |
| $h_2$ (Hz) | [0.000385] [d] | | 0.000782 (35) | [0.000767] [d] | [0.000653] [d] | [0.000586] [d] |
| $h_3$ (Hz) | [0.0000624] [d] | | [0.000139] [d] | [0.000140] [d] | [0.000118] [d] | [0.000105] [d] |
| $L_{JK}$ (mHz) | | 18.7 (47) | | | | |
| $L_{JKK}$ (mHz) | | −3545 (53) | | | | |
| $N_{lines}$ [e] | 94 | 86 | 344 | 204 | 240 | 171 |
| σ (MHz) | 0.046 | 0.030 | 0.034 | 0.043 | 0.042 | 0.047 |

[a] Constants as reported in Ref. [60] [b] $B_0$ values obtained from Eqn. (2) using the computed values for $B_e$ [CCSD(T))/cc-pCV6Z], vibration–rotation interaction, and electron-mass distribution [both evaluated using CCSD(T)/cc-pCVTZ]. Distortion constants computed using CCSD(T)/cc-pCVTZ. [c] Constant held fixed to value in Ref. [53] as stated by Ref [60]. [d] Constant held fixed at the CCSD(T)/cc-pCVTZ value. [e] Number of independent transitions. [f] Transitions reported by Brown *et al.*[28], Johnson *et al.*[25], and Guarnieri *et al.*[60] are included in the least-squares fit. See Supplementary Material for transitions used from previous works for non-standard isotopologues.

**TABLE 5.2 (Continued).** Experimental and computational spectroscopic constants for ketene (S-reduced Hamiltonian, $I^r$ representation) and experimental spectroscopic constants for several isotopologues in the ground vibrational state.

| | [2-$^2$H, $^{17}$O] | [2,2-$^2$H] | [2,2-$^2$H, 1-$^{13}$C] | [2,2-$^2$H, 2-$^{13}$C] | [2,2-$^2$H, $^{18}$O] | [2,2-$^2$H, $^{17}$O] |
|---|---|---|---|---|---|---|
| $A_0$ (MHz) | 194260.6 (27) | 141490.38 (28) | 141484.52 (67) | 141483.16 (65) | 141489.40 (85) | 141490.0(10) |
| $B_0$ (MHz) | 9383.1715 (13) | 9120.83067 (17) | 9119.42658 (65) | 8890.47351 (67) | 8641.83891 (56) | 8869.0621(17) |
| $C_0$ (MHz) | 8935.5431 (13) | 8552.69981 (16) | 8551.48444 (71) | 8349.84131 (61) | 8130.05311 (54) | 8330.8819(13) |
| $D_J$ (kHz) | 2.84576 (51) | 2.48404 (19) | 2.48496 (48) | 2.35860 (38) | 2.23474 (43) | 2.35569(55) |
| $D_{JK}$ (kHz) | 312.295 (66) | 322.962 (21) | 321.967 (38) | 310.142 (37) | 294.046 (43) | 307.799(76) |
| $D_K$ (kHz) | 15140 (840) | 5645 (100) | 5327 (225) | 5373 (209) | 5470 (359) | [5000] [d] |
| $d_1$ (kHz) | −0.20921 (58) | −0.220132 (37) | −0.22025 (14) | −0.20100 (12) | −0.18676 (15) | −0.20448(71) |
| $d_2$ (kHz) | −0.07596 (29) | −0.114212 (87) | −0.11415 (31) | −0.10309 (28) | −0.09366 (32) | −0.10311(28) |
| $H_J$ (Hz) | [0.0000211][d] | −0.001690 (47) | −0.00163 (12) | −0.001558 (95) | −0.001436 (96) | [−0.000862][d] |
| $H_{JK}$ (Hz) | 2.162 (37) | 2.0775 (46) | 2.0798 (93) | 1.8954 (93) | 1.690 (12) | 2.001(43) |
| $H_{KJ}$ (Hz) | −243.1 (22) | −127.50 (80) | −138.4 (14) | −124.0 (14) | −129.4 (15) | −129.1(27) |
| $H_K$ (Hz) | [4050] [d] | [787] [d] | [793] [d] | [781] [d] | [781] [d] | [784] [d] |
| $h_1$ (Hz) | [0.000178] [d] | [−0.0000144] [d] | [−0.0000146] [d] | [−0.0000142] [d] | [−0.000002] [d] | [−0.00000730] [d] |
| $h_2$ (Hz) | [0.000568] [d] | 0.001030 (30) | 0.00119 (12) | 0.00066 (11) | 0.000700 (97) | [0.000752] [d] |
| $h_3$ (Hz) | [0.000120] [d] | [0.000208] [d] | [0.000208] [d] | [0.000180] [d] | [0.000156] [d] | [0.000179] [d] |
| $N_{lines}$ [e] | 107 | 403 | 221 | 218 | 166 | 88 |
| σ (MHz) | 0.040 | 0.032 | 0.046 | 0.045 | 0.042 | 0.046 |

[a] Constants as reported in Ref. [60] [b] $B_0$ values obtained from Eqn. (2) using the computed values for $B_e$ [CCSD(T))/cc-pCV6Z], vibration–rotation interaction, and electron-mass distribution [both evaluated using CCSD(T)/cc-pCVTZ]. Distortion constants computed using CCSD(T)/cc-pCVTZ. [c] Constant held fixed to value in Ref. [53] as stated by Ref [60]. [d] Constant held fixed at the CCSD(T)/cc-pCVTZ value. [e] Number of independent transitions. [f] Transitions reported by Brown *et al.*[28], Johnson *et al.*[25], and Guarnieri *et al.*[60] are included in the least-squares fit. See Supplementary Material for transitions used from previous works for non-standard isotopologues.

Table 5.2 provides the experimental spectroscopic constants in the S reduction, $I^r$ representation for all 16 ketene isotopologues used in the semi-experimental equilibrium structure determination. The [1,2-$^{13}$C]-ketene spectroscopic constants provided in Table 5.2 are those reported by Guarnieri *et al.*[32] due to the inability to measure this isotopologue in this work. Table 5.2 includes, for the normal isotopologue, the previously determined spectroscopic constants by Guarnieri *et al.*[60] and the computed constants [CCSD(T)/cc-pCV6Z] for comparison to the experimental values determined in this work. The CCSD(T) values for all other isotopologues can be found in the Supplementary Material. Experimental rotational constants $B_0$ and $C_0$ determined by Guarnieri *et al.*[60] are in exceptional agreement with this work, but $A_0$ is not in such good agreement. The computed rotational constants are in good agreement with the experimentally determined ones previously reported, with the largest discrepancy being in $B_0$ (0.58%). Centrifugal distortion constants determined by Guarnieri *et al.*[60] are also in great agreement with those determined here with the largest difference in $d_2$ (0.81%). Neither work was able to determine $D_K$, but Guarnieri *et al*. used the previously determined value from Johns *et al.*,[53] while the present work used the CCSD(T) value. The CCSD(T) value was utilized to maintain a consistent treatment with the sextic centrifugal distortion constants, which were also held fixed at the CCSD(T) values since experimental values are not available. The CCSD(T) values for the centrifugal distortion constants display the expected level of agreement with the experimental values, with the largest discrepancy in $d_2$ (22%). There are only two sextic distortion constants that were determined both in this work and by Guarnieri *et al.*,[60] $H_{JK}$ and $H_{KJ}$, and both are in reasonable agreement (28%). $H_J$ was determined in this work, while it was held fixed in Guarnieri *et al*.,[60] similar to $D_K$. $H_K$ is held fixed at two different values in the two works for the same reason as for $D_K$. This work held the off-diagonal sextic centrifugal distortion constants, $h_1$, $h_2$, and $h_3$,

fixed at their respective CCSD(T) values, while they were held at zero in the previous works. This difference seemed to negate the need for the two octic centrifugal distortion constants utilized in the previous works for the frequency range and $K_a$ range measured in this work. The largest relative discrepancy in the CCSD(T) sextic centrifugal distortion constants that were determined is in $H_J$ (63%), which is not unexpected due to it being orders of magnitude smaller than the other constants.

The band structure for all ketene isotopologues is typical for a highly prolate molecule, with each band corresponding to a singular $J''+1$ value with different $K_a$ values. The transitions of the band structure lose $K_a$ degeneracy for $K_a$ = 3 for all isotopologues with the protio isotopologues losing degeneracy in bands at higher frequencies. The current work expanded the range of quantum numbers of the transitions assigned for ketene to include $J''+1$ = 7 to 41 and $K_a$ = 0 to 5. The breadth of the transitions assigned in this work is shown in Fig. 5.5, where all transitions newly measured are in black and previously measured transitions are in various colors indicating their source. All ketene isotopologue least-squares fits were limited to transitions with $K_a \leq 5$, even though transitions with higher $K_a$ were observed. This is because a single-state, distorted-rotor Hamiltonian was unable to provide a least-squares fit below the assumed measurement uncertainty of 50 kHz, when incorporating transitions above $K_a$ = 5. This failure of the single-state least-squares fit to model all of the observable transitions is due to coupling between the vibrational ground and excited states that has been extensively studied in the infrared spectra of ketene and summarized in the introduction.[44-49,51,52,54] An analysis of the vibrational coupling is beyond the scope of the current work. The cutoff of $K_a \leq 5$ was implemented for all isotopologues to maintain a consistent amount of spectroscopic information. A similar procedure was applied to previous works with $HN_3$, which also has a ground state coupled to the low-energy

fundamental states[110] and was shown to provide an $r_e^{SE}$ structure with complete consistency with the BTE.[83,87]

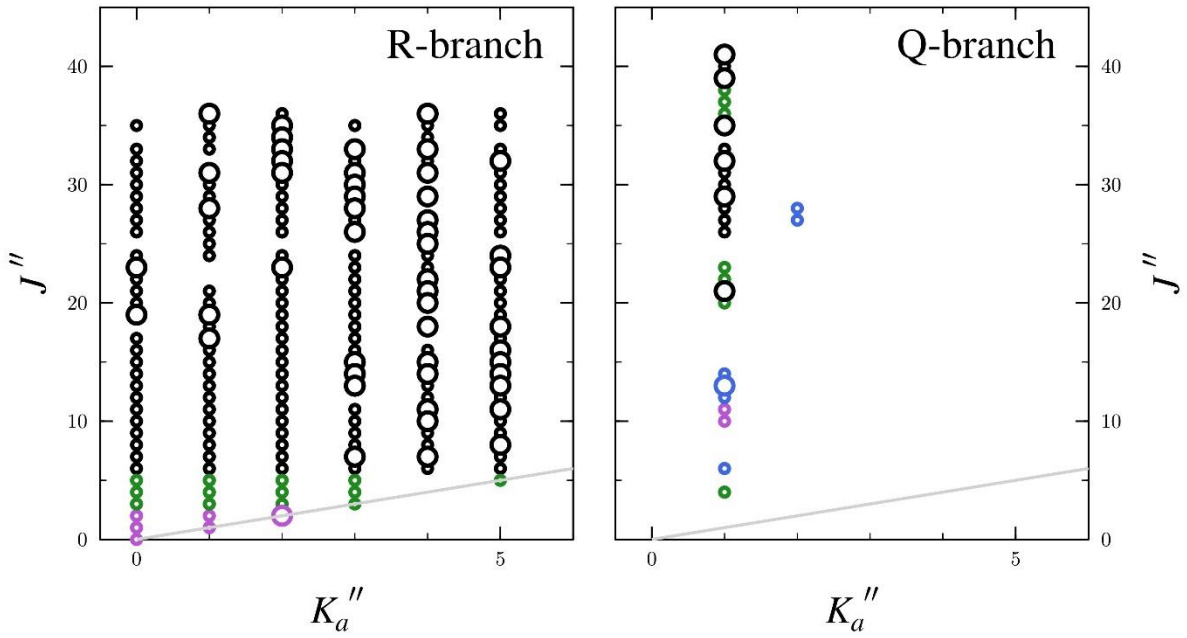


**FIG. 5.5.** Data distribution plot for the least-squares fit of spectroscopic data for the vibrational ground state of ketene. The size of the outlined circle is proportional to the value of $|(f_{obs.} - f_{calc.})/\delta f|$, where $\delta f$ is the frequency measurement uncertainty. The transitions are color coordinated as follows: Current work (black), Brown *et al.*[28] (purple), Johnson *et al.*[25] (blue), Guarnieri *et al.*[60](green). Transitions from previous works that overlapped with current measurements were omitted from the data set.

The heavy-atom isotopologues of ketene were observed at natural abundance from the synthesized protio sample of ketene, and only ${}^aR_{0,1}$ transitions could be observed and measured. The [2-$^2$H]-ketene and [2,2-$^2$H]-ketene isotopologues were the only other isotopologues where ${}^aQ_{0,-1}$ transitions could be measured. The [2-$^2$H]-ketene isotopologue has a small predicted *b*-dipole moment, $\mu_b$ = 0.048 D, but no *b*-type transitions were sufficiently intense to be observed in our spectrum. All of the heavy-atom isotopologues for [2-$^2$H]-ketene and [2,2-$^2$H]-ketene were observable at natural abundance from their deuterium-enriched samples. For the previously observed isotopologues, the published spectroscopic constants were used as predictions for the

spectral region measured in this work. Once rotational constants were obtained for several known isotopologues, a preliminary semi-experimental equilibrium structure was obtained, which provided very accurate equilibrium rotational constants for new isotopologues. Along with CCSD(T) vibrational and electronic corrections and centrifugal distortion constants, the predicted rotational constants were used to assign transitions for the previously unidentified isotopologues: [2-$^{2}$H, 1-$^{13}$C]-ketene, [2-$^{2}$H, 2-$^{13}$C]-ketene, [2-$^{2}$H, $^{18}$O]-ketene, [2-$^{2}$H, $^{17}$O]-ketene, and [2,2-$^{2}$H, $^{17}$O]-ketene. This technique greatly expedited the search for these transitions, as the CCSD(T)/cc-pCVTZ rotational constants predictions were not accurate enough to easily identify and assign the transitions. All heavy-atom isotopologue transitions measured from 500 GHz to 750 GHz and all three $^{17}$O isotopologues measured from 230 GHz to 500 GHz required 20 scans per transition due to low *S/N*. These low *S/N* transitions were collected by acquiring 10 MHz windows around each predicted transition. Despite the various isotopologue substitutions, the spectral pattern (Fig. 5.6) of ketene was relatively consistent due to the highly prolate nature of the molecule.

The rotational spectra of three separate ketene samples are shown in Fig. 5.6, where (a) corresponds to the protio isotopologue from 420 GHz to 434 GHz, (b) corresponds to the [2-$^{2}$H]-ketene isotopologue from 420 GHz to 434 GHz, and (c) corresponds to the [2,2-$^{2}$H]-ketene isotopologue from 411 GHz to 425 GHz along with their respective heavy-atom isotopologues. The rotational spectrum of ketene is sparse with of bands of R-branch transitions with constant *J* values, separated by ~ 16 GHz or ~2*C*, allowing for the assignment of multiple isotopologues within one sample spectrum. Thus, there was little issue with transitions overlapping, which would cause a poor determination of the transition frequencies. Each spectrum contains unassigned transitions belonging to excited vibrational states of ketene isotopologues, as demonstrated in Fig.

5.6. Data distribution plots for the isotopologues, showing the breadth of quantum numbers observed, are provided in the supplementary material.

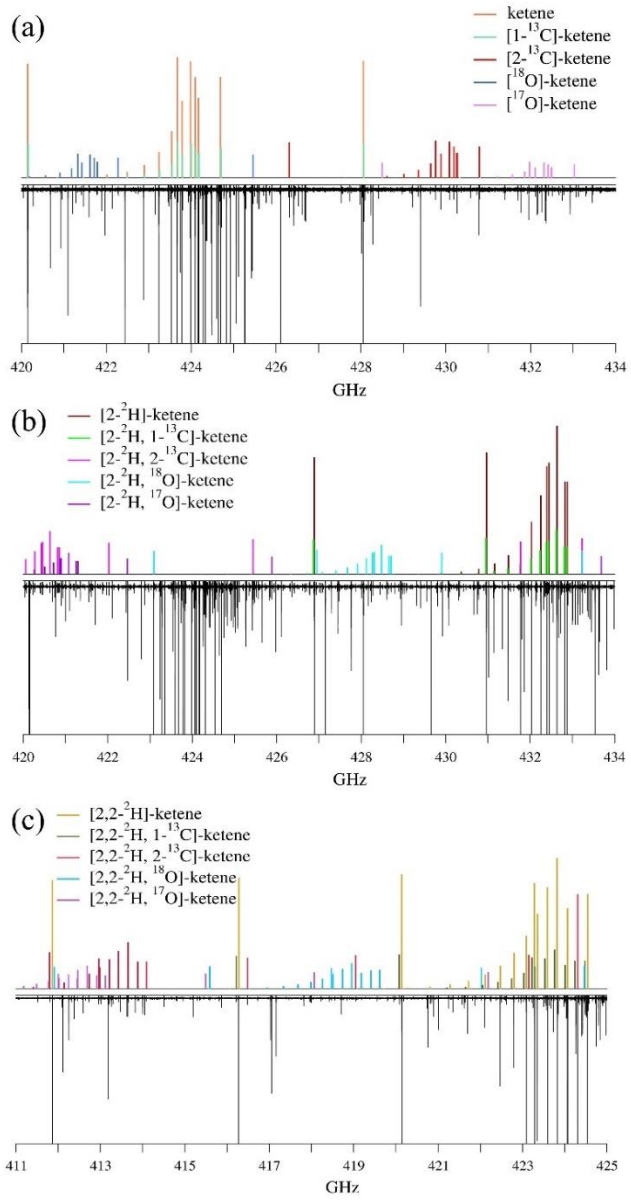


**FIG. 5.6.** (a) Stick spectra predicted from experimental spectroscopic constants from 420.0 to 434.0 GHz (top) and experimental spectrum (bottom) of the ketene and heavy-atom isotopologues. (b) Stick spectra predicted from experimental spectroscopic constants from 420.0 to 434.0 GHz (top) and experimental spectrum (bottom) of the [2-$^{2}$H]-ketene and heavy-atom isotopologues. (c) Stick spectra predicted from experimental spectroscopic constants from 411.0 to 425.0 GHz (top) and experimental spectrum (bottom) of the [2,2-$^{2}$H]-ketene and heavy-atom isotopologues. Transitions belonging to vibrationally excited states are also discernible.

**Semi-experimental Equilibrium Structure ($r_e^{SE}$)**

In contrast to several of our recent $r_e^{SE}$ structure determinations,[79-86] the spectroscopic constants determined in the S reduction ($B_0^{\beta(S)}$) were converted to equilibrium constants ($B_e^{\beta}$) and used directly in the least-squares fitting of the semi-experimental equilibrium structure without conversion to the determinable constants. In those previous works, with the exception of [1,3-$^2$H]-1*H*-1,2,4-triazole, the A-reduction and S-reduction rotational constants for each isotopologue were converted to the determinable constants in which the centrifugal distortion has been removed. These determinable constants are then averaged before converting to the equilibrium constants ($B_e^{\beta}$) for $r_e^{SE}$ structure determination. As noted previously, ketene is an extreme prolate top ($\kappa = -0.997$) with only *a*-type transitions, thus the A-reduction spectroscopic constants cannot be determined as accurately as the S-reduction constants. As a result, the S-reduction specific vibration-rotation interaction corrections determined in the CFOUR anharmonic frequency calculation were used to obtain the equilibrium rotational constants. Thus, the centrifugal distortion corrections used to determine the equilibrium rotational constants are the computed rather than the experimental ones. Ideally, the spectroscopic constants would be determined in both the A and S reductions, and each rotational constant would be converted to a determinable constant. If the determinable constants were similar, it would give confidence that the rotational and quartic centrifugal distortion constants were determined with sufficient accuracy to be included in the structure determination, regardless of the size of the transition data set. A similar problem might have arisen in the $HN_3$ semi-experimental equilibrium structure determinations,[83,87] but the $HN_3$ data set included *b*-type transitions, along with *a*-type transitions, which gave enough spectroscopic information to successfully determine the A-reduction spectroscopic constants.

In the current case, the S-reduction rotational constants were input to *xrefit*, along with vibration-rotation interaction and electron-mass distribution corrections predicted at the CCSD(T)/cc-pCVTZ level of theory. The *xrefit* module uses the values to calculate the equilibrium rotational constants ($B_e$) using Eq. (2), where the second term contains the vibration-rotation interaction correction, $\frac{m_e}{M_p}$ is the electron-proton mass ratio, $B_0^{\beta(S)}$ is the S-reduction rotational constant, and $g^{\beta\beta}$ is the corresponding magnetic $g$-tensor component.

$$B_e^{\beta} = B_0^{\beta(S)} + \frac{1}{2}\sum_i \alpha_i^{\beta} - \frac{m_e}{M_P} g^{\beta\beta} B^{\beta} \qquad (2)$$

These calculated equilibrium rotational constants are then used to calculate the inertial defect ($\Delta_i$), which is precisely zero for a rigid, planar molecule. For ketene, without either computational correction, the observed inertial defect $\Delta_{i0}$ is approximately 0.09 uÅ$^2$ (Table 5.3). Including the vibration-rotation interaction correction decreases the inertial defect to approximately 0.004 uÅ$^2$, while the inclusion of the electron-mass correction brings the inertial defect to slightly larger than 0.004 uÅ$^2$ (Table 5.3) in a similar manner to $HN_3$.[83] These two molecules stand in contrast to the trend observed for heterocyclic molecules,[79-82,111] where the vibration-rotation interaction correction results in a small negative value of $\Delta_{ie}$ and subsequent application of the electron-mass correction brings the magnitude of $\Delta_{ie}$ close to zero.[79-82,111] The similar inertial defect trend to $HN_3$ is likely due to the nature of the C−C−O backbone, where the electron mass is more-or-less cylindrically distributed in the combined in-plane and out-of-plane π orbitals.

**TABLE 5.3.** Inertial defects ($\Delta_i$) and second moments ($P_{bb}$) of ketene isotopologues**.**

| Isotopologue | $\Delta_{i0}$ (uÅ$^2$) [a] | $\Delta_{ie}$ (uÅ$^2$) [a,b] | $\Delta_{ie}$ (uÅ$^2$) [a,c] | $P_{bb}$ (uÅ$^2$) [c,d] | $P_{bb}$ / $m_H$ (Å$^2$) [c,d,e] |
|---|---|---|---|---|---|
| $H_2CCO$ | 0.0774 | 0.0035 | 0.0041 | 1.782 76 | 1.768 92 |
| [1-$^{13}$C]-$H_2CCO$ | 0.0772 | 0.0035 | 0.0040 | 1.782 77 | 1.768 93 |
| [2-$^{13}$C]-$H_2CCO$ | 0.0772 | 0.0035 | 0.0041 | 1.782 75 | 1.768 91 |
| [$^{18}$O]-$H_2CCO$ | 0.0779 | 0.0036 | 0.0042 | 1.782 70 | 1.768 86 |
| [$^{17}$O]-$H_2CCO$ | 0.0779 | 0.0038 | 0.0044 | 1.782 59 | 1.768 75 |
| [1,2-$^{13}$C]-$H_2CCO$ | 0.0766 | 0.0031 | 0.0037 | 1.782 95 | 1.769 11 |
| [2,2-$^{2}$H]-$H_2CCO$ | 0.1089 | 0.0036 | 0.0042 | 3.561 73 | 1.768 40 |
| [2,2-$^{2}$H, 2-$^{13}$C]-$H_2CCO$ | 0.1086 | 0.0036 | 0.0042 | 3.561 74 | 1.768 40 |
| [2,2-$^{2}$H, 1-$^{13}$C]-$H_2CCO$ | 0.1086 | 0.0036 | 0.0042 | 3.561 74 | 1.768 40 |
| [2,2-$^{2}$H, $^{18}$O]-$H_2CCO$ | 0.1095 | 0.0036 | 0.0042 | 3.561 75 | 1.768 40 |
| [2,2-$^{2}$H, $^{17}$O]-$H_2CCO$ | 0.1093 | 0.0037 | 0.0043 | 3.561 77 | 1.768 42 |
| [2-$^{2}$H]-$H_2CCO$ | 0.0964 | 0.0037 | 0.0043 | 2.594 89 | |
| [2-$^{2}$H, 2-$^{13}$C]-$H_2CCO$ | 0.0963 | 0.0037 | 0.0043 | 2.598 82 | |
| [2-$^{2}$H, 1-$^{13}$C]-$H_2CCO$ | 0.0961 | 0.0036 | 0.0042 | 2.595 32 | |
| [2-$^{2}$H, $^{18}$O]-$H_2CCO$ | 0.0969 | 0.0037 | 0.0043 | 2.595 58 | |
| [2-$^{2}$H, $^{17}$O]-$H_2CCO$ | 0.0966 | 0.0036 | 0.0042 | 2.595 31 | |
| **average** | 0.0918 | 0.0036 | 0.0042 | | |
| **std dev** | 0.0132 | 0.0001 | 0.0001 | | |

[a] $\Delta_i = I_c - I_a - I_b = -2P_{cc}$
[b] Vibration-rotation interaction corrections only.
[c] Vibration-rotation interaction and electron-mass corrections.
[d] $P_{bb} = (I_b - I_a - I_c)/-2$
[e] $m_H$ = 1.007825035 for $^1$H or 2.014101779 for $^2$H

The semi-experimental equilibrium structure parameters of ketene obtained from 16 isotopologues are depicted in Fig. 5.7 and enumerated in Table 5.4. The 2σ statistical uncertainties of the bond distances are all < 0.0007 Å, and the corresponding uncertainty in the bond angle is 0.014°. Overall, the precision and accuracy of the structural parameters are similar to those of $HN_3$[83] when comparing the $r_e^{SE}$ calculated at the same level of theory. The 2σ statistical uncertainties of heavy-atom bond lengths are nearly identical for $HN_3$ and ketene (0.000 74 for N1−N2; 0.000 75 for N2−N3; 0.0007 for both C1−C2 and C1−O). The 2σ statistical uncertainty

for the respective X−H bond is also quite similar (0.000 3 for $HN_3$ and 0.000 2 for ketene). More generally, the bond length accuracy of the $r_e^{SE}$ of ketene is similar to our other works including heterocyclic molecules[79-82,111] and is of the same order of magnitude for the accuracy in the angles, with that in ketene being more accurately determined. This improvement in accuracy is largely due to having 8× more independent moments of inertia than structural parameters (three bond lengths and one angle) for ketene. Included in Table 5.4 is the recommended presentation of the $r_e^{SE}$ structural parameters that has taken into account the limits of precision in their determination (*vide infra*).

**TABLE 5.4.** Equilibrium structural parameters of ketene.

| | $r_e^{SE}$ [a,b] East *et al.*[57] | $r_e^{SE}$ [a,c] Guarnieri *et al.*[58] | $r_e^{SE}$ this work | **$r_e^{SE}$ recommended** | CCSD(T) BTE | CCSD(T)/ cc-pCV6Z |
|---|---|---|---|---|---|---|
| $r_{C–C}$ (Å) | 1.312 12 (60) | 1.312 2 (12) | 1.312 18 (69) | **1.312 2 (7)** | 1.312 58 | 1.312 00 |
| $r_{C–H}$ (Å) | 1.075 76 (14) | 1.076 3 (2) | 1.075 93 (16) | **1.075 9 (2)** | 1.075 89 | 1.075 65 |
| $r_{C–O}$ (Å) | 1.160 30 (58) | 1.160 7 (12) | 1.160 64 (66) | **1.160 6 (7)** | 1.160 97 | 1.160 07 |
| $\theta_{C–C–H}$ (°) | 119.110 (12) | 119.115 (22) | 119.086 (14) | **119.086 (14)** | 119.077 | 119.067 |
| $N_{iso}$ [d] | 6 | 11 | 16 | **16** | | |

[a] 2σ uncertainties calculated based off of uncertainty presented in each work.
[b] Vibration-rotation corrections calculated at a mixed MP2 and CCSD(T) level.
[c] Vibration-rotation and electron-mass corrections calculated at the MP2/cc-pVTZ level.
[d] Number of isotopologues used in the structure determination.

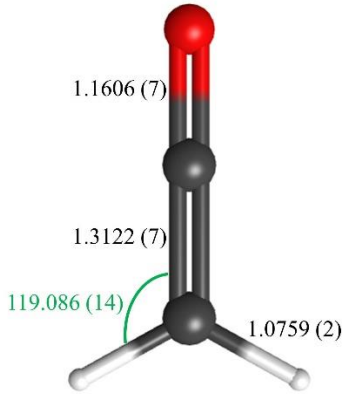


**FIG. 5.7.** Semi-experimental equilibrium structure ($r_e^{SE}$) of ketene with 2σ statistical uncertainties from least-squares fitting of the moments of inertia from 16 isotopologues. Distances are in Angstroms and the angle is in degrees.

**Discussion**

In accordance with previous structure determinations,[80-85] the effect of including the available isotopologues in the $r_e^{SE}$ structure is examined using *xrefiteration*.[82] Figure 5.8 shows a plot of parameter uncertainty as a function of number of incorporated isotopologues and reveals that the total uncertainty and the uncertainty of both the bond distances and bond angle have converged by the inclusion of the 11$^{th}$ isotopologue. Coincidentally, this is the same number of isotopologues used in the $r_e^{SE}$ determination published by Guarnieri *et al.*[58] The composition of the set of 11 isotopologues, however, is different in each case. Guarnieri *et al.*[58] determined the $r_e^{SE}$ with mainly protio and [2,2-$^2$H]-ketene isotopologues, while the first 11 isotopologues utilized by *xrefiteration* in the current work include a mix of protio, [2-$^2$H]-ketene, and [2,2-$^2$H]-ketene isotopologues. The addition of the five other isotopologues beyond the 11$^{th}$ neither decreases nor increases the total uncertainty, which is similar to the situation observed with $HN_3$[83] but unlike the cases of thiophene[80] and 1*H*- and 2*H*-1,2,3-triazole,[85] where the statistical uncertainty increases with the inclusion of the final isotopologues. Figure 5.9 shows the structural parameter values and their uncertainties as a function of number of ketene isotopologues, added in the same order as in Fig. 5.8. It is evident that the structural parameters are well-determined with the core set of isotopologues, because they agree with the respective BTE values. The addition of further isotopologues, however, decreases the 2σ uncertainties for all parameters until the addition of the eleventh isotopologue, similar to Fig. 5.8. The $r_{C–C}$ and $r_{C–O}$ bond lengths of the current $r_e^{SE}$ are both smaller than the respective BTE values (by 0.0003 and 0.0004 Å, respectively), while there is quite close agreement between the $r_{C–H}$ bond lengths ($r_{eC–H} - r_e^{SE}{}_{C–H}$ = 0.000 04 Å). The value of the bond angle, $\theta_{C–C–H}$, is slightly larger (0.009°) than the BTE value. Both heavy-atom bond distances of the $r_e$ BTE structure are too large (Fig. 5.9) relative to their $r_e^{SE}$ parameters, and the

observed residuals are very similar to those we observed in $HN_3$,[83] 0.000 35 Å for the central $r_{N1-N2}$ bond and 0.000 41 Å for the terminal $r_{N1-N2}$ bond. In the structural least-squares fitting from rotational constants, the most difficult atom to locate is the heavy atom nearest the center of mass, but an error in its location would tend to make one heavy-atom distance too long and one too short, contrary to the observations in ketene and $HN_3$. This may suggest that these residual discrepancies, which are not present in the distances involving H atoms, are due to some systematic shift in the BTE distances related to the heavy atom backbone of these molecules.

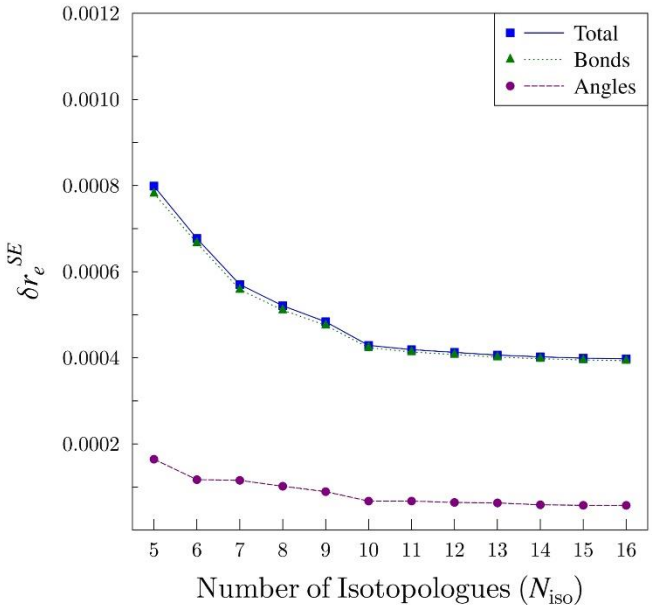


| $N_{iso}$ | Isotopologue Added |
|---|---|
| 5 | Core set |
| 6 | [2-$^2$H, $^{18}$O] |
| 7 | [2-$^2$H, 2-$^{13}$C] |
| 8 | [1,2-$^{13}$C] |
| 9 | [2,2-$^2$H, 2-$^{13}$C] |
| 10 | [2,2-$^2$H, $^{18}$O] |
| 11 | [$^{17}$O] |
| 12 | [2,2-$^2$H, 1-$^{13}$C] |
| 13 | [2-$^2$H, $^{17}$O] |
| 14 | [2,2-$^2$H, $^{17}$O] |
| 15 | [2,2-$^2$H] |
| 16 | [2-$^2$H, 1-$^{13}$C] |

**FIG. 5.8.** Plot of $r_e^{SE}$ *Uncertainty* ($\delta r_e^{SE}$) as a function of the number of isotopologues ($N_{iso}$) incorporated into the structure determination data set for ketene. The total relative statistical uncertainty ($\delta r_e^{SE}$, blue squares), the relative statistical uncertainty in the bond distances (green triangles), and the relative statistical uncertainty in the angle (purple circles) are presented.

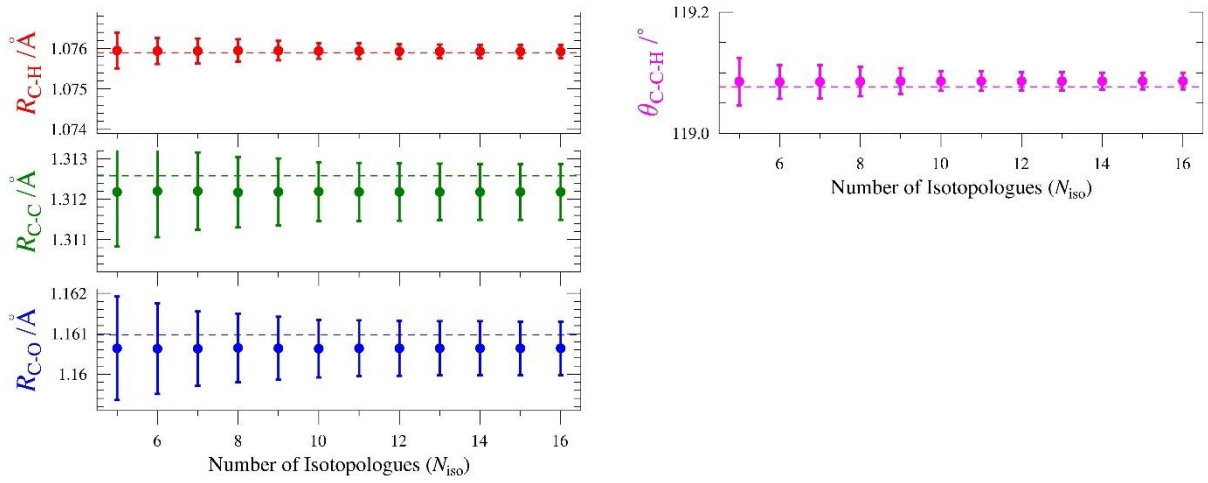


**FIG. 5.9.** Plots of the structural parameters of ketene as a function of the number of isotopologues ($N_{iso}$) and their 2σ uncertainties. Distance plots use consistent scales. Colored dashed lines indicate the BTE value. The table in Fig. 5.8 indicates the $x^{th}$ isotopologue added to the $r_e^{SE}$.

A graphical representation of all the structural parameters for the current $r_e^{SE}$, the $r_e^{SE}$ by East *et al.*,[57] the $r_e^{SE}$ by Guarnieri *et al.*,[58] the BTE, and various coupled-cluster calculations with different basis sets is shown in Fig. 5.10. Upon cursory inspection, it seems there is excellent agreement among all of the structural parameters of the three $r_e^{SE}$ structures (Table 5.4 and Fig. 5.10), and all are quoted to similar precision. Because separate sets of discrepancies are involved with respect to the two previous $r_e^{SE}$ structure determinations, we will discuss them separately. The heavy-atom distances from Guarnieri *et al.*[58] are essentially the same as our own, although with slightly larger 2σ uncertainties due to the smaller data set compared to the present work, and BTE results for both parameters easily fall within the quoted 2σ limit. The agreement for the two parameters involving the hydrogen-atom position is not quite as good. The $r_{C-H}$ bond distance from Guarnieri *et al.*[58] is in disagreement with our value to slightly more than the combined 2σ error estimates, and the BTE value falls well outside their 2σ error range. The angle, $\theta_{C-C-H}$, is indeed in agreement with our value within the combined estimated 2σ error limits, but the BTE value of this parameter falls significantly outside their 2σ error range. We believe the reason for

these discrepancies is due to the impact of untreated coupling between vibrational states impacting the rotational constants. It is known that the ground state of ketene at high $K_a$ values is affected by perturbations from low-lying vibrational states. We have chosen to employ only measurements for $K_a = 0 – 5$, which removed this problem. Guarnieri *et al.*,[58] however, used higher $K_a$ transitions in their least-squares fits, which required the inclusion of higher-order centrifugal distortion terms, $L_{JK}$ and $L_{JKK}$. These effective parameters distort the determined values of $A_0$ from the regression analysis, which may affect the structural parameters. We tested our conjecture by using our rotational constants for the set of isotopologues used by Guarnieri *et al.*[58] and found the resultant structure in essentially complete agreement with our own $r_e^{SE}$ structure (Table 5.4), which is consistent with the analysis of the structure shown in Fig. 5.9. This indicates that the five additional isotopologues that we measured and included were not required to achieve this improved accuracy.

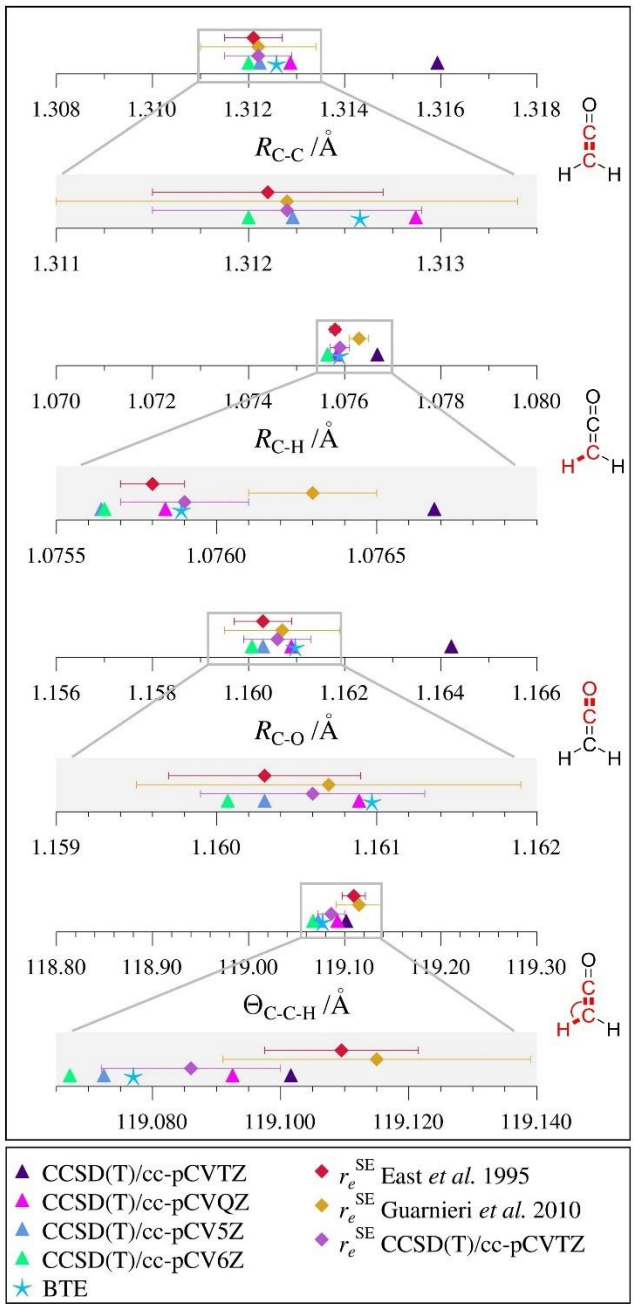


**FIG. 5.10.** Graphical comparison of the ketene structural parameters with bond distances in angstroms (Å) and angle in degrees (°). Bond distances are set to the same scale. Expansions are provided for each parameter in gray boxes. Statistical uncertainties for all $r_e^{SE}$ parameters are 2σ.

The situation with respect to the $r_e^{SE}$ structure from East *et al.*[57] is more straightforward. The bond distances and angles reported by East *et al.*[57] are in complete agreement with the current $r_e^{SE}$ values. This is somewhat surprising, given that the rotational constants are substantially less precise than the values determined in the present work and that the $A_0$ constant of [$^{18}$O]-ketene

used by East *et al.*[57] and determined experimentally by Brown *et al.*,[28] 287350 (910) MHz, is clearly too large by about 5 GHz. The values of $A_0$ for all heavy-atom isotopologues should be nearly the same, because they depend only on the distance of the hydrogen atoms from the *a*-axis. This is confirmed by the data in Table 5.2. The remaining rotational constants used by East *et al.*[57] are all similar to those in the present work. We obtained an $r_e^{SE}$ structure using the rotational constants and vibration-rotation interaction corrections presented in Table XIV of the East *et al.*[57] work and obtained a structure very closely resembling the one presented in that work for all parameters. This is also an interesting outcome as the vibration-rotation interaction corrections used in that work are clearly inadequate, as evidenced by the residual inertial defects presented in their Table XIV[57] that vary in sign and order of magnitude across the six isotopologues. Despite the inadequacy of the vibration-rotation interaction corrections, the $r_e^{SE}$ structure of East *et al.*[57] is in excellent agreement with the new $r_e^{SE}$, but not quite in agreement with the $\theta_{C–C–H}$ value from the $r_e$ BTE structure. These analyses are provided in the Supplementary Material and summarized in Table S-V and Table S-VI.

The $r_e^{SE}$ structure presented in this work, like the previously reported structures,[57,58] suffers from the impact of untreated Coriolis coupling between its ground state and its vibrationally excited states. Despite this limitation, the 2σ statistical uncertainties for the bond distances and bond angles are quite small (0.000 2 to 0.000 7 Å for the bond distances and 0.014° for the bond angle). For the bond distances, this statistical uncertainty is approaching the limit of the $r_e^{SE}$ structure determination, which requires the assumption that there is one mass-independent equilibrium geometry. The mass-independence of equilibrium structures is a tacitly accepted assumption of molecular structure determination by rotational spectroscopy that is no longer valid as the limits of accuracy and precision are extended, especially for parameters involving hydrogen

atoms. As a simple test of this assumption, optimized geometries were obtained for ketene and [2,2-$^2$H]-ketene with and without the diagonal Born-Oppenheimer correction (DBOC; SCF with the aug-cc-pCVTZ basis set). Of course, the $r_e$ structure obtained from the *normal* optimization without the DBOC resulted in the same equilibrium geometry for both isotopologues. With the DBOC, however, the equilibrium C–D distance decreased relative to the C–H distance by 0.000 06 Å. This value, which is similar to that obtained for benzene,[86] suggests that the limit and trustworthiness of the $r_e^{SE}$ structure for ketene and other C–H containing $r_e^{SE}$ structures is on the order of 0.000 1 Å or half of the 2σ statistical uncertainty of the $r_e^{SE}$ C–H distance in this work. As a result, we recommend that the structure of ketene be regarded as $r_{C–C}$ = 1.3122 (2) Å, $r_{C–H}$ = 1.0759 (2) Å, $r_{C–O}$ = 1.1606 (7) Å, and $\theta_{C–C–H}$ = 119.086 (14)°, as shown in Table 5.4.

The $C_{2v}$ symmetry of ketene-$h_2$ and ketene-$d_2$ allows for two independent confirmations of the quality of the spectroscopic analysis and computational corrections, $P_{bb}$ and $\Delta_{ie}$. The $\Delta_{ie}$ for a planar molecule is zero, as no nuclear mass exists off of the molecular plane. Any residual inertial defect after correction of the rotational constants for the vibration-rotation interaction and the electronic mass distribution potentially reveals room for improvements in the rotational constants or computational corrections. While all of the residual $\Delta_{ie}$ values are quite small (Table 5.3), their non-zero values demonstrate that further corrections may be possible. Their scatter reveals an interesting mass dependence. The ketene-$d_1$ and ketene-$d_2$ isotopologues have nearly identical inertial defects to four decimal places (0.004 2 or 0.004 3 uÅ$^2$), while the ketene-$h_2$ isotopologues have an average value of (0.004 2 uÅ$^2$) and range from 0.003 7 to 0.004 4 uÅ$^2$. To probe this mass dependence, we determined the $P_{bb}$ (second moments) value[112] for each isotopologue (Table 5.3), after computational corrections were applied to the rotational constants. To the extent that there is a single, mass-independent equilibrium geometry of ketene, the $P_{bb}$ value, corrected for the mass

of the hydrogen or deuterium atom in the $C_{2v}$ isotopologues (ketene-$h_2$ and ketene-$d_2$), should be the same for all isotopologues because it is only dependent on the location of the H atoms with respect to the perpendicular mirror plane. Also shown in Table 5.3, the $P_{bb}/m_H$ values are practically identical for all of the ketene-$d_2$ isotopologues (1.7684 Å$^2$). The $P_{bb}/m_H$ values for the protio ketene isotopologues show an increased scatter ranging from 1.7687 to 1.7691 Å$^2$ but have a higher average value as well (1.7689 Å$^2$). While these differences are small, their clear mass dependence leads us to conclude that we have not completely removed the impact of untreated Coriolis coupling from the rotational constants. The larger mass of $^2$H compared to $^1$H reduces the $A_0$ rotational constant by roughly a factor of two for the deuterium-containing isotopologues. The *a*-axis Coriolis $\zeta$ is unchanged between isotopologues, but the *a*-axis Coriolis coupling constants scale with the magnitude of the $A_0$ rotational constant. It is expected, therefore, that the protio ketenes would be subject to a slightly greater impact of untreated Coriolis coupling, which is consistent with this observation. The great constancy of the $P_{bb}/m_D$ values across all the [2,2-$^2$H]-ketene isotopologues (*vide supra*) leads us to believe that the corresponding *b*-coordinate of the $^2$H-atom (0.940 32 Å, determined by Eqn. 3) is one of the most reliably determined structural parameters of ketene.

$$b_H = \sqrt{\frac{P_{bb}}{2m_H}} \tag{3}$$

This assertion is supported by a comparison to its corresponding values calculated from the internal coordinates in Table 5.4: $r_e^{SE}$ = 0.940 25 Å, $r_e$ 6Z = 0.940 17 Å, and $r_e$ BTE = 0.940 29 Å. The very small difference from the BTE value (0.000 03 Å) is particularly notable and satisfying. The corresponding value for the *b*-coordinate of the $^1$H-atom in ketene is 0.940 45 Å, which is slightly

larger due to some combination of the true isotopic difference in the $r_{C–H}$ and $r_{C–D}$ equilibrium bond distances and the increased untreated Coriolis coupling in the protioketene isotopologues.

**Conclusion**

A new, highly precise, and accurate semi-experimental equilibrium ($r_e^{SE}$) structure for ketene ($H_2C=C=O$) has been determined from the rotational spectra of 16 isotopologues. The $2\sigma$ values for the $r_e^{SE}$ structure of ketene, and also the discrepancies between the Best Theoretical Estimate (BTE) and the $r_e^{SE}$ structural parameters, are strikingly similar to those for the previous $r_e^{SE}$ structure of hydrazoic acid (HNNN).[83] This outcome is noteworthy, although perhaps not surprising, given i) the structural similarity between the two species, and ii) the highly over-determined data sets, which are a consequence of the large number of isotopologues relative to the number of structural parameters. In both cases, we found that extrapolation to the complete basis set limit provided slightly better agreement with the $r_e^{SE}$ structure when the highest level calculation included in the extrapolation was CCSD(T)/cc-pCV6Z, as opposed to CCSD(T)/cc-pCV5Z. It is somewhat surprising that the high accuracy of the ketene structure did not require the full dataset from 16 isotopologues. The uncertainties in the structural parameters did not improve with the inclusion of the 'last' five isotopologues in the *xrefiteration* analysis. This case stands in contrast to other molecules that we have studied in which quite large numbers of isotopologues are required for convergence of the $r_e^{SE}$ parameters.[82,84,85] Previous studies were steering us toward a generalization that 'more is better' with respect to the number of isotopologues used in a structure determination, but the current case provides a counterexample. In the current case, the extra isotopologues do not degrade the quality of the structure, but they do not improve it. The current state of understanding of $r_e^{SE}$ structure determination does not enable a prediction

of the number of isotopologues that will be required for the statistical uncertainties of the structural parameters to converge.

The present work confirms the great utility of the BTE structure as a benchmark for the semi-experimental structures. Although both of the published $r_e^{SE}$ structures for ketene, to which we have compared our own results, are generally in excellent agreement with the present work, the comparison to the BTE structure clearly establishes that the present approach of limiting the data set to low $K_a$ values $(0 - 5)$ improved the results for a molecule in which perturbations of the ground state exist. There needs to be further investigation of why the BTE structure predicts heavy-atom bond distances that are longer than the $r_e^{SE}$ structure, when all of the other structural parameters agree so well. The BTE values for the heavy-atom distances do not fall outside the $2\sigma$ statistical uncertainty of the $r_e^{SE}$ values, but the small differences between BTE and $r_e^{SE}$ values have now been observed in both ketene and $HN_3$. The general applicability to similar molecules and the origin of the effect merit additional study.

The current studies enhance the capability for radioastronomers to search for ketene in different extraterrestrial environments by extending the measured frequency range of ketene to 750 GHz, as well as providing data for newly measured isotopologues, [2-$^2$H, 1-$^{13}$C]-ketene, [2-$^2$H, 2-$^{13}$C]-ketene, [2-$^2$H, $^{18}$O]-ketene, [2-$^2$H, $^{17}$O]-ketene, and [2,2-$^2$H, $^{17}$O]-ketene. These new data will also be valuable for identifying these species in laboratory experiments, *e.g.*, electric discharge, pyrolysis, photolysis. Finally, these spectra contain a great many transitions from vibrationally excited states, which should prove valuable in analyzing and quantifying the numerous perturbations that exist between these low-lying vibrational states. We hope to pursue this in the future.

## SUPPLEMENTARY MATERIAL

Computational output files, least-squares fitting for all isotopologues, data distribution plots for all non-standard isotopologues, *xrefiteration* outputs, equations used for calculating determinable constants and BTE corrections, and tables of S-reduction, A-reduction, and determinable constants, structural parameters, inertial defects, BTE corrections, and synthetic details are provided in the supplementary material.

## ACKNOWLEDGMENTS

We gratefully acknowledge funding from the U.S. National Science Foundation for support of this project (CHE-1954270 to R.J.M; CHE-1664325 to J.F.S.). We thank Maria Zdanovskaia for her assistance with generating figures. We thank Maria Zdanovskaia and Andrew Owen for their thoughtful commentary and review of the manuscript. We thank Tracy Drier for construction of the ketene lamp used in this work.

## AUTHOR DECLARATIONS

### Conflict of Interest

The authors have no conflicts to disclose.

## DATA AVAILABILITY

The data that support the findings of this study are available within the article and its supplementary material at https://doi.org/10.1063/5.0154770.

## REFERENCES


1. T. T. Tidwell, *Ketenes*; 2nd ed.; John Wiley & Sons: Hoboken, NJ, 2006.
2. In *Science of Synthesis*; Thieme, 2006; Vol. 23
3. A. D. Allen; T. T. Tidwell, "New Directions in Ketene Chemistry: The Land of Opportunity," Eur. J. Org. Chem., 1081-1096 (2012).
4. Y. Zhang; P. Gao; F. Jiao; Y. Chen; Y. Ding; G. Hou; X. Pan; X. Bao, "Chemistry of Ketene Transformation to Gasoline Catalyzed by H-SAPO-11," J. Am. Chem. Soc. **144** 18251−18258 (2022).
5. F. A. Leibfarth; C. J. Hawker, "The Emerging Utility of Ketenes in Polymer Chemistry," J. Polym. Sci., Part A: Polym. Chem. **51** 3769–3782 (2013).
6. M. J. Newland; G. J. Rea; L. P. Thüner; A. P. Henderson; B. T. Golding; A. R. Rickard; I. Barnes; J. Wenger, "Photochemistry of 2-butenedial and 4-oxo-2-pentenal under atmospheric boundary layer conditions," Phys. Chem. Chem. Phys. **21**, 1160 (2019).
7. W. Sun; J. Wang; C. Huang; N. Hansen; B. Yang, "Providing effective constraints for developing ketene combustion mechanisms: A detailed kinetic investigation of diacetyl flames," Combust. Flame **205**, 11-21 (2019).
8. R. L. Hudson; M. J. Loeffler, "Ketene Formation in Interstellar Ices: A Laboratory Study," Astrophys. J. **773**, 109 (2013).
9. B. E. Turner, "Microwave detection of interstellar ketene," Astrophys. J. **213**, L75-L79 (1977).
10. H. E. Matthews; T. J. Sears, "Interstellar Molecular Line Searches at 1.5 Centimeters," Astrophys. J. **300**, 766 (1986).
11. L. E. B. Johansson; C. Andersson; J. Ellder; P. Friberg; A. Hjalmarson; B. Hoglund; W. M. Irvine; H. Olofsson; G. Rydbeck, "Spectral scan of Orion A and IRC +10216 from 72 to 91 GHz," Astron. Astrophys. **130**, 227-256 (1984).
12. W. M. Irvine; P. Friberg; N. Kaifu; K. Kawaguchi; Y. Kitamura; H. E. Matthews; Y. Minh; S. Saito; N. Ukita; S. Yamamoto, "Observations of Some Oxygen-containing and Sulfur-containing Organic Molecules in Cold Dark Clouds," Astrophys. J. **342**, 871 (1989).
13. B. E. Turner; R. Terzieva; E. Herbst, "The Physics and Chemistry of Small Translucent Molecular Clouds. XII. More Complex Species Explainable by Gas-Phase Processes," Astrophys. J. **518**, 699 (1999).
14. A. Bacmann; V. Taquet; A. Faure; C. Kahane; C. Ceccarelli, "Detection of complex organic molecules in a prestellar core: a new challenge for astrochemical models," Astron. Astrophys **541**, L12 (2012).
15. J. K. Jørgensen; H. S. P. Müller; H. Calcutt; A. Coutens; M. N. Drozdovskaya; K. I. Öberg; M. V. Persson; V. Taquet; E. F. van Dishoeck; S. F. Wampfler, "The ALMA-PILS survey: isotopic composition of oxygen-containing complex organic molecules toward IRAS 16293–2422B," Astron. Astrophys **620** (2018).

16. S. Muller; A. Beelen; M. Guélin; S. Aalto; J. H. Black; F. Combes; S. J. Curran; P. Theule; S. N. Longmore, "Molecules at z = 0.89. A 4-mm-rest-frame absorption-line survey toward PKS 1830-211," Astron. Astrophys. **535**, A103 (2011).

17. H. Staudinger, *Die Ketene*; Enke Verlag: Stuttgart, 1912.

18. S. C. Wang; F. W. Schueler, "A simple ketene generator," J. Chem. Educ. **26**, 323 (1949).

19. G. Quadbeck, "Neuere Methoden der präparativen organischen Chemie II. Keten in der präparativen organischen Chemie," Angew. Chem. **68**, 361-370 (1956).

20. E. M. S. Maçôas; L. Khriachtchev; R. Fausto; M. Räsänen, "Photochemistry and Vibrational Spectroscopy of the *Trans* and *Cis* Conformers of Acetic Acid in Solid Ar," J. Phys. Chem. A **108**, 3380-3389 (2004).

21. X. K. Zhang; J. M. Parnis; E. G. Lewars; R. E. March, "FTIR spectroscopic investigation of matrix-isolated isomerization and decomposition products of ionized acetone: generation and characterization of 1-propen-2-ol," Can. J. Chem. **75**, 276-284 (1997).

22. B. J. Esselman; N. J. Hill, "Proper Resonance Depiction of Acylium Cation: A High-Level and Student Computational Investigation," J. Chem. Educ. **92**, 660-663 (2015).

23. J. Cernicharo; C. Cabezas; S. Bailleux; L. Margulès; R. Motiyenko; L. Zou; Y. Endo; C. Bermúdez; M. Agúndez; N. Marcelino; B. Lefloch; B. Tercero; P. de Vicente, "Discovery of the acetyl cation, $CH_3CO^+$, in space and in the laboratory," Astron. Astrophys. **646** (2021).

24. B. Bak; E. S. Knudsen; E. Madsen; J. Rastrup-Andersen, "Preliminary Analysis of the Microwave Spectrum of Ketene," Phys. Rev. **79**, 190-190 (1950).

25. H. R. Johnson; M. W. P. Strandberg, "The Microwave Spectrum of Ketene," J. Chem. Phys. **20**, 687-695 (1952).

26. A. P. Cox; L. F. Thomas; J. Sheridan, "Internuclear distances in keten from spectroscopic measurements," Spectrochim. Acta **15**, 542-543 (1959).

27. R. A. Beaudet, "Problems in molecular structure and internal rotation," Ph.D. Dissertation, Harvard University, 1962.

28. R. D. Brown; P. D. Godfrey; D. McNaughton; A. P. Pierlot; W. H. Taylor, "Microwave spectrum of ketene," J. Mol. Spectrosc. **140**, 340-352 (1990).

29. V. W. Weiss; W. H. Flygare, "Hydrogen Spin−Spin, Spin−Rotation, and Deuterium Nuclear Quadrupole Interactions in Ketene, Ketene-$d_1$, and Ketene-$d_2$," J. Chem. Phys. **45**, 3475-3476 (1966).

30. L. Nemes; M. Winnewisser, "Centrifugal distortion analysis of the microwave and millimeter wave spectra of deuterated ketenes," Z. Naturforsch., A **31A**, 272-282 (1976).

31. A. Guarnieri; A. Huckauf, "The Rotational Spectrum of ($^{17}$O)Ketene," Z. Naturforsch., A: Phys. Sci. **56**, 440-446 (2001).

32. A. Guarnieri, "The Millimeterwave Spectrum of Four Rare Ketene Isotopomers," Z. Naturforsch., A: Phys. Sci. **60**, 619-628 (2005).

33. L. Nemes; J. Demaison; G. Wlodarczak, "New measurements of sub-millimetre-wave rotational transitions for the ketene ($H_2CCO$) Molecule," Acta Phys. Hung. **61**, 135-138 (1987).

34. H. Gershinowitz; E. B. Wilson, "Infrared Absorption Spectrum of Ketene," J. Chem. Phys. **5**, 500-500 (1937).

35. F. Halverson; V. Z. Williams, "The Infra-Red Spectrum of Ketene," J. Chem. Phys. **15**, 552-559 (1947).

36. W. R. Harp; R. S. Rasmussen, "The Infra-Red Absorption Spectrum and Vibrational Frequency Assignment of Ketene," J. Chem. Phys. **15**, 778-785 (1947).

37. L. G. Drayton; H. W. Thompson, "The infra-red spectrum of keten.," J. Chem. Soc., 1416-1419 (1948).

38. B. Bak; F. A. Andersen, "The Infrared Spectrum of Ketene," J. Chem. Phys. **22**, 1050-1053 (1954).

39. P. E. B. Butler; D. R. Eaton; H. W. Thompson, "Vibration-rotation bands of keten," Spectrochim. Acta **13**, 223-235 (1958).

40. W. H. Fletcher; W. F. Arendale, "Infrared Spectra of $CD_2CO$ and CHDCO," J. Chem. Phys. **19**, 1431-1432 (1951).

41. W. F. Arendale; W. H. Fletcher, "Some Vibration-Rotation Bands of Ketene," J. Chem. Phys. **24**, 581-587 (1956).

42. W. F. Arendale; W. H. Fletcher, "Infrared Spectra of Ketene and Deuteroketenes," J. Chem. Phys. **26**, 793-797 (1957).

43. A. P. Cox; A. S. Esbitt, "Fundamental Vibrational Frequencies in Ketene and the Deuteroketenes," J. Chem. Phys. **38**, 1636-1643 (1963).

44. L. Nemes; Akad. Nauk SSSR, Sib. Otd., Inst. Opt. Atmos., 1974, p 2

45. L. Nemes, "Rotation-vibration analysis of the Coriolis-coupled $\nu_5$, $\nu_6$, $\nu_8$, and $\nu_9$ bands of $H_2CCO$," J. Mol. Spectrosc. **72**, 102-123 (1978).

46. F. Winther; F. Hegelund; L. Nemes, "The infrared spectrum of dideuteroketene below 620 $cm^{-1}$," J. Mol. Spectrosc. **117**, 388-402 (1986).

47. J. L. Duncan; A. M. Ferguson; J. Harper; K. H. Tonge; F. Hegelund, "High-resolution infrared rovibrational studies of the $A_1$ species fundamentals of isotopic ketenes," J. Mol. Spectrosc. **122**, 72-93 (1987).

48. J. L. Duncan; A. M. Ferguson, "High resolution infrared analyses of fundamentals and overtones in isotopic ketenes," Spectrochim. Acta A Mol. Biomol. Spectrosc. **43**, 1081-1086 (1987).

49. F. Hegelund; J. Kauppinen; F. Winther, "The high resolution infrared spectrum of the $\nu_9$, $\nu_6$ and $\nu_5$ bands in ketene-$d_2$," Mol. Phys. **61**, 261-273 (1987).

50. R. Escribano; J. L. Doménech; P. Cancio; J. Ortigoso; J. Santos; D. Bermejo, "The $\nu_1$ band of ketene," J. Chem. Phys. **101**, 937-949 (1994).

51. M. C. Campiña; E. Domingo; M. P. Fernández-Liencres; R. Escribano; L. Nemes, "Analysis of the high resolution spectra of the $\nu_5$ and $\nu_6$ bands of ketene," An. Quim., Int. Ed. **94**, 23-26 (1998).

52. M. Gruebele; J. W. C. Johns; L. Nemes, "Observation of the $\nu_6 + \nu_9$ Band of Ketene via Resonant Coriolis Interaction with $\nu_8$," J. Mol. Spectrosc. **198**, 376-380 (1999).

53. J. W. C. Johns; L. Nemes; K. M. T. Yamada; T. Y. Wang; J. Doménech; J. Santos; P. Cancio; D. Bermejo; J. Ortigoso; R. Escribano, "The ground state constants of ketene," J. Mol. Spectrosc. **156**, 501-503 (1992).

54. L. Nemes; D. Luckhaus; M. Quack; J. W. C. Johns, "Deperturbation of the low-frequency infrared modes of ketene ($CH_2CO$) " J. Mol. Struct. **517-518**, 217-226 (2000).

55. P. D. Mallinson; L. Nemes, "The Force Field and $r_z$ Structure of Ketene," J. Mol. Spectrosc. **59**, 470-481 (1976).

56. J. L. Duncan; B. Munro, "The ground state average structure of ketene," J. Mol. Struct. **161**, 311-319 (1987).

57. A. L. L. East; W. D. Allen; S. J. Klippenstein, "The anharmonic force field and equilibrium molecular structure of ketene," J. Chem. Phys. **102**, 8506-8532 (1995).

58. A. Guarnieri; J. Demaison; H. D. Rudolph, "Structure of ketene – Revisited $r_e$ (equilibrium) and $r_m$ (mass-dependent) structures," J. Mol. Struct. **969**, 1-8 (2010).

59. J. L. Duncan; A. M. Ferguson; J. Harper; K. H. Tonge, "A combined empirical-ab initio determination of the general harmonic force field of ketene," J. Mol. Spectrosc. **125**, 196-213 (1987).

60. A. Guarnieri; A. Huckauf, "The Rotational Spectrum of Ketene Isotopomers with $^{18}O$ and $^{13}C$ Revisited," Z. Naturforsch., A: Phys. Sci. **58**, 275-279 (2003).

61. C. C. Costain, "Determination of Molecular Structures from Ground State Rotational Constants," J. Chem. Phys. **29**, 864-874 (1958).

62. M. D. Harmony; V. W. Laurie; R. L. Kuczkowski; R. H. Schwendeman; D. A. Ramsay; F. J. Lovas; W. J. Lafferty; A. G. Maki, "Molecular structures of gas-phase polyatomic molecules determined by spectroscopic methods," J. Phys. Chem. Ref. Data **8**, 619-722 (1979).

63. P. Pulay; W. Meyer; J. E. Boggs, "Cubic force constants and equilibrium geometry of methane from Hartree–Fock and correlated wavefunctions," J. Chem. Phys. **68**, 5077-5085 (1978).

64. J. Demaison, "Experimental, semi-experimental and *ab initio* equilibrium structures," Mol. Phys. **105**, 3109-3138 (2007).

65. J. Vázquez; J. F. Stanton In *Equilibrium Molecular Structures: From Spectroscopy to Quantum Chemistry*; Demaison, J., Boggs, J. E., Császár, A. G., Eds.; Taylor & Francis Group: CRC Press, 2010, pp 53-87

66. M. Mendolicchio; E. Penocchio; D. Licari; N. Tasinato; V. Barone, "Development and Implementation of Advanced Fitting Methods for the Calculation of Accurate Molecular Structures," J. Chem. Theory Comput. **13**, 3060-3075 (2017).

67. C. Puzzarini; V. Barone, "Diving for Accurate Structures in the Ocean of Molecular Systems with the Help of Spectroscopy and Quantum Chemistry," Acc. Chem. Res. **51**, 548-556 (2018).

68. K. Raghavachari; G. W. Trucks; J. A. Pople; M. Head-Gordon, "A fifth-order perturbation comparison of electron correlation theories," Chem. Phys. Lett. **157**, 479-483 (1989).

69. J. M. L. Martin; P. R. Taylor, "The geometry, vibrational frequencies, and total atomization energy of ethylene. A calibration study," Chem. Phys. Lett. **248**, 336-344 (1996).

70. T. Helgaker; J. Gauss; P. Jørgensen; J. Olsen, "The prediction of molecular equilibrium structures by the standard electronic wave functions," J. Chem. Phys. **106**, 6430-6440 (1997).

71. K. A. Peterson; J. T. H. Dunning, "Benchmark calculations with correlated molecular wave functions. VIII. Bond energies and equilibrium geometries of the $CH_n$ and $C_2H_n$ ($n$=1–4) series," J. Chem. Phys. **106**, 4119-4140 (1997).

72. T. Helgaker; P. Jørgensen; J. Olsen, *Molecular Electronic-Structure Theory*; John Wiley & Sons, 2000.

73. K. L. Bak; J. Gauss; P. Jørgensen; J. Olsen; T. Helgaker; J. F. Stanton, "The Accurate Determination of Molecular Equilibrium Structures," J. Chem. Phys. **114**, 6548-6556 (2001).

74. S. Coriani; D. Marchesan; J. Gauss; C. Hättig; T. Helgaker; P. Jørgensen, "The accuracy of *ab initio* molecular geometries for systems containing second-row atoms," J. Chem. Phys. **123**, 184107 (2005).

75. C. Puzzarini, "Accurate molecular structures of small- and medium-sized molecules," Int. J. Quantum Chem. **116**, 1513-1519 (2016).

76. C. Puzzarini; J. F. Stanton, "Connections between the accuracy of rotational constants and equilibrium molecular structures," Phys. Chem. Chem. Phys. **25**, 1421-1429 (2023).

77. J. Gauss; J. F. Stanton, "Equilibrium structure of LiCCH," Int. J. Quantum Chem. **77**, 305-310 (2000).

78. M. Piccardo; E. Penocchio; C. Puzzarini; M. Biczysko; V. Barone, "Semi-Experimental Equilibrium Structure Determinations by Employing B3LYP/SNSD Anharmonic Force Fields: Validation and Application to Semirigid Organic Molecules," J. Phys. Chem. A **119**, 2058-2082 (2015).

79. Z. N. Heim; B. K. Amberger; B. J. Esselman; J. F. Stanton; R. C. Woods; R. J. McMahon, "Molecular structure determination: Equilibrium structure of pyrimidine ($m$-$C_4H_4N_2$) from rotational spectroscopy ($r_e^{SE}$) and high-level *ab initio* calculation ($r_e$) agree within the uncertainty of experimental measurement," J. Chem. Phys. **152**, 104303 (2020).

80. V. L. Orr; Y. Ichikawa; A. R. Patel; S. M. Kougias; K. Kobayashi; J. F. Stanton; B. J. Esselman; R. C. Woods; R. J. McMahon, "Precise equilibrium structure determination of thiophene ($c$-$C_4H_4S$) by rotational spectroscopy—Structure of a five-membered heterocycle containing a third-row atom," J. Chem. Phys. **154**, 244310 (2021).

81. B. J. Esselman; M. A. Zdanovskaia; A. N. Owen; J. F. Stanton; R. C. Woods; R. J. McMahon, "Precise equilibrium structure of thiazole (*c*-$C_3H_3NS$) from twenty-four isotopologues," J. Chem. Phys. **155**, 054302 (2021).

82. A. N. Owen; M. A. Zdanovskaia; B. J. Esselman; J. F. Stanton; R. C. Woods; R. J. McMahon, "Semi-Experimental Equilibrium ($r_e^{SE}$) and Theoretical Structures of Pyridazine (*o*-$C_4H_4N_2$)," J. Phys. Chem. A **125**, 7976-7987 (2021).

83. A. N. Owen; N. P. Sahoo; B. J. Esselman; J. F. Stanton; R. C. Woods; R. J. McMahon, "Semi-experimental equilibrium ($r_e^{SE}$) and theoretical structures of hydrazoic acid ($HN_3$)," J. Chem. Phys. **157**, 034303 (2022).

84. H. A. Bunn; B. J. Esselman; P. R. Franke; S. M. Kougias; R. J. McMahon; J. F. Stanton; S. L. Widicus Weaver; R. C. Woods, "Millimeter/Submillimeter-wave Spectroscopy and the Semi-experimental Equilibrium ($r_e^{SE}$) Structure of 1*H*-1,2,4-Triazole (*c*-$C_2H_3N_3$)," J. Phys. Chem. A **126**, 8196-8210 (2022).

85. M. A. Zdanovskaia; B. J. Esselman; S. M. Kougias; B. K. Amberger; J. F. Stanton; R. C. Woods; R. J. McMahon, "Precise equilibrium structures of 1*H*- and 2*H*-1,2,3-triazoles ($C_2H_3N_3$) by millimeter-wave spectroscopy," J. Chem. Phys. **157**, 084305 (2022).

86. B. J. Esselman; M. A. Zdanovskaia; A. N. Owen; J. F. Stanton; R. C. Woods; R. J. McMahon, "Precise Equilibrium Structure of Benzene," *unpublished work* (2023).

87. B. K. Amberger; B. J. Esselman; J. F. Stanton; R. C. Woods; R. J. McMahon, "Precise equilibrium structure determination of hydrazoic acid ($HN_3$) by millimeter-wave Spectroscopy," J. Chem. Phys. **143**, 104310 (2015).

88. B. J. Esselman; B. K. Amberger; J. D. Shutter; M. A. Daane; J. F. Stanton; R. C. Woods; R. J. McMahon, "Rotational spectroscopy of pyridazine and its isotopologs from 235–360 GHz: Equilibrium structure and vibrational satellites," J. Chem. Phys. **139**, 224304 (2013).

89. M. A. Zdanovskaia; B. J. Esselman; R. C. Woods; R. J. McMahon, "The 130 - 370 GHz Rotational Spectrum of Phenyl Isocyanide ($C_6H_5NC$)," J. Chem. Phys. **151**, 024301 (2019).

90. H. M. Pickett, "Determination of collisional linewidths and shifts by a convolution method," Appl. Opt. **19**, 2745-2749 (1980).

91. Z. Kisiel; L. Pszczółkowski; B. J. Drouin; C. S. Brauer; S. Yu; J. C. Pearson; I. R. Medvedev; S. Fortman; C. Neese, "Broadband rotational spectroscopy of acrylonitrile: Vibrational energies from perturbations," J. Mol. Spectrosc. **280**, 134-144 (2012).

92. Z. Kisiel; L. Pszczółkowski; I. R. Medvedev; M. Winnewisser; F. C. De Lucia; E. Herbst, "Rotational spectrum of *trans–trans* diethyl ether in the ground and three excited vibrational states," J. Mol. Spectrosc. **233**, 231-243 (2005).

93. H. M. Pickett, "The fitting and prediction of vibration-rotation spectra with spin interactions," J. Mol. Spectrosc. **148**, 371-377 (1991).

94. Z. Kisiel, "Assignment and Analysis of Complex Rotational Spectra," In *Spectroscopy from Space*; 1st ed.; Demaison, J., Sarka, K., Cohen, E. A., Eds.; Springer Netherlands: Dordrecht, 2001, pp 91-106.

95. "PROSPE - Programs for ROtational SPEctroscopy", http://info.ifpan.edu.pl/~kisiel/prospe.htm

96. "J.F. Stanton, J. Gauss, M.E. Harding, P.G. Szalay, with contributions from A.A. Auer, R.J. Bartlett, U. Benedikt, C. Berger, D.E. Bernholdt, Y.J. Bomble, L. Cheng, O. Christiansen, M. Heckert, O. Heun, C. Huber, T.-C. Jagau, D. Jonsson, J. Jusélius, K. Klein, W.J. Lauderdale, D.A. Matthews, T. Metzroth, L.A. Mück, D.P. O'Neill, D.R. Price, E. Prochnow, C. Puzzarini, K. Ruud, F. Schiffmann, W. Schwalbach, S. Stopkowicz, A. Tajti, J. Vázquez, F. Wang, J.D. Watts and the integral packages MOLECULE (J. Almlöf and P.R. Taylor), PROPS (P.R. Taylor), ABACUS (T. Helgaker, H.J. Aa. Jensen, P. Jørgensen, and J. Olsen), and ECP routines by A. V. Mitin and C. van Wüllen. *CFOUR, Coupled-Cluster techniques for Computational Chemistry*, a quantum-chemical program package. For the current version, see http://www.cfour.de".

97. J. F. Stanton; C. L. Lopreore; J. Gauss, "The equilibrium structure and fundamental vibrational frequencies of dioxirane," J. Chem. Phys. **108**, 7190-7196 (1998).

98. W. Schneider; W. Thiel, "Anharmonic Force Fields from Analytic Second Derivatives: Method and Application to Methyl Bromide," Chem. Phys. Lett. **157**, 367-373 (1989).

99. I. M. Mills, "Vibration-Rotation Structure in Asymmetric- and Symmetric-Top Molecules," In *Molecular Spectroscopy: Modern Research*; Rao, K. N., Mathews, C. W., Eds.; Academic Press: New York, 1972; Vol. 1, pp 115-140.

100. C. Puzzarini; J. Bloino; N. Tasinato; V. Barone, "Accuracy and Interpretability: The Devil and the Holy Grail. New Routes across Old Boundaries in Computational Spectroscopy," Chem. Rev. **119**, 8131-8191 (2019).

101. J. W. Williams; C. D. Hurd, "An Improved Apparatus for the Laboratory Preparation of Ketene and Butadiene," J. Org. Chem. **5**, 122-125 (1940).

102. P. J. Paulsen; W. D. Cooke, "Preparation of Deuterated Solvents for Nuclear Magnetic Resonance Spectrometry," Anal. Chem. **35**, 1560-1560 (1963).

103. J. K. G. Watson, "Determination of Centrifugal Distortion Coefficients of Asymmetric-Top Molecules," J. Chem. Phys. **46**, 1935-1949 (1967).

104. G. Winnewisser, "Millimeter Wave Rotational Spectrum of HSSH and DSSD. II. Anomalous *K* Doubling Caused by Centrifugal Distortion in DSSD," J. Chem. Phys. **56**, 2944-2954 (1972).

105. B. P. van Eijck, "Reformulation of quartic centrifugal distortion Hamiltonian," J. Mol. Spectrosc. **53**, 246-249 (1974).

106. V. Typke, "Centrifugal distortion analysis including $P^6$-terms," J. Mol. Spectrosc. **63**, 170-179 (1976).

107. L. Margulès; A. Perrin; J. Demaison; I. Merke; H. Willner; M. Rotger; V. Boudon, "Breakdown of the reduction of the rovibrational Hamiltonian: The case of $S^{18}O_2F_2$," J. Mol. Spectrosc. **256**, 232-237 (2009).

108. R. A. Motiyenko; L. Margulès; E. A. Alekseev; J. C. Guillemin; J. Demaison, "Centrifugal distortion analysis of the rotational spectrum of aziridine: Comparison of different Hamiltonians," J. Mol. Spectrosc. **264**, 94-99 (2010).

109. J. Doose; A. Guarnieri; W. Neustock; R. Schwarz; F. Winther; F. Hegelund, "Application of a PC-Controlled MW-Spectrometer for the Analysis of Ketene-$D_2$. Simultaneous Analysis of Vibrational Excited States Using Microwave and Infrared Spectra," Z. Naturforsch., A: Phys. Sci. **44**, 538-550 (1989).

110. K. Vávra; P. Kania; J. Koucký; Z. Kisiel; Š. Urban, "Rotational spectra of hydrazoic acid," J. Mol. Spectrosc. **337**, 27-31 (2017).

111. A. G. Császár; J. Demaison; H. D. Rudolph, "Equilibrium Structures of Three-, Four-, Five-, Six-, and Seven-Membered Unsaturated *N*-Containing Heterocycles," J. Phys. Chem. A **119**, 1731-1746 (2015).

112. R. K. Bohn; J. A. Montgomery, Jr. ; H. H. Michels; J. A. Fournier, "Second moments and rotational spectroscopy," J. Mol. Spectrosc. **325**, 42-49 (2016).

# Semi-experimental Equilibrium Structure of Methacrylonitrile ($r_e^{SE}$)

Houston H. Smith,[1] Samuel M. Kougias,[1] Madeleine Atwood,[1] Danny J. Lee,[1]
Bryan Changala,[3] Michael C. McCarthy,[3] Nitai Sahoo,[2] John F. Stanton,[2,*]
Brian J. Esselman,[1] R. Claude Woods,[1,*] Robert J. McMahon[1,*]
[1] *Department of Chemistry, University of Wisconsin–Madison, Madison, Wisconsin 53706, USA*

[2] *Quantum Theory Project, Departments of Physics and Chemistry, University of Florida, Gainesville, Florida 32611, United States*

[3] *Center for Astrophysics, Harvard and Smithsonian, 60 Garden Street, Cambridge, MA 02138-1516, United States*

* corresponding authors
E-mail address: johnstanton@chem.ufl.edu (J.F. Stanton)
E-mail address: rcwoods@wisc.edu (R.C. Woods)
E-mail address: robert.mcmahon@wisc.edu (R.J. McMahon)

## Abstract

The millimeter-wave rotational spectrum of methacrylonitrile has been collected and analyzed from 6 GHz to 40 GHz and from 130 GHz to 500 GHz, providing highly precise spectroscopic constants from A- and S- reduced Hamiltonians in the $I^r$ representation. The chemical synthesis of deuteriated samples allowed for 34 isotopologues to be observed and least-squares fit including the heavy-atoms of the protic and perdeutero species as well as every combination of deuteriated isotopologues. The main isotopologue was least-squares fit with the XIAM program accounting for internal rotation splitting, while all other isotopologues were fit with a distorted rotor Hamiltonian. The spectroscopic constants from 32 isotopologues along with vibration-rotation interaction and electron-mass distribution corrections from coupled-cluster calculations with single, double, and perturbative triple excitations [CCSD(T)/cc-pCVTZ] allowed for a highly precise and accurate semi-experimental ($r_e^{SE}$) structure to be determined. Due to three near-axis atoms, the experimental data cannot determine the precise location of those atoms. Our analysis determined the parameter ($\theta_{C2\text{-}C4\text{-}N}$) was most impacted by the near-axis problem. We

report a semi-experimental ($r_e^{SE}$) equilibrium structure where a parameter was held fixed at a computed value, resulting in a satisfactory structure. The 2σ uncertainties of the $r_e^{SE}$ parameters are ≤ 0.0008 Å and ≤ 0.053° for the bond distances and angles, respectively. In total 12 of the 16 $r_e^{SE}$ structural parameters agree with the "best theoretical estimate" (BTE) values, which are derived from a high-level computed $r_e$ structure [CCSD(T)/cc-pCV5Z] with corrections for use of a finite basis set, the incomplete treatment of electron correlation, relativistic effects, and the diagonal Born-Oppenheimer breakdown.

**Introduction**

Methacrylonitrile ($C_4H_5N$, Fig. 6.1) is a prolate, asymmetric rotor ($\kappa = -0.61$, $C_s$) that has previously been studied *via* various spectroscopic methods including rotational,[1,2] vibrational,[3-9] and ultraviolet[10] spectroscopies. The motivation for these studies was due to its perceived importance in the interstellar medium (ISM),[7] the nitrile functional group, and its ability to copolymerize to create , *e.g.*, methacrylonitrile/methylmethacrylate (A/M),[11] which is only one of many copolymers that have been reported. These various copolymers have been of great interest for industrial applications[12] and as photoresist materials.[13] Methacrylonitrile is a molecule of fundamental interest due to its small nature and that it contains the nitrile and methyl functional groups. Vibrational investigations were completed to understand how the vibrational spectra of nitriles[3,8] and methyl torsions[4] change between different molecules.

The first rotational spectroscopic investigation was performed by Norris *et al.*[1] in the microwave region from 8 – 40 GHz and determined the rotational constants, $V_3$ barrier, and the nuclear quadrupole coupling constants. The rotational spectrum was extended to 200 GHz by López *et al.*[2] but this measured frequency range was not continuous. López *et al.*[2] was able to

determine the rotational constants, quartic and partial sextic centrifugal distortion constants, $V_3$ barrier, and the molecular dipole moment from Stark-effect measurements. In the current work, we have measured the rotational spectrum from 6 – 40 GHz and 130 – 500 GHz for the main isotopologue. The extension of the frequency range to higher frequencies has allowed this work to determine a full set of the sextic centrifugal distortion constants in addition to all the spectroscopic parameters mentioned previously. The determination of all the sextic centrifugal distortion constants improves the accuracy in which rotational transitions can be predicted outside of the currently measured rotational spectrum. This improvement could prove helpful to radioastronomers because there has been a recent detection of methacrylonitrile in TMC-1 with the QUIJOTE line survey.[14] The current ISM detection is in the microwave region (< 45 GHz), but this work allows for assigned rotational transitions up to 500 GHz to be reliably used for the detection of methacrylonitrile at higher frequencies.

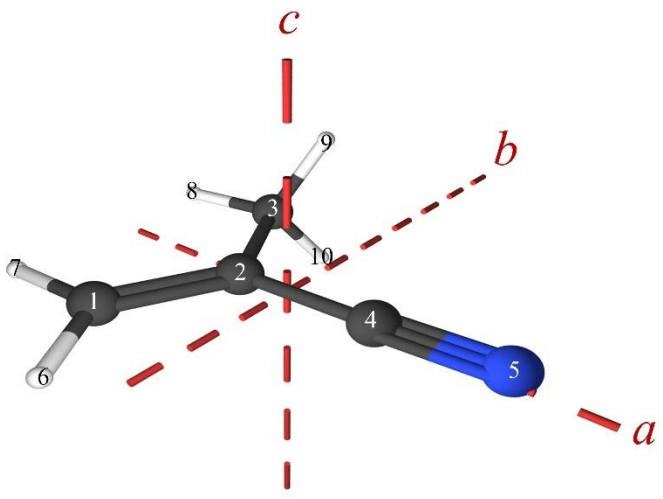


**FIG. 6.1.** Methacrylonitrile structure with principal inertial axes and standard atom numbering.

Despite all the spectroscopic investigations that have been completed, there has not been an attempt at a gas-phase, equilibrium structure determination of methacrylonitrile. Currently the semi-experimental equilibrium structure determination method utilizing CCSD(T)/cc-pCVTZ vibration-rotation interaction and electron-mass corrections has shown the closest agreement with high-level theoretical calculations.[15,16] The precision and accuracy of semi-experimental equilibrium structures ($r_e^{SE}$) has been thoroughly reviewed by Puzzarini[17] and Puzzarini and Stanton,[18] and is founded on the pioneering work of Pulay, Meyer, and Boggs.[19] Methacrylonitrile adds an additional component, internal rotation of the methyl group, that has to be satisfactorily addressed and which was not present in our previous works of highly precise and accurate $r_e^{SE}$ structures.[20-28] Semi-experimental equilibrium structures have been determined for various molecules[29-32] containing large amplitude motions (LAMs), and LAMs can be treated as a small-amplitude vibration if the potential energy function of this motion is harmonic.[33] In the case of methacrylonitrile, the methyl torsion has a high barrier (658 $cm^{-1}$, CCSD(T)), so it is expected that the small-amplitude vibration formalism will be appropriate. The least-squares fitting program XIAM[34] will be utilized to fit the vibrational ground state of the main isotopologue. XIAM was chosen due to speed and ability to return mostly unperturbed rotational constants, which are crucial for the structure determination.

Even though the structure is not similar to our previous works on thiophene[22], thiazole[21], or 2*H*-1,2,3-triazole[26], methacrylonitrile does have a similar problem with atoms extremely close to a principal inertial axis, and thus having an extremely small coordinate. Methacrylonitrile is the most egregious case out of the set due to its three atoms, C2, C4, and N, being close to the *a*-axis. This problem has been described in detail previously and attempts at mitigating the problem have been investigated.[35-39] Currently, there is no universal approach that solves this issue.

Methacrylonitrile gives us the ability to push the limits of semi-experimental equilibrium structure determination ($r_e^{SE}$) in relation to atoms close to a principal axis without having a third-row element or a cyclic structure.

In this work, a total of 34 isotopologues (Fig. 6.2) were observed, measured, and least-squares fit for frequencies ranging between 6 GHz to 500 GHz depending on the isotopologue being considered. Of the 34 isotopologues, the heavy-atom isotopologues of the protic and perdeutero isotopologue were observed at natural abundance in each respective spectrum. The remaining isotopologues are every combination of deuterium incorporation for methacrylonitrile, which was achieved by synthetic deuteration. Most isotopologues have a fully determined set of quartic and partial sextic centrifugal distortion constants, except for the heavy-atom isotopologues, due to their low abundance. Presently, the spectroscopic constants of 32 isotopologues are being utilized in the semi-experimental equilibrium structure of methacrylonitrile.

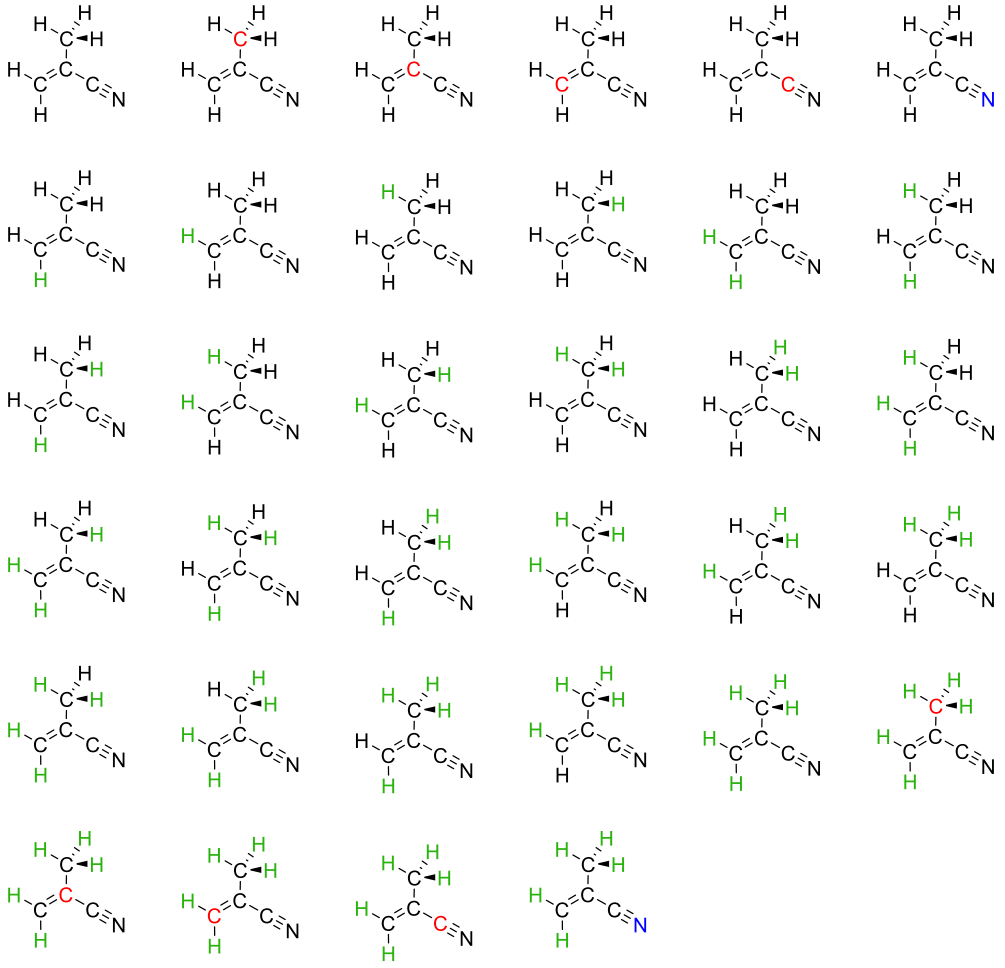

**FIG. 6.2.** Methacrylonitrile isotopologues measured in this work (34 in total). Black atoms correspond to the most naturally abundant isotope. Red carbon, blue nitrogen, and green hydrogen atoms correspond to $^{13}C$, $^{15}N$, and $^{2}H$, respectively.

**Experimental Methods**

The rotational spectra of synthesized samples of methacrylonitrile were continuously collected in segments from 130 – 230 GHz, 235 – 360 GHz, and 350 – 500 GHz and deuteriated methacrylonitrile samples were continuously collected in segments from 130 – 230 GHz and 235 – 360 GHz at the University of Wisconsin – Madison. The microwave spectrum of protic methacrylonitrile was also collected from 6 – 40 GHz at Harvard University by Bryan Changala and Mike McCarthy. The University of Wisconsin – Madison[28,40-42] and Harvard[43,44]

spectrometers have been described previously. The complete protic spectrum from 130 to 500 GHz and deuteriated spectra from 130 to 360 GHz were obtained using automated data collection software over approximately eight and five days, respectively, with these experimental parameters: 0.6 MHz/sec sweep rate, 10 ms time constant, and 50 kHz AM and 500 kHz FM modulation in a tone-burst design.[45] Additionally, the 80 – 135 GHz spectrum for the perdeutero sample was measured given the new acquisition of antenna horns and a VDI Zero-Bias Detector (ZBD) WR8.0ZBD in the pursuit of observing and measuring the heavy-atom isotopologues. The spectral segments for each respective spectrum were separately combined into a spectral file using Assignment and Analysis of Broadband Spectra (AABS) software.[46,47] A modified version of XIAM,[34] extending *J* to 100 was utilized in the least-squares fit of the vibrational ground state for protic methacrylonitrile, while ASFIT and ASROT[48] were used for all other methacrylonitrile isotopologues and were treated as distorted rotors. The microwave transitions were independently measured and incorporated into the XIAM least-squares fit. Additional programs created by Kisiel, XIARES, PLANM, and AC programs were used for analysis.[49,50] In our least-squares fits, we assume a uniform 50 kHz frequency measurement uncertainty for our measured transitions in spectra collected at the University of Wisconsin – Madison. The uncertainty for the microwave transitions acquired at Harvard University ranges from 2 to 10 kHz, depending on the intensity of the transition and if transitions are blended. A complete list of the transitions utilized in the least-squares fit with their measurement uncertainties are presented in the Supplementary Material.

**Computational Methods**

Calculations were carried out using a development version of CFOUR.[51] The methacrylonitrile structure was first optimized at the CCSD(T)/cc-pCVTZ level of theory. The optimized geometry and the same level of theory was subsequently used for an anharmonic, second-order vibrational perturbation theory (VPT2) calculation, wherein cubic force constants are evaluated using analytical second derivatives at displaced points.[52-54] Magnetic property calculations were performed for each isotopologue to obtain the electron-mass corrections to the corresponding rotational constants. The "best theoretical estimate" (BTE), as described previously,[20-28] is based on a CCSD(T)/cc-pCV5Z optimized structure with four additional corrections that address the following:

1. Residual basis set effects beyond cc-pCV5Z.
2. Residual electron correlation effects beyond the CCSD(T) treatment.
3. Effects of scalar (mass-velocity and Darwin) relativistic effects.
4. The fixed-nucleus approximation *via* the diagonal Born-Oppenheimer correction.

Equations used to calculate these corrections and the values of each of these corrections for methacrylonitrile are provided in the supplementary material (**Eq. S7– S13** and **Table S-VI**). One of the most important factors of the algorithm used to determine the BTE is the estimation of residual basis set effects, specifically estimated as the difference between the (directly computed) cc-pCV5Z geometry at the CCSD(T) level of theory and the estimate of the CCSD(T) geometry at the basis set limit. Following others,[55] the latter is estimated by assuming an exponential convergence pattern with respect to the highest angular momentum basis functions present in the basis. There were four angles, $\theta_{C3\text{-}C2\text{-}C1}$, $\theta_{C1\text{-}C2\text{-}C4}$, $\theta_{C2\text{-}C3\text{-}H8}$, and $\theta_{C2\text{-}C3\text{-}H9/H10}$, that either did not

follow a monotonic function or their rate of change did not show a convergence from cc-pCVTZ to cc-pCV5Z. There was a similar issue with the parameters in the BTE determination for 2*H*-1,2,3-triazole.[26] The correction for the finite basis set was set to zero for these angles by assuming the cc-pCV5Z value was the value at the basis set limit. In total these four angles only had three corrections to achieve their BTE values. A complete explanation of the BTE calculation is provided in the Supplementary Material.

The *xrefit* module of CFOUR calculates the moments of inertia and semi-experimental equilibrium structure using the experimental, determinable rotational constants and computational electron-mass distribution and vibration-rotation interaction corrections. X*refiteration*[23] was used to determine the suitability of the methacrylonitrile isotopologues for the structure determination. The routine begins by determining a structure using a single isotopic substitution at each position and then sequentially adds the most uncertainty-minimizing isotopologue to the structural least-squares fit until all available isotopologues are incorporated.

Computational output files are provided in the Supplementary Material.

**Synthesis of Methacrylonitrile Isotopologues**

For the preparation of methacrylonitrile, we followed two general routes depending on if we desired deuterium enrichment in the product (Scheme 6.1). For the preparation without deuterium enrichment, we found that methacrylonitrile could be distilled in high purity *via* the dehydration of methacrylamide (Scheme 6.1a). This process involves the mixing of both reagents and heating the mixture to 160 ºC. Methacrylonitrile is then distilled into a dry ice or liquid nitrogen receiving flask. For the preparation of deuterium-enriched samples of methacrylonitrile, an extended synthetic route was followed starting from acetone (Scheme 6.1b). In this method,

acetone is subjected to a strong base in the presence of $D_2O$, leading to deuterium enrichment through base-catalyzed tautomerization. Deuterium-enriched acetone is converted to deuterium-enriched acetone cyanohydrin *via* addition of potassium cyanide under acidic conditions. Acetone cyanohydrin is first converted to deuterium-enriched methacrylamide using sulfuric acid followed by dehydration with phosphorus pentoxide to yield deuterium-enriched methacrylonitrile. A third deuteriated sample was generated *via* using acetone-$d_6$ following Scheme 6.1b after skipping the first step and resulted in a mainly perdeutero methacrylonitrile sample.

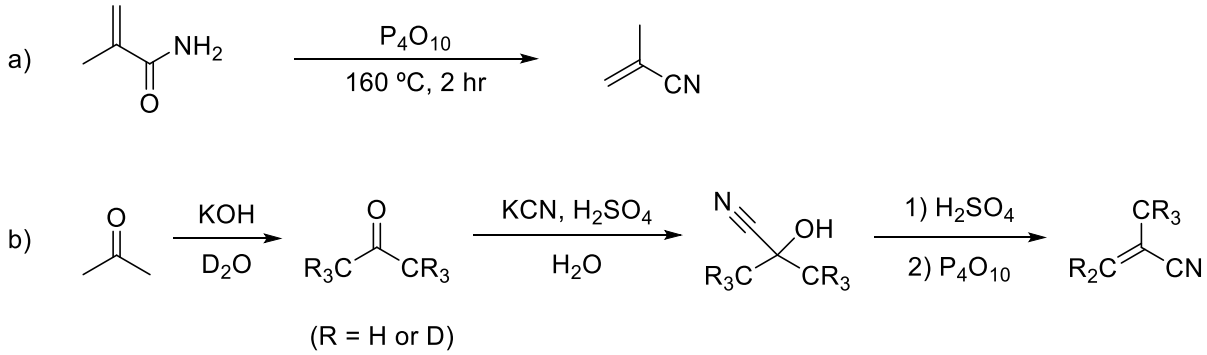


**Scheme 6.1**: Methods for producing methacrylonitrile (a), and deuterium-enriched methacrylonitrile (b).

**Analysis of Rotational Spectra**

The rotational spectrum of the vibrational ground state for the main isotopologue consisted of *a*-type R- and Q- branch transitions across the 130 to 500 GHz spectrum measured at the University of Wisconsin – Madison. The previously measured experimental dipole moments[2] of methacrylonitrile were determined to be $\mu_a$ = 3.940 (2) D and $\mu_b$ = 0.26 (5) D, however, no *b*-type rotational transitions were observed outside the microwave region (6 to 40 GHz) measured at Harvard. Figure 6.3 shows a small section of the experimental spectrum for methacrylonitrile, along with stick spectra predicted from experimental spectroscopic constants using XIAM[34] for both the A and E states (green and purple, respectively). Rotational transitions follow a pattern

where decreasing $J''+1$ and increasing $K_a$ occur as you progress lower in frequency beyond the band origin at $K_a$ = 0. Bandheads for methacrylonitrile appear as four transitions: two $^aR_{0,1}$ transitions ($J = K_a + K_c$ and $J + 1 = K_a + K_c$) for both the A and E states. The two bands shown in Fig. 6.3 undergo a turnaround and progress to higher frequency at $K_a$ = 8 and lose degeneracy at $K_a$ = 10.

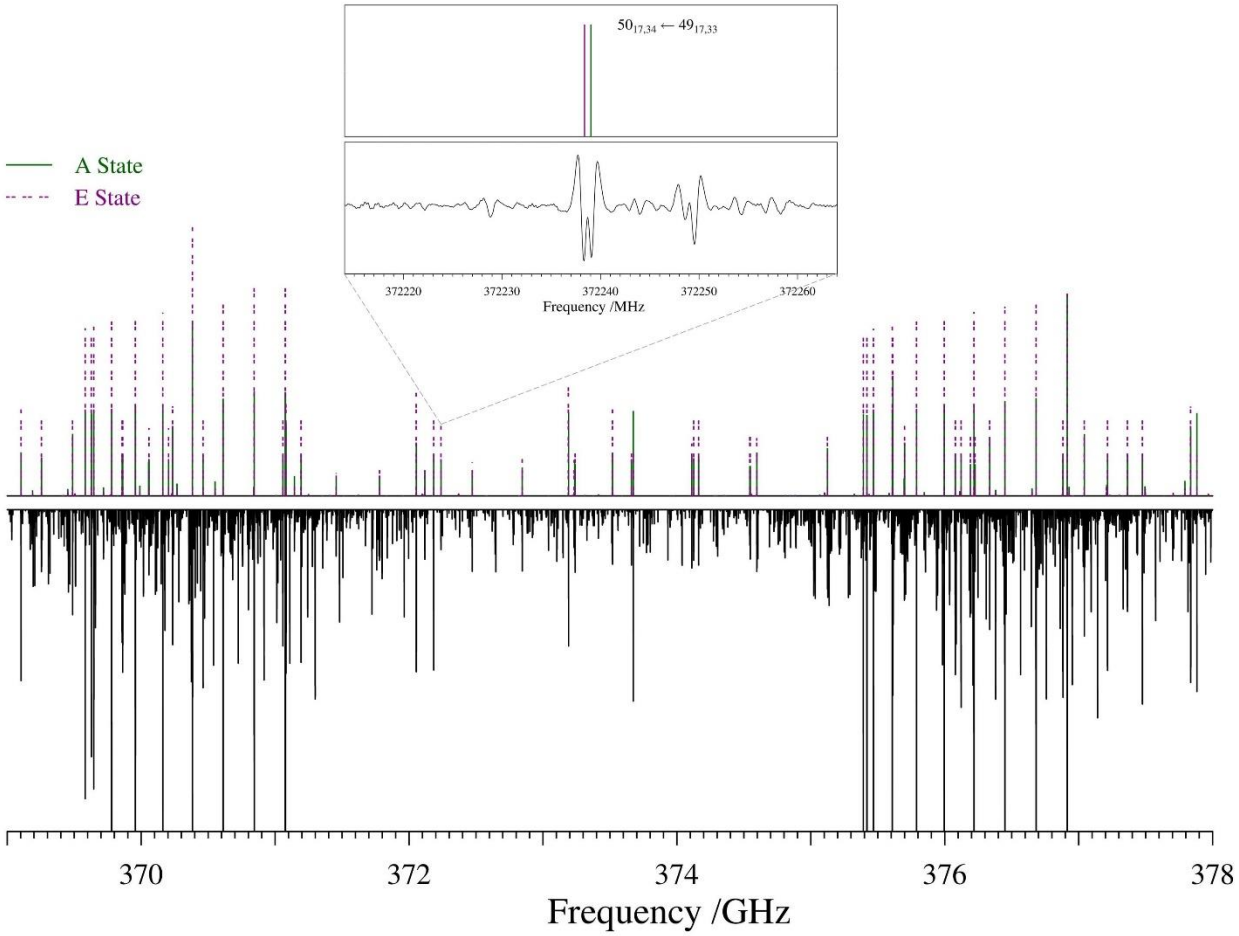


**FIG. 6.3.** Stick spectra for vibrational ground state of methacrylonitrile A state (green) and E state (purple) predicted from experimental spectroscopic constants from 369 to 378 GHz (top). The experimental spectrum of methacrylonitrile is on the bottom.

The splitting of A and E state transitions becomes resolvable at various $K_a$ values depending on the frequency, but an example is shown in the inset of Fig. 6.3 for $K_a$ = 17. Due to

the high barrier (~689 $cm^{-1}$) of methacrylonitrile, the frequency splitting is always small with the largest splitting observed only being a couple of MHz. This fact does lead to a large number of unresolvable or blended transitions involving both A and E states. The singly substituted heavy-atom isotopologues were observable at natural abundance in this spectrum. Only the main isotopologue utilized a Hamiltonian accounting for internal rotation splitting in the least-squares fitting because the heavy atom isotopologues were not intense enough to see transitions that had resolved A and E splittings. These fits were treated like distorted rotors and assumed every measured transition included both the corresponding A and E state.

Table 6.1 provides the spectroscopic constants for methacrylonitrile determined in this work alongside the previous works of Norris *et al.*[1] and López *et al.*[2] We present two least-squares fit of our experimental data, where one is a higher error fit, Fit I, and the other has an error below our experimental uncertainty of 50 kHz, Fit II. The unusual reporting of two least-squares fit for the same experimental data is due to the significant number of transitions that had to be removed from Fit I to achieve a total RMS below 50 kHz. A total of 1561 rotational transitions had to be removed, this large number of transitions is much higher than one would expect based on statistical probabilities or due to overlapping transitions of vibrationally excited states. Figures 4 and 5 show the range of quantum numbers included in the least-squares fit of Fit I and Fit II, respectively. It is apparent in Fig. 6.4 that there are a couple of systematic trends for the high error transitions (red circles). Both the A and E state data distribution plots show a collection of high error transitions progressing higher in $J''$ and $K_a''$ starting initially around $J''$ = 15 and $K_a''$ = 8 and another similar series to the left starting at around $J''$ = 30 and $K_a''$ = 5. These high error lines are attributed to four transitions in close proximity, A and E state $J = K_a + K_c$ and $J + 1 = K_a + K_c$ transitions, losing

degeneracy. The A and E state transitions lose degeneracy at different rates, thus there are experimental transitions that are distorted with all four transitions having different but similar frequencies. Most spectral fitting programs (such as SPFIT[56] and ASFIT[48]) try to take this into account by blending the transitions that have the same recorded experimental frequency in the initial least-squares fitting process. Unfortunately, XIAM does not blend transitions, so the observed minus calculated (*obs.* – *calc.*) are inaccurate because XIAM is assuming the observed frequency is the true unperturbed frequency for each transition. The large spectral range covered in the vibrational ground state (6 to 40 GHz and 130 to 500 GHz) results in a large quantity of these transitions being incorporated into the fit. A similar issue is possible for high $K_a$ transitions in the R-branch for the E state because four transitions are in close proximity, but in this case only the E state transitions are predicted not to be degenerate. Thus, high error results in the *obs.* – *calc.* value for at least one of the E state transitions. The Q-branch transitions for the E state do not experience this and are also high error. It seems the determined spectroscopic constants without accounting for these blended frequencies does not predict higher $K_a$ ($K_a$ >10) Q-branch transitions for the E state to within experimental uncertainty. It is of note that these transitions are the transitions that have the largest A and E splitting observed, couple of Megahertz, in our spectral coverage. It also cannot be ruled out that higher order centrifugal distortion constants beyond the sextic centrifugal distortion constants are needed to lower the error for high $J$ and $K_a$ transitions. Unfortunately, XIAM does not contain the capabilities of adding octic centrifugal distortion constants, so this assumption cannot be tested with this program. If all the transitions measured in this range could be adequately incorporated into the least-squares fit, we believe a large portion of these discrepancies would be resolved and would result in a low error fit without having to remove the large number of lines that is currently needed

**Table 6.1**. Experimental and computational spectroscopic constants for methacrylonitrile, normal isotopologue, ground vibrational sate (A-reduced Hamiltonian, $I^r$ representation).

| | CCSD(T)/cc-pCVTZ | Current Work Fit I | Current Work Fit II | López *et al.*[2] | Norris *et al*[1] |
|---|---|---|---|---|---|
| $A_0$ (MHz) | 9253 | 9291.31245 (35) | 9291.32169 (66) | 9291.3161 (28) | 9297.48 (30) |
| $B_0$ (MHz) | 4143 | 4166.48697 (22) | 4166.48195 (41) | 4166.43628 (79) | 4166.33 (01) |
| $C_0$ (MHz) | 2909 | 2924.60173 (21) | 2924.60355 (39) | 2924.65852 (77) | 2924.68 (01) |
| $\Delta_J$ (kHz) | 0.743 | 0.764922 (41) | 0.763823 (48) | 0.76525 (61) | |
| $\Delta_{JK}$ (kHz) | 13.8 | 13.92443 (23) | 13.92925 (24) | 13.8812 (36) | |
| $\Delta_K$ (kHz) | −5.21 | −5.4036 (28) | −5.3466 (42) | −5.094 (42) | |
| $\delta_J$ (kHz) | 0.256 | 0.264520 (21) | 0.264115 (23) | 0.26503 (22) | |
| $\delta_K$ (kHz) | 8.48 | 8.63005 (35) | 8.62943 (30) | 8.5996 (94) | |
| $\Phi_J$ (Hz) | 0.000504 | 0.0004930 (70) | 0.0002890 (90) | | |
| $\Phi_{JK}$ (Hz) | 0.120 | 0.11473 (11) | 0.11440 (11) | 0.0495 (97) | |
| $\Phi_{KJ}$ (Hz) | −0.243 | −0.23117 (37) | −0.22762 (42) | | |
| $\Phi_K$ (Hz) | 0.145 | 0.2522 (48) | 0.3668 (81) | −0.393 (40) | |
| $\phi_J$ (Hz) | 0.000246 | 0.000241 (3) | 0.000147 (5) | | |
| $\phi_{JK}$ (Hz) | 0.0620 | 0.059526 (71) | 0.058336 (83) | | |
| $\phi_K$ (Hz) | 0.264 | 0.26184 (74) | 0.26092 (79) | | |
| $\chi_{aa}$ (MHz) | −4.13 | −4.2330 (23) | −4.2361 (23) | | −4.18 (02) |
| $\chi_{bb} - \chi_{cc}$ (MHz) | 0.0511 | 0.0222 (45) | | | |
| $V_3$ (MHz) | | 19974070. (15000) | 20663280. (19000) | | |
| $V_3$ ($cm^{-1}$) | 657.6 | 666.26 (51) | 689.25 (64) | 694.7 (21) | 710. (21) |
| $D_{\pi 2K}$ (MHz) | | −1.46 (11) | −7.503 (78) | | |
| $D_{\pi 2-}$ (MHz) | | −0.237 (18) | −0.957 (14) | | |
| $N_{lines}$ | | 3937 | 2376 | 81 | 15 |
| $\sigma_{fit}$ (MHz) | | 0.089 | 0.047 | 0.037 | |
| $\Delta_i$ (u$Å^2$) | | −2.886156 (14) | −2.886355 (26) | −2.89096 (5) | −2.859 (2) |

Both Fit I and II are able to accurately predict transitions for the entire spectral range of this work and the reported transitions frequencies would allow for confirmed observational detection in different interstellar sources. The rotational and quartic distortion constants that are determined by both fits are of similar quality and precision when compared to López *et al.*,[2] with notable improvement in $\Delta_K$, presumably due to the larger data set and better determination of the sextic centrifugal distortion constants. The CCSD(T) $B_0$ value has the largest difference in the rotational constants when compared to either Fit I and II (0.57%). The CCSD(T) quartic centrifugal distortion constants have the largest disagreement with $\Delta_K$ (3.6%) and $\delta_J$ (3.0%) for Fit I and II, respectively. There are larger differences between Fit I and II with sextic centrifugal distortion constants, especially $\Phi_J$ (70.6%), $\Phi_K$ (31.2%) and $\phi_J$ (63.9%), where Fit II has smaller $\Phi_J$ and $\phi_J$ but larger $\Phi_K$. The on-diagonal sextic constants that show poor agreement between the two least-squares fits are the values that are generally the most difficult to determine ($\Phi_J$ and $\Phi_K$). Fit I has closer agreement between all the sextic centrifugal distortion constants and their respective CCSD(T) values. It is possible that the removal of high error lines in XIAM due to the lack of blended line treatment to achieve Fit II, may have distorted the sextic centrifugal distortion constants from the true physically meaningful values. Fit I should be treated as the more reliable determination of the spectroscopic constants despite its larger $\sigma_{fit}$ value. The $V_3$ parameter for Fit II, 689.25 (64) $cm^{-1}$, is closer in agreement to López *et al*., 694.7 (21) $cm^{-1}$, than Fit I, 666.26 (51) $cm^{-1}$, however, Fit I is closer to the CCSD(T) predicted value of 657.6 $cm^{-1}$. The $V_3$ parameter for Fit II, even though there is close agreement, is outside the quoted statistical uncertainty of López *et al*.[2] The two higher order internal rotation parameters, $D_{\pi 2K}$ and $D_{\pi 2-}$ are significantly different between each fit, and Fit II has significantly more precision in the determination of both parameters. As the rotational constants in both Fit I and Fit II agree to within 9 kHz, either set of

spectroscopic constants would be useful for the $r_e^{SE}$ structure determination. The rotational constants from Fit II will be used in the structure determination, because its $\sigma_{fit}$ value is similar to those of all the other isotopologues measured in this work.

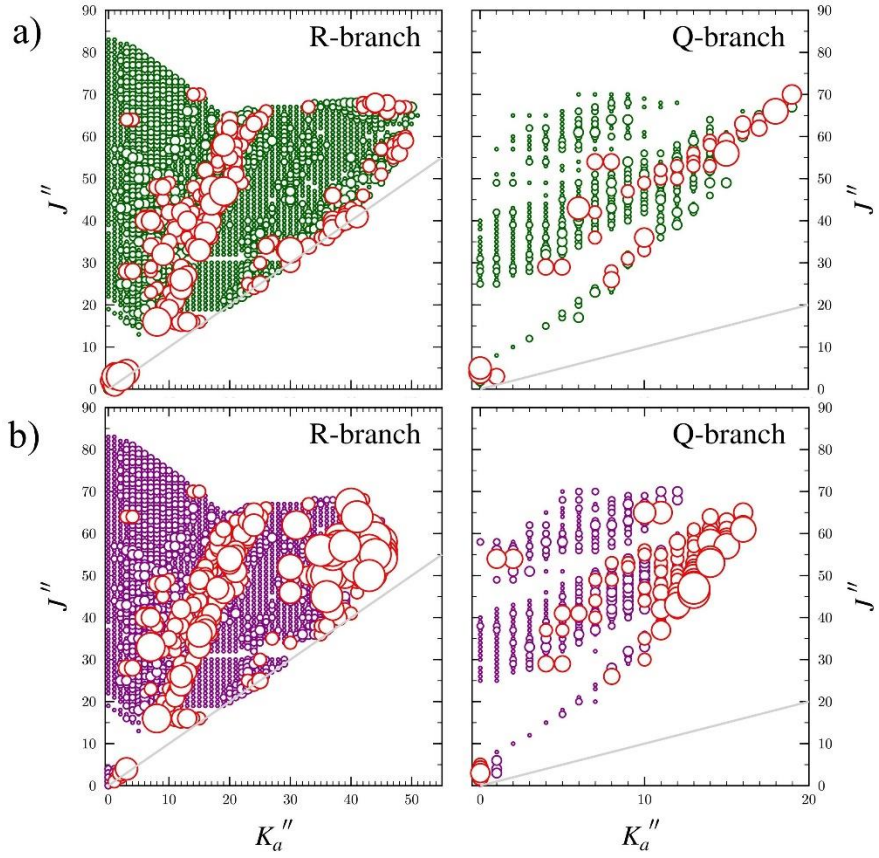


**Fig. 6.4.** Data distribution plot for the least-squares fit of spectroscopic data for the vibrational ground state of methacrylonitrile (Fit I). The size of the outlined circle is proportional to the value of $|(f_{obs.} - f_{calc.})/\delta f|$, where $\delta f$ is the frequency measurement uncertainty, and values greater than 3 are outlined in red. A and E state transitions are green and purple, respectively.

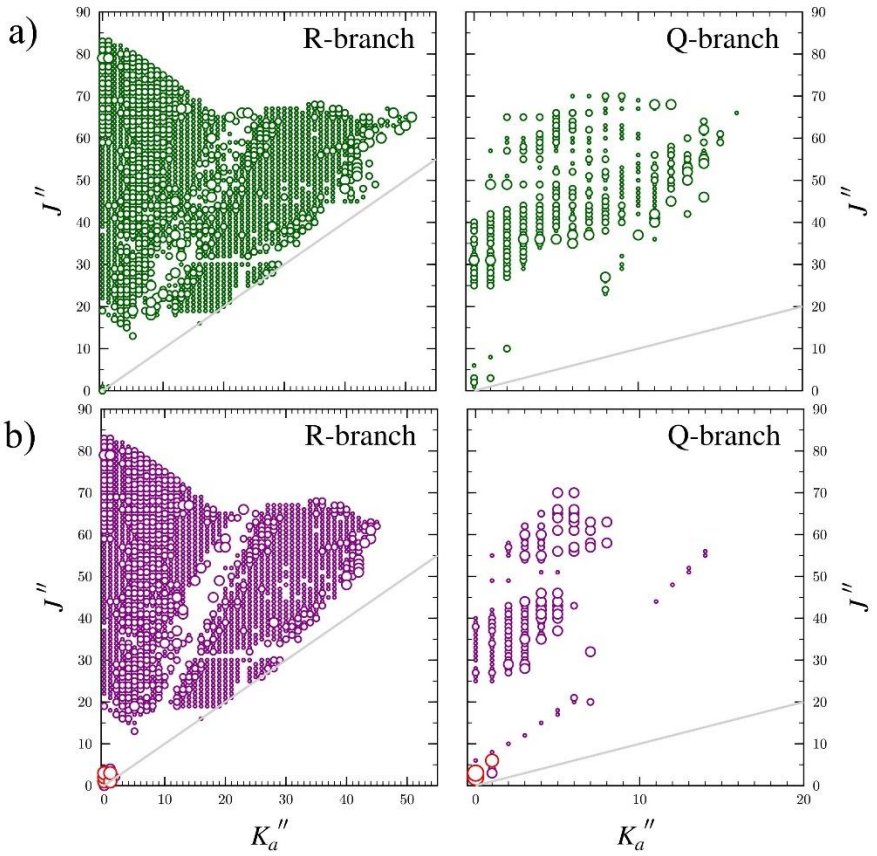


**Fig. 6.5.** Data distribution plot for the least-squares fit of spectroscopic data for the vibrational ground state of methacrylonitrile (Fit II). The size of the outlined circle is proportional to the value of $|(f_{obs.} - f_{calc.})/\delta f|$, where $\delta f$ is the frequency measurement uncertainty, and values greater than 3 are outlined in red. A and E state transitions are green and purple, respectively.

All three deuteriated samples of methacrylonitrile allowed for every combination of deuterium substituted isotopologues excluding heavy-atom substituted isotopologues to be observed. The fully deuteriated methacrylonitrile was sufficiently pure to allow an additional set of heavy-atom substituted isotopologues to be observed. This resulted in rotational constants being determined for a total of 34 isotopologues, and the transitions of all of these deuteriated isotopologues were modeled with distorted rotor Hamiltonians. This assumption was rigorously valid for any isotopologue that contained at least one deuterium in the methyl rotor because every observable transition was able to be assigned and incorporated into a least-squares fit below the experimental uncertainty of 50 kHz. The resulting A and E splitting with at least one deuterium

in the methyl rotor was thus experimentally unresolvable. The only isotopologues that this did not occur for were [1-$^{2}H_{cis}$]-, [1-$^{2}H_{trans}$]-, and [1,1-$^{2}H$]-methacrylonitrile. These isotopologues were treated similar to the heavy atom isotopologues of the primary isotopologue, where only transitions measured were those with no observable A or E state splitting. The intensity of the rotational transitions for these isotopologues were quite weak in our deuteriated spectra because all had quite high deuterium incorporation. Table 6.2 shows the CCSD(T)/cc-pCVTZ and experimental spectroscopic constants for every singly-substituted isotopologue in the A-Reduced Hamiltonian, $I^{r}$ representation.

**Table 6.2**. Experimental and computational spectroscopic constants for the ground vibrational state of singly-substituted methacrylonitrile isotopologues (A-reduced Hamiltonian, $I^r$ representation).

| | [1-$^{13}$C] | | [2-$^{13}$C] | | [3-$^{13}$C] | | [4-$^{13}$C] | |
|---|---|---|---|---|---|---|---|---|
| | CCSD(T) | Present Work | CCSD(T) | Present Work | CCSD(T) | Present Work | CCSD(T) | Present Work |
| $A_0$ (MHz) | 8983 | 9020.071 (15) | 9252 | 9290.32 (11) | 9016 | 9053.0230 (42) | 9253 | 9291.1612 (74) |
| $B_0$ (MHz) | 4102 | 4125.8648 (40) | 4135 | 4158.418 (25) | 4091 | 4114.67031 (55) | 4113 | 4136.4437 (12) |
| $C_0$ (MHz) | 2862 | 2877.49168 (21) | 2905 | 2920.60185 (32) | 2860 | 2875.37323 (23) | 2895 | 2909.84776 (22) |
| $\Delta_J$ (kHz) | 0.700 | 0.7305 (32) | 0.734 | 0.794 (19) | 0.764 | 0.78682 (22) | 0.738 | 0.75817 (72) |
| $\Delta_{JK}$ (kHz) | 13.7 | 13.674 (48) | 13.9 | 13.38 (30) | 12.7 | 12.8131 (24) | 13.4 | 13.638 (15) |
| $\Delta_K$ (kHz) | −5.91 | [−5.91] | −5.27 | [−5.27] | −4.17 | −4.662 (12) | −4.84 | −5.10 (11) |
| $\delta_J$ (kHz) | 0.241 | 0.2537 (16) | 0.253 | 0.2800 (98) | 0.269 | 0.27751 (11) | 0.254 | 0.26118 (36) |
| $\delta_K$ (kHz) | 8.28 | 8.3785 (79) | 8.49 | 8.546 (41) | 8.06 | 8.1856 (21) | 8.31 | 8.4907 (90) |
| $\Phi_J$ (Hz) | 0.000456 | [0.000456] | 0.000485 | 0.000493 (10) | 0.000544 | 0.000565 (61) | 0.000503 | [0.000503] |
| $\Phi_{JK}$ (Hz) | 0.115 | 0.11558 (34) | 0.120 | 0.12203 (59) | 0.115 | 0.1166 (10) | 0.115 | 0.11205 (57) |
| $\Phi_{KJ}$ (Hz) | −0.224 | [−0.224] | −0.243 | [−0.243] | −0.24 | −0.3720 (74) | −0.236 | −0.1936 (97) |
| $\Phi_K$ (Hz) | 0.125 | [0.125] | 0.145 | [0.145] | 0.152 | [0.152] | 0.143 | [0.143] |
| $\phi_J$ (Hz) | 0.000224 | [0.000224] | 0.000237 | [0.000237] | 0.000265 | 0.000282 (30) | 0.000246 | [0.000246] |
| $\phi_{JK}$ (Hz) | 0.0591 | [0.0591] | 0.0620 | [0.0620] | 0.0593 | 0.05936 (64) | 0.0596 | [0.0596] |
| $\phi_K$ (Hz) | 0.243 | [0.243] | 0.265 | [0.265] | 0.241 | 0.1863 (49) | 0.258 | [0.258] |
| $N_{lines}$ | | 171 | | 161 | | 348 | | 242 |
| $\sigma_{fit}$ (MHz) | | 0.046 | | 0.047 | | 0.048 | | 0.051 |
| $\Delta_i$ (uÅ$^2$) | | −2.88693 (15) | | −2.89067 (97) | | −2.886846 (34) | | −2.891852 (57) |

**Table 6.2 Continued.** Experimental and computational spectroscopic constants for the ground vibrational state of singly-substituted methacrylonitrile isotopologues (A-reduced Hamiltonian, $I^r$ representation).

| | [$^{15}$N] | | [1-$^{2}$H$_{cis}$] | | [1-$^{2}$H$_{trans}$] | | [3-$^{2}$H$_{anti}$] | |
|---|---|---|---|---|---|---|---|---|
| | CCSD(T) | Present Work | CCSD(T) | Present Work | CCSD(T) | Present Work | CCSD(T) | Present Work |
| $A_0$ (MHz) | 9252 | 9289.46 (10) | 8500 | 8535.428 (11) | 8967 | 9004.6838 (83) | 9084 | 9121.4543 (71) |
| $B_0$ (MHz) | 4000 | 4023.271 (21) | 4134 | 4157.5686 (39) | 3985 | 4007.96416 (88) | 3968 | 3990.11748 (59) |
| $C_0$ (MHz) | 2838 | 2853.15251 (28) | 2826 | 2841.08838 (59) | 2803 | 2818.20879 (66) | 2806 | 2821.09365 (61) |
| $\Delta_J$ (kHz) | 0.687 | 0.867 (23) | 0.721 | 0.7362 (29) | 0.625 | 0.64225 (42) | 0.707 | 0.72896 (24) |
| $\Delta_{JK}$ (kHz) | 13.5 | 11.00 (37) | 13.5 | 13.324 (89) | 12.9 | 13.0220 (29) | 11.1 | 11.2505 (24) |
| $\Delta_K$ (kHz) | −4.89 | [−4.89] | −7.26 | −5.89 (47) | −4.54 | −4.643 (61) | −1.14 | −1.270 (51) |
| $\delta_J$ (kHz) | 0.233 | 0.320 (11) | 0.255 | 0.2596 (15 | 0.212 | 0.21750 (22) | 0.248 | 0.25636 (13) |
| $\delta_K$ (kHz) | 8.27 | 8.051 (52) | 8.14 | 8.080 (51) | 7.71 | 7.8176 (90) | 7.30 | 7.4274 (82) |
| $\Phi_J$ (Hz) | 0.000449 | [0.000449] | 0.000498 | [0.000498] | 0.000379 | [0.000379] | 0.000564 | [0.000564] |
| $\Phi_{JK}$ (Hz) | 0.114 | [0.114] | 0.115 | [0.115] | 0.100 | 0.0963 (19) | 0.0966 | 0.0972 (13) |
| $\Phi_{KJ}$ (Hz) | −0.229 | [−0.229] | −0.225 | [−0.225] | −0.196 | −0.1827 (38) | −0.209 | −0.2108 (17) |
| $\Phi_K$ (Hz) | 0.137 | [0.137] | 0.124 | [0.124] | 0.109 | [0.109] | 0.147 | [0.147] |
| $\phi_J$ (Hz) | 0.000219 | [0.000219] | 0.000245 | [0.000245] | 0.000187 | [0.000187] | 0.000276 | [0.000276] |
| $\phi_{JK}$ (Hz) | 0.0587 | [0.0587] | 0.0594 | [0.0594] | 0.0516 | 0.0408 (43) | 0.0504 | 0.0444 (40) |
| $\phi_K$ (Hz) | 0.271 | [0.271] | 0.209 | [0.209] | 0.230 | [0.230] | 0.228 | [0.228] |
| $N_{lines}$ | | 73 | | 115 | | 267 | | 397 |
| $\sigma_{fit}$ (MHz) | | 0.049 | | 0.042 | | 0.043 | | 0.044 |
| $\Delta_i$ (uÅ$^2$) | | −2.88741 (88) | | −2.88377 (14) | | −2.89139 (72) | | −2.920267 (61) |

**Table 6.2 Continued.** Experimental and computational spectroscopic constants for the ground vibrational state of singly-substituted methacrylonitrile isotopologues (A-reduced Hamiltonian, $I^r$ representation).

| | [3-$^2$H$_{gauche}$] | |
|---|---|---|
| | CCSD(T) | Present Work |
| $A_0$ (MHz) | 8627 | 8662.2956 (50) |
| $B_0$ (MHz) | 4086 | 4109.80874 (48) |
| $C_0$ (MHz) | 2840 | 2855.08247 (52) |
| $\Delta_J$ (kHz) | 0.800 | 0.82388 (21) |
| $\Delta_{JK}$ (kHz) | 12.4 | 12.6232 (20) |
| $\Delta_K$ (kHz) | −5.30 | −5.552 (32) |
| $\delta_J$ (kHz) | 0.285 | 0.29476 (12) |
| $\delta_K$ (kHz) | 7.69 | 7.8357 (60) |
| $\Phi_J$ (Hz) | 0.000490 | [0.000490] |
| $\Phi_{JK}$ (Hz) | 0.115 | 0.1110 (12) |
| $\Phi_{KJ}$ (Hz) | −0.235 | −0.2275 (15) |
| $\Phi_K$ (Hz) | 0.144 | [0.144] |
| $\phi_J$ (Hz) | 0.000236 | [0.000236] |
| $\phi_{JK}$ (Hz) | 0.0594 | 0.0614 (30) |
| $\phi_K$ (Hz) | 0.210 | [0.210] |
| $N_{lines}$ | | 408 |
| $\sigma_{fit}$ (MHz) | | 0.037 |
| $\Delta_i$ (uÅ$^2$) | | −4.301071 (49) |

**Semi-experimental Equilibrium Structure ($r_e^{SE}$)**

The spectroscopic constants were determined in both the A and S reductions for all 32 isotopologues utilized in the semi-experimental equilibrium structure ($r_e^{SE}$). The rotational constants ($B_0$) for each reduction were converted to determinable constants ($B''$) using Eqns. S(1) – S(6) in the supplementary material. The agreement between the two sets of determinable constants (within 0.07 and 0.02 MHz when including and not including heavy-atom substituted isotopologues, respectively) confirms that the rotational constants and quartic centrifugal distortion constants determined for all isotopologues are physically meaningful and gives confidence in their inclusion in the least-squares fit of the structure determination. The respective determinable rotational constants were averaged together and input into *xrefit* along with vibration-rotation interaction and electron-mass distribution corrections predicted at the CCSD(T)/cc-pCVTZ level of theory. *Xrefit* uses the given rotational constants and corrections to calculate the equilibrium rotational constants ($B_e$) using Eq. (1), where the second term is the vibration-rotation interaction correction, $\frac{m_e}{M_p}$ is the electron-to-proton mass ratio, $B''$ is the determinable constant, and $g^{\beta\beta}$ is the corresponding magnetic $g$-tensor component.

$$B_e^{\beta} = B''^{\beta} + \frac{1}{2}\sum_i \alpha_i^{\beta} - \frac{m_e}{M_P} g^{\beta\beta} B^{\beta} \quad (1)$$

The rotational constants are then used to calculate the inertial defect ($\Delta_i$) for each isotopologue. Unlike our previous works including all planar molecules,[20-28] the inertial defect is non-zero for methacrylonitrile, due to the two out-of-plane hydrogen atoms on the methyl rotor. The inertial defects provide important insight into the quality of the computational corrections to the experimental rotational constants. Without either computational correction, the observed $\Delta_{i0}$ ranges from −2.8866 uÅ$^2$ to −6.0229 uÅ$^2$ for [1,1-$^2$H] and [3,3,3-$^2$H], respectively. The $\Delta_{i0}$ inertial

defect for $H_2$, HD, and $D_2$ isotopologues are −2.898 (14) uÅ$^2$, −4.319 (19)uÅ$^2$, and −6.006 (15) uÅ$^2$. The $\Delta_{ie}$ inertial defect for $H_2$, HD, and $D_2$ isotopologues are −3.1142 (14) uÅ$^2$, −4.5461 (44) uÅ$^2$, and −6.2180 (22) uÅ$^2$. When both the vibration-rotation interaction and electron-mass corrections have been taken into account, the $\Delta_{ie}$ decreases by ~ 0.2 uÅ$^2$, and the standard deviation between isotopologues is drastically decreased. There is a nearly linear trend in the number of $^2$H atoms out-of-plane and the inertial defects (**Fig. S34**). The slight non-linearity is presumably due to the $^1$H/$^2$H isotopologues, which also experience a slight rotation in the inertial planes due to the loss of symmetry. The planar second moment $P_{cc}$ ($-2\Delta_{ie}$) when corrected for the mass of the out-of-plane atoms ($^1$H or $^2$H) is remarkably consistent across all isotopologues, which will be discussed in greater detail below.

**Table 6.3.** Inertial defects ($\Delta_i$) and second moments ($P_{cc}$) of methacrylonitrile isotopologues.

| Isotopologue | $\Delta_{i0}$ (uÅ$^2$) [a] | $\Delta_{ie}$ (uÅ$^2$) [b] | $P_{cc}$ (uÅ$^2$) [b,c] | $P_{cc}$ / $m_H$ (Å$^2$)[b,c,d] |
|---|---|---|---|---|
| $C_4H_5N$ | −2.8872 | −3.10984 | 1.55492 | 1.54285 |
| [1-$^{13}$C] | −2.8877 | −3.11419 | 1.55709 | 1.54500 |
| [2-$^{13}$C] | −2.8915 | −3.11392 | 1.55696 | 1.54487 |
| [3-$^{13}$C] | −2.8875 | −3.11408 | 1.55704 | 1.54495 |
| [4-$^{13}$C] | −2.8926 | −3.11423 | 1.55711 | 1.54502 |
| [$^{15}$N] | −2.8882 | −3.11383 | 1.55692 | 1.54483 |
| [1-$^2$H$_{cis}$] | −2.8845 | −3.11418 | 1.55709 | 1.54500 |
| [1-$^2$H$_{trans}$] | −2.8920 | −3.11432 | 1.55716 | 1.54507 |
| [3-$^2$H$_{anti}$] | −2.9209 | −3.11549 | 1.55775 | 1.54565 |
| [3-$^2$H$_{gauche}$] | −4.3018 | −4.53974 | | |
| [1,1-$^2$H] | −2.8866 | −3.11409 | 1.55705 | 1.54496 |
| [1-$^2$H$_{cis}$,3-$^2$H$_{anti}$] | −2.9135 | −3.11552 | 1.55776 | 1.54567 |
| [1-$^2$H$_{cis}$,3-$^2$H$_{gauche}$] | −4.2984 | −4.54383 | | |
| [1-$^2$H$_{trans}$,3-$^2$H$_{anti}$] | −2.9209 | −3.11574 | 1.55787 | 1.54578 |
| [1-$^2$H$_{trans}$,3-$^2$H$_{gauche}$] | −4.3023 | −4.54054 | | |
| [3-$^2$H$_{anti}$,3-$^2$H$_{gauche}$] | −4.3398 | −4.54764 | | |
| [3-$^2$H$_{gauche}$,3-$^2$H$_{gauche}$] | −5.9890 | −6.21804 | 3.10902 | 1.54363 |
| [1,1-$^2$H,3-$^2$H$_{anti}$] | −2.9154 | −3.11569 | 1.55784 | 1.54575 |
| [1,1-$^2$H,3-$^2$H$_{gauche}$] | −4.3006 | −4.54444 | | |
| [1-$^2$H$_{cis}$,3-$^2$H$_{anti}$,3-$^2$H$_{gauche}$] | −4.3360 | −4.55167 | | |
| [1-$^2$H$_{cis}$,3-$^2$H$_{gauche}$,3-$^2$H$_{gauche}$] | −5.980 | −6.21792 | 3.10896 | 1.54360 |
| [1-$^2$H$_{trans}$,3-$^2$H$_{anti}$,3-$^2$H$_{gauche}$] | −4.3398 | −4.54850 | | |
| [1-$^2$H$_{trans}$,3-$^2$H$_{gauche}$,3-$^2$H$_{gauche}$] | −5.9883 | −6.21873 | 3.10937 | 1.54380 |
| [3,3,3-$^2$H] | −6.0229 | −6.21980 | 3.1099 | 1.54406 |
| [1,1-$^2$H,3-$^2$H$_{anti}$,3-$^2$H$_{gauche}$] | −4.3377 | −4.55217 | | |
| [1,1-$^2$H,3-$^2$H$_{gauche}$,3-$^2$H$_{gauche}$] | −5.9821 | −6.21836 | 3.10918 | 1.54370 |
| [1-$^2$H$_{cis}$,3,3,3-$^2$H] | −6.0144 | −6.21854 | 3.10927 | 1.54375 |
| [1-$^2$H$_{trans}$,3,3,3-$^2$H] | −6.0218 | −6.21912 | 3.10956 | 1.54389 |
| [1,1,3,3,3-$^2$H] | −6.0154 | −6.22028 | 3.11014 | 1.54418 |
| [1,1,3,3,3-$^2$H,1-$^{13}$C] | −6.0131 | −6.21962 | 3.10981 | 1.54402 |
| [1,1,3,3,3-$^2$H,2-$^{13}$C] | −6.0137 | −6.21703 | 3.10851 | 1.54337 |
| [1,1,3,3,3-$^2$H,3-$^{13}$C] | −6.0113 | −6.21824 | 3.10912 | 1.54367 |
| [1,1,3,3,3-$^2$H,4-$^{13}$C] | −6.0184 | −6.21102 | 3.10551 | 1.54188 |
| [1,1,3,3,3-$^2$H,$^{15}$N] | −6.0096 | −6.21685 | 3.10843 | 1.54333 |
| Average $\bar{x}$ | | | | 1.54432 |
| std dev s | | | | 0.00094 |

[a] An average between A- and S-reduced ground rotational constants, $B_0$, to obtain $\Delta_i = I_c - I_a - I_b$ .

[b] Vibration-rotation interaction and electron-mass corrections.

[c] $P_{cc} = (I_c - I_a - I_b)/-2$

[d] $m_H$ = 1.007825035 for $^1$H or 2.014101779 for $^2$H

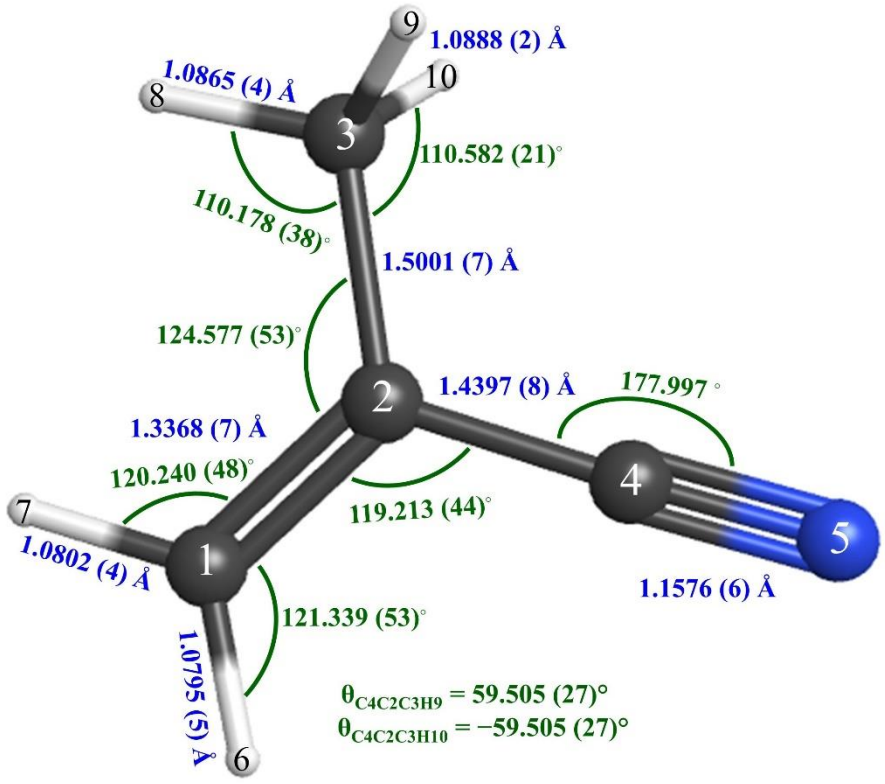


**FIG. 6.6.** Semi-experimental equilibrium structure ($r_e^{SE}$) of methacrylonitrile with 2σ statistical uncertainties from least-squares fitting of the moments of inertia from 32 isotopologues. Distances are in Angstroms and the angles are in degrees.

The semi-experimental equilibrium structure ($r_e^{SE}$) determined from 32 isotopologues is presented in Fig. 6.6 and enumerated in Table 6.4. The 2σ statistical uncertainties for the bond distances are all ≤ 0.0008 Å with the largest uncertainties corresponding to heavy atom bond distances. The uncertainties for the bond angles are all ≤ 0.053° with most bond angles having similar precision besides the angles corresponding to the methyl group, which are determined to a higher level of precision. The $r_e^{SE}$ of methacrylonitrile is the first non-planar molecule determined to this level of precision or accuracy. A similar level of precision was achieved to the recently reported $r_e^{SE}$ structure determinations of planar heteroaromatics[20-24,26] and small molecules.[25,28] It is the only structure where a parameter was held constant at its BTE value during the least-squares

fitting process in *xrefit* in order to obtain a satisfactory structure. The discussion on the origin of the structural issue and how this parameter was identified will be discussed further below.

**Table 6.4.** Equilibrium structural parameters of methacrylonitrile.

| | $r_e^{SE}$ CCSD(T)/ cc-pCVTZ | $r_e$ CCSD(T) BTE | $r_e$ CCSD(T)/ cc-pCV5Z |
|---|---|---|---|
| $r_{C1-C2}$ | 1.3368 (7) | 1.3370 | 1.3364 |
| $r_{C2-C3}$ | 1.5001 (7) | 1.5003 | 1.5003 |
| $r_{C2-C4}$ | 1.4396 (8) | 1.4395 | 1.4399 |
| $r_{C4-N}$ | 1.1576 (6) | 1.1590 | 1.1581 |
| $r_{C1-H6}$ | 1.0795 (5) | 1.0793 | 1.0793 |
| $r_{C1-H7}$ | 1.0801 (4) | 1.0803 | 1.0803 |
| $r_{C3-H8}$ | 1.0865 (4) | 1.0870 | 1.0869 |
| $r_{C3-H9/H10}$ | 1.0888 (2) | 1.0891 | 1.0891 |
| $\theta_{C3-C2-C1}$ | 124.575 (53) | 124.562 | 124.585 |
| $\theta_{C1-C2-C4}$ | 119.215 (44) | 119.247 | 119.228 |
| $\theta_{C2-C4-N}$ | [177.997][a] | 177.997 | 178.054 |
| $\theta_{C2-C1-H6}$ | 121.337 (53) | 121.347 | 121.392 |
| $\theta_{C2-C1-H7}$ | 120.242 (48) | 120.226 | 120.257 |
| $\theta_{C2-C3-H8}$ | 110.179 (37) | 110.182 | 110.184 |
| $\theta_{C2-C3-H9/H10}$ | 110.581 (21) | 110.571 | 110.573 |
| $\theta_{C4-C2-C3-H9}$ | 59.505 (27) | 59.465 | 59.472 |
| $\theta_{C4-C2-C3-H10}$ | −59.505 (27) | −59.465 | −59.472 |
| $N_{iso}$ | 32 | | |

[a]Parameter held fixed at BTE value.

## Discussion

The *xrefiteration* program[23] was used to examine the effects of including all available isotopologues in the $r_e^{SE}$ structure similar to our previous structure determinations.[23-28] Figure 6.7 is a plot of parameter uncertainty versus the number of isotopologues incorporated into the least-squares fit. A steady decrease in the total uncertainty is experienced as more isotopologues are added until approximately the 20$^{th}$ isotopologue, however, a smaller decrease is seen until the penultimate isotopologue is added. A small increase in total uncertainty is observed with the inclusion of the last isotopologue. By the 28$^{th}$ isotopologue added, the least-squares fit seems to be fully converged. There was no observed drastic increase in the total uncertainty as the last few

isotopologues were added into the least-squares fit unlike what was observed for thiophene[22] and 1*H*- and 2*H*-1,2,3-triazole.[26] It is worth noting, the first three isotopologues added beyond the core set are the [$^{13}$C]-isotopologues of the perdeutero species. These isotopologues provide important structural information about the location of those carbon atoms that is apparently not contained within the core set of isotopologues and lower the total uncertainty the most. Figure 6.8 shows the structural parameter values and their uncertainties as a function of isotopologues added by *xrefiteration*, and the specific order of isotopologues added is shown in the table of Fig. 6.7. Not until approximately the 24$^{th}$ isotopologue is included in the $r_e^{SE}$ structure, does it appear that every structural parameter is converged to its finalized value. These two observations support the inclusion of as many isotopologues as practical in a structure determination, because it is not clear *a priori* which isotopologues will be critically important or how many isotopologues will be needed to achieve a converged structure. Beyond the 24$^{th}$ isotopologue, the statistical uncertainties for the parameters are rather consistent and show small changes, indicating that this structure may be approaching the limit of what is achievable for an $r_e^{SE}$ structure in general or from the current data set.

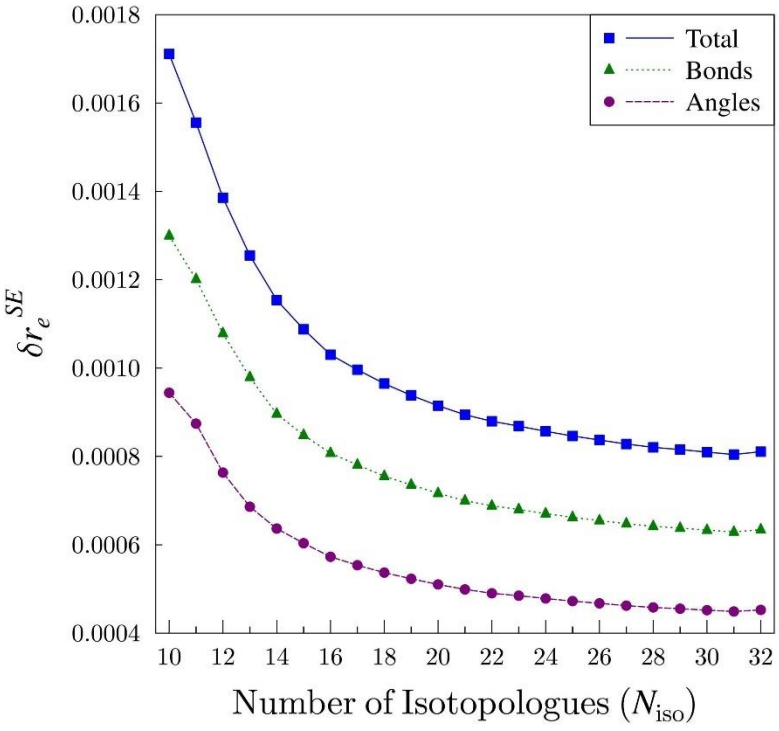


| $N_{iso}$ | Isotopologue Added |
|---|---|
| 10 | Core set |
| 11 | [1,1,3,3,3-$^2$H,2-$^{13}$C] |
| 12 | [1,1,3,3,3-$^2$H,1-$^{13}$C] |
| 13 | [1,1,3,3,3-$^2$H,3-$^{13}$C] |
| 14 | [1,1-$^2$H] |
| 15 | [1-$^2$H$_{trans}$, 3-$^2$H$_{gauche}$, 3-$^2$H$_{gauche}$] |
| 16 | [1-$^2$H$_{cis}$, 3-$^2$H$_{gauche}$, 3-$^2$H$_{gauche}$] |
| 17 | [1,1-$^2$H, 3-$^2$H$_{gauche}$, 3-$^2$H$_{gauche}$] |
| 18 | [1-$^2$H$_{trans}$, 3-$^2$H$_{gauche}$] |
| 19 | [3-$^2$H$_{gauche}$, 3-$^2$H$_{gauche}$] |
| 20 | [1,1-$^2$H, 3-$^2$H$_{gauche}$] |
| 21 | [1-$^2$H$_{cis}$, 3-$^2$H$_{gauche}$] |
| 22 | [1-$^2$H$_{cis}$, 3-$^2$H$_{anti}$] |
| 23 | [3,3,3-$^2$H] |
| 24 | [1-$^2$H$_{trans}$, 3,3,3-$^2$H] |
| 25 | [3-$^2$H$_{anti}$, 3-$^2$H$_{gauche}$] |
| 26 | [1-$^2$H$_{trans}$, 3-$^2$H$_{anti}$, 3-$^2$H$_{gauche}$] |
| 27 | [1,1-$^2$H, 3-$^2$H$_{anti}$] |
| 28 | [1-$^2$H$_{trans}$, 3-$^2$H$_{anti}$] |
| 29 | [1,1-$^2$H, 3-$^2$H$_{anti}$, 3-$^2$H$_{gauche}$] |
| 30 | [1-$^2$H$_{cis}$, 3-$^2$H$_{anti}$, 3-$^2$H$_{gauche}$] |
| 31 | [1-$^2$H$_{cis}$, 3,3,3-$^2$H] |
| 32 | [1,1,3,3,3-$^2$H] |

**FIG. 6.7.** Plot of $r_e^{SE}$ *Uncertainty* ($\delta r_e^{SE}$) as a function of the number of isotopologues ($N_{iso}$) incorporated into the structure determination data set for methacrylonitrile. The total relative statistical uncertainty ($\delta r_e^{SE}$, blue squares), the relative statistical uncertainty in the bond distances (green triangles), and the relative statistical uncertainty in the angles (purple circles) are presented.

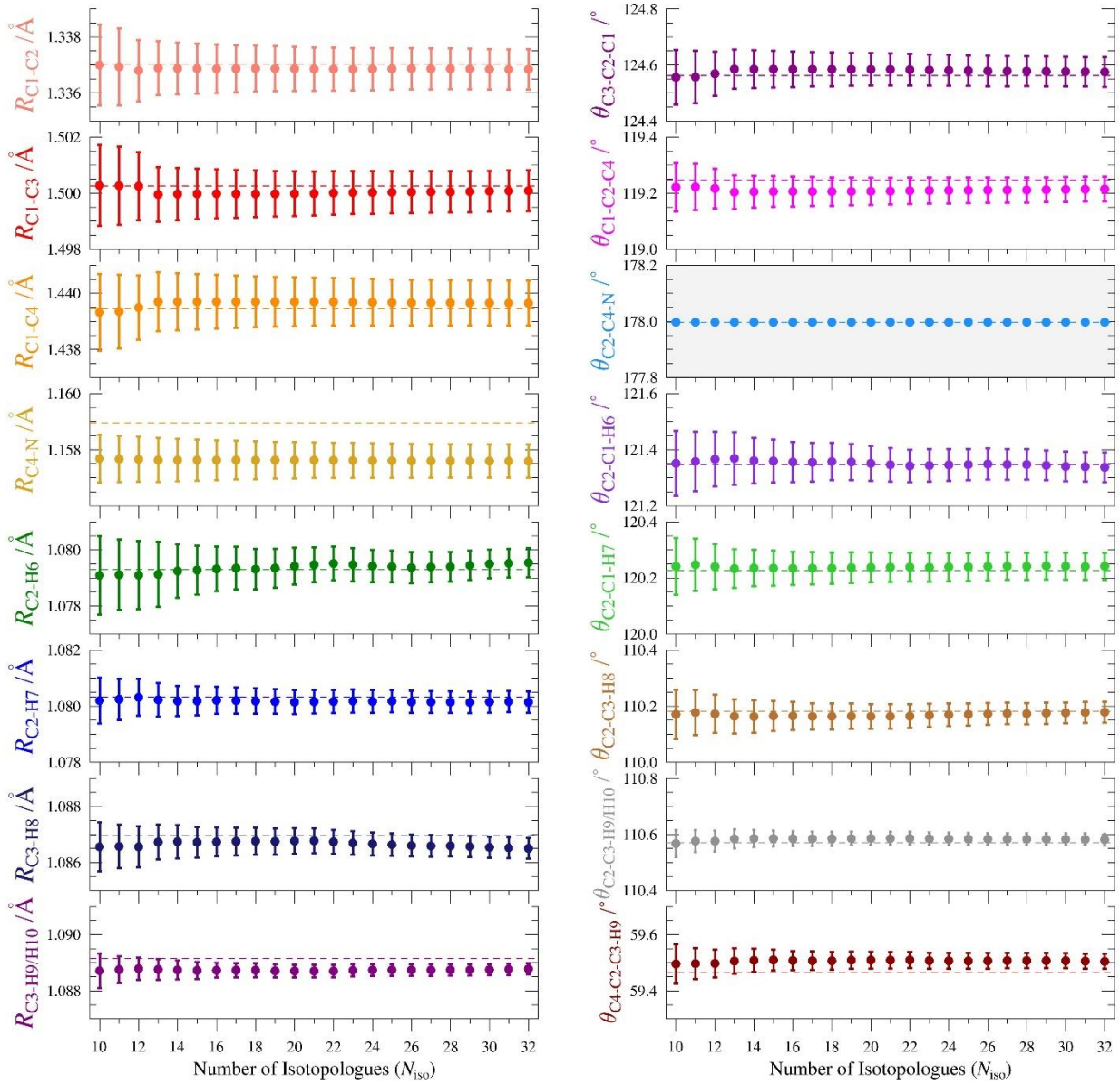


**FIG. 6.8.** Plots of the structural parameters of methacrylonitrile as a function of the number of isotopologues ($N_{iso}$) and their 2σ uncertainties. Distance and angle plots use consistent scales, respectively. Colored dashed lines indicate the BTE value. $\theta_{C2-C4-N}$ is held fixed at the BTE value and is shaded in gray. The table in Fig. 6.7 indicates the $x^{th}$ isotopologue added to the $r_e^{SE}$.

Providing complimentary analysis to the parameter convergence plots in Fig. 6.8, Fig. 6.9 is a graphical representation of all the structural parameters for the current $r_e^{SE}$, BTE, and various coupled-cluster calculations with different basis sets. As can be seen in both figures, 12 of the 16 independent structural parameters agree with their respective $r_e$ BTE value within its 2σ

uncertainty. The four parameter values that do not agree between the $r_e^{SE}$ and $r_e$ BTE structures are three bond lengths, $r_{C4-N}$, $r_{C3-H8}$, and $r_{C3-H9/H10}$, and one bond angle, $\theta_{C4-C2-C3-H9}$. The parameter with the largest discrepancy is the $r_{C4-N}$ bond distance, despite it seemingly converging with only the core set of single-substitution isotopologues. The $r_e^{SE}$ value is in agreement with the CCSD(T)/cc-pCV5Z value, however, considering the reliability of the BTE calculations previously,[20-28] this is likely somewhat accidental. It is more likely holding the $\theta_{C2-C4-N}$ angle at the BTE value is the cause of this discrepancy, by constraining the ability of the least squares fit to determine the location of the C4 and N atoms. All three remaining parameters involve the methyl group, and all the discrepancies may be due to an overestimation of the precision from the least-squares fit of the structure. These atoms are substituted in many of the isotopologues, and the parameters are well-converged. The three parameters have differences from the BTE values similar to other parameters, $r_{C3-H8} = -0.00046$ Å, $r_{C3-H9/H10} = -0.00037$ Å, and $\theta_{C4-C2-C3-H9} = 0.040°$. While this supports the idea that the precision associated with these parameters might be overestimated, the origin of this discrepancy is somewhat ambiguous.

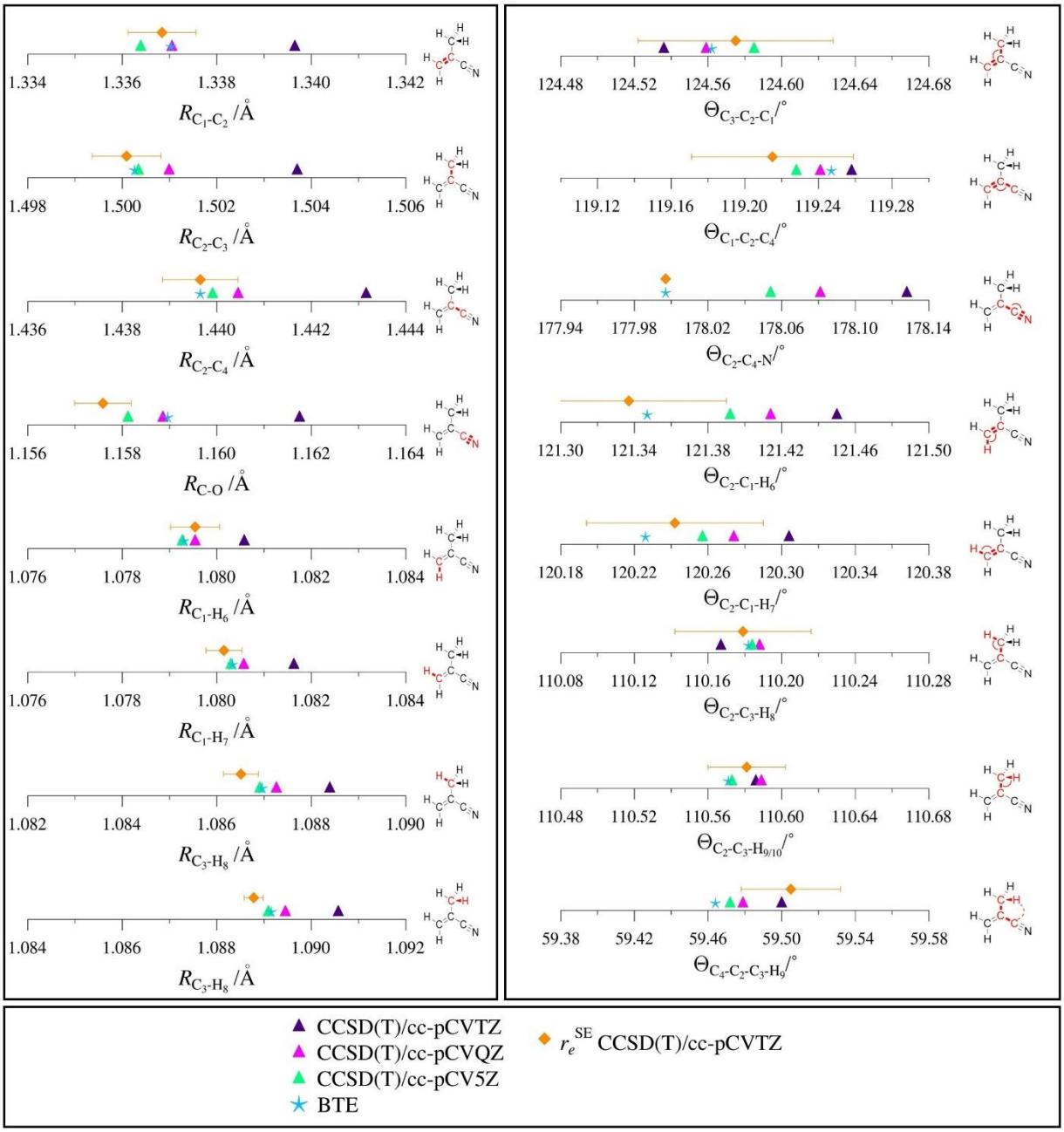


**FIG. 6.9.** Graphical comparison of the methacrylonitrile structural parameters with bond distances in angstroms (Å) and angles in degrees (°). Bond distances and bond angles are set to the same scales, respectively. Statistical uncertainties for all $r_e^{SE}$ parameters are 2σ besides $\theta_{C2\text{-}C4\text{-}N}$ which was held fixed at the BTE value.

Unlike previous works,[20-28] an angle, $\theta_{C2\text{-}C4\text{-}N}$, was held fixed at the determined BTE value because the structure determined with all parameters varying resulted in statistical uncertainties significantly higher for various parameters and resulted in more structural parameters not agreeing with their respective BTE value. The structure with all parameters varying is presented in the Supplementary Material (**Fig. S35**). This structure does not have the precision that is typical for an $r_e^{SE}$ structure determination, and it is likely due to three atoms, C2, C4, and N, having extremely small *b*-axis coordinates (Fig. 6.1). The poor determination of an atom location due to its proximity to a principal axis is widely known in structure determination methods,[35-39] but there is no universal solution to this problem. Our works with thiophene[22] and thiazole[21] had similar problems but to a lesser degree because they involved fewer problematic atom locations. In all three structures (thiophene, thiazole, and methacrylonitrile) the mass of the atoms and molecular geometry prevents moving of the problematic atoms significantly away from the nearby principal inertial axis. In the case of methacrylonitrile, the near-axis atom issue is exacerbated by having three connected atoms nearly colinear with its *a*-axis. The angle between these three problematic atoms was chosen to be held fixed at the BTE value to attempt to constrain the viable structures that could result from the least-squares fit in *xrefit*. When atoms are close to a principal axis, there are numerous structures that are possible minima resulting from the least-squares fit. Slight changes in $\theta_{C2\text{-}C4\text{-}N}$ result in large differences in the resulting structure due to its core relationship to the molecule. The high-level theoretical calculations to determine the BTE parameter are likely the best way to determine this parameter because computational calculations are not affected by this close proximity to a principal axis. The support for this method is the resulting structure has parameters that are more precisely determined and agree with their respective BTE values.

The $C_s$ symmetry of methacrylonitrile isotopologues that contain the same isotope of hydrogen for both out-of-plane hydrogen atoms in the methyl group allows for second moments[57] ($P_{cc}$, Table 6.3) to be analyzed to assess the quality of the spectroscopic constants and computational corrections utilized in the $r_e^{SE}$ structure determination. If corrected for vibration-rotation interaction and electron-mass corrections, the $P_{cc}$ for each separate group of isotopologues should be the same and any deviation indicates room for improvement in the rotational constants or computational corrections. The average of the $P_{cc}$ for the isotopologues with only $^1$H or $^2$H atoms out-of-plane is 1.5571 (7) and 3.1093 (5) uÅ$^2$, respectively. The $^1$H isotopologues have a greater standard deviation than the $^2$H isotopologues, however, if the main isotopologue is removed, the standard deviation is decreased to 0.0004 uÅ$^2$. The noticeable difference in the $P_{cc}$ value of the main isotopologue from the rest is likely due to the main isotopologue being fit with XIAM, and its full treatment of the internal rotation splitting. Furthermore, the mass dependence can attempt to be removed by considering the last column in Table 6.3, $P_{cc}$ / $m_H$. All isotopologues that maintain $C_s$ symmetry (all $^1$H or $^2$H atoms out of plane) should have the same value of $P_{cc}$ / $m_H$. The values range from 1.54285 Å$^2$ to 1.54578 Å$^2$ for the $^1$H isotopologues and 1.54337 Å$^2$ to 1.54418 Å$^2$ for the $^2$H isotopologues. These differences are larger than the ones observed for ketene[28], which could indicate a less accurate determination of the rotational constants or computational corrections. It is also feasible since the number of atoms has doubled, in addition to the two out-of-plane atoms being comprised in a methyl group, that the precision obtained in ketene is not possible for methacrylonitrile. The *c*-coordinate (out-of-plane distance) can be calculated for the $^1$H and $^2$H isotopologues given Eqn. 2, where $^1$H-atom = 0.87893 Å and $^2$H-atom = 0.87858 Å.

$$c_H = \sqrt{\frac{P_{cc}}{2m_H}} \quad (2)$$

The 0.00035 Å difference between the values is larger than the expected isotopic difference in the $r_{C–H}$ and $r_{C–D}$ equilibrium bond distances.[27,28] Given the resulting structures from the $r_e^{SE}$ and BTE, a similar approach can be implemented given their rotational constants. The *c*-coordinate is 0.87828 Å and 0.87829 Å for the $r_e^{SE}$ and BTE, respectively. The extremely small difference, 0.00001 Å, between these two gives confidence in the overall quality of the semi-experimental equilibrium structure and BTE structure determined in this work.

**Conclusion**

A highly precise and accurate semi-experimental equilibrium ($r_e^{SE}$) structure for methacrylonitrile has been determined from the spectroscopic constants of 32 isotopologues. The methacrylonitrile $r_e^{SE}$ needed significantly more isotopologues than the core set to reach a converged structure and is a counter example to $HN_3$[25] and ketene,[28] where those structures were mostly converged after the core set. The overall precision of the structural parameters was similar to our previous heteroaromatic structure determinations.[20-24,26] The BTE values for structural parameters fall within the 2σ uncertainties for the respective $r_e^{SE}$ parameter for 12 out of the 16 independent structural parameters determined in this work. We have also observed worse percentages of structural parameters that did not agree with BTE values for thiophene[22] and thiazole.[21] Each of the cases where there are significant deviations from the BTE values occur with molecules that have atom(s) close to a principal axis.

Methacrylonitrile is the first molecule where we held a structural parameter at its respective BTE value, due to the inability to determine the parameter with a high level of precision. This issue was attributed to C2, C4, and N atoms lying extremely close to the principal *a*-axis, and

the inability of any of the 32 isotopologues to significantly rotate the principal axis away from these three atoms. The solution in this work with holding the $\theta_{C2\text{-}C4\text{-}N}$ fixed to the BTE value is an empirical solution to the near-axis problem. Ideally, every parameter would be able to be varied in the least-squares fit of the structure determination, but in this case, it was at the detriment of the entire structure. We believe the BTE value determined in this work is likely within $2\sigma$ of a representative error given the other angle uncertainties. Additionally, we have presented an analysis of the impact of each rotational constant on each structural parameter, which revealed the $\theta_{C2\text{-}C4\text{-}N}$ parameter as being the most sensitive to changes in the data set. This is the first example where such an analysis was used to identify which structural parameter should be held at a constant value. This analysis and the solution applied in this work may be generalized to other molecules that have this near-axis problem and where a precise $r_e^{SE}$ structure cannot be determined.

The current spectroscopic investigation of methacrylonitrile from 6 GHz to 500 GHz has allowed a complete determination of the spectroscopic constants through the sextic centrifugal distortion constants. With methacrylonitrile's recent detection in TMC-1,[14] it has renewed interest in searching for methacrylonitrile in other extraterrestrial environments in different frequency ranges. The current spectroscopic constants improve the accuracy of rotational transitions predicted through 500 GHz. It is also evident from the spectra that there were a significant number of vibrationally excited states that were observable, but they were not within the scope of this work. Preliminary assignments of rotational transitions have been made for the vibrationally excited states, including the first vibrationally excited torsional motion of the methyl rotor. A more complete rotational analyses of vibrational states and treatment of the internal rotation of the vibrationally excited states is possible with the currently available spectra and may be the subject of future studies.

## SUPPLEMENTARY MATERIAL

Computational output files, least-squares fitting for all isotopologues, data distribution plots for all non-standard isotopologues, *xrefiteration* outputs, equations used for calculating determinable constants and BTE corrections, and tables of S-reduction, A-reduction, and determinable constants, structural parameters, BTE corrections, and synthetic details are provided in Appendix A.

## ACKNOWLEDGMENTS

We gratefully acknowledge funding from the U.S. National Science Foundation for support of this project (CHE-1954270). We thank Ha Vinh Lam Nguyen for providing the modified version of XIAM.

## AUTHOR DECLARATIONS

### Conflict of Interest

The authors have no conflicts to disclose.

## DATA AVAILABILITY

The data that support the findings of this study are available within the article and its supplementary material.

## REFERENCES


1. C. L. Norris; W. H. Flygare, "The microwave spectrum, barrier to internal rotation of the methyl group, and $^{14}N$ nuclear quadrupole coupling constants in methacrylonitrile," *J. Mol. Spectrosc.* **40**, 40-51 (1971).
2. J. C. López; J. Demaison; A. Gomez; J. L. Alonso; G. Wlodarczak, "The rotational spectrum of methacrylonitrile: Dipole moment, internal rotation, and centrifugal distortion," *J. Mol. Spectrosc.* **141**, 317-324 (1990).
3. A. Tramer; K. L. Wierzchowski, "Vibration spectra and force constants of nitriles," *Bulletin de l'Académie polonaise des sciences* **5**, 335-341 (1957).
4. F. Winther; D. O. Hummel, "The combination band of the methyl group torsion and antisymmetrical stretching frequency—I. Molecules with one methyl rotor," *Spectrochim. Acta - A: Mol. Biomol.* **25**, 417-423 (1969).
5. J. Bragin; K. L. Kizer; J. R. Durig, "The vibrational spectra and normal modes of vibration of 2-cyanopropene and 2-cyanopropene-d5," *J. Mol. Spectrosc.* **38**, 289-305 (1971).
6. T. S. Abilova; N. N. Sarvanova; R. M. Akhmedov; S. I. Mekhtiev, "IR spectra and normal vibrations of methacrylonitrile," *Dokl. Akad. Nauk SSR* **38** (1982).
7. F. Cerceau; F. Raulin; R. Courtin; D. Gautier, "Infrared spectra of gaseous mononitriles: Application to the atmosphere of Titan," *Icarus* **62**, 207-220 (1985).
8. M. P. Bernstein; S. A. Sandford; L. J. Allamandola, "The Infrared Spectra of Nitriles and Related Compounds Frozen in Ar and H2O," *Astrophys. J.* **476**, 932 (1997).
9. C. Y. Panicker; H. T. Varghese; B. Harikumar; A. Chandran, "Vibrational spectroscopic investigations of methacrylonitrile," *Material Science Research India* **8**, 297-300 (2011).
10. C. Y. Oh; S. K. Shin; H. L. Kim; C. R. Park, "Photodissociation of Methacrylonitrile at 193 nm: The CN Radical Product Channel," *J. Phys. Chem. A* **107**, 4333-4338 (2003).
11. A. S. Brar; D. R. Pradhan, "Complete Assignment of 1H and 13C NMR Spectra of Methacrylonitrile/Methylmethacrylate Copolymers," *Polym. J.* **33**, 602-609 (2001).
12. H. F. Mark; N. M. Bikales; C. G. Overberger; G. Menges In *Encyclopedia of Polymer Science and Engineering*; 2nd ed.; John Wiley and Sons, 1985; Vol. 1, p 843
13. B.-C. Ho; W.-K. Chin; Y.-D. Lee, "Solubility parameters of polymethacrylonitrile, poly(methacrylic acid) and methacrylonitrile/methacrylic acid copolymer," *J. Appl. Polym. Sci.* **42**, 99-106 (1991).
14. J. Cernicharo; R. Fuentetaja; C. Cabezas; M. Agúndez; N. Marcelino; B. Tercero; J. R. Pardo; P. de Vicente, "Discovery of five cyano derivatives of propene with the QUIJOTE line survey," *Astron. Astrophys.* **663**, L5 (2022).
15. J. Gauss; J. F. Stanton, "Equilibrium structure of LiCCH," *Int. J. Quantum Chem.* **77**, 305-310 (2000).
16. K. L. Bak; J. Gauss; P. Jørgensen; J. Olsen; T. Helgaker; J. F. Stanton, "The Accurate Determination of Molecular Equilibrium Structures," *J. Chem. Phys.* **114**, 6548-6556 (2001).
17. C. Puzzarini, "Accurate molecular structures of small- and medium-sized molecules," *Int. J. Quantum Chem.* **116**, 1513-1519 (2016).
18. C. Puzzarini; J. F. Stanton, "Connections between the accuracy of rotational constants and equilibrium molecular structures," *Phys. Chem. Chem. Phys.* **25**, 1421-1429 (2023).
19. P. Pulay; W. Meyer; J. E. Boggs, "Cubic force constants and equilibrium geometry of methane from Hartree–Fock and correlated wavefunctions," *J. Chem. Phys.* **68**, 5077-5085 (1978).
20. Z. N. Heim; B. K. Amberger; B. J. Esselman; J. F. Stanton; R. C. Woods; R. J. McMahon, "Molecular structure determination: Equilibrium structure of pyrimidine (*m*-$C_4H_4N_2$) from rotational spectroscopy ($r_e^{SE}$) and high-level *ab initio* calculation ($r_e$) agree within the uncertainty of experimental measurement," *J. Chem. Phys.* **152**, 104303 (2020).

21. B. J. Esselman; M. A. Zdanovskaia; A. N. Owen; J. F. Stanton; R. C. Woods; R. J. McMahon, "Precise equilibrium structure of thiazole (*c*-$C_3H_3NS$) from twenty-four isotopologues," *J. Chem. Phys.* **155**, 054302 (2021).
22. V. L. Orr; Y. Ichikawa; A. R. Patel; S. M. Kougias; K. Kobayashi; J. F. Stanton; B. J. Esselman; R. C. Woods; R. J. McMahon, "Precise equilibrium structure determination of thiophene (*c*-$C_4H_4S$) by rotational spectroscopy—Structure of a five-membered heterocycle containing a third-row atom," *J. Chem. Phys.* **154**, 244310 (2021).
23. A. N. Owen; M. A. Zdanovskaia; B. J. Esselman; J. F. Stanton; R. C. Woods; R. J. McMahon, "Semi-Experimental Equilibrium ($r_e^{SE}$) and Theoretical Structures of Pyridazine (*o*-$C_4H_4N_2$)," *J. Phys. Chem. A* **125**, 7976-7987 (2021).
24. H. A. Bunn; B. J. Esselman; P. R. Franke; S. M. Kougias; R. J. McMahon; J. F. Stanton; S. L. Widicus Weaver; R. C. Woods, "Millimeter/Submillimeter-wave Spectroscopy and the Semi-experimental Equilibrium ($r_e^{SE}$) Structure of 1*H*-1,2,4-Triazole (*c*-$C_2H_3N_3$)," *J. Phys. Chem. A* **126**, 8196-8210 (2022).
25. A. N. Owen; N. P. Sahoo; B. J. Esselman; J. F. Stanton; R. C. Woods; R. J. McMahon, "Semi-experimental equilibrium ($r_e^{SE}$) and theoretical structures of hydrazoic acid ($HN_3$)," *J. Chem. Phys.* **157**, 034303 (2022).
26. M. A. Zdanovskaia; B. J. Esselman; S. M. Kougias; B. K. Amberger; J. F. Stanton; R. C. Woods; R. J. McMahon, "Precise equilibrium structures of 1*H*- and 2*H*-1,2,3-triazoles ($C_2H_3N_3$) by millimeter-wave spectroscopy," *J. Chem. Phys.* **157**, 084305 (2022).
27. B. J. Esselman; M. A. Zdanovskaia; A. N. Owen; J. F. Stanton; R. C. Woods; R. J. McMahon, "Precise Equilibrium Structure of Benzene," *unpublished work* (2023).
28. H. H. Smith; B. J. Esselman; S. A. Wood; J. F. Stanton; R. C. Woods; R. J. McMahon, "Improved semi-experimental equilibrium structure and high-level theoretical structures of ketene," *J. Chem. Phys.* **158**, 244304 (2023).
29. J. Demaison; L. Margulès; I. Kleiner; A. G. Császár, "Equilibrium structure in the presence of internal rotation: A case study of cis-methyl formate," *J. Mol. Spectrosc.* **259**, 70-79 (2010).
30. N. Vogt; J. Demaison; J. Vogt; H. D. Rudolph, "Why it is sometimes difficult to determine the accurate position of a hydrogen atom by the semiexperimental method: Structure of molecules containing the OH or the CH3 group," *J. Comput. Chem.* **35**, 2333-2342 (2014).
31. E. Penocchio; M. Piccardo; V. Barone, "Semiexperimental Equilibrium Structures for Building Blocks of Organic and Biological Molecules: The B2PLYP Route," *J. Chem. Theory Comput.* **11**, 4689-4707 (2015).
32. J. Demaison; N. C. Craig; R. Gurusinghe; M. J. Tubergen; H. D. Rudolph; L. H. Coudert; P. G. Szalay; A. G. Császár, "Fourier Transform Microwave Spectrum of Propene-3-d1 ($CH_2$═$CHCH_2D$), Quadrupole Coupling Constants of Deuterium, and a Semiexperimental Equilibrium Structure of Propene," *J. Phys. Chem. A* **121**, 3155-3166 (2017).
33. I. V. Kochikov; Y. I. Tarasov; N. Vogt; V. P. Spiridonov, "Large-amplitude motion in 1,4-cyclohexadiene and 1,4-dioxin: theoretical background for joint treatment of spectroscopic, electron diffraction and ab initio data," *J. Mol. Struct.* **607**, 163-174 (2002).
34. H. Hartwig; H. Dreizler In *Z NATURFORSCH A*, 1996; Vol. 51, p 923
35. L. Pierce, "Note on the use of ground-state rotational constants in the determination of molecular structures," *J. Mol. Spectrosc.* **3**, 575-580 (1959).
36. B. P. Stoicheff, "The variation of carbon-carbon bond lengths with environment as determined by spectroscopic studies of simple polyatomic molecules," *Tetrahedron* **17**, 135-145 (1962).
37. H. D. Rudolph, "Contribution to the systematics of r0-derived molecular structure determinations from rotational parameters," *Struct. Chem.* **2**, 581-588 (1991).
38. H. D. Rudolph, "Accurate molecular structure from microwave rotational spectroscopy," *Advances in Molecular Structure Research* **1**, 63-114 (1995).

39. J. Demaison; H. D. Rudolph, "When Is the Substitution Structure Not Reliable?," *J. Mol. Spectrosc.* **215**, 78-84 (2002).
40. B. K. Amberger; B. J. Esselman; J. F. Stanton; R. C. Woods; R. J. McMahon, "Precise Equilibrium Structure Determination of Hydrazoic Acid ($HN_3$) by Millimeter-wave Spectroscopy," *J. Chem. Phys.* **143**, 104310 (2015).
41. B. J. Esselman; B. K. Amberger; J. D. Shutter; M. A. Daane; J. F. Stanton; R. C. Woods; R. J. McMahon, "Rotational spectroscopy of pyridazine and its isotopologs from 235–360 GHz: Equilibrium structure and vibrational satellites," *J. Chem. Phys.* **139**, 224304 (2013).
42. M. A. Zdanovskaia; B. J. Esselman; R. C. Woods; R. J. McMahon, "The 130 - 370 GHz Rotational Spectrum of Phenyl Isocyanide ($C_6H_5NC$)," *J. Chem. Phys.* **151**, 024301 (2019).
43. M. C. McCarthy; W. Chen; M. J. Travers; P. Thaddeus, "Microwave Spectra of 11 Polyyne Carbon Chains," *Astrophys. J., Suppl. Ser.* **129**, 611 (2000).
44. J.-U. Grabow; E. S. Palmer; M. C. McCarthy; P. Thaddeus, "Supersonic-jet cryogenic-resonator coaxially oriented beam-resonator arrangement Fourier transform microwave spectrometer," *Rev. Sci. Instrum.* **76**, 093106 (2005).
45. H. M. Pickett, "Determination of collisional linewidths and shifts by a convolution method," *Appl. Opt.* **19**, 2745-2749 (1980).
46. Z. Kisiel; L. Pszczółkowski; B. J. Drouin; C. S. Brauer; S. Yu; J. C. Pearson; I. R. Medvedev; S. Fortman; C. Neese, "Broadband rotational spectroscopy of acrylonitrile: Vibrational energies from perturbations," *J. Mol. Spectrosc.* **280**, 134-144 (2012).
47. Z. Kisiel; L. Pszczółkowski; I. R. Medvedev; M. Winnewisser; F. C. De Lucia; E. Herbst, "Rotational spectrum of *trans–trans* diethyl ether in the ground and three excited vibrational states," *J. Mol. Spectrosc.* **233**, 231-243 (2005).
48. Z. Kisiel; E. Białkowska-Jaworska, "Sextic Centrifugal Distortion in Fluorobenzene and Phenylacetylene from cm-Wave Rotational Spectroscopy," *J. Mol. Spectrosc.* **359**, 16-21 (2019).
49. Z. Kisiel, "Assignment and Analysis of Complex Rotational Spectra," In *Spectroscopy from Space*; 1st ed.; Demaison, J., Sarka, K., Cohen, E. A., Eds.; Springer Netherlands: Dordrecht, 2001, pp 91-106.
50. "PROSPE - Programs for ROtational SPEctroscopy", http://info.ifpan.edu.pl/~kisiel/prospe.htm
51. "J.F. Stanton, J. Gauss, M.E. Harding, P.G. Szalay, with contributions from A.A. Auer, R.J. Bartlett, U. Benedikt, C. Berger, D.E. Bernholdt, Y.J. Bomble, L. Cheng, O. Christiansen, M. Heckert, O. Heun, C. Huber, T.-C. Jagau, D. Jonsson, J. Jusélius, K. Klein, W.J. Lauderdale, D.A. Matthews, T. Metzroth, L.A. Mück, D.P. O'Neill, D.R. Price, E. Prochnow, C. Puzzarini, K. Ruud, F. Schiffmann, W. Schwalbach, S. Stopkowicz, A. Tajti, J. Vázquez, F. Wang, J.D. Watts and the integral packages MOLECULE (J. Almlöf and P.R. Taylor), PROPS (P.R. Taylor), ABACUS (T. Helgaker, H.J. Aa. Jensen, P. Jørgensen, and J. Olsen), and ECP routines by A. V. Mitin and C. van Wüllen. *CFOUR, Coupled-Cluster techniques for Computational Chemistry*, a quantum-chemical program package. For the current version, see http://www.cfour.de".
52. J. F. Stanton; C. L. Lopreore; J. Gauss, "The equilibrium structure and fundamental vibrational frequencies of dioxirane," *J. Chem. Phys.* **108**, 7190-7196 (1998).
53. W. Schneider; W. Thiel, "Anharmonic Force Fields from Analytic Second Derivatives: Method and Application to Methyl Bromide," *Chem. Phys. Lett.* **157**, 367-373 (1989).
54. I. M. Mills, "Vibration-Rotation Structure in Asymmetric- and Symmetric-Top Molecules," In *Molecular Spectroscopy: Modern Research*; Rao, K. N., Mathews, C. W., Eds.; Academic Press: New York, 1972; Vol. 1, pp 115-140.
55. C. Puzzarini; J. Bloino; N. Tasinato; V. Barone, "Accuracy and Interpretability: The Devil and the Holy Grail. New Routes across Old Boundaries in Computational Spectroscopy," *Chem. Rev.* **119**, 8131-8191 (2019).
56. H. M. Pickett, "The fitting and prediction of vibration-rotation spectra with spin interactions," *J. Mol. Spectrosc.* **148**, 371-377 (1991).

57. R. K. Bohn; J. A. Montgomery, Jr. ; H. H. Michels; J. A. Fournier, "Second moments and rotational spectroscopy," *J. Mol. Spectrosc.* **325**, 42-49 (2016).

# Supplementary Material

## Semi-experimental Equilibrium Structure of Methacrylonitrile ($r_e^{SE}$)

Houston H. Smith,[1] Samuel M. Kougias,[1] Madeleine Atwood,[1] Danny J. Lee,[1]
Bryan Changala,[3] Michael C. McCarthy,[3] Nitai Sahoo,[2] John F. Stanton,[2,*]
Brian J. Esselman,[1] R. Claude Woods,[1,*] Robert J. McMahon[1,*]

[1] *Department of Chemistry, University of Wisconsin–Madison, Madison, Wisconsin 53706, USA*

[2] *Quantum Theory Project, Departments of Physics and Chemistry, University of Florida, Gainesville, Florida 32611, United States*

[3] *Center for Astrophysics, Harvard and Smithsonian, 60 Garden Street, Cambridge, MA 02138-1516, United States*

* corresponding authors
E-mail address: johnstanton@chem.ufl.edu (J.F. Stanton)
E-mail address: rcwoods@wisc.edu (R.C. Woods)
E-mail address: robert.mcmahon@wisc.edu (R.J. McMahon)

| Table of Contents | Page |
|---|---|

| | |
|---|---|
| Low error least-squares fitting input and output files for methacrylonitrile standard isotopologue (methacrylonitrile_gs_fit_A.res/xo/xi and methacrylonitrile_gs_fit_S.res/xo/xi) | Separate Files |
| Least-squares fitting output files for methacrylonitrile non-standard isotopologues fitted in this work (methacrylo_iso#_*S*.res and methacrylo_iso#_*A*.res) | Separate Files |
| VPT2 anharmonic output files for methacrylonitrile isotopologues, CCSD(T)/cc-pCVTZ (out.ISOMASS###) | Separate Files |
| Magnetic calculations for methacrylonitrile isotopologues (methacrylonitrile_mag_###.out) | Separate Files |
| Geometry optimizations of methacrylonitrile, CCSD(T)/cc-pCVTZ (methacrylonitrile_opt_pCVTZ.out) | Separate Files |
| Geometry optimization of methacrylonitrile, CCSD(T)/cc-pCVQZ (methacrylonitrile_opt_pCVQZ.out) | Separate Files |
| Geometry optimizations of methacrylonitrile, CCSD(T)/cc-pC5TZ (methacrylonitrile_opt_pCV5Z.out) | Separate Files |
| Geometry optimizations of methacrylonitrile, CCSD(T)/cc-pCVTZ, Relativistic (methacrylonitrile_opt_cc-pCVTZ-Relativistic.out) | Separate Files |
| Geometry optimizations of methacrylonitrile, CCSD(T)/pVDZ (methacrylonitrile_opt_CCSDT-pVDZ.out) | Separate Files |
| Geometry optimizations of methacrylonitrile, CCSDT(Q)/pVDZ (methacrylonitrile_opt_CCSDTQ-pVDZ.out) | Separate Files |
| Geometry optimizations of methacrylonitrile, SCF/pVTZ (methacrylonitrile_opt_SCF_pVTZ.out) | Separate Files |
| Geometry optimizations of methacrylonitrile, SCF/pVTZ with DBOC (methacrylonitrile_opt_SCF_pVTZ-DBOC.out) | Separate Files |
| *xrefiteration* output files for methacrylonitrile (xrefiteration methacrylonitrile-results.csv) | Separate Files |
| *xrefit* output files including all corrections for methacrylonitrile with A3 angle fixed (methacrylonitrile_ReSE.out) | Separate Files |
| *xrefit* output files including all corrections for methacrylonitrile with all parameters varying (methacrylonitrile_ReSE_total.out) | |

**Table S-I.** Experimental and computational spectroscopic constants for standard methacrylonitrile isotopologue, ground vibrational state (S-reduced Hamiltonian, $I^r$ representation)

| | CCSD(T)/ cc-pCVTZ | Current Work Version 2 |
|---|---|---|
| $A_0$ (MHz) | 9253 | 9291.31630 (57) |
| $B_0$ (MHz) | 4143 | 4166.46243 (39) |
| $C_0$ (MHz) | 2909 | 2924.62307 (37) |
| $D_J$ (kHz) | 0.293 | 0.298408 (39) |
| $D_{JK}$ (kHz) | 16.5 | 16.73021 (22) |
| $D_K$ (kHz) | −7.46 | −7.7931 (22) |
| $d_1$ (kHz) | −0.256 | −0.264578 (19) |
| $d_2$ (kHz) | −0.225 | −0.2332210 (80) |
| $H_J$ (Hz) | −0.00217 | −0.0022350 (50) |
| $H_{JK}$ (Hz) | 0.0733 | 0.071840 (36) |
| $H_{KJ}$ (Hz) | −0.0463 | −0.04219 (11) |
| $H_K$ (Hz) | −0.194 | [−0.00194] |
| $h_1$ (Hz) | −0.000172 | −0.0001660 (30) |
| $h_2$ (Hz) | 0.00134 | 0.0013650 (20) |
| $h_3$ (Hz) | 0.000418 | 0.0004240 (10) |
| $V_3$ (MHz) | | 20607634. (17268) |
| $V_3$ ($cm^{-1}$) | | 687.39 (57) |
| $D_{pi2K}$ (MHz) | | −7.596 (80) |
| $D_{pi2-}$ (MHz) | | −1.001 (14) |
| $N_{lines}$ | | 2376 |
| $\sigma_{fit}$ (MHz) | | 0.048 |
| $\Delta_i$ ($uÅ^2$) | | −2.888108 (25) |

**Table S-II.** Experimental and computational spectroscopic constants for non-standard methacrylonitrile isotopologues, ground vibrational state (A-reduced Hamiltonian, $I^r$ representation)

| | [1-$^{13}$C] | | [2-$^{13}$C] | | [3-$^{13}$C] | | [4-$^{13}$C] | |
|---|---|---|---|---|---|---|---|---|
| | CCSD(T) | Present Work | CCSD(T) | Present Work | CCSD(T) | Present Work | CCSD(T) | Present Work |
| $A_0$ (MHz) | 8983 | 9020.071 (15) | 9252 | 9290.32 (11) | 9016 | 9053.0230 (42) | 9253 | 9291.1612 (74) |
| $B_0$ (MHz) | 4102 | 4125.8648 (40) | 4135 | 4158.418 (25) | 4091 | 4114.67031 (55) | 4113 | 4136.4437 (12) |
| $C_0$ (MHz) | 2862 | 2877.49168 (21) | 2905 | 2920.60185 (32) | 2860 | 2875.37323 (23) | 2895 | 2909.84776 (22) |
| $\Delta_J$ (kHz) | 0.700 | 0.7305 (32) | 0.734 | 0.794 (19) | 0.764 | 0.78682 (22) | 0.738 | 0.75817 (72) |
| $\Delta_{JK}$ (kHz) | 13.7 | 13.674 (48) | 13.9 | 13.38 (30) | 12.7 | 12.8131 (24) | 13.4 | 13.638 (15) |
| $\Delta_K$ (kHz) | −5.91 | [−5.91] | −5.27 | [−5.27] | −4.17 | −4.662 (12) | −4.84 | −5.10 (11) |
| $\delta_J$ (kHz) | 0.241 | 0.2537 (16) | 0.253 | 0.2800 (98) | 0.269 | 0.27751 (11) | 0.254 | 0.26118 (36) |
| $\delta_K$ (kHz) | 8.28 | 8.3785 (79) | 8.49 | 8.546 (41) | 8.06 | 8.1856 (21) | 8.31 | 8.4907 (90) |
| $\Phi_J$ (Hz) | 0.000456 | [0.000456] | 0.000485 | 0.000493 (10) | 0.000544 | 0.000565 (61) | 0.000503 | [0.000503] |
| $\Phi_{JK}$ (Hz) | 0.115 | 0.11558 (34) | 0.120 | 0.12203 (59) | 0.115 | 0.1166 (10) | 0.115 | 0.11205 (57) |
| $\Phi_{KJ}$ (Hz) | −0.224 | [−0.224] | −0.243 | [−0.243] | −0.24 | −0.3720 (74) | −0.236 | −0.1936 (97) |
| $\Phi_K$ (Hz) | 0.125 | [0.125] | 0.145 | [0.145] | 0.152 | [0.152] | 0.143 | [0.143] |
| $\phi_J$ (Hz) | 0.000224 | [0.000224] | 0.000237 | [0.000237] | 0.000265 | 0.000282 (30) | 0.000246 | [0.000246] |
| $\phi_{JK}$ (Hz) | 0.0591 | [0.0591] | 0.0620 | [0.0620] | 0.0593 | 0.05936 (64) | 0.0596 | [0.0596] |
| $\phi_K$ (Hz) | 0.243 | [0.243] | 0.265 | [0.265] | 0.241 | 0.1863 (49) | 0.258 | [0.258] |
| $N_{lines}$ | | 171 | | 161 | | 348 | | 242 |
| $\sigma_{fit}$ (MHz) | | 0.046 | | 0.047 | | 0.048 | | 0.051 |
| $\Delta_i$ (uÅ$^2$) | | −2.88693 (15) | | −2.89067 (97) | | −2.886846 (34) | | −2.891852 (57) |

**Table S-II continued.** Experimental and computational spectroscopic constants for non-standard methacrylonitrile isotopologues, ground vibrational state (A-reduced Hamiltonian, $I^r$ representation)

| | [$^{15}$N] | | [1-$^2$H$_{cis}$] | | [1-$^2$H$_{trans}$] | | [3-$^2$H$_{anti}$] | |
|---|---|---|---|---|---|---|---|---|
| | CCSD(T) | Present Work | CCSD(T) | Present Work | CCSD(T) | Present Work | CCSD(T) | Present Work |
| $A_0$ (MHz) | 9252 | 9289.46 (10) | 8500 | 8535.428 (11) | 8967 | 9004.6838 (83) | 9084 | 9121.4543 (71) |
| $B_0$ (MHz) | 4000 | 4023.271 (21) | 4134 | 4157.5686 (39) | 3985 | 4007.96416 (88) | 3968 | 3990.11748 (59) |
| $C_0$ (MHz) | 2838 | 2853.15251 (28) | 2826 | 2841.08838 (59) | 2803 | 2818.20879 (66) | 2806 | 2821.09365 (61) |
| $\Delta_J$ (kHz) | 0.687 | 0.867 (23) | 0.721 | 0.7362 (29) | 0.625 | 0.64225 (42) | 0.707 | 0.72896 (24) |
| $\Delta_{JK}$ (kHz) | 13.5 | 11.00 (37) | 13.5 | 13.324 (89) | 12.9 | 13.0220 (29) | 11.1 | 11.2505 (24) |
| $\Delta_K$ (kHz) | −4.89 | [−4.89] | −7.26 | −5.89 (47) | −4.54 | −4.643 (61) | −1.14 | −1.270 (51) |
| $\delta_J$ (kHz) | 0.233 | 0.320 (11) | 0.255 | 0.2596 (15) | 0.212 | 0.21750 (22) | 0.248 | 0.25636 (13) |
| $\delta_K$ (kHz) | 8.27 | 8.051 (52) | 8.14 | 8.080 (51) | 7.71 | 7.8176 (90) | 7.30 | 7.4274 (82) |
| $\Phi_J$ (Hz) | 0.000449 | [0.000449] | 0.000498 | [0.000498] | 0.000379 | [0.000379] | 0.000564 | [0.000564] |
| $\Phi_{JK}$ (Hz) | 0.114 | [0.114] | 0.115 | [0.115] | 0.100 | 0.0963 (19) | 0.0966 | 0.0972 (13) |
| $\Phi_{KJ}$ (Hz) | −0.229 | [−0.229] | −0.225 | [−0.225] | −0.196 | −0.1827 (38) | −0.209 | −0.2108 (17) |
| $\Phi_K$ (Hz) | 0.137 | [0.137] | 0.124 | [0.124] | 0.109 | [0.109] | 0.147 | [0.147] |
| $\phi_J$ (Hz) | 0.000219 | [0.000219] | 0.000245 | [0.000245] | 0.000187 | [0.000187] | 0.000276 | [0.000276] |
| $\phi_{JK}$ (Hz) | 0.0587 | [0.0587] | 0.0594 | [0.0594] | 0.0516 | 0.0408 (43) | 0.0504 | 0.0444 (40) |
| $\phi_K$ (Hz) | 0.271 | [0.271] | 0.209 | [0.209] | 0.230 | [0.230] | 0.228 | [0.228] |
| $N_{lines}$ | | 73 | | 115 | | 267 | | 397 |
| $\sigma_{fit}$ (MHz) | | 0.049 | | 0.042 | | 0.043 | | 0.044 |
| $\Delta_i$ (uÅ$^2$) | | −2.88741 (88) | | −2.88377 (14) | | −2.89139 (72) | | −2.920267 (61) |

**Table S-II continued.** Experimental and computational spectroscopic constants for non-standard methacrylonitrile isotopologues, ground vibrational state (A-reduced Hamiltonian, $I^r$ representation)

| | [3-$^2$H$_{gauche}$] | |
|---|---|---|
| | CCSD(T) | Present Work |
| $A_0$ (MHz) | 8627 | 8662.2956 (50) |
| $B_0$ (MHz) | 4086 | 4109.80874 (48) |
| $C_0$ (MHz) | 2840 | 2855.08247 (52) |
| $\Delta_J$ (kHz) | 0.800 | 0.82388 (21) |
| $\Delta_{JK}$ (kHz) | 12.4 | 12.6232 (20) |
| $\Delta_K$ (kHz) | −5.30 | −5.552 (32) |
| $\delta_J$ (kHz) | 0.285 | 0.29476 (12) |
| $\delta_K$ (kHz) | 7.69 | 7.8357 (60) |
| $\Phi_J$ (Hz) | 0.000490 | [0.000490] |
| $\Phi_{JK}$ (Hz) | 0.115 | 0.1110 (12) |
| $\Phi_{KJ}$ (Hz) | −0.235 | −0.2275 (15) |
| $\Phi_K$ (Hz) | 0.144 | [0.144] |
| $\phi_J$ (Hz) | 0.000236 | [0.000236] |
| $\phi_{JK}$ (Hz) | 0.0594 | 0.0614 (30) |
| $\phi_K$ (Hz) | 0.210 | [0.210] |
| $N_{lines}$ | | 408 |
| $\sigma_{fit}$ (MHz) | | 0.037 |
| $\Delta_i$ (uÅ$^2$) | | −4.301071 (49) |

**Table S-II continued.** Experimental and computational spectroscopic constants for non-standard methacrylonitrile isotopologues, ground vibrational state (A-reduced Hamiltonian, $I^r$ representation)

| | [1,1-$^2$H] | | [1-$^2$H$_{cis}$, 3-$^2$H$_{anti}$] | | [1-$^2$H$_{cis}$, 3-$^2$H$_{gauche}$] | | [1-$^2$H$_{trans}$, 3-$^2$H$_{anti}$] | |
|---|---|---|---|---|---|---|---|---|
| | CCSD(T) | Present Work | CCSD(T) | Present Work | CCSD(T) | Present Work | CCSD(T) | Present Work |
| $A_0$ (MHz) | 8282 | 8317.003 (10) | 8338 | 8372.5550 (62) | 7946 | 7979.3456 (42) | 8771 | 8807.6316 (68) |
| $B_0$ (MHz) | 3975 | 3997.7284 (40) | 3963 | 3985.17468 (57) | 4080 | 4103.43120 (52) | 3833 | 3854.66817 (66) |
| $C_0$ (MHz) | 2728 | 2742.22544 (54) | 2728 | 2742.7013 (10) | 2759 | 2773.78490 (54) | 2709 | 2723.42121 (60) |
| $\Delta_J$ (kHz) | 0.616 | 0.6147 (33) | 0.686 | 0.70974 (65) | 0.771 | 0.79541 (23) | 0.593 | 0.61207 (25) |
| $\Delta_{JK}$ (kHz) | 12.4 | 11.893 (70) | 11.1 | 11.1682 (23) | 12.2 | 12.3873 (20) | 10.8 | 10.9414 (28) |
| $\Delta_K$ (kHz) | −6.32 | −2.58 (44) | −3.62 | −3.717 (34) | −6.95 | −7.148 (24) | −1.66 | −1.963 (47) |
| $\delta_J$ (kHz) | 0.215 | 0.2116 (17) | 0.25 | 0.25453 (17) | 0.281 | 0.29102 (13) | 0.204 | 0.21063 (13) |
| $\delta_K$ (kHz) | 7.37 | 7.067 (44) | 7.03 | 7.1678 (66) | 7.40 | 7.5197 (49) | 6.75 | 6.8610 (76) |
| $\Phi_J$ (Hz) | 0.000398 | [0.000398] | 0.000531 | 0.00158 (26) | 0.000465 | [0.000465] | 0.000388 | [0.000388] |
| $\Phi_{JK}$ (Hz) | 0.0957 | [0.0957] | 0.0938 | 0.0919 (14) | 0.110 | 0.1094 (12) | 0.0833 | 0.0870 (14) |
| $\Phi_{KJ}$ (Hz) | −0.183 | [−0.183] | −0.196 | −0.1955 (19) | −0.219 | −0.2213 (17) | −0.173 | −0.1486 (58) |
| $\Phi_K$ (Hz) | 0.0952 | [0.0952] | 0.127 | [0.127] | 0.126 | [0.126] | 0.109 | [0.109] |
| $\phi_J$ (Hz) | 0.000197 | [0.000197] | 0.000262 | [0.000262] | 0.000226 | [0.000226] | 0.000191 | [0.000191] |
| $\phi_{JK}$ (Hz) | 0.0493 | [0.0493] | 0.0487 | 0.0553 (30) | 0.0566 | 0.0526 (22) | 0.0432 | 0.0341 (34) |
| $\phi_K$ (Hz) | 0.184 | [0.184] | 0.180 | [0.180] | 0.165 | [0.165] | 0.199 | [0.199] |
| $N_{lines}$ | | 107 | | 370 | | 399 | | 328 |
| $\sigma_{fit}$ (MHz) | | 0.042 | | 0.043 | | 0.040 | | 0.040 |
| $\Delta_i$ (uÅ$^2$) | | −2.88589 (15) | | −2.912921 (83) | | −4.297658 (51) | | −2.920277 (64) |

**Table S-II continued.** Experimental and computational spectroscopic constants for non-standard methacrylonitrile isotopologues, ground vibrational state (A-reduced Hamiltonian, $I^r$ representation)

| | [1-$^2$H$_{trans}$, 3-$^2$H$_{gauche}$] | | [3-$^2$H$_{anti}$, 3-$^2$H$_{gauche}$] | | [3-$^2$H$_{gauche}$, 3-$^2$H$_{gauche}$] | | [1,1-$^2$H, 3-$^2$H$_{anti}$] | |
|---|---|---|---|---|---|---|---|---|
| | CCSD(T) | Present Work | CCSD(T) | Present Work | CCSD(T) | Present Work | CCSD(T) | Present Work |
| $A_0$ (MHz) | 8347 | 8381.8612 (46) | 8504 | 8538.1328 (49) | 8100 | 8133.5658 (58) | 8095 | 8128.2452 (51) |
| $B_0$ (MHz) | 3940 | 3961.92121 (45) | 3914 | 3936.49164 (45) | 4025 | 4048.02050 (64) | 3827 | 3848.57372 (52) |
| $C_0$ (MHz) | 2739 | 2753.33029 (48) | 2744 | 2758.09552 (55) | 2778 | 2792.25657 (60) | 2638 | 2651.83802 (33) |
| $\Delta_J$ (kHz) | 0.658 | 0.67809 (17) | 0.761 | 0.78520 (18) | 0.826 | 0.84853 (26) | 0.580 | 0.59819 (20) |
| $\Delta_{JK}$ (kHz) | 12.0 | 12.2014 (17) | 9.92 | 10.0509 (18) | 11.1 | 11.2360 (25) | 10.6 | 10.6939 (12) |
| $\Delta_K$ (kHz) | −5.32 | −5.534 (28) | −1.55 | −1.771 (33) | −5.04 | −5.290 (33) | −3.81 | −3.997 (30) |
| $\delta_J$ (kHz) | 0.229 | 0.23670 (10) | 0.276 | 0.28515 (10) | 0.299 | 0.30820 (14) | 0.205 | 0.21137 (10) |
| $\delta_K$ (kHz) | 7.11 | 7.2407 (52) | 6.60 | 6.7125 (59) | 6.64 | 6.7276 (67) | 6.49 | 6.6091 (22) |
| $\Phi_J$ (Hz) | 0.000353 | [0.000353] | 0.000600 | [0.000600] | 0.000529 | [0.000529] | 0.000384 | 0.000426 (21) |
| $\Phi_{JK}$ (Hz) | 0.096 | 0.09243 (99) | 0.0916 | 0.0897 (10) | 0.103 | 0.1023 (15) | 0.0803 | 0.0809 (13) |
| $\Phi_{KJ}$ (Hz) | −0.183 | −0.1813 (14) | −0.201 | −0.1983 (14) | −0.210 | −0.2091 (28) | −0.162 | −0.1643 (36) |
| $\Phi_K$ (Hz) | 0.0996 | [0.0996] | 0.143 | 0.143264 | 0.129 | [0.129] | 0.0941 | [0.0941] |
| $\phi_J$ (Hz) | 0.000171 | [0.000171] | 0.000291 | 0.0002913 | 0.000253 | [0.000253] | 0.000190 | [0.000190] |
| $\phi_{JK}$ (Hz) | 0.0495 | 0.0510 (23) | 0.0482 | 0.0452 (26) | 0.0545 | 0.0516 (32) | 0.0415 | 0.04246 (57) |
| $\phi_K$ (Hz) | 0.186 | [0.186] | 0.183 | 0.182526 | 0.152 | [0.152] | 0.159 | 0.1670 (57) |
| $N_{lines}$ | | 430 | | 424 | | 335 | | 458 |
| $\sigma_{fit}$ (MHz) | | 0.037 | | 0.036 | | 0.042 | | 0.046 |
| $\Delta_i$ (uÅ$^2$) | | −4.301541 (48) | | −4.33914 (52) | | −5.987907 (62) | | −2.914705 (49) |

**Table S-II continued.** Experimental and computational spectroscopic constants for non-standard methacrylonitrile isotopologues, ground vibrational state (A-reduced Hamiltonian, $I^r$ representation)

| | [1,1-$^2$H, 3-$^2$H$_{gauche}$] | | [1-$^2$H$_{cis}$, 3-$^2$H$_{anti}$, 3-$^2$H$_{gauche}$] | | [1-$^2$H$_{cis}$, 3-$^2$H$_{gauche}$, 3-$^2$H$_{gauche}$] | | [1-$^2$H$_{trans}$, 3-$^2$H$_{anti}$, 3-$^2$H$_{gauche}$] | |
|---|---|---|---|---|---|---|---|---|
| | CCSD(T) | Present Work | CCSD(T) | Present Work | CCSD(T) | Present Work | CCSD(T) | Present Work |
| $A_0$ (MHz) | 7729 | 7761.8471 (23) | 7827 | 7859.1776 (27) | 7479 | 7509.9623 (47) | 8199 | 8233.2754 (36) |
| $B_0$ (MHz) | 3932 | 3953.97836 (32) | 3911 | 3933.18242 (31) | 4021 | 4043.87547 (62) | 3789 | 3810.33797 (37) |
| $C_0$ (MHz) | 2665 | 2679.26496 (25) | 2668 | 2681.62402 (27) | 2699 | 2712.88299 (34) | 2651 | 2664.41880 (27) |
| $\Delta_J$ (kHz) | 0.641 | 0.66189 (13) | 0.737 | 0.76080 (13) | 0.794 | 0.81649 (26) | 0.629 | 0.64866 (13) |
| $\Delta_{JK}$ (kHz) | 11.6 | 11.79469 (57) | 9.84 | 9.94597 (60) | 10.9 | 11.0224 (14) | 9.98 | 10.10814 (86) |
| $\Delta_K$ (kHz) | −6.69 | −6.8989 (67) | −3.50 | −3.6498 (77) | −6.37 | −6.538 (23) | −2.51 | −2.763 (16) |
| $\delta_J$ (kHz) | 0.229 | 0.236988 (78) | 0.274 | 0.283066 (76) | 0.294 | 0.30369 (13) | 0.223 | 0.230147 (72) |
| $\delta_K$ (kHz) | 6.81 | 6.9331 (11) | 6.35 | 6.4612 (13) | 6.43 | 6.5210 (19) | 6.20 | 6.3146 (15) |
| $\Phi_J$ (Hz) | 0.000369 | 0.000494 (38) | 0.000548 | 0.000514 (37) | 0.000473 | 0.000461 (21) | 0.000394 | 0.000368 (15) |
| $\Phi_{JK}$ (Hz) | 0.0910 | 0.09127 (41) | 0.0889 | 0.08882 (42) | 0.0992 | 0.0971 (14) | 0.0795 | 0.07900 (88) |
| $\Phi_{KJ}$ (Hz) | −0.172 | −0.1755 (15) | −0.192 | −0.1925 (16) | −0.201 | −0.2006 (38) | −0.164 | −0.1675 (24) |
| $\Phi_K$ (Hz) | 0.0879 | [0.0879] | 0.128 | [0.128] | 0.118 | [0.118] | 0.102 | [0.102] |
| $\phi_J$ (Hz) | 0.000181 | 0.000227 (20) | 0.000268 | 0.000250 (19) | 0.000229 | [0.000229] | 0.000191 | [0.000191] |
| $\phi_{JK}$ (Hz) | 0.0470 | 0.04748 (31) | 0.0463 | 0.04623 (34) | 0.0521 | 0.05099 (64) | 0.0414 | 0.04097 (40) |
| $\phi_K$ (Hz) | 0.148 | 0.1547 (23) | 0.142 | 0.1444 (25) | 0.118 | 0.1166 (43) | 0.161 | 0.1670 (39) |
| $N_{lines}$ | | 787 | | 844 | | 425 | | 620 |
| $\sigma_{fit}$ (MHz) | | 0.041 | | 0.042 | | 0.047 | | 0.042 |
| $\Delta_i$ (uÅ$^2$) | | −4.299991 (28) | | −4.335376 (31) | | −5.979871 (52) | | −4.339125 (35) |

**Table S-II continued.** Experimental and computational spectroscopic constants for non-standard methacrylonitrile isotopologues, ground vibrational state (A-reduced Hamiltonian, $I^r$ representation)

| | [1-$^2$H$_{trans}$, 3-$^2$H$_{gauche}$, 3-$^2$H$_{gauche}$] | | [3,3,3-$^2$H] | | [1,1-$^2$H, 3-$^2$H$_{anti}$, 3-$^2$H$_{gauche}$] | | [1,1-$^2$H, 3-$^2$H$_{gauche}$, 3-$^2$H$_{gauche}$] | |
|---|---|---|---|---|---|---|---|---|
| | CCSD(T) | Present Work | CCSD(T) | Present Work | CCSD(T) | Present Work | CCSD(T) | Present Work |
| $A_0$ (MHz) | 7825 | 7857.5701 (49) | 8011 | 8043.2251 (57) | 7587 | 7618.2151 (27) | 7262 | 7292.4000 (20) |
| $B_0$ (MHz) | 3889 | 3910.99132 (56) | 3857 | 3878.61251 (55) | 3784 | 3805.86045 (24) | 3883 | 3905.23085 (31) |
| $C_0$ (MHz) | 2681 | 2694.63682 (33) | 2687 | 2700.97991 (34) | 2581 | 2594.46930 (21) | 2609 | 2622.19322 (23) |
| $\Delta_J$ (kHz) | 0.669 | 0.68654 (24) | 0.785 | 0.80753 (21) | 0.612 | 0.630830 (81) | 0.647 | 0.66476 (11) |
| $\Delta_{JK}$ (kHz) | 11.0 | 11.2142 (12) | 8.74 | 8.8726 (12) | 9.76 | 9.87864 (40) | 10.7 | 10.86299 (49) |
| $\Delta_K$ (kHz) | −5.58 | −5.843 (28) | −1.66 | −1.876 (34) | −4.17 | −4.301 (11) | −6.66 | −6.8447 (41) |
| $\delta_J$ (kHz) | 0.236 | 0.24217 (12) | 0.289 | 0.29730 (11) | 0.222 | 0.229410 (47) | 0.234 | 0.240657 (66) |
| $\delta_K$ (kHz) | 6.25 | 6.3371 (20) | 5.67 | 5.7471 (22) | 5.96 | 6.07146 (90) | 6.03 | 6.12134 (89) |
| $\Phi_J$ (Hz) | 0.000357 | 0.000389 (22) | 0.000656 | 0.000645 (22) | 0.000381 | 0.000348 (22) | 0.000358 | 0.000232 (29) |
| $\Phi_{JK}$ (Hz) | 0.0864 | 0.0854 (13) | 0.0814 | 0.0812 (14) | 0.0764 | 0.07467 (27) | 0.0826 | 0.08157 (24) |
| $\Phi_{KJ}$ (Hz) | −0.162 | −0.1622 (36) | −0.178 | −0.1766 (43) | −0.155 | −0.1493 (11) | −0.154 | −0.15003 (95) |
| $\Phi_K$ (Hz) | 0.0850 | [0.0850] | 0.126 | [0.126] | 0.0902 | 0.139 (17) | 0.0772 | [0.0772] |
| $\phi_J$ (Hz) | 0.000171 | [0.000171] | 0.000317 | [0.000317] | 0.000187 | 0.000168 (11) | 0.000174 | 0.000108 (15) |
| $\phi_{JK}$ (Hz) | 0.0457 | 0.04610 (58) | 0.0441 | 0.04353 (62) | 0.0396 | 0.03890 (22) | 0.0434 | 0.04272 (21) |
| $\phi_K$ (Hz) | 0.137 | 0.1516 (52) | 0.132 | 0.1354 (68) | 0.128 | 0.1270 (14) | 0.109 | 0.1064 (12) |
| $N_{lines}$ | | 460 | | 447 | | 1320 | | 1032 |
| $\sigma_{fit}$ (MHz) | | 0.045 | | 0.045 | | 0.038 | | 0.043 |
| $\Delta_i$ (uÅ$^2$) | | −5.987696 (50) | | −6.022295 (54) | | −4.337029 (30) | | −5.981527 (27) |

**Table S-II continued.** Experimental and computational spectroscopic constants for non-standard methacrylonitrile isotopologues, ground vibrational state (A-reduced Hamiltonian, $I^r$ representation)

| | [1-$^2H_{cis}$, 3,3,3-$^2H$] | | [1-$^2H_{trans}$, 3,3,3-$^2H$] | | [1,1,3,3,3-$^2H$] | | [1,1,3,3,3-$^2H$, 1-$^{13}C$] | |
|---|---|---|---|---|---|---|---|---|
| | CCSD(T) | Present Work | CCSD(T) | Present Work | CCSD(T) | Present Work | CCSD(T) | Present Work |
| $A_0$ (MHz) | 7392 | 7421.9316 (30) | 7714 | 7745.4763 (25) | 7154 | 7183.19513 (65) | 6980 | 7009.271 (14) |
| $B_0$ (MHz) | 3855 | 3876.71022 (31) | 3741 | 3761.86174 (29) | 3738 | 3758.87771 (10) | 3712 | 3733.1798 (25) |
| $C_0$ (MHz) | 2612 | 2626.14133 (25) | 2597 | 2610.83600 (24) | 2529 | 2542.271244 (76) | 2496 | 2508.52903 (35) |
| $\Delta_J$ (kHz) | 0.761 | 0.78374 (11) | 0.642 | 0.660289 (98) | 0.622 | 0.640849 (49) | 0.588 | 0.71978 (95) |
| $\Delta_{JK}$ (kHz) | 8.63 | 8.74011 (52) | 9.08 | 9.21772 (45) | 8.87 | 8.99239 (19) | 8.94 | 7.731 (19) |
| $\Delta_K$ (kHz) | −3.19 | −3.285 (12) | −2.92 | −3.1406 (62) | −4.21 | −4.3594 (33) | −4.67 | [−4.67] |
| $\delta_J$ (kHz) | 0.287 | 0.296177 (64) | 0.230 | 0.236999 (58) | 0.229 | 0.236117 (25) | 0.216 | 0.27967 (47) |
| $\delta_K$ (kHz) | 5.49 | 5.5712 (10) | 5.43 | 5.5088 (10) | 5.26 | 5.33611 (28) | 5.20 | 5.0852 (76) |
| $\Phi_J$ (Hz) | 0.000584 | 0.000534 (31) | 0.000413 | 0.000401 (23) | 0.000387 | 0.000400 (12) | 0.000349 | [0.000349] |
| $\Phi_{JK}$ (Hz) | 0.0797 | 0.07805 (34) | 0.0715 | 0.07100 (30) | 0.0691 | 0.06810 (11) | 0.0668 | 0.07003 (73) |
| $\Phi_{KJ}$ (Hz) | −0.174 | −0.1675 (14) | −0.144 | −0.1423 (11) | −0.138 | −0.13494 (46) | −0.130 | −0.1712 (92) |
| $\Phi_K$ (Hz) | 0.118 | 0.155 (18) | 0.0868 | [0.0868] | 0.0799 | 0.1054 (54) | 0.0708 | [0.0708] |
| $\phi_J$ (Hz) | 0.000285 | 0.000257 (15) | 0.000199 | 0.000190 (11) | 0.000189 | 0.0001902 (62) | 0.000171 | [0.000171] |
| $\phi_{JK}$ (Hz) | 0.0424 | 0.04177 (27) | 0.0382 | 0.03759 (24) | 0.0365 | 0.035997 (99) | 0.0352 | [0.0352] |
| $\phi_K$ (Hz) | 0.103 | 0.1012 (15) | 0.118 | 0.1185 (19) | 0.0941 | 0.09507 (64) | 0.0886 | [0.0886] |
| $N_{lines}$ | | 1047 | | 1097 | | 1725 | | 123 |
| $\sigma_{fit}$ (MHz) | | 0.043 | | 0.043 | | 0.037 | | 0.046 |
| $\Delta_i$ (uÅ$^2$) | | −6.013842 (35) | | −6.021270 (29) | | −6.014824 (9) | | −6.01217 (17) |

**Table S-II continued.** Experimental and computational spectroscopic constants for non-standard methacrylonitrile isotopologues, ground vibrational state (A-reduced Hamiltonian, $I^r$ representation)

| | [1,1,3,3,3-$^2$H, 2-$^{13}$C] | | [1,1,3,3,3-$^2$H, 3-$^{13}$C] | | [1,1,3,3,3-$^2$H, 4-$^{13}$C] | | [1,1,3,3,3-$^2$H, $^{15}$N] | |
|---|---|---|---|---|---|---|---|---|
| | CCSD(T) | Present Work | CCSD(T) | Present Work | CCSD(T) | Present Work | CCSD(T) | Present Work |
| $A_0$ (MHz) | 7153 | 7182.482 (79) | 7021 | 7050.341 (13) | 7154 | 7182.98 (74) | 7152 | [7181.76] |
| $B_0$ (MHz) | 3734 | 3754.717 (23) | 3700 | 3720.9253 (65) | 3708 | 3729.21 (20) | 3611 | 3631.3134 (60) |
| $C_0$ (MHz) | 2527 | 2540.25827 (41) | 2495 | 2508.18775 (34) | 2516 | 2528.68030 (84) | 2470 | 2483.03392 (49) |
| $\Delta_J$ (kHz) | 0.617 | 0.623 (13) | 0.642 | 0.6997 (16) | 0.617 | 0.603 (12) | 0.576 | 0.5530 (32) |
| $\Delta_{JK}$ (kHz) | 8.92 | 8.78 (15) | 8.17 | 7.848 (16) | 8.63 | 8.60 (11) | 8.77 | 8.803 (31) |
| $\Delta_K$ (kHz) | −4.25 | [−4.25] | −3.50 | [−3.50] | −3.97 | [−3.97] | −4.09 | [−4.09] |
| $\delta_J$ (kHz) | 0.227 | 0.2366 (70) | 0.240 | 0.26673 (82) | 0.226 | 0.2293 (60) | 0.209 | 0.2047 (16) |
| $\delta_K$ (kHz) | 5.27 | 5.257 (21) | 5.02 | 5.0332 (34) | 5.15 | [5.14] | 5.17 | [5.17] |
| $\Phi_J$ (Hz) | 0.000374 | [0.000374] | 0.000413 | [0.000413] | 0.000390 | [0.000390] | 0.000351 | [0.000351] |
| $\Phi_{JK}$ (Hz) | 0.0693 | [0.0693] | 0.0668 | 0.06840 (60) | 0.0660 | [0.0660] | 0.0659 | [0.0659] |
| $\Phi_{KJ}$ (Hz) | −0.139 | [−0.139] | −0.139 | [−0.139] | −0.133 | [−0.133] | −0.131 | [−0.131] |
| $\Phi_K$ (Hz) | 0.0803 | [0.0803] | 0.0846 | [0.0846] | 0.0776 | [0.0776] | 0.0750 | [0.0750] |
| $\phi_J$ (Hz) | 0.000183 | [0.000183] | 0.000202 | [0.000202] | 0.000191 | [0.000191] | 0.000171 | [0.000171] |
| $\phi_{JK}$ (Hz) | 0.0366 | [0.0366] | 0.0353 | [0.0353] | 0.0350 | [0.0350] | 0.0348 | [0.0348] |
| $\phi_K$ (Hz) | 0.0945 | [0.0945] | 0.0870 | [0.0870] | 0.0925 | [0.0925] | 0.0992 | [0.0992] |
| $N_{lines}$ | | 38 | | 100 | | 24 | | 39 |
| $\sigma_{fit}$ (MHz) | | 0.047 | | 0.047 | | 0.048 | | 0.056 |
| $\Delta_i$ (uÅ$^2$) | | −6.0133 (11) | | −6.01059 (27) | | −6.018 (10) | | −6.0094 (98) |

**Table S-III.** Experimental and computational spectroscopic constants for methacrylonitrile isotopologues, ground vibrational state (S-reduced Hamiltonian, $I^r$ representation)

| | [1-$^{13}$C] | | [2-$^{13}$C] | | [3-$^{13}$C] | | [4-$^{13}$C] | |
|---|---|---|---|---|---|---|---|---|
| | CCSD(T) | Present Work | CCSD(T) | Present Work | CCSD(T) | Present Work | CCSD(T) | Present Work |
| $A_0$ (MHz) | 8983 | 9020.083 (15) | 9252 | 9290.38 (15) | 9016 | 9053.0262 (44) | 9253 | 9291.1635 (78) |
| $B_0$ (MHz) | 4102 | 4125.8424 (39) | 4135 | 4158.383 (33) | 4091 | 4114.65224 (45) | 4113 | 4136.4250 (13) |
| $C_0$ (MHz) | 2862 | 2877.50747 (20) | 2905 | 2920.61811 (34) | 2860 | 2875.38850 (23) | 2895 | 2909.86401 (29) |
| $D_J$ (kHz) | 0.241 | 0.2542 (36) | 0.286 | 0.317 (28) | 0.323 | 0.330013 (68) | 0.304 | 0.30659 (61) |
| $D_{JK}$ (kHz) | 16.5 | 16.536 (51) | 16.5 | 16.36 (41) | 15.3 | 15.5557 (27) | 16.0 | 16.344 (18) |
| $D_K$ (kHz) | −8.21 | [−8.21] | −7.51 | [−7.51] | −6.37 | −6.932 (12) | −7.01 | −7.29 (11) |
| $d_1$ (kHz) | −0.241 | −0.2524 (16) | −0.253 | −0.271 (12) | −0.269 | −0.277250 (59) | −0.254 | −0.26097 (36) |
| $d_2$ (kHz) | −0.230 | −0.23690 (23) | −0.224 | −0.2304 (16) | −0.220 | −0.228144 (59) | −0.217 | −0.22568 (23) |
| $H_J$ (Hz) | −0.00214 | [−0.00214] | −0.00217 | −0.002163 (11) | −0.00217 | −0.002310 (29) | −0.00204 | −0.002279 (61) |
| $H_{JK}$ (Hz) | 0.0684 | 0.06609 (34) | 0.0731 | 0.07096 (88) | 0.0722 | 0.0824 (12) | 0.0701 | 0.0752 (20) |
| $H_{KJ}$ (Hz) | −0.0305 | [−0.0305] | −0.0462 | [−0.0462] | −0.0567 | −0.2017 (92) | −0.0475 | [−0.0475] |
| $H_K$ (Hz) | −0.0192 | [−0.0192] | −0.00177 | [−0.00177] | 0.0141 | [0.0141] | 0.00207 | [0.00207] |
| $h_1$ (Hz) | −0.000206 | [−0.000206] | −0.000179 | [−0.000179] | −0.000138 | [−0.000138] | −0.000148 | [−0.000148] |
| $h_2$ (Hz) | 0.00130 | [0.00130] | 0.00133 | [0.00133] | 0.00136 | 0.001357 (16) | 0.00127 | 0.001395 (30) |
| $h_3$ (Hz) | 0.000430 | [0.000430] | 0.000417 | [0.000417] | 0.000403 | 0.0003455 (62) | 0.000394 | [0.000394] |
| $N_{lines}$ | | 171 | | 161 | | 348 | | 242 |
| $\sigma_{fit}$ (MHz) | | 0.046 | | 0.047 | | 0.050 | | 0.051 |
| $\Delta_i$ (uÅ$^2$) | | −2.88848 (15) | | −2.8923 (13) | | −2.888299 (33) | | −2.893361 (62) |

**Table S-III continued.** Experimental and computational spectroscopic constants for methacrylonitrile isotopologues, ground vibrational state (S-reduced Hamiltonian, $I^r$ representation)

| | [$^{15}$N] | | [1-$^2$H$_{cis}$] | | [1-$^2$H$_{trans}$] | | [3-$^2$H$_{anti}$] | |
|---|---|---|---|---|---|---|---|---|
| | CCSD(T) | Present Work | CCSD(T) | Present Work | CCSD(T) | Present Work | CCSD(T) | Present Work |
| $A_0$ (MHz) | 9252 | 9289.40 (12) | 8500 | 8535.431 (11) | 8967 | 9004.7012 (97) | 9084 | 9121.4623 (78) |
| $B_0$ (MHz) | 4000 | 4023.260 (24) | 4134 | 4157.5517 (38) | 3985 | 4007.94913 (91) | 3968 | 3990.10201 (59) |
| $C_0$ (MHz) | 2838 | 2853.16809 (37) | 2826 | 2841.10356 (56) | 2803 | 2818.22159 (54) | 2806 | 2821.10674 (47) |
| $D_J$ (kHz) | 0.282 | 0.475 (29) | 0.198 | 0.2086 (26) | 0.222 | 0.22603 (37) | 0.341 | 0.34864 (21) |
| $D_{JK}$ (kHz) | 15.9 | 13.20 (45) | 16.7 | 16.48 (10) | 15.3 | 15.5158 (20) | 13.3 | 13.5289 (13) |
| $D_K$ (kHz) | −6.92 | [−6.92] | −9.88 | −8.53 (47) | −6.56 | −6.695 (61) | −2.98 | −3.143 (49) |
| $d_1$ (kHz) | −0.233 | −0.324 (13) | −0.255 | −0.2596 (15) | −0.212 | −0.21811 (21) | −0.248 | −0.25647 (12) |
| $d_2$ (kHz) | −0.203 | −0.2000 (16) | −0.261 | −0.2639 (16) | −0.202 | −0.20773 (23) | −0.183 | −0.18977 (21) |
| $H_J$ (Hz) | −0.00189 | [−0.00189] | −0.00244 | [−0.00244] | −0.00176 | [−0.00176] | −0.00163 | [−0.00163] |
| $H_{JK}$ (Hz) | 0.0685 | 0.0553 (17) | 0.0687 | [0.0687] | 0.0590 | 0.0567 (12) | 0.0612 | 0.05992 (81) |
| $H_{KJ}$ (Hz) | −0.0431 | [−0.0431] | −0.0254 | [−0.0254] | −0.0269 | [−0.0269] | −0.0577 | −0.0568 (15) |
| $H_K$ (Hz) | −0.000959 | [−0.000959] | −0.0259 | [−0.0259] | −0.0169 | [−0.0169] | 0.0333 | [0.0333] |
| $h_1$ (Hz) | −0.000145 | [−0.000145] | −0.000271 | [−0.000271] | −0.000166 | [−0.000166] | −0.0000288 | [−0.0000288] |
| $h_2$ (Hz) | 0.00117 | [0.00117] | 0.00147 | [0.00147] | 0.00107 | 0.00074 (11) | 0.00110 | 0.00092 (10) |
| $h_3$ (Hz) | 0.000364 | [0.000364] | 0.000516 | [0.000516] | 0.000353 | [0.000353] | 0.000305 | [0.000305] |
| $N_{lines}$ | | 73 | | 115 | | 267 | | 397 |
| $\sigma_{fit}$ (MHz) | | 0.048 | | 0.042 | | 0.044 | | 0.044 |
| $\Delta_i$ (uÅ$^2$) | | −2.8891 (10) | | −2.88519 (14) | | −2.892569 (75) | | −2.921541 (59) |

**Table S-III continued.** Experimental and computational spectroscopic constants for methacrylonitrile isotopologues, ground vibrational state (S-reduced Hamiltonian, $I^r$ representation)

| | [3-$^2H_{gauche}$] | |
|---|---|---|
| | CCSD(T) | Present Work |
| $A_0$ (MHz) | 8627 | 8662.2963 (75) |
| $B_0$ (MHz) | 4086 | 4109.79230 (54) |
| $C_0$ (MHz) | 2840 | 2855.09844 (85) |
| $D_J$ (kHz) | 0.343 | 0.35046 (65) |
| $D_{JK}$ (kHz) | 15.2 | 15.4695 (14) |
| $D_K$ (kHz) | −7.58 | −7.903 (51) |
| $d_1$ (kHz) | −0.285 | −0.29454 (15) |
| $d_2$ (kHz) | −0.228 | −0.23727 (21) |
| $H_J$ (Hz) | −0.00246 | −0.00214 (28) |
| $H_{JK}$ (Hz) | 0.0751 | 0.07135 (85) |
| $H_{KJ}$ (Hz) | −0.0584 | −0.0489 (13) |
| $H_K$ (Hz) | 0.0101 | 0.0100628 |
| $h_1$ (Hz) | −0.000190 | −0.0001896 |
| $h_2$ (Hz) | 0.00148 | 0.00155 (14) |
| $h_3$ (Hz) | 0.000426 | 0.000400 (63) |
| $N_{lines}$ | | 408 |
| $\sigma_{fit}$ (MHz) | | 0.036 |
| $\Delta_i$ (uÅ$^2$) | | −4.302548 (75) |

**Table S-III continued.** Experimental and computational spectroscopic constants for methacrylonitrile isotopologues, ground vibrational state (S-reduced Hamiltonian, $I^r$ representation)

| | [1,1-$^2$H] | | [1-$^2$H$_{cis}$, 3-$^2$H$_{anti}$] | | [1-$^2$H$_{cis}$, 3-$^2$H$_{gauche}$] | | [1-$^2$H$_{trans}$, 3-$^2$H$_{anti}$] | |
|---|---|---|---|---|---|---|---|---|
| | CCSD(T) | Present Work | CCSD(T) | Present Work | CCSD(T) | Present Work | CCSD(T) | Present Work |
| $A_0$ (MHz) | 8282 | 8317.002 (10) | 8338 | 8372.5638 (59) | 7946 | 7979.3479 (49) | 8771 | 8807.6456 (77) |
| $B_0$ (MHz) | 3975 | 3997.7138 (39) | 3963 | 3985.15953 (57) | 4080 | 4103.41515 (53) | 3833 | 3854.65343 (68) |
| $C_0$ (MHz) | 2728 | 2742.23883 (51) | 2728 | 2742.71271 (44) | 2759 | 2773.79952 (91) | 2709 | 2723.43244 (46) |
| $D_J$ (kHz) | 0.156 | 0.1667 (21) | 0.257 | 0.26383 (21) | 0.239 | 0.24553 (66) | 0.253 | 0.25950 (22) |
| $D_{JK}$ (kHz) | 15.2 | 14.589 (84) | 13.6 | 13.8358 (14) | 15.4 | 15.6895 (14) | 12.9 | 13.0435 (19) |
| $D_K$ (kHz) | −8.62 | −4.89 (44) | −5.76 | −5.901 (31) | −9.61 | −9.890 (24) | −3.36 | −3.647 (46) |
| $d_1$ (kHz) | −0.215 | −0.2117 (17) | −0.247 | −0.25478 (12) | −0.281 | −0.29088 (17) | −0.204 | −0.21076 (13) |
| $d_2$ (kHz) | −0.230 | −0.2242 (13) | −0.214 | −0.22236 (18) | −0.266 | −0.27522 (18) | −0.170 | −0.17564 (19) |
| $H_J$ (Hz) | −0.00194 | [−0.00194] | −0.00192 | [−0.00192] | −0.00276 | −0.00227 (26) | −0.00143 | [−0.00143] |
| $H_{JK}$ (Hz) | 0.0554 | [0.0554] | 0.0591 | 0.05985 (97) | 0.0708 | 0.06805 (98) | 0.0512 | 0.0538 (11) |
| $H_{KJ}$ (Hz) | −0.0137 | [−0.0137] | −0.0437 | −0.0436 (17) | −0.0408 | −0.0384 (17) | −0.0390 | [−0.0390] |
| $H_K$ (Hz) | −0.0316 | [−0.0316] | 0.0121 | [0.0121] | −0.0103 | [−0.0103] | 0.00838 | [0.00838] |
| $h_1$ (Hz) | −0.000227 | [−0.000227] | −0.000114 | [−0.000114] | −0.000298 | [−0.000298] | −0.00008 | [−0.00008] |
| $h_2$ (Hz) | 0.00117 | [0.00117] | 0.00123 | 0.001516 (86) | 0.00161 | 0.001495 (88) | 0.000908 | 0.000678 (89) |
| $h_3$ (Hz) | 0.000424 | [0.000424] | 0.000376 | [0.000376] | 0.000524 | [0.000524] | 0.000271 | [0.000271] |
| $N_{lines}$ | | 107 | | 370 | | 399 | | 328 |
| $\sigma_{fit}$ (MHz) | | 0.042 | | 0.043 | | 0.040 | | 0.042 |
| $\Delta_i$ (uÅ$^2$) | | −2.88726 (15) | | −2.914106 (55) | | −4.299082 (73) | | −2.921452 (64) |

**Table S-III continued.** Experimental and computational spectroscopic constants for methacrylonitrile isotopologues, ground vibrational state (S-reduced Hamiltonian, $I^r$ representation)

| | [1-$^2$H$_{trans}$, 3-$^2$H$_{gauche}$] | | [3-$^2$H$_{anti}$, 3-$^2$H$_{gauche}$] | | [3-$^2$H$_{gauche}$, 3-$^2$H$_{gauche}$] | | [1,1-$^2$H, 3-$^2$H$_{anti}$] | |
|---|---|---|---|---|---|---|---|---|
| | CCSD(T) | Present Work | CCSD(T) | Present Work | CCSD(T) | Present Work | CCSD(T) | Present Work |
| $A_0$ (MHz) | 8347 | 8381.8630 (53) | 8504 | 8538.1359 (58) | 8100 | 8133.5728 (68) | 8095 | 8128.2478 (49) |
| $B_0$ (MHz) | 3940 | 3961.90597 (46) | 3914 | 3936.47757 (45) | 4025 | 4048.00634 (64) | 3827 | 3848.55980 (51) |
| $C_0$ (MHz) | 2739 | 2753.34444 (79) | 2744 | 2758.10829 (86) | 2778 | 2792.2682 (10) | 2638 | 2651.85034 (33) |
| $D_J$ (kHz) | 0.238 | 0.24314 (55) | 0.394 | 0.40445 (60) | 0.392 | 0.40000 (80) | 0.188 | 0.19293 (16) |
| $D_{JK}$ (kHz) | 14.6 | 14.8135 (11) | 12.1 | 12.3362 (11) | 13.7 | 13.9245 (17) | 12.9 | 13.1256 (14) |
| $D_K$ (kHz) | −7.42 | −7.700 (27) | −3.39 | −3.664 (33) | −7.21 | −7.513 (33) | −5.76 | −6.018 (29) |
| $d_1$ (kHz) | −0.229 | −0.23659 (13) | −0.276 | −0.28511 (14) | −0.299 | −0.30830 (19) | −0.205 | −0.21139 (10) |
| $d_2$ (kHz) | −0.210 | −0.21770 (16) | −0.184 | −0.19043 (17) | −0.217 | −0.22394 (23) | −0.196 | −0.202665 (67) |
| $H_J$ (Hz) | −0.00198 | −0.00192 (21) | −0.00180 | −0.00161 (23) | −0.00253 | −0.00261 (33) | −0.00162 | −0.001663 (34) |
| $H_{JK}$ (Hz) | 0.0589 | 0.05580 (70) | 0.0624 | 0.05923 (65) | 0.0746 | 0.0730 (11) | 0.0489 | 0.04809 (87) |
| $H_{KJ}$ (Hz) | −0.0261 | −0.0220 (12) | −0.0680 | −0.0621 (12) | −0.0706 | −0.0669 (27) | −0.0273 | −0.0228 (15) |
| $H_K$ (Hz) | −0.0186 | [−0.0186] | 0.0414 | [0.0414] | 0.0206 | 0.020643 | −0.00731 | [−0.00731] |
| $h_1$ (Hz) | −0.000203 | [−0.000203] | −0.0000127 | [−0.0000127] | −0.000127 | −0.0001266 | −0.000137 | [−0.000137] |
| $h_2$ (Hz) | 0.00117 | 0.001230 (75) | 0.00120 | 0.001126 (81) | 0.00153 | 0.00142 (11) | 0.00100 | 0.001064 (21) |
| $h_3$ (Hz) | 0.000375 | [0.000375] | 0.000304 | [0.000304] | 0.000380 | 0.0003796 | 0.000328 | 0.0003501 (91) |
| $N_{lines}$ | | 430 | | 424 | | 335 | | 458 |
| $\sigma_{fit}$ (MHz) | | 0.037 | | 0.036 | | 0.042 | | 0.046 |
| $\Delta_i$ (uÅ$^2$) | | −4.302962 (67) | | −4.340426 (71) | | −5.989044 (85) | | −2.916046 (48) |

**Table S-III continued.** Experimental and computational spectroscopic constants for methacrylonitrile isotopologues, ground vibrational state (S-reduced Hamiltonian, $I^r$ representation)

| | [1,1-$^2$H, 3-$^2$H$_{gauche}$] | | [1-$^2$H$_{cis}$, 3-$^2$H$_{anti}$, 3-$^2$H$_{gauche}$] | | [1-$^2$H$_{cis}$, 3-$^2$H$_{gauche}$, 3-$^2$H$_{gauche}$] | | [1-$^2$H$_{trans}$, 3-$^2$H$_{anti}$, 3-$^2$H$_{gauche}$] | |
|---|---|---|---|---|---|---|---|---|
| | CCSD(T) | Present Work | CCSD(T) | Present Work | CCSD(T) | Present Work | CCSD(T) | Present Work |
| $A_0$ (MHz) | 7729 | 7761.8518 (23) | 7827 | 7859.1820 (26) | 7479 | 7509.9655 (46) | 8199 | 8233.2777 (34) |
| $B_0$ (MHz) | 3932 | 3953.96421 (33) | 3911 | 3933.16927 (31) | 4021 | 4043.86144 (61) | 3789 | 3810.32470 (36) |
| $C_0$ (MHz) | 2665 | 2679.27762 (25) | 2668 | 2681.63589 (26) | 2699 | 2712.89483 (33) | 2651 | 2664.43064 (27) |
| $D_J$ (kHz) | 0.161 | 0.165098 (97) | 0.308 | 0.316907 (92) | 0.285 | 0.29129 (21) | 0.279 | 0.28664 (11) |
| $D_{JK}$ (kHz) | 14.5 | 14.77746 (35) | 12.4 | 12.61123 (34) | 13.9 | 14.1732 (17) | 12.1 | 12.28023 (96) |
| $D_K$ (kHz) | −9.09 | −9.3778 (63) | −5.65 | −5.8642 (73) | −8.91 | −9.157 (22) | −4.25 | −4.567 (15) |
| $d_1$ (kHz) | −0.229 | −0.237141 (80) | −0.273 | −0.283203 (77) | −0.294 | −0.30368 (14) | −0.223 | −0.230152 (72) |
| $d_2$ (kHz) | −0.240 | −0.248548 (43) | −0.214 | −0.222088 (45) | −0.254 | −0.262598 (78) | −0.175 | −0.181033 (43) |
| $H_J$ (Hz) | −0.00216 | −0.002110 (23) | −0.00213 | −0.002193 (21) | −0.00290 | −0.002895 (49) | −0.00158 | −0.001613 (22) |
| $H_{JK}$ (Hz) | 0.0549 | 0.05448 (11) | 0.0610 | 0.06090 (10) | 0.0717 | 0.0691 (11) | 0.0516 | 0.04968 (59) |
| $H_{KJ}$ (Hz) | −0.0135 | −0.01159 (35) | −0.0584 | −0.05686 (35) | −0.0585 | −0.0570 (25) | −0.0414 | −0.0396 (10) |
| $H_K$ (Hz) | −0.0316 | [−0.0316] | 0.0256 | [0.0256] | 0.00650 | [0.00650] | 0.00900 | [0.00900] |
| $h_1$ (Hz) | −0.000270 | −0.000207 (18) | −0.000103 | −0.000092 (17) | −0.000244 | [−0.000244] | −0.0000888 | [−0.0000888] |
| $h_2$ (Hz) | 0.00126 | 0.001343 (12) | 0.00134 | 0.001392 (12) | 0.00169 | 0.001679 (31) | 0.000989 | 0.001004 (13) |
| $h_3$ (Hz) | 0.000451 | 0.0004817 (45) | 0.000371 | 0.0003871 (45) | 0.000472 | 0.000478 (11) | 0.000280 | 0.0002961 (53) |
| $N_{lines}$ | | 787 | | 844 | | 425 | | 620 |
| $\sigma_{fit}$ (MHz) | | 0.042 | | 0.042 | | 0.047 | | 0.042 |
| $\Delta_i$ (uÅ$^2$) | | −4.301301 (28) | | −4.336604 (30) | | −5.981089 (51) | | −4.340413 (34) |

**Table S-III continued.** Experimental and computational spectroscopic constants for methacrylonitrile isotopologues, ground vibrational state (S-reduced Hamiltonian, $I^r$ representation)

| | [1-$^2$H$_{trans}$, 3-$^2$H$_{gauche}$, 3-$^2$H$_{gauche}$] | | [3,3,3-$^2$H] | | [1,1-$^2$H, 3-$^2$H$_{anti}$, 3-$^2$H$_{gauche}$] | | [1,1-$^2$H, 3-$^2$H$_{gauche}$, 3-$^2$H$_{gauche}$] | |
|---|---|---|---|---|---|---|---|---|
| | CCSD(T) | Present Work | CCSD(T) | Present Work | CCSD(T) | Present Work | CCSD(T) | Present Work |
| $A_0$ (MHz) | 7825 | 7857.5728 (48) | 8011 | 8043.2271 (57) | 7587 | 7618.2159 (18) | 7262 | 7292.4046 (19) |
| $B_0$ (MHz) | 3889 | 3910.97798 (55) | 3857 | 3878.60036 (54) | 3784 | 3805.84809 (23) | 3883 | 3905.21835 (31) |
| $C_0$ (MHz) | 2681 | 2694.64853 (33) | 2687 | 2700.99062 (34) | 2581 | 2594.48052 (19) | 2609 | 2622.20420 (23) |
| $D_J$ (kHz) | 0.259 | 0.26357 (19) | 0.440 | 0.45164 (18) | 0.209 | 0.215010 (53) | 0.174 | 0.177589 (80) |
| $D_{JK}$ (kHz) | 13.5 | 13.7523 (15) | 10.8 | 11.0080 (14) | 12.2 | 12.37513 (17) | 13.5 | 13.78757 (27) |
| $D_K$ (kHz) | −7.63 | −7.952 (27) | −3.39 | −3.652 (34) | −6.18 | −6.4057 (40) | −9.02 | −9.2780 (38) |
| $d_1$ (kHz) | −0.236 | −0.24221 (12) | −0.289 | −0.29730 (11) | −0.222 | −0.229573 (46) | −0.234 | −0.240815 (66) |
| $d_2$ (kHz) | −0.205 | −0.211548 (69) | −0.173 | −0.177961 (71) | −0.201 | −0.208057 (28) | −0.236 | −0.243718 (35) |
| $H_J$ (Hz) | −0.00206 | −0.002085 (37) | −0.00180 | −0.001822 (36) | −0.00179 | −0.001796 (10) | −0.00226 | −0.002371 (17) |
| $H_{JK}$ (Hz) | 0.0582 | 0.05414 (93) | 0.0612 | 0.06018 (90) | 0.0493 | 0.049106 (44) | 0.0544 | 0.054523 (77) |
| $H_{KJ}$ (Hz) | −0.0319 | −0.0199 (20) | −0.0736 | −0.0689 (17) | −0.0318 | −0.030702 (91) | −0.0207 | −0.01940 (15) |
| $H_K$ (Hz) | −0.0147 | [−0.0147] | 0.0444 | [0.0444] | −0.00334 | [−0.00334] | −0.0250 | [−0.0250] |
| $h_1$ (Hz) | −0.000179 | [−0.000179] | 0.0000511 | [0.0000511] | −0.000151 | −0.0001243 (89) | −0.000255 | −0.000283 (14) |
| $h_2$ (Hz) | 0.00121 | 0.001271 (23) | 0.00123 | 0.001241 (24) | 0.00108 | 0.0011160 (69) | 0.00131 | 0.0013379 (94) |
| $h_3$ (Hz) | 0.000351 | 0.0003886 (98) | 0.000266 | 0.000276 (10) | 0.000338 | 0.0003444 (23) | 0.000429 | 0.0004361 (30) |
| $N_{lines}$ | | 460 | | 447 | | 1320 | | 1032 |
| $\sigma_{fit}$ (MHz) | | 0.045 | | 0.045 | | 0.037 | | 0.043 |
| $\Delta_i$ (uÅ$^2$) | | −5.988930 (49) | | −6.023430 (54) | | −4.338295 (23) | | −5.982704 (27) |

**Table S-III continued.** Experimental and computational spectroscopic constants for methacrylonitrile isotopologues, ground vibrational state (S-reduced Hamiltonian, $I^r$ representation)

| | [1-$^2$H$_{cis}$, 3,3,3-$^2$H] | | [1-$^2$H$_{trans}$, 3,3,3-$^2$H] | | [1,1,3,3,3-$^2$H] | | [1,1,3,3,3-$^2$H, 1-$^{13}$C] | |
|---|---|---|---|---|---|---|---|---|
| | CCSD(T) | Present Work | CCSD(T) | Present Work | CCSD(T) | Present Work | CCSD(T) | Present Work |
| $A_0$ (MHz) | 7392 | 7421.9306 (20) | 7714 | 7745.4801 (24) | 7154 | 7183.19528 (38) | 6980 | 7009.2875 (95) |
| $B_0$ (MHz) | 3855 | 3876.69826 (18) | 3741 | 3761.85039 (18) | 3738 | 3758.866518 (98) | 3712 | 3733.1688 (25) |
| $C_0$ (MHz) | 2612 | 2626.15179 (20) | 2597 | 2610.84628 (21) | 2529 | 2542.281042 (73) | 2496 | 2508.53813 (27) |
| $D_J$ (kHz) | 0.356 | 0.366319 (60) | 0.305 | 0.312718 (56) | 0.232 | 0.238602 (40) | 0.185 | 0.3181 (10) |
| $D_{JK}$ (kHz) | 11.1 | 11.24550 (25) | 11.1 | 11.30451 (24) | 11.2 | 11.40663 (12) | 11.4 | 10.162 (11) |
| $D_K$ (kHz) | −5.21 | −5.3951 (42) | −4.61 | −4.8745 (56) | −6.16 | −6.3828 (10) | −6.68 | [−6.68] |
| $d_1$ (kHz) | −0.289 | −0.296207 (18) | −0.230154 | −0.237036 (16) | −0.229 | −0.236206 (23) | −0.216 | −0.27951 (46) |
| $d_2$ (kHz) | −0.202 | −0.208775 (30) | −0.169 | −0.173841 (29) | −0.195 | −0.201207 (10) | −0.201 | −0.200643 (85) |
| $H_J$ (Hz) | −0.00217 | −0.002224 (10) | −0.00162 | −0.0016402 (92) | −0.00185 | −0.0018376 (77) | −0.00183 | [−0.00183] |
| $H_{JK}$ (Hz) | 0.0609 | 0.060896 (63) | 0.0507 | 0.050604 (57) | 0.0489 | 0.048774 (31) | 0.0460 | 0.04150 (44) |
| $H_{KJ}$ (Hz) | −0.0695 | −0.06807 (14) | −0.0442 | −0.04235 (15) | −0.0374 | −0.036254 (56) | −0.0276 | [−0.0276] |
| $H_K$ (Hz) | 0.0352 | [0.0352] | 0.00973 | [0.00973] | 0.00140 | [0.00140] | −0.00827 | [−0.00827] |
| $h_1$ (Hz) | −0.0000408 | [−0.0000408] | −0.000057 | [−0.000057] | −0.000123 | −0.0000966 (49) | −0.000157 | [−0.000157] |
| $h_2$ (Hz) | 0.00138 | 0.0014048 (73) | 0.00102 | 0.0010321 (68) | 0.00112 | 0.0011451 (30) | 0.00109 | [0.00109] |
| $h_3$ (Hz) | 0.000326 | 0.0003258 (29) | 0.000256 | 0.0002620 (28) | 0.000312 | 0.0003179 (12) | 0.000328 | [0.000328] |
| $N_{lines}$ | 1047 | | 1097 | | 1725 | | 123 | |
| $\sigma_{fit}$ (MHz) | 0.043 | | 0.043 | | 0.036 | | 0.046 | |
| $\Delta_i$ (uÅ$^2$) | −6.015020 (24) | | −6.022405 (26) | | −6.015989 (5) | | −6.01313 (13) | |

**Table S-III continued.** Experimental and computational spectroscopic constants for methacrylonitrile isotopologues, ground vibrational state (S-reduced Hamiltonian, $I^r$ representation)

| | [1,1,3,3,3-$^2$H, 2-$^{13}$C] | | [1,1,3,3,3-$^2$H, 3-$^{13}$C] | | [1,1,3,3,3-$^2$H, 4-$^{13}$C] | | [1,1,3,3,3-$^2$H, $^{15}$N] | |
|---|---|---|---|---|---|---|---|---|
| | CCSD(T) | Present Work | CCSD(T) | Present Work | CCSD(T) | Present Work | CCSD(T) | Present Work |
| $A_0$ (MHz) | 7153 | 7182.44(13) | 7021 | 7050.323(14) | 7154 | 7182.79 (63) | 7152 | [7181.76] |
| $B_0$ (MHz) | 3734 | 3754.723(41) | 3700 | 3720.9148(67) | 3708 | 3729.26 (17) | 3611 | 3631.3217 (60) |
| $C_0$ (MHz) | 2527 | 2540.26821(51) | 2495 | 2508.19745(34) | 2516 | 2528.69017 (77) | 2470 | 2483.04381 (46) |
| $D_J$ (kHz) | 0.227 | 0.234(24) | 0.262 | 0.3131(19) | 0.242 | 0.2748 (81) | 0.222 | 0.2470 (28) |
| $D_{JK}$ (kHz) | 11.3 | 11.24(50) | 10.5 | 10.143(18) | 10.9 | 10.316 (73) | 10.9 | 10.349 (26) |
| $D_K$ (kHz) | −6.20 | −6.9(14) | −5.40 | [−5.40] | −5.85 | [−5.85] | −5.87 | [−5.87] |
| $d_1$ (kHz) | −0.227 | −0.2429(96) | −0.240 | −0.26674(85) | −0.226 | -0.2521 (40) | −0.209 | −0.2289 (14) |
| $d_2$ (kHz) | −0.195 | −0.2005(75) | −0.190 | −0.19339(13) | −0.187 | [−0.187] | −0.177 | [−0.177] |
| $H_J$ (Hz) | −0.00185 | [−0.00185] | −0.00186 | [−0.00186] | −0.00173 | [−0.00173] | −0.00161 | [−0.00161] |
| $H_{JK}$ (Hz) | 0.0489 | [0.0489] | 0.0490 | 0.04822(58) | 0.0466 | [0.0466] | 0.0455 | [0.0455] |
| $H_{KJ}$ (Hz) | −0.0375 | [−0.0375] | −0.0455 | [−0.0455] | −0.0365 | [−0.0365] | −0.0331 | [−0.0331] |
| $H_K$ (Hz) | 0.00153 | [0.00153] | 0.0114 | [0.0114] | 0.00250 | [0.00250] | −0.0000944 | [−0.0000944] |
| $h_1$ (Hz) | −0.000129 | [−0.000129] | −0.0000956 | [−0.0000956] | −0.000102 | [−0.000102] | −0.000105 | [−0.000105] |
| $h_2$ (Hz) | 0.00111 | [0.00111] | 0.00114 | [0.00114] | 0.00106 | [0.00106] | 0.000981 | [0.000981] |
| $h_3$ (Hz) | 0.000312 | [0.000312] | 0.000297 | [0.000297] | 0.000293 | [0.000293] | 0.000276 | [0.000276] |
| $N_{lines}$ | | 38 | | 100 | | 24 | | 39 |
| $\sigma_{fit}$ (MHz) | | 0.048 | | 0.048 | | 0.043 | | 0.054 |
| $\Delta_i$ (uÅ$^2$) | | −6.0142 (19) | | −6.01193 (28) | | −6.0189 (87) | | −6.0099 (98) |

**Equations for Calculating the Determinable Constants**

$$A_0'' = A_0^{(A)} + 2\Delta_J \quad \text{(S1)}$$
$$B_0'' = B_0^{(A)} + 2\Delta_J + \Delta_{JK} - 2\delta_J - 2\delta_K \quad \text{(S2)}$$
$$C_0'' = C_0^{(A)} + 2\Delta_J + \Delta_{JK} + 2\delta_J + 2\delta_K \quad \text{(S3)}$$

$$A_0'' = A_0^{(S)} + 2D_J + 6d_2 \quad \text{(S4)}$$
$$B_0'' = B_0^{(S)} + 2D_J + D_{JK} + 2d_1 + 4d_2 \quad \text{(S5)}$$
$$C_0'' = C_0^{(S)} + 2D_J + D_{JK} - 2d_1 + 4d_2 \quad \text{(S6)}$$

**TABLE S-IV.** Averaged determinable constants for ketene isotopologues and differences between A and S reduction determinable constants ($I^r$ representation).

| Isotopologue | methacrylonitrile | [1-$^{13}$C] | [2-$^{13}$C] | [3-$^{13}$C] | [4-$^{13}$C] | [$^{15}$N] |
|---|---|---|---|---|---|---|
| $A_0$" (MHz) | 9291.3194 | 9053.02503 | 9290.356 | 9020.0773 | 9291.162738 | 9289.431 |
| $B_0$" (MHz) | 4166.469 | 4114.659 | 4158.399 | 4125.851 | 4136.432 | 4023.262 |
| $C_0$" (MHz) | 2924.629 | 2875.396 | 2920.625 | 2877.514 | 2909.871 | 2853.174 |
| $A_0$" diff (MHz) | 0.0077 | −0.00092 | −0.066 | −0.0096 | −0.000043 | 0.062 |
| $B_0$" diff (MHz) | −0.018 | −0.017 | −0.002 | −0.015 | −0.018 | −0.022 |
| $C_0$" diff (MHz) | −0.022 | −0.017 | −0.019 | −0.020 | −0.019 | −0.016 |

**TABLE S-IV continued.** Averaged determinable constants for ketene isotopologues and differences between A and S reduction determinable constants ($I^r$ representation).

| Isotopologue | [1-$^2$H$_{cis}$] | [1-$^2$H$_{trans}$] | [3-$^2$H$_{anti}$] | [3-$^2$H$_{gauche}$] | [1,1-$^2$H] | [1-$^2$H$_{cis}$, 3-$^2$H$_{anti}$] | [1-$^2$H$_{cis}$, 3-$^2$H$_{gauche}$] |
|---|---|---|---|---|---|---|---|
| $A_0$" (MHz) | 8535.42965 | 9004.693 | 9121.4588 | 8662.2964 | 8317.0026 | 8372.5597 | 7979.34697 |
| $B_0$" (MHz) | 4157.557 | 4007.954 | 3990.109 | 4109.798 | 3997.720 | 3985.165 | 4103.420 |
| $C_0$" (MHz) | 2841.110 | 2818.229 | 2821.115 | 2855.105 | 2742.246 | 2742.720 | 2773.805 |
| $A_0$" diff (MHz) | −0.00036 | −0.015 | −0.0061 | 0.0017 | 0.0032 | −0.0066 | 0.00045 |
| $B_0$" diff (MHz) | −0.020 | −0.019 | −0.013 | −0.018 | −0.015 | −0.015 | −0.020 |
| $C_0$" diff (MHz) | −0.019 | −0.016 | −0.012 | −0.019 | −0.015 | −0.013 | −0.020 |

**TABLE S-IV continued.** Averaged determinable constants for ketene isotopologues and differences between A and S reduction determinable constants ($I^r$ representation).

| Isotopologue | [1-$^2H_{trans}$, 3-$^2H_{anti}$] | [1-$^2H_{trans}$, 3-$^2H_{gauche}$] | [3-$^2H_{anti}$, 3-$^2H_{gauche}$] | [3-$^2H_{gauche}$, 3-$^2H_{gauche}$] | [1,1-$^2H$, 3-$^2H_{anti}$] | [1,1-$^2H$, 3-$^2H_{gauche}$] |
|---|---|---|---|---|---|---|
| $A_0$" (MHz) | 8807.639 | 8381.86237 | 8538.1350 | 8133.5699 | 8128.24668 | 7761.8495 |
| $B_0$" (MHz) | 3854.660 | 3961.911 | 3936.483 | 4048.011 | 3848.565 | 3953.968 |
| $C_0$" (MHz) | 2723.440 | 2753.350 | 2758.115 | 2792.275 | 2651.856 | 2679.283 |
| $A_0$" diff (MHz) | −0.012 | 0.00038 | −0.0012 | −0.0048 | −0.00057 | −0.0022 |
| $B_0$" diff (MHz) | −0.013 | −0.018 | −0.012 | −0.017 | −0.015 | −0.019 |
| $C_0$" diff (MHz) | −0.011 | −0.018 | −0.012 | −0.016 | −0.015 | −0.018 |

**TABLE S-IV continued.** Averaged determinable constants for ketene isotopologues and differences between A and S reduction determinable constants ($I^r$ representation).

| Isotopologue | [1-$^2H_{cis}$, 3-$^2H_{anti}$, 3-$^2H_{gauche}$] | [1-$^2H_{cis}$, 3-$^2H_{gauche}$, 3-$^2H_{gauche}$] | [1-$^2H_{trans}$, 3-$^2H_{anti}$, 3-$^2H_{gauche}$] | [1-$^2H_{trans}$, 3-$^2H_{gauche}$, 3-$^2H_{gauche}$] | [3,3,3-$^2H$] | [1,1-$^2H$, 3-$^2H_{anti}$, 3-$^2H_{gauche}$] |
|---|---|---|---|---|---|---|
| $A_0$" (MHz) | 7859.1802 | 7509.9642 | 8233.27694 | 7857.57177 | 8043.22683 | 7618.2157 |
| $B_0$" (MHz) | 3933.174 | 4043.866 | 3810.330 | 3910.982 | 3878.606 | 3805.852 |
| $C_0$" (MHz) | 2681.642 | 2712.900 | 2664.437 | 2694.654 | 2700.997 | 2594.486 |
| $A_0$" diff (MHz) | −0.0022 | −0.00057 | −0.00049 | −0.00058 | −0.00022 | 0.0013 |
| $B_0$" diff (MHz) | −0.014 | −0.018 | −0.013 | −0.017 | −0.011 | −0.015 |
| $C_0$" diff (MHz) | −0.013 | −0.017 | −0.013 | −0.017 | −0.011 | −0.014 |

**TABLE S-IV continued.** Averaged determinable constants for ketene isotopologues and differences between A and S reduction determinable constants ($I^r$ representation).

| Isotopologue | [1,1-$^2$H, 3-$^2$H$_{gauche}$, 3-$^2$H$_{gauche}$] | [1-$^2$H$_{cis}$, 3,3,3-$^2$H] | [1-$^2$H$_{trans}$, 3,3,3-$^2$H] | [1,1,3,3,3-$^2$H] | [1,1,3,3,3-$^2$H, 1-$^{13}$C] | [1,1,3,3,3-$^2$H, 2-$^{13}$C] |
|---|---|---|---|---|---|---|
| $A_0$" (MHz) | 7292.4024 | 7421.9316 | 7745.4787 | 7183.1955 | 7050.333 | 7182.462 |
| $B_0$" (MHz) | 3905.222 | 3876.703 | 3761.855 | 3758.870 | 3720.918 | 3754.718 |
| $C_0$" (MHz) | 2622.209 | 2626.157 | 2610.852 | 2542.286 | 2508.202 | 2540.273 |
| $A_0$" diff (MHz) | −0.0022 | 0.0031 | −0.0021 | 0.0019 | 0.019 | 0.044 |
| $B_0$" diff (MHz) | −0.018 | −0.012 | −0.013 | −0.014 | −0.012 | −0.031 |
| $C_0$" diff (MHz) | −0.017 | −0.012 | −0.012 | −0.013 | −0.012 | −0.013 |

**TABLE S-IV continued.** Averaged determinable constants for ketene isotopologues and differences between A and S reduction determinable constants ($I^r$ representation).

| Isotopologue | [1,1,3,3,3-$^2$H, 3-$^{13}$C] | [1,1,3,3,3-$^2$H, 4-$^{13}$C] | [1,1,3,3,3-$^2$H, $^{15}$N] |
|---|---|---|---|
| $A_0$" (MHz) | 7009.280 | 7182.89 | 7181.7636 |
| $B_0$" (MHz) | 3733.172 | 3729.240 | 3631.316 |
| $C_0$" (MHz) | 2508.543 | 2528.695 | 2483.048 |
| $A_0$" diff (MHz) | −0.014 | 0.19 | 0.0017 |
| $B_0$" diff (MHz) | −0.012 | −0.076 | −0.032 |
| $C_0$" diff (MHz) | −0.012 | −0.012 | −0.013 |

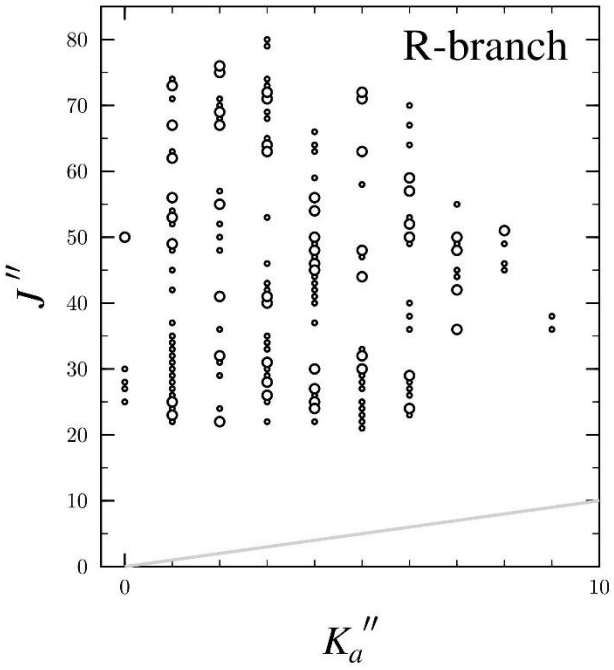


**Fig. S1.** Data distribution plot for the least-squares fits of spectroscopic data for the vibrational ground states of [1-$^{13}$C]. The size of the outlined circle is proportional to the value of $|(f_{obs.} - f_{calc.})/\delta f|$, where $\delta f$ is the frequency measurement uncertainty, and all values represented are smaller than 3.

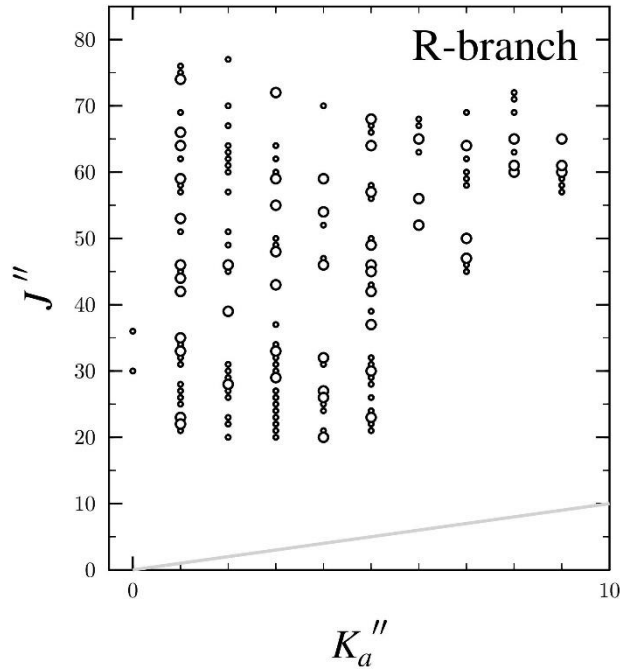


**Fig. S2.** Data distribution plot for the least-squares fits of spectroscopic data for the vibrational ground states of [2-$^{13}$C]. The size of the outlined circle is proportional to the value of $|(f_{obs.} - f_{calc.})/\delta f|$, where $\delta f$ is the frequency measurement uncertainty, and all values represented are smaller than 3.

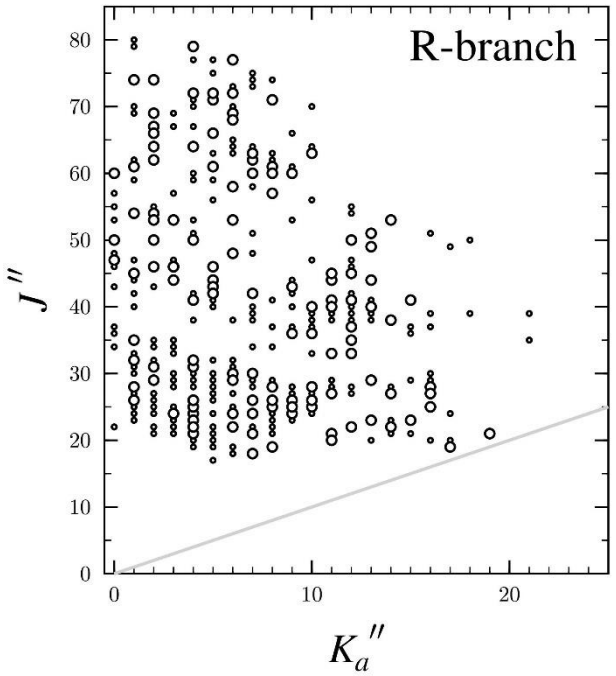


**Fig. S3.** Data distribution plot for the least-squares fits of spectroscopic data for the vibrational ground states of [3-$^{13}$C]. The size of the outlined circle is proportional to the value of $|(f_{obs.} - f_{calc.})/\delta f|$, where $\delta f$ is the frequency measurement uncertainty, and all values represented are smaller than 3.

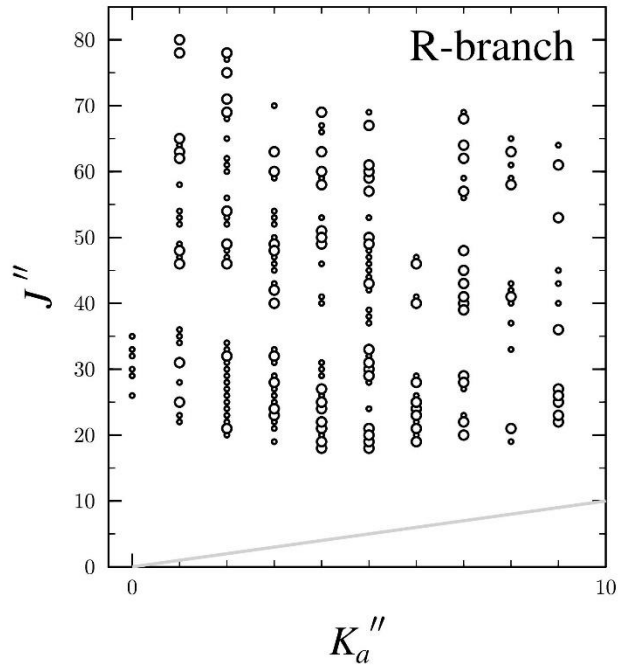


**Fig. S4.** Data distribution plot for the least-squares fits of spectroscopic data for the vibrational ground states of [4-$^{13}$C]. The size of the outlined circle is proportional to the value of $|(f_{obs.} - f_{calc.})/\delta f|$, where $\delta f$ is the frequency measurement uncertainty, and all values represented are smaller than 3.

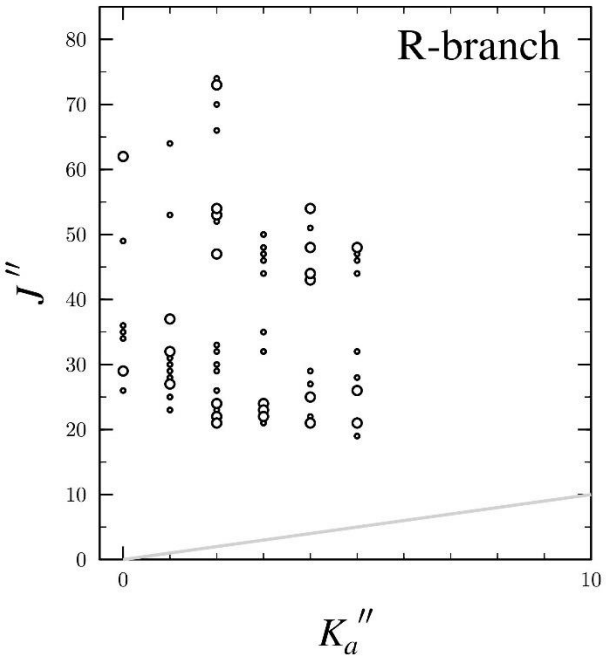


**Fig. S5.** Data distribution plot for the least-squares fits of spectroscopic data for the vibrational ground states of [$^{15}$N]. The size of the outlined circle is proportional to the value of $|(f_{obs.} - f_{calc.})/\delta f|$, where $\delta f$ is the frequency measurement uncertainty, and all values represented are smaller than 3.

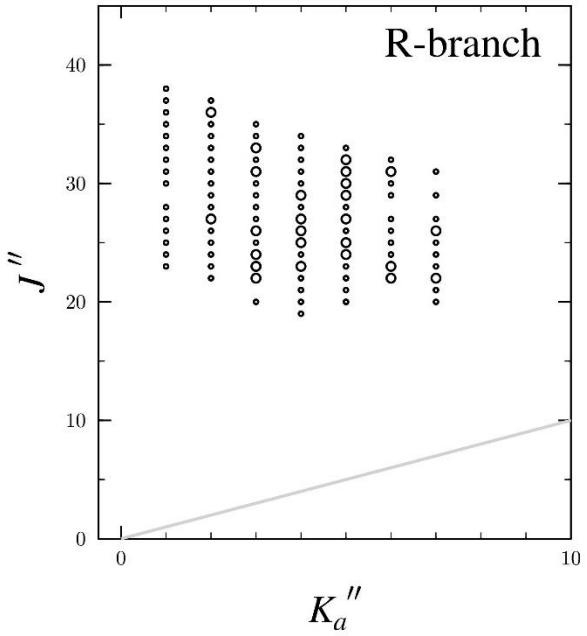


**Fig. S6.** Data distribution plot for the least-squares fits of spectroscopic data for the vibrational ground states of [1-$^{2}$H$_{cis}$]. The size of the outlined circle is proportional to the value of $|(f_{obs.} - f_{calc.})/\delta f|$, where $\delta f$ is the frequency measurement uncertainty, and all values represented are smaller than 3.

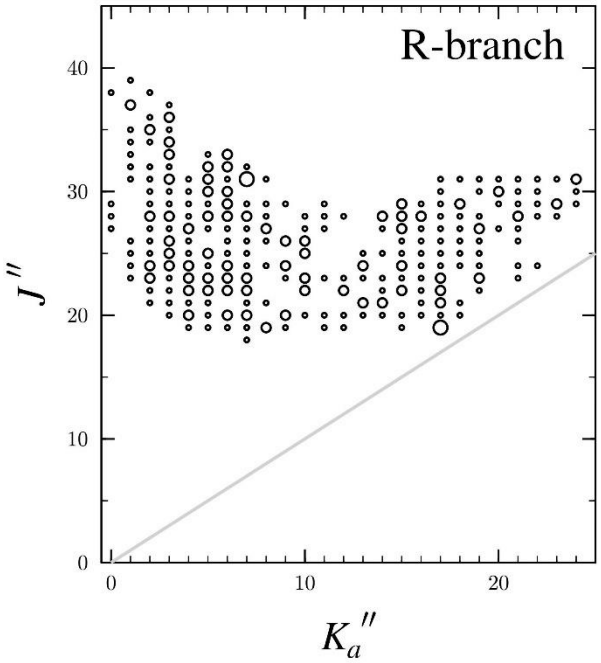


**Fig. S7.** Data distribution plot for the least-squares fits of spectroscopic data for the vibrational ground states of [1-$^2$H$_{trans}$]. The size of the outlined circle is proportional to the value of $|(f_{obs.} - f_{calc.})/\delta f|$, where $\delta f$ is the frequency measurement uncertainty, and all values represented are smaller than 3.

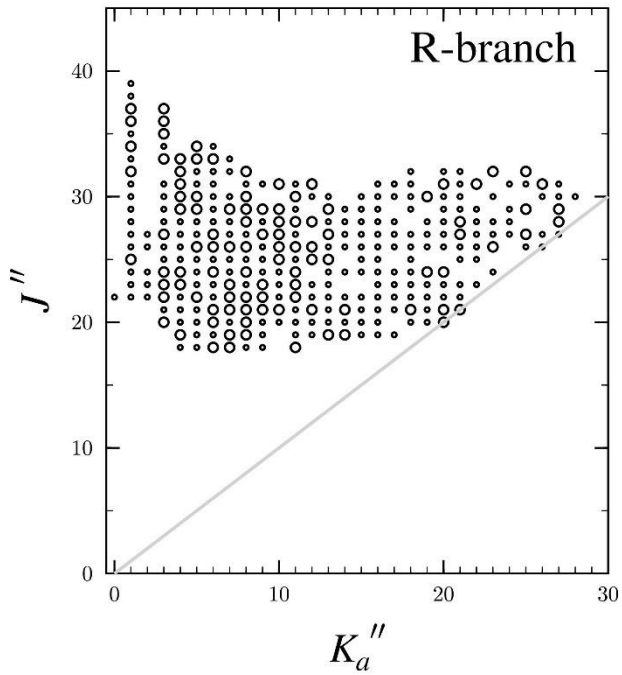


**Fig. S8.** Data distribution plot for the least-squares fits of spectroscopic data for the vibrational ground states of [3-$^2$H$_{anti}$]. The size of the outlined circle is proportional to the value of $|(f_{obs.} - f_{calc.})/\delta f|$, where $\delta f$ is the frequency measurement uncertainty, and all values represented are smaller than 3.

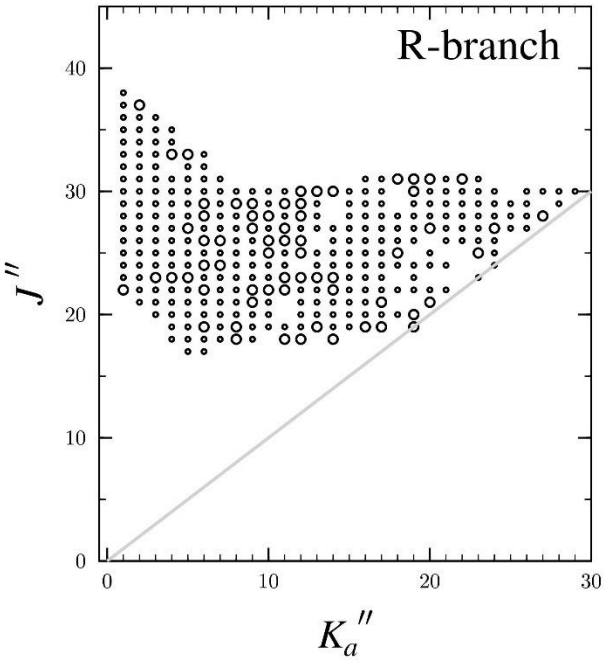


**Fig. S9.** Data distribution plot for the least-squares fits of spectroscopic data for the vibrational ground states of [3-$^2$H$_{gauche}$]. The size of the outlined circle is proportional to the value of $|(f_{obs.} - f_{calc.})/\delta f|$, where $\delta f$ is the frequency measurement uncertainty, and all values represented are smaller than 3.

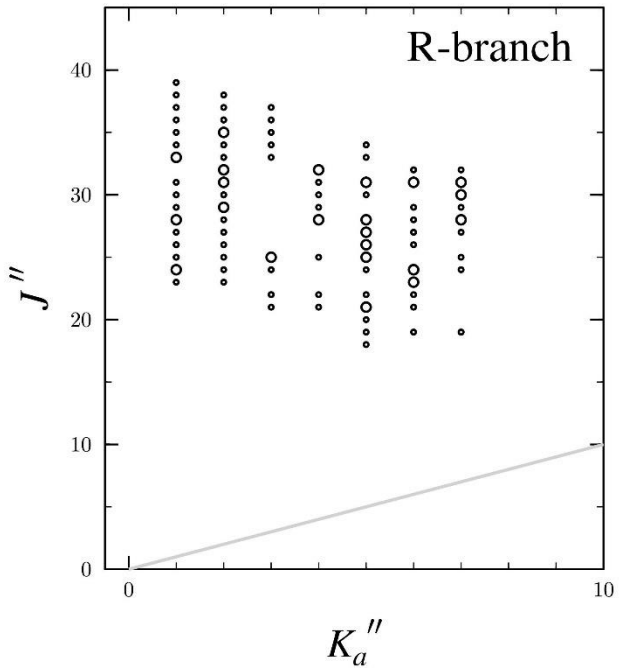


**Fig. S10.** Data distribution plot for the least-squares fits of spectroscopic data for the vibrational ground states of [1,1-$^2$H]. The size of the outlined circle is proportional to the value of $|(f_{obs.} - f_{calc.})/\delta f|$, where $\delta f$ is the frequency measurement uncertainty, and all values represented are smaller than 3.

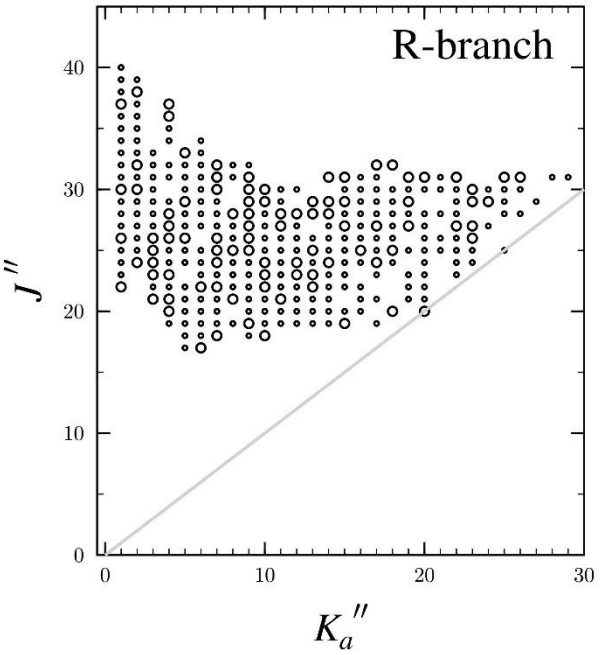


**Fig. S11.** Data distribution plot for the least-squares fits of spectroscopic data for the vibrational ground states of [1-$^2$H$_{cis}$, 3-$^2$H$_{anti}$]. The size of the outlined circle is proportional to the value of $|(f_{obs.} - f_{calc.})/\delta f|$, where $\delta f$ is the frequency measurement uncertainty, and all values represented are smaller than 3.

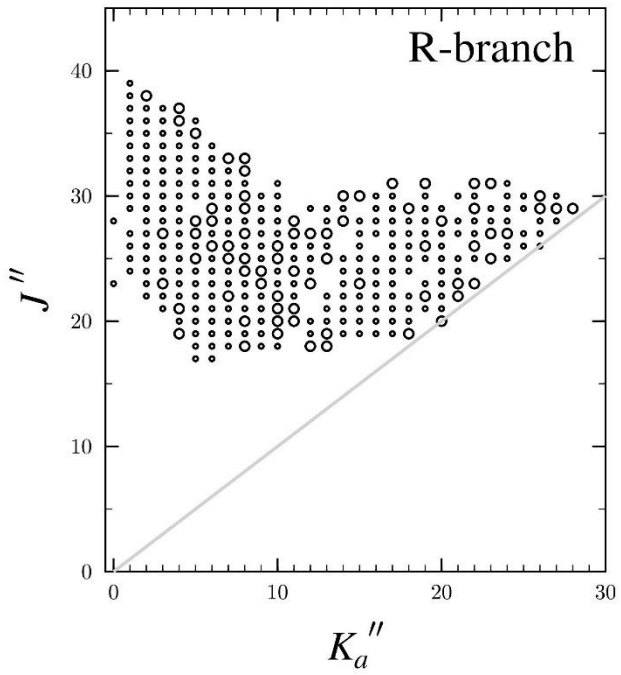


**Fig. S12.** Data distribution plot for the least-squares fits of spectroscopic data for the vibrational ground states of [1-$^2$H$_{cis}$, 3-$^2$H$_{gauche}$]. The size of the outlined circle is proportional to the value of $|(f_{obs.} - f_{calc.})/\delta f|$, where $\delta f$ is the frequency measurement uncertainty, and all values represented are smaller than 3.

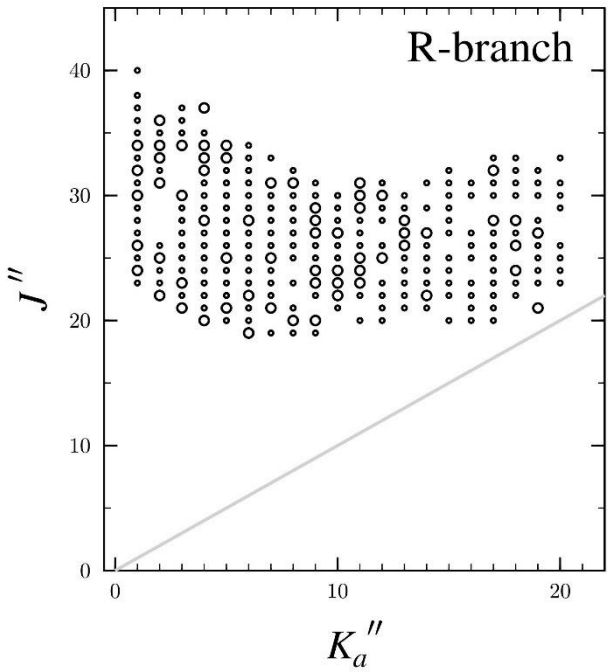


**Fig. S13.** Data distribution plot for the least-squares fits of spectroscopic data for the vibrational ground states of [1-$^2$H$_{trans}$, 3-$^2$H$_{anti}$]. The size of the outlined circle is proportional to the value of $|(f_{obs.} - f_{calc.})/\delta f|$, where $\delta f$ is the frequency measurement uncertainty, and all values represented are smaller than 3.

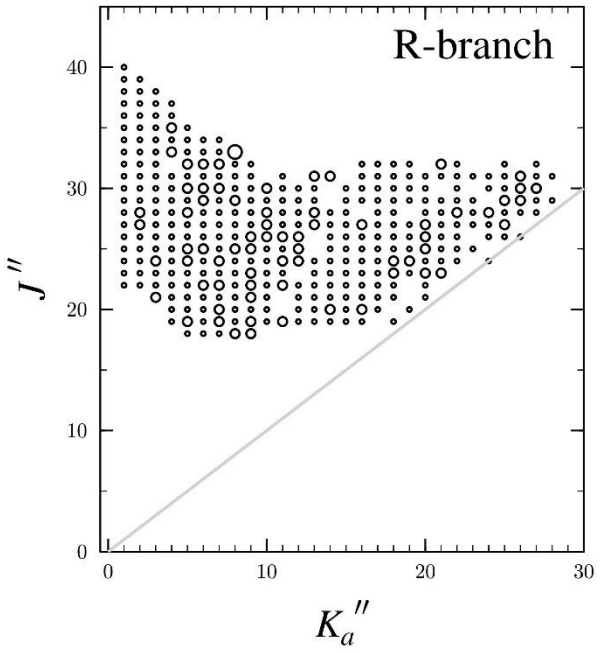


**Fig. S14.** Data distribution plot for the least-squares fits of spectroscopic data for the vibrational ground states of [1-$^2$H$_{trans}$, 3-$^2$H$_{gauche}$]. The size of the outlined circle is proportional to the value of $|(f_{obs.} - f_{calc.})/\delta f|$, where $\delta f$ is the frequency measurement uncertainty, and all values represented are smaller than 3.

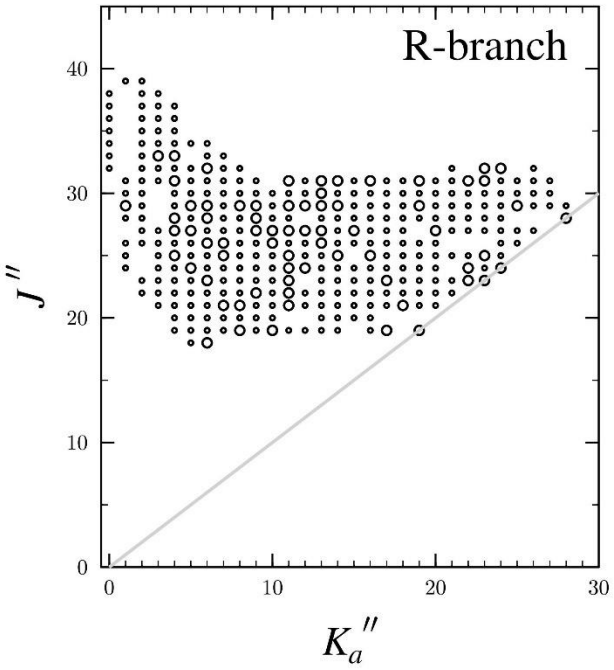


**Fig. S15.** Data distribution plot for the least-squares fits of spectroscopic data for the vibrational ground states of [3-$^2$H$_{anti}$, 3-$^2$H$_{gauche}$]. The size of the outlined circle is proportional to the value of $|(f_{obs.} - f_{calc.})/\delta f|$, where $\delta f$ is the frequency measurement uncertainty, and all values represented are smaller than 3.

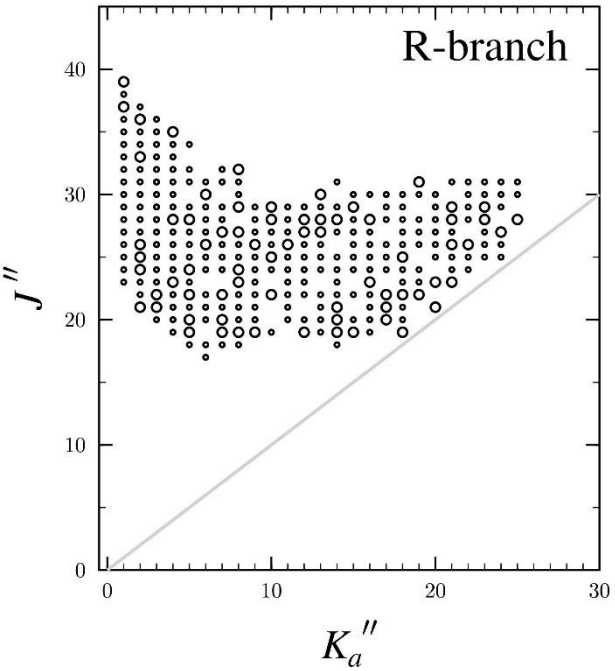


**Fig. S16.** Data distribution plot for the least-squares fits of spectroscopic data for the vibrational ground states of [3-$^2$H$_{gauche}$, 3-$^2$H$_{gauche}$]. The size of the outlined circle is proportional to the value of $|(f_{obs.} - f_{calc.})/\delta f|$, where $\delta f$ is the frequency measurement uncertainty, and all values represented are smaller than 3.

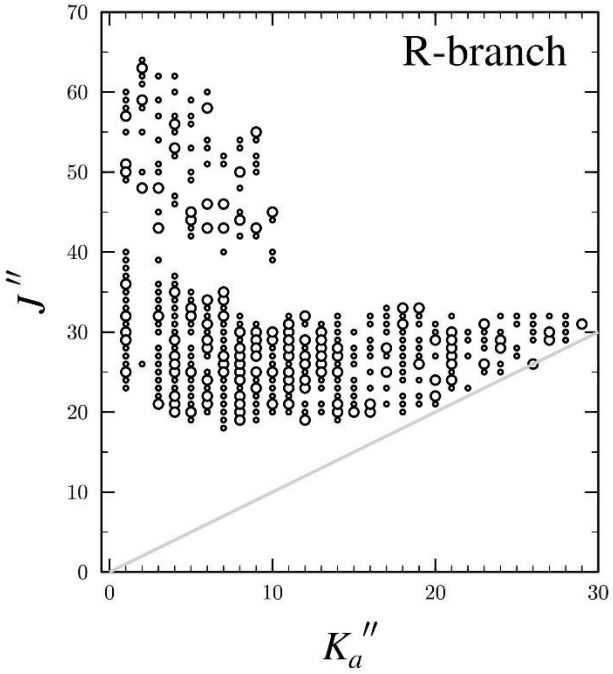


**Fig. S17.** Data distribution plot for the least-squares fits of spectroscopic data for the vibrational ground states of [1,1-$^2$H, 3-$^2$H$_{anti}$]. The size of the outlined circle is proportional to the value of $|(f_{obs.} - f_{calc.})/\delta f|$, where $\delta f$ is the frequency measurement uncertainty, and all values represented are smaller than 3.

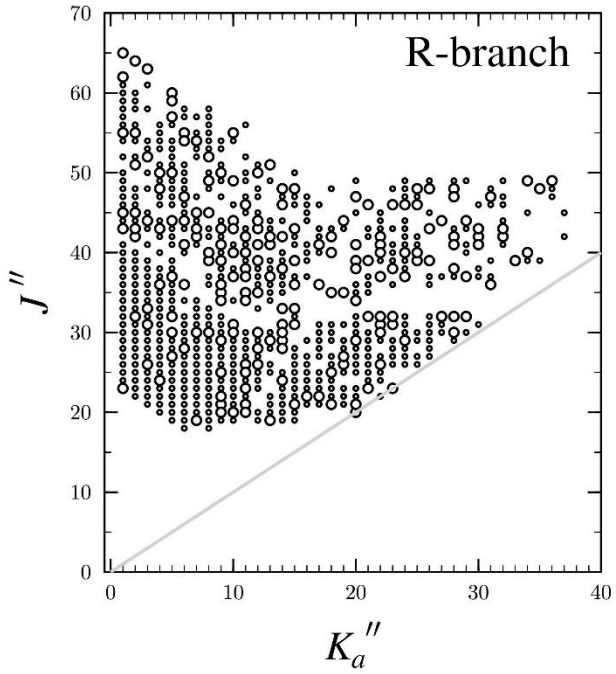


**Fig. S18.** Data distribution plot for the least-squares fits of spectroscopic data for the vibrational ground states of [1,1-$^2$H, 3-$^2$H$_{gauche}$]. The size of the outlined circle is proportional to the value of $|(f_{obs.} - f_{calc.})/\delta f|$, where $\delta f$ is the frequency measurement uncertainty, and all values represented are smaller than 3.

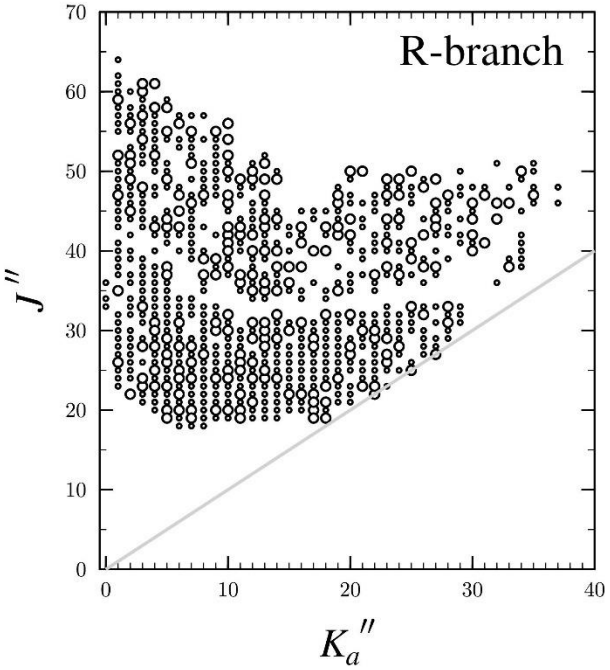


**Fig. S19.** Data distribution plot for the least-squares fits of spectroscopic data for the vibrational ground states of [1-$^2$H$_{cis}$, 3-$^2$H$_{anti}$, 3-$^2$H$_{gauche}$]. The size of the outlined circle is proportional to the value of $|(f_{obs.} - f_{calc.})/\delta f|$, where $\delta f$ is the frequency measurement uncertainty, and all values represented are smaller than 3.

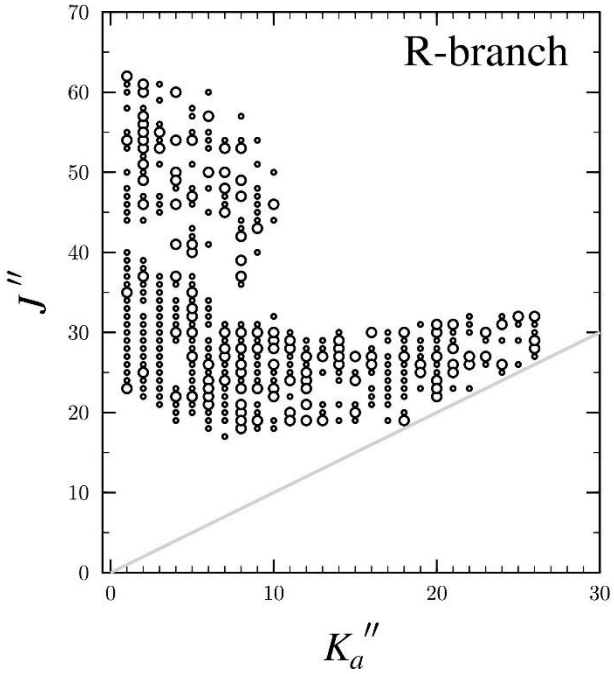


**Fig. S20.** Data distribution plot for the least-squares fits of spectroscopic data for the vibrational ground states of [1-$^2$H$_{cis}$, 3-$^2$H$_{gauche}$, 3-$^2$H$_{gauche}$]. The size of the outlined circle is proportional to the value of $|(f_{obs.} - f_{calc.})/\delta f|$, where $\delta f$ is the frequency measurement uncertainty, and all values represented are smaller than 3.

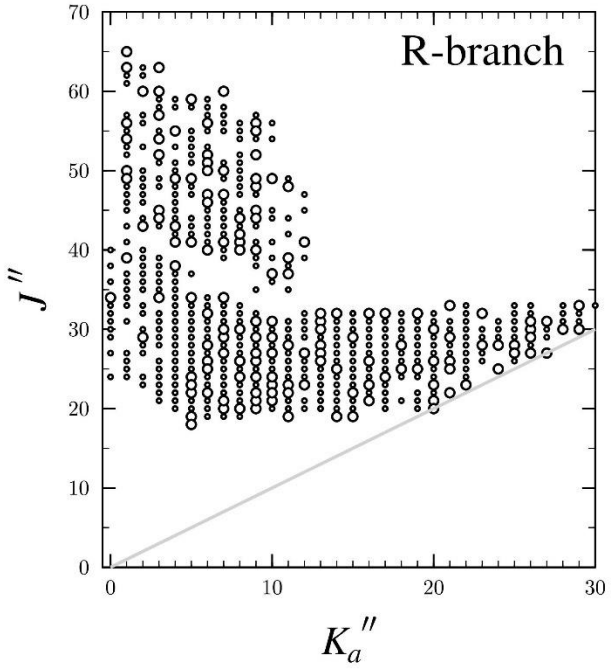


**Fig. S21.** Data distribution plot for the least-squares fits of spectroscopic data for the vibrational ground states of [1-$^2$H$_{trans}$, 3-$^2$H$_{anti}$, 3-$^2$H$_{gauche}$]. The size of the outlined circle is proportional to the value of $|(f_{obs.} - f_{calc.})/\delta f|$, where $\delta f$ is the frequency measurement uncertainty, and all values represented are smaller than 3.

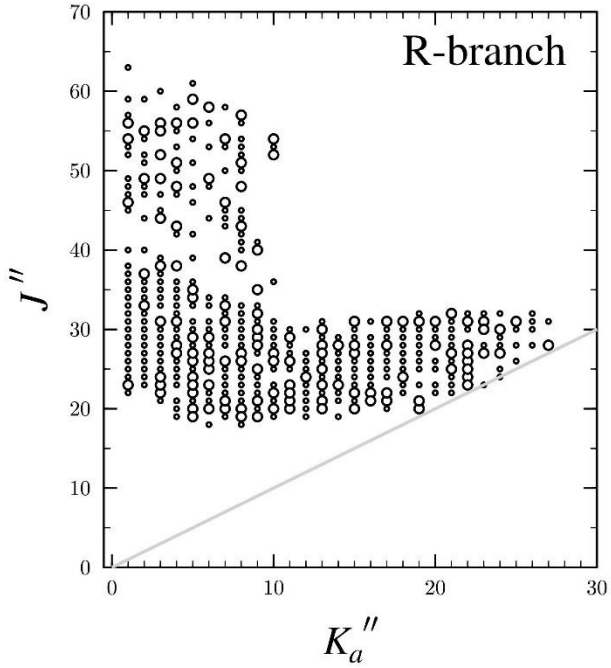


**Fig. S22.** Data distribution plot for the least-squares fits of spectroscopic data for the vibrational ground states of [1-$^2$H$_{trans}$, 3-$^2$H$_{gauche}$, 3-$^2$H$_{gauche}$]. The size of the outlined circle is proportional to the value of $|(f_{obs.} - f_{calc.})/\delta f|$, where $\delta f$ is the frequency measurement uncertainty, and all values represented are smaller than 3.

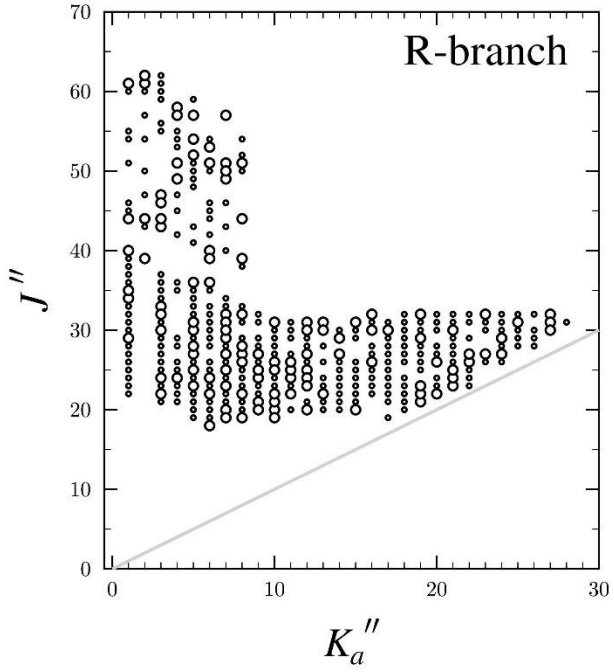


**Fig. S23.** Data distribution plot for the least-squares fits of spectroscopic data for the vibrational ground states of [3,3,3-$^2$H]. The size of the outlined circle is proportional to the value of $|(f_{obs.} - f_{calc.})/\delta f|$, where $\delta f$ is the frequency measurement uncertainty, and all values represented are smaller than 3.

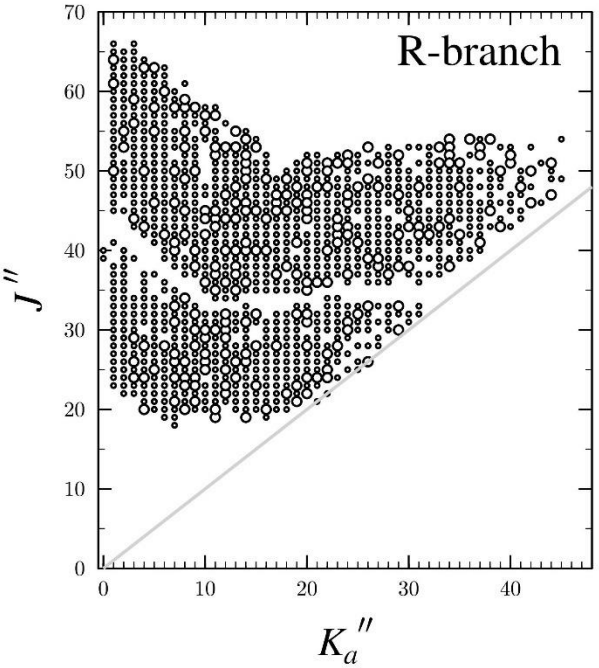


**Fig. S24.** Data distribution plot for the least-squares fits of spectroscopic data for the vibrational ground states of [1,1-$^2$H, 3-$^2$H$_{anti}$, 3-$^2$H$_{gauche}$]. The size of the outlined circle is proportional to the value of $|(f_{obs.} - f_{calc.})/\delta f|$, where $\delta f$ is the frequency measurement uncertainty, and all values represented are smaller than 3.

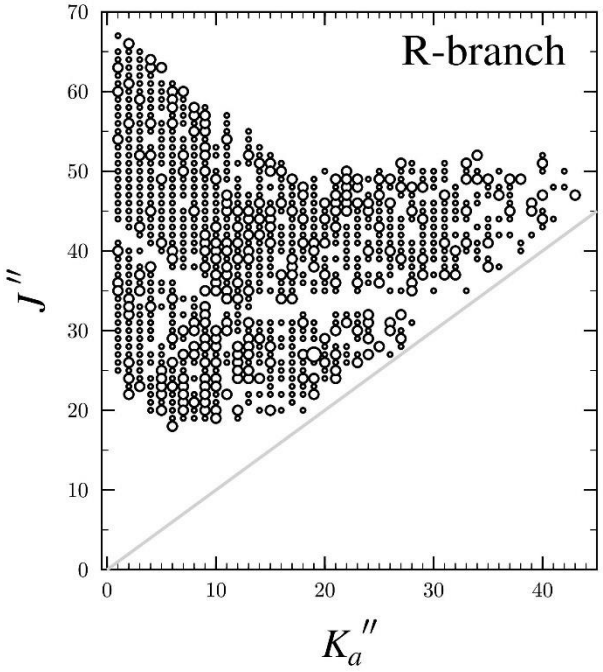


**Fig. S25.** Data distribution plot for the least-squares fits of spectroscopic data for the vibrational ground states of [1,1-$^2$H, 3-$^2$H$_{gauche}$, 3-$^2$H$_{gauche}$]. The size of the outlined circle is proportional to the value of $|(f_{obs.} - f_{calc.})/\delta f|$, where $\delta f$ is the frequency measurement uncertainty, and all values represented are smaller than 3.

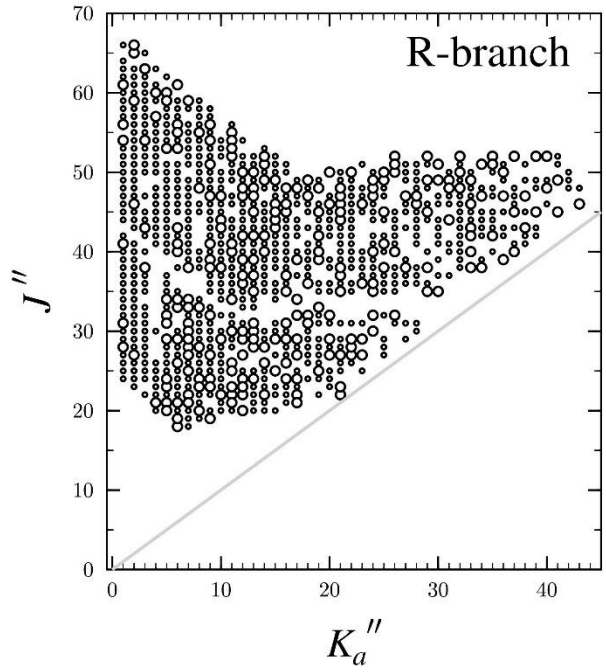


**Fig. S26.** Data distribution plot for the least-squares fits of spectroscopic data for the vibrational ground states of [1-$^2$H$_{cis}$, 3,3,3-$^2$H]. The size of the outlined circle is proportional to the value of $|(f_{obs.} - f_{calc.})/\delta f|$, where $\delta f$ is the frequency measurement uncertainty, and all values represented are smaller than 3.

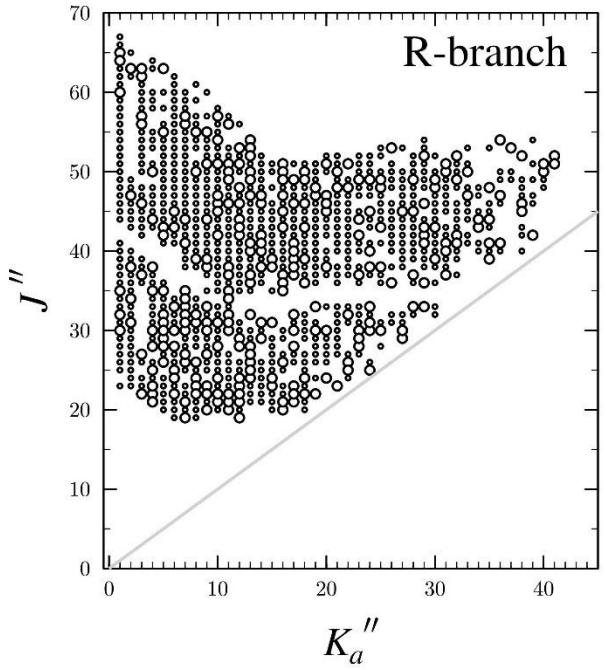


**Fig. S27.** Data distribution plot for the least-squares fits of spectroscopic data for the vibrational ground states of [1-$^2$H$_{trans}$, 3,3,3-$^2$H]. The size of the outlined circle is proportional to the value of $|(f_{obs.} - f_{calc.})/\delta f|$, where $\delta f$ is the frequency measurement uncertainty, and all values represented are smaller than 3.

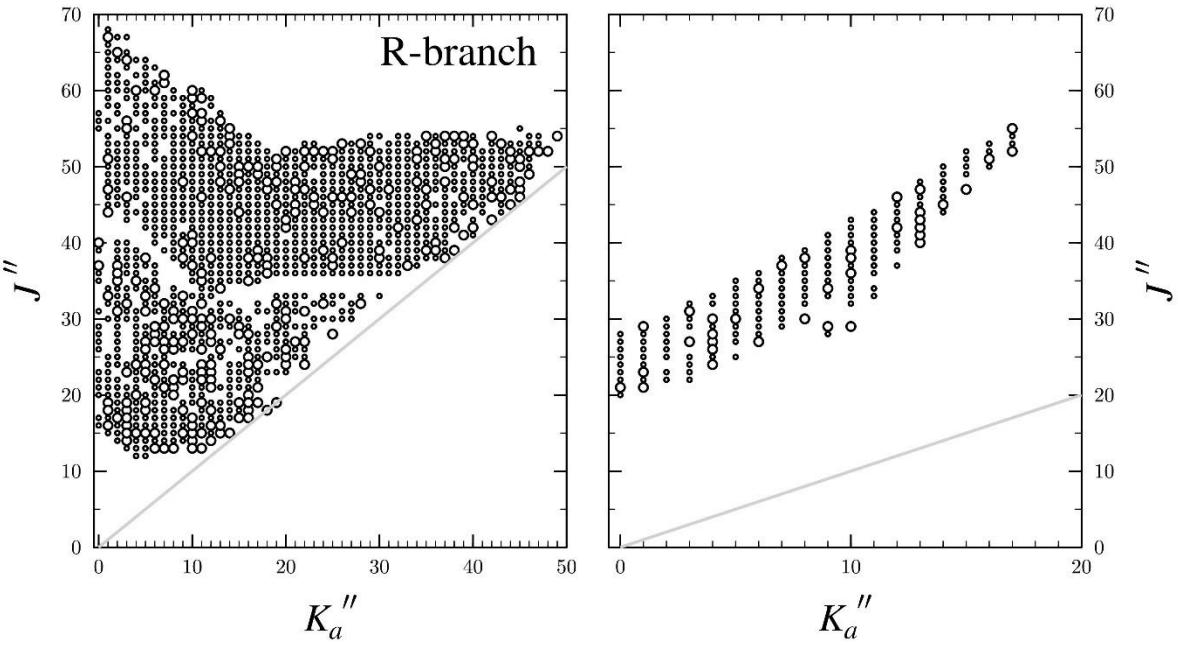


**Fig. S28.** Data distribution plot for the least-squares fits of spectroscopic data for the vibrational ground states of [1,1,3,3,3-$^2$H]. The size of the outlined circle is proportional to the value of $|(f_{obs.} - f_{calc.})/\delta f|$, where $\delta f$ is the frequency measurement uncertainty, and all values represented are smaller than 3.

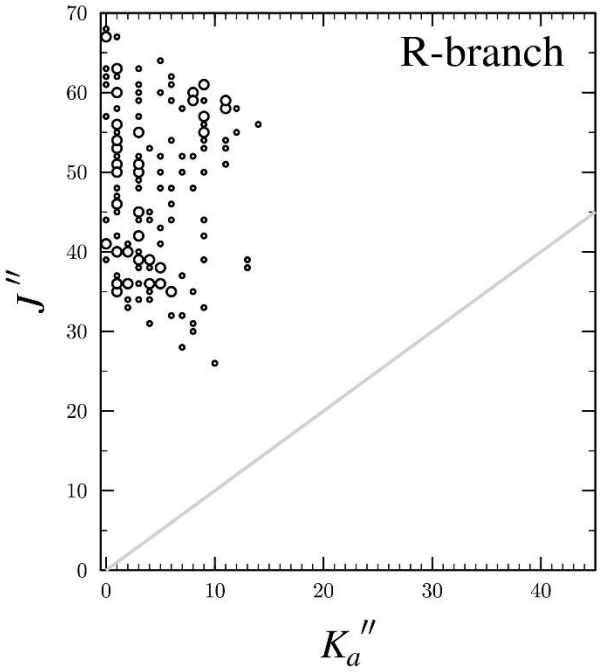


**Fig. S29.** Data distribution plot for the least-squares fits of spectroscopic data for the vibrational ground states of [1,1,3,3,3-$^{2}$H, 1-$^{13}$C]. The size of the outlined circle is proportional to the value of $|(f_{obs.} - f_{calc.})/\delta f|$, where $\delta f$ is the frequency measurement uncertainty, and all values represented are smaller than 3.

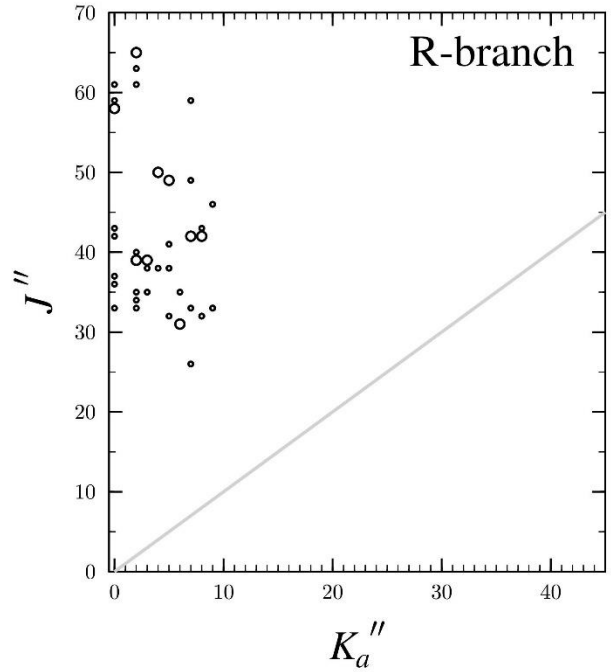


**Fig. S30.** Data distribution plot for the least-squares fits of spectroscopic data for the vibrational ground states of [1,1,3,3,3-$^{2}$H, 2-$^{13}$C]. The size of the outlined circle is proportional to the value of $|(f_{obs.} - f_{calc.})/\delta f|$, where $\delta f$ is the frequency measurement uncertainty, and all values represented are smaller than 3.

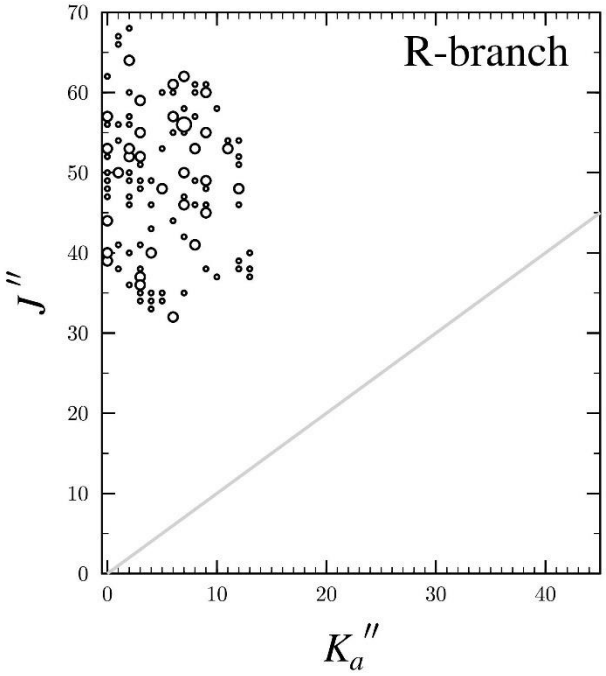


**Fig. S31.** Data distribution plot for the least-squares fits of spectroscopic data for the vibrational ground states of [1,1,3,3,3-$^{2}$H, 3-$^{13}$C]. The size of the outlined circle is proportional to the value of $|(f_{obs.} - f_{calc.})/\delta f|$, where $\delta f$ is the frequency measurement uncertainty, and all values represented are smaller than 3.

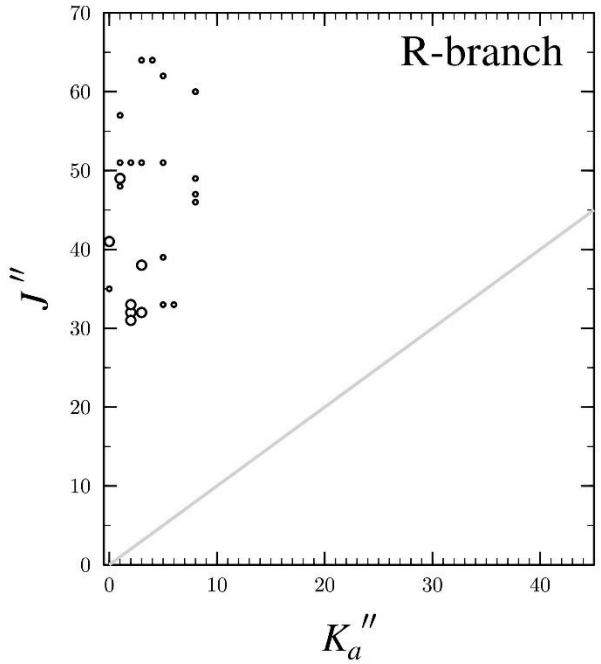


**Fig. S32.** Data distribution plot for the least-squares fits of spectroscopic data for the vibrational ground states of [1,1,3,3,3-$^{2}$H, 4-$^{13}$C]. The size of the outlined circle is proportional to the value of $|(f_{obs.} - f_{calc.})/\delta f|$, where $\delta f$ is the frequency measurement uncertainty, and all values represented are smaller than 3.

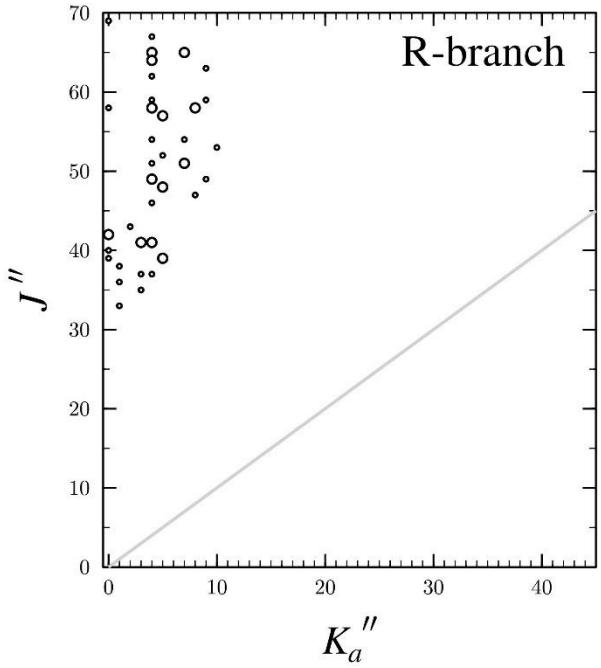


**Fig. S33.** Data distribution plot for the least-squares fits of spectroscopic data for the vibrational ground states of [1,1,3,3,3-$^{2}$H, $^{15}$N]. The size of the outlined circle is proportional to the value of $|(f_{obs.} - f_{calc.})/\delta f|$, where $\delta f$ is the frequency measurement uncertainty, and all values represented are smaller than 3.

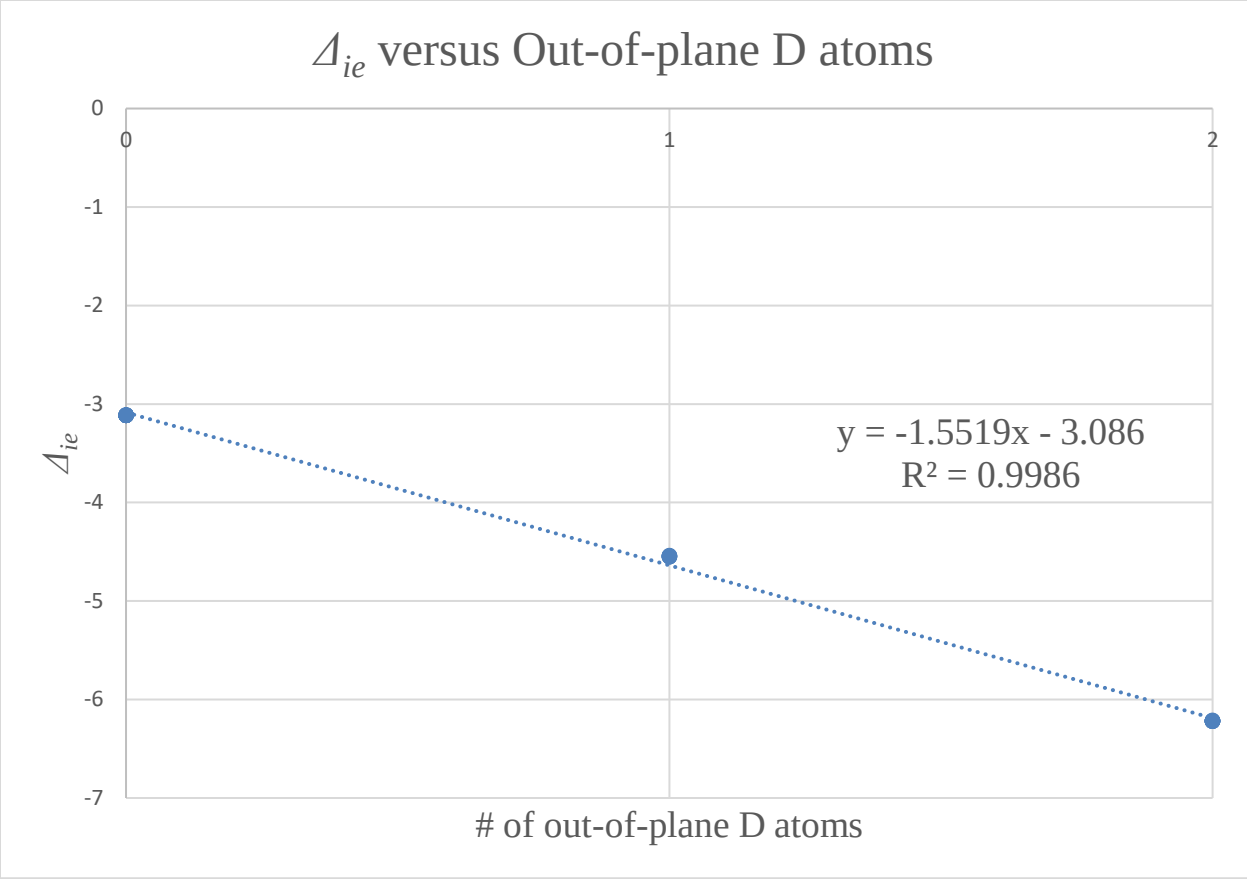


**Fig. S34.** The averaged inertial defects $\Delta_{ie}$ for isotopologues that have the same number of out-of-plane deuterium atoms.

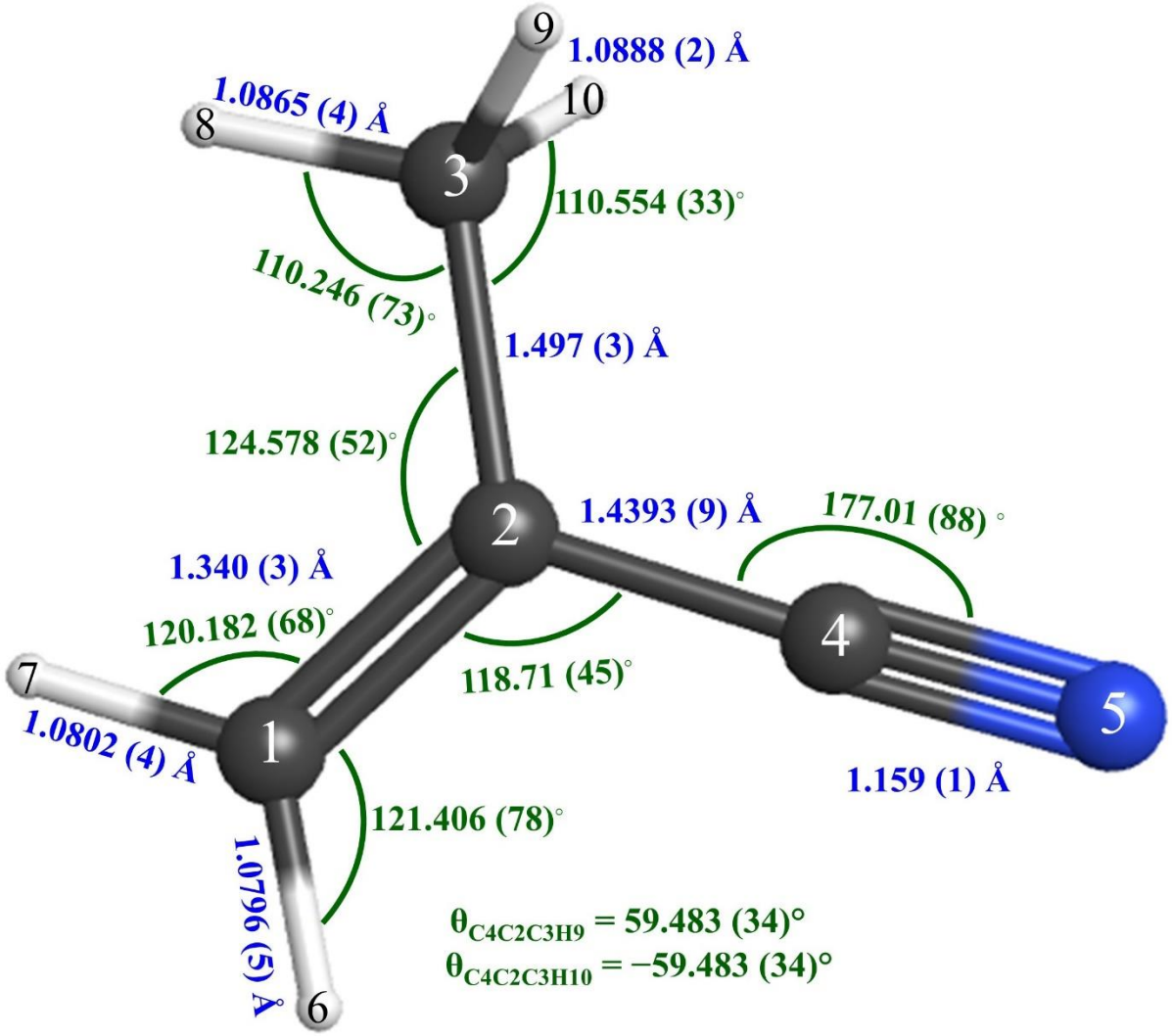


**FIG. S35.** Semi-experimental equilibrium structure ($r_e^{SE}$) of methacrylonitrile with 2σ statistical uncertainties from least-squares fitting of the moments of inertia from 32 isotopologues with varying $\theta_{C2\text{-}C4\text{-}N}$. Distances are in Angstroms and the angles are in degree

**TABLE S-V.** Structural parameters of methacrylonitrile.

| | $r_e^{SE}$ | $r_e^{SE}$ | CCSD(T) | CCSD(T)/ | CCSD(T)/ | CCSD(T)/ |
|---|---|---|---|---|---|---|
| | This Work | This Work[a] | BTE | cc-pCV5Z | cc-pCVQZ | cc-pCVTZ |
| $r_{C1-C2}$ | 1.3368 (7) | 1.340 (3) | 1.33703 | 1.33639 | 1.33705 | 1.33965 |
| $r_{C2-C3}$ | 1.5001 (7) | 1.497 (3) | 1.50026 | 1.50034 | 1.50099 | 1.50370 |
| $\theta_{C3-C2-C1}$ | 124.577 (53) | 124.578 (52) | 124.562 | 124.58500 | 124.55900 | 124.53600 |
| $r_{C2-C4}$ | 1.4397 (8) | 1.4393 (9) | 1.43946 | 1.43991 | 1.44045 | 1.44316 |
| $\theta_{C1-C2-C4}$ | 119.213 (45) | 118.71 (45) | 119.247 | 119.22800 | 119.24100 | 119.25800 |
| $r_{C4-N}$ | 1.1576 (6) | 1.159 (1) | 1.15896 | 1.15812 | 1.15886 | 1.16175 |
| $\theta_{C2-C4-N}$ | [177.997][b] | 177.01 (88) | 177.997 | 178.05400 | 178.08100 | 178.12800 |
| $r_{C1-H6}$ | 1.0795 (5) | 1.0796 (5) | 1.07930 | 1.07927 | 1.07954 | 1.08058 |
| $\theta_{C2-C1-H6}$ | 121.339 (53) | 121.406 (78) | 121.347 | 121.39200 | 121.41400 | 121.45000 |
| $r_{C1-H7}$ | 1.0802 (4) | 1.0802 (4) | 1.08033 | 1.08030 | 1.08057 | 1.08163 |
| $\theta_{C2-C1-H7}$ | 120.240 (48) | 120.182 (68) | 120.226 | 120.25700 | 120.27400 | 120.30400 |
| $r_{C3-H8}$ | 1.0865 (4) | 1.0865 (4) | 1.08696 | 1.08691 | 1.08726 | 1.08839 |
| $\theta_{C2-C3-H8}$ | 110.178 (37) | 110.246 (73) | 110.182 | 110.18400 | 110.18800 | 110.16700 |
| $r_{C3-H9/H10}$ | 1.0888 (2) | 1.0888 (2) | 1.08915 | 1.08909 | 1.08945 | 1.09057 |
| $\theta_{C2-C3-H9/H10}$ | 110.582 (21) | 110.554 (33) | 110.571 | 110.57300 | 110.58900 | 110.58600 |
| $\theta_{C4-C2-C3-H9}$ | 59.505 (27) | 59.483 (34) | 59.465 | 59.47200 | 59.47900 | 59.50000 |
| $\theta_{C4-C2-C3-H10}$ | −59.505 (27) | −59.483 (34) | −59.465 | -59.47200 | −59.47900 | −59.50000 |
| $N_{isotopologues}$ | 32 | | | | | |

[a]All structural parameters were varied during the least-squares fit of *xrefit*.
[b]Parameter held fixed at BTE value.

**Equations for Calculating the Best Theoretical Estimate (BTE)**

1. Residual basis set effects beyond cc-pCV6Z: To estimate the correction needed to approach the infinite basis set limit,[9,10] equilibrium structural parameters obtained with the cc-pCVXZ (X = Q, 5, and 6) basis sets were extrapolated using the empirical exponential[11] expression in Eq. (S7).

$$R(x) = R(\infty) + Ae^{-Bx} \tag{S7}$$

R($x$) are the values of the parameters obtained using the various basis sets ($x$ = 4, 5, and 6), and R($\infty$) is the desired basis set limit estimate. Using three basis sets ($x$ = 4, 5, and 6), the system of equations using Eq. (S7) can be solved, yielding Eq. (S8).

$$R(\infty) = -\frac{R(5)^2 - R(4)R(6)}{R(4) + R(6) - 2R(5)} \tag{S8}$$

The correction to the structure due to a finite basis set is estimated by Eq. (S9).

$$\Delta R(\text{basis}) = R(\infty) - R(\text{CCSD(T)/cc-pCV6Z}) \tag{S9}$$

2. Residual electron correlation effects beyond the CCSD(T) treatment: Residual correlation effects are assessed by doing geometry optimizations at the CCSDT(Q) level[12] and then estimating the correlation correction in Eq. (S10).

$$\Delta R(\text{cor}) = R(\text{CCSDT(Q)}) - R(\text{CCSD(T)}) \tag{S10}$$

As calculations at the CCSDT(Q) level of theory are quite expensive, these two calculations are obtained with the cc-pVDZ basis, in the frozen-core approximation.

3. Effects of scalar (mass-velocity and Darwin) relativistic effects: The relativistic corrections are obtained by subtraction of the equilibrium parameters obtained with a standard non-relativistic calculation from those obtained with the X2C-1e variant of coupled-cluster theory,[13-15] as shown in Eq. (S11).

$$\Delta\text{R(rel)} = R(\text{CCSD(T)/cc-pCVTZ})_{\text{SFX2C-1e}} - R(\text{CCSD(T)/cc-pCVTZ})_{NR} \tag{S11}$$

4. The diagonal Born-Oppenheimer correction (DBOC): The diagonal Born-Oppenheimer correction (DBOC)[16,17] is obtained from Eq. (S12).

$$\Delta R(\text{DBOC}) = R(\text{SCF/cc-pVTZ})_{DBOC} - R(\text{SCF/cc-pVTZ})_{NR} \tag{S12}$$

Here, the first value is obtained by minimizing the DBOC-corrected SCF energy with respect to nuclear positions, and the latter is again the traditional calculation.

The sum of the above-described corrections is used to obtain the best equilibrium structural parameters, given by Eq. (S13).

$$\Delta R(\text{best}) = \Delta R(\text{basis}) + \Delta R(\text{cor}) + \Delta R(\text{rel}) + \Delta R(\text{DBOC}) \tag{S13}$$

The sum of the corrections, $\Delta R$(best), is applied to the CCSD(T)/cc-pCV6Z structural parameters.

**TABLE S-VI.** Corrections used in determining the best theoretical estimate of equilibrium structural parameters of methacrylonitrile.

| | pCV*X*Z basis set correction $\Delta R$(basis) | correlation correction $\Delta R$(corr) | relativistic correction $\Delta R$(rel) | DBOC correction $\Delta R$(DBOC) | pCV*X*Z sum of corrections $\Delta R$(best) | CCSD(T)/ cc-pCV5Z | pCVXZ CCSD(T) BTE |
|---|---|---|---|---|---|---|---|
| $r_{C1-C2}$ | −0.000218 | 0.001117 | −0.000276 | 0.000021 | 0.000645 | 1.33639 | 1.33703 |
| $r_{C2-C3}$ | −0.000207 | 0.000337 | −0.000223 | 0.000017 | −0.000076 | 1.50034 | 1.50026 |
| $\theta_{C3-C2-C1}$ | 0.000000 | −0.033191 | 0.004212 | 0.005868 | −0.023111 | 124.58500 | 124.562 |
| $r_{C2-C4}$ | −0.000135 | −0.000148 | −0.000211 | 0.000046 | −0.000448 | 1.43991 | 1.43946 |
| $\theta_{C1-C2-C4}$ | 0.000000 | 0.021472 | 0.000011 | −0.002325 | 0.019158 | 119.22800 | 119.247 |
| $r_{C4-N}$ | −0.000253 | 0.001283 | −0.000199 | 0.000014 | 0.000845 | 1.15812 | 1.15896 |
| $\theta_{C2-C4-N}$ | −0.033693 | −0.018719 | −0.003912 | −0.000421 | −0.056745 | 178.05400 | 177.997 |
| $r_{C1-H6}$ | −0.000093 | 0.000126 | −0.000133 | 0.000134 | 0.000033 | 1.07927 | 1.07930 |
| $\theta_{C2-C1-H6}$ | −0.035360 | −0.002742 | −0.000894 | −0.005753 | −0.044749 | 121.39200 | 121.347 |
| $r_{C1-H7}$ | −0.000097 | 0.000126 | −0.000128 | 0.000133 | 0.000034 | 1.08030 | 1.08033 |
| $\theta_{C2-C1-H7}$ | −0.020480 | −0.001965 | −0.003866 | −0.004822 | −0.031133 | 120.25700 | 120.226 |
| $r_{C3-H8}$ | −0.000155 | 0.000213 | −0.000115 | 0.000109 | 0.000051 | 1.08691 | 1.08696 |
| $\theta_{C2-C3-H8}$ | 0.000000 | 0.002746 | −0.004263 | −0.000407 | −0.001924 | 110.18400 | 110.182 |
| $r_{C3-H9/H10}$ | −0.000158 | 0.000223 | −0.000120 | 0.000112 | 0.000057 | 1.08909 | 1.08915 |
| $\theta_{C2-C3-H9/H10}$ | 0.000000 | 0.002090 | −0.002362 | −0.001421 | −0.001694 | 110.57300 | 110.571 |
| $\theta_{C4-C2-C3-H9}$ | −0.004081 | −0.002557 | 0.000298 | −0.000731 | −0.007071 | 59.47200 | 59.465 |
| $\theta_{C4-C2-C3-H10}$ | 0.004081 | 0.002557 | −0.000298 | 0.000731 | 0.007071 | −59.47200 | −59.465 |

**List of Isotopologue Numbering for Supplementary Material Files**

| **Methacrylonitrile** | |
|---|---|
| Normal isotopologue | Isomass1 or no number |
| [1–$^{13}$C]– | Isomass004 |
| [2–$^{13}$C]– | Isomass003 |
| [3–$^{13}$C]– | Isomass002 |
| [4–$^{13}$C]– | Isomass005 |
| [$^{15}$N]– | Isomass006 |
| [1–$^{2}H_{cis}$]– | Isomass007 |
| [1–$^{2}H_{trans}$]– | Isomass008 |
| [3–$^{2}H_{anti}$]– | Isomass009 |
| [3–$^{2}H_{gauche}$]– | Isomass010 |
| [1,1–$^{2}$H]– | Isomass011 |
| [1–$^{2}H_{cis}$, 3–$^{2}H_{anti}$]– | Isomass012 |
| [1–$^{2}H_{cis}$, 3–$^{2}H_{gauche}$]– | Isomass013 |
| [1–$^{2}H_{trans}$, 3–$^{2}H_{anti}$]– | Isomass014 |
| [1–$^{2}H_{trans}$, 3–$^{2}H_{gauche}$]– | Isomass015 |
| [3–$^{2}H_{anti}$, 3–$^{2}H_{gauche}$]– | Isomass016 |
| [3–$^{2}H_{gauche}$, 3–$^{2}H_{gauche}$]– | Isomass017 |
| [1,1–$^{2}$H, 3–$^{2}H_{anti}$]– | Isomass018 |
| [1,1–$^{2}$H, 3–$^{2}H_{gauche}$]– | Isomass019 |
| [1–$^{2}H_{cis}$, 3–$^{2}H_{anti}$, 3–$^{2}H_{gauche}$]– | Isomass020 |
| [1–$^{2}H_{cis}$, 3–$^{2}H_{gauche}$, 3–$^{2}H_{gauche}$]– | Isomass021 |
| [1–$^{2}H_{trans}$, 3–$^{2}H_{anti}$, 3–$^{2}H_{gauche}$]– | Isomass022 |
| [1–$^{2}H_{trans}$, 3–$^{2}H_{gauche}$, 3–$^{2}H_{gauche}$]– | Isomass023 |
| [3,3,3–$^{2}$H]– | Isomass024 |
| [1,1–$^{2}$H, 3–$^{2}H_{anti}$ ,3–$^{2}H_{gauche}$]– | Isomass025 |
| [1,1–$^{2}$H, 3–$^{2}H_{gauche}$, 3–$^{2}H_{gauche}$]– | Isomass026 |
| [1–$^{2}H_{cis}$, 3,3,3–$^{2}$H]– | Isomass027 |
| [1–$^{2}H_{trans}$, 3,3,3–$^{2}$H]– | Isomass028 |
| [1,1,3,3,3–$^{2}$H]– | Isomass029 |
| [1,1,3,3,3–$^{2}$H, 1–$^{13}$C]– | Isomass032 |
| [1,1,3,3,3–$^{2}$H, 2–$^{13}$C]– | Isomass031 |
| [1,1,3,3,3–$^{2}$H, 3–$^{13}$C]– | Isomass030 |
| [1,1,3,3,3–$^{2}$H, 4–$^{13}$C]– | Isomass033 |
| [1,1,3,3,3–$^{2}$H, $^{15}$N]– | Isomass034 |

# Appendix B: Electrical Discharges of Different Molecules

## Introduction

The rotational spectrometer the McMahon | Woods group uses is skeletally the same as the original design of Claude Woods and described in detail in various publications.[1-3] Additional adaptations have been made over the decades, but the major changes are the implementation of a solenoid magnet to create a homogenous magnetic field up to 300 G around the discharge cell based on DeLucia *et al.*[4] and is described in detail in previous publications,[5,6] There have been recent changes to the way mm/sub-mm wave radiation is generated and detected, and these have been described previously.[7-10] The group has long been interested in the generation and laboratory detection of the acylium or acetyl cation ($CH_3CO^+$). With the recent astronomical and laboratory detection of acylium,[11] we thought this would be a great opportunity to test out the discharge capabilities of our instrument for small organic molecules, because our group has further interest in examining other organic molecule discharges.

Before we began the discharge experiments to try to observe acylium, we wanted to benchmark our spectrometer and familiarize ourselves with how to optimize discharge conditions. We selected $ArH^+$, $ArD^+$, $KrH^+$, $XeD^+$, $H_2D^+$, and $N_2OH^+$ as our discharge targets because these molecules have been detected previously with our spectrometer or similar types of spectrometers. In the past decade, the liquid nitrogen cooling system that was originally used for all the publications at the University of Wisconsin – Madison was replaced with a chiller system to reach ~ −80 °C because these temperatures suited studying reactive neutral molecules. The first step in repeating the previously studied discharge experiments at the University of Wisconsin – Madison was to disconnect the chiller, remove all the chiller fluid from the system, and refit the spectrometer to allow for liquid nitrogen cooling to be used. Thus, all the discharges discussed in this chapter

utilized liquid nitrogen through a set of four Teflon tubes wrapped around the discharge tube to cool the system to ~ 77 K. Once these molecules were examined, we attempted to repeat the laboratory detection of acylium[11], and to detect acylium for the first time in a ketene ($H_2CCO$), Ar, and $H_2$ discharge.

**$ArH^+$ and $ArD^+$**

The first experiments were in an argon and $H_2$ discharge with the pressure of the argon at 70 mTorr in the inlet manifold and trace amounts of $H_2$ gas controlled by an MKS mass flow controller. The experiments were carried out in a negative-glow configuration with the magnet at 270 Gauss with a discharge voltage of 1425 V. The vibrational ground-state rotational transition from $J = 0$ to $J = 1$ was easily observable, as shown in Fig. B.1, and was previously measured at 615858.4 MHz.[12] The first vibrationally excited-state rotational transition from $J = 0$ to $J = 1$ was observable with an average of 50 scans (Fig. B.2.). The first vibrationally excited-state transition was predicted using the molecular constants provided by James and Summer[13], and the observed transition was only 0.031 MHz away from the prediction of 593512.18 MHz. James and Summer[13] measured the infrared emission spectrum of $ArH^+$ *via* carbon hollow cathode lamp. Bowman *et al.*[14] measured the $J = 0$ to 1 rotational transition for three isotopologues of $ArD^+$. Given the experimental vibration-rotation interaction constant for $ArH^+$ and the experimental rotational constant of $ArD^+$, we applied an empirical shift to the vibration-rotation interaction constant based on the change in the reduced mass between $ArH^+$ and $ArD^+$. The predicted vibration-rotation interaction constant was then used to calculate the rotational constant for the first vibrationally excited state of $ArD^+$. Similar corrections were made to the quartic distortion constant, and the distorted rotor energy expression for diatomic molecules was used to calculate the $J = 1$ to $J = 2$ rotational transition. We predicted the first vibrationally excited-state from $J = 1$ to $J = 2$ for $ArD^+$

at 618174.89 MHz. A tentative detection at 618176.25 MHz can be observed in Fig. B.3, which required an average of 50 scans to obtain. The ~ 1 MHz difference between the predicted and observed frequencies is not surprising given the prediction method, and we believe this may be the first detection of this rotational transition.

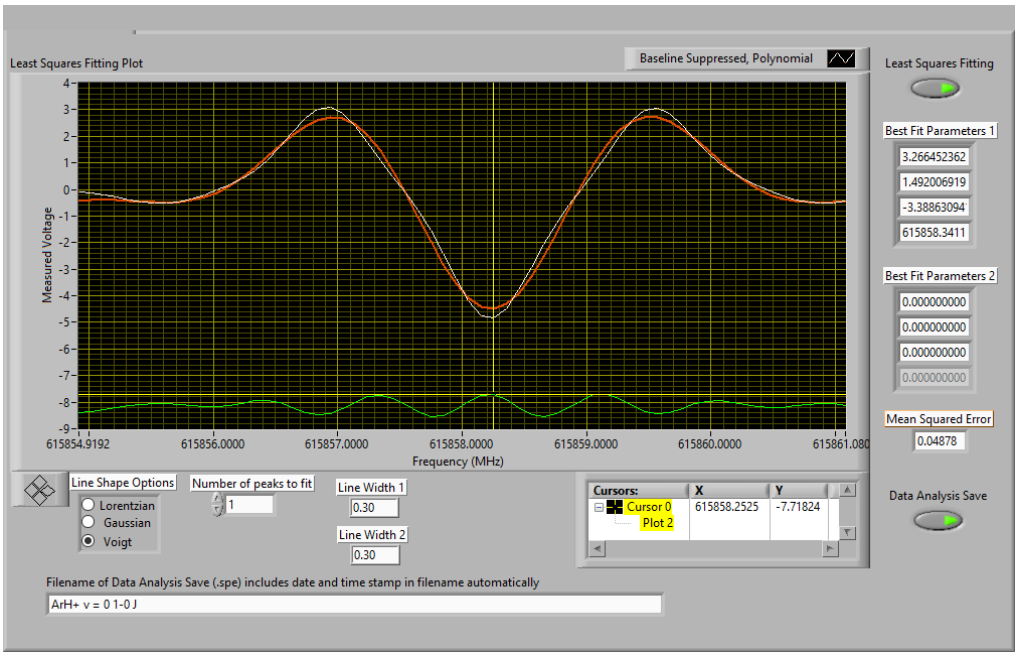


**Fig. B.1.** $ArH^+$ vibrational ground-state rotational transition from $J = 0$ to $J = 1$ observed at 615858.25 MHz.

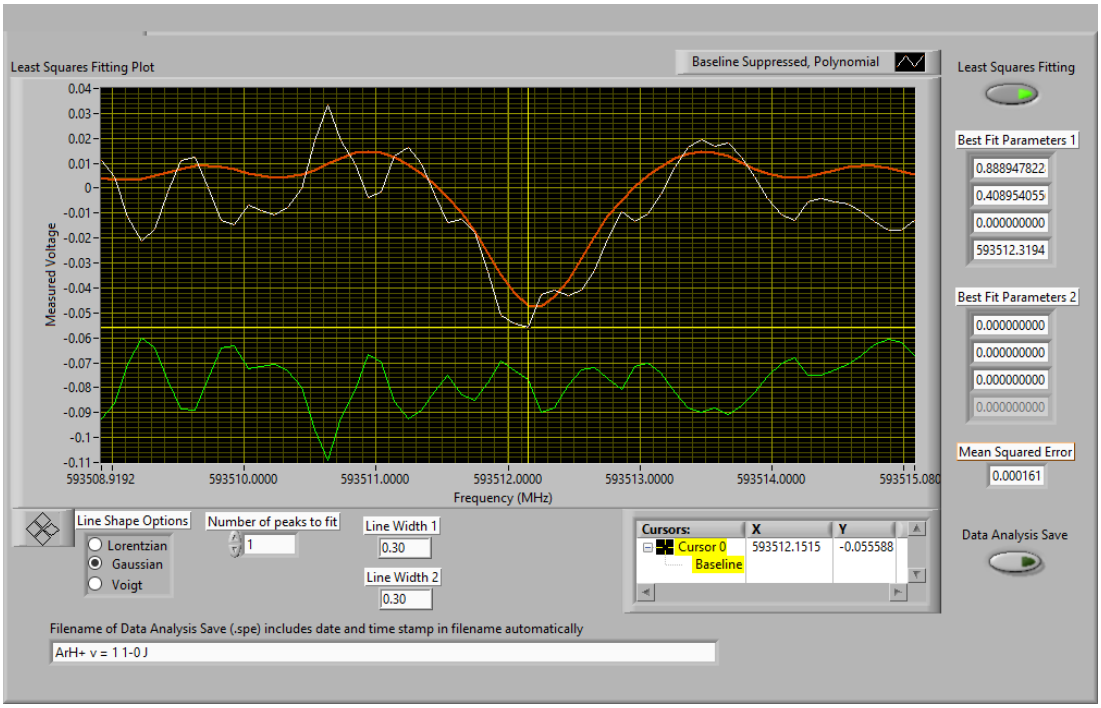


**Fig. B.2.** $ArH^+$ first vibrationally excited-state rotational transition from $J = 0$ to $J = 1$ observed at 593512.15 MHz.

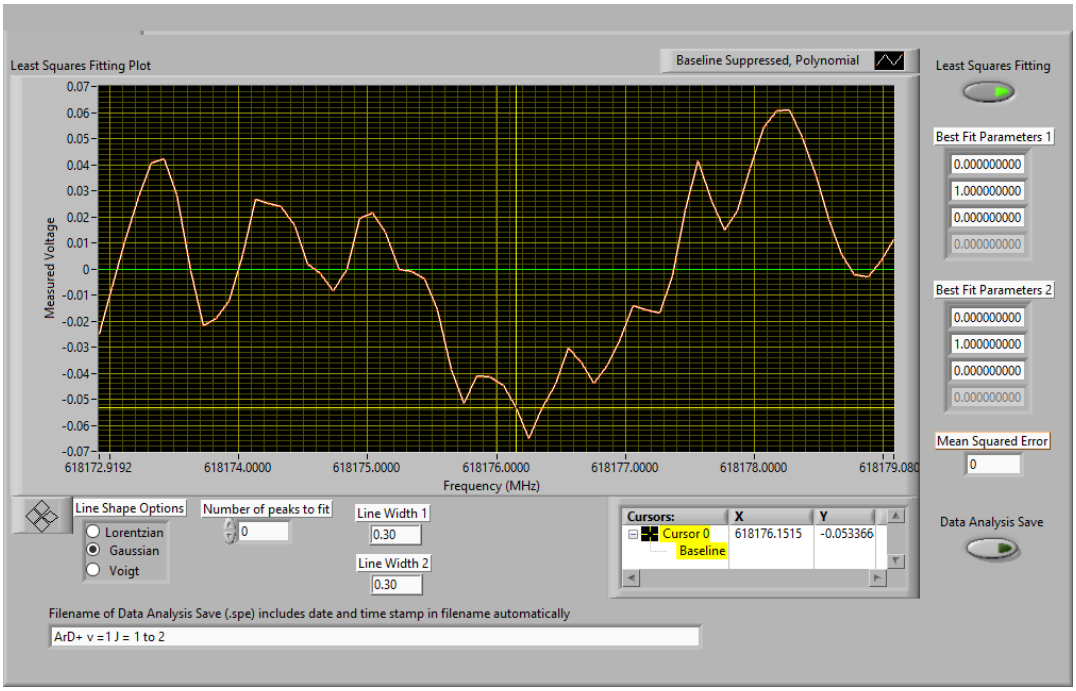


**Fig. B.3.** $ArD^+$ first vibrationally excited-state rotational transition from $J = 1$ to $J = 2$ observed at 618176.25 MHz.

**$KrH^+$**

The $J$ = 0 to 1 rotational transition of $KrH^+$ was easily observed at 494515.35 MHz (Fig. B4), which was only 0.025 MHz away from our predicted frequency. Linnartz *et al.*[15] measured the Zeeman effect on this transition and were able to determine an electric dipole moment of 3.0 (6) D. Our prediction was calculated by taking the average of the highest and lowest frequencies observed by Linnartz *et al.*[15] The experimental conditions utilized were based on those from the published work of $KrD^+$ at the University of Wisconsin – Madison.[6] These conditions were 1 mTorr $H_2$, 12 mTorr Kr, discharge voltage of 1500 V, and 300 Gauss for the solenoid magnet.

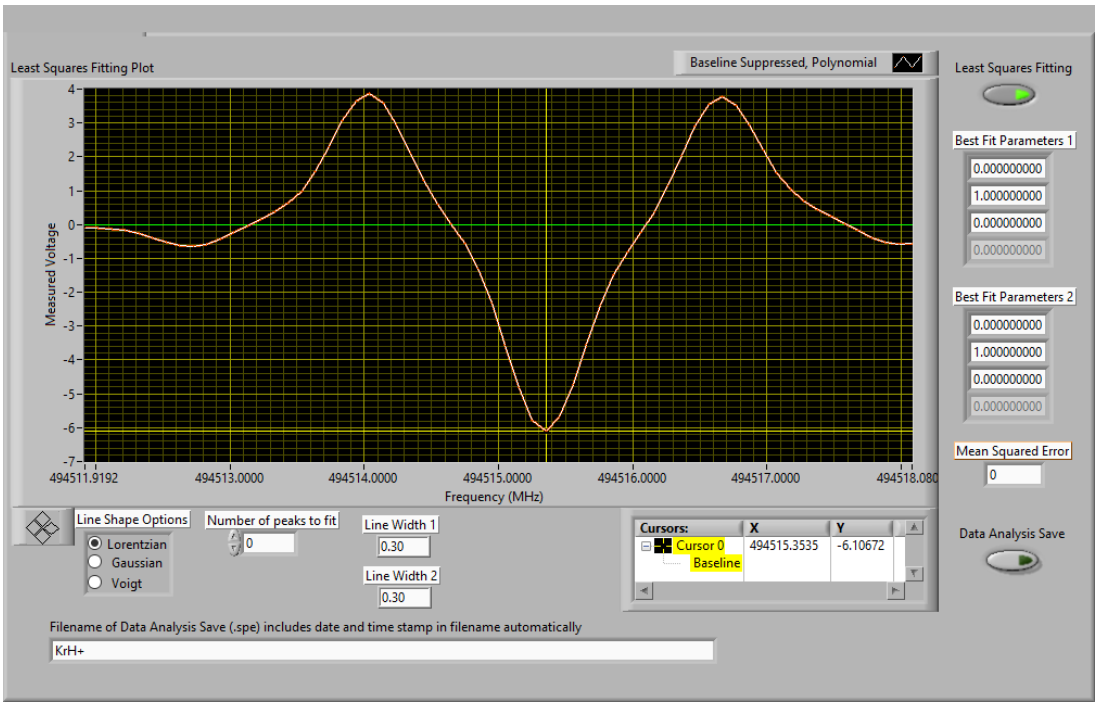


**Fig. B.4.** $KrH^+$ vibrational ground-state rotational transition from $J$ = 0 to $J$ = 1 observed at 494515.35 MHz.

**$XeD^+$**

The next experiment was the discharge of xenon, deuterium, and argon gas to create $XeD^+$. Using argon as a carrier gas for this discharge was previously shown with this spectrometer at the University of Wisconsin – Madison to greatly increase the abundance of $XeD^+$ and $XeH^+$.[16] The previous work with this spectrometer setup examined the $J = 1$ to $J = 2$ transitions for various xenon isotopologues ($^{136}Xe$, $^{134}Xe$, $^{132}Xe$, $^{131}Xe$, $^{130}Xe$, $^{129}Xe$, $^{128}Xe$, $^{126}Xe$, and $^{124}Xe$).[16] The spectroscopic constants from a previous publication[17] were utilized to predict the transition frequencies for $^{132}Xe$, $^{129}Xe$, $^{131}Xe$, $^{134}Xe$, and $^{136}Xe$ isotopologues. Ohtaki *et al.*[17] measured the rotational transitions of these isotopologues from 1 – 5 THz using a far-infrared spectrometer and a tunable radiation source. The remaining isotopologues, $^{130}Xe$, $^{128}Xe$, $^{126}Xe$, and $^{124}Xe$, were observed by applying empirical shifts to the $J = 1$ to $J = 2$ transitions observed previously. The experimental conditions we used were as follows: 8 mTorr chamber pressure, 0.2 mTorr xenon pressure, 0.8 mTorr $D_2$ pressure, 7 mTorr argon pressure, 1800 V discharge voltage, and 240 Gauss for the magnet. Figure B.5 shows a 600 MHz spectrum segment highlighting various isotopologues ($^{134}XeD^+$, $^{132}XeD^+$, $^{130}XeD^+$, $^{129}XeD^+$, and $^{128}XeD^+$); hyperfine components of $^{131}XeD^+$ are observed. The least abundant xenon isotopes, $^{126}Xe$ and $^{124}Xe$, at 0.089 % and 0.095 %, respectively, are tentatively observed in Fig. B.6 and Fig. B.7. Fig. B.6 and Fig. B.7 required averaging 50 scans for the tentative detection and likely more would be needed for a definitive detection. We are confident that the predicted transition frequencies of 589213.60 MHz and 589362.47 MHz for $^{126}Xe$ and $^{124}Xe$ isotopologues, respectively, are accurate because these tentative detections were reproducible.

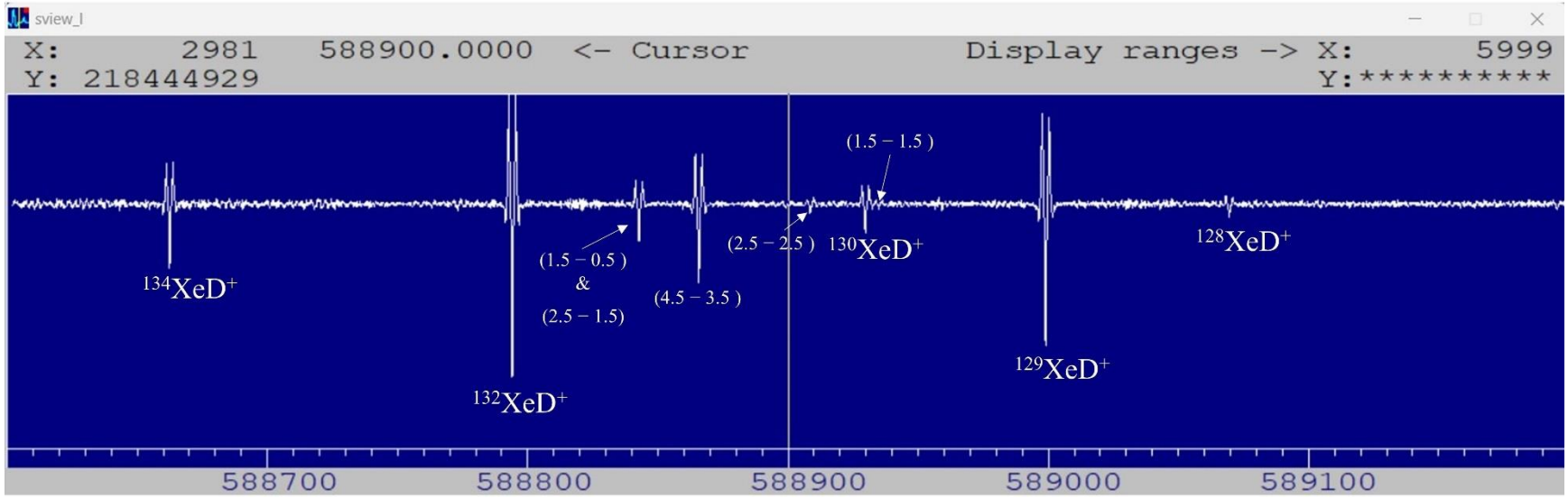


**Fig. B.5.** $XeD^+$ rotational spectrum from 588600 MHz to 589200 MHz and contains several isotopologues and hyperfine transitions of $^{131}XeD^+$.

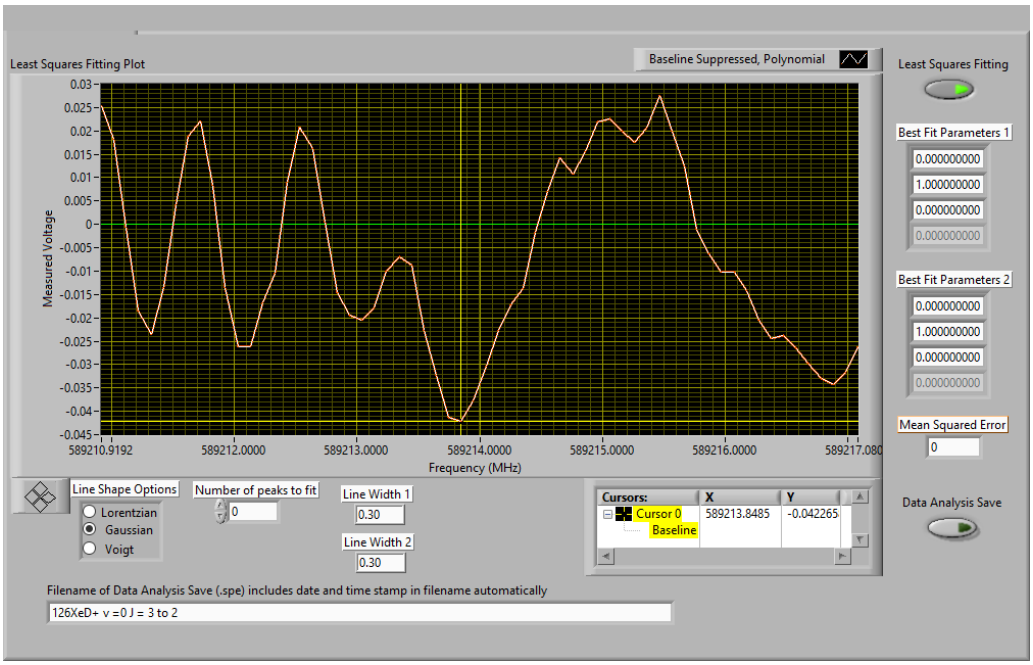


**Fig. B.6.** $^{126}XeD^{+}$ vibrational ground-state rotational transition from $J$ = 2 to $J$ = 3 observed at 589213.85 MHz.

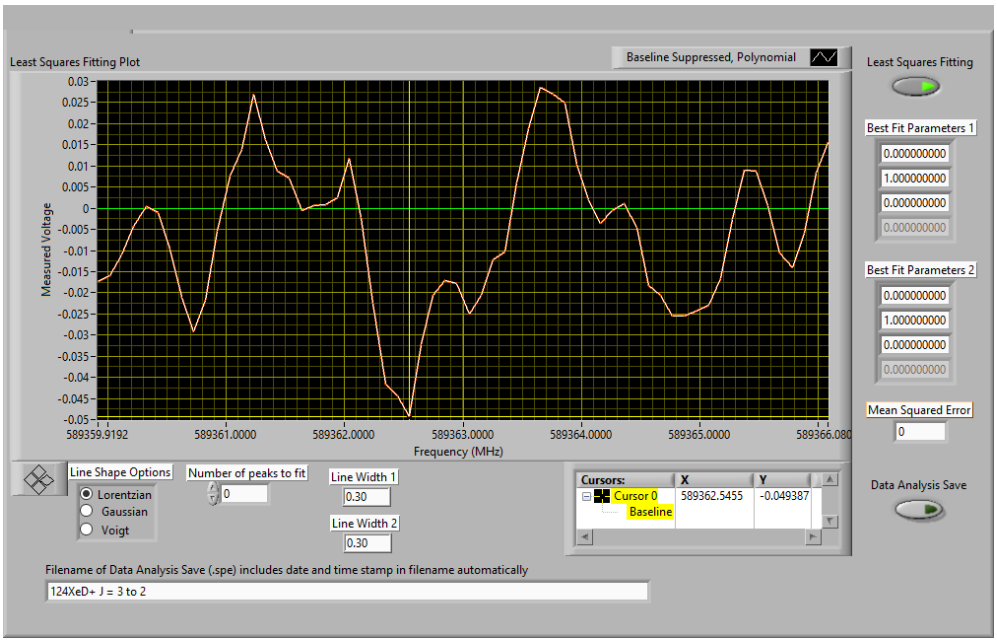


**Fig. B.7.** $^{124}XeD^{+}$ vibrational ground-state rotational transition from $J$ = 2 to $J$ = 3 observed at 589362.55 MHz.

**$H_2D^+$ and $N_2OH^+$**

The last two benchmark experiments were the observations of $H_2D^+$ and $N_2OH^+$. The experimental conditions were copied from the previous publication[5] using the University of Wisconsin – Madison spectrometer for the $H_2D^+$ discharge, which were, solenoid magnet at 300 Gauss, 1900 V discharge voltage, 8 mTorr Ar, 3 mTorr $H_2$, and 1.5 mTorr $D_2$. The same transition, $1_{10} \leftarrow 1_{11}$, was observed at 372421.47 MHz, and the signal-to-noise ratio is great with an average of 100 scans as shown in Fig. B.8. Two other works have been published on the rotational spectrum of $H_2D^+$ and $D_2H^+$. Amano and Hirao[18] improved the accuracy of rest frequencies of known transitions and measured a new transition for $H_2D^+$, $J = 3_{21} \leftarrow 3_{22}$, at 646430.293(50) MHz. They used combination differences to obtain spectroscopic constants for both species. Jusko *et al.*[19] measured the rotational spectrum of both species up to 1.5 THz using double resonance action spectroscopy. They determined spectroscopic parameters from these observed rotational transitions using the Euler formalism.

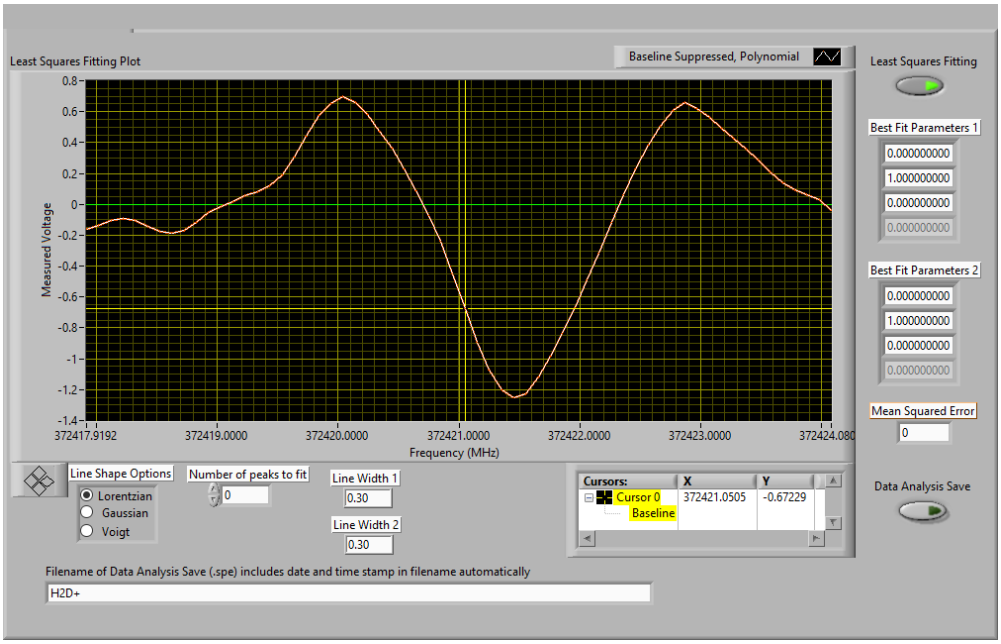


**Fig. B.8.** $H_2D^+$ vibrational ground-state rotational transition, $1_{1,0} \leftarrow 1_{1,1}$, observed at 372421.47 MHz.

The $N_2OH^+$ discharge parameters are as follows: 2 mTorr $N_2O$, 2 mTorr $H_2$, 8 mTorr argon, 2000 V for discharge voltage, and 290 Gauss for the solenoid magnet. The above parameters are the optimal parameters we found to observe the $N_2OH^+$ rotational transition at 402764.28 MHz with an average of 50 scans (Fig. B.9). The predicted transitional frequency based on the spectroscopic constants from McCarthy and Thaddeus[20] of 402764.57 MHz gives confidence that the transition observed belongs to the O-protonated form of $N_2OH^+$. McCarthy and Thaddeus[20] measured the Fourier transformed microwave spectrum of $NNOH^+$ from 5 GHz to 43 GHz using a jet pulsed supersonic expansion. The N-protonated form ~ 2000 K higher in energy was looked for given the predictions from McCarthy *et al.*[21], but it was not observed in our experiment. McCarthy *et al.*[21] measured the Fourier transformed microwave spectrum of $HNNO^+$ from 5 GHz to 43 GHz using a jet pulsed supersonic expansion. They were also able to determine several spectroscopic parameters.

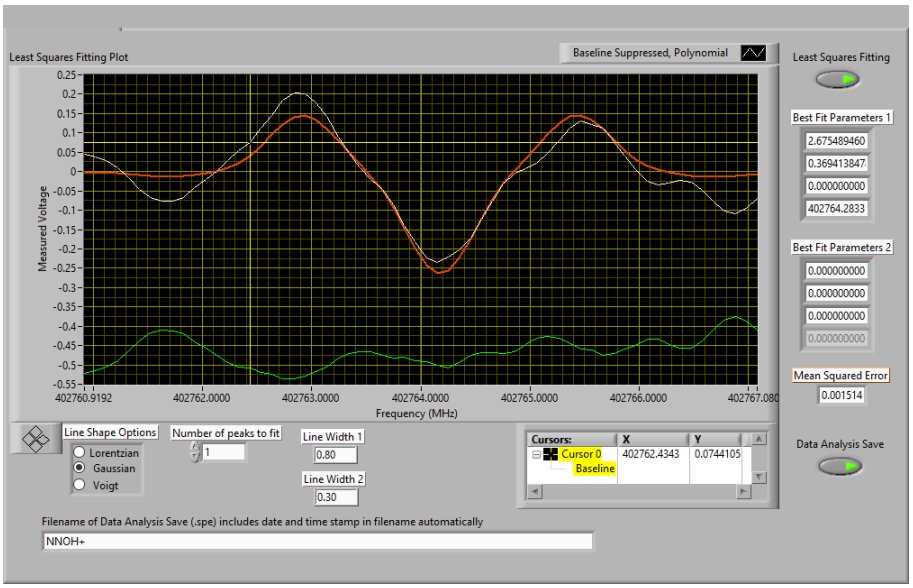


**Fig. B.9.** $N_2OH^+$ vibrational ground-state rotational transition, $18_{0,18} \leftarrow 17_{0,17}$, observed at 402764.28 MHz.

**$CH_3CO^+$ *via* CO and $CH_4$**

We attempted to repeat the experiment of Cernicharo *et al.*[11] using CO, $CH_4$, and argon gases to generate and observe the acylium cation ($CH_3CO^+$). Table B.1 contains the attempts to vary the experimental parameters to increase the abundance of acylium. Our first attempt was to use the same ratio of pressures for the gases as was done previously, which is shown in Trial 1 (Fig. B.10). All the spectra shown searching for acylium consisted of an average of 50 scans and centered around the previously observed transition at 438233.877 MHz. There is a possible detection in Fig. B.10, but the signal-to-noise ratio is barely detectable. The subsequent trials where the discharge voltage was increased did not result in any observable signals. We found Trial 29 (Fig. B.11) to have the greatest signal-to-noise ratio (~ 5), and this is where the partial pressures of CO and $CH_4$ gases were increased with respect to argon. Even after all these attempts, we were unable to achieve the signal-to-noise ratio that was obtained by Cernicharo *et al.*[11]

**Table B.1.** Experimental Conditions utilized in search for acylium rotational transition at 438233.877 MHz using CO, $CH_4$, and Ar gases.

| Trial # | CO (mTorr) | $CH_4$ (mTorr) | Ar (mTorr) | Discharge Voltage (V) | Magnet (Gauss) | Chamber (mTorr) |
|---|---|---|---|---|---|---|
| 1 | 33 | 33 | 120 | 1600 | 270 | 11 |
| 2 | 33 | 33 | 120 | 2000 | 270 | 11 |
| 3 | 33 | 33 | 120 | 2500 | 270 | 11 |
| 4 | 33 | 33 | 120 | 2300 | 270 | 11 |
| 5 | 33 | 33 | 120 | 2100 | 270 | 11 |
| 6 | 33 | 33 | 120 | 1900 | 270 | 11 |
| 7 | 33 | 33 | 120 | 1700 | 270 | 11 |
| 8 | 33 | 33 | 120 | 1500 | 270 | 11 |
| 9 | 33 | 33 | 120 | 1300 | 270 | 11 |
| 10 | 33 | 33 | 120 | 1500 | 234 | 11 |
| 11 | 33 | 33 | 120 | 1500 | 198 | 11 |
| 12 | 33 | 33 | 120 | 1500 | 162 | 11 |
| 13 | 33 | 33 | 120 | 1500 | 126 | 11 |
| 14 | 33 | 33 | 120 | 1500 | 300 | 11 |
| 15 | 33 | 33 | 80 | 1500 | 300 | 11 |

| | | | | | | |
|---|---|---|---|---|---|---|
| 16 | 33 | 33 | 60 | 1500 | 300 | 11 |
| 17 | 33 | 33 | 40 | 1500 | 300 | 11 |
| 18 | 33 | 33 | 150 | 1500 | 300 | 11 |
| 19 | 33 | 33 | 170 | 1500 | 300 | 11 |
| 20 | 33 | 33 | 190 | 1500 | 300 | 11 |
| 21 | 33 | 33 | 130 | 1500 | 300 | 11 |
| 22 | 33 | 33 | 110 | 1500 | 300 | 11 |
| 23 | 33 | 33 | 90 | 1500 | 300 | 11 |
| 24 | 66 | 66 | 120 | 1500 | 300 | 11 |
| 25 | 66 | 66 | 100 | 1500 | 300 | 11 |
| 26 | 99 | 99 | 120 | 1500 | 300 | 11 |
| 27 | 132 | 132 | 120 | 1500 | 300 | 11 |
| 28 | 165 | 165 | 120 | 1500 | 300 | 11 |
| 29 | 132 | 132 | 120 | 1500 | 300 | 11 |

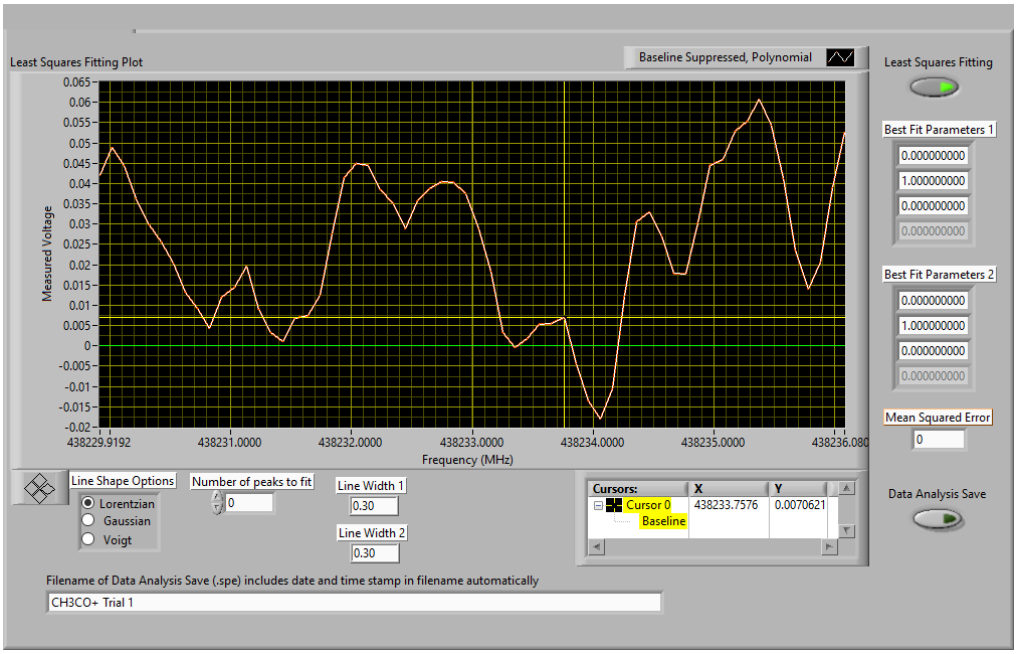


**Fig. B.10.** Trial 1 of $CH_3CO^+$ vibrational ground-state rotational transition, $24_0 \leftarrow 23_0$, previously observed at 438233.877 MHz.

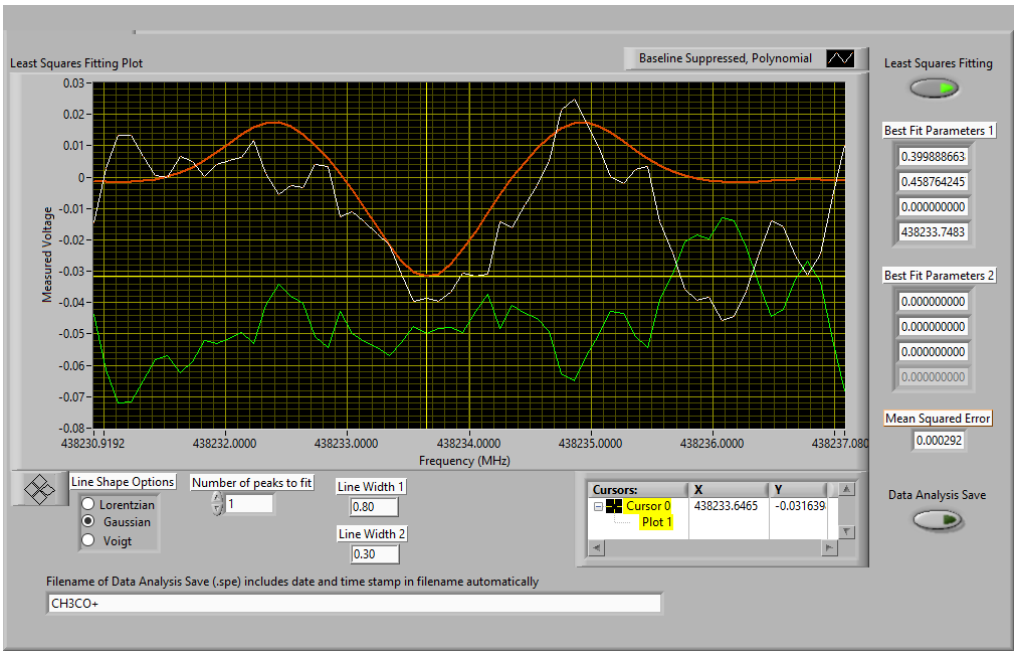


**Fig. B.11.** Trial 29 of $CH_3CO^+$ vibrational ground-state rotational transition, $24_0 \leftarrow 23_0$, previously observed at 438233.877 MHz.

### $CH_3CO^+$ *via* $H_2CCO$ and $H_2$

Our research group was interested in attempting to generate the acylium cation from a discharge comprised of ketene ($H_2CCO$), Ar, and $H_2$ gases. We believed this discharge would preferentially make acylium because both $ArH^+$ and $H_3^+$ will be generated in the electrical discharge and serve as proton sources to generate acylium. Ketene has a proton affinity of 807 kJ/mol, while Ar and $H_2$ have proton affinities of 371 kJ/mol and 421 kJ/mol, respectively.[22,23] Thus, ketene has a higher proton affinity than the other discharge components and at least thermodynamically can be protonated in this environment. Furthermore, protonation of ketene could create the acylium cation because it is the lowest-energy protonated-ketene isomer by 176.2 kJ/mol.[24] The various different experimental discharge conditions utilized to try to optimize the generation of acylium are shown in Table B.2. Figure B.12 is the experimental conditions (Trial 2) that had the greatest signal-to-noise ratio. Most of the parameters were similar to the CO, $CH_4$,

and Ar discharge except for the partial pressure of ketene, which needed to be much higher than CO or $CH_4$. This is exemplified by Fig. B.13, where no acylium signal was observed and corresponds to the lowest partial pressure of ketene utilized in the trials. Tentative detections are present in Fig. B.14 and Fig. B.15, where higher partial pressures of ketene were used in comparison to trial 7 but lower than the best signal-to-noise of trial 2. Changes in the discharge voltage and solenoid magnet seem to only worsen the signal-to-noise. Separate trials were tried previously of different magnetic fields, but they are not shown here because the signal disappeared similar to the previous experiment. In total, it seems the use of ketene, Ar, and $H_2$ as a precursor to create acylium was equivalent to using CO and $CH_4$, however, neither experiment had the expected signal-to-noise of Cernicharo *et al*.[11]

We hypothesize that the difference in the signal-to-noise observed in this work when using ketene as a precursor gas compared to Cernicharo *et al.*[11] comes from how the sample gases were mixed and cooled to liquid nitrogen temperature before entering the sample cell. Once ketene was introduced into our spectrometer, it was shown to immediately condense at liquid nitrogen temperature and resulted in very little ketene being observed in the gas phase. This depletion in ketene is one possible explanation as to why higher abundances of the acylium cation were not observed. It is also possible that the o-protonated from of ketene was kinetically favored in our discharge so high-level theoretical calculations have been completed to try to determine accurate molecular constants to predict rotational transitions and aid in its possible assignment. It is of note that Mosley *et al.*[24] found that both isomers, acylium cation and o-protonated ketene were observed depending on the small organic precursors used in a nozzle-pulsed discharge source, albeit the abundance of o-protonated ketene is less. Work is currently underway to be able to reliably control

the temperature of our spectrometer between liquid nitrogen and room temperature, and we believe this will increase the abundance of acylium observed from the ketene discharge.

**Table B.2.** Experimental Conditions utilized in search for acylium rotational transition at 438233.877 MHz using ketene, $H_2$, and Ar gases.

| Trial # | Ketene (mTorr) | $H_2$ (mTorr) | Ar (mTorr) | Discharge Voltage (V) | Magnet (Gauss) | Chamber (mTorr) |
|---|---|---|---|---|---|---|
| 1 | 150 | 60 | 115 | 2000 | 160 | 10 |
| 2 | 150 | 60 | 115 | 1500 | 160 | 10 |
| 3 | 150 | 60 | 115 | 1500 | 160 | 10 |
| 4 | 150 | 60 | 115 | 2000 | 160 | 10 |
| 5 | 150 | 60 | 115 | 2000 | 160 | 15 |
| 6 | 150 | 40 | 115 | 2000 | 160 | 15 |
| 7 | 8 | 40 | 115 | 2000 | 160 | 15 |
| 8 | 8 | 10 | 115 | 2000 | 160 | 15 |
| 9 | 150 | 100 | 115 | 2000 | 160 | 15 |
| 10 | 150 | 150 | 115 | 2000 | 160 | 15 |
| 11 | 50 | 50 | 115 | 2000 | 160 | 15 |
| 12 | 100 | 50 | 115 | 2000 | 160 | 15 |
| 13 | 100 | 50 | 115 | 2000 | 100 | 15 |
| 14 | 100 | 50 | 115 | 1500 | 160 | 10 |

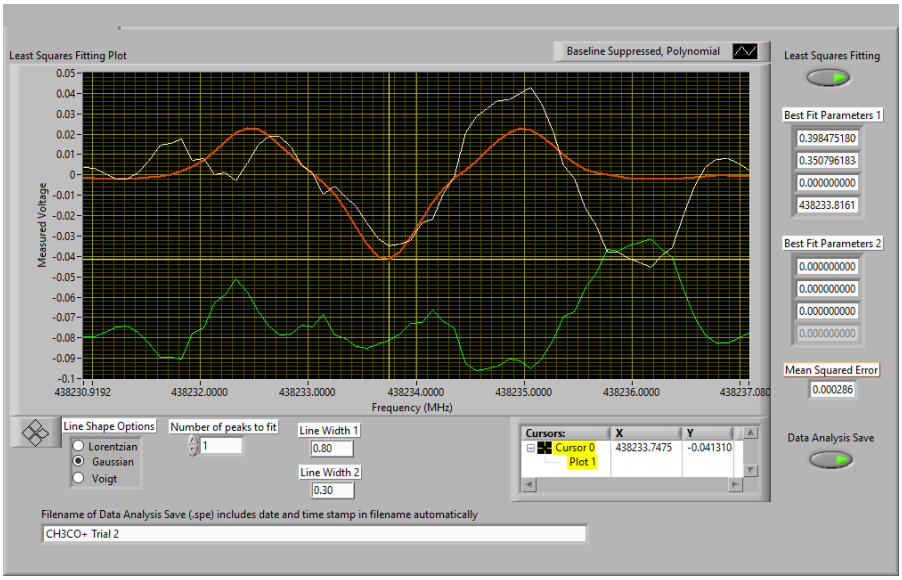


**Fig. B.12.** Trial 2 of $CH_3CO^+$ vibrational ground-state rotational transition, $24_0 \leftarrow 23_0$, previously observed at 438233.877 MHz.

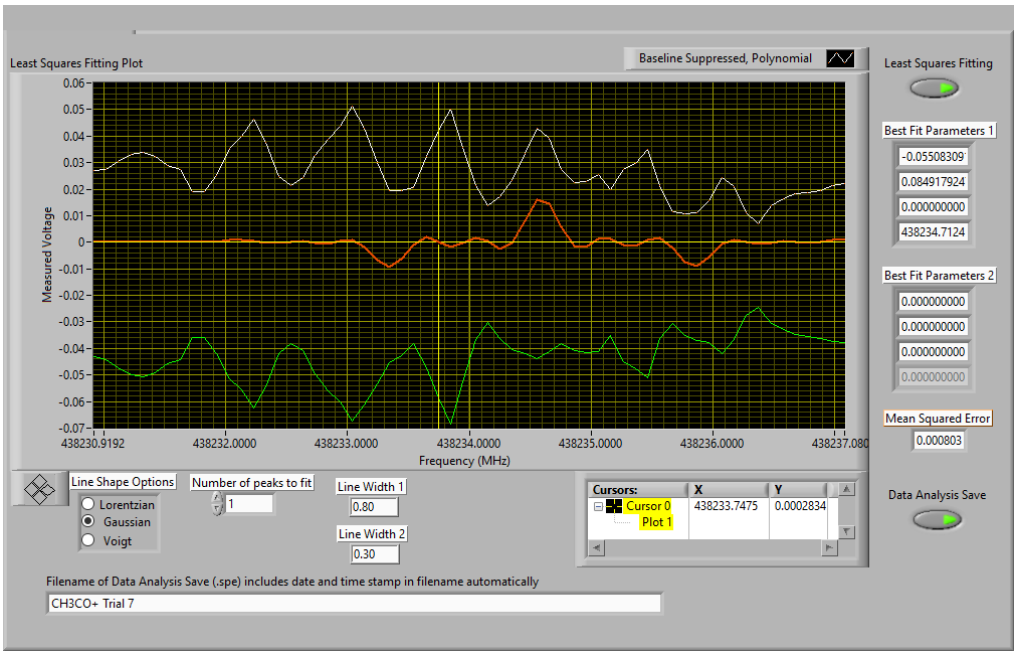


**Fig. B.13.** Trial 7 of $CH_3CO^+$ vibrational ground-state rotational transition, $24_0 \leftarrow 23_0$, previously observed at 438233.877 MHz.

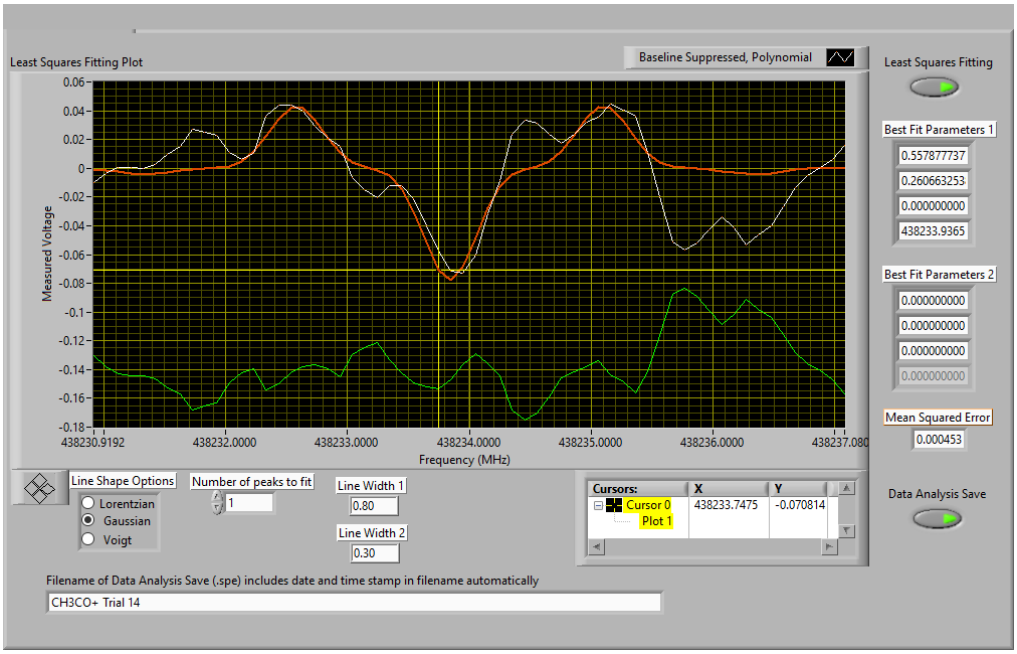


**Fig. B.14.** Trial 14 of $CH_3CO^+$ vibrational ground-state rotational transition, $24_0 \leftarrow 23_0$, previously observed at 438233.877 MHz.

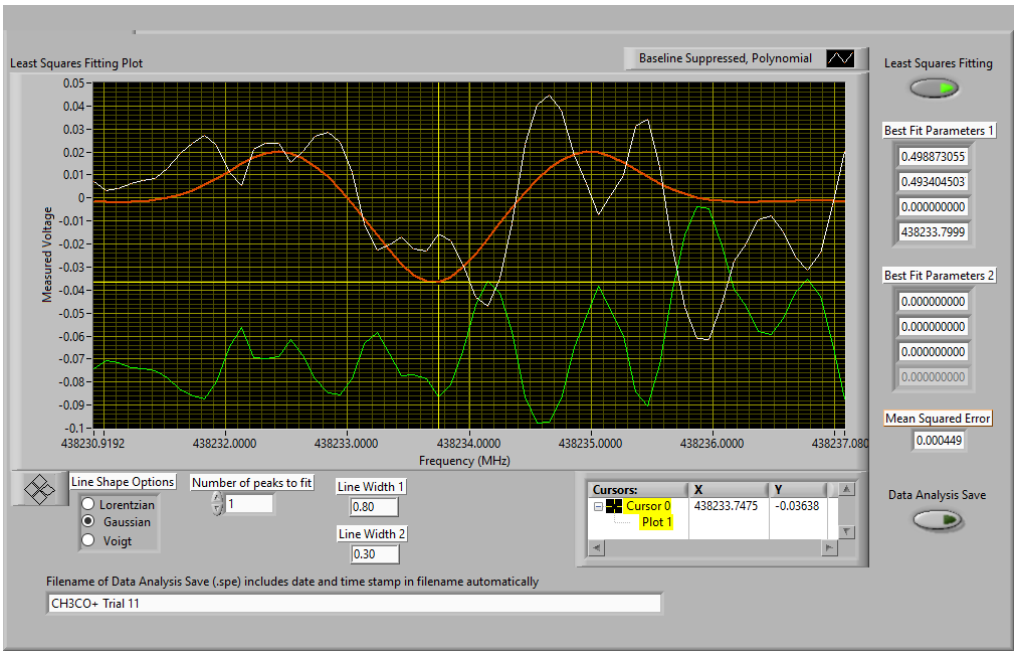


**Fig. B.15.** Trial 11 of $CH_3CO^+$ vibrational ground-state rotational transition, $24_0 \leftarrow 23_0$, previously observed at 438233.877 MHz.

# References


1. R. C. Woods, "A Microwave Spectrometer with an Internal Glow Discharge," *Rev. Sci. Instrum.* **44**, 282-288 (1973).
2. T. A. Dixon; R. C. Woods, "Microwave Absorption Spectrum of the $CO^+$ Ion," *Phys. Rev. Lett.* **34**, 61-63 (1975).
3. R. C. Woods; T. A. Dixon; R. J. Saykally; P. G. Szanto, "Laboratory Microwave Spectrum of $HCO^+$," *Phys. Rev. Lett.* **35**, 1269-1272 (1975).
4. F. C. De Lucia; E. Herbst; G. M. Plummer; G. A. Blake, "The production of large concentrations of molecular ions in the lengthened negative glow region of a discharge," *J. Chem. Phys.* **78**, 2312-2316 (1983).
5. H. E. Warner; W. T. Conner; R. H. Petrmichl; R. C. Woods, "Laboratory detection of the $1_{10}\leftarrow1_{11}$ submillimeter wave transition of the $H_2D$+ ion," *J. Chem. Phys.* **81**, 2514-2514 (1984).
6. H. E. Warner; W. T. Conner; R. C. Woods, "The lowest rotational transition of several isotopic forms of KrD+," *J. Chem. Phys.* **81**, 5413-5416 (1984).
7. B. J. Esselman; B. K. Amberger; J. D. Shutter; M. A. Daane; J. F. Stanton; R. C. Woods; R. J. McMahon, "Rotational spectroscopy of pyridazine and its isotopologs from 235–360 GHz: Equilibrium structure and vibrational satellites," *J. Chem. Phys.* **139**, 224304 (2013).
8. B. K. Amberger; B. J. Esselman; J. F. Stanton; R. C. Woods; R. J. McMahon, "Precise Equilibrium Structure Determination of Hydrazoic Acid ($HN_3$) by Millimeter-wave Spectroscopy," *J. Chem. Phys.* **143**, 104310 (2015).
9. M. A. Zdanovskaia; B. J. Esselman; R. C. Woods; R. J. McMahon, "The 130 - 370 GHz Rotational Spectrum of Phenyl Isocyanide ($C_6H_5NC$)," *J. Chem. Phys.* **151**, 024301 (2019).
10. H. H. Smith; B. J. Esselman; S. A. Wood; J. F. Stanton; R. C. Woods; R. J. McMahon, "Improved semi-experimental equilibrium structure and high-level theoretical structures of ketene," *J. Chem. Phys.* **158**, 244304 (2023).
11. J. Cernicharo; C. Cabezas; S. Bailleux; L. Margulès; R. Motiyenko; L. Zou; Y. Endo; C. Bermúdez; M. Agúndez; N. Marcelino; B. Lefloch; B. Tercero; P. de Vicente, "Discovery of the acetyl cation, $CH3CO^+$, in space and in the laboratory," *A&A* **646** (2021).
12. K. B. Laughlin; G. A. Blake; R. C. Cohen; D. C. Hovde; R. J. Saykally, "Determination of the dipole moment of $ArH^+$ from the rotational Zeeman effect by tunable far infrared laser spectroscopy," *Phys. Rev. Lett.* **58**, 996-999 (1987).
13. W. B. James; P. D. Summer, "Fundamental Vibration-Rotation Bands and Molecular Constants for the ArH+ Ground State (1Σ+)," *Phys. Scr.* **25**, 268 (1982).
14. W. C. Bowman; G. M. Plummer; E. Herbst; F. C. De Lucia, "Measurement of the J=0→1 rotational transitions of three isotopes of ArD+," *J. Chem. Phys.* **79**, 2093-2095 (1983).
15. H. Linnartz; M. Havenith; E. Zwart; W. Leo Meerts; J. J. ter Meulen, "Determination of the electric dipole moment of KrH+," *J. Mol. Spectrosc.* **153**, 710-717 (1992).
16. K. A. Peterson; R. H. Petrmichl; R. L. McClain; R. C. Woods, "Submillimeter wave spectroscopy of XeH+ and XeD+," *J. Chem. Phys.* **95**, 2352-2360 (1991).
17. Y. Ohtaki; F. Matsushima; H. Odashima; K. Takagi, "Rotational Spectra of XeH+ and Its Isotopic Species," *J. Mol. Spectrosc.* **210**, 271-274 (2001).

18. T. Amano; T. Hirao, "Accurate rest frequencies of submillimeter-wave lines of H2D+ and D2H+," *J. Mol. Spectrosc.* **233**, 7-14 (2005).
19. P. Jusko; M. Töpfer; H. S. P. Müller; P. N. Ghosh; S. Schlemmer; O. Asvany, "Double resonance rotational action spectroscopy of cold H2D+ and D2H+," *J. Mol. Spectrosc.* **332**, 33-37 (2017).
20. M. C. McCarthy; P. Thaddeus, "High-resolution rotational spectroscopy of NNOH+, DCS+, Ar···D3+, Ar···DCO+, and Ar···HN2+," *J. Mol. Spectrosc.* **263**, 71-77 (2010).
21. M. C. McCarthy; O. Martinez, Jr.; K. N. Crabtree; V. Lattanzi; S. E. Novick; S. Thorwirth, "Detection of Nitrogen-Protonated Nitrous Oxide (HNNO+) by Rotational Spectroscopy," *J. Phys. Chem. A* **117**, 9968-9974 (2013).
22. G. B. Debrou; J. E. Fulford; E. G. Lewars; R. E. March, "Ketene: Ion chemistry and proton affinity," *International Journal of Mass Spectrometry and Ion Physics* **26**, 345-352 (1978).
23. W. L. Jolly, *Modern Inorganic Chemistry*; McGraw-Hill: New York, 1991.
24. J. D. Mosley; J. W. Young; M. A. Duncan, "Infrared spectroscopy of the acetyl cation and its protonated ketene isomer," *J. Chem. Phys.* **141**, 024306 (2014).

THE JOURNAL OF PHYSICAL CHEMISTRY A
A JOURNAL OF THE AMERICAN CHEMICAL SOCIETY



pubs.acs.org/JPCA Article

# Synthesis, Purification, and Rotational Spectroscopy of 1-Cyanocyclobutene ($C_5H_5N$)

*Published as part of The Journal of Physical Chemistry virtual special issue "10 Years of the ACS PHYS Astrochemistry Subdivision".*

Houston H. Smith, Samuel M. Kougias, Brian J. Esselman, R. Claude Woods,* and Robert J. McMahon*

Cite This: *J. Phys. Chem. A* 2022, 126, 1980–1993 Read Online



**ABSTRACT:** The rotational spectrum of 1-cyanocyclobutene from 130 to 360 GHz has been observed, assigned, and least-squares fit for the ground state and the two lowest-energy vibrationally excited states. Synthesis by UV photochemical dimerization of acrylonitrile and subsequent base-catalyzed dehydrocyanation affords a highly pure sample, yielding several thousand observable rotational transitions for this small organic nitrile. Over 2500 *a*-type, R-branch transitions of the ground state have been least-squares fit to low error with partial-octic A- and S-reduced Hamiltonians, providing precise determinations of the corresponding spectroscopic constants. In both reductions, computed spectroscopic constants are in close agreement with their experimentally determined counterparts. Two vibrationally excited states ($\nu_{27}$ and $\nu_{17}$) form a Coriolis-coupled dyad, displaying many *a*-type and *b*-type local resonances and related nominal interstate transitions. Somewhat unexpectedly, despite the very small permanent *b*-axis dipole moment, a number of *b*-type transitions could be observed for the $\nu_{17}$ state; this is explained in terms of state mixing by the Coriolis perturbations. Over 2200 transitions for each of these states have been least-squares fit to a low-error, two-state, partial-octic, A-reduced Hamiltonian with nine Coriolis-coupling terms ($G_a$ , $G_a^J$, $G_a^K$, $G_a^{JJ}$, $F_{bc}$ , $F_{bc}^K$, $G_b$ , $G_b^J$, and $F_{ac}$). The availability of so many observed rotational transitions, including resonant transitions and nominal interstate transitions, enables a very accurate and precise determination of the energy difference ($\Delta E_{27,17}$ = 14.0588093 (43) cm$^{-1}$) between $\nu_{27}$ and $\nu_{17}$. The spectroscopic constants presented herein provide a starting point for future astronomical searches for 1-cyanocyclobutene.

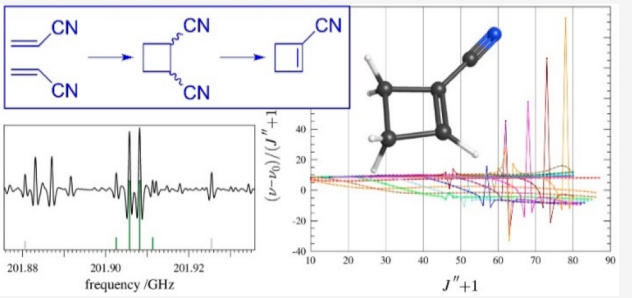


## INTRODUCTION

The interstellar medium (ISM) and circumstellar shells are known to contain complex and diverse chemical environments, with almost 250 molecules currently detected, including many new detections in the past few years.[1,2] Organic nitriles comprise an important subset of interstellar molecules because of their chemical relationship to molecules of prebiotic relevance, *e.g.*, pyridine. The cyano moiety is prevalent among organic species detected in the ISM because the typically large permanent dipole moments lead to a higher likelihood that molecules containing this functional group may be detected via radioastronomy, relative to other functionalities. The assignment of laboratory rotational spectra of organic nitriles is highly desirable to facilitate the detection of new molecules in the ISM. We have been interested in expanding two areas of organic nitrile assignments: aryl nitriles/isonitriles[3−6] and nitrile-containing isomers of pyridine.[7−10] The aryl nitriles/isonitriles are of interest as possible tracer molecules for molecular species, e.g., benzene, pyridine, pyrimidine, pyrazine, and pyridazine. While pyridine, pyrimidine, and pyridazine have permanent dipole moments, they have been sought unsuccessfully in the ISM.[11] The addition of the cyano substituent could be beneficial by significantly increasing the dipole moment, allowing the substituted species to serve as a tracer molecule for the parent species. Benzene and pyrazine do not have a permanent dipole, while the former has been detected by infrared spectroscopy, tracer molecules are necessary for their existence in the ISM to be inferred by radioastronomy. The recent detections of benzonitrile,[12] 1- and 2-cyanoaphthalene,[13] and 1-cyano-1,3-cyclopentadiene[14] signify great advances utilizing this technique and encourage further studies of the laboratory rotational spectra of nitrile-containing tracer molecules.

Nitrogen-containing isomers of pyridine ($C_5H_5N$) provide similar motivation as tracers of pyridine's presence in various environments. Importantly, the detection, or lack thereof, of

**Received:** January 17, 2022
**Revised:** February 24, 2022
**Published:** March 22, 2022

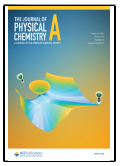







https://doi.org/10.1021/acs.jpca.2c00384
*J. Phys. Chem. A* 2022, 126, 1980−1993

particular $C_5H_5N$ isomers could help elucidate the reaction chemistry of small organic nitriles and/or pathways for formation of aromatic molecules such as pyridine. We have recently investigated seven structural isomers of pyridine (including the present case) that are shown in Figure 1, several

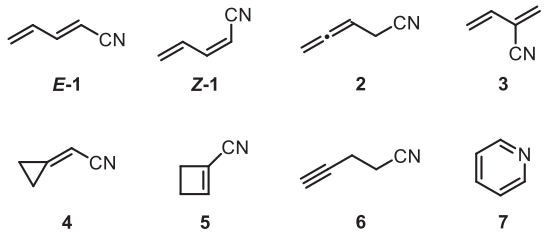


**Figure 1.** $C_5H_5N$ isomers that have been studied by rotational spectroscopy: (*E*)-1-cyano-1,3-butadiene (*E*-**1**), (*Z*)-1-cyano-1,3-butadiene (*Z*-**1**), 4-cyano-1,2-butadiene (**2**), 2-cyano-1,3-butadiene (**3**), (cyanomethylene)cyclopropane (**4**), 1-cyanocyclobutene (**5**), 4-cyano-1-butyne (**6**), and pyridine (**7**).

of which are proposed to be a part of complex, astrochemically relevant processes.[15−17] Two derivatives, *E*- and *Z*-1-cyano-1,3-butadiene (*E*-**1**, *Z*-**1**) have recently been detected *via* laboratory rotational spectroscopy in various chemical environments.[18,19] Another 1,3-butadiene derivative, 2-cyano-1,3-butadiene (**3**), has been generated by UV irradiation of cyanoacetylene and ethylene.[20] In terms of potential relevance to astrochemistry, 1-cyanocyclobutene (**5**) has been generated by photolysis of 2-cyano-1,3-butadiene,[21] and the reverse transformation can be achieved by thermolysis.[22,23] Due to their proposed importance and recent detection in reactive environments, the astronomical search for these isomers seems warranted.

1-Cyanocyclobutene (**5**), the pyridine isomer presented in this work, has a planar, four-membered ring. The $\pi$ bond within the ring enforces the planarity of the ring by greatly restricting the ability of the carbon atoms to move out-of-plane. Structurally similar, four-membered ring molecules with $\pi$-conjugated substituents have been studied by rotational spectroscopy, *e.g.*, $\beta$-propiolactone (**10**)[24−26] and diketene (**11**) (Figure 2).[27] Each of these species, like cyanocyclobutene,

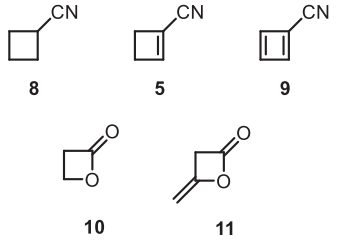


**Figure 2.** Structurally similar four-membered ring species: cyanocyclobutane (**8**), 1-cyanocyclobutene (**5**), cyano-1,3-cyclobutadiene (**9**), $\beta$-propiolactone (**10**), and diketene (**11**).

has a planar ring due to the presence of $sp^2$-hybridized carbon atoms in the ring or conjugation between ring atoms and substituents. Unlike the molecules mentioned above, rotational or vibrational spectra of 1-cyanocyclobutene (**5**) have not been reported in the literature. Cyanocyclobutane (**8**), due to its fully saturated ring, exhibits two nonplanar conformers (−CN equatorial or axial), which have been well-studied by rotational and vibrational spectroscopy.[28−32] While the fully unsaturated cyanocyclobutadiene (**9**) has been generated and characterized under matrix-isolation conditions,[33] it has not been analyzed *via* gas-phase spectroscopy. Exploration of the spectroscopy and structures of these similar compounds allows meaningful comparisons to be made of these strained four-membered ring systems.

## EXPERIMENTAL AND THEORETICAL METHODS

**Synthesis.** 1-Cyanocyclobutene (**5**) has been prepared *via* a number of synthetic methods: photoinduced 4$\pi$ electrocyclization from 2-cyano-1,3-butadiene (**3**),[21] ring expansion from 1-cyano-bicyclo[1.1.0]butane,[34] base-induced elimination from 1-chloro-2-cyanocyclobutane[22,35] or 1,2-dicyanocyclobutane,[22,35] dehydration of 1-cyclobutene-1-carboxamide,[36] or photochemical [2 + 2] cycloaddition of ethylene and cyanoacetylene.[37] To prepare a sample for analysis *via* rotational spectroscopy, the base-induced elimination of 1,2-dicyanocyclobutane described by Gale and Cherkofsky[22] was utilized. By this route, 1-cyanocyclobutene (**5**) could be selectively obtained on multigram scale in a two-step synthesis starting from acrylonitrile and isolated from the 1,2-dicyanocyclobutanes by distillation. As shown in Scheme 1, acrylonitrile (**12**) was

**Scheme 1. Syntheses of 1,2-Dicyanocyclobutane (13) and 1-Cyanocyclobutene (5)**

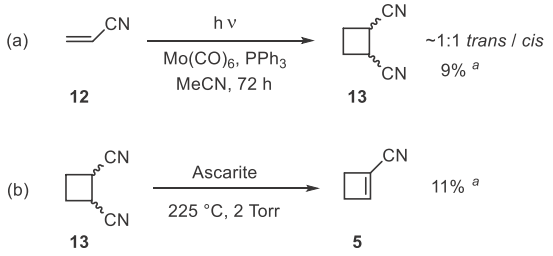


[a]Isolated yield.

photodimerized to generate 1,2-dicyanocyclobutane (**13**) *via* a [2 + 2] cycloaddition in 9% yield using $Mo(CO)_6$ as a photosensitizer.[38] Depending on the reaction conditions, this dimerization produces predominantly the *trans* stereoisomers of 1,2-dicyanocyclobutane[39] or a mixture (58:42) of *trans*- and *cis*-(1,2-dicyanocyclobutane) isomers.[40] As evidenced by the $^1$H NMR data provided in the Supporting Information, our reaction yielded an approximately 1:1 mixture of the *trans* and *cis* diastereomers. Dehydrocyanation of the mixture of 1,2-dicyanocyclobutane isomers (**13**) by passing through a heated quartz tube packed with Ascarite afforded the desired compound, 1-cyanocyclobutene (**5**), in 11% yield.

**Spectroscopy.** Using a millimeter-wave spectrometer previously described,[4,41] the rotational spectrum of 1-cyanocyclobutene was collected from 130 to 230 GHz and from 235 to 360 GHz, in a continuous flow at room temperature, with a sample pressure of 4 mTorr. The separate spectral segments were combined into a single broadband spectrum using Kisiel's Assignment and Analysis of Broadband Spectra (AABS) software.[42,43] Pickett's SPFIT/SPCAT[44] was used for least-squares fits and spectral predictions, along with the PIFORM, PLANM, and AC programs for analysis.[45,46] A uniform frequency measurement uncertainty of 50 kHz was assumed for all measurements.

**Computation.** Electronic structure calculations were carried out with Gaussian 16[47] using the WebMO[48] interface to obtain predicted values for various spectroscopic constants. Optimized


https://doi.org/10.1021/acs.jpca.2c00384
J. Phys. Chem. A 2022, 126, 1980−1993

geometries at the B3LYP/6-311+G(2d,p) and the MP2/6-311+G(2d,p) levels were obtained using "verytight" convergence criteria and an "ultrafine" integration grid, and subsequent anharmonic vibrational frequency calculations were carried out. Although the B3LYP predictions of the spectroscopic constants were adequate to begin the analysis, they did not have the expected agreement with the experimental spectroscopic constants. Thus, MP2 calculations were performed, and these had slightly closer agreement with the experimental constants. All computational output files can be found in the Supporting Information.

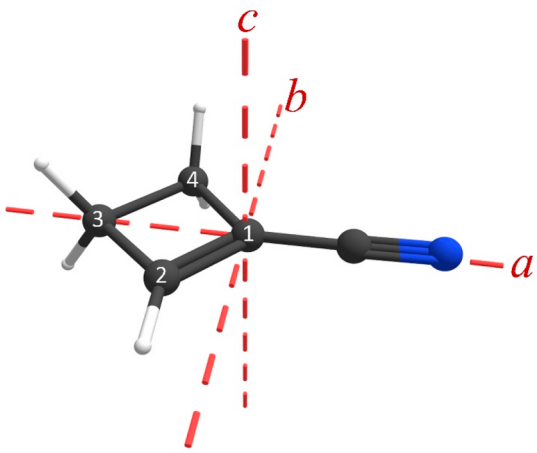


**Figure 3.** 1-Cyanocyclobutene (**5**, $C_s$, $C_5H_5N$) structure with principal inertial axes ($\mu_a$ = 4.2 D, $\mu_b$ = 0.07 D, MP2/6-311+G(2d,p)).

## RESULTS AND DISCUSSION

**Ground Vibrational State.** 1-Cyanocyclobutene (Figure 3) is a highly prolate, asymmetric top molecule ($\kappa = -0.94$) with a strong dipole moment along its *a*-principal axis ($\mu_a$ = 4.2 D, MP2) and much weaker *b*-component ($\mu_b$ = 0.07 D, MP2). The experimental spectrum from 130−360 GHz is dominated by $^aR_{0,1}$ transitions that appear in clearly observable bands sharing a single *J* value (Figure 4). In this frequency range, the (+) and (−) symmetry $^aR_{0,1}$ transitions are degenerate for the initial series, $K_a = 0^+$ and $K_a = 1^-$ but lose degeneracy at higher $K_a$. The (+) and (−) symmetry transitions become degenerate at different *J* values depending on the particular band. As the $K_a$ quantum number increases, transitions of the two symmetries attain $K_a$ degeneracy. The transitions in the series shown in Figure 4 become prolate ($K_a$) degenerate at $K_a$ = 10. This series continues to even lower frequency as the $K_a$ value increases until the transitions become too weak to be observed. These bands are separated by approximately $B_0 + C_0$ (~4.5 GHz). Transitions for the singly substituted heavy isotopologues, $^{13}C$ and $^{15}N$, could not be detected at their natural abundance. We attribute this to the spectral density arising from the ground and vibrationally excited states of the main isotopologue. Thus, the work presented herein addresses only the analysis of the ground vibrational state and first two vibrationally excited states of the normal species.

Over 2500 transitions, represented in Figure 5, have been measured and least-squares fit to partial-octic, distorted-rotor Hamiltonians in the $I^r$ representation for both the A ($\sigma_{fit}$ = 0.024 MHz) and S reductions ($\sigma_{fit}$ = 0.024 MHz). The resulting values of the spectroscopic constants are shown in Table 1, along with their computational counterparts. The computed rotational constants (MP2/6-311+G(2d,p)) are within 1% of the experimental values. Even with this relatively small difference, the predicted sum of $B_0 + C_0$ is approximately 37 MHz too small, which results in $^aR_{0,1}$ band locations off by 1.3−4.1 GHz with $J'' + 1$ ranging from 32 to 87. While line assignments inside these obvious bands are initially challenging from computational predictions, the R-branch $K_a = 0$ series, which are outside of these bands and have spacing that mainly depends on $C_0$, are the first targets for assignment. This series has been readily identified *via* a Loomis−Wood plot and subsequent assignment and least-squares fitting has been straightforward. The computed quartic centifugal distortion constants agree quite well with the experimental values, the largest discrepancies being in $\delta_J$ (5%) and in $d_2$ (6%) for the A and S reductions, respectively. Likewise, there is satisfactory agreement between the computed and experimental sextic distortion constants, with the largest discrepancies being in $\varphi_J$ (32%) and in $h_3$ (9%) for the A and S reductions, respectively. The transitions included in the final data set are insufficient to satisfactorily determine the sextic constants $\Phi_K$, $Hk$, or $h_1$. These constants are held at their computed values, in a manner similar to that in previous works where there were only *a*-type transitions across a similar range of *J* and *K* values.[4,5] Even with the inability to determine a complete set of sextic distortion constants, three octic centrifugal distortion constants, $L_{JJK}$, $L_{JK}$, and $L_{KKJ}$, have been satisfactorily determined and their inclusion improves the $\sigma_{fit}$. Presently, no commonly available computational software is able to predict octic centrifugal distortion constants, so the octic constants that are not determined have been held at zero in the least-squares fit. This likely affects the reported octic distortion constants and somewhat reduces their physical meaningfulness compared to the well-determined quartic and sextic distortion constants.

**Fundamental Vibrational States $\nu_{27}$ and $\nu_{17}$.** The vibrational energy manifold of 1-cyanocyclobutene below 550 $cm^{-1}$ (Figure 6) consists of the ground state and three sets of vibrationally excited states. The first set is a Coriolis-coupled dyad of the two lowest-energy vibrationally excited states ($\nu_{27}$ and $\nu_{17}$). The next-lowest-energy set of vibrational states consists of a likely Coriolis-, Fermi-, and Darling−Dennison-coupled tetrad of the corresponding two-quanta vibrational states ($2\nu_{27}$, $\nu_{27} + \nu_{17}$, and $2\nu_{17}$) and fundamental $\nu_{26}$. Near 500 $cm^{-1}$, the three-quanta states of $\nu_{27}$ and $\nu_{17}$ form a complex polyad with $\nu_{27} + \nu_{26}$, $\nu_{17} + \nu_{26}$, $\nu_{25}$, and $\nu_{16}$. While all of these states are sufficiently intense to be observed in the current spectral data, this work strictly focuses on the Coriolis-coupled dyad of $\nu_{27}$ and $\nu_{17}$ at ca. 165 $cm^{-1}$. The lowest-energy fundamental state, $\nu_{27}$ (A″, 159 $cm^{-1}$), is an out-of-plane bend of the cyano substituent, with a simultaneous distortion of the cyclobutene ring by a large motion of the $C(3)H_2$ group with respect to C(1). The second-lowest-energy fundamental state, $\nu_{17}$ (A′, 173 $cm^{-1}$), is an in-plane bend of the cyano substituent, combined with some in-plane distortion of the cyclobutene ring. The two lowest-energy vibrational states are expected to have strong interactions, due to the small predicted energy separation (14 $cm^{-1}$) and the combination of relatively large $A_\nu$ rotational constants, Coriolis $\zeta$ values, and *J* values observed in this frequency range. As expected, a single-state model cannot adequately predict or fit the transitions observed for either vibrationally excited state. Therefore, a two-state, partial-octic, A-reduced Hamiltonian has been employed to model $\nu_{27}$ and $\nu_{17}$ in a manner similar to that in our previous work on (cyanomethylene)cyclopropane.[10] The least-squares fit incor-


https://doi.org/10.1021/acs.jpca.2c00384
J. Phys. Chem. A 2022, 126, 1980−1993

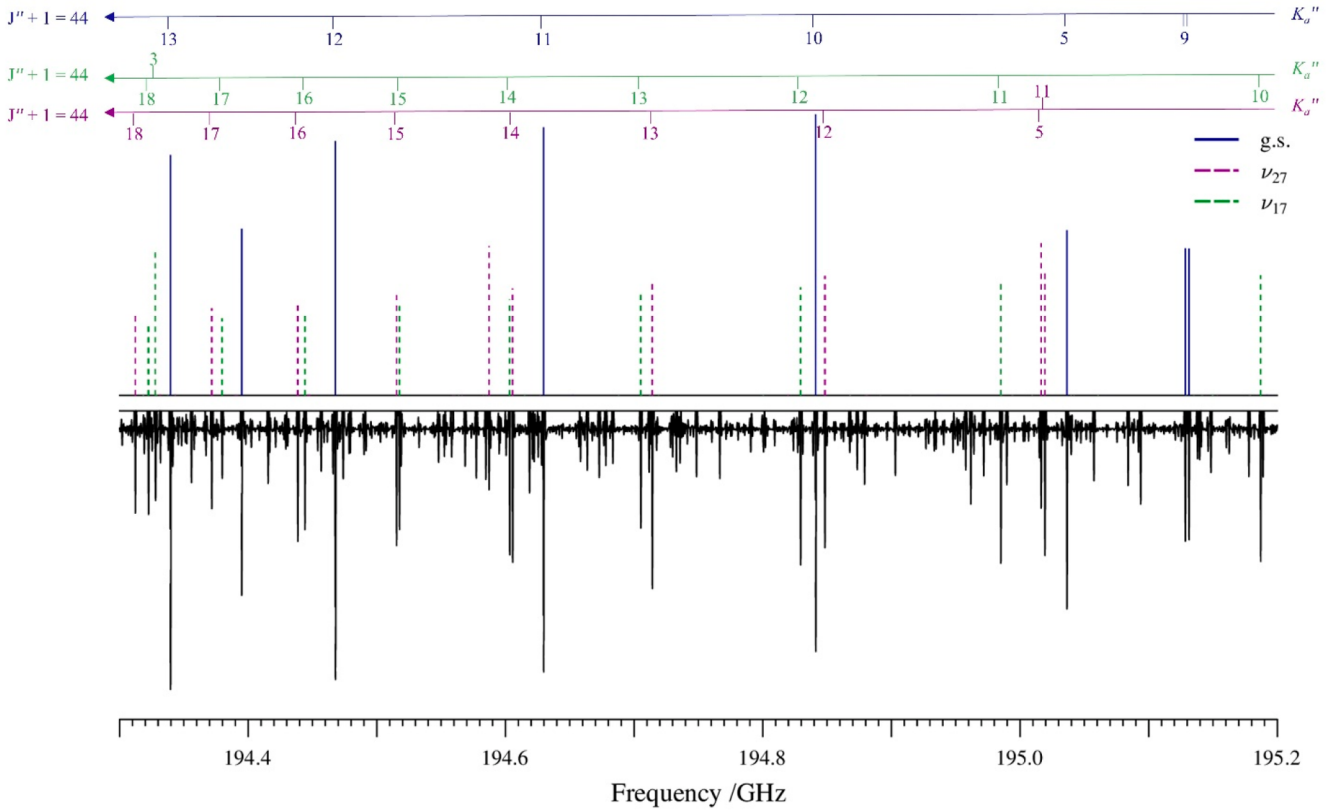


**Figure 4.** Predicted (top) and experimental (bottom) rotational spectra of 1-cyanocyclobutene (**5**) from 194.3 to 195.2 GHz. Ground-state transitions for the $J'' + 1 = 44$ band appear in dark blue, $\nu_{27}$ in purple, and $\nu_{17}$ in green. The complete frequency spectrum from 130 to 360 GHz was obtained automatically over approximately 6 days given these experimental parameters: 0.6 MHz/s sweep rate, 10 ms time constant, and 50 kHz AM and 500 kHz FM modulation in a tone burst design.

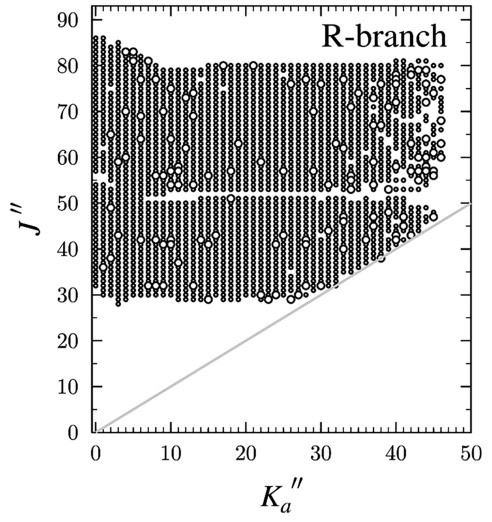


**Figure 5.** Data distribution plots for the least-squares fit of spectroscopic data for the vibrational ground state of 1-cyanocyclobutene (**5**). R-branch transitions are represented by black circles. The size of the symbol is proportional to the value of $|(f_{obs} - f_{calc})/\delta f|$, where $\delta f$ is the frequency measurement uncertainty, and all values are smaller than 3.

porates at least 2200 transitions for each vibrationally excited state and has a low statistical error ($\sigma_{fit}$ = 0.031 MHz). The wide range of $J$ (28−87) and $K_a$ (0−46 and 43 for $\nu_{27}$ and $\nu_{17}$, respectively) quantum numbers recorded is illustrated in the data set distribution plot (Figure 7). This distribution of least-squares fit transitions is only slightly diminished in comparison to the vibrational ground state, due to the low energy (and thus high population) of these vibrationally excited states.

The spectroscopic constants resulting from the final least-squares fit (Table 2) include a precise determination of the rotational constants for each vibrational state. The rotational constants are well determined for each state, and the largest experimental uncertainty appears in the values of the $A_v$ constants, whose relative statistical uncertainties are only 0.003% of their values. The near-absence of *b*-type transitions (*vide infra*), due to the very small $\mu_b$ value, contributes to this diminished precision of $A_v$, as in the ground state. As has been shown for similar cases,[3−5,49] the Coriolis-coupled dyad increases the uncertainty in the $A_v$ rotational constants somewhat, due to the high correlation between $A_v$ and the *a*-type Coriolis parameters. A full set of quartic distortion constants and a few ($\Phi_J$ , $\Phi_{JK}$ , and $\Phi_{KJ}$) sextic distortion constants have been determined for each vibrational state. All distortion constants that cannot be determined in the fit have been held constant at their corresponding ground-state values. There are no clear signs of Coriolis coupling being absorbed by the quartic distortion constants, and all are within expected deviations from the ground state (<10%, except $\Delta_K$ at 15% for $\nu_{27}$).

**Coriolis-Coupling Analysis.** The least-squares fit determines a precise energy separation ($\Delta E_{27,17}$ = 421472.50 (13) MHz; 14.0588093 (43) cm$^{-1}$) between $\nu_{27}$ and $\nu_{17}$. The computed energy difference (13.8 cm$^{-1}$; MP2) agrees very well


https://doi.org/10.1021/acs.jpca.2c00384
J. Phys. Chem. A 2022, 126, 1980−1993

**Table 1. Spectroscopic Constants for the Ground Vibrational State of 1-Cyanocyclobutene (S- and A-Reduced Hamiltonian, $I^r$ Representation)**

| | S Reduction, $I^r$ representation | | | A Reduction, $I^r$ representation | |
|---|---|---|---|---|---|
| | Experimental | MP2 [a] | | Experimental | MP2 [a] |
| $A_0$ (MHz) | 12492.5719 (78) | 12418 | $A_0$ (MHz) | 12492.5807 (81) | 12418 |
| $B_0$ (MHz) | 2364.413212 (66) | 2344 | $B_0$ (MHz) | 2364.41929 (11) | 2344 |
| $C_0$ (MHz) | 2038.935375 (72) | 2022 | $C_0$ (MHz) | 2038.929419 (99) | 2022 |
| $D_J$ (kHz) | 0.112235 (11) | 0.108 | $\Delta_J$ (kHz) | 0.135307 (18) | 0.129 |
| $D_{JK}$ (kHz) | 5.513431 (92) | 5.39 | $\Delta_{JK}$ (kHz) | 5.37497 (12) | 5.26 |
| $D_K$ (kHz) | 3.046 (74) | 3.18 | $\Delta_K$ (kHz) | 3.252 (75) | 3.28 |
| $d_1$ (kHz) | −0.0204606 (23) | −0.0194 | $\delta_J$ (kHz) | 0.020490 (11) | 0.0194 |
| $d_2$ (kHz) | −0.0115338 (69) | −0.0108 | $\delta_K$ (kHz) | 2.9188 (18) | 2.80 |
| $H_J$ (Hz) | −0.00004395 (77) | −0.0000441 | $\Phi_J$ (Hz) | 0.0000146 (19) | 0.0000103 |
| $H_{JK}$ (Hz) | 0.011349 (15) | 0.0109 | $\Phi_{JK}$ (Hz) | 0.01604 (32) | 0.0155 |
| $H_{KJ}$ (Hz) | −0.070845 (85) | −0.0718 | $\Phi_{KJ}$ (Hz) | −0.0875 (11) | −0.0880 |
| $H_K$ (Hz) | [0.0710] | 0.071 | $\Phi_K$ (Hz) | [0.0825] | 0.0825 |
| $h_1$ (Hz) | [−0.000000621] | −0.000000621 | $\phi_J$ (Hz) | 0.00000622 (99) | 0.00000417 |
| $h_2$ (Hz) | 0.00002895 (78) | 0.0000272 | $\phi_{JK}$ (Hz) | 0.00802 (20) | 0.00774 |
| $h_3$ (Hz) | 0.00000527 (33) | 0.00000479 | $\phi_K$ (Hz) | 0.163 (14) | 0.165 |
| $L_{JJK}$ (μHz) | −0.0000326 (12) | | $L_{JJK}$ (μHz) | −0.0000387 (12) | |
| $L_{JK}$ (μHz) | 0.0004759 (53) | | $L_{JK}$ (μHz) | 0.000300 (16) | |
| $L_{KKJ}$ (μHz) | −0.005681 (28) | | $L_{KKJ}$ (μHz) | −0.005089 (57) | |
| $\Delta_i$ (uÅ$^2$) [b,c] | −6.334144 (27) | | $\Delta_i$ (uÅ$^2$) [b,c] | −6.332842 (31) | |
| $N_{lines}$ [d] | 2529 | | $N_{lines}$ [d] | 2529 | |
| $\sigma_{fit}$ (MHz) | 0.024 | | $\sigma_{fit}$ (MHz) | 0.024 | |

[a]Evaluated with the 6-311+G(2d,p) basis set. [b]Inertial defect, $\Delta_i = I_c - I_a - I_b$. [c]Calculated using PLANM from the $B_0$ constants. [d]Number of fitted transition frequencies

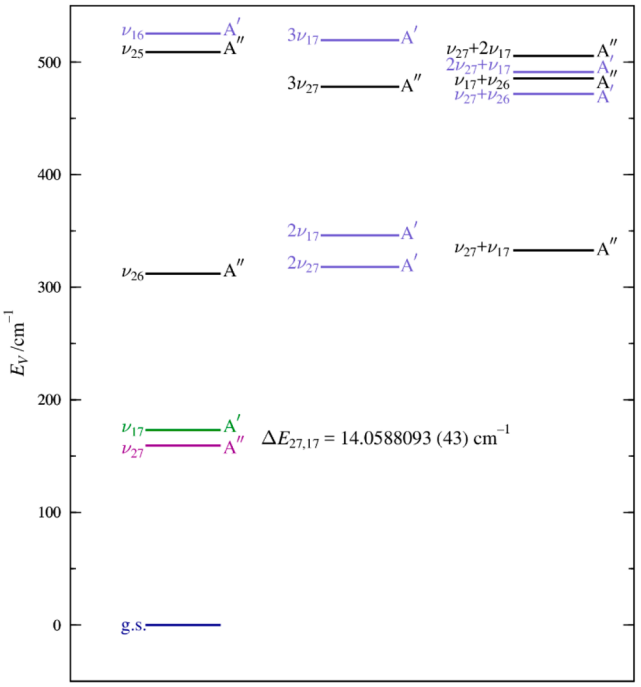


**Figure 6.** Vibrational energy levels of 1-cyanocyclobutene (**5**) below 550 cm$^{-1}$ from computed fundamental frequencies (MP2/6-311+G-(2d,p)). The value of $\Delta E_{27,17}$ results from the experimental perturbation analysis of $\nu_{27}$ and $\nu_{17}$ in this work.

with the experimentally determined value. The B3LYP computed value (17.9 cm$^{-1}$) is slightly overpredicted (ca. 5 cm$^{-1}$), as is the case in several similar works involving coupled dyads.[3−6,9] The high precision of the experimental value of $\Delta E_{27,17}$ arises because the data set includes all of the following: (i) numerous rotational transitions involved in global interactions between the two fundamentals, (ii) rotational transitions involved in local resonances occurring from energy-level crossings, and (iii) (formally forbidden) interstate transitions that involve changes in both rotational and vibrational quantum numbers. The symmetries of the two fundamentals, $\nu_{27}$ (A″, 159 cm$^{-1}$) and $\nu_{17}$ (A′, 173 cm$^{-1}$), allow for both *a*- and *b*-type Coriolis coupling between the states. The final least-squares fit requires incorporation of nine Coriolis-coupling terms ($G_a$ , $G_a^J$, $G_a^K$, $G_a^{JJ}$, $F_{bc}$ , $F_{bc}^K$, $G_b$ , $G_b^J$, $F_{ac}$) to quantitatively account for both of these types of coupling across the observed spectrum.

The initial fitting process of the first several $K_a$ series for each vibrational state has been accomplished by varying the energy separation and the $G_a$ value to account for, and adequately predict, the global undulation that is present for each series. This global undulation in Figure 8 appears to be small relative to the magnitude of the local resonances at higher $J$ and $K_a$. Figures 9 and 10, however, better illustrate the substantial impact of the global undulation on several $K_a$ series. The undulation is observed at low $J$ for low $K_a$ series and progresses higher in $J$ as $K_a$ increases until approximately $K_a$ = 20 for $\nu_{27}$ (lower for $\nu_{17}$) where the position of the global undulation has increased to $J$ values beyond the range investigated in this experiment. The values of $J$ for a particular $K_a$ at which the global undulation is most apparent are always those that correspond to the changeover from oblate asymmetric top behavior at low $J$ to prolate-like at high $J$. During fitting, if any local resonances are predicted in the $K_a$ series, transitions involved in the resonance, along with several transitions at lower and higher $J$ values, are omitted from the fit until the global undulation is treated well. Once the global perturbation is well predicted, the local


https://doi.org/10.1021/acs.jpca.2c00384
J. Phys. Chem. A 2022, 126, 1980−1993

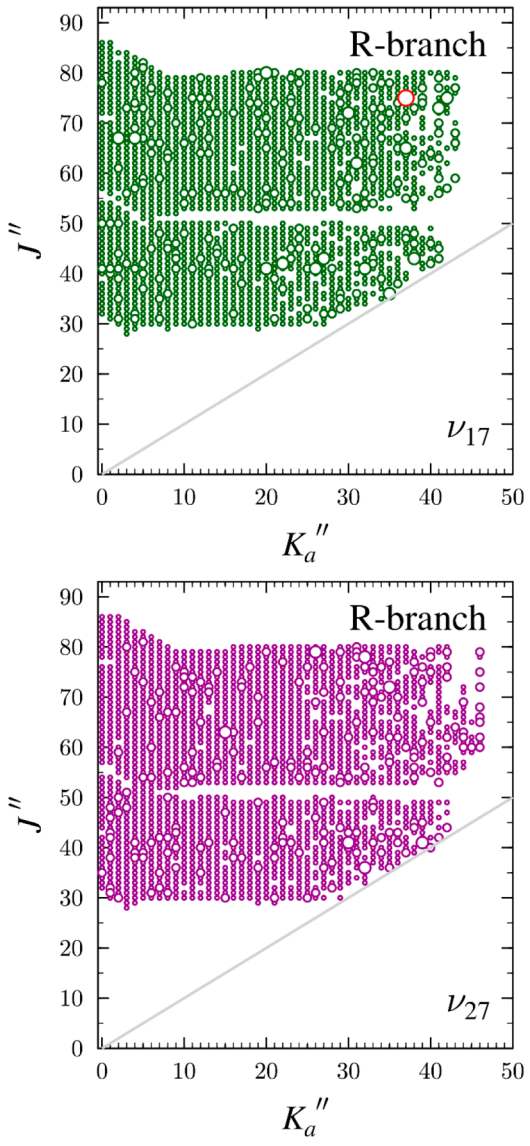


**Figure 7.** Data distribution plot for data in the two-state fit of $\nu_{27}$ and $\nu_{17}$ of 1-cyanocyclobutene (**5**). The size of the plotted symbol is proportional to the value of $|(f_{obs} - f_{calc})/\delta f|$, where $\delta f$ is frequency measurement uncertainty, and values greater than or equal to 3 are marked in red.

resonances can be more readily assigned. As more transitions are incorporated into the least-squares fit, additional coupling terms are needed to account for the complex interactions between the two fundamental states. During the fitting process, all centrifugal distortion constants are monitored for signs of absorbed Coriolis perturbation or unfavorable correlations between distortion and coupling constants. This iterative process allows for a fully predictive fit to be achieved, which in turn makes it possible to perform a final frequency sweep measuring and recording every visible transition for each fundamental. Lastly, the nominal interstate transitions are measured and included in the least-squares fit in all cases where confident assignments can be made (*vide infra*).

Figure 8 illustrates the regularity of the *a*-type local resonances, which begin at $K_a = 4^-$ at $J = 48$ and subsequently increase in $J$ by five until the end of the measured frequency range. As the local resonances progress to higher $J$, their magnitude increases with the largest resonance occurring at $K_a = 10^-$. This most displaced transition at $J = 78$ is approximately 9 GHz away from its unperturbed predicted position. A significant number of resonances (~40) are observed, with the majority being *a*-type resonances. The *a*-type resonances are also significantly larger in magnitude than *b*-type resonances, as can be seen in Figures 9 and 10.

A few *a*-type resonances are shown in Figure 9a; the $K_a = 1^-$ series of $\nu_{17}$ has two *a*-type resonances, at $J = 37$ and 47, with $\Delta K_a = 4$ and 2 selection rules, respectively. The paired resonance at $J = 37$ is in Figure 9c with the $K_a = 5^+$ ($\Delta K_a = 4$) series of $\nu_{27}$ and is obscured by the global undulation. The magnitude of the resonance and $J$ value are exactly the same in the two series, although the different scale factors in the plots make this more difficult to see in the figure. The second paired local resonance at $J = 47$ is shown in Figure 9b with the $K_a = 3^+$ ($\Delta K_a = 2$) series of $\nu_{27}$, and in this case the symmetry is more visually obvious. Figure 9d containing the $K_a = 3^-$ series of $\nu_{17}$ is included because it shows another paired resonance for the $K_a = 5^+$ series of $\nu_{27}$ at $J = 58$. The $K_a = 3^-$ series of $\nu_{17}$ has a second resonance at $J = 43$, which is paired with the $K_a = 7^+$ series of $\nu_{27}$ (not shown). An example of a *b*-type local resonance at $J = 72,73$ is shown in Figure 10, between the $K_a = 9^+$ series of $\nu_{17}$ and the $K_a = 12^+$ series of $\nu_{27}$ ($\Delta K_a = 3$). The $\Delta K_a$ selection rule is always even for *a*-type and odd for *b*-type resonances; in addition, there is a change in symmetry for *a*-type and no change in symmetry for *b*-type coupling.

An additional indication of unaddressed Coriolis coupling would be if the vibration−rotation interaction constants for $\nu_{27}$ and $\nu_{17}$ exhibit large, equal and opposite values. The $B_0 - B_v$ and $C_0 - C_v$ values presented in Table 3 are relatively small in magnitude, exhibit the same sign, and show excellent agreement between experiment and theory. These observations support the interpretation that these values are physically meaningful and that their corresponding rotational constants are well determined and likely free of residual Coriolis-coupling effects. The experimental and computational $A_0 - A_v$ values are in quite poor agreement and are much larger in magnitude than the $B_0 - B_v$ or $C_0 - C_v$ values for each vibrational state. It is unclear to what extent these large values of $A_0 - A_v$ and the disagreement between their theoretical and experimental values are caused by residual unaddressed Coriolis coupling or by poorly estimated $A_0 - A_v$ values. A similar observation was made for the $A_0 - A_v$ values in the analogous Coriolis-coupled dyad of (cyanomethylene)cyclopropane.[10] The discrepancy is larger for 1-cyanocyclobutene (**5**), but, for both molecules, the computed values for these interactions are of opposite sign than the fitted ones. Given the close agreement in the averages of these values, at least some untreated coupling must be manifest in the experimental and/or theoretical values. The very large data sets and the overall quality of the least-squares fits, however, make it possible that $A_{27}$ and $A_{17}$ are close to their true values, despite the discrepancy with the theoretical calculations.

The lowest-order spectroscopic Coriolis coupling parameters, $G_a$ and $G_b$ can be predicted, given the Coriolis constant $\zeta$, by eq 1, where $\omega$ is the harmonic vibrational frequency of the corresponding mode and $x$ is the corresponding inertial axis.

$$G_x = \frac{\omega_{27} + \omega_{17}}{\sqrt{\omega_{27} \times \omega_{17}}} \zeta^x_{27,17} B^x_e \approx 2\zeta^x_{27,17} B^x_e \quad (1)$$

The experimental $\zeta$ values in Table 3 are calculated from eq 1 using harmonic frequencies computed by MP2, the exper-


https://doi.org/10.1021/acs.jpca.2c00384
J. Phys. Chem. A 2022, 126, 1980−1993

**Table 2. Spectroscopic Constants for Vibrationally Excited States $\nu_{27}$ and $\nu_{17}$ of 1-Cyanocyclobutene (5) (A-Reduced Hamiltonian, $I^r$ Representation)**

| | Ground State | $\nu_{27}$ (A", 159 cm$^{-1}$) [a,b] | $\nu_{17}$ (A', 173 cm$^{-1}$) [a,b] |
|---|---|---|---|
| $A_0$ (MHz) | 12492.5807 (81) | 12576.09 (31) | 12402.39 (31) |
| $B_0$ (MHz) | 2364.41929 (11) | 2367.99024 (40) | 2370.86901 (39) |
| $C_0$ (MHz) | 2038.929419 (99) | 2043.148392 (65) | 2041.224377 (62) |
| $\Delta_J$ (kHz) | 0.135307 (18) | 0.138684 (12) | 0.139633 (12) |
| $\Delta_{JK}$ (kHz) | 5.37497 (12) | 5.53104 (59) | 5.16909 (58) |
| $\Delta_K$ (kHz) | 3.252 (75) | 3.744 (25) | 3.233 (29) |
| $\delta_J$ (kHz) | 0.020490 (11) | 0.0205743 (24) | 0.0219861 (20) |
| $\delta_K$ (kHz) | 2.9188 (18) | 2.92104 (42) | 2.99398 (54) |
| $\Phi_J$ (Hz) | 0.0000146 (19) | 0.00002013 (98) | 0.0000183 (10) |
| $\Phi_{JK}$ (Hz) | 0.01604 (32) | 0.016545 (44) | 0.015331 (43) |
| $\Phi_{KJ}$ (Hz) | −0.0875 (11) | −0.10018 (25) | −0.06685 (23) |
| $\Phi_K$ (Hz) | [0.0825] | [0.0825] | [0.0825] |
| $\phi_J$ (Hz) | 0.00000622 (99) | [0.00000622] | [0.00000622] |
| $\phi_{JK}$ (Hz) | 0.00802 (20) | [0.00802] | [0.00802] |
| $\phi_K$ (Hz) | 0.163 (14) | [0.163] | [0.163] |
| $\Delta E$ | | 421472.50 (13) MHz / 14.0588093 (43) cm$^{-1}$ | |
| $G_a$ (MHz) | | 19993.0 (33) | |
| $G_a^J$ (MHz) | | −0.016787 (14) | |
| $G_a^K$ (MHz) | | −0.2226 (14) | |
| $G_a^{JJ}$ (MHz) | | 0.00000003739 (26) | |
| $F_{bc}$ (MHz) | | −0.1191 (29) | |
| $F_{bc}^K$ (MHz) | | −0.00010156 (99) | |
| $G_b$ (MHz) | | 97.09 (85) | |
| $G_b^J$ (MHz) | | −0.780 (57) | |
| $F_{ac}$ (MHz) | | −0.0004476 (74) | |
| $\Delta_i$ (uÅ$^2$) [c,d] | −6.332842 (31) | −6.25371 (99) | −6.3242 (10) |
| $N_{lines}$ [e] | 2529 | 2300 | 2233 |
| $\sigma_{fit}$ (MHz) | 0.024 | 0.030 | 0.032 |

[a]Fundamental frequencies calculated using MP2/6-311+G(2d,p). [b]Octic centrifugal distortion constants (not shown) were held constant at their ground-state values. [c]Inertial defect, $\Delta_i = I_c - I_a - I_b$. [d]Calculated using PLANM from the $B_0$ constants. [e]Number of fitted transition frequencies.

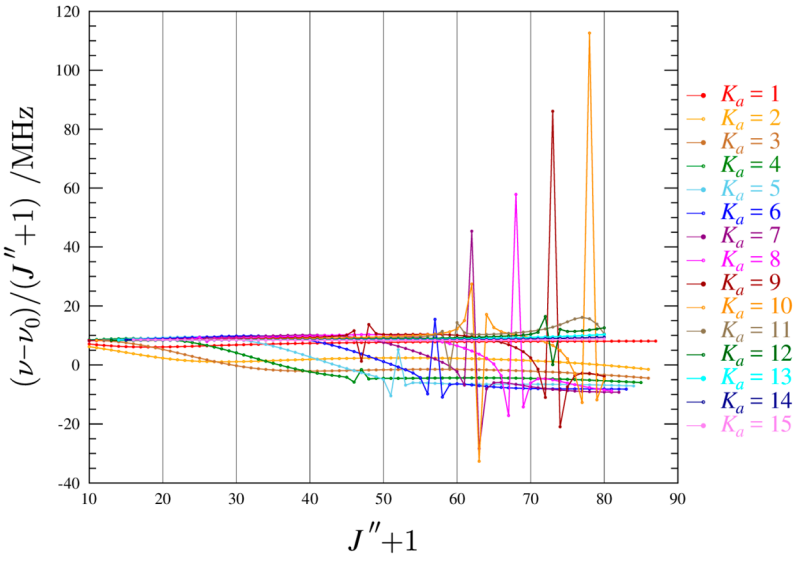


**Figure 8.** Superimposed resonance plots of $\nu_{27}$ for $^aR_{0,1}$ $K_a^-$ series from 1 to 15 for 1-cyanocyclobutene (**5**). Measured transitions are omitted for clarity, but they are indistinguishable from the plotted values on this scale. The plotted values are frequency differences between excited-state transitions and their ground-state counterparts, scaled by $(J'' + 1)$.

imentally determined $G_x$, and rotational constants corrected by half the sum of the corresponding MP2 vibration−rotation interaction constants for all vibrations. The experimental value of $\zeta^a_{27,17}$ is slightly greater than the computational predictions, while the experimental value of $\zeta^b_{27,17}$ is smaller by a similar magnitude.

The observed resonances are a result of state mixing between $\nu_{27}$ and $\nu_{17}$. This state mixing can result in interstate transitions, where simultaneous changes in rotational and vibrational quantum numbers occur. The energy separation in the Coriolis-coupled dyad, $\nu_{27}$ and $\nu_{17}$ (14.0588093 (43) cm$^{-1}$), is small enough to cause intense local resonances and state mixing,


https://doi.org/10.1021/acs.jpca.2c00384
J. Phys. Chem. A 2022, 126, 1980−1993

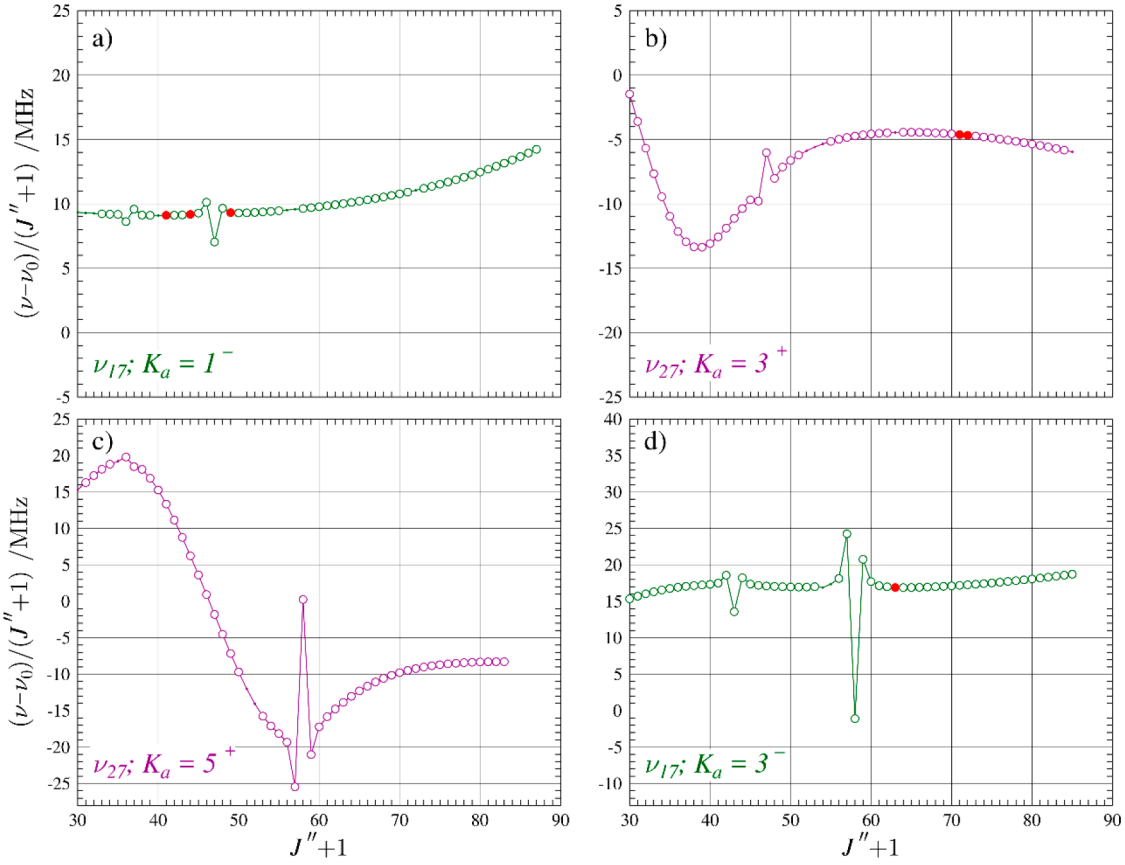


**Figure 9.** Resonance plots for 1-cyanocyclobutene (**5**) showing the $K_a = 1^-$ and $3^-$ series for $\nu_{17}$ and $K_a = 3^+$ and $5^+$ series for $\nu_{27}$. These are examples of resonances conforming to the $\Delta K_a = 2$ or 4 selection rules for *a*-type resonances. The plotted values are frequency differences between excited-state transitions and their ground-state counterparts, scaled by $(J'' + 1)$ in order to make the plots more horizontal. Measured transitions are represented by circles: $\nu_{27}$ (purple), $\nu_{17}$ (green). The measured transitions with $|(f_{obs} - f_{calc})/\delta f| > 3$ are marked in red. Predictions from the final coupled fit are represented by a solid, colored line.

and this allows a significant number (57) of nominal interstate transitions to be assigned. These transitions are assigned by comparison of the experimental and predicted frequencies, as well as by comparison of the observed average frequencies, which should ideally be exactly the same for matched sets of corresponding inter- and intrastate transitions. Two nominal interstate transitions, along with their corresponding intrastate transitions, are shown in Figure 11. Each measured transition includes its *obs.*−*calc.* value in parentheses. The average frequencies of the inter- and intrastate transitions shown in Figure 11 differ by only 62 kHz, illustrating the accuracy of the measurements and the correctness of the assignments. The corresponding intrastate resonances ($J'' + 1 = 73$) from the $K_a = 9^-$ series of $\nu_{27}$ and the $K_a = 5^+$ series of $\nu_{17}$ are displayed in Figure 11 to illustrate that the resonances and observable interstate transitions occur at the same $J$ values, as a result of significant state mixing. For example, the smallest energy separation, $\Delta E = 8984$ MHz, occurs between $73_{9,65}$ for $\nu_{27}$ and $73_{5,68}$ for $\nu_{17}$, which corresponds to the intrastate transitions most shifted in frequency for each vibrational state.

A rarely reported type of intensity enhancement by state mixing has been found in this spectrum. 1-Cyanocyclobutene has a quite small *b*-type dipole moment ($\mu_a = 4.2$ D, $\mu_b = 0.07$ D, MP2), which prevents observation of any *b*-type transitions in the ground state or in $\nu_{27}$. Due to the Coriolis-coupling between $\nu_{27}$ and $\nu_{17}$, however, indirect state mixing enhances the intensity of approximately 35 *b*-type transitions for $\nu_{17}$ sufficiently that they become measurable and are included in the least-squares fit of the coupled dyad. As exemplified in the Loomis−Wood plot in Figure 12, many of these intense *b*-type transitions occur near the *J*-levels where degeneracy of the $^aR_{0,1}$ $K_a^+$ and $K_a^-$ series is established, and also near, but not necessarily exactly coincident with, *J* values where local resonances are observed between the two vibrational states. In most $K_a^+/K_a^-$ series for $\nu_{17}$, the rigid-rotor asymmetry splitting results in only the expected doublet at low *J* values. In the case of the $K_a^+/K_a^- = 1$ and 2 series shown, however, the two transitions involving the $J = 48$ level both exhibit the formation of a quartet that includes observably intense *b*-type transitions. At lower *J*-levels, the *b*-type transitions disappear, and the series progresses with the expected doublet pattern. Due to strong, local perturbation, transitions in the $J'' + 1 = 50-53$ range are nondegenerate but do not exhibit a clear doublet structure. The $K_a^+/K_a^- = 1$ and 2 series become degenerate after the resonances at $J'' + 1 = 57$. These *b*-type transitions are allowed, to a negligible extent, due to the small *b*-type dipole moment component. They are much more intense, however, due to intensity borrowing from *a*-type transitions with the same *J* values. Although the closest relevant resonance with $\nu_{27}$ is at $J = 51$, this is still a *J* region of significant state mixing with $\nu_{27}$, which has the effect of perturbing the energy levels of $\nu_{17}$. The perturbation causes two of the $\nu_{17}$ energy levels to cross at or near the *J* value where the observed *b*-type transitions are most intense. In some of the observed cases, the mixing is sufficiently strong that SPFIT and SPCAT reverse the labels of


https://doi.org/10.1021/acs.jpca.2c00384
J. Phys. Chem. A 2022, 126, 1980−1993

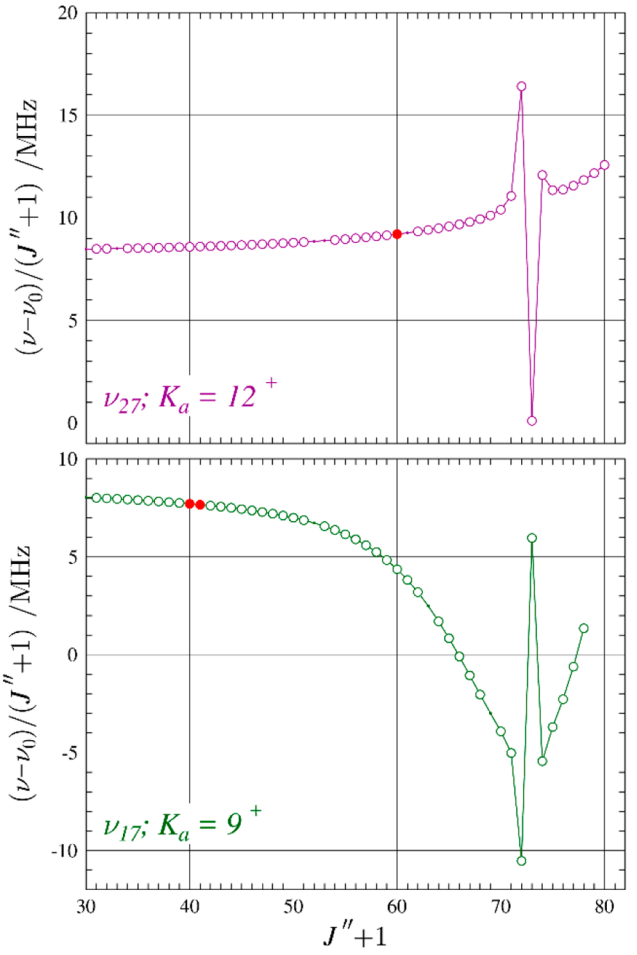


**Figure 10.** Resonance plots for 1-cyanocyclobutene (**5**) showing the $K_a = 9^+$ series for $\nu_{17}$ and $K_a = 12^+$ series for $\nu_{27}$. These two resonances conform to the $\Delta K_a = 3$ selection rule for *b*-type resonances. The plotted values are frequency differences between excited-state transitions and their ground-state counterparts, scaled by $(J'' + 1)$ in order to make the plots more horizontal. Measured transitions are represented by circles: $\nu_{27}$ (purple), $\nu_{17}$ (green). The measured transitions with $|(f_{obs} - f_{calc})/\delta f| > 3$ are marked in red. Predictions from the final coupled fit are represented by a solid, colored line.

**Table 3. Vibration−Rotation Interaction and Coriolis-Coupling Constants of 1-Cyanocyclobutene (5)**

| | Experimental | B3LYP [a] | MP2 [a] |
|---|---|---|---|
| $A_0 - A_{27}$ (MHz) | −83.41 (31) | 17.8 | 17.4 |
| $B_0 - B_{27}$ (MHz) | −3.57095 (41) | −3.42 | −3.25 |
| $C_0 - C_{27}$ (MHz) | −4.21897 (12) | −4.07 | −3.94 |
| $A_0 - A_{17}$ (MHz) | 90.19 (31) | −11.1 | −7.26 |
| $B_0 - B_{17}$ (MHz) | −6.44972 (41) | −6.11 | −6.29 |
| $C_0 - C_{17}$ (MHz) | −2.29495 (12) | −2.14 | −2.26 |
| $\frac{(A_0-A_{27})+(A_0-A_{17})}{2}$ (MHz) | 3.38 (22) | 3.36 | 5.05 |
| $\frac{(B_0-B_{27})+(B_0-B_{17})}{2}$ (MHz) | −5.01033 (29) | −4.77 | −4.77 |
| $\frac{(C_0-C_{27})+(C_0-C_{17})}{2}$ (MHz) | −3.256965 (83) | −3.10 | −3.10 |
| $\zeta^a_{27,17}$ | 0.807 | 0.751 | 0.744 |
| $\zeta^b_{27,17}$ | 0.021 | 0.027 | 0.0227 |

[a]Evaluated with the 6-311+G(2d,p) basis set.

the mixed energy levels, resulting in an apparent exchange of the *a*-type and *b*-type identification of the transitions in the quartet. An example of that can be seen in the $J = 48−49$ transitions in Figure 12, where SPFIT and SPCAT misidentify the *a*- and *b*-type transitions. Because of this problem, we manually shifted this frequency segment in the Loomis−Wood plot by ∼3 MHz to visually align all (lower-frequency) *a*-type transitions for clarity. In an extreme case of intensity borrowing, $J'' + 1 = 81$ for $K_a^+/K_a^- = 5$ and 6 transitions, almost all of the intensity is transferred from the *a*-type to *b*-type transitions. In all cases, SPCAT does accurately reproduce the observed pattern of the quartet, including the relative intensities. A summary listing of all *b*-type transitions included in the least-squares fit is provided in the Supporting Information.

There are several important clues to the quantum mechanical origin of the intensity enhancement of the nominally *b*-type transitions. First, this quartet phenomenon requires having both *a*- and *b*-type Coriolis coupling between $\nu_{27}$ and $\nu_{17}$, which is easily confirmed by setting the *b*-type Coriolis parameters to zero in SPCAT, in which case the predicted intensities of the lines in question are not greater than they are in the ground-state spectrum, i.e., negligible. Second, unlike the local resonances observed between states, the enhancement effect is not present in the spectra of both vibrational levels; it is present only in $\nu_{17}$ (to be explained below). Finally, the frequency splittings of the quartets and the intensities of the "*b*-type" peaks are both highly dependent upon the energy-level splittings of the two near-degenerate rotational levels in $\nu_{17}$ and on the distance of these two levels from the Coriolis-connected rotational levels in $\nu_{27}$, although not in a simply recognizable way. All these observations can be clearly understood by consideration of the diagonalization of the two-state Hamiltonian matrix for the $J$ involved, focusing on the three or four vib-rotational levels of most interest. Figure 13 shows an example of four vib-rotational levels, where the $48_{1,47}$ and $48_{2,47}$ energy levels for $\nu_{17}$ are connected to the $48_{5,44}$ and $48_{4,44}$ energy levels, respectively, for $\nu_{27}$ through *a*-type Coriolis coupling. These $\nu_{17}$ energy levels are also connected to the other two rotational energy levels ($48_{1,47}$ to $48_{4,44}$ and $48_{2,47}$ to $48_{5,44}$) through *b*-type coupling (to a lesser extent). This double coupling in the matrix allows the $48_{1,47}$ and $48_{2,47}$ energy levels to indirectly mix with each other. The degree of this mixing is normally small, but it is greatly amplified when the two levels are very close to each other, i.e., near-degenerate, ultimately leading to the *b*-type transitions we have observed. In general, two connecting states in $\nu_{27}$, *e.g.*, both $48_{5,44}$ and $48_{4,44}$ in the above instance, are not required for this effect, and cases of only one rotational energy level of $\nu_{27}$ interacting strongly with the two near-degenerate energy levels of $\nu_{17}$ are observed here. At first glance, one would suspect, from the symmetry of the interaction and the quantum number types involved, that the same phenomenon could be observed in $\nu_{27}$. It must be remembered, however, that because $\nu_{27}$ has the lower vibrational energy, its resonances must always have the higher $K_a$ value. The higher $K_a$ value implies a greater oblate asymmetry (lower $K_c$) at any particular $J$ value, which in turn yields much larger asymmetry splittings. This renders the indirect mixing of the two rotational states in $\nu_{27}$ inconsequential. An interesting aspect of the "*b*-type" intensities predicted by SPCAT is that they do, in fact, depend on the value of $\mu_b$ to a noticeable extent (about 10% when going from 0 to 0.07 D). This behavior is understood by considering that the intensities are proportional to the absolute square of a sum of (large) $\mu_a$ and (small) $\mu_b$ matrix elements. Thus, the cross term is more substantial than the square of the $\mu_b$ term (which leads to negligible intensity by itself) and does produce significant increases or decreases in predicted intensity. This example of a quantum interference


https://doi.org/10.1021/acs.jpca.2c00384
J. Phys. Chem. A 2022, 126, 1980−1993

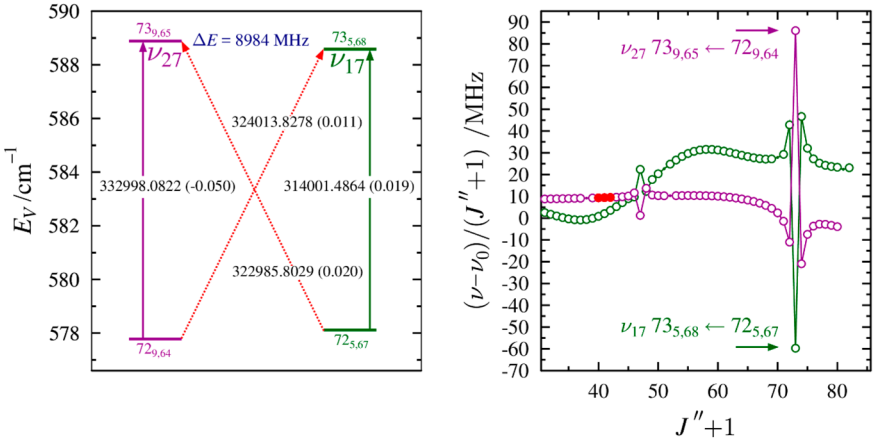


**Figure 11.** Energy diagram (left) depicting a representative matched pair of nominal interstate transitions between the $\nu_{27}$ (purple) and $\nu_{17}$ (green) vibrational states of 1-cyanocyclobutene (**5**). Standard $^aR_{0,1}$ transitions within vibrational states are denoted by vertical arrows. The diagonal, dashed arrows indicate nominal interstate transitions that are formally forbidden but enabled as a result of rotational energy level mixing. Values printed on each of the arrows are the corresponding transition frequency (in MHz) with its obs−calc value in parentheses. The marked energy separation is between the two strongly interacting rotational energy levels. Resonance plots (right) of the $K_a$ series of $\nu_{27}$ and $\nu_{17}$ that contain the corresponding resonant transitions labeled with their quantum numbers and marked by colored arrows.

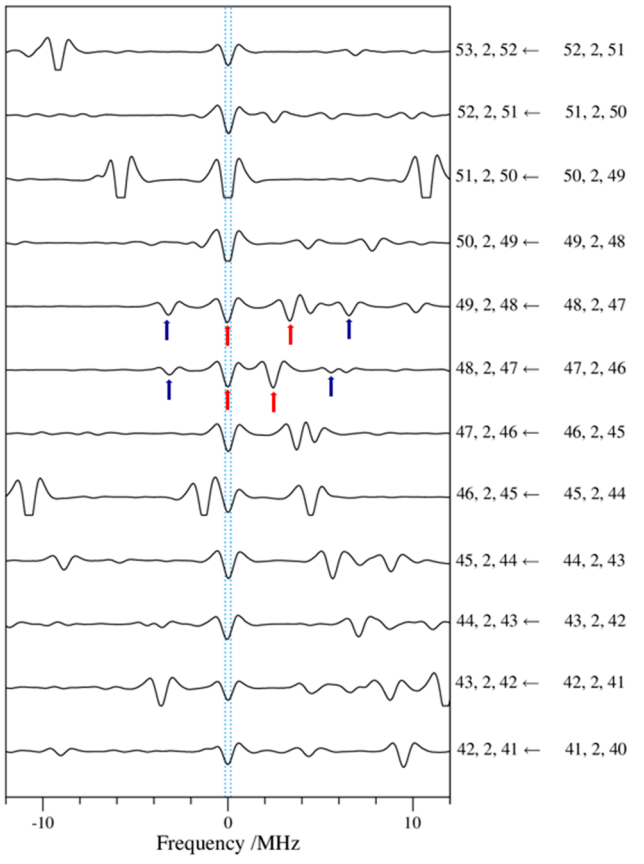


**Figure 12.** Loomis−Wood plot centered on the $K_a = 2^-$ series for $\nu_{17}$ ranging in $J'' + 1 = 42-53$. The $K_a = 1^+$ can be seen higher in frequency below $J'' + 1 = 47$ in a typical doublet pattern progressing further away in frequency as $J'' + 1$ decreases. A quartet of *a*-type (red) and *b*-type (blue) transitions is then observed for $J'' + 1 = 48$ and 49. The Loomis−Wood frequency segment corresponding to $J'' + 1 = 49$ was shifted lower in frequency by 3 MHz for this figure due to the SPCAT misassignment of the *a*- and *b*-type transitions.

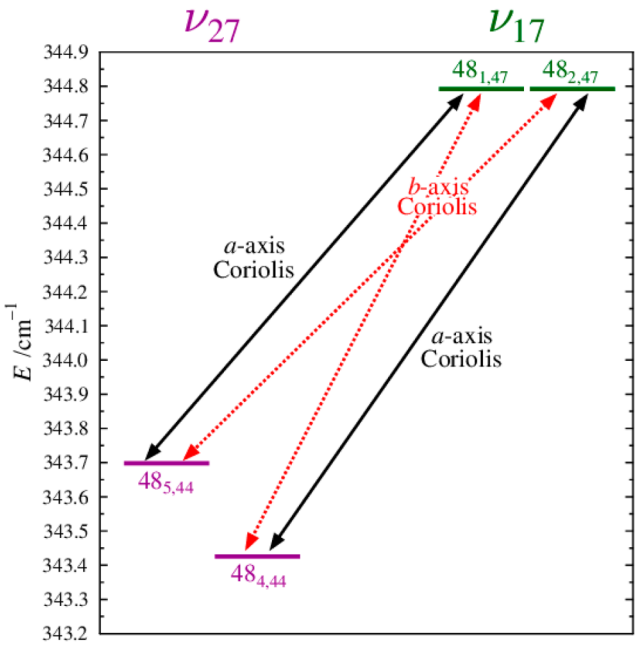


**Figure 13.** Four-state vib-rotational energy level diagram showing the states involved in creating an observable quartet in the $K_a^+/K_a^- = 1$ and 2 series. The red and black arrows indicate the *b*- and *a*-axis Coriolis interactions, respectively, that allow for state mixing between states.

effect may well be more important in other molecules with a somewhat larger $\mu_b$. Meanwhile, this phenomenon is not possible in a molecule where the second dipole component is *exactly* zero, since the molecular symmetry that causes it will also mean that only one type of Coriolis coupling is allowed between any two vibrational states. Of course, if both dipole moment components are comparable in magnitude, the effects of the indirect coupling may not even be noticed.

Higher up the vibrational manifold, at approximately 330 cm$^{-1}$, the two-quanta vibrational states of $\nu_{27}$ (A″) and $\nu_{17}$ (A′) form a coupled tetrad with $\nu_{26}$. This tetrad is expected to be well-isolated from other vibrationally excited states and of sufficient intensity that the rotational spectra of all four states can be measured, assigned, and least-squares fit, using the spectral data we have already acquired. Despite the complicating interaction


https://doi.org/10.1021/acs.jpca.2c00384
J. Phys. Chem. A 2022, 126, 1980−1993

with $\nu_{26}$ (A″), this tetrad can be addressed using the same general methodology recently employed with benzonitrile, where the triad consisting of the overtones and simple combination of the two lowest-lying states is analyzed very successfully.[50] In that study, the harmonic and anharmonic vibrational constants for the states involved are well predicted by the *xguinea* routine of CFOUR, as was the Darling−Dennison coupling term connecting the two overtone states. Furthermore, it has been found that the higher-order Coriolis coupling coefficients, *e.g.*, $G_a^J$ or $F_{bc}$, for the triad scale rather closely as a factor of $\sqrt{2}$ from the corresponding ones of the dyad. Equivalent predictions and scaling for 1-cyanocyclobutene should greatly expedite assignment of the tetrad, and a successful fit would provide a further test of the accuracy of the predicted and scaled parameters. The $\nu_{26}$ fundamental should be coupled by anharmonic resonance to the combination state and by higher-order Coriolis interactions to all three triad states. Acquisition and analysis of the modestly strong $\nu_{17}$ band, its two hot bands, and possibly the weaker $\nu_{27}$ and $\nu_{26}$ bands, by high-resolution infrared spectroscopy, and a successful perturbation analysis of the tetrad, in addition to the results of this study, can potentially provide highly accurate absolute vibrational energies of the lowest six excited vibrational levels of 1-cyanocyclobutene.

## CONCLUSION

The ground-state spectroscopic constants of 1-cyanocyclobutene (**5**) from this work should provide an excellent foundation for predicting frequencies for an astronomical search, even for transitions well outside the range explored here. In the lower microwave region and for the lower *J* transitions most often used in radioastronomy, these predictions would require inclusion of the effects of nuclear hyperfine structure. The needed quadrupole coupling constants can be well estimated computationally, or they could be much better determined by measuring and analyzing a few resolved hyperfine multiplets for low-*J* transitions occurring in the lower microwave region. Unlike several other $C_5H_5N$ isomers,[8] the ground-state of 1-cyanocyclobutene (**5**) is well fit by a single-state Hamiltonian model, so the present centrifugal distortion analysis should provide accurate frequency estimates well above the current range. The accuracy is of course expected to degrade gradually as one encounters quantum number values further removed from those sampled in this study.

The experimentally well-determined higher-order Coriolis coupling parameters for interacting fundamental states in 1-cyanocyclobutene (**5**) contribute to a steadily growing list of organic molecules that have been analyzed in this level of detail. A similar statement can be made about the quartic centrifugal distortion constants for the two vibrationally excited states. Neither these higher-order Coriolis constants nor the changes between the ground-state and vibrationally excited-state centrifugal distortion constants, however, can be meaningfully estimated *via* any readily available computational software package. A practical computational approach to obtaining these constants thus remains a pressing challenge for theory. Not only would such computed values serve as a measure of quality for a least-squares fit, but they would also likely improve the initial predictions of excited-state rotational spectra and thereby facilitate the early stage of the fitting process. Incorporation of these computed values in the least-squares fit for all constants that could not be adequately determined should also improve the accuracy of those constants that can be varied and fit.

## GENERAL EXPERIMENTAL METHODS

All commercial reagents were purchased from Sigma-Aldrich or Oakwood Chemical and used as received, unless otherwise noted. $^1$H NMR spectra (400 or 500 MHz) and $^{13}$C NMR spectra (100 or 125 MHz) were obtained in $CDCl_3$ on a Bruker 400 MHz AVANCE III or Bruker 500 MHz DCH AVANCE III spectrometer; chemical shifts ($\delta$) are reported as ppm downfield from internal standard $SiMe_4$ or referenced to residual solvent signals. Mass spectra were acquired using electrospray ionization (ESI) or the atmospheric solids analysis probe (ASAP) on a Thermo Scientific Q-Exactive Plus mass spectrometer. GC/MS analysis was performed on a Shimadzu GCMS-2010S instrument. IR spectra were obtained on a Bruker TENSOR Fourier transform infrared instrument as neat samples using an attenuated total reflectance accessory (Bruker PLATINUM ATR).

**Mixture of *trans*- and *cis*-1,2-Dicyanocyclobutane (13).** ***Note:*** *Exposure of the reaction mixture to short-wavelength UV−C (254 nm) is critical and necessitates the use of a quartz reaction vessel or immersion probe.*

Photolyses were carried out in an immersion-type quartz photochemical reactor (Ace Glass # 7861-250) having an inner annular volume of 500 mL and equipped with a magnetic stirrer. Into the water-cooled quartz immersion probe was inserted a centrally positioned 450 W medium-pressure mercury arc lamp (Hanovia # 679A36, 122 mm arc length). The quartz lamp chamber was continuously purged with a slow, steady stream of dry $N_2$ to prevent ozone generation/damage during lamp operation. Molybdenum hexacarbonyl ($Mo(CO)_6$, 5.43 g, 20.6 mmol), triphenylphosphine ($PPh_3$, 5.42 g, 20.7 mmol), hydroquinone (350 mg, 3.2 mmol), acrylonitrile (195 mL, 160 g, 3 mol), and acetonitrile (143 mL) were added to the annular reactor compartment, and the mixture was stirred until most of the solids were dissolved. The reaction mixture was purged under a steady stream of dry $N_2$ for 5 min. The reactor vessel was then maintained under a nitrogen atmosphere. With the immersion probe coolant flowing, the lamp was ignited, and the temperature of the stirred reaction was maintained at 55−60 °C by the heat of the mercury lamp throughout the course of the photolysis. Any remaining undissolved reactants dissolved within minutes of igniting the lamp as the reaction temperature increased. The reaction progress was monitored *via* $^1$H NMR over the 72 h photolysis. After the irradiation time had elapsed, the photolysis was halted, and the reaction vessel was cooled to room temperature. The amber-colored reactor contents were filtered through a coarse glass-fritted funnel and concentrated *in vacuo* to remove acetonitrile and acrylonitrile. The resulting deep-red oil was purified *via* short-path vacuum distillation to afford a mixture of 1,2-dicyanocyclobutane stereoisomers (**13**) as a viscous amber oil that solidified upon cooling to room temperature (14.6 g, 0.138 mol, 9%, bp = 110−125 °C at 2 Torr). $^1$H NMR ($CDCl_3$, 500 MHz): $\delta$ (ppm) 3.42−3.60 (m, 2H), 2.42−2.62 (m, 4H). *trans* $^{13}$C{$^1$H}-NMR ($CDCl_3$, 125 MHz): $\delta$ (ppm) 118.6, 26.6, 24.8. *cis* $^{13}$C{$^1$H}-NMR ($CDCl_3$, 125 MHz): $\delta$ (ppm) 118.3, 26.7, 24.8. IR (neat): ($cm^{-1}$) 2969 (m), 2242 (s), 1444 (m), 1244 (w), 1205 (m), 751 (w), 492 (w). HRMS (ASAP-MS), *m*/*z*: $[M + H]^+$ Calcd for $C_6H_7N_2$: 107.0604. Found: 107.0604.

**1-Cyanocyclobutene (5).** A vertical quartz tube 50 cm long and 2.5 cm in diameter, with 20 cm of its length packed with


https://doi.org/10.1021/acs.jpca.2c00384
J. Phys. Chem. A 2022, 126, 1980−1993

Ascarite (Aldrich, 20−30 mesh), was heated in a 40 cm long cylindrical tube furnace to 200 °C for 2 h under a steady stream of dry $N_2$ to remove water or absorbed gases from the Ascarite bed. A stoppered pressure-equalizing dropping funnel containing 1,2-dicyanocyclobutane (**13**, 9.95 g, 94 mmol) was connected to the top of the quartz reactor tube and the bottom was connected to a vacuum manifold through a series of three dry ice/acetone cooled traps. The temperature of the tube furnace was set to 225 °C, and the system was evacuated to a pressure of 500 mTorr. The dropping funnel at the top of the reactor was lightly heated with a heat gun until the 1,2-dicyanocyclobutane was thoroughly melted and degassed. The 1,2-dicyanocyclobutane melt was added dropwise to the heated reaction tube. The rate of addition was sufficient to maintain an internal pressure below 2 Torr. The complete dropwise delivery of molten **13** to the heated reactor bed was achieved over a course of 2 h. A total of 1.56 g of hazy, colorless liquid was recovered from the traps after the addition of **13** was completed. The collected distillate was cooled to 0 °C on ice and allowed to separate. The clear organic supernatant layer was separated and dried over granular anhydrous $Na_2SO_4$ to yield 1-cyanocyclobutene (**5**) as a colorless oil (834 mg, 10.6 mmol, 11%). $^1$H NMR ($CDCl_3$, 500 MHz): $\delta$ (ppm) 6.78 (t, $J$ = 1.4 Hz, 1H), 2.84 (dd, $J$ = 3.4 Hz, 2H), 2.63 (ddd, $J$ = 3.4 Hz, 3.2 Hz, 1.4 Hz, 2H). $^{13}$C{$^1$H}-NMR ($CDCl_3$, 125 MHz): $\delta$ (ppm) 153.0, 117.2, 113.9, 32.4, 30.3. IR (neat): ($cm^{-1}$) 2978 (w), 2937 (m), 2835 (w), 2218 (m), 1584 (w), 1425 (w), 1252 (m), 1213 (w), 1162 (w), 1073 (w), 936 (w), 910 (m), 867 (m), 757 (m), 684 (w), 584 (w), 516 (s). HRMS (ASAP-MS), $m/z$: $[M + H]^+$ Calcd for $C_5H_6N$: 80.0495. Found: 80.0494.

## ■ ASSOCIATED CONTENT

### Supporting Information

The Supporting Information is available free of charge at https://pubs.acs.org/doi/10.1021/acs.jpca.2c00384.

Table of *b*-type transitions observed in $\nu_{17}$ paired with the corresponding *a*-type transitions; experimental IR, $^1$H NMR, $^{13}$C NMR, and mass spectra of all compounds (PDF)

Computational chemistry output files and least-squares fitting output files from SPFIT (ZIP)

## ■ AUTHOR INFORMATION

### Corresponding Authors

**R. Claude Woods** − *Department of Chemistry, University of Wisconsin−Madison, Madison, Wisconsin 53706-1322, United States;* orcid.org/0000-0003-0865-4693; Email: rcwoods@wisc.edu

**Robert J. McMahon** − *Department of Chemistry, University of Wisconsin−Madison, Madison, Wisconsin 53706-1322, United States;* orcid.org/0000-0003-1377-5107; Email: robert.mcmahon@wisc.edu

### Authors

**Houston H. Smith** − *Department of Chemistry, University of Wisconsin−Madison, Madison, Wisconsin 53706-1322, United States;* orcid.org/0000-0002-3762-1842

**Samuel M. Kougias** − *Department of Chemistry, University of Wisconsin−Madison, Madison, Wisconsin 53706-1322, United States;* orcid.org/0000-0002-9877-0817

**Brian J. Esselman** − *Department of Chemistry, University of Wisconsin−Madison, Madison, Wisconsin 53706-1322, United States;* orcid.org/0000-0002-9385-8078

Complete contact information is available at: https://pubs.acs.org/10.1021/acs.jpca.2c00384

### Notes

The authors declare no competing financial interest.

## ■ ACKNOWLEDGMENTS

We gratefully acknowledge the National Science Foundation for support of this project (CHE-1954270). We thank Michael McCarthy for the loan of an amplification-multiplication chain and Aatmik R. Patel for stimulating discussions regarding the synthesis of 1-cyanocyclobutene precursors and the assessment of synthetic routes. We thank the following organizations and individuals for support of shared departmental facilities: Bruker AVANCE 400 NMR spectrometer (NSF CHE-1048642), Bruker AVANCE 500 NMR spectrometer (gift from Paul J. and Margaret M. Bender), and Thermo Scientific Q Exactive Plus mass spectrometer (NIH 1S10 OD020022-1).

## ■ REFERENCES

(1) Müller, H. S. P.; Schlöder, F.; Stutzki, J.; Winnewisser, G. The Cologne Database for Molecular Spectroscopy, CDMS: a Useful Tool for Astronomers and Spectroscopists. *J. Mol. Struct.* **2005**, *742*, 215−227.

(2) Müller, H. S. P.; Thorwirth, S.; Roth, D. A.; Winnewisser, G. The Cologne Database for Molecular Spectroscopy, CDMS. *Astron. Astrophys.* **2001**, *370*, L49−L52.

(3) Zdanovskaia, M. A.; Esselman, B. J.; Lau, H. S.; Bates, D. M.; Woods, R. C.; McMahon, R. J.; Kisiel, Z. The 103 - 360 GHz Rotational Spectrum of Benzonitrile, the First Interstellar Benzene Derivative Detected by Radioastronomy. *J. Mol. Spectrosc.* **2018**, *351*, 39−48.

(4) Zdanovskaia, M. A.; Esselman, B. J.; Woods, R. C.; McMahon, R. J. The 130 - 370 GHz Rotational Spectrum of Phenyl Isocyanide ($C_6H_5NC$). *J. Chem. Phys.* **2019**, *151*, 024301.

(5) Dorman, P. M.; Esselman, B. J.; Park, J. E.; Woods, R. C.; McMahon, R. J. Millimeter-Wave Spectrum of 4-Cyanopyridine in its Ground State and Lowest-Energy Vibrationally Excited States, $\nu_{20}$ and $\nu_{30}$. *J. Mol. Spectrosc.* **2020**, *369*, 111274.

(6) Dorman, P. M.; Esselman, B. J.; Woods, R. C.; McMahon, R. J. An Analysis of the Rotational Ground State and Lowest-energy Vibrationally Excited Dyad of 3-Cyanopyridine: Low Symmetry Reveals Rich Complexity of Perturbations, Couplings, and Interstate Transitions. *J. Mol. Spectrosc.* **2020**, *373*, 111373.

(7) Kougias, S. M.; Knezz, S. N.; Owen, A. N.; Sanchez, R. A.; Hyland, G. E.; Lee, D. J.; Patel, A. R.; Esselman, B. J.; Woods, R. C.; McMahon, R. J. Synthesis and Characterization of Cyanobutadiene Isomers—Molecules of Astrochemical Significance. *J. Org. Chem.* **2020**, *85*, 5787−5798.

(8) Zdanovskaia, M. A.; Dorman, P. M.; Orr, V. L.; Owen, A. N.; Kougias, S. M.; Esselman, B. J.; Woods, R. C.; McMahon, R. J. Rotational Spectra of Three Cyanobutadiene Isomers ($C_5H_5N$) of Relevance to Astrochemistry and Other Harsh Reaction Environments. *J. Am. Chem. Soc.* **2021**, *143*, 9551−9564.

(9) Zdanovskaia, M. A.; Esselman, B. J.; Kougias, S. M.; Patel, A. R.; Woods, R. C.; McMahon, R. J. The 130−360 GHz rotational spectrum of *syn*-2-cyano-1,3-butadiene ($C_5H_5N$) - a molecule of astrochemical relevance. *Mol. Phys.* **2021**, *119*, No. e1964629.

(10) Esselman, B. J.; Kougias, S. M.; Zdanovskaia, M. A.; Woods, R. C.; McMahon, R. J. Synthesis, Purification, and Rotational Spectroscopy of (Cyanomethylene)Cyclopropane—An Isomer of Pyridine. *J. Phys. Chem. A* **2021**, *125*, 5601−5614.

(11) Charnley, S. B.; Kuan, Y.-J.; Huang, H.-C.; Botta, O.; Butner, H. M.; Cox, N.; Despois, D.; Ehrenfreund, P.; Kisiel, Z.; Lee, Y.-Y.; et al.

Astronomical Searches for Nitrogen Heterocycles. *Adv. Space Res.* **2005**, *36*, 137−145.
(12) McGuire, B. A.; Burkhardt, A. M.; Kalenskii, S. V.; Shingledecker, C. N.; Remijan, A. J.; Herbst, E.; McCarthy, M. C. Detection of the Aromatic Molecule Benzonitrile (*c*-$C_6H_5CN$) in the Interstellar Medium. *Science* **2018**, *359*, 202−205.
(13) McGuire, B. A.; Loomis, R. A.; Burkhardt, A. M.; Lee, K. L. K.; Shingledecker, C. N.; Charnley, S. B.; Cooke, I. R.; Cordiner, M. A.; Herbst, E.; Kalenskii, S.; et al. Detection of Two Interstellar Polycyclic Aromatic Hydrocarbons via Spectral Matched Filtering. *Science* **2021**, *371*, 1265−1269.
(14) McCarthy, M. C.; Lee, K. L. K.; Loomis, R. A.; Burkhardt, A. M.; Shingledecker, C. N.; Charnley, S. B.; Cordiner, M. A.; Herbst, E.; Kalenskii, S.; Willis, E. R.; et al. Interstellar Detection of the Highly Polar Five-Membered Ring Cyanocyclopentadiene. *Nat. Astron.* **2021**, *5*, 176−180.
(15) Morales, S. B.; Bennett, C. J.; Le Picard, S. D.; Canosa, A.; Sims, I. R.; Sun, B. J.; Chen, P. H.; Chang, A. H. H.; Kislov, V. V.; Mebel, A. M.; et al. A Crossed Molecular Beam, Low-Temperature Kinetics, and Theoretical Investigation of the Reaction of the Cyano Radical (CN) with 1,3-Butadiene ($C_4H_6$). A Route to Complex Nitrogen-Bearing Molecules in Low-Temperature Extraterrestrial Environments. *Astrophys. J.* **2011**, *742*, 26.
(16) Sun, B. J.; Huang, C. H.; Chen, S. Y.; Chen, S. H.; Kaiser, R. I.; Chang, A. H. H. Theoretical Study on Reaction Mechanism of Ground-State Cyano Radical with 1,3-Butadiene: Prospect of Pyridine Formation. *J. Phys. Chem. A* **2014**, *118*, 7715−7724.
(17) Jamal, A.; Mebel, A. M. Theoretical Investigation of the Mechanism and Product Branching Ratios of the Reactions of Cyano Radical with 1- and 2-Butyne and 1,2-Butadiene. *J. Phys. Chem. A* **2013**, *117*, 741−755.
(18) Mishra, P.; Fritz, S. M.; Herbers, S.; Mebel, A. M.; Zwier, T. S. Gas-phase Pyrolysis of *Trans* 3-Pentenenitrile: Competition Between Direct and Isomerization-Mediated Dissociation. *Phys. Chem. Chem. Phys.* **2021**, *23*, 6462−6471.
(19) McCarthy, M. C.; Lee, K. L. K.; Carroll, P. B.; Porterfield, J. P.; Changala, P. B.; Thorpe, J. H.; Stanton, J. F. Exhaustive Product Analysis of Three Benzene Discharges by Microwave Spectroscopy. *J. Phys. Chem. A* **2020**, *124*, 5170−5181.
(20) Guillemin, J. C.; Ferris, J. P. Photochemistry of Unsaturated Nitriles on Titan. *Symposium on Titan*; ESA, 1992; pp 177−181.
(21) Gale, D. M. 1-Cyanobicyclo[1.1.0]butane and 1-cyanocyclobutene by photolysis of 2-cyano-1,3-butadiene. Patent number 3459647, 1969.
(22) Gale, D. M.; Cherkofsky, S. C. Dehydrocyanation of Dinitriles. Preparation of 1-Cyclobutenecarbonitrile by Direct Dehydrocyanation of 1,2-Cyclobutanedicarbonitrile. *J. Org. Chem.* **1973**, *38*, 475−478.
(23) Sarner, S. F.; Gale, D. M.; Hall, H. K.; Richmond, A. B. Gas-phase Thermolysis Kinetics of Small Ring Nitriles. *J. Phys. Chem.* **1972**, *76*, 2817−2819.
(24) Kwak, N.; Simmons, J. W.; Goldstein, J. H. Microwave Spectrum of Propiolactone. *J. Chem. Phys.* **1955**, *23*, 2450−2450.
(25) Boone, D. W.; Britt, C. O.; Boggs, J. E. Microwave Spectrum, Dipole Moment, and Ring-Puckering Vibration of $\beta$-Propiolactone. *J. Chem. Phys.* **1965**, *43*, 1190−1194.
(26) Chen, Z.; van Wijngaarden, J. A Combined *ab Initio*, Fourier Transform Microwave and Fourier Transform Infrared Spectroscopic Investigation of $\beta$-Propiolactone: The $\nu_8$ and $\nu_{12}$ bands. *J. Mol. Spectrosc.* **2009**, *257*, 164−169.
(27) Orr, V. L.; Esselman, B. J.; Dorman, P. M.; Amberger, B. K.; Guzei, I. A.; Woods, R. C.; McMahon, R. J. Millimeter-wave Spectroscopy, X-ray Crystal Structure, and Quantum Chemical Studies of Diketene - Resolving Ambiguities Concerning the Structure of the Ketene Dimer. *J. Phys. Chem. A* **2016**, *120*, 7753−7763.
(28) Durig, J. R.; Carreira, L. A.; Lafferty, W. J. Spectra and Structure of Small Ring Compounds. Microwave Spectrum of Cyanocyclobutane. *J. Mol. Spectrosc.* **1973**, *46*, 187−193.
(29) Fong, M. Y.; Harmony, M. D. Microwave Spectrum, Dipole Moment, Quadrupole Coupling Constants, and Conformation of Cyanocyclobutane. *J. Chem. Phys.* **1973**, *58*, 4260−4264.
(30) Caminati, W.; Velino, B.; Della Valle, R. G. Rotational Spectra of Several Vibrational Excited States of Axial and Equatorial Cyanocyclobutane and Potential Energy Function of the Ring Puckering. *J. Mol. Spectrosc.* **1988**, *129*, 284−292.
(31) Durig, J. R.; Ganguly, A.; Klaassen, J. J.; Guirgis, G. A. The $r_0$ Structural Parameters, Conformational Stability, and Vibrational Assignment of Equatorial and Axial Cyanocyclobutane. *J. Mol. Struct.* **2009**, *923*, 28−38.
(32) Caminati, W.; Velino, B.; Dakkouri, M.; Schäfer, L.; Siam, K.; Ewbank, J. D. Reinvestigation of the Microwave Spectrum of Cyanocyclobutane: Assignment of the Axial Conformer. *J. Mol. Spectrosc.* **1987**, *123*, 469−475.
(33) Menke, J. L.; McMahon, R. J. Photochemistry of matrix-isolated 5-cyano-2H-pyran-2-one ($\delta$-cyano-$\alpha$-pyrone) and cyanocyclobuta-1,3-diene. *Can. J. Chem.* **2011**, *89*, 186−194.
(34) Miki, S.; Matsumura, S.-i.; Ohno, T.; Yoshida, Z.-i. Co(II)-porphyrin Catalyzed Isomerization of Bicyclobutanecarbonitrile. *Tetrahedron Lett.* **1986**, *27*, 3669−3672.
(35) Gale, D. M., Mono- and Dichlorocyclobutanecarbonitriles by Cycloaddition of Vinyl Chloride and an Acrylonitrile. Patent number 3642859, 1972.
(36) Tietz, R. F.; Kenyon, W. G. 1-Cyanocyclobutene Monomer and Polymer and Their Preparation. Patent number 3468861, Sep 23, 1969.
(37) Ferris, J. P.; Guillemin, J. C. Photochemical Cycloaddition Reactions of Cyanoacetylene and Dicyanoacetylene. *J. Org. Chem.* **1990**, *55*, 5601−5606.
(38) Hughes, W. B. Photodimerization of Acrylonitrile. Patent number 3623966, Nov 30, 1971.
(39) Miyashita, A.; Ikezu, S.; Nohira, H. Stereospecific Photodimerization of Unsaturated Compounds Induced by Nickel Complexes. *Chem. Lett.* **1985**, *14*, 1235−1238.
(40) Hosaka, S.; Wakamatsu, S. Photodimerization of Acrylonitrile. *Tetrahedron Lett.* **1968**, *9*, 219−220.
(41) Esselman, B. J.; Amberger, B. K.; Shutter, J. D.; Daane, M. A.; Stanton, J. F.; Woods, R. C.; McMahon, R. J. Rotational Spectroscopy of Pyridazine and its Isotopologs from 235−360 GHz: Equilibrium Structure and Vibrational Satellites. *J. Chem. Phys.* **2013**, *139*, 224304.
(42) Kisiel, Z.; Pszczółkowski, L.; Drouin, B. J.; Brauer, C. S.; Yu, S.; Pearson, J. C.; Medvedev, I. R.; Fortman, S.; Neese, C. Broadband Rotational Spectroscopy of Acrylonitrile: Vibrational Energies from Perturbations. *J. Mol. Spectrosc.* **2012**, *280*, 134−144.
(43) Kisiel, Z.; Pszczółkowski, L.; Medvedev, I. R.; Winnewisser, M.; De Lucia, F. C.; Herbst, E. Rotational Spectrum of *Trans-Trans* Diethyl Ether in the Ground and Three Excited Vibrational States. *J. Mol. Spectrosc.* **2005**, *233*, 231−243.
(44) Pickett, H. M. The Fitting and Prediction of Vibration-rotation Spectra with Spin Interactions. *J. Mol. Spectrosc.* **1991**, *148*, 371−377.
(45) Kisiel, Z., PROSPE - Programs for ROtational SPEctroscopy; http://info.ifpan.edu.pl/~kisiel/prospe.htm (accessed April 3, 2021).
(46) Kisiel, Z. Assignment and Analysis of Complex Rotational Spectra. In *Spectroscopy from Space*, 1st ed.; Demaison, J., Sarka, K., Cohen, E. A., Eds.; Springer Netherlands: Dordrecht, 2001; pp 91−106.
(47) Frisch, M. J.; Trucks, G. W.; Schlegel, H. B.; Scuseria, G. E.; Robb, M. A.; Cheeseman, J. R.; Scalmani, G.; Barone, V.; Petersson, G. A.; Nakatsuji, H.; et al. *Gaussian 16*, rev C.01; Gaussian, Inc.: Wallingford, CT, USA, 2016.
(48) Schmidt, J. R.; Polik, W. F. *WebMO Enterprise, version 20.0*; WebMO LLC: Madison, WI, USA, 2020; http://www.webmo.net (accessed April 2021).
(49) Kisiel, Z.; Kraśnicki, A. The Millimetre-Wave Rotational Spectrum of Phenylacetylene. *J. Mol. Spectrosc.* **2010**, *262*, 82−88.
(50) Zdanovskaia, M. A.; Martin-Drumel, M.-A.; Kisiel, Z.; Pirali, O.; Esselman, B. J.; Woods, R. C.; McMahon, R. J. The eight lowest-energy vibrational states of benzonitrile: analysis of Coriolis and Darling-

Dennison couplings by millimeter-wave and far-infrared spectroscopy.
*J. Mol. Spectrosc.* **2022**, *383*, 111568.





https://doi.org/10.1021/acs.jpca.2c00384
*J. Phys. Chem. A* 2022, 126, 1980−1993

Journal of Molecular Spectroscopy 391 (2023) 111737

Contents lists available at ScienceDirect

Journal of Molecular Spectroscopy

journal homepage: www.elsevier.com/locate/yjmsp

# The 130–500 GHz rotational spectrum of 2-cyanopyrimidine

Houston H. Smith, Brian J. Esselman, Maria A. Zdanovskaia, R. Claude Woods *, Robert J. McMahon *

*Department of Chemistry, University of Wisconsin–Madison, Madison, Wisconsin 53706, USA*

ARTICLE INFO

*Keywords:*
Rotational spectroscopy
Vibrational spectroscopy
Coriolis coupling
Interstellar molecule
Astrochemistry

ABSTRACT

The rotational spectrum of 2-cyanopyrimidine has been obtained from 130 GHz to 500 GHz. Over 7500 vibrational ground-state transitions have been assigned and least-squares fit to partial octic, A- and S-reduced Hamiltonians with low error ($\sigma_{fit}$ = 36 kHz). The two lowest-energy fundamental modes, the out-of-plane ($\nu_{18}$) and in-plane ($\nu_{27}$) nitrile bending modes, form a Coriolis-coupled dyad similar to the analogous fundamental states of other cyanoarenes. The coupled dyad was least-squares fit to a partial octic, A-reduced Hamiltonian ($\sigma_{fit}$ = 47 kHz) with over 6700 transitions for each vibrational state, including transitions that are perturbed or involved in resonances, as well as symmetry-allowed nominal interstate transitions resulting from Coriolis coupling. The spectroscopic information from these transitions enabled the determination of a highly precise energy separation ($\Delta E_{18,27}$ = 38.9673191 (77) cm$^{-1}$) and six Coriolis-coupling coefficients ($G_a$, $G_a^J$, $G_a^K$, $G_a^{JJ}$, $F_{bc}$, and $F_{bc}^K$). The spectroscopic constants and transitions presented in this work provide the foundation for future radioastronomical searches for 2-cyanopyrimidine.

## 1. Introduction

There has been long-standing interest in elucidating the molecular composition of various extraterrestrial environments, with particular attention on aromatic compounds. The detection of benzene *via* infrared spectroscopy in proto-planetary nebula CRL 618 [1] was a catalyst to search for other aromatic molecules; the search for aromatic heterocycles, however, has been unsuccessful [2–5]. Pyrimidine is of particular interest as an astronomical target because its core is present in various biological and prebiotic molecules. These include thymine, uracil, cytosine, thiamine (vitamin B1), and alloxan, as well as various synthetic drugs [6]. Therefore, detection of pyrimidine in an extraterrestrial environment would signify detection of a biologically relevant molecule in a harsh, possibly prebiotic environment. Despite multiple attempts, there have been no reported interstellar detections of this molecule [2,5,7]. Radioastronomy, which relies on the population of the species in the source observed and on the intrinsic intensity of its rotational transitions due to its dipole moment, is the preferred method of detection because it is reasonably unambiguous in molecular identification. The inability to detect nonpolar or weakly polar aromatic molecules has led to attempts to detect simple derivatives of those molecules with nitrile substituents, which tend to bestow a large dipole moment. The larger dipole moment leads to a greater chance of detection by radioastronomy, which is illustrated by the prevalence of nitrile-containing molecules detected in the interstellar medium (ISM) [8,9]. Such attempts to detect nitrile-containing derivatives have been successful for benzonitrile [10] and cyanonaphthalenes [11], suggesting their parent molecules are also present in space. These astronomical detections rely on the availability of accurate spectroscopic constants determined from laboratory spectra. Given the success of nitrile-substituted detections, our group reported the rotational spectral analyses of several nitrile-containing aromatic and heteroaromatic compounds (Fig. 1), including benzonitrile [12,13], 2-cyanopyridine [14], 3-cyanopyridine [15], 4-cyanopyridine [16], cyanopyrazine [17], and 2-cyanopyrimidine (presented in this work) in their ground and vibrationally excited states. In contrast to the situation with benzonitrile and the cyanopyridines, for which some spectroscopic data had been previously available [18–21], 2-cyanopyrimidine and cyanopyrazine did not have previously reported rotational spectra.

The two lowest-energy vibrational modes for molecules containing a π-conjugated nitrile moiety are typically the in-plane and out-of-plane bending modes of the nitrile, and these modes are often sufficiently close in energy that Coriolis coupling is observed in the millimeter-wave frequency transitions. Analysis of the rotational spectra for these vibrational modes for benzonitrile [12,13], 3-cyanopyridine [15], 4-cyanopyridine [16], cyanopyrazine [17], 1-cyanocyclobutene [22],

* Corresponding authors.
*E-mail addresses:* rcwoods@wisc.edu (R.C. Woods), robert.mcmahon@wisc.edu (R.J. McMahon).

https://doi.org/10.1016/j.jms.2023.111737
Received 8 December 2022; Received in revised form 6 January 2023; Accepted 8 January 2023
Available online 10 January 2023

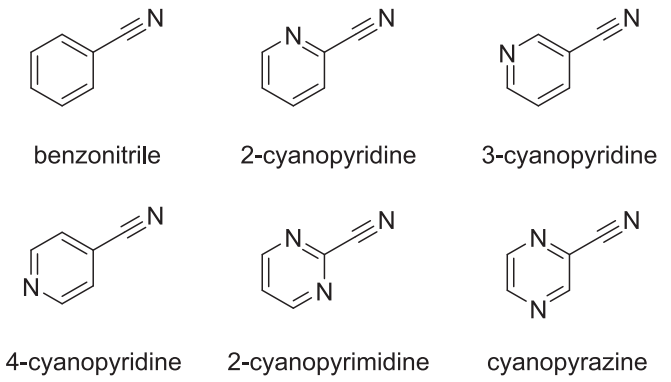


**Fig. 1.** Cyanoarenes derived from benzene, pyridine, pyrimidine, and pyrazine.

**Table 1**
Energy differences between out-of-plane and in-plane nitrile bending modes for molecules containing a π-conjugated nitrile moiety.

| | out-of-plane | in-plane | $\Delta E_{ip-oop}$ ($cm^{-1}$) |
|---|---|---|---|
| benzonitrile [12,13] | $\nu_{22}$, $B_1$ | $\nu_{33}$, $B_2$ | 19.1081701(74) |
| 3-cyanopyridine [15] | $\nu_{30}$, A″ | $\nu_{21}$, A′ | 15.7524693 (37) |
| 4-cyanopyridine [16] | $\nu_{20}$, $B_1$ | $\nu_{30}$, $B_2$ | 18.806554 (11) |
| cyanopyrazine [17] | $\nu_{27}$, A″ | $\nu_{19}$, A′ | 24.8245962 (60) |
| 2-cyanopyrimidine (this work) | $\nu_{18}$, $B_1$ | $\nu_{27}$, $B_2$ | 38.9673191 (77) |
| 1-cyanocyclobutene [22] | $\nu_{27}$, A″ | $\nu_{17}$, A′ | 14.0588093 (43) |
| (cyanomethylene)cyclopropane [23] | $\nu_{27}$, A″ | $\nu_{17}$, A′ | −29.8975453 (33) |
| acrylonitrile [24,25] | $\nu_{15}$, A″ | $\nu_{11}$, A′ | −104.378277 (6) |

(cyanomethylene)cyclopropane [23], and acrylonitrile [24] required the use of vibrationally coupled Hamiltonians to assign the observed rotational transitions and resulted in the determination of highly accurate and precise energy separations between the two fundamental states (Table 1). For each of the cyano-substituted aromatic compounds observed, the out-of-plane nitrile bending mode is lower in energy (Table 1). The coupling and state mixing result in rotational transitions influenced by Coriolis perturbation. This perturbation results in the appearance of local resonances, *i.e.*, transitions whose frequencies are drastically shifted from where they would be expected in the absence of perturbation, and formally forbidden, nominal interstate transitions. While band origins can be determined from high-resolution infrared spectroscopy, as has been done for benzonitrile [13] and acrylonitrile [24], it is the various coupling interactions affecting the rotational transition frequencies that enable the highly precise determination of the energy separation between vibrational states. This work presents the rotational spectroscopy and analysis of the ground and two lowest-energy vibrationally excited states of 2-cyanopyrimidine from 130 GHz to 500 GHz.

## 2. Experimental methods

A commercial sample of 2-cyanopyrimidine (Oakwood, 99% purity) was used without further purification. Using a millimeter-wave spectrometer that has been previously described [26,27], the rotational spectrum of 2-cyanopyrimidine was collected from 130 to 230 and from 235 to 360 GHz in a continuous flow at room temperature, with a sample pressure of 3 mTorr. Additional spectral data were obtained with a newly acquired amplification and multiplication chain that extended the frequency range to 500 GHz with a sample pressure of 4 mTorr. The separate spectral segments were combined into a single broadband spectrum using Kisiel's Assignment and Analysis of Broadband Spectra (AABS) software [24,28]. The complete spectrum from 130 to 500 GHz was obtained using automated data collection software over approximately nine days given these experimental parameters: 0.6 MHz/sec sweep rate, 10 ms time constant, and 50 kHz AM and 500 kHz FM modulation in a tone-burst design [29]. Pickett's SPFIT/SPCAT programs [30] were used for least-squares fits and spectral predictions, along with Kisiel's PIFORM, PLANM, and AC programs for analysis [31,32]. A uniform frequency measurement uncertainty of 0.050 MHz was assumed for all measurements.

## 3. Computational methods

Electronic structure calculations were carried out with Gaussian 16 [33] using the WebMO interface [34] to obtain theoretical spectroscopic constants. Optimized geometries at the B3LYP/6–311+(2d,p) and MP2/6–311+(2d,p) levels were obtained using "verytight" convergence criteria and an "ultrafine" integration grid. Subsequent anharmonic

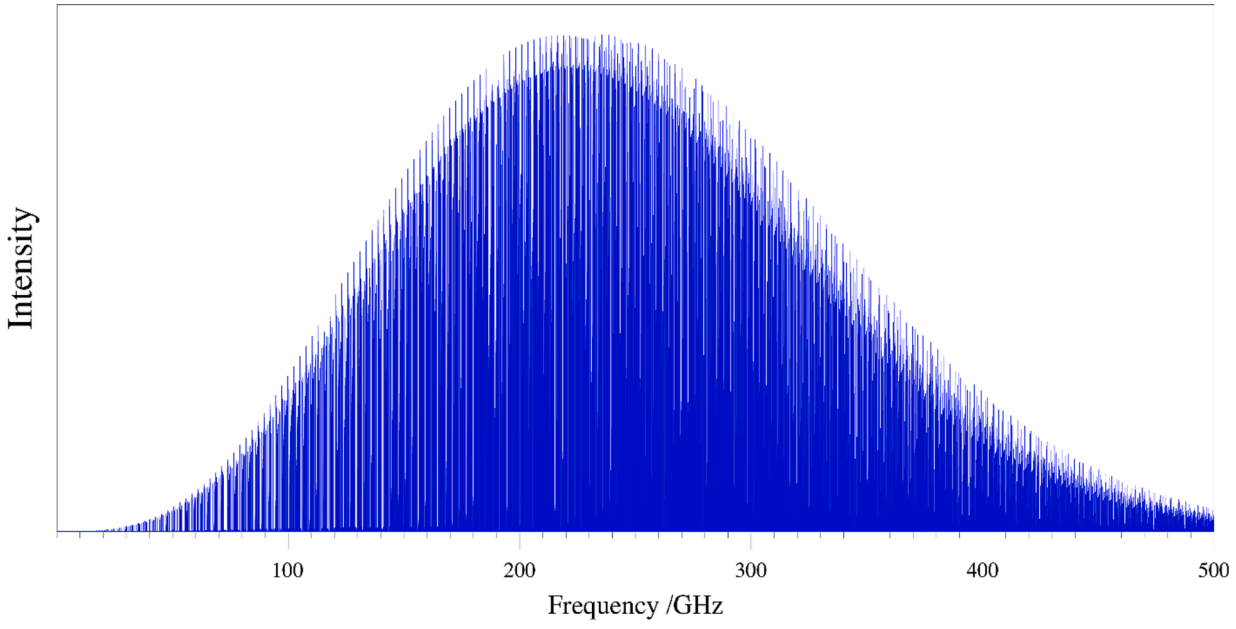


**Fig. 2.** Predicted rotational spectrum of the ground vibrational state of 2-cyanopyrimidine at 292 K.

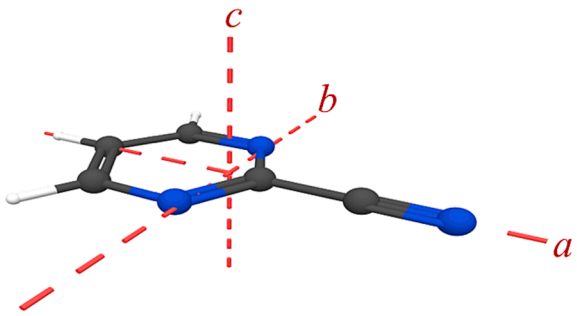


**Fig. 3.** 2-Cyanopyrimidine ($C_{2v}$, $\mu_a$ = 6.5 D, B3LYP) structure with principal inertial axes.

vibrational frequency calculations were carried out to obtain vibration–rotation interaction constants and predictions of the centrifugal distortion constants. These methods have been effective to generate the necessary spectroscopic constants for adequate *a priori* predictions for other cyanoarenes [12,13,15–17]. From the optimized geometries, magnetic calculations were also performed to obtain theoretical nuclear quadrupole coupling constants. Computational output files can be found in the supplementary material.

## 4. 2-Cyanopyrimidine rotational spectrum

The rotational spectrum of 2-cyanopyrimidine was obtained from 130 to 500 GHz. This frequency range satisfactorily covered the most intense rotational transitions, as judged by comparison to the predicted rotational populations in the 2-cyanopyrimidine spectrum at ambient temperature (Fig. 2). While the peak transition intensities occur near 220 GHz, there is still substantial intensity well beyond 400 GHz. As will be discussed below, this extension in the frequency range to 500 GHz was vital in the analysis of the Coriolis-coupled dyad of $\nu_{18}$ and $\nu_{27}$, because most resonances were observed between 375 and 500 GHz, providing crucial coupling information.

### 4.1. Ground-State spectral analysis

The rotational spectrum of 2-cyanopyrimidine ($\mu$ = 6.5 D (B3LYP), $\kappa = -0.851$) has not been previously reported. As a consequence of $C_{2v}$ symmetry and the nitrile substituent lying along the *a*-principal axis (Fig. 3), 2-cyanopyrimidine exhibits only *a*-type rotational transitions. The rotational spectrum of this prolate, asymmetric top is thus dominated by $^aR_{0,1}$ ground-state and vibrationally excited-state transitions across the frequency range studied. Fig. 4 shows a small subset of the spectrum from 198 GHz to 199 GHz along with predicted stick spectra for the ground state and the two lowest-energy vibrationally excited states, $\nu_{18}$ and $\nu_{27}$. It is apparent that the spectrum also includes unassigned transitions that are due to higher-energy vibrationally excited states, but they are not addressed in this work. Similar to other monosubstituted arenes, despite being a near-prolate top ($\kappa = -0.851$), the most prominent band structure for the ground state of 2-cyanopyrimidine follows the recognizable oblate-type band pattern at low $K_a$ [12,13,15–17,35]. Bands start at $K_a = 0$ and increase in $K_a$ as $J''$ decreases. The band in Fig. 4 begins with a $K_c$-degenerate pair of $^aR_{0,1}$ transitions, which lose degeneracy at higher $K_a$ values. The degenerate $^aR_{0,1}$ transitions have quantum numbers that follow either $K_a + K_c = J$ or $K_a + K_c = J + 1$, and $K_a$ series with these selection rules are subsequently referred to as $K_a^+$ and $K_a^-$, respectively.

The vibrational ground state of 2-cyanopyrimidine has been least-squares fit to partial octic A- and S-reduced, single-state Hamiltonians with low error ($\sigma_{fit}$ = 36 kHz). As shown in Fig. 5, the final transition data set (~7600 transitions) encompasses an extensive range of quantum numbers with $J'' + 1 = 42$ to 189 and $K_a = 0$ to 63. The resulting spectroscopic constants are reported in Table 2 along with respective computed values (B3LYP and MP2). Though a partial octic Hamiltonian was utilized, no computational comparison is possible for the octic centrifugal distortion constants, because there is no readily available software to compute these values. As a result, octic terms that were undeterminable in the least-squares fit were set to a value of zero. There were an insufficient number of nuclear quadrupole coupling-resolved transitions to obtain experimental nuclear quadrupole coupling constants, therefore these terms were not included in the Hamiltonian. Least-squares fitting files and computed nuclear quadrupole coupling constants can be found in the supplementary material.

The MP2-computed rotational constants are in satisfactory agreement with the experimental values (within ~ 1%), but the B3LYP-computed rotational constants are closer in agreement (within ~ 0.13%). This result is similar to the situation observed for cyanopyrazine [17]. The B3LYP-computed quartic centrifugal distortion constants are also in good agreement with the experimental values (within 10%), with $\Delta_K$ and $D_K$ having the largest difference from experiment. The MP2

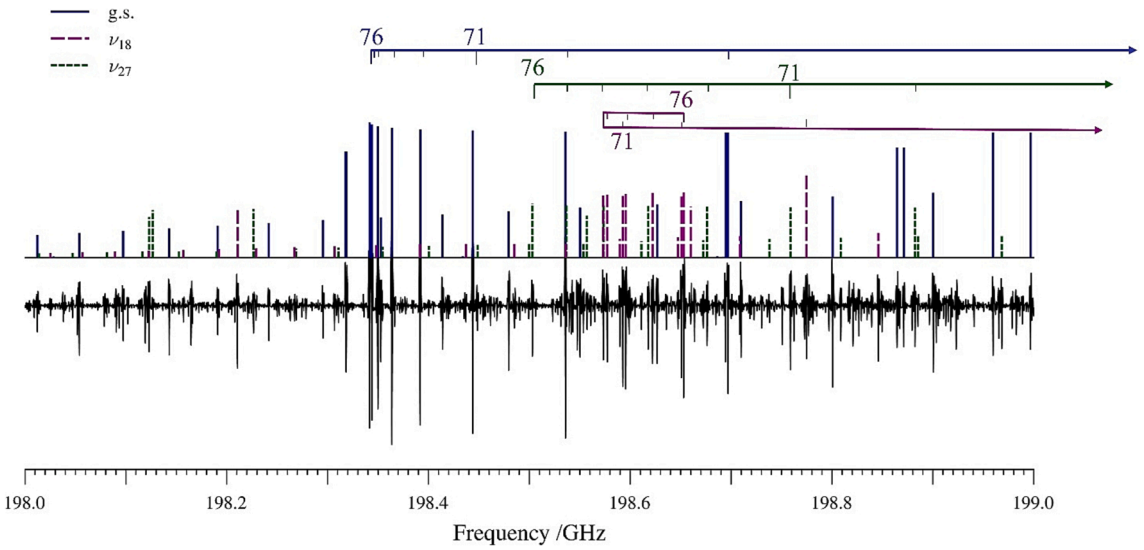


**Fig. 4.** Experimental rotational spectrum (bottom) of 2-cyanopyrimidine from 198 to 199 GHz and stick spectra (top) from experimental spectroscopic constants. The ground state (blue), $\nu_{18}$ (magenta), and $\nu_{27}$ (green) are labeled by the upper energy-level quantum number, $J'' + 1$. (For interpretation of the references to colour in this figure legend, the reader is referred to the web version of this article.)

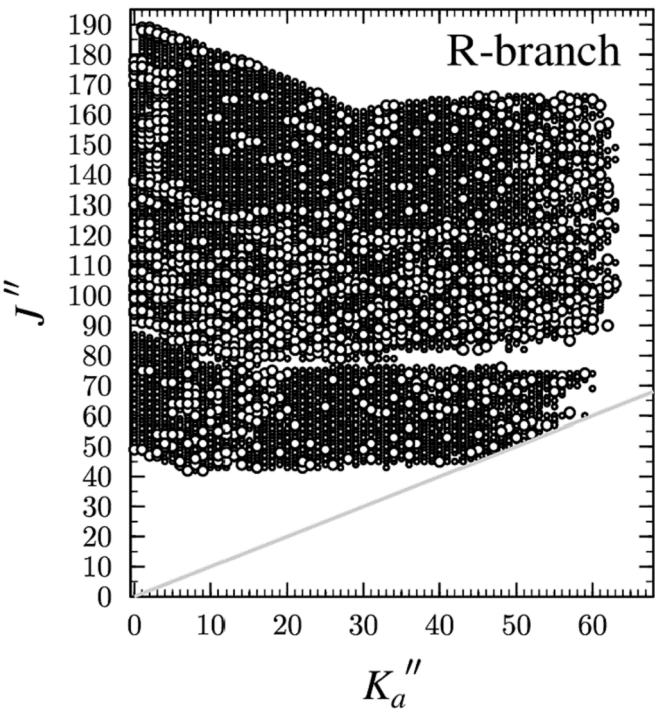


**Fig. 5.** Data distribution plot for the least-squares fit of spectroscopic data for the vibrational ground state of 2-cyanopyrimidine. The size of the outlined circle is proportional to the value of $|(f_{obs.} - f_{calc.})/\delta f|$, where $\delta f$ is the frequency measurement uncertainty and all values are less than 3.

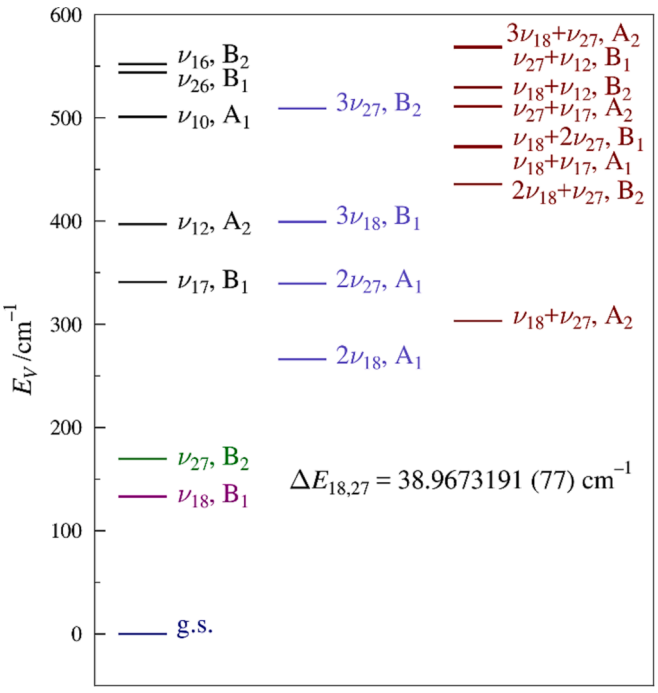


**Fig. 6.** Vibrational energy levels of 2-cyanopyrimidine below 600 $cm^{-1}$ from computed fundamental frequencies (B3LYP/6–311+G(2d,p)). The value of $\Delta E_{18,27}$ results from the experimental perturbation analysis of $\nu_{18}$ and $\nu_{27}$ in this work (*vide infra*).

quartic centrifugal distortion constants are in slightly closer agreement with the experimental values (within 5%), with $\delta_J$ and $d_1$ having the largest discrepancies. There is poorer agreement for the sextic centrifugal distortion constants for both sets of computed values. With the exception of $\Phi_K$ and $\phi_J$, the B3LYP values are within ~ 15%, and the MP2 values are within 10%, excluding $H_K$, and $h_1$. The B3LYP values of $\Phi_K$ and $H_K$ are approximately half of their experimental values, and the MP2 values are only slightly closer. The values of $\phi_J$ and $h_1$ are the smallest of the sextic centrifugal distortion constants, so it is not surprising that their predictions have large relative errors. The worst of

**Table 2**
Experimental and computational spectroscopic constants for the ground vibrational state of 2-cyanopyrimidine (A- and S-reduced Hamiltonians, $I^r$ representation).

| A Reduction, $I^r$ representation | | | | S Reduction, $I^r$ representation | | | |
|---|---|---|---|---|---|---|---|
| | Experimental [a] | B3LYP [b] | MP2 [b] | | Experimental [a] | B3LYP [b] | MP2 [b] |
| $A_0$ (MHz) | 6043.4539 (12) | 6051 | 5986 | $A_0$ (MHz) | 6043.4535 (12) | 6051 | 5986 |
| $B_0$ (MHz) | 1651.140609 (36) | 1649 | 1635 | $B_0$ (MHz) | 1651.139276 (36) | 1649 | 1635 |
| $C_0$ (MHz) | 1296.639905 (39) | 1295 | 1284 | $C_0$ (MHz) | 1296.641199 (39) | 1295 | 1284 |
| $\Delta_J$ (kHz) | 0.0483056 (22) | 0.0464 | 0.0460 | $D_J$ (kHz) | 0.0354922 (20) | 0.0345 | 0.0338 |
| $\Delta_{JK}$ (kHz) | 1.037502 (25) | 0.976 | 1.01 | $D_{JK}$ (kHz) | 1.114400 (26) | 1.05 | 1.08 |
| $\Delta_K$ (kHz) | 0.3608 (18) | 0.389 | 0.351 | $D_K$ (kHz) | 0.3003 (18) | 0.330 | 0.290 |
| $\delta_J$ (kHz) | 0.01154427 (86) | 0.0111 | 0.0110 | $d_1$ (kHz) | −0.01154436 (86) | −0.0111 | −0.0110 |
| $\delta_K$ (kHz) | 0.660687 (56) | 0.621 | 0.635 | $d_2$ (kHz) | −0.00640999 (54) | −0.00594 | −0.00611 |
| $\Phi_J$ (Hz) | 0.000001716 (84) | 0.00000174 | 0.00000187 | $H_J$ (Hz) | −0.000012737 (77) | −0.0000117 | −0.0000129 |
| $\Phi_{JK}$ (Hz) | 0.0017323 (24) | 0.00149 | 0.00163 | $H_{JK}$ (Hz) | 0.0011987 (19) | 0.00103 | 0.00115 |
| $\Phi_{KJ}$ (Hz) | −0.008505 (15) | −0.00739 | −0.00819 | $H_{KJ}$ (Hz) | −0.006498 (16) | −0.00566 | −0.00634 |
| $\Phi_K$ (Hz) | 0.0107 (10) | 0.00653 | 0.00718 | $H_K$ (Hz) | 0.0116 (10) | 0.00528 | 0.00583 |
| $\phi_J$ (Hz) | 0.000001226 (19) | 0.000000881 | 0.000000922 | $h_1$ (Hz) | −0.000000239 (19) | −0.000000409 | −0.00000046 |
| $\phi_{JK}$ (Hz) | 0.0008021 (15) | 0.000751 | 0.000824 | $h_2$ (Hz) | 0.000007394 (15) | 0.00000674 | 0.00000740 |
| $\phi_K$ (Hz) | 0.008258 (34) | 0.00731 | 0.00779 | $h_3$ (Hz) | 0.0000014737 (48) | 0.00000129 | 0.00000139 |
| $L_J$ (mHz) | 0.0000000167 (12) | | | $L_J$ (mHz) | 0.0000000114 (12) | | |
| $L_{JJK}$ (mHz) | −0.000002409 (17) | | | $L_{JJK}$ (mHz) | −0.000002025 (17) | | |
| $L_{JK}$ (mHz) | 0.00001448 (22) | | | $L_{JK}$ (mHz) | 0.00001835 (22) | | |
| $L_{KKJ}$ (mHz) | −0.0001149 (31) | | | $L_{KKJ}$ (mHz) | −0.0001301 (31) | | |
| $L_K$ (mHz) | [0.] | | | $L_K$ (mHz) | [0.] | | |
| $\Delta_i$ (uÅ$^2$) [c,d] | 0.057658 (21) | | | $\Delta_i$ (uÅ$^2$) [c,d] | 0.057568 (21) | | |
| $N_{lines}$ [e] | 7591 | | | $N_{lines}$ [e] | 7591 | | |
| $\sigma_{fit}$ (MHz) | 0.036 | | | $\sigma_{fit}$ (MHz) | 0.036 | | |

[a] Off-diagonal octic centrifugal distortion terms (not shown in table) were held constant at a value of zero.
[b] Evaluated with the 6–311+G(2d,p) basis set.
[c] Inertial defect, $\Delta_i = I_c - I_a - I_b$.
[d] Calculated using PLANM from the $B_0$ constants.
[e] Number of fitted transition frequencies.

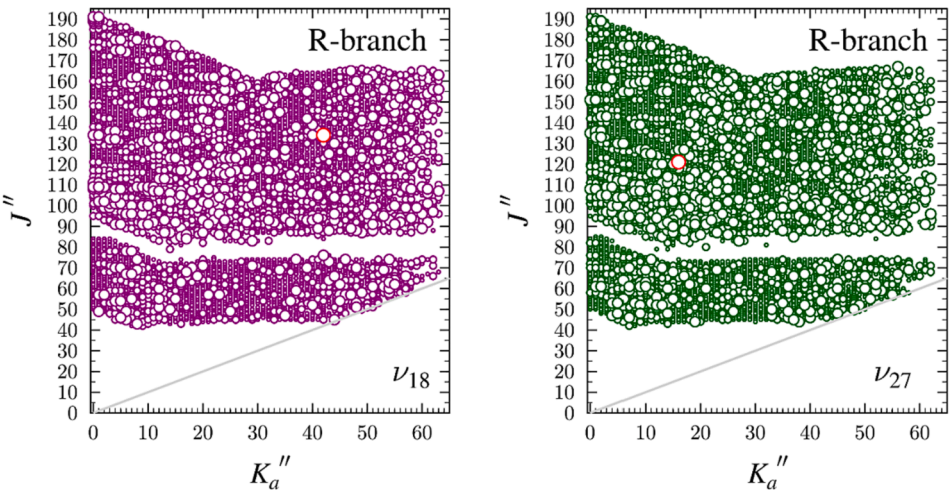


**Fig. 7.** Data distribution plots for the least-squares fit of spectroscopic data for the lowest-energy fundamental states of 2-cyanopyrimidine, $\nu_{18}$ (magenta) and $\nu_{27}$ (green). The size of the symbol is proportional to the value of $|(f_{obs.} - f_{calc.})/\delta f|$, where $\delta f$ is the frequency measurement uncertainty, and values greater than 3 are depicted in red. (For interpretation of the references to colour in this figure legend, the reader is referred to the web version of this article.)

these, the MP2 prediction of $h_1$, is approximately twice the size of the experimental value. Unlike the case of cyanopyrazine [17], however, no sign change in the value of $h_1$ was observed for 2-cyanopyrimidine. On average, the MP2 computed distortion constants are in closer agreement with experiment than the B3LYP values. Despite the discrepancies described for each set of computed values, they provide very good *a priori* predictions of the rotational spectrum and are important in assisting the early stage of least-squares fitting.

### 4.2. Spectral analysis of $\nu_{18}$ and $\nu_{27}$

The two lowest-energy vibrationally excited states of 2-cyanopyrimidine are an isolated, Coriolis-coupled dyad, similar to those seen in other cyanoarenes [12,13,15–17]. The lower-energy vibration, $\nu_{18}$ ($B_1$, 132 $cm^{-1}$ B3LYP), is an out-of-plane bend of the nitrile group with respect to the aromatic ring, while $\nu_{27}$ ($B_2$, 175 $cm^{-1}$ B3LYP) involves an in-plane bend of the nitrile group. The vibrational manifold of 2-cyanopyrimidine below 600 $cm^{-1}$ is presented in Fig. 6, which depicts additional possible coupled states, especially above 450 $cm^{-1}$. This work focuses only on the coupled dyad of $\nu_{18}$ and $\nu_{27}$. The initial assignment of $\nu_{18}$ and

**Table 3**
Experimentally determined spectroscopic constants for the ground and vibrationally excited states $\nu_{18}$ and $\nu_{27}$ of 2-cyanopyrimidine (A-reduced Hamiltonian, $I^r$ representation).

| | ground state [a] | $\nu_{18}$ ($B_1$, 133 $cm^{-1}$) [a,b] | $\nu_{27}$ ($B_2$, 175 $cm^{-1}$) [a,b] |
|---|---|---|---|
| $A_v$ (MHz) | 6043.4539 (12) | 6051.08 (13) | 6032.06 (13) |
| $B_v$ (MHz) | 1651.140609 (36) | 1653.012774 (36) | 1654.267680 (36) |
| $C_v$ (MHz) | 1296.639905 (39) | 1298.754909 (32) | 1297.555132 (34) |
| $\Delta_J$ (MHz) | 0.0483056 (22) | 0.0492650 (13) | 0.0493417 (13) |
| $\Delta_{JK}$ (MHz) | 1.037502 (25) | 1.06773 (49) | 0.98437 (49) |
| $\Delta_K$ (MHz) | 0.3608 (18) | [0.3608] | 0.4143 (13) |
| $\delta_J$ (MHz) | 0.01154427 (86) | 0.01162990 (85) | 0.01194518 (88) |
| $\delta_K$ (MHz) | 0.660687 (56) | 0.663053 (60) | 0.662360 (57) |
| $\Phi_J$ (MHz) | 0.000001716 (84) | 0.000002372 (31) | 0.000002309 (31) |
| $\Phi_{JK}$ (MHz) | 0.0017323 (24) | 0.0017797 (84) | 0.0016502 (88) |
| $\Phi_{KJ}$ (MHz) | −0.008505 (15) | −0.008081 (11) | [−0.008505] |
| $\Phi_K$ (MHz) | 0.0107 (10) | [0.0107] | [0.0107] |
| $\phi_J$ (MHz) | 0.000001226 (19) | 0.000001384 (18) | 0.000001592 (18) |
| $\phi_{JK}$ (MHz) | 0.0008021 (15) | 0.0008179 (11) | 0.0007685 (11) |
| $\phi_K$ (MHz) | 0.008258 (34) | 0.008228 (26) | 0.008475 (27) |
| $\Delta E_{18,27}$ (MHz) | | 1168210.84 (23) | |
| $\Delta E_{18,27}$ ($cm^{-1}$) | | 38.9673191 (77) | |
| $G_a$ (MHz) | | 10666.3 (75) | |
| $G_a^J$ (MHz) | | −0.006165 (29) | |
| $G_a^K$ (MHz) | | −0.00466 (14) | |
| $G_a^{JJ}$ (MHz) | | 0.00000000635 (44) | |
| $F_{bc}$ (MHz) | | −0.3779 (26) | |
| $F_{bc}^k$ (kHz) | | −0.000006992 (97) | |
| $\Delta_i$ (uÅ$^2$) [c,d] | 0.057658 (21) | −0.1214 (19) | 0.1997 (19) |
| $N_{lines}$ [e] | 7591 | 7114 | 6712 |
| $\sigma_{fit}$ (MHz) | 0.036 | 0.046 | 0.048 |

[a] Octic centrifugal distortion constants are not shown and, for the excited states, are held constant at their ground-state values in Table 2.
[b] Fundamental frequencies calculated using B3LYP/6–311+G(2d,p).
[c] Inertial defect, $\Delta_i = I_c - I_a - I_b$.
[d] Calculated using PLANM from the $B_v$ constants.
[e] Number of fitted transition frequencies.

**Table 4**
Vibration-rotation interaction and Coriolis-coupling constants of the 2-cyanopyrimidine $\nu_{18}$-$\nu_{27}$ dyad.

| | Experimental | B3LYP [a] | MP2 [a] |
|---|---|---|---|
| $A_0 - A_{18}$ (MHz) | −7.62 (13) | 81.13 | 95.75 |
| $B_0 - B_{18}$ (MHz) | −1.872165 (51) | −1.84 | −1.77 |
| $C_0 - C_{18}$ (MHz) | −2.115004 (50) | −2.09 | −2.03 |
| $A_0 - A_{27}$ (MHz) | 11.39 (13) | −77.53 | −92.33 |
| $B_0 - B_{27}$ (MHz) | −3.127071 (51) | −2.96 | −3.08 |
| $C_0 - C_{27}$ (MHz) | −0.915227 (52) | −0.85 | −0.91 |
| $\frac{(A_0 - A_{18}) + (A_0 - A_{27})}{2}$(MHz) | 1.88 (09) | 1.80 | 1.71 |
| $\frac{(B_0 - B_{18}) + (B_0 - B_{27})}{2}$(MHz) | −2.499618 (36) | −2.40 | −2.43 |
| $\frac{(C_0 - C_{18}) + (C_0 - C_{27})}{2}$(MHz) | −1.515115 (36) | −1.47 | −1.47 |
| $\left\|\zeta^a_{18,27}\right\|$ | 0.873 | 0.809 | 0.810 |
| $\Delta E_{18,27}$ (cm$^{-1}$) | 38.9673191 (77) | 42.70 | 36.64 |

[a] Evaluated with the 6–311+G(2d,p) basis set.

$\nu_{27}$ was performed using a single-state, distorted-rotor Hamiltonian for each vibrational state. Computationally predicted rotational constants and ground-state distortion constants were used for initial predictions. This technique allowed for the assignment of three series corresponding to $K_a = 0$, 1, and 2 for both states, but there was apparent perturbation in each least-squares fit that was untreated in a single-state model. Thus, a two-state model was adopted, initially using the $\Delta E_{18,27}$ and $G_a$ values predicted by B3LYP and the rotational constants $A_0$, $B_v$ and $C_v$ ($A_0$ is the experimental ground-state value and $B_v$ and $C_v$ are the experimental ground-state values corrected by the respective B3LYP vibration–rotation interaction constants, $\alpha_B$ and $\alpha_C$, for each vibrational state). The vibration–rotation interaction constant, $\alpha_A$, was not used because it showed clear signs of absorbed perturbation (equal magnitude but opposite sign for each state; *vide infra*). Quartic, sextic, and octic distortion constants were set to their ground-state values, and in the initial least-squares fitting process, only $\Delta E$ and $C_v$ were allowed to vary. As transitions were added to the least-squares fit, additional rotational, centrifugal, and Coriolis-coupling coefficients were varied to model the experimental spectrum until all observed transitions for each vibrational state were assigned across the frequency region measured. The extent of the rotational transitions measured is shown in Fig. 7, and the spectroscopic constants determined in the least-squares fit are provided in Table 3.

The final least-squares fit is an exhaustive collection of transitions across the frequency region and totals over 7100 transitions for $\nu_{18}$ and 6700 for $\nu_{27}$. The totals are only slightly lower than that for the ground state (~7600), which is expected due to the somewhat lower intensity of vibrationally excited states. The observed transitions range from 42 to 192 in $J'' + 1$ for both states and $K_a = 0$ to 63 and 62 for $\nu_{18}$ and $\nu_{27}$, respectively. The data set includes transition frequencies that are shifted *via* global perturbations and intense resonances and includes 17 transitions that are formally forbidden, coupling-allowed interstate transitions. To achieve a satisfactory fit, it was necessary to extend the frequency range beyond 360 GHz, because most resonances occur in this region. These highly perturbed resonant transitions are critical in determining accurate and precise Coriolis-coupling constants. The importance of data in the higher frequency region was noted in the earlier case of cyanopyrazine [17], and it is even more important for 2-cyanopyrimidine. Attempts to obtain a satisfactory least-squares fit using only data from the 130 GHz to 360 GHz frequency range were ultimately unsuccessful. Least-squares fitting of the final data set, including resonant transitions and symmetry-allowed interstate transitions, provides a precise energy separation between $\nu_{18}$ and $\nu_{27}$ ($\Delta E_{18,27}$ = 38.9673191 (77) cm$^{-1}$). Based on similar results in molecules where the band origins have been measured independently by high-resolution infrared spectroscopy [13], the accuracy is presumed to be comparable to the precision. This large energy separation required much higher values of $J$ and $K$ of $\nu_{18}$ before the energy levels are sufficiently close to create resonances than in some previous works with smaller energy separations between the coupled modes [12,13,15,16,35]. Along with a precise value of $\Delta E_{18,27}$, the least-squares fit provides a nearly complete set of quartic and sextic distortion constants, excluding $\Delta_K$ for $\nu_{18}$, $\Phi_{KJ}$ for $\nu_{27}$ and $\Phi_K$ for both $\nu_{18}$ and $\nu_{27}$. Unfortunately, $\Delta_K$ of $\nu_{18}$ could not be determined, which is attributed to the high correlation of $\Delta_K$ with $A_{18}$ and the limitation of being able to measure only $^aR_{0,1}$ transitions. In addition, six Coriolis-coupling terms ($G_a$, $G_a^J$, $G_a^K$, $G_a^{JJ}$, $F_{bc}$, and $F_{bc}^K$) were determined. The inclusion of all of these coupling terms was needed to obtain a satisfactory least-squares fit with a total error lower than the measurement uncertainty of 50 kHz.

A measure of the quality of the least-squares fit comes from the comparison of the computed rotational constants to those experimentally determined, to establish whether or not any of the computed constants show signs of untreated Coriolis coupling. The vibration–rotation interaction constants (Table 4) provide a straightforward comparison between the experimental and computed values, where unaddressed Coriolis coupling appears as large values with opposing

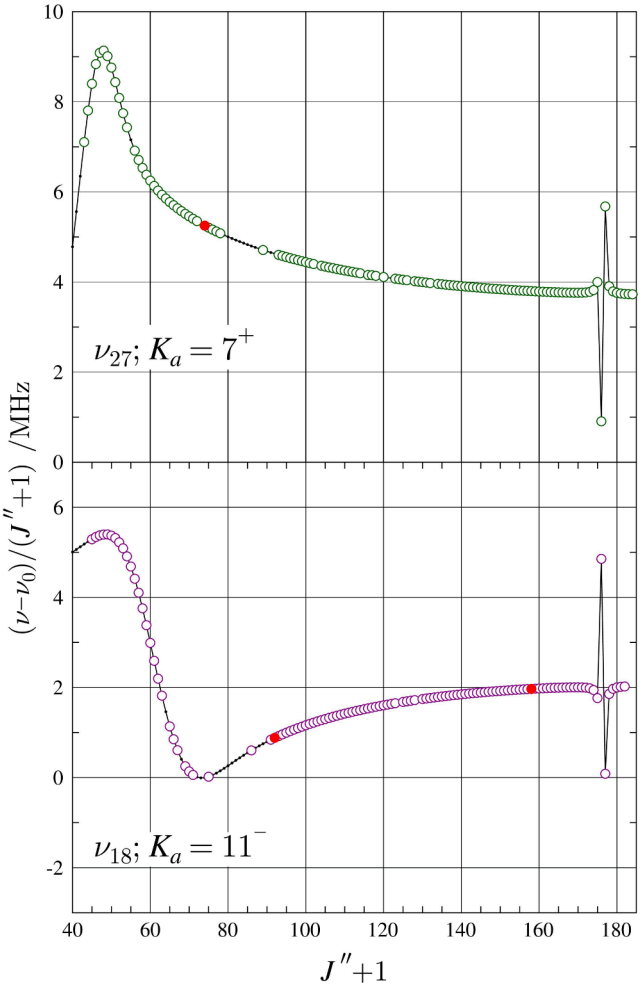


**Fig. 8.** Resonance plots for 2-cyanopyrimidine showing the $K_a = 11^-$ series for $\nu_{18}$ and $K_a = 7^+$ series for $\nu_{27}$. These two resonances conform to the $\Delta K_a = 4$ selection rule for *a*-type resonances. The plotted values are frequency differences between excited-state transitions and their ground-state counterparts, scaled by ($J'' + 1$) in order to make the plots more horizontal. Measured transitions are represented by circles: $\nu_{18}$ (magenta), $\nu_{27}$ (green). Red circles indicate transitions whose *obs.* – *calc.* values are more than three times the experimental uncertainty. Predictions from the final coupled fit are represented by a solid black line. (For interpretation of the references to colour in this figure legend, the reader is referred to the web version of this article.)

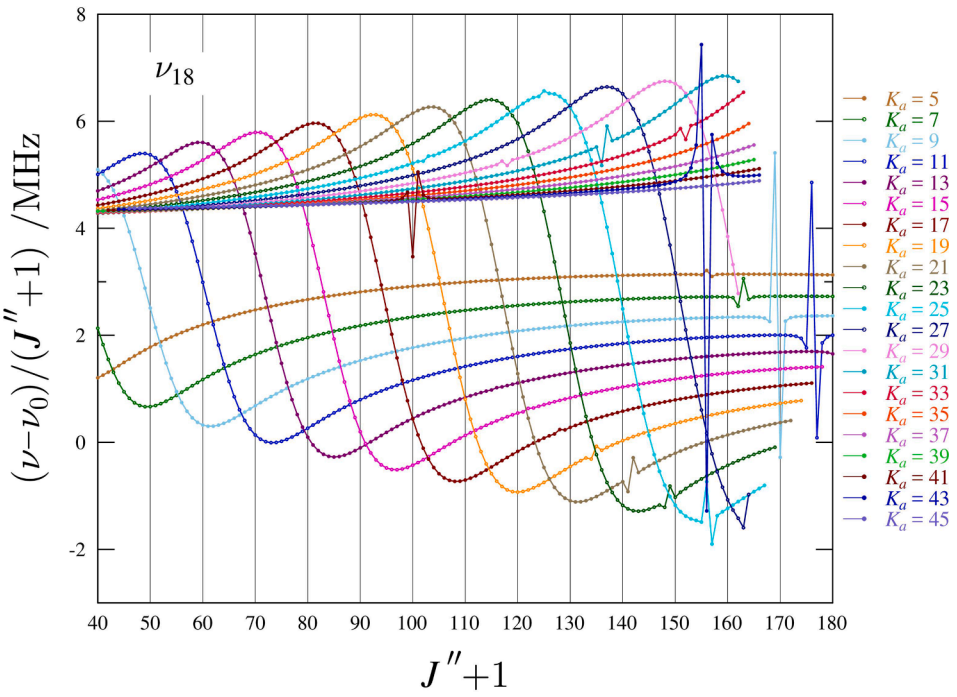


**Fig. 9.** Superimposed resonance plots of $\nu_{18}$ for $^aR_{0,1}$ odd-$K_a$ series from 5 to 45 for 2-cyanopyrimidine. Measured transitions are omitted for clarity, but they are indistinguishable from the plotted values on this scale. The plotted values are frequency differences between excited-state transitions and their ground-state counterparts, scaled by $(J'' + 1)$.

sign between the two vibrational states. The MP2 values of $B_0 - B_v$ and $C_0 - C_v$ are in excellent agreement with the experimental values (within 6%), which provides confidence in the method to determine the vibration–rotation interaction constants. The corresponding B3LYP values are approximately as accurate as the MP2 values for $B_0 - B_v$ and $C_0 - C_v$ (within 7%). In contrast, both the B3LYP and MP2 values of $A_0 - A_v$ show poor agreement with the experimental values, each having similarly large discrepancies and much larger magnitudes than the experimental values (Table 4). The disagreement indicates the presence of untreated Coriolis coupling in both computational results or in the experimental values. The fact that the experimental values are significantly smaller than either computed value suggests that the least-squares fit may be performing a better job of treating the Coriolis coupling. This situation, in which the experimental $A_0 - A_v$ values have different signs than the computed values, was also noted in previous works [17,22]. The average of the computed $A_0 - A_v$ values for $\nu_{18}$ and $\nu_{27}$ cancels out the unaddressed Coriolis effects, and these averages are in excellent agreement with the experimental average (Table 4). Unsurprisingly, the corresponding average values for the $B_v$ and $C_v$ values are also in excellent agreement between both theoretical treatments and experiment. The $\Delta E_{18,27}$ values for both computational methods are in close agreement; the B3LYP value is approximately 4 $cm^{-1}$ too large and the MP2 value is approximately 2 $cm^{-1}$ too small. The experimental Coriolis $\zeta^a_{18,27}$ value is also in satisfactory agreement with both the MP2 and B3LYP values with the experimental value being slightly larger (7%). The agreement between experimental and computational Coriolis $\zeta^a_{18,27}$ values, along with a low $\sigma_{fit}$ value, indicate a satisfactory treatment of the Coriolis coupling that is present in the $\nu_{18}$-$\nu_{27}$ dyad of 2-cyanopyrimidine.

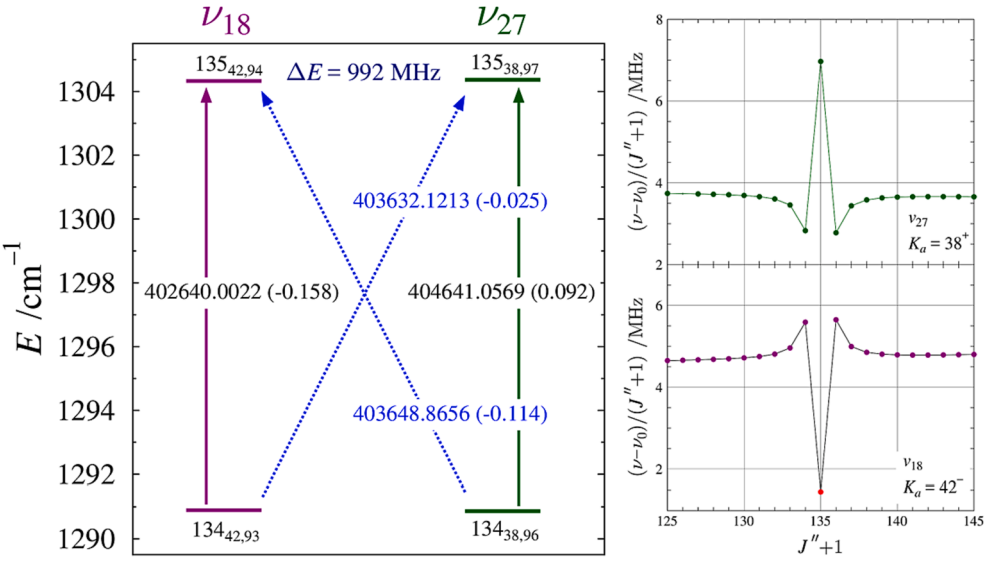


**Fig. 10.** Energy diagram (left) depicting a representative matched pair of nominal interstate transitions between the $\nu_{18}$ (magenta) and $\nu_{27}$ (green) vibrational states of 2-cyanopyrimidine. Standard $^aR_{0,1}$ transitions within vibrational states are denoted by vertical arrows. The diagonal, dashed arrows indicate nominal interstate transitions that are formally forbidden but enabled as a result of rotational energy-level mixing. Values printed on each of the arrows are the corresponding transition frequency (in MHz) with its *obs.* – *calc.* value in parentheses. The marked energy separation is between the two strongly interacting rotational energy levels. Resonance plots (right) of the $K_a$ series of $\nu_{18}$ and $\nu_{27}$ show the corresponding resonant intrastate transitions. (For interpretation of the references to colour in this figure legend, the reader is referred to the web version of this article.)

**Table 5**
Experimental energy separations for selected organic species for the out-of-plane and in-plane nitrile bending modes.

| | $\Delta E_{ip-oop}$ ($cm^{-1}$) | *ortho* N | *meta* N | *para* N |
|---|---|---|---|---|
| benzonitrile [12,13] | 19.1081701(74) | 0 | 0 | 0 |
| 3-cyanopyridine [15] | 15.7524693 (37) | 0 | 1 | 0 |
| 4-cyanopyridine [16] | 18.806554 (11) | 0 | 0 | 1 |
| cyanopyrazine [17] | 24.8245962 (60) | 1 | 1 | 0 |
| cyanopyrimidine (this work) | 38.9673191 (77) | 2 | 0 | 0 |

The successful incorporation of many resonant and nominal interstate transitions into the data set indicates an adequate treatment of the dyad by the Hamiltonian, since these transitions are highly dependent on $\Delta E_{18,27}$ and the Coriolis-coupling coefficients utilized in the least-squares fit. One example of the state mixing between vibrational states is shown in Fig. 8, where a sharp resonance occurs between the $K_a = 11^-$ series of $\nu_{18}$ and $K_a = 7^+$ series of $\nu_{27}$ ($\Delta K_a = 4$). The most-perturbed transition, at $J'' + 1 = 176$, is ~ 500 MHz from its unperturbed location. Each of these series also displays large undulations occurring from both global coupling perturbation and centrifugal distortion. The progression of the global undulation, from low to high frequencies as $K_a$ increases, is displayed in Fig. 9. This plot highlights several of the resonances present for the $\nu_{18}$-$\nu_{27}$ dyad, and the most perturbed transition, located in $K_a = 43$, is ~ 1 GHz from its unperturbed location. Most resonances are above $J'' + 1 = 130$, reaffirming the utility of the extension of the frequency range to 500 GHz.

A total of 17 independent nominal interstate transitions were measured and incorporated into the least-squares fit, and they were crucial in finalizing several Coriolis-coupling constants and confirming the assignment of some resonant transitions. These nominal interstate transitions occur when rotational energy levels from each vibrational state are close enough in energy that intense state-mixing occurs. In many cases, it is possible to measure corresponding intrastate and interstate transitions for each level to create a matched set of four transitions (Fig. 10). As these four transitions involve the same energy levels, the average of the interstate transition frequencies must be the same as the intrastate transition frequencies. This condition confirms the assignment of all transitions when the difference between the sets of transitions is less than the measurement uncertainty of 50 kHz. The frequency difference between the transitions in Fig. 10 is only 36 kHz despite the higher *obs*. – *calc*. for individual transitions, *e.g.*, the intrastate transition of $\nu_{18}$, where it is one of two transitions in the fit that is greater than three times the measurement uncertainty and is shown in red in the resonance plot of Fig. 10 and in the data distribution plot (Fig. 7). The typical working procedure for least-squares fitting is to scrutinize transitions with greater than two times the measurement uncertainty with regards to including such transitions in the least-squares fit. This transition displays an abnormal line shape, which is likely due to another underlying transition distorting its true frequency. Although this would typically warrant the exclusion of this transition, the very limited number of these important resonant and nominal interstate transitions in the data set make even this imperfectly measured transition highly valuable for the coupling information it provides. As a result, it was retained in the final data set with explicably high error.

Measurement of the precise and accurate value of the energy difference for the out-of-plane and in-plane nitrile bending modes for a variety C($sp^2$)–CN-containing organic molecules, including the previously studied cyanoarenes, allows for an analysis of the structural factors that impact the vibrational mode energies. As shown in Fig. 1, the structure of each of the cyanoarenes recently studied in our group [15–17] differs from benzonitrile [12,13] by *N*-atom substitution in the aromatic ring. Similar to benzonitrile, 3-cyanopyridine [15] and 4-cyanopyridine [16] have *ortho* C–H groups adjacent to the nitrile. Cyanopyrazine [17] has an *ortho* C–H group and a nitrogen atom. 2-Cyanopyrimidine from this work completes this series by providing analogous data for a cyanoarene with two *ortho* nitrogen atoms. There is a monotonic increase in the $\Delta E_{ip-oop}$ values with increasing substitutions of *ortho* C–H groups with nitrogen atoms shown in Table 5. There is a smaller change to $\Delta E_{ip-oop}$ with *meta* substitution in the reverse direction, such that the effects of *ortho* and *meta* substitution are approximately +10 and −3 $cm^{-1}$, respectively.

## 5. Conclusion

To expand the search for heterocyclic aromatic molecules in the interstellar medium, the current study provides the necessary laboratory data for 2-cyanopyrimidine. The larger dipole moment of 2-cyanopyrimidine (6.5 D) vs pyrimidine (2.3 D) increases the possibility of detection in the ISM if these species were to have similar abundances. The combination of the spectroscopic constants provided here, along with computed (provided in Supplementary Material) or experimental nuclear quadrupole coupling constants, would reliably predict transition frequencies much lower or slightly higher in frequency than the frequency range of the current measurements (130–500 GHz). The least-squares fit of the Coriolis-coupled dyad of $\nu_{18}$ and $\nu_{27}$ allows for a precise determination of the energy separation of the fundamental modes, $\Delta E_{18,27}$, although high-resolution infrared spectroscopy is needed to determine the fundamental frequencies. This infrared study would be challenging, however, since $\nu_{18}$ and $\nu_{27}$ have quite low predicted intensities (0.1 and 0.6 km/mol (MP2), respectively). Of the cyanoarenes studied to date, 2-cyanopyrimidine exhibits the largest energy difference for the out-of-plane and in-plane nitrile bending modes ($\Delta E_{ip-oop}$ = 38.9673191 (77) $cm^{-1}$). This large energy separation notwithstanding, a two-state Hamiltonian is required to adequately address the transition frequencies observed for each vibrational state – even in the 130 – 360 GHz range. At the same time, highly-perturbed transition frequencies (resonances) above 360 GHz are required to adequately describe the Coriolis perturbation and obtain a satisfactory least-squares fit. This behavior demonstrates how broadly Coriolis perturbation can affect transition frequencies, even those that are not “highly” perturbed as resonances, and that the resonant transitions provide important constraints on the determination of the spectroscopic parameters that cannot be obtained from transition frequencies influenced by the global Coriolis interaction alone.

## Declaration of Competing Interest

The authors declare that they have no known competing financial interests or personal relationships that could have appeared to influence the work reported in this paper.

## Data availability

Data are provided in the article and in the Supplementary Material.

## Acknowledgments

We gratefully acknowledge funding from the U.S. National Science Foundation for support of this project (CHE-1954270). We thank Michael McCarthy for the loan of an amplification-multiplication chain and the Harvey Spangler Award (to B.J.E) for support of the purchase of the corresponding zero-bias detector.

## Appendix A. Supplementary material

Supplementary data to this article can be found online at https://doi.org/10.1016/j.jms.2023.111737.

## References

[1] J. Cernicharo, A.M. Heras, A.G.G.M. Tielens, J.R. Pardo, F. Herpin, M. Guélin, L.B. F.M. Waters, Infrared Space Observatory's Discovery of $C_4H_2$, $C_6H_2$, and Benzene in CRL 618, Astrophys. J. 546 (2001) L123–L126.
[2] T.J. Barnum, M.A. Siebert, K.L.K. Lee, R.A. Loomis, P.B. Changala, S.B. Charnley, M.L. Sita, C. Xue, A.J. Remijan, A.M. Burkhardt, B.A. McGuire, I.R. Cooke, A Search for Heterocycles in GOTHAM Observations of TMC-1, J. Phys. Chem. A 126 (2022) 2716–2728.
[3] M.L. Kutner, D.E. Machnik, K.D. Tucker, R.L. Dickman, Search for interstellar pyrrole and furan, Astrophys. J. 242 (1980) 541–544.
[4] Y.-J. Kuan, C.-H. Yan, S.B. Charnley, Z. Kisiel, P. Ehrenfreund, H.-C. Huang, A search for interstellar pyrimidine, Mon. Not. R. Astron. Soc. 345 (2003) 650–656.
[5] S.B. Charnley, Y.-J. Kuan, H.-C. Huang, O. Botta, H.M. Butner, N. Cox, D. Despois, P. Ehrenfreund, Z. Kisiel, Y.-Y. Lee, A.J. Markwick, Z. Peeters, S.D. Rodgers, Astronomical searches for nitrogen heterocycles, Adv. Space Res. 36 (2005) 137–145.
[6] J. Basha N, N.M. Goudgaon, A comprehensive review on pyrimidine analogs-versatile scaffold with medicinal and biological potential, J. Mol. Struct. 1246 (2021) 131168.
[7] M.N. Simon, M. Simon, Search for Interstellar Acrylonitrile, Pyrimidine, and Pyridine, Astrophys. J. 184 (1973) 757–762.
[8] H.S.P. Müller, S. Thorwirth, D.A. Roth, G. Winnewisser, The Cologne Database for Molecular Spectroscopy, CDMS, Astron. Astrophys. 370 (2001) L49–L52.
[9] H.S.P. Müller, F. Schlöder, J. Stutzki, G. Winnewisser, The Cologne Database for Molecular Spectroscopy, CDMS: a Useful Tool for Astronomers and Spectroscopists, J. Mol. Struct. 742 (2005) 215–227.
[10] B.A. McGuire, A.M. Burkhardt, S.V. Kalenskii, C.N. Shingledecker, A.J. Remijan, E. Herbst, M.C. McCarthy, Detection of the Aromatic Molecule Benzonitrile (*c*-$C_6H_5CN$) in the Interstellar Medium, Science 359 (2018) 202–205.
[11] B.A. McGuire, R.A. Loomis, A.M. Burkhardt, K.L.K. Lee, C.N. Shingledecker, S. B. Charnley, I.R. Cooke, M.A. Cordiner, E. Herbst, S. Kalenskii, M.A. Siebert, E. R. Willis, C. Xue, A.J. Remijan, M.C. McCarthy, Detection of two interstellar polycyclic aromatic hydrocarbons via spectral matched filtering, Science 371 (2021) 1265–1269.
[12] M.A. Zdanovskaia, B.J. Esselman, H.S. Lau, D.M. Bates, R.C. Woods, R.J. McMahon, Z. Kisiel, The 103–360 GHz rotational spectrum of benzonitrile, the first interstellar benzene derivative detected by radioastronomy, J. Mol. Spectrosc. 351 (2018) 39–48.
[13] M.A. Zdanovskaia, M.-A. Martin-Drumel, Z. Kisiel, O. Pirali, B.J. Esselman, R. C. Woods, R.J. McMahon, The eight lowest-energy vibrational states of benzonitrile: analysis of Coriolis and Darling-Dennison couplings by millimeter-wave and far-infrared spectroscopy, J. Mol. Spectrosc. 383 (2022), 111568.
[14] P.M. Dorman, B.J. Esselman, R.C. Woods, R.J. McMahon, The 130 to 500 GHz rotational spectrum of 2-cyanopyridine (*o*-$C_5H_4N$-CN), manuscript in preparation (2023).
[15] P.M. Dorman, B.J. Esselman, R.C. Woods, R.J. McMahon, An analysis of the rotational ground state and lowest-energy vibrationally excited dyad of 3-cyano-pyridine: Low symmetry reveals rich complexity of perturbations, couplings, and interstate transitions, J. Mol. Spectrosc. 373 (2020), 111373.
[16] P.M. Dorman, B.J. Esselman, J.E. Park, R.C. Woods, R.J. McMahon, Millimeter-wave spectrum of 4-cyanopyridine in its ground state and lowest-energy vibrationally excited states, $\nu_{20}$ and $\nu_{30}$, J. Mol. Spectrosc. 369 (2020), 111274.
[17] B.J. Esselman, M.A. Zdanovskaia, H.H. Smith, R.C. Woods, R.J. McMahon, The 130–500 GHz Rotational Spectroscopy of Cyanopyrazine ($C_4H_3N_2$-CN), J. Mol. Spectrosc. 389 (2022), 111703.
[18] S. Doraiswamy, S.D. Sharma, Microwave spectrum of 2-cyanopyridine, Curr. Sci. 40 (1971) 398–399.
[19] R.G. Ford, The microwave spectra and dipole moments of the cyanopyridines, J. Mol. Spectrosc. 58 (1975) 178–184.
[20] N. Heineking, H. Dreizler, Nuclear Quadrupole Coupling Effects in the Rotational Spectrum of 4-Cyanopyridine, Z. Naturforsch. A 42 (1987) 83–86.
[21] N. Vogt, K.P.R. Nair, J.-U. Grabow, J. Demaison, Microwave rotational spectrum and ab initio computations on 4-cyanopyridine: molecular structure and hyperfine interactions, Mol. Phys. 116 (2018) 3530–3537.
[22] H.H. Smith, S.M. Kougias, B.J. Esselman, R.C. Woods, R.J. McMahon, Synthesis, Purification, and Rotational Spectroscopy of 1-Cyanocyclobutene ($C_5H_5N$), J. Phys. Chem. A 126 (2022) 1980–1993.
[23] B.J. Esselman, S.M. Kougias, M.A. Zdanovskaia, R.C. Woods, R.J. McMahon, Synthesis, Purification, and Rotational Spectroscopy of (Cyanomethylene) Cyclopropane—An Isomer of Pyridine, J. Phys. Chem. A 125 (2021) 5601–5614.
[24] Z. Kisiel, M.-A. Martin-Drumel, O. Pirali, Lowest vibrational states of acrylonitrile from microwave and synchrotron radiation spectra, J. Mol. Spectrosc. 315 (2015) 83–91.
[25] G. Cazzoli, Z. Kisiel, The rotational spectrum of acrylonitrile in excited states of the two low-frequency CCN bending vibrational modes, J. Mol. Spectrosc. 130 (1988) 303–315.
[26] B.K. Amberger, B.J. Esselman, J.F. Stanton, R.C. Woods, R.J. McMahon, Precise Equilibrium Structure Determination of Hydrazoic Acid ($HN_3$) by Millimeter-wave Spectroscopy, J. Chem. Phys. 143 (2015), 104310.
[27] B.J. Esselman, B.K. Amberger, J.D. Shutter, M.A. Daane, J.F. Stanton, R.C. Woods, R.J. McMahon, Rotational Spectroscopy of Pyridazine and its Isotopologs from 235–360 GHz: Equilibrium Structure and Vibrational Satellites, J. Chem. Phys. 139 (2013), 224304.
[28] Z. Kisiel, L. Pszczółkowski, I.R. Medvedev, M. Winnewisser, F.C. De Lucia, E. Herbst, Rotational spectrum of *trans–trans* diethyl ether in the ground and three excited vibrational states, J. Mol. Spectrosc. 233 (2005) 231–243.
[29] H.M. Pickett, Determination of collisional linewidths and shifts by a convolution method, Applied Optics 19 (1980) 2745–2749.
[30] H.M. Pickett, The fitting and prediction of vibration-rotation spectra with spin interactions, J. Mol. Spectrosc. 148 (1991) 371–377.
[31] Z. Kisiel, Assignment and Analysis of Complex Rotational Spectra, in: J. Demaison, K. Sarka, E.A. Cohen (Eds.), Spectroscopy From Space, Springer, Netherlands, Dordrecht, 2001, pp. 91–106.
[32] Z. Kisiel, PROSPE - Programs for ROtational SPEctroscopy. http://info.ifpan.edu.pl/~kisiel/prospe.htm.
[33] M.J. Frisch, G.W. Trucks, H.B. Schlegel, G.E. Scuseria, M.A. Robb, J.R. Cheeseman, G. Scalmani, V. Barone, G.A. Petersson, H. Nakatsuji, X. Li, M. Caricato, A.V. Marenich, J. Bloino, B.G. Janesko, R. Gomperts, B. Mennucci, H.P. Hratchian, J.V. Ortiz, A.F. Izmaylov, J.L. Sonnenberg, Williams, F. Ding, F. Lipparini, F. Egidi, J. Goings, B. Peng, A. Petrone, T. Henderson, D. Ranasinghe, V.G. Zakrzewski, J. Gao, N. Rega, G. Zheng, W. Liang, M. Hada, M. Ehara, K. Toyota, R. Fukuda, J. Hasegawa, M. Ishida, T. Nakajima, Y. Honda, O. Kitao, H. Nakai, T. Vreven, K. Throssell, J.A. Montgomery Jr., J.E. Peralta, F. Ogliaro, M.J. Bearpark, J.J. Heyd, E.N. Brothers, K.N. Kudin, V.N. Staroverov, T.A. Keith, R. Kobayashi, J. Normand, K. Raghavachari, A.P. Rendell, J.C. Burant, S.S. Iyengar, J. Tomasi, M. Cossi, J.M. Millam, M. Klene, C. Adamo, R. Cammi, J.W. Ochterski, R.L. Martin, K. Morokuma, O. Farkas, J.B. Foresman, D.J. Fox, Gaussian 16 Rev. C.01. Wallingford, CT, 2016.
[34] J.R. Schmidt, W.F. Polik, WebMO Enterprise. 17.0.012e ed.; WebMO, LLC., Holland, MI, USA, 2017.
[35] M.A. Zdanovskaia, B.J. Esselman, R.C. Woods, R.J. McMahon, The 130–370 GHz rotational spectrum of phenyl isocyanide ($C_6H_5NC$), J. Chem. Phys. 151 (2019), 024301.

Journal of Molecular Spectroscopy 389 (2022) 111703

Contents lists available at ScienceDirect

Journal of Molecular Spectroscopy

journal homepage: www.elsevier.com/locate/yjmsp

# The 130–500 GHz rotational spectroscopy of cyanopyrazine ($C_4H_3N_2$-CN)

Brian J. Esselman, Maria A. Zdanovskaia, Houston H. Smith, R. Claude Woods *, Robert J. McMahon *

*Department of Chemistry, University of Wisconsin–Madison, Madison, WI 53706, USA*

ARTICLE INFO

*Keywords:*
Rotational spectroscopy
Coriolis coupling
Interstellar molecule
Astrochemistry

ABSTRACT

The rotational spectrum of cyanopyrazine (2-pyrazinecarbonitrile, *p*-$C_4H_3N_2$-CN) has been obtained from 130 to 500 GHz. Rotational transitions of cyanopyrazine have been measured, assigned, and least-squares fit for the first time. Over 7000 transitions of the ground vibrational state have been least-squares fit to partial octic, A- and S-reduced Hamiltonians with low statistical uncertainty ($\sigma_{fit}$ = 34 kHz). Similar to other cyanoarenes, the first two fundamental modes are the out-of-plane ($\nu_{27}$, A″) and in-plane ($\nu_{19}$, A′) nitrile bending modes, which form an *a*- and *b*-axis Coriolis-coupled dyad. Greater than 5800 transitions from each of these vibrational modes were fit to a partial octic, A-reduced Hamiltonian ($\sigma_{fit}$ = 38 kHz), and the analysis reveals the precise energy separation, $\Delta E_{27,19}$, between the coupled vibrational states, as well as values for eight *a*- and *b*-type Coriolis-coupling coefficients, $G_a$, $G_a^J$, $G_a^K$, $G_a^{JJ}$, $F_{bc}^K$, $G_b$, $G_b^J$, and $F_{ac}$. Cyanopyrazine is a strongly polar derivative of pyrazine, thus cyanopyrazine can serve as a potential tracer molecule for its nonpolar parent compound in extraterrestrial environments. The transition frequencies and spectroscopic constants provided in this work, combined with theoretical or experimental nuclear quadrupole coupling constants, provide the foundation for future radioastronomical searches for cyanopyrazine.

## 1. Introduction

The feasibility of radioastronomical detection of a molecule depends upon its population in the source of interest and on the intrinsic intensity of its rotational transitions due to its dipole moment. The direct detections of benzene [1] and other nonpolar species [1,2] in extraterrestrial environments rely upon infrared spectroscopy, but can be supported or suggested by detection of their polar, substituted derivatives by radioastronomy. The recent radioastronomical detections of benzonitrile [3] and two cyanonaphthalenes [4] not only provide confirmation of these species in the interstellar medium (ISM), but also suggest the presence of their parent species, benzene and naphthalene. The presence of these nitrile-substituted aromatic molecules and the many other nitrile-containing organic species in the ISM [5–7] inspired the recent rotational spectral analyses of several nitrile-containing heteroaromatic compounds (Fig. 1) by our group, including benzonitrile [8,9], 3-cyanopyridine [10], and 4-cyanopyridine [11] up to 360 GHz in their ground and vibrationally excited states. Similarly inspired, McNaughton *et al.* reported the 2 to 100 GHz spectroscopy of several polycyclic aromatic nitriles (1-cyanonaphthalene, 2-cyanonaphthalene, 9-cyanoanthracene, and 9-cyanophenanthrene) [12]. To facilitate astronomical searches for additional cyanoarenes, we have measured the laboratory rotational spectra of cyanopyrazine (presented in this work), 2-cyanopyridine [13], and 2-cyanopyrimidine [14].

Unlike its isomeric dinitrogen-containing benzene analogues, pyridazine ($\mu_a$ = 4.22 D [15]) and pyrimidine ($\mu_a$ = 2.334 D [16]), pyrazine ($D_{2h}$, $\mu$ = 0) does not possess a permanent dipole moment due to the *para* relationship of the nitrogen atoms and cannot be the direct target of a radioastronomical search. While neither pyridazine nor pyrimidine has been detected in the ISM [17–20], and both molecules are part of a larger dilemma regarding the apparent absence of aromatic heterocycles in the list of organic molecules in the ISM, pyrazine represents an intriguing possibility as an astrochemical species. Pyrazine is nearly isoenergetic with pyrimidine, both of which are 19.7 kcal/mol more stable than pyridazine [21–23]. Due to its lack of a permanent dipole moment, tracer molecules are required to explore the potential contribution of pyrazine to interstellar organic chemistry. Substituted pyrazines have not garnered significant attention in the spectroscopy community. Transition frequencies and rotational constants have been provided for chloropyrazine [24,25], but not for other substituted pyrazines. Given the prevalence of organic nitriles in the ISM, cyanopyrazine is an ideal tracer molecule for pyrazine. Detection of any

* Corresponding authors.
*E-mail addresses:* rcwoods@wisc.edu (R.C. Woods), robert.mcmahon@wisc.edu (R.J. McMahon).

https://doi.org/10.1016/j.jms.2022.111703
Received 25 August 2022; Received in revised form 3 October 2022; Accepted 4 October 2022
Available online 10 October 2022

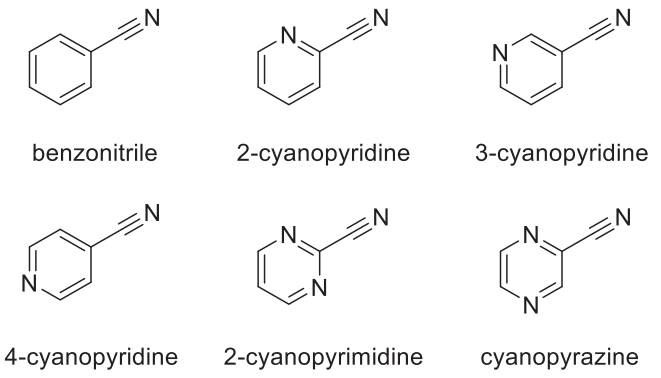


**Fig. 1.** Cyanoarenes derived from benzene, pyridine, pyrimidine, and pyrazine.

**Table 1**
Energy differences between out-of-plane and in-plane nitrile bending modes for cyanoarenes.

| | out-of-plane | in-plane | $\Delta E$ ($cm^{-1}$) |
|---|---|---|---|
| benzonitrile [8,9] | $\nu_{22}$, $B_1$ | $\nu_{33}$, $B_2$ | 19.1081701(74) |
| 3-cyanopyridine [10] | $\nu_{30}$, $A''$ | $\nu_{21}$, $A'$ | 15.7524693 (37) |
| 4-cyanopyridine [11] | $\nu_{20}$, $B_1$ | $\nu_{30}$, $B_2$ | 18.806554 (11) |

heterocycle or substituted heterocycle in the ISM would represent a dramatic breakthrough for the field [17–20], because derivatives of the parent aromatic compounds are ubiquitous in biologically relevant molecules. Alkylated pyrazines are found in various natural sources, including coffee beans, cocoa beans, and vegetables and are produced by insects, fungi, and bacteria [26].

The two lowest-energy vibrational modes of the cyanoarenes are typically the out-of-plane and in-plane nitrile bending modes, which are often sufficiently close in energy to observe Coriolis coupling between them at millimeter-wave frequencies. Analysis of the rotational spectra for these vibrational modes for benzonitrile [8,9], 3-cyanopyridine [10], and 4-cyanopyridine [11] provided highly accurate and precise relative energy values, Table 1. The Coriolis coupling and resultant state mixing necessitate that transitions of the vibrational modes are least-squares fit as a Coriolis-coupled dyad. It is this interaction that results in numerous resonant transitions and coupling-allowed, nominal interstate transitions that provide the accurate and precise vibrational energy spacing. Only for benzonitrile have the precise band origins of each mode been measured by high-resolution infrared spectroscopy [9]. Herein, we report the rotational spectroscopy and analysis of the ground and two lowest-energy vibrationally excited states of cyanopyrazine from 130 to 500 GHz.

## 2. Experimental methods

A commercial sample of cyanopyrazine was used without further purification for all spectroscopic measurements. The rotational spectrum was collected using a millimeter-wave spectrometer that has been previously described [27,28] in the 130 to 230 and 235 to 360 GHz frequency ranges, in a continuous flow at room temperature, with sample pressures of 3 to 12 mTorr. Additional spectral data were obtained with a newly acquired amplification and multiplication chain that extends the frequency range to 500 GHz. The separate spectral segments were combined into a single broadband spectrum using Kisiel's Assignment and Analysis of Broadband Spectra (AABS) software [29,30]. The complete spectrum from 130 to 500 GHz was obtained automatically over approximately nine days using the following experimental parameters: 0.045 kHz frequency increment, 0.6 MHz/s sweep rate, 10 ms time constant, and 50 kHz AM and 500 kHz FM modulation in a tone-burst design. Pickett's SPFIT/SPCAT [31] were used for least-squares fits and spectral predictions, along with Kisiel's PIFORM, PLANM, and AC programs for analysis [32]. A uniform frequency measurement uncertainty of 0.050 MHz was assumed for all measurements.

## 3. Computational methods and results

Electronic structure calculations were carried out with Gaussian 16 [33] using the WebMO interface [34] to obtain theoretical spectroscopic constants. Optimized geometries at the B3LYP/6-311+(2d,p) and MP2/

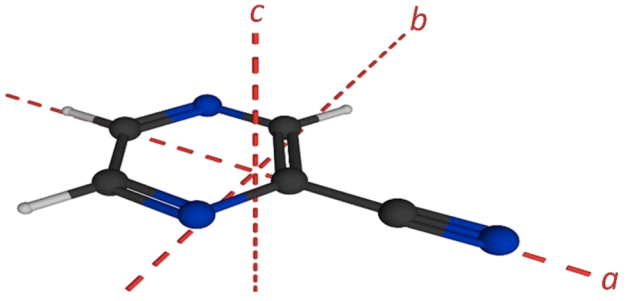


**Fig. 3.** Cyanopyrazine ($C_s$, $\mu_a$ = 4.2 D, $\mu_b$ = 0.1 D, B3LYP) structure with principal inertial axes.

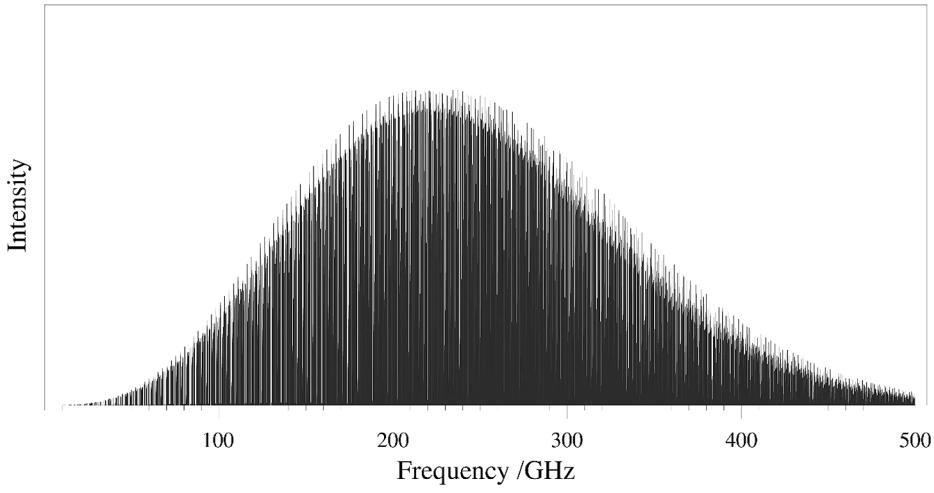


**Fig. 2.** Predicted spectrum (SPCAT) of the ground vibrational state of cyanopyrazine at 292 K.

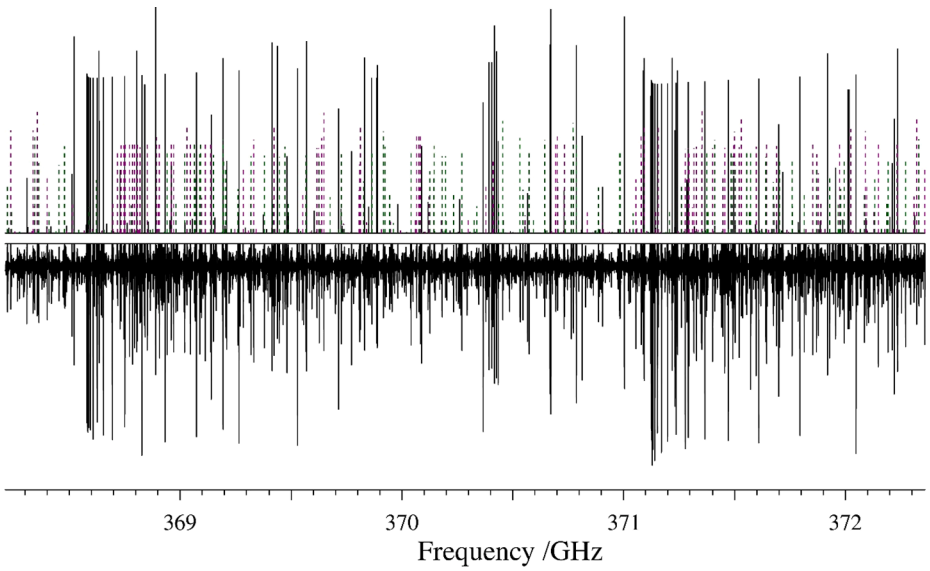


**Fig. 4.** Predicted (top) and experimental (bottom) rotational spectra of cyanopyrazine from 368.2 to 372.4 GHz. Ground-state cyanopyrazine with prominent transitions for the $J'' + 1 = 144$ and $J'' + 1 = 145$ bands appear in black. Transitions for $\nu_{27}$ are in purple and transitions for $\nu_{19}$ are in dark green. Unassigned transitions are attributable to other vibrationally excited states of cyanopyrazine. (For interpretation of the references to colour in this figure legend, the reader is referred to the web version of this article.)

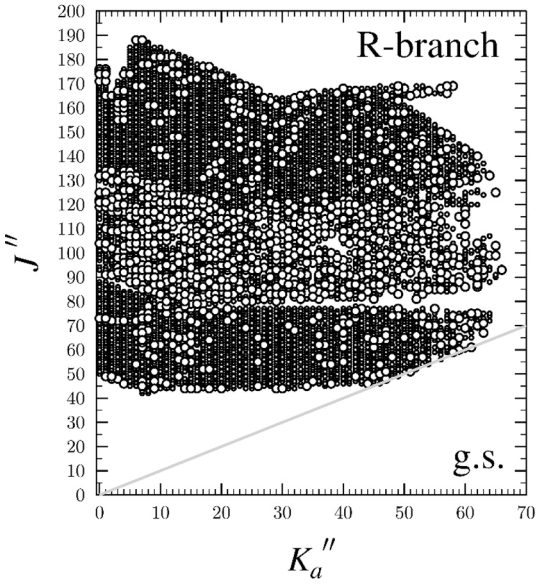


**Fig. 5.** Data distribution plot for the least-squares fit of spectroscopic data for the vibrational ground state of cyanopyrazine. The size of the symbol is proportional to the value of $|(f_{obs.} - f_{calc.})/\delta f|$, where $\delta f$ is the frequency measurement uncertainty, and all values are smaller than 3.

6-311+(2d,p) levels of theory were obtained using "verytight" convergence criteria and an "ultrafine" integration grid, and subsequent anharmonic vibrational frequency calculations were carried out using second-order vibrational perturbation theory (VPT2). All computational output files can be found in the supplemental material.

## 4. Cyanopyrazine rotational spectra

The recently expanded frequency range of our instrument allowed us to measure the spectrum of cyanopyrazine up to 500 GHz, a frequency coverage beyond that used in previous works on cyanoarenes (up to 375 GHz) [8–11]. This range is nearly optimal for cyanopyrazine at the ambient laboratory temperature (Fig. 2), as it covers the most intense transitions based upon the rotational populations. The expanded frequency coverage was also advantageous for the least-squares fitting of $\nu_{27}$ and $\nu_{19}$, due to the high $J'' + 1$ values of the most intense transitions of these vibrationally excited states (*vide infra*). The relatively low value of $C_0$ (~1276 MHz) for all cyanopyrazine vibrational states results in the $K_a = 0$ series transition near 130 GHz having a value of $J'' + 1 = 51$ and increasing to $J'' + 1 = 195$ just below 500 GHz. This range of $J'' + 1$ (and the resulting range of $K_a$) quantum numbers provides a wealth of spectroscopic information on the centrifugal distortion and necessitates a high-order Hamiltonian to adequately model the spectrum.

### 4.1. Ground-state spectral analysis

The ground-state spectrum of cyanopyrazine ($\mu_a = 4.2$ D, $\mu_b = 0.1$ D, B3LYP; $\kappa = -0.854$) has not been reported, despite this benzonitrile analog being commercially available. The strong electron-withdrawing effect of the nitrile group results in a dipole moment nearly coincidental with that substituent (Fig. 3) and the *a* principal axis. Due to the asymmetry of the ring caused by the nitrile substitution, there is also a slight *b*-axis dipole component. The large difference in the *a*- and *b*-axis dipole components results in *a*-type transitions that are roughly 2000 times more intense than the *b*-type transitions. As a result, the rotational spectrum of cyanopyrazine is dominated by intense $^{a}R_{0,1}$ transitions across the frequency range (Fig. 4). Despite being a prolate molecule, cyanopyrazine and other substituted arenes [8–11,35] have prominent oblate-type bands, in which transitions in the bands begin at $K_a = 0$ and increase in $K_a$ as frequency increases. Cyanopyrazine displays prolate-type bands at high $K_a$, though the spacing and intensity make them much less prominent. The much weaker Q-branch transitions could not be observed and assigned for cyanopyrazine owing to the spectral density created by excited vibrational states of cyanopyrazine. Thus, the final transition data set for the ground vibrational state contained only *a*-type, R-branch transitions. As shown in Fig. 5, these transitions cover a broad range of quantum numbers, including $J'' + 1 = 42$ to 189 and $K_a = 0$ to 66. The spectral density and frequency range investigated allowed for the measurement, assignment, and least-squares fitting of 7078 independent transition frequencies to partial octic, A- and S-reduced Hamiltonians with low error ($\sigma_{fit} = 34$ kHz). The resulting spectroscopic constants are reported in Table 2, along with their corresponding computed values. Though several octic terms are required in the A and S reduction least-squares fits, no readily available computational software is able to provide these values for comparison. Thus, $L_K$ and the off-diagonal octic terms that could not be satisfactorily determined were held at values of zero in the least-squares fitting.

The B3LYP-computed rotational constants are in excellent agreement with the experimental values, similar to that seen for 3- and 4-

**Table 2**
Experimental and computational spectroscopic constants for the ground vibrational state of cyanopyrazine (S- and A-reduced Hamiltonians, $I^r$ representation).

| | S reduction, $I^r$ representation | | | | A reduction, $I^r$ representation | | |
|---|---|---|---|---|---|---|---|
| | Experimental | B3LYP [a] | MP2 [a] | | Experimental | B3LYP [a] | MP2 [a] |
| $A_0$ (MHz) | 6003.12984 (58) | 6016.1 | 5950.4 | $A_0$ (MHz) | 6003.12822 (58) | 6016.1 | 5950.4 |
| $B_0$ (MHz) | 1621.517450 (24) | 1619.4 | 1605.5 | $B_0$ (MHz) | 1621.518806 (24) | 1619.4 | 1605.5 |
| $C_0$ (MHz) | 1276.428481 (25) | 1276.7 | 1264.1 | $C_0$ (MHz) | 1276.427155 (25) | 1276.7 | 1264.1 |
| $D_J$ (kHz) | 0.0359497 (18) | 0.0348 | 0.0345 | $\Delta_J$ (kHz) | 0.0492594 (19) | 0.0471 | 0.0472 |
| $D_{JK}$ (kHz) | 1.182301 (25) | 1.11 | 1.15 | $\Delta_{JK}$ (kHz) | 1.102415 (24) | 1.04 | 1.07 |
| $D_K$ (kHz) | 0.2897 (13) | 0.317 | 0.282 | $\Delta_K$ (kHz) | 0.3525 (13) | 0.379 | 0.345 |
| $d_1$ (kHz) | −0.01183021 (59) | −0.0112 | −0.0113 | $\delta_J$ (kHz) | 0.01182909 (60) | 0.0112 | 0.0113 |
| $d_2$ (kHz) | −0.00665773 (39) | −0.00616 | −0.00636 | $\delta_K$ (kHz) | 0.702668 (42) | 0.660 | 0.677 |
| $H_J$ (Hz) | −0.000014359 (71) | −0.0000123 | −0.0000135 | $\Phi_J$ (Hz) | 0.000001797 (74) | 0.00000275 | 0.00000306 |
| $H_{JK}$ (Hz) | 0.0013660 (16) | 0.00117 | 0.00129 | $\Phi_{JK}$ (Hz) | 0.0019713 (18) | 0.00170 | 0.00185 |
| $H_{KJ}$ (Hz) | −0.007530 (15) | −0.00646 | −0.00718 | $\Phi_{KJ}$ (Hz) | −0.009803 (15) | −0.00845 | −0.00932 |
| $H_K$ (Hz) | 0.01171 (81) | 0.00594 | 0.00652 | $\Phi_K$ (Hz) | 0.01097 (83) | 0.00738 | 0.00807 |
| $h_1$ (Hz) | 0.000000244 (14) | −0.000000153 | −0.000000148 | $\phi_J$ (Hz) | 0.000001844 (15) | 0.00000129 | 0.00000142 |
| $h_2$ (Hz) | 0.000008265 (11) | 0.00000756 | 0.00000829 | $\phi_{JK}$ (Hz) | 0.0009204 (11) | 0.000864 | 0.000945 |
| $h_3$ (Hz) | 0.0000016326 (42) | 0.00000145 | 0.00000156 | $\phi_K$ (Hz) | 0.009580 (31) | 0.00862 | 0.00925 |
| $L_J$ (mHz) | 0.0000000295 (10) | | | $L_J$ (mHz) | 0.0000000361 (10) | | |
| $L_{JJK}$ (mHz) | −0.000002512 (15) | | | $L_{JJK}$ (mHz) | −0.000002972 (15) | | |
| $L_{JK}$ (mHz) | 0.00002268 (18) | | | $L_{JK}$ (mHz) | 0.00001795 (19) | | |
| $L_{KKJ}$ (mHz) | −0.0001332 (26) | | | $L_{KKJ}$ (mHz) | −0.0001153 (26) | | |
| $L_K$ (mHz) | [0.] | | | $L_K$ (mHz) | [0.] | | |
| $\Delta_i$ (uÅ$^2$) [b,c] | 0.075770 (12) | | | $\Delta_i$ (uÅ$^2$) [b,c] | 0.076419 (12) | | |
| $N_{lines}$ [d] | 7078 | | | $N_{lines}$ [d] | 7078 | | |
| $\sigma_{fit}$ (MHz) | 0.034 | | | $\sigma_{fit}$ (MHz) | 0.034 | | |

[a] Evaluated with the 6–311+G(2d,p) basis set.
[b] Inertial defect, $\Delta_i = I_c - I_a - I_b$.
[c] Calculated using PLANM from the $B_0$ constants.
[d] Number of fitted transition frequencies.

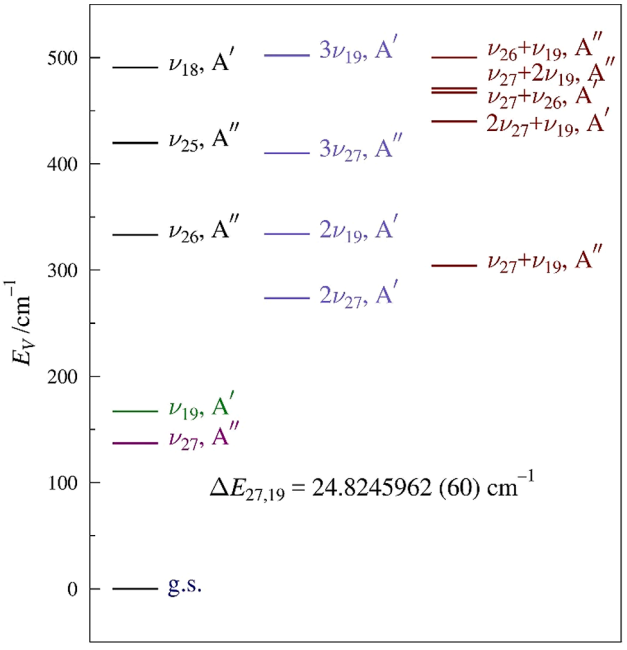


**Fig. 6.** Vibrational energy levels of cyanopyrazine below 500 cm$^{-1}$ from computed fundamental frequencies (B3LYP/6-311+G(2d,p)). The value of $\Delta E_{27,19}$ results from the experimental perturbation analysis of $\nu_{27}$ and $\nu_{19}$ in this work.

cyanopyridine [10,11]. The largest discrepancy between the experimental and computed rotational constant values is for $A_0$, which is overestimated by 13 MHz (0.21%). The B3LYP values of $B_0$ and $C_0$ are within 2.1 MHz and 0.3 MHz of their experimental values, respectively. All of the B3LYP quartic centrifugal distortion constants are in good agreement (within 10% of their experimental values) in both reductions. There is much poorer agreement between the computed sextic distortion constants and the experimental values, typically varying from 6 to 30%. Both $\Phi_J$ and $H_K$, however, differ by about 50% from their computed values, while $h_1$ is the wrong sign. At first glance, it appears that the MP2 computed values are worse than their B3LYP counterparts. Though the agreement of the MP2 values is inferior for the rotational constants, the deviations from the experimental values all remain less than 1%. For nearly all of the remaining spectroscopic constants, the MP2 value is closer to the experimental value than the B3LYP-computed value. All of the MP2 quartic centrifugal distortion constants are within 5% of their experimental values, and all of them show better agreement than the B3LYP values. With regard to the sextic centrifugal distortion constants, the general agreement of the MP2-computed constants is between 0.2 and 6%. The exceptions are $\Phi_J$, $\Phi_K$, $\phi_J$, $H_K$, and $h_1$, with large discrepancies of 70%, −26%, −23%, −44%, and −160%, respectively. As with the B3LYP value of $h_1$, its MP2 value has the incorrect sign. Despite the issues with both sets of computed spectroscopic constants, both B3LYP and MP2 values provide *a priori* predictions of the rotational spectrum of cyanopyrazine sufficient to identify and assign its transitions in the experimental spectrum.

### 4.2. Spectral analysis of $\nu_{27}$ and $\nu_{19}$

Similar to other cyanoarenes [8–11], the first two fundamental modes of cyanopyrazine are the out-of-plane and in-plane nitrile bending modes, $\nu_{27}$ and $\nu_{19}$, respectively. These two vibrational states form a Coriolis-coupled dyad that is well separated in energy from the ground state and the next vibrationally excited state, $2\nu_{27}$. The previous low-resolution infrared (IR) spectroscopy of cyanopyrazine provides an assignment of most of the cyanopyrazine vibrational modes [36–39], though there is some ambiguity about the assignment of the modes at 160, 173, and 339 cm$^{-1}$, with both of the lower modes assigned A″ symmetry [38]. The two lowest-frequency modes, $\nu_{27}$ (A″) and $\nu_{19}$ (A′), are predicted to have energies of 137 and 167 cm$^{-1}$ (B3LYP) or 136 and 162 cm$^{-1}$ (MP2). It is likely that the mode at 339 cm$^{-1}$, designated A′ in the solution phase IR and Raman vibrational study, is $\nu_{26}$ (A″), but it is not clear whether either of the modes observed at 160 and 173 cm$^{-1}$ are $\nu_{27}$ (A″) or $\nu_{19}$ (A′). As a result of that ambiguity, the vibrational state

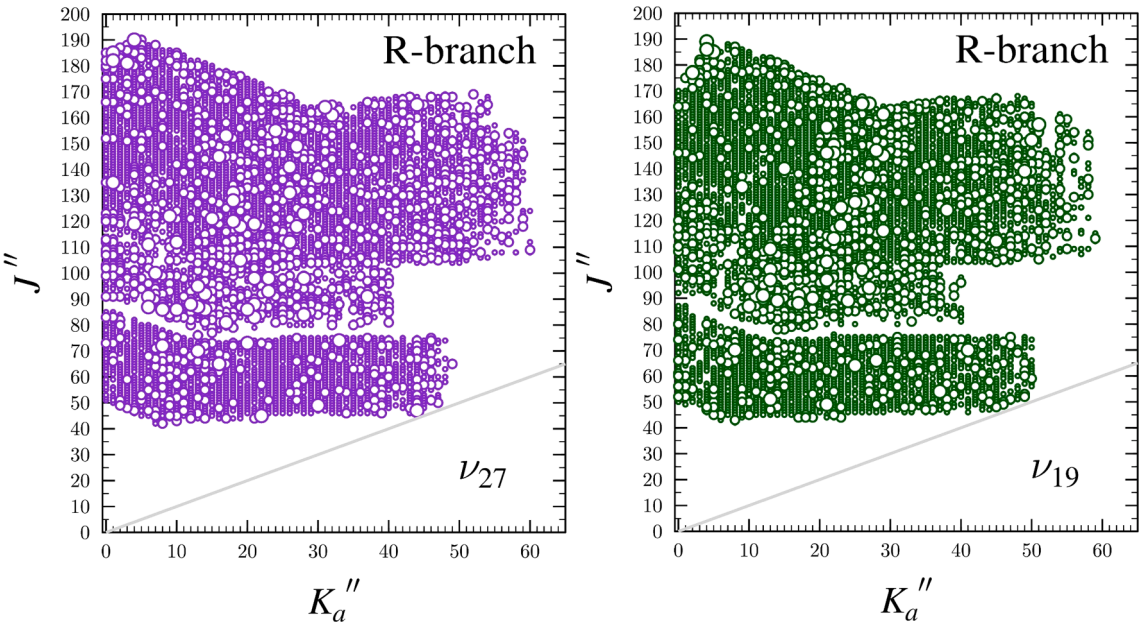


**Fig. 7.** Data distribution plots for the least-squares fit of spectroscopic data for the lowest-energy fundamental states of cyanopyrazine, $\nu_{27}$ (purple) and $\nu_{19}$ (dark green). The size of the symbol is proportional to the value of $|(f_{obs.} - f_{calc.})/\delta f|$, where $\delta f$ is the frequency measurement uncertainty, and all values are smaller than 3. (For interpretation of the references to colour in this figure legend, the reader is referred to the web version of this article.)

diagram shown Fig. 6. is based upon the computed (B3LYP) fundamental frequencies. The initial predictions for these vibrational states were based upon the experimental ground-state rotational constants, computational vibration–rotation interaction constants, and the ground-state centrifugal distortion constants. After initial measurement, assignment, and least-squares fitting of these fundamental states, it became clear that a single-state Hamiltonian was insufficient to model their rotational spectra. To address this problem, a Coriolis-coupled dyad Hamiltonian was employed similar to our previous works [8–11,35,40,41]. The A″ and A′ symmetries of these states allow both *a*- and *b*-axis Coriolis coupling. Thus, initially, computed $G_a$, $G_b$, and $\Delta E_{27,19}$ values were added to the least-squares fit. As transitions were added to the fit, these parameters were allowed to vary, and additional parameters were included until the available transitions could be modeled adequately. The breadth of transitions is shown in Fig. 7, and the resulting spectroscopic constants are provided in Table 3.

The final least-squares fit of the Coriolis-coupled dyad ($\nu_{27}$ and $\nu_{19}$) contained over 12,000 transitions, including many transitions involving energy levels perturbed by the coupling, many intensely shifted resonant transitions created by nearly degenerate energy levels of $\nu_{27}$ and $\nu_{19}$, and 37 formally forbidden, coupling-allowed, nominal interstate transitions. Due to the intensity of the transitions for each vibrationally excited state, the number of transitions for each state in the final data set for $\nu_{27}$ and $\nu_{19}$ (6257 and 5893, respectively) is decreased only slightly from that of the ground state (7078). In the frequency range studied, the observed transitions range from 42 to 191 in $J'' + 1$ and from 0 to 60 in $K_a$. Since many of the intense resonant transitions and nominal interstate transitions occur beyond 360 GHz, extending the measured spectral range to 500 GHz was an important factor in obtaining a satisfactory least-squares fit. Data from the higher frequency range had not been necessary in previous works on analogous species [8–11] and can be attributed to the larger energy difference between the coupled states in cyanopyrazine, relative to the previously studied compounds (Table 1).

In cyanopyrazine, the energy separation between $\nu_{27}$ and $\nu_{19}$ ($\Delta E_{27,19}$ = 24.8245962 (60) cm$^{-1}$) requires higher values of $J$ and $K$ for the energy levels of $\nu_{27}$ to approach those of $\nu_{19}$ closely enough to create resonances (*vide infra*). It is important to note that this energy difference varies substantially from the frequencies reported for the two lowest-energy fundamentals in the previously reported low-resolution IR and Raman spectroscopic data [38] of 173 and 160 cm$^{-1}$, casting doubt on the previous liquid-phase IR assignments. In addition to determining a highly accurate and precise $\Delta E_{27,19}$ value, the least-squares fit provides a nearly complete set of spectroscopic constants of a sextic centrifugally distorted, A-reduced Hamiltonian (excluding the off-diagonal terms $\phi_{JK}$ and $\phi_K$) and eight Coriolis-coupling coefficients ($G_a$, $G_a^J$, $G_a^K$, $G_a^{JJ}$, $F_{bc}^K$, $G_b$, $G_b^J$, and $F_{ac}$). Attempts to include $F_{bc}$ in the least-squares fit were made, but were not successful. In view of that result, we found it surprising that $F_{bc}^K$ was necessary to achieve a reasonable fit and could be well determined.

The computed spectroscopic constants $B_v$ and $C_v$ are in quite close agreement with their experimentally determined values (Table 4). At both the MP2 and B3LYP levels, the predicted vibration–rotation interaction constants ($B_0 - B_v$) differ by less than 10% from their experimental values, with the MP2 values in slightly closer agreement than the B3LYP values. The very close agreement seen for the $B_0 - B_v$ values provides evidence that the deperturbation of the constants in the computational results and the treatment of the Coriolis-coupling were both reasonably effective. For the $A_0 - A_v$ values, however, there is a very large discrepancy between the computed and experimental values. At both levels of theory, the magnitudes of the $A_0 - A_v$ values are computed to be five or six times larger than the experimental values. This is largely due to residual Coriolis coupling in the computed values, given the very large magnitudes of the values and the smaller magnitudes of the experimental $A_0 - A_v$ values in this and similar works. The B3LYP-predicted values are slightly closer to the experimental ones than the MP2 values, in this case. Given the fairly large experimental $A_0 - A_v$

**Table 3**
Experimentally determined parameters for the ground state and vibrationally excited states $\nu_{27}$ and $\nu_{19}$ of cyanopyrazine (A-reduced Hamiltonian, $I^r$ representation).

| | ground state [a] | $\nu_{27}$ (A″, 136 cm$^{-1}$) [a,b] | $\nu_{19}$ (A′, 162 cm$^{-1}$) [a,b] |
|---|---|---|---|
| $A_v$ (MHz) | 6003.12822 (58) | 6026.492 (18) | 5977.166 (18) |
| $B_v$ (MHz) | 1621.518806 (24) | 1623.29554 (16) | 1624.75111 (17) |
| $C_v$ (MHz) | 1276.427155 (25) | 1278.422236 (28) | 1277.400270 (27) |
| $\Delta_J$ (kHz) | 0.0492594 (19) | 0.05013381 (98) | 0.0504064 (10) |
| $\Delta_{JK}$ (kHz) | 1.102415 (24) | 1.12777 (17) | 1.05278 (17) |
| $\Delta_K$ (kHz) | 0.3525 (13) | 0.3421 (28) | 0.4081 (42) |
| $\delta_J$ (kHz) | 0.01182909 (60) | 0.01191174 (61) | 0.01227503 (66) |
| $\delta_K$ (kHz) | 0.702668 (42) | 0.704032 (38) | 0.706581 (29) |
| $\Phi_J$ (Hz) | 0.000001797 (74) | 0.000002534 (20) | 0.000002850 (20) |
| $\Phi_{JK}$ (Hz) | 0.0019713 (18) | 0.0020104 (37) | 0.0018932 (37) |
| $\Phi_{KJ}$ (Hz) | −0.009803 (15) | −0.0104488 (91) | −0.008731 (12) |
| $\Phi_K$ (Hz) | 0.01097 (83) | 0.00672 (61) | 0.00602 (53) |
| $\phi_J$ (Hz) | 0.000001844 (15) | 0.000002043 (12) | 0.000002359 (14) |
| $\phi_{JK}$ (Hz) | 0.0009204 (11) | [0.0009204] | [0.0009204] |
| $\phi_K$ (Hz) | 0.009580 (31) | [0.009580] | [0.009580] |
| $\Delta E_{27,19}$ (MHz) | | 744222.67 (18) | |
| $\Delta E_{27,19}$ (cm$^{-1}$) | | 24.8245962 (60) | |
| $G_a$ (MHz) | | 10789.33 (63) | |
| $G_a{}^J$ (MHz) | | −0.0052515 (62) | |
| $G_a{}^K$ (MHz) | | −0.029393 (77) | |
| $G_a{}^{JJ}$ (MHz) | | 0.00000000517 (11) | |
| $F_{bc}{}^K$ (MHz) | | −0.00001287 (20) | |
| $G_b$ (MHz) | | −134.02 (45) | |
| $G_b{}^J$ (MHz) | | 0.0000378 (12) | |
| $F_{ac}$ (MHz) | | −1.079 (12) | |
| $\Delta_i$ (uÅ$^2$) [c] | | 0.012604 (26) | 0.02917 (26) |
| $N_{\text{lines}}$ [e] | | 6257 | 5893 |
| $\sigma_{\text{fit}}$ (MHz) | | 0.038 | 0.037 |

[a] Octic centrifugal distortion constants not shown and held constant at their ground-state values in Table 2.
[b] Fundamental frequencies calculated using MP2/6-311+G(2d,p).
[c] Inertial defect, $\Delta_i = I_c - I_a - I_b$.
[d] Calculated using PLANM from the $B_0$ constants.
[e] Number of fitted transition frequencies.

values, it is possible that they also retain untreated Coriolis coupling, though to a much lesser extent than the computed values. The MP2 $\Delta E_{27,19}$ value of 26.4 cm$^{-1}$ is in excellent agreement with the very precise experimental value, while the B3LYP value is an overestimate by 6 cm$^{-1}$. The Coriolis $\zeta^x_{27,19}$ values show very good agreement between theory and experiment at the B3LYP and MP2 levels of theory, which, combined with the low $\sigma_{\text{fit}}$ value, indicates a satisfactory treatment of the *a*-axis and *b*-axis Coriolis coupling in the least-squares fit.

Further evidence of an adequate treatment of the dyad by the Hamiltonian model is the ability to include many resonant and nominal interstate transitions in the data set, whose prediction is heavily dependent on the $\Delta E_{27,19}$ value and Coriolis-coupling constants. Sharp *a*-type and *b*-type resonances are observed due to mixing of $\nu_{27}$ and $\nu_{19}$ energy levels that are nearly degenerate, as shown in Fig. 8. A "minus" superscript on the $K_a$ value indicates that $K_a + K_c = J + 1$, whereas a "plus" superscript indicates that $K_a + K_c = J$. At $J'' + 1 = 157$, there is an intense *a*-type resonance between $\nu_{27}$ and $\nu_{19}$ with a $\Delta K_a = 2$ selection rule. The resonant transitions are displaced from their unperturbed transition frequencies by about 1.5 GHz. There are additional small resonances in the $K_a = 16^-$ series of $\nu_{19}$ that correspond to resonances in different $\nu_{27}$ series. Each of these series displays the large undulations due to centrifugal distortion and Coriolis coupling between these states. Fig. 9 shows how these resonances and undulations progress across the $K_a{}^+$ series of $\nu_{27}$. The undulations and resonances become more pronounced and move to progressively higher $J''+1$ values as a function of $K_a$. While it is generally possible to obtain quartic distortion constants and preliminary values of the energy difference and Coriolis-coupling constants from the undulations, many local resonances are often needed to obtain precise determinations of the latter constants. The resonance progression plot shows that, for cyanopyrazine, most of the intense resonances occur after $J'' + 1 = 100$, reiterating the importance of obtaining the higher-frequency data (360 – 500 GHz) used in this

**Table 4**
Vibration-rotation interaction and Coriolis-coupling constants of cyanopyrazine.

| | Experimental | B3LYP [a] | MP2 [a] |
|---|---|---|---|
| $A_0 - A_{27}$ (MHz) | −23.364 (18) | 112.0 | 138.7 |
| $B_0 - B_{27}$ (MHz) | −1.77673 (17) | −1.71 | −1.66 |
| $C_0 - C_{27}$ (MHz) | −1.995081 (37) | −1.97 | −1.92 |
| $A_0 - A_{19}$ (MHz) | 25.962 (18) | −109.5 | −136.4 |
| $B_0 - B_{19}$ (MHz) | −3.23230 (17) | −3.07 | −3.18 |
| $C_0 - C_{19}$ (MHz) | −0.973115 (37) | −0.90 | −0.95 |
| $\frac{(A_0 - A_{27}) + (A_0 - A_{19})}{2}$(MHz) | 1.299 (13) | 1.29 | 1.14 |
| $\frac{(B_0 - B_{27}) + (B_0 - B_{19})}{2}$(MHz) | −2.50452 (12) | −2.39 | −2.42 |
| $\frac{(C_0 - C_{27}) + (C_0 - C_{19})}{2}$(MHz) | −1.484098 (26) | −1.43 | −1.44 |
| $\lvert\zeta^a_{27,19}\rvert$ | 0.899 | 0.804 | 0.808 |
| $\lvert\zeta^b_{27,19}\rvert$ | 0.0413 | 0.036 | 0.037 |
| $\Delta E_{27,19}$ (cm$^{-1}$) | 24.8245962 (60) | 30.6 | 26.4 |

[a]Evaluated with the 6-311+G(2d,p) basis set.

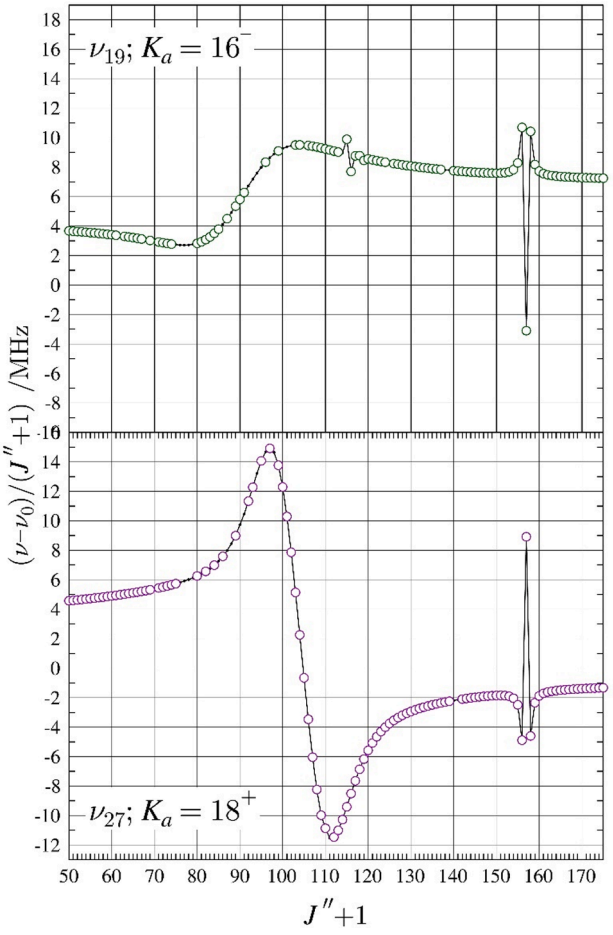


**Fig. 8.** Resonance plots for cyanopyrazine showing the $K_a = 16^-$ series for $\nu_{19}$ and $K_a = 18^+$ series for $\nu_{27}$. These two resonances conform to the $\Delta K_a = 2$ selection rule for *a*-type resonances. The plotted values are frequency differences between excited-state transitions and their ground-state counterparts, scaled by $(J''+1)$ in order to make the plots more horizontal. Measured transitions are represented by circles: $\nu_{27}$ (purple), $\nu_{19}$ (green). Predictions from the final coupled fit are represented by a solid, colored line. (For interpretation of the references to colour in this figure legend, the reader is referred to the web version of this article.)

work.

Two additional types of transitions are observed in the excited-state spectra of cyanopyrazine that are made possible by the coupling of the fundamental states: *b*-type transitions that are more intense than they would be due purely to the *b*-axis dipole moment and nominal interstate transitions. As observed with cyanocyclobutene [41], the state mixing of $\nu_{27}$ and $\nu_{19}$ allows intensity transfer from *a*-type transitions to *b*-type transitions. In this case, *b*-type transitions are observed for each vibrationally excited state, unlike cyanocyclobutene where they were only observed in $\nu_{17}$. The result is that there are many *b*-type, R-branch transitions assigned, measured, and least-squares fit for the dyad despite the very small $\mu_b$ (approximately 42 times smaller than $\mu_a$). Formally forbidden, nominal interstate rotational transitions are observable from the energy levels with the most intense state-mixing. They share at least one energy level with a transition involved in a resonance and borrow intensity from those resonant transitions. In some cases, the intensity borrowing is so profound that the intrastate resonant transitions have vanishingly small intensities and cannot be observed. In other cases, such as the one highlighted in Fig. 10, all four transitions (two intrastate resonant transitions and two interstate transitions) can be observed and included in the least-squares fit. Since the four transitions involve the same four energy levels, the average of the nominal interstate frequencies should be the same as that of the intrastate frequencies. For the particular set depicted in Fig. 10, the averages differ by only 25 kHz, giving confidence in their assignment and in the dyad least-squares fit overall. The inclusion of the many *b*-type transitions and the nominal interstate transitions provides a substantial constraint on the $\Delta E_{27,19}$ value and Coriolis-coupling constants. As a result, we are confident that the spectroscopic constants provided are well-determined and likely to be physically meaningful and predictive beyond the studied frequency range.

## 5. Conclusion

The transition frequencies and spectroscopic constants for cyanopyrazine, presented in this work, provide the necessary laboratory data for future astronomical searches for this potential pyrazine tracer. Combined with computed or experimental nuclear quadrupole coupling constants, the spectroscopic constants should reliably predict transition frequencies to much lower or slightly higher frequencies for the ground and two lowest-energy fundamental states. While this work provides the precise and accurate energy separation between vibrational modes $\nu_{27}$ and $\nu_{19}$, high-resolution infrared spectroscopy or other spectroscopy that would provide a direct measurement of the frequency of either $\nu_{27}$ or $\nu_{19}$ is needed to determine both fundamental frequencies. This measurement would be somewhat challenging due to the low predicted IR intensities of $\nu_{27}$ and $\nu_{19}$ (1.5 and 0.4 km/mol, respectively; MP2). Such an investigation would also resolve the ambiguity concerning the proper assignment of these two modes from the previous low-resolution infrared study. A high-resolution infrared study would further provide the necessary information to begin to address the complex set of interacting vibrationally excited states higher in energy than $\nu_{27}$ and $\nu_{19}$. The two-quanta states of $\nu_{27}$ and $\nu_{19}$ are expected to form a complicated tetrad of states with $\nu_{26}$ (0.8 km/mol, MP2), as shown in Fig. 6. Although the millimeter-wave intensities of these transitions are expected to be strong enough to readily observe their spectra, and many perturbation constants can be predicted by scaling the coupling constants between $\nu_{27}$ and $\nu_{19}$ by a factor of $\sqrt{2}$, achieving a satisfactory least-squares fit will still be a challenging endeavor.

## Declaration of Competing Interest

The authors declare that they have no known competing financial interests or personal relationships that could have appeared to influence the work reported in this paper.

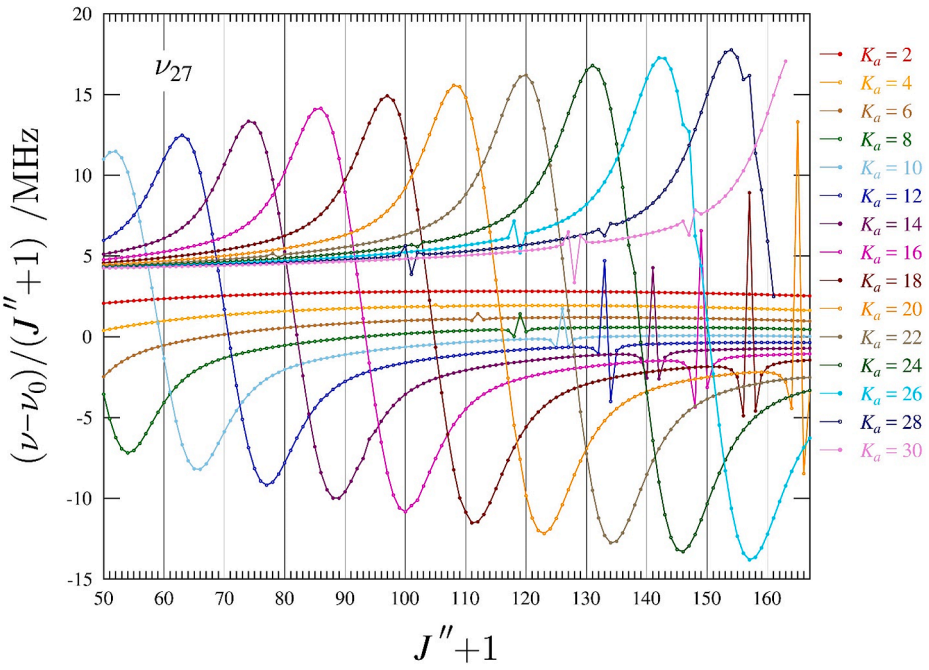


**Fig. 9.** Superimposed resonance plots of $\nu_{27}$ for $^{a}R_{0,1}$ even-$K_a^{+}$ series from 2 to 30 for cyanopyrazine. Measured transitions are omitted for clarity, but they are indistinguishable from the plotted values on this scale. The plotted values are frequency differences between excited-state transitions and their ground-state counterparts, scaled by $(J'' + 1)$.

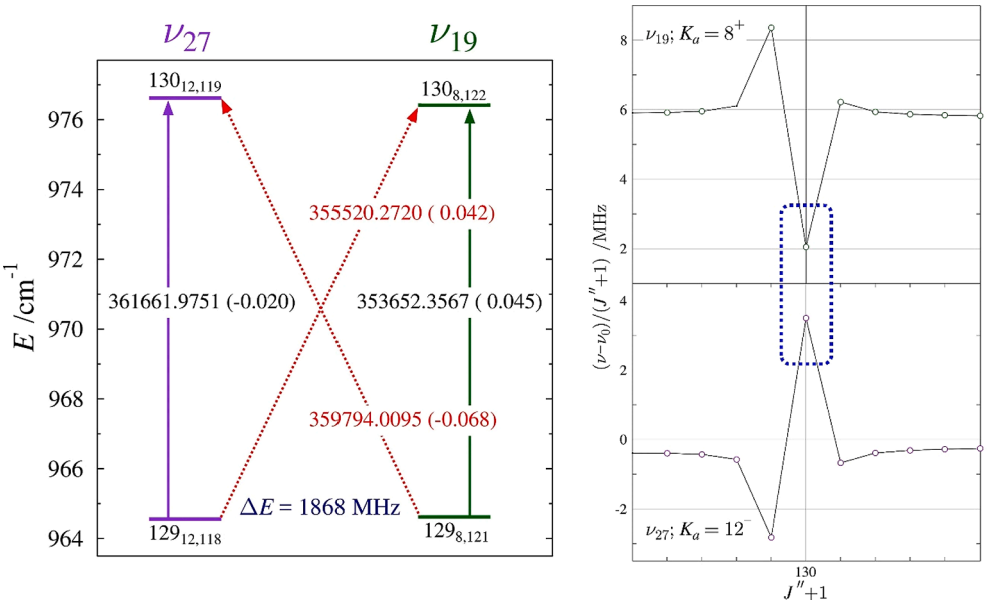


**Fig. 10.** Energy diagram (left) depicting a representative matched pair of nominal interstate transitions between the $\nu_{27}$ (purple) and $\nu_{19}$ (dark green) vibrational states of cyanopyrazine. Standard $^{a}R_{0,1}$ transitions within vibrational states are denoted by vertical arrows. The diagonal, dashed arrows indicate nominal interstate transitions that are formally forbidden, but enabled as a result of rotational energy-level mixing. The value printed on each of the arrows is the corresponding transition frequency (in MHz) with its *obs.* – *calc.* value in parentheses. The marked energy separation is between the two strongly interacting rotational energy levels. Resonance plots (right) of the $K_a$ series of $\nu_{27}$ and $\nu_{19}$ that contain the corresponding resonant transitions, which are identified with a blue box. (For interpretation of the references to colour in this figure legend, the reader is referred to the web version of this article.)

## Data availability

Data will be made available on request.

## Acknowledgments

We gratefully acknowledge funding from the U.S. National Science Foundation for support of this project (CHE-1664912 and CHE-1954270). We thank Michael McCarthy for the loan of an amplification-multiplication chain and the Harvey Spangler Award (to B.J.E.) for support of the purchase of the corresponding zero-bias detector.

## Appendix A. Supplementary material

Supplementary data to this article can be found online at https://doi.org/10.1016/j.jms.2022.111703.

## References

[1] J. Cernicharo, A.M. Heras, A.G.G.M. Tielens, J.R. Pardo, F. Herpin, M. Guélin, L.B.F.M. Waters, Infrared Space Observatory's Discovery of $C_4H_2$, $C_6H_2$, and Benzene in CRL 618, Astrophys. J. 546 (2) (2001) L123–L126.

[2] S.T. Ridgway, D.N.B. Hall, S.G. Kleinmann, D.A. Weinberger, R.S. Wojslaw, Circumstellar acetylene in the infrared spectrum of IRC +10° 216, Nature 264 (5584) (1976) 345–346.

[3] B.A. McGuire, A.M. Burkhardt, S.V. Kalenskii, C.N. Shingledecker, A.J. Remijan, E. Herbst, M.C. McCarthy, Detection of the Aromatic Molecule Benzonitrile (*c*-$C_6H_5CN$) in the Interstellar Medium, Science 359 (6372) (2018) 202–205.
[4] B.A. McGuire, A. Loomis Ryan, A.M. Burkhardt, K. Lee Kin Long, C. N. Shingledecker, S.B. Charnley, I.R. Cooke, M.A. Cordiner, E. Herbst, S. Kalenskii, M.A. Siebert, E.R. Willis, C. Xue, A.J. Remijan, M.C. McCarthy, Detection of two interstellar polycyclic aromatic hydrocarbons via spectral matched filtering, Science 371 (6535) (2021) 1265–1269.
[5] M.C. McCarthy, B.A. McGuire, Aromatics and Cyclic Molecules in Molecular Clouds: A New Dimension of Interstellar Organic Chemistry, J. Phys. Chem. A 125 (16) (2021) 3231–3243.
[6] H.S.P. Müller, F. Schlöder, J. Stutzki, G. Winnewisser, The Cologne Database for Molecular Spectroscopy, CDMS: a Useful Tool for Astronomers and Spectroscopists, J. Mol. Struct. 742 (1–3) (2005) 215–227.
[7] H.S.P. Müller, S. Thorwirth, D.A. Roth, G. Winnewisser, The Cologne Database for Molecular Spectroscopy, CDMS, Astron. Astrophys. 370 (3) (2001) L49–L52.
[8] M.A. Zdanovskaia, B.J. Esselman, H.S. Lau, D.M. Bates, R.C. Woods, R.J. McMahon, Z. Kisiel, The 103–360 GHz rotational spectrum of benzonitrile, the first interstellar benzene derivative detected by radioastronomy, J. Mol. Spectrosc. 351 (2018) 39–48.
[9] M.A. Zdanovskaia, M.-A. Martin-Drumel, Z. Kisiel, O. Pirali, B.J. Esselman, R. C. Woods, R.J. McMahon, The eight lowest-energy vibrational states of benzonitrile: analysis of Coriolis and Darling-Dennison couplings by millimeter-wave and far-infrared spectroscopy, J. Mol. Spectrosc. 383 (2022), 111568.
[10] P.M. Dorman, B.J. Esselman, R.C. Woods, R.J. McMahon, An analysis of the rotational ground state and lowest-energy vibrationally excited dyad of 3-cyano-pyridine: Low symmetry reveals rich complexity of perturbations, couplings, and interstate transitions, J. Mol. Spectrosc. 373 (2020), 111373.
[11] P.M. Dorman, B.J. Esselman, J.E. Park, R.C. Woods, R.J. McMahon, Millimeter-wave spectrum of 4-cyanopyridine in its ground state and lowest-energy vibrationally excited states, $\nu_{20}$ and $\nu_{30}$, J. Mol. Spectrosc. 369 (2020), 111274.
[12] D. McNaughton, M.K. Jahn, M.J. Travers, D. Wachsmuth, P.D. Godfrey, J.-U. Grabow, Laboratory rotational spectroscopy of cyano substituted polycyclic aromatic hydrocarbons, Mon. Not. R. Astron. Soc. 476 (4) (2018) 5268–5273.
[13] P.M. Dorman, B.J. Esselman, R.C. Woods, R.J. McMahon, Unpublished work, 2022.
[14] H.H. Smith, B.J. Esselman, R.C. Woods, R.J. McMahon, Unpublished work, 2022.
[15] W. Werner, H. Dreizler, H.D. Rudolph, Zum Mikrowellenspektrum des Pyridazins, Z. Naturforsch. A 22 (4) (1967) 531–543.
[16] G.L. Blackman, R.D. Brown, F.R. Burden, The microwave spectrum, dipole moment, and nuclear quadrupole coupling constants of pyrimidine, J. Mol. Spectrosc. 35 (3) (1970) 444–454.
[17] T.J. Barnum, M.A. Siebert, K.L.K. Lee, R.A. Loomis, P.B. Changala, S.B. Charnley, M.L. Sita, C. Xue, A.J. Remijan, A.M. Burkhardt, B.A. McGuire, I.R. Cooke, A Search for Heterocycles in GOTHAM Observations of TMC-1, J. Phys. Chem. A 126 (17) (2022) 2716–2728.
[18] E.E. Etim, R.O.A. Adelagun, C. Andrew, O. Enock Oluwole, Optimizing the searches for interstellar heterocycles, Adv. Space Res. 68 (8) (2021) 3508–3520.
[19] S.B. Charnley, Y.-J. Kuan, H.-C. Huang, O. Botta, H.M. Butner, N. Cox, D. Despois, P. Ehrenfreund, Z. Kisiel, Y.-Y. Lee, A.J. Markwick, Z. Peeters, S.D. Rodgers, Astronomical searches for nitrogen heterocycles, Adv. Space Res. 36 (2) (2005) 137–145.
[20] Y.-J. Kuan, C.-H. Yan, S.B. Charnley, Z. Kisiel, P. Ehrenfreund, H.-C. Huang, A search for interstellar pyrimidine, Mon. Not. R. Astron. Soc. 345 (2003) 650–656.
[21] M. Nabavian, R. Sabbah, R. Chastel, M. Laffitte, Thermodynamique de composés azotés-II.—Étude thermochimique des acides aminobenzoïques, de la pyrimidine, de l'uracile et de la thymine, J. Chim. Phys. 74 (1977) 115–126.
[22] J. Tjebbes, The heats of combustion and formation of the three diazines and their resonance energies, Acta Chem. Scand. 16 (4) (1962) 916–921.
[23] Z.N. Heim, B.K. Amberger, B.J. Esselman, J.F. Stanton, R.C. Woods, R.J. McMahon, Molecular structure determination: Equilibrium structure of pyrimidine (*m*-$C_4H_4N_2$) from rotational spectroscopy ($r_e^{SE}$) and high-level ab initio calculation ($r_e$) agree within the uncertainty of experimental measurement, J. Chem. Phys. 152 (10) (2020), 104303.
[24] S. Akavipat, C.F. Su, R.L. Cook, Microwave spectra of chloropyrazine, J. Mol. Spectrosc. 111 (1) (1985) 209–210.
[25] P.M. Higgins, B.J. Esselman, M.A. Zdanovskaia, R.C. Woods, R.J. McMahon, Millimeter-wave spectroscopy of the chlorine isotopologues of chloropyrazine and twenty-two of their vibrationally excited states, J. Mol. Spectrosc. 364 (2019), 111179.
[26] F.B. Mortzfeld, C. Hashem, K. Vranková, M. Winkler, F. Rudroff, Pyrazines: Synthesis and Industrial Application of these Valuable Flavor and Fragrance Compounds, Biotechnol. J. 15 (11) (2020) 2000064.
[27] B.K. Amberger, B.J. Esselman, J.F. Stanton, R.C. Woods, R.J. McMahon, Precise Equilibrium Structure Determination of Hydrazoic Acid ($HN_3$) by Millimeter-wave Spectroscopy, J. Chem. Phys. 143 (10) (2015), 104310.
[28] B.J. Esselman, B.K. Amberger, J.D. Shutter, M.A. Daane, J.F. Stanton, R.C. Woods, R.J. McMahon, Rotational Spectroscopy of Pyridazine and its Isotopologs from 235–360 GHz: Equilibrium Structure and Vibrational Satellites, J. Chem. Phys. 139 (2013), 224304.
[29] Z. Kisiel, L. Pszczółkowski, B.J. Drouin, C.S. Brauer, S. Yu, J.C. Pearson, I. R. Medvedev, S. Fortman, C. Neese, Broadband rotational spectroscopy of acrylonitrile: Vibrational energies from perturbations, J. Mol. Spectrosc. 280 (2012) 134–144.
[30] Z. Kisiel, L. Pszczółkowski, I.R. Medvedev, M. Winnewisser, F.C. De Lucia, E. Herbst, Rotational spectrum of *trans–trans* diethyl ether in the ground and three excited vibrational states, J. Mol. Spectrosc. 233 (2) (2005) 231–243.
[31] H.M. Pickett, The fitting and prediction of vibration-rotation spectra with spin interactions, J. Mol. Spectrosc. 148 (2) (1991) 371–377.
[32] Z. Kisiel, PROSPE - Programs for ROtational SPEctroscopy, 2020. http://info.ifpan.edu.pl/~kisiel/prospe.htm. (Accessed 07-11-2020.
[33] M.J. Frisch, G.W. Trucks, H.B. Schlegel, G.E. Scuseria, M.A. Robb, J.R. Cheeseman, G. Scalmani, V. Barone, G.A. Petersson, H. Nakatsuji, X. Li, M. Caricato, A.V. Marenich, J. Bloino, B.G. Janesko, R. Gomperts, B. Mennucci, H.P. Hratchian, J.V. Ortiz, A.F. Izmaylov, J.L. Sonnenberg, D. Williams-Young, F. Ding, F. Lipparini, F. Egidi, J. Goings, B. Peng, A. Petrone, T. Henderson, D. Ranasinghe, V.G. Zakrzewski, J. Gao, N. Rega, G. Zheng, W. Liang, M. Hada, M. Ehara, K. Toyota, R. Fukuda, J. Hasegawa, M. Ishida, T. Nakajima, Y. Honda, O. Kitao, H. Nakai, T. Vreven, K. Throssell, J.A. Montgomery, Jr. , J.E. Peralta, F. Ogliaro, M.J. Bearpark, J.J. Heyd, E.N. Brothers, K.N. Kudin, V.N. Staroverov, T.A. Keith, R. Kobayashi, J. Normand, K. Raghavachari, A.P. Rendell, J.C. Burant, S.S. Iyengar, J. Tomasi, M. Cossi, J.M. Millam, M. Klene, C. Adamo, R. Cammi, J.W. Ochterski, R.L. Martin, K. Morokuma, O. Farkas, J.B. Foresman, D.J. Fox, Gaussian 16 rev C.01, Gaussian, Inc., Wallingford, CT, USA, 2016.
[34] J.R. Schmidt, W.F. Polik, WebMO Enterprise, version 19.0; WebMO LLC: Madison, WI, USA, 2019; http://www.webmo.net (accessed August, 2019).
[35] M.A. Zdanovskaia, B.J. Esselman, R.C. Woods, R.J. McMahon, The 130–370 GHz rotational spectrum of phenyl isocyanide ($C_6H_5NC$), J. Chem. Phys. 151 (2) (2019), 024301.
[36] H. Shindo, Studies on the Infrared Spectra of Heterocyclic Compound. VIII. Infrared Spectra of Substituted Pyrazines and their *N*-Oxides, Chem. Pharm. Bull. 8 (1) (1960) 33–45.
[37] J. Bus, T.J. Liefkens, W. Schwaiger, Infrared spectrometry of pyrazines, Recl. Trav. Chim. Pays-Bas 92 (1) (1973) 123–126.
[38] M.J.M. Delgado, F. Márquez, M.I. Suero, J.I. Marcos, Vibrational spectra of pyrazincarbonitrile and [$^{15}$N]pyrazincarbonitrile, J. Raman Spectrosc. 20 (2) (1989) 63–65.
[39] K.V. Shuvaev, T.S.M. Abedin, C.A. McClary, L.N. Dawe, J.L. Collins, L. K. Thompson, Ligand directed self-assembly *vs.* metal ion coordination algorithm—when does the ligand or the metal take control? Dalton Trans. 16 (2009) 2926–2939.
[40] B.J. Esselman, S.M. Kougias, M.A. Zdanovskaia, R.C. Woods, R.J. McMahon, Synthesis, Purification, and Rotational Spectroscopy of (Cyanomethylene) Cyclopropane—An Isomer of Pyridine, J. Phys. Chem. A 125 (25) (2021) 5601–5614.
[41] H.H. Smith, S.M. Kougias, B.J. Esselman, R.C. Woods, R.J. McMahon, Synthesis, Purification, and Rotational Spectroscopy of 1-Cyanocyclobutene ($C_5H_5N$), J. Phys. Chem. A 126 (12) (2022) 1980–1993.

The Journal of Chemical Physics

RESEARCH ARTICLE | JUNE 23 2023

# Improved semi-experimental equilibrium structure and high-level theoretical structures of ketene



Houston H. Smith ; Brian J. Esselman ; Samuel A. Wood ; John F. Stanton ;
R. Claude Woods ; Robert J. McMahon



*J. Chem. Phys.* 158, 244304 (2023)
https://doi.org/10.1063/5.0154770

# Improved semi-experimental equilibrium structure and high-level theoretical structures of ketene

Cite as: J. Chem. Phys. 158, 244304 (2023); doi: 10.1063/5.0154770
Submitted: 15 April 2023 • Accepted: 25 May 2023 •
Published Online: 23 June 2023



Houston H. Smith,[1] Brian J. Esselman,[1] Samuel A. Wood,[1] John F. Stanton,[2,a)] R. Claude Woods,[1,a)] and Robert J. McMahon[1,a)]

## AFFILIATIONS

[1] Department of Chemistry, University of Wisconsin–Madison, Madison, Wisconsin 53706, USA
[2] Quantum Theory Project, Departments of Physics and Chemistry, University of Florida, Gainesville, Florida 32611, USA

[a)] **Authors to whom correspondence should be addressed:** johnstanton@chem.ufl.edu; rcwoods@wisc.edu; and robert.mcmahon@wisc.edu

## ABSTRACT

The millimeter-wave rotational spectrum of ketene ($H_2C{=}C{=}O$) has been collected and analyzed from 130 to 750 GHz, providing highly precise spectroscopic constants from a sextic, S-reduced Hamiltonian in the $I^r$ representation. The chemical synthesis of deuteriated samples allowed spectroscopic measurements of five previously unstudied ketene isotopologues. Combined with previous work, these data provide a new, highly precise, and accurate semi-experimental ($r_e^{SE}$) structure for ketene from 32 independent moments of inertia. This $r_e^{SE}$ structure was determined with the experimental rotational constants of each available isotopologue, together with computed vibration–rotation interaction and electron-mass distribution corrections from coupled-cluster calculations with single, double, and perturbative triple excitations [CCSD(T)/cc-pCVTZ]. The 2σ uncertainties of the $r_e^{SE}$ parameters are ≤0.0007 Å and 0.014° for the bond distances and angle, respectively. Only S-reduced spectroscopic constants were used in the structure determination due to a breakdown in the A-reduction of the Hamiltonian for the highly prolate ketene species. All four $r_e^{SE}$ structural parameters agree with the "best theoretical estimate" (BTE) values, which are derived from a high-level computed $r_e$ structure [CCSD(T)/cc-pCV6Z] with corrections for the use of a finite basis set, the incomplete treatment of electron correlation, relativistic effects, and the diagonal Born–Oppenheimer breakdown. In each case, the computed value of the geometric parameter lies within the statistical experimental uncertainty (2σ) of the corresponding semi-experimental coordinate. The discrepancies between the BTE structure and the $r_e^{SE}$ structure are 0.0003, 0.0000, and 0.0004 Å for $r_{C\text{-}C}$, $r_{C\text{-}H}$, and $r_{C\text{-}O}$, respectively, and 0.009° for $\theta_{C\text{-}C\text{-}H}$.





## INTRODUCTION

Ketenes ($R_2C{=}C{=}O$) represent an important functional group in organic chemistry.[1,2] The reactivity of ketenes, albeit modulated by the nature of the substituents, is generally very high with respect to cycloaddition reactions and the addition of nucleophiles. As such, ketenes are precursors to the family of carboxylic acid derivatives, including anhydrides, carboxylic acids, esters, and amides (Scheme 1). It is the central relationship to these and other functional groups that places ketenes as important intermediates in diverse areas of science, including synthetic organic chemistry,[1–3] petroleum refining,[4] photolithography,[5] atmospheric chemistry,[6] combustion,[7] and astrochemistry.[8] The parent molecule of the family, ketene ($H_2C{=}C{=}O$), is a paradigm in terms of structure, bonding, and reactivity. It is a cornerstone of structural organic chemistry and has attracted substantial interest from both experimental and theoretical communities. In the current study, we describe the determination of a highly precise, gas-phase molecular structure for ketene using state-of-the-art methods for both experiment and theory.

Ketene ($H_2C{=}C{=}O$, $C_{2v}$, ethenone) has been identified as an interstellar molecule, with its initial detection in Sgr B2 in 1977.[9] Its detection in that source was later confirmed,[10] and various subsequent studies detected ketene in other galactic[11–15] and extragalactic[16] sources. Ketene has been generated from the photolysis

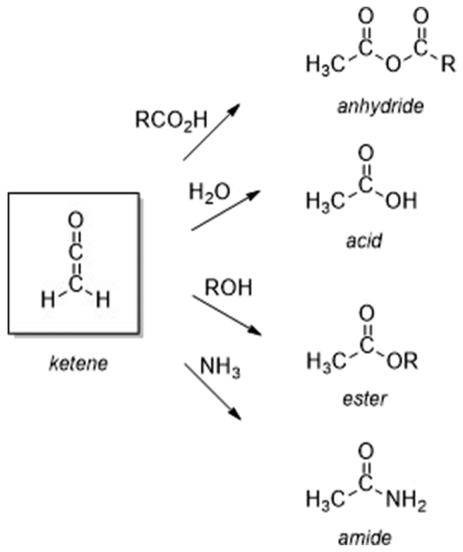


**SCHEME 1.** Reactions of ketene with various nucleophiles.

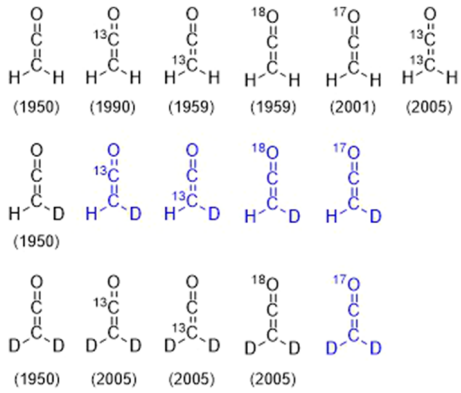


**FIG. 1.** Ketene isotopologues previously measured (black) and newly measured in this work (blue). Ketene, [2-$^2$H]-ketene, and [2,2-$^2$H]-ketene were measured by Bak *et al.*[24] [2-$^{13}$C]-ketene and [$^{18}$O]-ketene were measured by Cox *et al.*[26] [1-$^{13}$C]-ketene was measured by Brown *et al.*[28] [$^{17}$O]-ketene was measured by Guarnieri and Huckauf[31] [1,2-$^{13}$C]-ketene, [2,2-$^2$H, 1-$^{13}$C]-ketene, [2,2-$^2$H, 2-$^{13}$C]-ketene, and [2,2-$^2$H, $^{18}$O]-ketene were measured by Guarnieri.[32] The date listed indicates the first literature report of that isotopologue.

of interstellar ice analogs comprising a variety of chemical compositions ($O_2$ + $C_2H_2$, $CO_2$ + $C_2H_4$, CO + $CH_4$).[8] The central, electrophilic carbon atom of ketene reacts with common interstellar molecules $H_2O$, $NH_3$, $CH_3OH$, and HCN to form acetic acid, acetamide, methyl acetate, and pyruvonitrile, respectively.[17–19] Some of these reaction products have potential prebiotic importance in the interstellar medium. Ketene can also be generated from the decomposition of two known interstellar molecules: acetic acid[20] and acetone.[21] The acylium cation ($H_3C–C{\equiv}O^+$, $C_{3v}$),[22] which has recently been detected in the ISM,[23] is a protonated form of ketene. Due to its prevalence and possible role in the chemical reactions of extraterrestrial environments, the observation of rotational transitions of ketene in its ground and vibrationally excited states is important to radioastronomers. Previously, the rotational spectra of various ketene isotopologues have been observed and assigned up to a frequency of 350 GHz. In this work, we extended the frequency range to 750 GHz for 15 ketene isotopologues, including all singly substituted heavy-atom isotopologues of ketene, ketene-$d_1$, and ketene-$d_2$. The doubling of the spectral range for ketene isotopologues, along with new isotopologue analyses, expands the capabilities for radioastronomers to search for ketene spectral lines in different extra-terrestrial environments.

The pure rotational spectra of ketene and its isotopologues have been extensively studied for over seventy years. The rotational spectrum of ketene and its two deuteriated isotopologues, [2-$^2$H]-ketene (HDC=C=O) and [2,2-$^2$H]-ketene ($D_2$C=C=O), were measured in the early 1950s.[24,25] Subsequently, heavy-atom substituted isotopologues [2-$^{13}$C]-ketene and [$^{18}$O]-ketene were measured in 1959 and 1963,[26,27] but the final single-substitution isotopologue, [1-$^{13}$C]-ketene, was not reported until 1990.[28] In 1966, the proton spin–rotation and deuterium nuclear quadrupole constants were determined for ketene, [2-$^2$H]-ketene, and [2,2-$^2$H]-ketene.[29] In 1976, the frequency range was extended into the millimeter-wave region (up to 220 GHz) for [2-$^2$H]-ketene and [2,2-$^2$H]-ketene, permitting analysis of their centrifugal distortion.[30] More recent studies expanded the measured frequency range to 350 GHz for various isotopologues, refined the least-squares fits, and measured the spectra of new isotopologues [$^{17}$O]-ketene,[31] [1,2-$^{13}$C]-ketene,[32] [2,2-$^2$H, 1-$^{13}$C]-ketene,[32] [2,2-$^2$H, 2-$^{13}$C]-ketene,[32] and [2,2-$^2$H, $^{18}$O]-ketene.[32] For ketene, itself, Nemes *et al.* reported the measurement of 82 *a*-type, $\Delta K_a$ = 0 transitions up to 800 GHz.[33] Figure 1 shows the 11 isotopologues for which rotational spectra have previously been reported (black) and the five isotopologues newly measured in this work (blue).

The gas-phase infrared spectrum of ketene was recorded nearly 85 years ago.[34] The rotational structure in the infrared spectrum was first analyzed by Halverson and Williams,[35] followed by Harp and Rasmussen,[36] Drayton and Thompson,[37] Bak and Andersen,[38] and Butler *et al.*[39] The infrared spectra of [2-$^2$H]-ketene and [2,2-$^2$H]-ketene were reported in 1951,[40] and the first vibration-rotation bands of ketene and [2,2-$^2$H]-ketene were observed by Arendale and Fletcher in 1956.[41,42] The first complete analysis of the rotationally resolved infrared spectra of the nine fundamental states present in ketene, [2-$^2$H]-ketene, and [2,2-$^2$H]-ketene was performed by Cox and Esbitt in 1963.[43] Nemes explored the Coriolis coupling present in $\nu_5$, $\nu_6$, $\nu_8$, and $\nu_9$ of ketene in two separate studies in 1974 and 1978.[44,45] A similar study was done on [2,2-$^2$H]-ketene by Winther *et al.*, where $\nu_5$, $\nu_6$, $\nu_8$, and $\nu_9$ were examined.[46] A high-resolution infrared analysis of the four $A_1$ vibrational states for ketene, [2-$^2$H]-ketene, and [2,2-$^2$H]-ketene was performed by Duncan *et al.*,[47] followed by the high-resolution infrared study of $\nu_5$, $\nu_6$, $\nu_7$, and $\nu_8$ fundamental states and two overtone states for ketene by Duncan and Ferguson.[48] The $\nu_9$, $\nu_6$, and $\nu_5$ bands in [2,2-$^2$H]-ketene were analyzed with high-resolution infrared spectroscopy by Hegelund *et al.*[49] Escribano *et al.*[50] examined the $\nu_1$ band of ketene in 1994, which is coupled to other vibrational modes. The fundamental states, $\nu_5$ and $\nu_6$, were re-examined by Campiña *et al.*[51] in 1998 along with the observation of $\nu_6$ + $\nu_9$ in 1999 by Gruebele *et al.*[52] Johns *et al.*[53] were able to update the ground-state

spectroscopic constants derived from millimeter-wave data along with the infrared data provided by Campiña *et al.*[51] and Escribano *et al.*[50] Nemes *et al.*[54] revisited the non-linear least-squares fitting of $\nu_5$, $\nu_6$, and $\nu_9$ and were able to remove most of the Coriolis perturbation contributions to the $A_v$ rotational constants and derive new experimental Coriolis ζ constants. The vibrational energy manifold up to 3400 $cm^{-1}$ is shown in Fig. 2, using the experimental frequencies where available and supplementing with computed values where experimental values are not available.

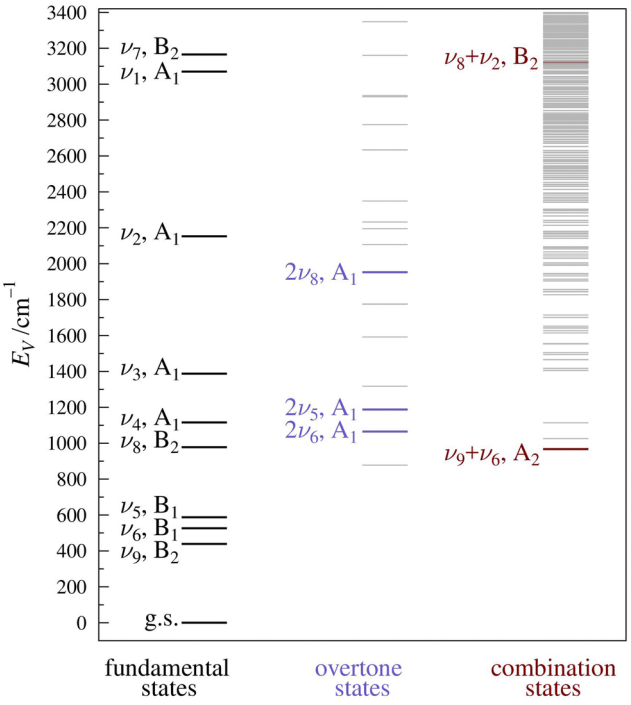


**FIG. 2.** Vibrational energy levels of ketene below 3400 $cm^{-1}$. Experimentally observed vibrational energy levels (black, purple, and maroon) are each taken from the most recent literature report and labeled.[44–54] Unobserved vibrational energy levels (gray) are depicted using the computed fundamental frequencies [CCSD(T)/cc-pVTZ]. Overtone and combination states are provided up to five quanta.

The observation and assignment of various ketene isotopologues have been used for several structural determinations presented in Table I.[28,55–58] The first zero-point average structure ($r_z$), accounting for harmonic vibrational corrections, centrifugal distortion, and electronic corrections, was determined in 1976.[55] A second $r_z$ structure was calculated in 1987,[56] after several studies examining the vibrational spectra of ketene isotopologues facilitated a more physically realistic general harmonic force field to be applied to the structure calculation.[47,48,59] The additional measurement of [1-$^{13}$C]-ketene by Brown *et al.*[28] enabled the first complete substitution structure ($r_s$) determination, where every atom was isotopically substituted at least once in the structure determination. The first semi-experimental equilibrium structure ($r_e^{SE}$), using vibration–rotation interaction corrections calculated from an anharmonic force field, was calculated in 1995 with the rotational constants of the six isotopologues available at that time.[57] The six isotopologues in this $r_e^{SE}$ structure provide 12 independent moments of inertia, which is more than sufficient to determine the four structural parameters of ketene. Guarnieri *et al.*[31,32,60] measured and assigned rotational transitions for five new isotopologues and determined an updated $r_e^{SE}$ from the rotational constants of 11 isotopologues (22 independent moments of inertia) using vibration–rotation corrections calculated at the MP2/cc-pVTZ level in 2010.[58] The two $r_e^{SE}$ structures are generally in good agreement but disagree somewhat with respect to the $r_{C-H}$ value.

The foundation for semi-experimental equilibrium ($r_e^{SE}$) structure determination was pioneered by Pulay, Meyer, and Boggs,[63] and the accuracy of the structures obtained using this approach has been exemplified in various studies.[64–67] The accuracy of semi-experimental structures using different computational methods was investigated in the 1990s and 2000s[68–74] and was comprehensively reviewed by Puzzarini[75] and Puzzarini and Stanton.[76] The coupled-cluster method for both geometry optimizations and anharmonic force-field calculations, along with sufficiently large basis sets for the molecule of interest, was shown to provide the most accurate structural parameters.[73,77] For larger molecules, where coupled-cluster methods are not feasible, structural parameters derived from density

**TABLE I.** Select previously reported structures of ketene.

| | Mallinson and Nemes[55] $r_z$ 1976 | Duncan and Munro[56] $r_z$ 1987 | Brown *et al.*[28] $r_s$ 1990 | East *et al.*[57] $r_e^{SE}$ 1995 | Guarnieri *et al.*[58] $r_e^{SE}$ 2010 |
|---|---|---|---|---|---|
| $r_{C-C}$ | 1.3171 (20)[a] | 1.316 5 (15)[b] | 1.314 (72)[c] | 1.312 12 (60)[d] | 1.3122 (12)[d] |
| $r_{C-H}$ | 1.0797 (10)[a] | 1.080 02 (33)[b] | 1.0825 (15)[c] | 1.075 76 (14)[d] | 1.0763 (2)[d] |
| $r_{C-O}$ | 1.1608 (20)[a] | 1.161 4 (14)[b] | 1.162 (72)[c] | 1.160 30 (58)[d] | 1.1607 (12)[d] |
| $\theta_{C-C-H}$ | 119.02 (10)[a] | 119.011 (31)[b] | 118.72 (5)[c] | 119.110 (12)[d] | 119.115 (22)[d] |
| $N_{iso}$[e] | 5 | 5 | 6 | 6 | 11 |

[a]Uncertainties as stated in Mallinson and Nemes.[55]
[b]3σ values.
[c]Uncertainties estimated as recommended by Costain[61] and Harmony *et al.*[62]
[d]All statistical uncertainties adjusted from previous reports to be 2σ values.
[e]Number of isotopologues used in the structure determination.

functional methods, e.g., B3LYP/SNSD, display reasonable accuracy.[78] A number of our recent studies have shown remarkable agreement of CCSD(T)/cc-pCV5Z or CCSD(T)/cc-pCV6Z $r_e$ structures with $r_e^{SE}$ structures determined using CCSD(T)/cc-pCVTZ vibration–rotation corrections.[79–86] The small number of atoms in ketene allows the coupled-cluster approach to be utilized in this work, affording an $r_e^{SE}$ structure of similar precision and accuracy to those recent studies.

## EXPERIMENTAL METHODS

The rotational spectra of synthesized samples of ketene and deuteriated ketene, described later, were continuously collected in the segments 130–230, 235–360, 350–500, and 500–750 GHz. The instrument covering the 130–360 GHz range has previously been described.[87–89] The 350–500 and 500–750 GHz segments were obtained with a newly acquired amplification and multiplication chain. VDI Mini SGX (SGX-M) signal generator, with external multipliers WR4.3X2 and WR2.2X2, generates 350-500 GHz and, with external multipliers WR4.3X2 and WR1.5X3, generates 500-750 GHz. These spectral segments were detected by using VDI zero-bias detectors WR2.2ZBD and WR1.5ZBD, respectively. The complete spectrum from 130 to 750 GHz was obtained using automated data collection software over ~12 days with these experimental parameters: 0.6 MHz/s sweep rate, 10 ms time constant, and 50 kHz AM and 500 kHz FM modulation in a tone-burst design.[90] The frequency spectra were combined into a single spectral file using Assignment and Analysis of Broadband Spectra (AABS) software.[91,92] Pickett's SPFIT/SPCAT programs[93] were used for least-squares fits and spectral predictions, along with Kisiel's PIFORM, PLANM, and AC programs for analysis.[94,95] Additional short-frequency ranges of the spectrum were collected with an increased number of scans for low-abundance isotopologues. In our least-squares fits, we assume a uniform 50 kHz frequency measurement uncertainty for our measured transitions, 50 kHz for literature values that did not specify an uncertainty, and 25 kHz for transitions reported by Guarnieri *et al.*[31,32,60] Least-squares fitting output files are provided in the supplementary material.

In this study, we measured and assigned the rotational spectrum from 130 to 750 GHz for the primary (Fig. 3) and deuterium-substituted ketene isotopologues, including their heavy-atom isotopologues, $^{13}C$ and $^{18}O$. All $^{17}O$-substituted isotopologues, including the new detection of [2-$^{2}$H, $^{17}$O]-ketene and [2,2-$^{2}$H, $^{17}$O]-ketene, were measured from 230 to 500 GHz. The reduced frequency coverage is due to lower signal-to-noise ratios ($S/N$) for the hardware configurations outside that range. Transitions of [1,2-$^{13}$C]-ketene could not be measured or assigned due to the proximity of its transitions to those of [2-$^{13}$C]-ketene and the inherently lower $S/N$ for an isotopologue ~0.0121% the intensity of the main isotopologue. Thus, we were unable to improve upon the spectroscopic constants presented by Guarnieri.[32] Due to the planarity condition, each isotopologue provides two independent moments of inertia. With 16 isotopologues used for the new structure determination, an $r_e^{SE}$ structure for ketene was obtained by using 32 independent moments of inertia.

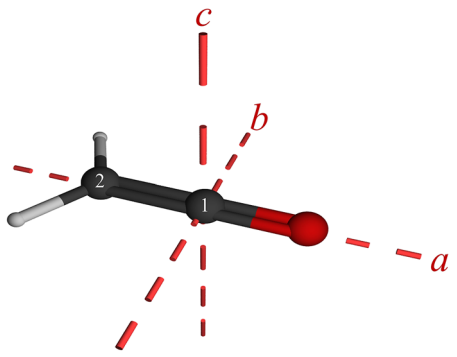


**FIG. 3.** Ketene structure with principal inertial axes and carbon atom numbering.

## COMPUTATIONAL METHODS

Calculations were carried out using a development version of CFOUR.[96] The ketene structure was first optimized at the CCSD(T)/cc-pCVTZ level of theory. The optimized geometry and the same level of theory were subsequently used for an anharmonic, second-order vibrational perturbation theory (VPT2) calculation, wherein cubic force constants are evaluated using analytical second derivatives at displaced points.[97–99] Magnetic property calculations were performed for each isotopologue to obtain the electron-mass corrections to the corresponding rotational constants. The "best theoretical estimate" (BTE), as described previously, is based on a CCSD(T)/cc-pCV6Z optimized structure with four additional corrections[79–86] that address the following:

1. Residual basis set effects beyond cc-pCV6Z.
2. Residual electron correlation effects beyond the CCSD(T) treatment.
3. Effects of scalar (mass–velocity and Darwin) relativistic effects.
4. The fixed-nucleus approximation via the diagonal Born–Oppenheimer correction.

The equations used to calculate these corrections and the values of each of these corrections for ketene are provided in the supplementary material (S7–S13 and Table S-V). One of the most important factors of the algorithm used to determine the BTE is the estimation of residual basis set effects, specifically estimated as the difference between the (directly computed) cc-pCV6Z geometry at the CCSD(T) level of theory and the estimate of the CCSD(T) geometry at the basis set limit. Following others,[100] the latter is estimated by assuming an exponential convergence pattern with respect to the highest angular momentum basis functions present in the basis. A complete explanation of the BTE calculation is provided in the supplementary material.

The *xrefit* module of CFOUR calculates the moments of inertia and the semi-experimental equilibrium structure using the experimental, S-reduced rotational constants and computational electron-mass distribution and vibration–rotation corrections. The *xrefiteration* program was used to reveal insight into the contributions of additional isotopologues in refining the structure.[82] The routine begins by determining a structure using a single isotopic substitution at each position and then sequentially adding the most uncertainty-minimizing isotopologue to the structural least-squares

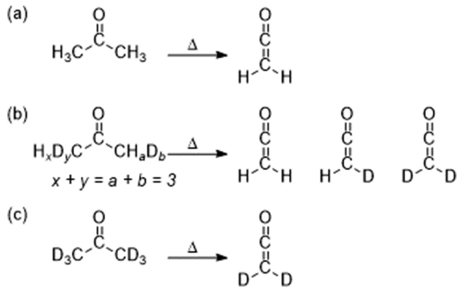


**SCHEME 2.** Ketene isotopologue synthesis: (a) ketene-$h_2$ by pyrolysis of acetone-$h_6$, (b) mixture of ketene isotopologues by pyrolysis of 50% deuterium-enriched acetone, and (c) ketene-$d_2$ by pyrolysis of acetone-$d_6$.

fit until all available isotopologues are incorporated. The routine is also useful in assessing the quality of the fit for each isotopologue, since a problematic fit may be readily apparent as a deviation in the *xrefiteration* plot.

Computational output files are provided in the supplementary material.

## SYNTHESIS OF KETENE ISOTOPOLOGUES

Ketene was synthesized by pyrolysis of acetone (HPLC grade, Sigma-Aldrich) at atmospheric pressure using a lamp described by Williams and Hurd[101] and collected in a −130 °C cold trap [Scheme 2(a)]. After collection, the cold trap was isolated from the pyrolysis apparatus and placed under vacuum to remove volatile impurities; ketene was then transferred to a stainless-steel cold trap for spectroscopic investigation. A mixed deuterio-/protio-solution of acetone-$d_x$ was produced by a procedure modified from Paulsen and Cooke,[102] using acetone, $D_2O$, and lithium deuteroxide (LiOD). The reaction mixture was distilled, yielding ~50% deuterium-enriched acetone. Pyrolysis and purification of this mixture produced ketene, [2-$^2$H]-ketene, and [2,2-$^2$H]-ketene [Scheme 2(b)]. An independent sample of [2,2-$^2$H]-ketene [Scheme 2(c)] with high deuterium incorporation was generated by pyrolysis of acetone-$d_6$ (99.5%, Oakwood Chemical).

## ANALYSIS OF ROTATIONAL SPECTRA

The rotational spectrum of ketene is dominated by $^aR_{0,1}$ transitions, but a select few low-intensity $^aQ_{0,-1}$ transitions were observable in the lower frequency range. Ketene has an *a*-axis dipole, $\mu_a$ = 1.414 (10) D,[25] and is extremely close to a prolate top [$\kappa$ = −0.997 for the main isotopologue, Eq. (1)], which can result in a breakdown of the A-reduction least-squares fit ($I^r$ representation) of the Hamiltonian,

$$\kappa = \left(\frac{2B - A - C}{A - C}\right). \quad (1)$$

The A-reduction breakdown for molecules that approach a spherical top, a prolate top (in the $I^{r/l}$ representation), or an oblate top (in the $III^{r/l}$ representation) has been discussed previously.[84,103–108] (The output files of least-squares fitting for each isotopologue to sextic, A- and S-reduction Hamiltonians in the $I^r$ representation are

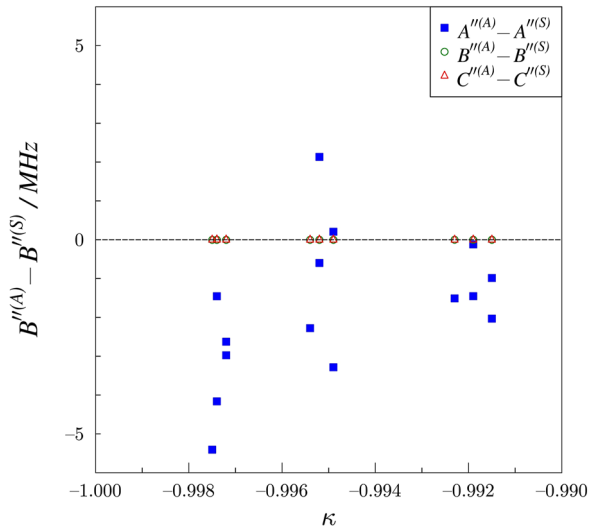


**FIG. 4.** Difference between the determinable constants ($A_0''$, $B_0''$, and $C_0''$) derived using the A- and the S-reduced Hamiltonians for ketene isotopologues as a function of $\kappa$. The symbols for the *b*- and *c*-axis differences are so close to zero that they are overlapped and difficult to distinguish on the plot. Note the increase in scatter and the deviation from zero for the *a*-axis differences as $\kappa$ approaches the prolate limit of −1.000.

provided in the supplementary material.) For ketene, the experimental and computed A-reduction spectroscopic constants do not appear to display the unreasonably large *K*-dependent centrifugal distortion constants that have been noted in other cases where the A-reduction breaks down. There is, however, a significant difference between the A- and S-reduction determinable constants (Eqs. S1–S6 in the supplementary material) from the least-squares fits in the A- and S-reductions. The $\kappa$ values for the ketene isotopologues vary from −0.9915 ([2,2-$^2$H]-ketene) to −0.9975 ([$^{18}$O]-ketene). The greatest discrepancies in the determinable constants occur for the $A_0$ constant of the isotopologues with the greatest $\kappa$ values, [$^{18}$O]-ketene and [$^{17}$O]-ketene. Figure 4 shows the differences in the determinable constants (nominal $B''$ values) in the A- and S-reductions as a function of $\kappa$. While the trend does not show a clearly defined behavior, the variability in $A_0''$ increases as $\kappa$ approaches the prolate-top limit (−1.000). Additionally, in each case, the A-reduction fits have a larger statistical uncertainty than the S-reduction fits. Doose *et al.*[109] observed similar issues with [2,2-$^2$H]-ketene ($\kappa$ = −0.9915), including high uncertainties and high correlations for some parameters when only pure rotational transitions were used in the least-squares fit. For these reasons, only the S-reduction spectroscopic constants are presented in the main text of this work and used in the $r_e^{SE}$ structure determination. The S-reduction spectroscopic constants for all ketene isotopologues are presented in Table II.

Table II provides the experimental spectroscopic constants in the S-reduction and $I^r$ representation for all 16 ketene isotopologues used in the semi-experimental equilibrium structure determination. The [1,2-$^{13}$C]-ketene spectroscopic constants provided in Table II are those reported by Guarnieri *et al.*[32] due to the inability to measure this isotopologue in this work. Table II includes, for the normal isotopologue, the previously determined spectroscopic constants by Guarnieri and Huckauf[50] and the computed constants

**TABLE II.** Spectroscopic constants for ketene isotopologues, ground vibrational state (S-reduced Hamiltonian, $I^r$ representation).

| | Normal isotopologue | | | | | |
|---|---|---|---|---|---|---|
| | Guarnieri *et al.* 2003[a] | CCSD(T)[b] | Current work | [1-$^{13}$C] | [2-$^{13}$C] | [$^{18}$O] |
| $A_0$ (MHz) | 282 032 (22) | 281 680 | 282 121.6 (18) | 282 104.2 (25) | 282 108.1 (26) | 282 142.0 (40) |
| $B_0$ (MHz) | 10 293.319 63 (81) | 10 234 | 10 293.318 94 (24) | 10 293.629 59 (44) | 9 960.977 88 (37) | 9 761.237 01 (38) |
| $C_0$ (MHz) | 9 915.903 93 (80) | 9861 | 9 915.903 04 (24) | 9 916.210 87 (44) | 9 607.139 42 (35) | 9 421.124 72 (37) |
| $D_J$ (kHz) | 3.280 4 (18) | 3.15 | 3.281 23 (30) | 3.279 63 (49) | 3.090 08 (35) | 2.949 28 (14) |
| $D_{JK}$ (kHz) | 478.27 (11) | 477 | 477.384 (31) | 476.701 (43) | 451.182 (36) | 434.455 (47) |
| $D_K$ (kHz) | [22 840][c] | 20 700 | [20 700][d] | [20 700][d] | [20 700][d] | [20 700][d] |
| $d_1$ (kHz) | −0.147 57 (84) | −0.125 | −0.147 726 (11) | −0.147 875 (96) | −0.132 961 (89) | −0.125 48 (11) |
| $d_2$ (kHz) | −0.056 21 (51) | −0.043 3 | −0.055 755 (57) | −0.055 96 (11) | −0.049 28 (11) | −0.045 47 (17) |
| $H_J$ (Hz) | [−0.002 04] [c] | −0.000 466 | −0.001 25 (13) | −0.001 11 (21) | −0.001 10 (14) | [−0.000 319 4] |
| $H_{JK}$ (Hz) | 2.27 (21) | 2.80 | 2.914 2 (89) | 2.976 (13) | 2.587 6 (91) | 2.495 (13) |
| $H_{KJ}$ (Hz) | −526.2 (45) | −711 | −647.7 (11) | −673.7 (15) | −603.0 (13) | −614.2 (17) |
| $H_K$ (Hz) | [5230][c] | 5890 | [5890][d] | [5930][d] | [5850][d] | [5850][d] |
| $h_1$ (Hz) | | 0.000 026 4 | [0.000 026 4][d] | [0.000 025 9][d] | [0.000 023 7][d] | [0.000 025][d] |
| $h_2$ (Hz) | | 0.000 442 | [0.000 442][d] | [0.000 444][d] | [0.000 369][d] | [0.000 339][d] |
| $h_3$ (Hz) | | 0.000 072 4 | [0.000 0724][d] | [0.000 073][d] | [0.000 059 5][d] | [0.000 054 4][d] |
| $L_{JK}$ (mHz) | −21.3 (46) | | | | | |
| $L_{JKK}$ (mHz) | 3475 (59) | | | | | |
| $N_{lines}$[e] | 156 | | 307[f] | 209 | 230 | 189 |
| σ (MHz) | 0.040 | | 0.037 | 0.048 | 0.041 | 0.041 |
| | [$^{17}$O] | [1,2-$^{13}$C] | [2-$^{2}$H] | [2-$^{2}$H, 1-$^{13}$C] | [2-$^{2}$H, 2-$^{13}$C] | [2-$^{2}$H,$^{18}$O] |
| $A_0$ (MHz) | 282 175 (13) | 282 031 (22) | 194 292.2 (13) | 194 256.1 (23) | 193 984.2 (26) | 194 243.2 (31) |
| $B_0$ (MHz) | 10 013.472 2 (14) | 9 960.865 0 (25) | 9 647.065 33 (21) | 9 646.687 07 (65) | 9 373.431 43 (63) | 9 145.129 30 (76) |
| $C_0$ (MHz) | 9 655.909 6 (13) | 9 607.055 0 (27) | 9 174.643 51 (20) | 9 174.260 89 (64) | 8 926.177 92 (60) | 8 719.333 31 (72) |
| $D_J$ (kHz) | 3.099 97 (63) | 3.088 1 (21) | 3.004 61 (37) | 3.005 29 (64) | 2.827 55 (61) | 2.699 45 (58) |
| $D_{JK}$ (kHz) | 454.371 (92) | 451.12 (11) | 328.426 (25) | 327.242 (41) | 315.948 (35) | 297.756 (44) |
| $D_K$ (kHz) | [20 700][d] | [22 840][c] | 17 400 (674) | 15 380 (1098) | 17 090 (1276) | 16 760 (1576) |
| $d_1$ (kHz) | −0.134 67 (76) | −0.133 1 (27) | −0.226 195 (49) | −0.226 86 (15) | −0.203 28 (16) | −0.191 48 (17) |
| $d_2$ (kHz) | −0.048 45 (60) | −0.050 9 (11) | −0.084 10 (15) | −0.083 75 (26) | −0.075 65 (27) | −0.068 77 (30) |
| $H_J$ (Hz) | [−0.003 84][d] | [−0.002 04][c] | −0.001 380 (80) | −0.001 04 (15) | −0.001 03 (12) | [−0.000 111 7][d] |
| $H_{JK}$ (Hz) | 2.561 (89) | 2.07 (23) | 2.284 3 (67) | 2.316 (11) | 2.065 5 (83) | 1.948 (11) |
| $H_{KJ}$ (Hz) | −635.8 (33) | −506.9 (42) | −254.39 (89) | −264.6 (15) | −240.3 (13) | −238.6 (15) |
| $H_K$ (Hz) | [5870][d] | [5230][c] | [4070][d] | [3970][d] | [4060][d] | [4040][d] |
| $h_1$ (Hz) | [0.000 025 8][d] | | [0.000 194][d] | [0.000 195][d] | [0.000 161][d] | [0.000 165][d] |
| $h_2$ (Hz) | [0.000 385][d] | | 0.000 782 (35) | [0.000 767][d] | [0.000 653][d] | [0.000 586][d] |
| $h_3$ (Hz) | [0.000 062 4][d] | | [0.000 139][d] | [0.000 140][d] | [0.000 118][d] | [0.000 105][d] |
| $L_{JK}$ (mHz) | | 18.7 (47) | | | | |
| $L_{JKK}$ (mHz) | | −3545 (53) | | | | |
| $N_{lines}$[e] | 94 | 86 | 344 | 204 | 240 | 171 |
| σ (MHz) | 0.046 | 0.030 | 0.034 | 0.043 | 0.042 | 0.047 |

**TABLE II.** (*Continued.*)

| | [2-$^{2}$H,$^{17}$O] | [2,2-$^{2}$H] | [2,2-$^{2}$H, 1-$^{13}$C] | [2,2-$^{2}$H, 2-$^{13}$C] | [2,2-$^{2}$H,$^{18}$O] | [2,2-$^{2}$H,$^{17}$O] |
|---|---|---|---|---|---|---|
| $A_0$ (MHz) | 194 260.6 (27) | 141 490.38 (28) | 141 484.52 (67) | 141 483.16 (65) | 141 489.40 (85) | 141 490.0(10) |
| $B_0$ (MHz) | 9 383.171 5 (13) | 9 120.830 67 (17) | 9 119.426 58 (65) | 8 890.473 51 (67) | 8 641.838 91 (56) | 8 869.062 1(17) |
| $C_0$ (MHz) | 8 935.543 1 (13) | 8 552.699 81 (16) | 8 551.484 44 (71) | 8 349.841 31 (61) | 8 130.053 11 (54) | 8 330.881 9(13) |
| $D_J$ (kHz) | 2.845 76 (51) | 2.484 04 (19) | 2.484 96 (48) | 2.358 60 (38) | 2.234 74 (43) | 2.355 69(55) |
| $D_{JK}$ (kHz) | 312.295 (66) | 322.962 (21) | 321.967 (38) | 310.142 (37) | 294.046 (43) | 307.799(76) |
| $D_K$ (kHz) | 15 140 (840) | 5645 (100) | 5327 (225) | 5373 (209) | 5470 (359) | [5000][d] |
| $d_1$ (kHz) | −0.209 21 (58) | −0.220 132 (37) | −0.220 25 (14) | −0.201 00 (12) | −0.186 76 (15) | −0.204 48(71) |
| $d_2$ (kHz) | −0.075 96 (29) | −0.114 212 (87) | −0.114 15 (31) | −0.103 09 (28) | −0.093 66 (32) | −0.103 11(28) |
| $H_J$ (Hz) | [0.000 021 1][d] | −0.001 690 (47) | −0.001 63 (12) | −0.001 558 (95) | −0.001 436 (96) | [−0.000 862][d] |
| $H_{JK}$ (Hz) | 2.162 (37) | 2.077 5 (46) | 2.079 8 (93) | 1.895 4 (93) | 1.690 (12) | 2.001(43) |
| $H_{KJ}$ (Hz) | −243.1 (22) | −127.50 (80) | −138.4 (14) | −124.0 (14) | −129.4 (15) | −129.1(27) |
| $H_K$ (Hz) | [4050][d] | [787][d] | [793][d] | [781][d] | [781][d] | [784][d] |
| $h_1$ (Hz) | [0.000 178][d] | [−0.000 014 4][d] | [−0.000 014 6][d] | [−0.000 014 2][d] | [−0.000 002][d] | [−0.000 007 30][d] |
| $h_2$ (Hz) | [0.000 568][d] | 0.001 030 (30) | 0.001 19 (12) | 0.000 66 (11) | 0.000 700 (97) | [0.000 752][d] |
| $h_3$ (Hz) | [0.000 120][d] | [0.000 208][d] | [0.000 208][d] | [0.000 180][d] | [0.000 156][d] | [0.000 179][d] |
| $N_{lines}$[e] | 107 | 403 | 221 | 218 | 166 | 88 |
| σ (MHz) | 0.040 | 0.032 | 0.046 | 0.045 | 0.042 | 0.046 |

[a] Constants as reported in Ref. 60.
[b] $B_0$ values obtained from Eq. (2) using the computed values for $B_e$, vibration–rotation interaction, and electron-mass distribution [each evaluated using CCSD(T)/cc-pCVTZ]. Distortion constants computed using CCSD(T)/cc-pCVTZ.
[c] Constant held fixed to value in Ref. 53 as stated by Ref. 60.
[d] Constant held fixed at the CCSD(T)/cc-pCVTZ value.
[e] Number of independent transitions.
[f] Transitions reported by Brown *et al.*,[28] Johnson and Strandberg,[25] and Guarnieri and Huckauf[30] are included in the least-squares fit. See the supplementary material for transitions used from previous studies for non-standard isotopologues.

[CCSD(T)/cc-pCV6Z] for comparison to the experimental values determined in this work. The CCSD(T) values for all other isotopologues can be found in the supplementary material. Experimental rotational constants $B_0$ and $C_0$ determined by Guarnieri and Huckauf[60] are in exceptional agreement with this work, but $A_0$ is not in such good agreement. The computed rotational constants are in good agreement with the experimentally determined ones previously reported, with the largest discrepancy being in $B_0$ (0.58%). Centrifugal distortion constants determined by Guarnieri and Huckauf[60] are also in excellent agreement with those determined here, with the largest difference in $d_2$ (0.81%). Neither work was able to determine $D_K$, but Guarnieri *et al.* used the previously determined value from Johns *et al.*,[53] while the present work used the CCSD(T) value. The CCSD(T) value was utilized to maintain a consistent treatment with the sextic centrifugal distortion constants, which were also held fixed at the CCSD(T) values since experimental values are not available. The CCSD(T) values for the centrifugal distortion constants display the expected level of agreement with the experimental values, with the largest discrepancy in $d_2$ (22%). There are only two sextic distortion constants that were determined both in this work and by Guarnieri and Huckauf,[60] $H_{JK}$ and $H_{KJ}$, and both are in reasonable agreement (28%). $H_J$ was determined in this work, while it was held fixed in Guarnieri and Huckauf,[60] similar to $D_K$. $H_K$ is held fixed at two different values in the two works for the same reason as $D_K$. This work held the off-diagonal sextic centrifugal distortion constants, $h_1$, $h_2$, and $h_3$, fixed at their respective CCSD(T) values, while they were held at zero in the previous studies. This difference seemed to negate the need for the two octic centrifugal distortion constants utilized in the previous studies for the frequency range and $K_a$ range measured in this work. The largest relative discrepancy in the CCSD(T) sextic centrifugal distortion constants that were determined is in $H_J$ (63%), which is not unexpected due to it being orders of magnitude smaller than the other constants.

The band structure for all ketene isotopologues is typical for a highly prolate molecule, with each band corresponding to a singular $J''+1$ value with different $K_a$ values. The transitions of the band structure lose $K_a$ degeneracy for $K_a = 3$ for all isotopologues, with the protio-isotopologues losing degeneracy in bands at higher frequencies. The current work expanded the range of quantum numbers of the transitions assigned for ketene to include $J''+1 = 7$ to 41 and $K_a = 0$ to 5. The breadth of the transitions assigned in this work is shown in Fig. 5, where all transitions newly measured are in black and previously measured transitions are in various colors indicating their source. All ketene isotopologue least-squares fits were limited to transitions with $K_a \leq 5$, even though transitions with higher $K_a$ were observed. This is because a single-state, distorted-rotor Hamiltonian was unable to provide a least-squares fit below the assumed measurement uncertainty of 50 kHz when incorporating transitions above $K_a = 5$. This failure of the single-state least-squares fit to model all of the observable transitions is due to coupling between the vibrational ground and excited states that has been extensively studied in the infrared spectra of ketene and summarized in the Introduction.[44–49,51,52,54] An analysis of the vibrational coupling is beyond the scope of the current work. The cutoff of $K_a \leq 5$ was implemented for all isotopologues to maintain a consistent amount of spectroscopic information. A similar procedure was applied to previous studies with $HN_3$, which also has a ground state coupled to low-energy fundamental states,[110] and was shown to provide an $r_e^{SE}$ structure with complete consistency with the BTE.[83,87]

The heavy-atom isotopologues of ketene were observed at natural abundance from the synthesized protio-sample of ketene, and only $^aR_{0,1}$ transitions could be observed and measured. The



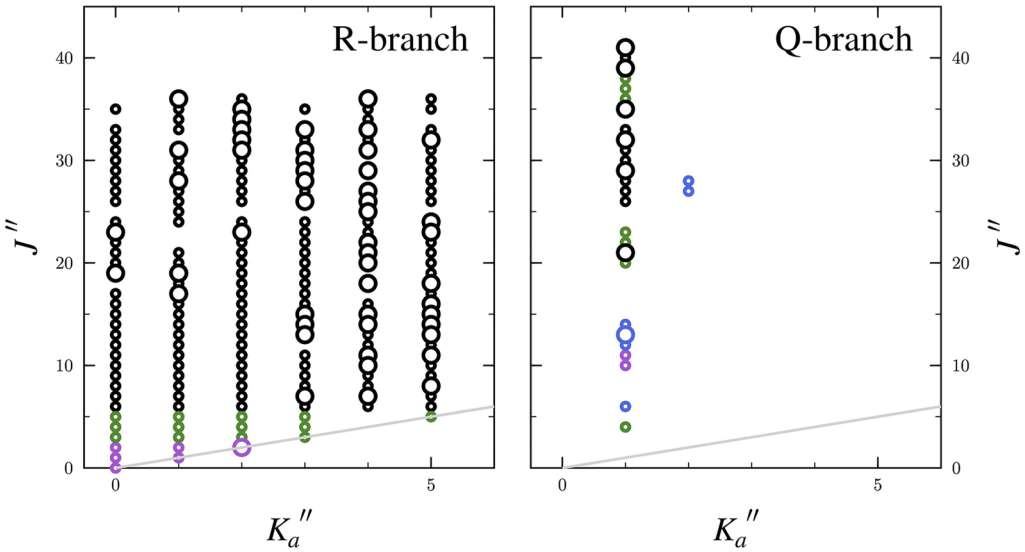


**FIG. 5.** Data distribution plot for the least-squares fit of spectroscopic data for the vibrational ground state of ketene. The size of the outlined circle is proportional to the value of $|(f_{obs.} - f_{calc.})/\delta f|$, where $\delta f$ is the frequency measurement uncertainty. The transitions are color coordinated as follows: Current work (black), Brown *et al.*[28] (purple), Johnson and Strandberg[25] (blue), and Guarnieri and Huckauf[60](green). Transitions from previous studies that overlapped with current measurements were omitted from the dataset.

[2-$^2$H]-ketene and [2,2-$^2$H]-ketene isotopologues were the only other isotopologues where $^aQ_{0,-1}$ transitions could be measured. The [2-$^2$H]-ketene isotopologue has a small predicted *b*-dipole moment, $\mu_b$ = 0.048 D, but no *b*-type transitions were sufficiently intense to be observed in our spectrum. All of the heavy-atom isotopologues for [2-$^2$H]-ketene and [2,2-$^2$H]-ketene were observable at natural abundance in their deuterium-enriched samples. For the previously observed isotopologues, the published spectroscopic constants were used as predictions for the spectral region measured in this work. Once rotational constants were obtained for several known isotopologues, a preliminary semi-experimental equilibrium structure was obtained, which provided very accurate equilibrium rotational constants for new isotopologues. Along with CCSD(T) vibrational and electronic corrections and centrifugal distortion constants, the predicted rotational constants were used to assign transitions for the previously unidentified isotopologues: [2-$^2$H, 1-$^{13}$C]-ketene, [2-$^2$H, 2-$^{13}$C]-ketene, [2-$^2$H, $^{18}$O]-ketene, [2-$^2$H, $^{17}$O]-ketene, and [2,2-$^2$H, $^{17}$O]-ketene. This technique greatly expedited the search for these transitions, as the CCSD(T)/cc-pCVTZ rotational constants predictions were not accurate enough to easily identify and assign the transitions. All heavy-atom isotopologue transitions measured from 500 to 750 GHz and all three $^{17}$O-isotopologues measured from 230 to 500 GHz required averaging 20 scans due to low *S/N*. These low *S/N* transitions were collected by acquiring 10 MHz windows around each predicted transition. Despite the various isotopologue substitutions, the spectral pattern (Fig. 6) of ketene was relatively consistent due to the highly prolate nature of the molecule.

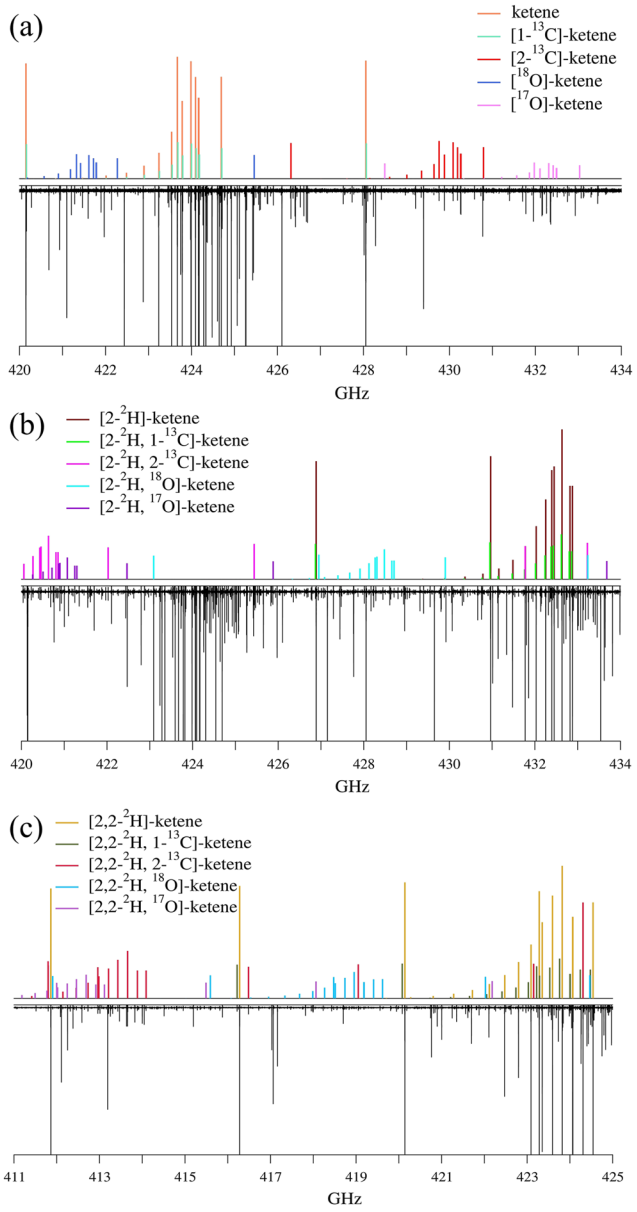


**FIG. 6.** (a) Stick spectra predicted from experimental spectroscopic constants from 420.0 to 434.0 GHz (top) and experimental spectrum (bottom) of the ketene and heavy-atom isotopologues. (b) Stick spectra predicted from experimental spectroscopic constants from 420.0 to 434.0 GHz (top) and experimental spectrum (bottom) of the [2-$^2$H]-ketene and heavy-atom isotopologues. (c) Stick spectra predicted from experimental spectroscopic constants from 411.0 to 425.0 GHz (top) and experimental spectrum (bottom) of the [2,2-$^2$H]-ketene and heavy-atom isotopologues. Transitions belonging to vibrationally excited states are also discernible.

The rotational spectra of three separate ketene samples are shown in Fig. 6, where (a) corresponds to the protio-isotopologue from 420 to 434 GHz, (b) corresponds to the [2-$^2$H]-ketene isotopologue from 420 to 434 GHz, and (c) corresponds to the [2,2-$^2$H]-ketene isotopologue from 411 to 425 GHz along with their respective heavy-atom isotopologues. The rotational spectrum of ketene is sparse with the bands of R-branch transitions with constant *J* values, separated by ~16 GHz or ~2*C*, allowing for the assignment of multiple isotopologues within one sample spectrum. Thus, there was little issue with transitions overlapping, which would cause a poor determination of the transition frequencies. Each spectrum contains unassigned transitions belonging to excited vibrational states of ketene isotopologues, as shown in Fig. 6. Data distribution plots for the isotopologues, showing the breadth of quantum numbers observed, are provided in the supplementary material.

## SEMI-EXPERIMENTAL EQUILIBRIUM STRUCTURE ($r_e^{SE}$)

In contrast to several of our recent $r_e^{SE}$ structure determinations,[79–86] the spectroscopic constants determined in the S-reduction ($B_0^{\beta(S)}$) were converted to equilibrium constants ($B_e^{\beta}$) and used directly in the least-squares fitting of the semi-experimental equilibrium structure without conversion to the determinable constants. In those previous studies, with the exception of [1,3-$^2$H]-1*H*-1,2,4-triazole, the A-reduction and S-reduction rotational constants for each isotopologue were converted to the determinable constants from which the centrifugal distortion has been removed. These determinable constants are then averaged before converting to the equilibrium constants ($B_e^{\beta}$) for $r_e^{SE}$ structure determination. As noted previously, ketene is an extreme prolate top ($\kappa$ = −0.997) with only *a*-type transitions; thus, the A-reduction spectroscopic constants cannot be determined as

accurately as the S-reduction constants. As a result, the S-reduction specific vibration–rotation interaction corrections determined in the CFOUR anharmonic frequency calculation were used to obtain the equilibrium rotational constants. Thus, the centrifugal distortion corrections used to determine the equilibrium rotational constants are the computed ones rather than the experimental ones. Ideally, the spectroscopic constants would be determined in both the A- and S-reductions, and each rotational constant would be converted to a determinable constant. If the determinable constants were similar, it would give confidence that the rotational and quartic centrifugal distortion constants were determined with sufficient accuracy to be included in the structure determination, regardless of the size of the transition dataset. A similar problem might have arisen in the $HN_3$ semi-experimental equilibrium structure determinations,[83,87] but the $HN_3$ dataset included *b*-type transitions, along with *a*-type transitions, which gave enough spectroscopic information to successfully determine the A-reduction spectroscopic constants.

In the current case, the S-reduction rotational constants were input to *xrefit*, along with vibration–rotation interaction and electron-mass distribution corrections predicted at the CCSD(T)/cc-pCVTZ level of theory. The *xrefit* module uses the values to calculate the equilibrium rotational constants ($B_e$) using Eq. (2), where the second term contains the vibration–rotation interaction correction, $\frac{m_e}{M_p}$ is the electron–proton mass ratio, $B_0^{\beta(S)}$ is the S-reduction rotational constant, and $g^{\beta\beta}$ is the corresponding magnetic *g*-tensor component,

$$B_e^{\beta} = B_0^{\beta(S)} + \frac{1}{2}\sum_i \alpha_i^{\beta} - \frac{m_e}{M_P} g^{\beta\beta} B^{\beta}. \quad (2)$$

These calculated equilibrium rotational constants are then used to calculate the inertial defect ($\Delta_i$), which is precisely zero for a rigid, planar molecule. For ketene, without either computational correction, the observed inertial defect $\Delta_{i0}$ is ~0.09 $\mu$Å$^2$ (Table III). Including the vibration–rotation interaction correction decreases the inertial defect to ~0.004 $\mu$Å$^2$, while the inclusion of the electron-mass correction brings the inertial defect to slightly larger than 0.004 $\mu$Å$^2$ (Table III) in a similar manner to $HN_3$.[83] These two molecules stand in contrast to the trend observed for heterocyclic molecules,[79–82,111] where the vibration–rotation interaction correction results in a small negative value of $\Delta_{ie}$ and subsequent application of the electron-mass correction brings the magnitude of $\Delta_{ie}$ close to zero.[79–82,111] The similar inertial defect trend to $HN_3$ is likely due to the nature of the C–C–O backbone, where the electron mass is more-or-less cylindrically distributed in the combined in-plane and out-of-plane π orbitals.

The semi-experimental equilibrium structure parameters of ketene obtained from 16 isotopologues are shown in Fig. 7 and enumerated in Table IV. The 2σ statistical uncertainties of the bond distances are all <0.0007 Å, and the corresponding uncertainty in the bond angle is 0.014°. Overall, the precision and accuracy of the structural parameters are similar to those of $HN_3$[83] when comparing the $r_e^{SE}$ calculated at the same level of theory. The 2σ statistical

**TABLE III.** Inertial defects ($\Delta_i$) and second moments ($P_{bb}$) of ketene isotopologues.

| Isotopologue | $\Delta_{i0}$ ($\mu$Å$^2$)[a] | $\Delta_{ie}$ ($\mu$Å$^2$)[a,b] | $\Delta_{ie}$ ($\mu$Å$^2$)[a,c] | $P_{bb}$ ($\mu$Å$^2$)[c,d] | $P_{bb}/m_H$ (Å$^2$)[c,d,e] |
|---|---|---|---|---|---|
| $H_2CCO$ | 0.0774 | 0.0035 | 0.0041 | 1.782 76 | 1.768 92 |
| [1-$^{13}$C]-$H_2CCO$ | 0.0772 | 0.0035 | 0.0040 | 1.782 77 | 1.768 93 |
| [2-$^{13}$C]-$H_2CCO$ | 0.0772 | 0.0035 | 0.0041 | 1.782 75 | 1.768 91 |
| [$^{18}$O]-$H_2CCO$ | 0.0779 | 0.0036 | 0.0042 | 1.782 70 | 1.768 86 |
| [$^{17}$O]-$H_2CCO$ | 0.0779 | 0.0038 | 0.0044 | 1.782 59 | 1.768 75 |
| [1,2-$^{13}$C]-$H_2CCO$ | 0.0766 | 0.0031 | 0.0037 | 1.782 95 | 1.769 11 |
| [2,2-$^2$H]-$H_2CCO$ | 0.1089 | 0.0036 | 0.0042 | 3.561 73 | 1.768 40 |
| [2,2-$^2$H, 2-$^{13}$C]-$H_2CCO$ | 0.1086 | 0.0036 | 0.0042 | 3.561 74 | 1.768 40 |
| [2,2-$^2$H, 1-$^{13}$C]-$H_2CCO$ | 0.1086 | 0.0036 | 0.0042 | 3.561 74 | 1.768 40 |
| [2,2-$^2$H,$^{18}$O]-$H_2CCO$ | 0.1095 | 0.0036 | 0.0042 | 3.561 75 | 1.768 40 |
| [2,2-$^2$H,$^{17}$O]-$H_2CCO$ | 0.1093 | 0.0037 | 0.0043 | 3.561 77 | 1.768 42 |
| [2-$^2$H]-$H_2CCO$ | 0.0964 | 0.0037 | 0.0043 | 2.594 89 | |
| [2-$^2$H, 2-$^{13}$C]-$H_2CCO$ | 0.0963 | 0.0037 | 0.0043 | 2.598 82 | |
| [2-$^2$H, 1-$^{13}$C]-$H_2CCO$ | 0.0961 | 0.0036 | 0.0042 | 2.595 32 | |
| [2-$^2$H,$^{18}$O]-$H_2CCO$ | 0.0969 | 0.0037 | 0.0043 | 2.595 58 | |
| [2-$^2$H,$^{17}$O]-$H_2CCO$ | 0.0966 | 0.0036 | 0.0042 | 2.595 31 | |
| Average ($\bar{x}$) | 0.0918 | 0.0036 | 0.0042 | | |
| Std dev (s) | 0.0132 | 0.0001 | 0.0001 | | |

[a] $\Delta_i = I_c - I_a - I_b = -2P_{cc}$.
[b] Vibration–rotation interaction corrections only.
[c] Vibration–rotation interaction and electron-mass corrections.
[d] $P_{bb} = (I_b - I_a - I_c)/-2$.
[e] $m_H$ = 1.007 825 035 for $^1$H or 2.014 101 779 for $^2$H.

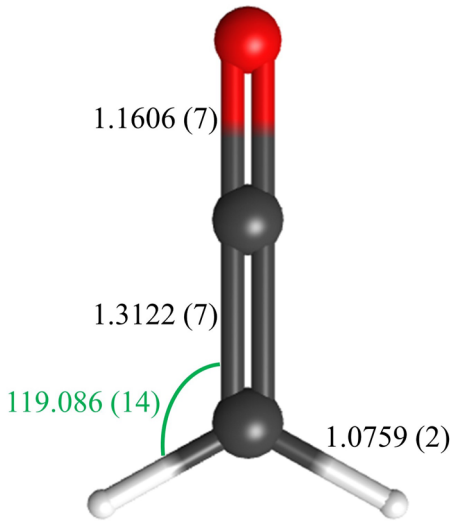


**FIG. 7.** Semi-experimental equilibrium structure ($r_e^{SE}$) of ketene with 2σ statistical uncertainties from least-squares fitting of the moments of inertia from 16 isotopologues. Distances are in angstroms, and the angle is in degrees.

uncertainties of heavy-atom bond lengths are nearly identical for $HN_3$ and ketene (0.000 74 for N1–N2; 0.000 75 for N2–N3; and 0.000 69 for C1-C2; 0.000 66 for C1-O). The 2σ statistical uncertainty for the respective X–H bond is also quite similar (0.0003 for $HN_3$ and 0.0002 for ketene). More generally, the bond length accuracy of the $r_e^{SE}$ of ketene is similar to our other works, including heterocyclic molecules,[79–82,111] and is of the same order of magnitude for the accuracy in the angles, with that in ketene being more accurately determined. This improvement in accuracy is largely due to having 8× more independent moments of inertia than structural parameters (three bond lengths and one angle) for ketene. Table IV presents the $r_e^{SE}$ structural parameters determined in the complete analysis, as well as the recommended $r_e^{SE}$ structural parameters, which take into account the limits of precision in their determination. The distinction between these sets of values is discussed in greater detail in the next section.

## DISCUSSION

In accordance with previous structure determinations,[80–85] the effect of including the available isotopologues in the $r_e^{SE}$ structure is examined using *xrefiteration*.[82] Figure 8 shows a plot of parameter uncertainty as a function of the number of incorporated isotopologues and reveals that the total uncertainty and the uncertainty of both the bond distances and bond angle have converged with the inclusion of the 11th isotopologue. Coincidentally, this is the same number of isotopologues used in the $r_e^{SE}$ determination published by Guarnieri *et al.*[58] The composition of the set of 11 isotopologues, however, is different in each case. Guarnieri *et al.*[58] determined the $r_e^{SE}$ with mainly protio- and [2,2-$^2$H]-ketene isotopologues, while the first 11 isotopologues utilized by *xrefiteration* in the current work include a mix of protio-, [2-$^2$H]-ketene, and [2,2-$^2$H]-ketene isotopologues. The addition of the five other isotopologues beyond the 11th neither decreases nor increases the total uncertainty, which is similar to the situation observed with $HN_3$[83] but unlike the cases of thiophene[80] and 1*H*- and 2*H*-1,2,3-triazole,[85] where the statistical uncertainty increases with the inclusion of the final isotopologues. Figure 9 shows the structural parameter values and their uncertainties as a function of the number of ketene isotopologues, added in the same order as in Fig. 8. It is evident that the structural parameters are well-determined with the core set of isotopologues because they agree with the respective BTE values. The addition of further isotopologues, however, decreases the 2σ uncertainties for all parameters until the addition of the 11th isotopologue, similar to Fig. 8. The $r_{C-C}$ and $r_{C-O}$ bond lengths of the current $r_e^{SE}$ are both smaller than the respective BTE values (by 0.0003 and 0.0004 Å, respectively), while there is quite close agreement between the $r_{C-H}$ bond lengths ($r_{eC-H} - r_e^{SE}{}_{C-H}$ = 0.000 04 Å). The value of the bond angle, $\theta_{C-C-H}$, is slightly larger (0.009°) than the BTE value. Both heavy-atom bond distances of the $r_e$ BTE structure are too large (Fig. 9) relative to their $r_e^{SE}$ parameters, and the observed residuals are very similar to those we observed in $HN_3$,[83] 0.000 35 Å for the central $r_{N1-N2}$ bond and 0.000 41 Å for the terminal RN2-N3 bond. In the structural least-squares fitting from rotational constants, the most difficult atom to locate is the heavy atom nearest to the center of mass, but an error in its location would tend to make one heavy-atom distance too long and one too short, contrary to the observations in ketene and $HN_3$. This may suggest that these residual discrepancies, which are not present in the distances involving H

**TABLE IV.** Equilibrium structural parameters of ketene. Boldface indicates recommended values.

| | $r_e^{SE}$[a,b] East *et al.*[57] | $r_e^{SE}$[a,c] Guarnieri *et al.*[58] | $r_e^{SE}$ this work | **$r_e^{SE}$ recommended** | CCSD(T) BTE | CCSD(T)/cc-pCV6Z |
|---|---|---|---|---|---|---|
| $r_{C-C}$ (Å) | 1.312 12 (60) | 1.3122 (12) | 1.312 18 (69) | **1.3122 (7)** | 1.312 58 | 1.312 00 |
| $r_{C-H}$ (Å) | 1.075 76 (14) | 1.0763 (2) | 1.075 93 (16) | **1.0759 (2)** | 1.075 89 | 1.075 65 |
| $r_{C-O}$ (Å) | 1.160 30 (58) | 1.1607 (12) | 1.160 64 (66) | **1.1606 (7)** | 1.160 97 | 1.160 07 |
| $\theta_{C-C-H}$ (deg) | 119.110 (12) | 119.115 (22) | 119.086 (14) | **119.086 (14)** | 119.077 | 119.067 |
| $N_{iso}$[d] | 6 | 11 | 16 | **16** | | |

[a] 2σ uncertainties calculated based on the uncertainty presented in each work.
[b] Vibration–rotation corrections calculated at a mixed MP2 and CCSD(T) level.
[c] Vibration–rotation and electron-mass corrections calculated at the MP2/cc-pVTZ level.
[d] Number of isotopologues used in the structure determination.

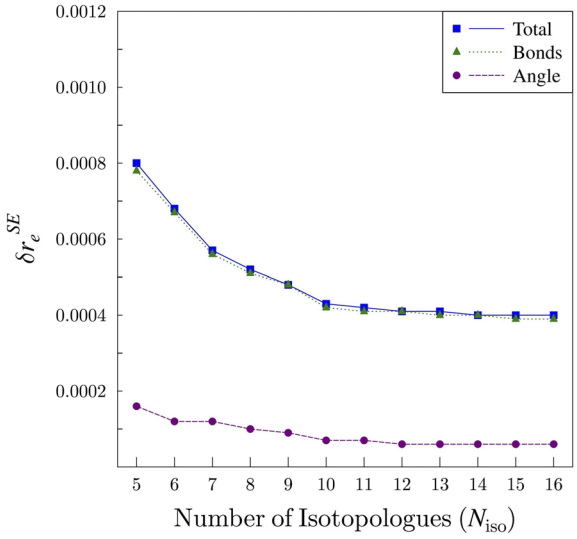


| $N_{iso}$ | Isotopologue Added |
|---|---|
| 5 | Core set |
| 6 | [2-$^2$H, $^{18}$O] |
| 7 | [2-$^2$H, 2-$^{13}$C] |
| 8 | [1,2-$^{13}$C] |
| 9 | [2,2-$^2$H, 2-$^{13}$C] |
| 10 | [2,2-$^2$H, $^{18}$O] |
| 11 | [$^{17}$O] |
| 12 | [2,2-$^2$H, 1-$^{13}$C] |
| 13 | [2-$^2$H, $^{17}$O] |
| 14 | [2,2-$^2$H, $^{17}$O] |
| 15 | [2,2-$^2$H] |
| 16 | [2-$^2$H, 1-$^{13}$C] |

**FIG. 8.** Plot of $r_e^{SE}$ *uncertainty* ($\delta r_e^{SE}$) as a function of the number of isotopologues ($N_{iso}$) incorporated into the structure determination dataset for ketene. The total relative statistical uncertainty ($\delta r_e^{SE}$, blue squares), the relative statistical uncertainty in the bond distances (green triangles), and the relative statistical uncertainty in the angle (purple circles) are presented.

atoms, are due to some systematic shift in the BTE distances related to the heavy atom backbone of these molecules.

A graphical representation of all the structural parameters for the current $r_e^{SE}$, the $r_e^{SE}$ by East *et al.*,[57] the $r_e^{SE}$ by Guarnieri *et al.*,[58] the BTE, and various coupled-cluster calculations with different basis sets is shown in Fig. 10. Upon cursory inspection, it seems there is excellent agreement among all of the structural parameters of the three $r_e^{SE}$ structures (Table IV and Fig. 10), and all are quoted to similar precision. Because separate sets of discrepancies are involved with respect to the two previous $r_e^{SE}$ structure determinations, we will discuss them separately. The heavy-atom distances from Guarnieri *et al.*[58] are essentially the same as our own, although with slightly larger 2σ uncertainties due to the smaller dataset compared to the present work, and BTE results for both parameters easily fall within the quoted 2σ limit. The agreement for the two parameters involving the hydrogen-atom position is not quite as good. The $r_{C\text{-}H}$ bond distance from Guarnieri *et al.*[58] is in disagreement with our value by slightly more than the combined 2σ error estimates, and the BTE value falls well outside their 2σ error range. The angle, $\theta_{C\text{-}C\text{-}H}$, is, indeed, in agreement with our value within the combined estimated 2σ error limits, but the BTE value of this parameter falls significantly outside their 2σ error range. We believe that the reason for these discrepancies is the impact of untreated coupling between vibrational states impacting the rotational constants. It is

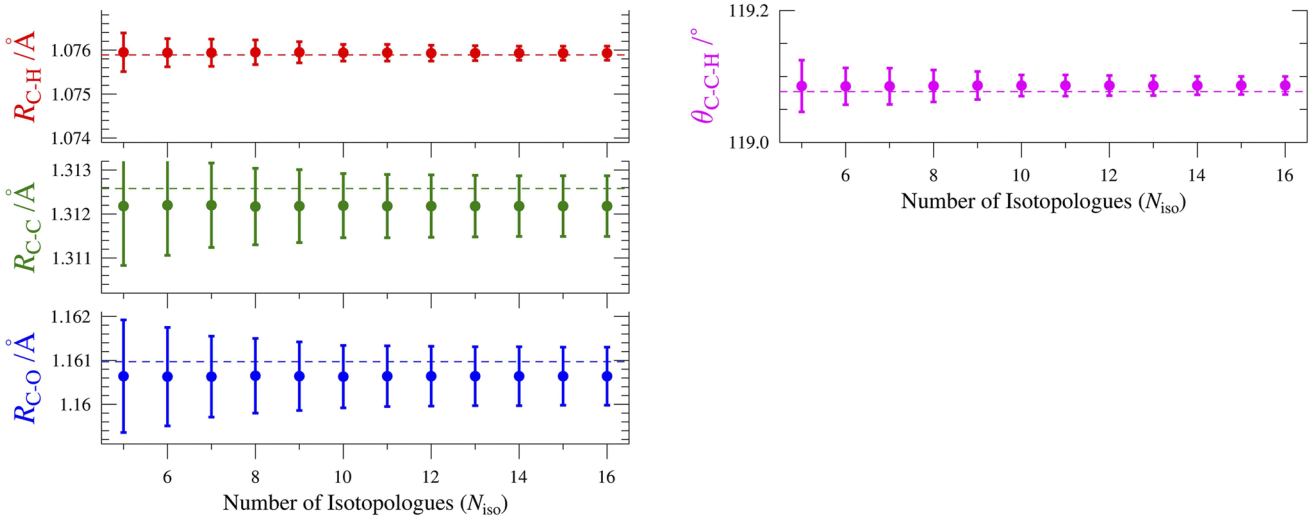


**FIG. 9.** Plots of the structural parameters of ketene as a function of the number of isotopologues ($N_{iso}$) and their 2σ uncertainties. Plots of bond distance use consistent scales. The colored dashed lines indicate the BTE value. The table in Fig. 8 indicates the *x*th isotopologue added to the $r_e^{SE}$.

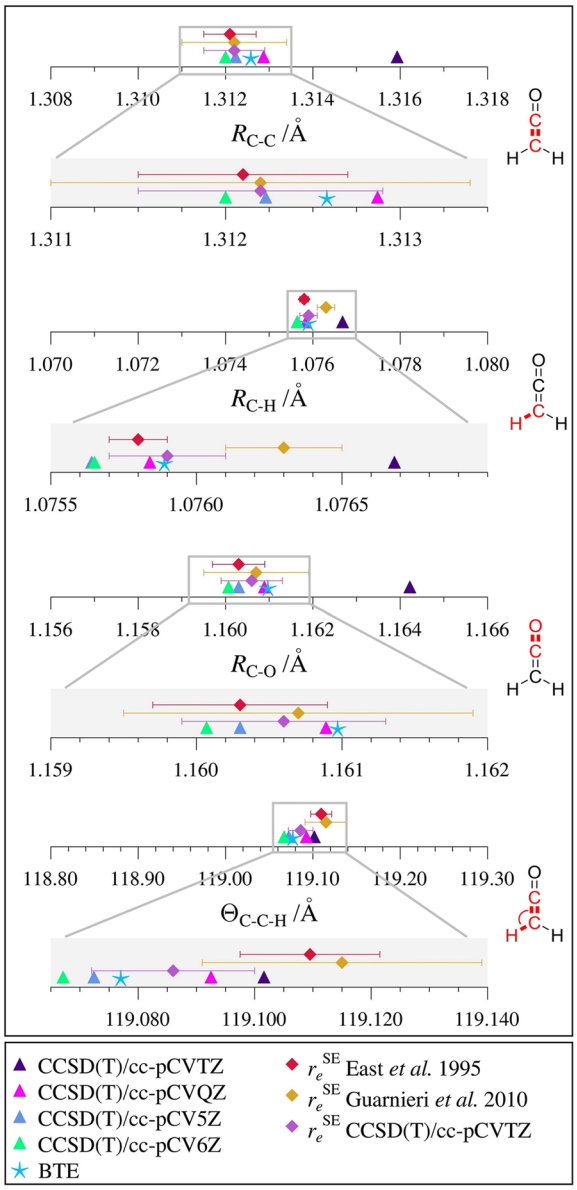


**FIG. 10.** Graphical comparison of the ketene structural parameters with bond distances in angstroms (Å) and angles in degrees (°). Plots of bond distance use the same scale. Expansions are provided for each parameter in gray boxes. The statistical uncertainties for all $r_e^{SE}$ parameters are 2σ.

known that the ground state of ketene at high $K_a$ values is affected by perturbations from low-lying vibrational states. We have chosen to employ only measurements for $K_a$ = 0–5, which removed this problem. Guarnieri *et al.*,[58] however, used higher $K_a$ transitions in their least-squares fits, which required the inclusion of higher-order centrifugal distortion terms, $L_{JK}$ and $L_{JKK}$. These effective parameters distort the determined values of $A_0$ from the regression analysis, which may affect the structural parameters. We tested our conjecture by using our rotational constants for the set of isotopologues used by Guarnieri *et al.*[58] and found the resultant structure in essentially complete agreement with our own $r_e^{SE}$ structure (Table IV), which is consistent with the analysis of the structure shown in Fig. 9. This indicates that the five additional isotopologues that we measured and included were not required to achieve this improved accuracy.

The situation with respect to the $r_e^{SE}$ structure from East *et al.*[57] is more straightforward. The bond distances and angles reported by East *et al.*[57] are in complete agreement with the current $r_e^{SE}$ values. This is somewhat surprising, given that the rotational constants are substantially less precise than the values determined in the present work and that the $A_0$ constant of [$^{18}$O]-ketene used by East *et al.*[57] and determined experimentally by Brown *et al.*,[28] 287 350 (910) MHz, is clearly too large by about 5 GHz. The values of $A_0$ for all heavy-atom isotopologues should be nearly the same because they depend only on the distance of the hydrogen atoms from the *a*-axis. This is confirmed by the data in Table II. The remaining rotational constants used by East *et al.*[57] are all similar to those in the present work. We obtained an $r_e^{SE}$ structure using the rotational constants and vibration–rotation interaction corrections presented in Table XIV of the East *et al.*[57] work and obtained a structure very closely resembling the one presented in that work for all parameters. This is also an interesting outcome, as the vibration–rotation interaction corrections used in that work are clearly inadequate, as evidenced by the residual inertial defects presented in their Table XIV[57] that vary in sign and order of magnitude across the six isotopologues. Despite the inadequacy of the vibration–rotation interaction corrections, the $r_e^{SE}$ structure of East *et al.*[57] is in excellent agreement with the new $r_e^{SE}$ but not quite in agreement with the $\theta_{C\text{–}C\text{–}H}$ value from the $r_e$ BTE structure. These analyses are provided in the supplementary material and summarized in Tables S-V and S-VI.

The $r_e^{SE}$ structure presented in this work, like the previously reported structures,[57,58] suffers from the impact of untreated Coriolis coupling between its ground state and its vibrationally excited states. Despite this limitation, the 2σ statistical uncertainties for the bond distances and bond angles are quite small (0.0002 to 0.0007 Å for the bond distances and 0.014° for the bond angle). For the bond distances, this statistical uncertainty is approaching the limit of the $r_e^{SE}$ structure determination, which requires the assumption that there is one mass-independent equilibrium geometry. The mass independence of equilibrium structures is a tacitly accepted assumption of molecular structure determination by rotational spectroscopy that is no longer valid as the limits of accuracy and precision are extended, especially for parameters involving hydrogen atoms. As a simple test of this assumption, optimized geometries were obtained for ketene and [2,2-$^2$H]-ketene with and without the diagonal Born–Oppenheimer correction (DBOC; SCF with the aug-cc-pCVTZ basis set). Of course, the $r_e$ structure obtained from the *normal* optimization without the DBOC resulted in the same equilibrium geometry for both isotopologues. With the DBOC, however, the equilibrium C–D distance decreased relative to the C–H distance by 0.000 06 Å. This value, which is similar to that obtained for benzene,[86] suggests that the limit and trustworthiness of the $r_e^{SE}$ structure for ketene and other C–H containing $r_e^{SE}$ structures is on the order of 0.0001 Å, which is half of the 2σ statistical uncertainty of the $r_e^{SE}$ C–H distance in this work. As a consequence of these relationships, our recommended values for the structural parameters of ketene are $r_{C\text{–}C}$ = 1.3122 (7) Å,

$r_{C-H}$ = 1.0759 (2) Å, $r_{C-O}$ = 1.1606 (7) Å, and $\theta_{C-C-H}$ = 119.086 (14)°, as shown in Fig. 7 and Table IV.

The $C_{2v}$ symmetry of ketene-$h_2$ and ketene-$d_2$ allows for two independent confirmations of the quality of the spectroscopic analysis and computational corrections, $P_{bb}$ and $\Delta_{ie}$. $\Delta_{ie}$ for a planar molecule is zero, as no nuclear mass exists off of the molecular plane. Any residual inertial defect after correction of the rotational constants for the vibration–rotation interaction and the electronic mass distribution potentially reveals room for improvements in the rotational constants or computational corrections. While all of the residual $\Delta_{ie}$ values are quite small (Table III), their non-zero values demonstrate that further corrections may be possible. Their scatter reveals an interesting mass dependence. The ketene-$d_1$ and ketene-$d_2$ isotopologues have nearly identical inertial defects to four decimal places (0.0042 or 0.0043 $\mu$Å$^2$), while the ketene-$h_2$ isotopologues have an average value of (0.0042 $\mu$Å$^2$) and a range from 0.0037 to 0.0044 $\mu$Å$^2$. To probe this mass dependence, we determined the $P_{bb}$ (second moments) value[112] for each isotopologue (Table III), after computational corrections were applied to the rotational constants. To the extent that there is a single, mass-independent equilibrium geometry of ketene, the $P_{bb}$ value, corrected for the mass of the hydrogen or deuterium atom in the $C_{2v}$ isotopologues (ketene-$h_2$ and ketene-$d_2$), should be the same for all isotopologues because it is only dependent on the location of the H atoms with respect to the perpendicular mirror plane. Also shown in Table III are the $P_{bb}/m_H$ values, which are practically identical for all of the ketene-$d_2$ isotopologues (1.7684 Å$^2$). The $P_{bb}/m_H$ values for the protio-ketene isotopologues show an increased scatter ranging from 1.7687 to 1.7691 Å$^2$ but have a higher average value as well (1.7689 Å$^2$). While these differences are small, their clear mass dependence leads us to conclude that we have not completely removed the impact of untreated Coriolis coupling from the rotational constants. The larger mass of $^2$H compared to $^1$H reduces the $A_0$ rotational constant by roughly a factor of two for the deuterium-containing isotopologues. The $a$-axis Coriolis $\zeta$ is unchanged between isotopologues, but the $a$-axis Coriolis coupling constants scale with the magnitude of the $A_0$ rotational constant. It is expected, therefore, that the protio-ketenes would be subject to a slightly greater impact of untreated Coriolis coupling, which is consistent with this observation. The great constancy of the $P_{bb}/m_D$ values across all the [2,2-$^2$H]-ketene isotopologues (*vide supra*) leads us to believe that the corresponding $b$-coordinate of the $^2$H-atom [0.940 32 Å, determined by Eq. (3)] is one of the most reliably determined structural parameters of ketene,

$$b_H = \sqrt{\frac{P_{bb}}{2m_H}}. \tag{3}$$

This assertion is supported by a comparison to its corresponding values calculated from the internal coordinates in Table IV: $r_e^{SE}$ = 0.940 25 Å, $r_e$ 6Z = 0.940 17 Å, and $r_e$ BTE = 0.940 29 Å. The very small difference from the BTE value (0.000 03 Å) is particularly notable and satisfying. The corresponding value for the $b$-coordinate of the $^1$H-atom in ketene is 0.940 45 Å, which is slightly larger due to some combination of the true isotopic difference in the $r_{C-H}$ and $r_{C-D}$ equilibrium bond distances and the increased untreated Coriolis coupling in the protio-ketene isotopologues.

## CONCLUSION

A new, highly precise, and accurate semi-experimental equilibrium ($r_e^{SE}$) structure for ketene ($H_2C{=}C{=}O$) has been determined from the rotational spectra of 16 isotopologues. The 2$\sigma$ values for the $r_e^{SE}$ structure of ketene, and also the discrepancies between the best theoretical estimate (BTE) and the $r_e^{SE}$ structural parameters, are strikingly similar to those for the previous $r_e^{SE}$ structure of hydrazoic acid (HNNN).[83] This outcome is noteworthy, although perhaps not surprising, given (i) the structural similarity between the two species and (ii) the highly over-determined datasets, which are a consequence of the large number of isotopologues relative to the number of structural parameters. In both cases, we found that extrapolation to the complete basis set limit provided slightly better agreement with the $r_e^{SE}$ structure when the highest level calculation included in the extrapolation was CCSD(T)/cc-pCV6Z, as opposed to CCSD(T)/cc-pCV5Z. It is somewhat surprising that the high accuracy of the ketene structure did not require the full dataset from 16 isotopologues. The uncertainties in the structural parameters did not improve with the inclusion of the "last" five isotopologues in the *xrefiteration* analysis. This case stands in contrast to other molecules that we have studied, in which quite large numbers of isotopologues are required for convergence of the $r_e^{SE}$ parameters.[82,84,85] Previous studies were steering us toward a generalization that "more is better" with respect to the number of isotopologues used in a structure determination, but the current case provides a counterexample. In the current case, the extra isotopologues do not degrade the quality of the structure, but they do not improve it. The current state of understanding of $r_e^{SE}$ structure determination does not enable a prediction of the number of isotopologues that will be required for the statistical uncertainties of the structural parameters to converge.

The present work confirms the great utility of the BTE structure as a benchmark for the semi-experimental structures. Although both of the published $r_e^{SE}$ structures for ketene, to which we have compared our own results, are generally in excellent agreement with the present work, the comparison to the BTE structure clearly establishes that the present approach of limiting the dataset to low $K_a$ values (0–5) improved the results for a molecule in which perturbations of the ground state exist. There need to be further investigations of why the BTE structure predicts heavy-atom bond distances that are longer than the $r_e^{SE}$ structure when all of the other structural parameters agree so well. The BTE values for the heavy-atom distances do not fall outside the 2$\sigma$ statistical uncertainty of the $r_e^{SE}$ values, but the small differences between BTE and $r_e^{SE}$ values have now been observed in both ketene and $HN_3$. The general applicability to similar molecules and the origin of the effect merit additional study.

The current studies enhance the capability for radioastronomers to search for ketene in different extraterrestrial environments by extending the measured frequency range of ketene to 750 GHz as well as providing data for newly measured isotopologues, [2-$^2$H, 1-$^{13}$C]-ketene, [2-$^2$H, 2-$^{13}$C]-ketene, [2-$^2$H, $^{18}$O]-ketene, [2-$^2$H, $^{17}$O]-ketene, and [2,2-$^2$H, $^{17}$O]-ketene. These new data will also be valuable for identifying these species in laboratory experiments, e.g., electric discharge, pyrolysis, and photolysis. Finally, these spectra contain a great many transitions from vibrationally excited states, which should prove valuable in analyzing and quantifying the numerous perturbations that exist between these

low-lying vibrational states. We hope to pursue this topic in the future.

## SUPPLEMENTARY MATERIAL

Computational output files, least-squares fitting for all isotopologues, data distribution plots for all non-standard isotopologues, *xrefiteration* outputs, equations used for calculating determinable constants and BTE corrections, and tables of S-reduction, A-reduction, and determinable constants, structural parameters, inertial defects, BTE corrections, and synthetic details are provided in the supplementary material.

## ACKNOWLEDGMENTS

We gratefully acknowledge the funding from the U.S. National Science Foundation for the support of this project (Grant No. CHE-1954270 to R.J.M and Grant No. CHE-1664325 to J.F.S.). We thank Maria Zdanovskaia for her assistance with generating figures. We thank Maria Zdanovskaia and Andrew Owen for their thoughtful commentary and review of the manuscript. We thank Tracy Drier for the construction of the ketene lamp used in this work.

## AUTHOR DECLARATIONS

### Conflict of Interest

The authors have no conflicts to disclose.

### Author Contributions

**Houston H. Smith**: Formal analysis (equal); Investigation (equal); Writing – original draft (equal); Writing – review & editing (equal). **Brian J. Esselman**: Conceptualization (equal); Formal analysis (equal); Investigation (equal); Supervision (equal); Writing – original draft (equal); Writing – review & editing (equal). **Samuel A. Wood**: Investigation (equal); Methodology (equal); Writing – review & editing (equal). **John F. Stanton**: Formal analysis (equal); Investigation (equal); Software (equal); Writing – review & editing (equal). **R. Claude Woods**: Conceptualization (equal); Formal analysis (equal); Investigation (equal); Supervision (equal); Writing – review & editing (equal). **Robert J. McMahon**: Funding acquisition (lead); Investigation (equal); Project administration (equal); Supervision (equal); Writing – review & editing (equal).

## DATA AVAILABILITY

The data that support the findings of this study are available within the article and its supplementary material.

## REFERENCES

[1]T. T. Tidwell, *Ketenes*, 2nd ed. (John Wiley & Sons, Hoboken, NJ, 2006).
[2]R. L. Danheiser, *Science of Synthesis: Three Carbon-Heteroatom Bonds: Ketenes and Derivatives* (Georg Thieme Verlag, Stuttgart, 2006), Vol. 23.
[3]A. D. Allen and T. T. Tidwell, "New directions in ketene chemistry: The land of opportunity," Eur. J. Org. Chem. **2012**, 1081–1096.
[4]Y. Zhang, P. Gao, F. Jiao, Y. Chen, Y. Ding, G. Hou, X. Pan, and X. Bao, "Chemistry of ketene transformation to gasoline catalyzed by H-SAPO-11," J. Am. Chem. Soc. **144** 18251–18258 (2022).
[5]F. A. Leibfarth and C. J. Hawker, "The emerging utility of ketenes in polymer chemistry," J. Polym. Sci., Part A: Polym. Chem. **51**, 3769–3782 (2013).
[6]M. J. Newland, G. J. Rea, L. P. Thüner, A. P. Henderson, B. T. Golding, A. R. Rickard, I. Barnes, and J. Wenger, "Photochemistry of 2-butenedial and 4-oxo-2-pentenal under atmospheric boundary layer conditions," Phys. Chem. Chem. Phys. **21**, 1160 (2019).
[7]W. Sun, J. Wang, C. Huang, N. Hansen, and B. Yang, "Providing effective constraints for developing ketene combustion mechanisms: A detailed kinetic investigation of diacetyl flames," Combust. Flame **205**, 11–21 (2019).
[8]R. L. Hudson and M. J. Loeffler, "Ketene formation in interstellar ices: A laboratory study," Astrophys. J. **773**, 109 (2013).
[9]B. E. Turner, "Microwave detection of interstellar ketene," Astrophys. J. **213**, L75–L79 (1977).
[10]H. E. Matthews and T. J. Sears, "Interstellar molecular line searches at 1.5 centimeters," Astrophys. J. **300**, 766–772 (1986).
[11]L. E. B. Johansson, C. Andersson, J. Ellder, P. Friberg, A. Hjalmarson, B. Hoglund, W. M. Irvine, H. Olofsson, and G. Rydbeck, "Spectral scan of Orion A and IRC+10216 from 72 to 91 GHz," Astron. Astrophys. **130**, 227–256 (1984).
[12]W. M. Irvine, P. Friberg, N. Kaifu, K. Kawaguchi, Y. Kitamura, H. E. Matthews, Y. Minh, S. Saito, N. Ukita, and S. Yamamoto, "Observations of some oxygen-containing and sulfur-containing organic molecules in cold dark clouds," Astrophys. J. **342**, 871–875 (1989).
[13]B. E. Turner, R. Terzieva, and E. Herbst, "The physics and chemistry of small translucent molecular clouds. XII. More complex species explainable by gas-phase processes," Astrophys. J. **518**, 699–732 (1999).
[14]A. Bacmann, V. Taquet, A. Faure, C. Kahane, and C. Ceccarelli, "Detection of complex organic molecules in a prestellar core: A new challenge for astrochemical models," Astron. Astrophys. **541**, L12 (2012).
[15]J. K. Jørgensen, H. S. P. Müller, H. Calcutt, A. Coutens, M. N. Drozdovskaya, K. I. Öberg, M. V. Persson, V. Taquet, E. F. van Dishoeck, and S. F. Wampfler, "The ALMA-PILS survey: Isotopic composition of oxygen-containing complex organic molecules toward IRAS 16293–2422B," Astron. Astrophys. **620**, A170 (2018).
[16]S. Muller, A. Beelen, M. Guélin, S. Aalto, J. H. Black, F. Combes, S. J. Curran, P. Theule, and S. N. Longmore, "Molecules at z = 0.89. A 4-mm-rest-frame absorption-line survey toward PKS 1830-211," Astron. Astrophys. **535**, A103 (2011).
[17]H. Staudinger, *Die Ketene* (Enke Verlag, Stuttgart, 1912).
[18]S. C. Wang and F. W. Schueler, "A simple ketene generator," J. Chem. Educ. **26**, 323 (1949).
[19]G. Quadbeck, "Neuere Methoden der präparativen organischen Chemie II. Keten in der präparativen organischen Chemie," Angew. Chem. **68**, 361–370 (1956).
[20]E. M. S. Maçôas, L. Khriachtchev, R. Fausto, and M. Räsänen, "Photochemistry and vibrational spectroscopy of the *trans* and *cis* conformers of acetic acid in solid Ar," J. Phys. Chem. A **108**, 3380–3389 (2004).
[21]X. K. Zhang, J. M. Parnis, E. G. Lewars, and R. E. March, "FTIR spectroscopic investigation of matrix-isolated isomerization and decomposition products of ionized acetone: Generation and characterization of 1-propen-2-ol," Can. J. Chem. **75**, 276–284 (1997).
[22]B. J. Esselman and N. J. Hill, "Proper resonance depiction of Acylium cation: A high-level and student computational investigation," J. Chem. Educ. **92**, 660–663 (2015).
[23]J. Cernicharo, C. Cabezas, S. Bailleux, L. Margulès, R. Motiyenko, L. Zou, Y. Endo, C. Bermúdez, M. Agúndez, N. Marcelino, B. Lefloch, B. Tercero, and P. de Vicente, "Discovery of the acetyl cation, $CH_3CO^+$, in space and in the laboratory," Astron. Astrophys. **646**, L7 (2021).
[24]B. Bak, E. S. Knudsen, E. Madsen, and J. Rastrup-Andersen, "Preliminary analysis of the microwave spectrum of ketene," Phys. Rev. **79**, 190 (1950).
[25]H. R. Johnson and M. W. P. Strandberg, "The microwave spectrum of ketene," J. Chem. Phys. **20**, 687–695 (1952).
[26]A. P. Cox, L. F. Thomas, and J. Sheridan, "Internuclear distances in keten from spectroscopic measurements," Spectrochim. Acta **15**, 542–543 (1959).
[27]R. A. Beaudet, "Problems in molecular structure and internal rotation," Ph.D. dissertation (Harvard University, 1962).

[28]R. D. Brown, P. D. Godfrey, D. McNaughton, A. P. Pierlot, and W. H. Taylor, "Microwave spectrum of ketene," J. Mol. Spectrosc. **140**, 340–352 (1990).
[29]V. W. Weiss and W. H. Flygare, "Hydrogen spin–spin, spin–rotation, and deuterium nuclear quadrupole interactions in ketene, ketene-$d_1$, and ketene-$d_2$," J. Chem. Phys. **45**, 3475–3476 (1966).
[30]L. Nemes and M. Winnewisser, "Centrifugal distortion analysis of the microwave and millimeter wave spectra of deuterated ketenes," Z. Naturforsch., A **31**, 272–282 (1976).
[31]A. Guarnieri and A. Huckauf, "The rotational spectrum of ($^{17}$O) ketene," Z. Naturforsch., A: Phys. Sci. **56**, 440–446 (2001).
[32]A. Guarnieri, "The millimeterwave spectrum of four rare ketene isotopomers," Z. Naturforsch., A: Phys. Sci. **60**, 619–628 (2005).
[33]L. Nemes, J. Demaison, and G. Wlodarczak, "New measurements of sub-millimetre-wave rotational transitions for the ketene ($H_2CCO$) Molecule," Acta Phys. Hung. **61**, 135–138 (1987).
[34]H. Gershinowitz and E. B. Wilson, "Infrared absorption spectrum of ketene," J. Chem. Phys. **5**, 500 (1937).
[35]F. Halverson and V. Z. Williams, "The infra-red spectrum of ketene," J. Chem. Phys. **15**, 552–559 (1947).
[36]W. R. Harp and R. S. Rasmussen, "The infra-red absorption spectrum and vibrational frequency assignment of ketene," J. Chem. Phys. **15**, 778–785 (1947).
[37]L. G. Drayton and H. W. Thompson, "The infra-red spectrum of keten," J. Chem. Soc. **1948**, 1416–1419.
[38]B. Bak and F. A. Andersen, "The infrared spectrum of ketene," J. Chem. Phys. **22**, 1050–1053 (1954).
[39]P. E. B. Butler, D. R. Eatcw, and H. W. Thompson, "Vibration-rotation bands of keten," Spectrochim. Acta **13**, 223–235 (1958).
[40]W. H. Fletcher and W. F. Arendale, "Infrared spectra of $CD_2CO$ and CHDCO," J. Chem. Phys. **19**, 1431–1432 (1951).
[41]W. F. Arendale and W. H. Fletcher, "Some vibration-rotation bands of ketene," J. Chem. Phys. **24**, 581–587 (1956).
[42]W. F. Arendale and W. H. Fletcher, "Infrared spectra of ketene and deuteroketenes," J. Chem. Phys. **26**, 793–797 (1957).
[43]A. P. Cox and A. S. Esbitt, "Fundamental vibrational frequencies in ketene and the deuteroketenes," J. Chem. Phys. **38**, 1636–1643 (1963).
[44]L. Nemes, "Multiple Coriolis perturbations in the vibrational-rotational spectra of ketene and dideuteroketene," Tezisy Dokl. - Simp. Mol. Spektrosk. Vys. Sverkhvys. Razresheniya, 2nd; Akad. Nauk SSSR, Sib. Otd., Inst. Opt. Atmos. 2 (1974).
[45]L. Nemes, "Rotation-vibration analysis of the Coriolis-coupled $\nu_5$, $\nu_6$, $\nu_8$, and $\nu_9$ bands of $H_2CCO$," J. Mol. Spectrosc. **72**, 102–123 (1978).
[46]F. Winther, F. Hegelund, and L. Nemes, "The infrared spectrum of dideuteroketene below 620 cm$^{-1}$," J. Mol. Spectrosc. **117**, 388–402 (1986).
[47]J. L. Duncan, A. M. Ferguson, J. Harper, K. H. Tonge, and F. Hegelund, "High-resolution infrared rovibrational studies of the $A_1$ species fundamentals of isotopic ketenes," J. Mol. Spectrosc. **122**, 72–93 (1987).
[48]J. L. Duncan and A. M. Ferguson, "High resolution infrared analyses of fundamentals and overtones in isotopic ketenes," Spectrochim. Acta, Part A **43**, 1081–1086 (1987).
[49]F. Hegelund, J. Kauppinen, and F. Winther, "The high resolution infrared spectrum of the $\nu_9$, $\nu_6$ and $\nu_5$ bands in ketene-$d_2$," Mol. Phys. **61**, 261–273 (1987).
[50]R. Escribano, J. L. Doménech, P. Cancio, J. Ortigoso, J. Santos, and D. Bermejo, "The $\nu_1$ band of ketene," J. Chem. Phys. **101**, 937–949 (1994).
[51]M. C. Campiña, E. Domingo, M. P. Fernández-Liencres, R. Escribano, and L. Nemes, "Analysis of the high resolution spectra of the $\nu_5$ and $\nu_6$ bands of ketene," An. Quim., Int. Ed. **94**, 23–26 (1998)..
[52]M. Gruebele, J. W. C. Johns, and L. Nemes, "Observation of the $\nu_6 + \nu_9$ band of ketene via resonant Coriolis interaction with $\nu_8$," J. Mol. Spectrosc. **198**, 376–380 (1999).
[53]J. W. C. Johns, L. Nemes, K. M. T. Yamada, T. Y. Wang, J. Doménech, J. Santos, P. Cancio, D. Bermejo, J. Ortigoso, and R. Escribano, "The ground state constants of ketene," J. Mol. Spectrosc. **156**, 501–503 (1992).
[54]L. Nemes, D. Luckhaus, M. Quack, and J. W. C. Johns, "Deperturbation of the low-frequency infrared modes of ketene ($CH_2CO$)," J. Mol. Struct. **517-518**, 217–226 (2000).
[55]P. D. Mallinson and L. Nemes, "The force field and $r_z$ structure of ketene," J. Mol. Spectrosc. **59**, 470–481 (1976).
[56]J. L. Duncan and B. Munro, "The ground state average structure of ketene," J. Mol. Struct. **161**, 311–319 (1987).
[57]A. L. L. East, W. D. Allen, and S. J. Klippenstein, "The anharmonic force field and equilibrium molecular structure of ketene," J. Chem. Phys. **102**, 8506–8532 (1995).
[58]A. Guarnieri, J. Demaison, and H. D. Rudolph, "Structure of ketene—Revisited $r_e$ (equilibrium) and $r_m$ (mass-dependent) structures," J. Mol. Struct. **969**, 1–8 (2010).
[59]J. L. Duncan, A. M. Ferguson, J. Harper, and K. H. Tonge, "A combined empirical-ab initio determination of the general harmonic force field of ketene," J. Mol. Spectrosc. **125**, 196–213 (1987).
[60]A. Guarnieri and A. Huckauf, "The rotational spectrum of ketene isotopomers with $^{18}$O and $^{13}$C revisited," Z. Naturforsch., A: Phys. Sci. **58**, 275–279 (2003).
[61]C. C. Costain, "Determination of molecular structures from ground state rotational constants," J. Chem. Phys. **29**, 864–874 (1958).
[62]M. D. Harmony, V. W. Laurie, R. L. Kuczkowski, R. H. Schwendeman, D. A. Ramsay, F. J. Lovas, W. J. Lafferty, and A. G. Maki, "Molecular structures of gas-phase polyatomic molecules determined by spectroscopic methods," J. Phys. Chem. Ref. Data **8**, 619–722 (1979).
[63]P. Pulay, W. Meyer, and J. E. Boggs, "Cubic force constants and equilibrium geometry of methane from Hartree–Fock and correlated wavefunctions," J. Chem. Phys. **68**, 5077–5085 (1978).
[64]J. Demaison, "Experimental, semi-experimental and *ab initio* equilibrium structures," Mol. Phys. **105**, 3109–3138 (2007).
[65]J. Vázquez and J. F. Stanton, in *Equilibrium Molecular Structures: From Spectroscopy to Quantum Chemistry*, edited by J. Demaison, J. E. Boggs, and A. G. Császár (Taylor & Francis Group; CRC Press, 2010), pp 53–87.
[66]M. Mendolicchio, E. Penocchio, D. Licari, N. Tasinato, and V. Barone, "Development and implementation of advanced fitting methods for the calculation of accurate molecular structures," J. Chem. Theory Comput. **13**, 3060–3075 (2017).
[67]C. Puzzarini and V. Barone, "Diving for accurate structures in the ocean of molecular systems with the help of spectroscopy and quantum chemistry," Acc. Chem. Res. **51**, 548–556 (2018).
[68]K. Raghavachari, G. W. Trucks, J. A. Pople, and M. Head-Gordon, "A fifth-order perturbation comparison of electron correlation theories," Chem. Phys. Lett. **157**, 479–483 (1989).
[69]J. M. L. Martin and P. R. Taylor, "The geometry, vibrational frequencies, and total atomization energy of ethylene. A calibration study," Chem. Phys. Lett. **248**, 336–344 (1996).
[70]T. Helgaker, J. Gauss, P. Jørgensen, and J. Olsen, "The prediction of molecular equilibrium structures by the standard electronic wave functions," J. Chem. Phys. **106**, 6430–6440 (1997).
[71]K. A. Peterson and T. H. Dunning, Jr., "Benchmark calculations with correlated molecular wave functions. VIII. Bond energies and equilibrium geometries of the $CH_n$ and $C_2H_n$ ($n$=1–4) series," J. Chem. Phys. **106**, 4119–4140 (1997).
[72]T. Helgaker, P. Jørgensen, and J. Olsen, *Molecular Electronic-Structure Theory* (John Wiley & Sons, 2000).
[73]K. L. Bak, J. Gauss, P. Jørgensen, J. Olsen, T. Helgaker, and J. F. Stanton, "The accurate determination of molecular equilibrium structures," J. Chem. Phys. **114**, 6548–6556 (2001).
[74]S. Coriani, D. Marchesan, J. Gauss, C. Hättig, T. Helgaker, and P. Jørgensen, "The accuracy of *ab initio* molecular geometries for systems containing second-row atoms," J. Chem. Phys. **123**, 184107 (2005).
[75]C. Puzzarini, "Accurate molecular structures of small- and medium-sized molecules," Int. J. Quantum Chem. **116**, 1513–1519 (2016).
[76]C. Puzzarini and J. F. Stanton, "Connections between the accuracy of rotational constants and equilibrium molecular structures," Phys. Chem. Chem. Phys. **25**, 1421–1429 (2023).
[77]J. Gauss and J. F. Stanton, "Equilibrium structure of LiCCH," Int. J. Quantum Chem. **77**, 305–310 (2000).
[78]M. Piccardo, E. Penocchio, C. Puzzarini, M. Biczysko, and V. Barone, "Semi-experimental equilibrium structure determinations by employing B3LYP/SNSD

anharmonic force fields: Validation and application to semirigid organic molecules," J. Phys. Chem. A **119**, 2058–2082 (2015).
[79]Z. N. Heim, B. K. Amberger, B. J. Esselman, J. F. Stanton, R. C. Woods, and R. J. McMahon, "Molecular structure determination: Equilibrium structure of pyrimidine ($m$-$C_4H_4N_2$) from rotational spectroscopy ($r_e^{SE}$) and high-level *ab initio* calculation ($r_e$) agree within the uncertainty of experimental measurement," J. Chem. Phys. **152**, 104303 (2020).
[80]V. L. Orr, Y. Ichikawa, A. R. Patel, S. M. Kougias, K. Kobayashi, J. F. Stanton, B. J. Esselman, R. C. Woods, and R. J. McMahon, "Precise equilibrium structure determination of thiophene ($c$-$C_4H_4S$) by rotational spectroscopy—Structure of a five-membered heterocycle containing a third-row atom," J. Chem. Phys. **154**, 244310 (2021).
[81]B. J. Esselman, M. A. Zdanovskaia, A. N. Owen, J. F. Stanton, R. C. Woods, and R. J. McMahon, "Precise equilibrium structure of thiazole ($c$-$C_3H_3NS$) from twenty-four isotopologues," J. Chem. Phys. **155**, 054302 (2021).
[82]A. N. Owen, M. A. Zdanovskaia, B. J. Esselman, J. F. Stanton, R. C. Woods, and R. J. McMahon, "Semi-experimental equilibrium ($r_e^{SE}$) and theoretical structures of pyridazine ($o$-$C_4H_4N_2$)," J. Phys. Chem. A **125**, 7976–7987 (2021).
[83]A. N. Owen, N. P. Sahoo, B. J. Esselman, J. F. Stanton, R. C. Woods, and R. J. McMahon, "Semi-experimental equilibrium ($r_e^{SE}$) and theoretical structures of hydrazoic acid ($HN_3$)," J. Chem. Phys. **157**, 034303 (2022).
[84]H. A. Bunn, B. J. Esselman, P. R. Franke, S. M. Kougias, R. J. McMahon, J. F. Stanton, S. L. Widicus Weaver, and R. C. Woods, "Millimeter/Submillimeter-wave spectroscopy and the semi-experimental equilibrium ($r_e^{SE}$) structure of 1*H*-1,2,4-Triazole ($c$-$C_2H_3N_3$)," J. Phys. Chem. A **126**, 8196–8210 (2022).
[85]M. A. Zdanovskaia, B. J. Esselman, S. M. Kougias, B. K. Amberger, J. F. Stanton, R. C. Woods, and R. J. McMahon, "Precise equilibrium structures of 1*H*- and 2*H*-1,2,3-triazoles ($C_2H_3N_3$) by millimeter-wave spectroscopy," J. Chem. Phys. **157**, 084305 (2022).
[86]B. J. Esselman, M. A. Zdanovskaia, A. N. Owen, J. F. Stanton, R. C. Woods, and R. J. McMahon, "Precise equilibrium structure of benzene" (unpublished) (2023).
[87]B. K. Amberger, B. J. Esselman, J. F. Stanton, R. C. Woods, and R. J. McMahon, "Precise equilibrium structure determination of hydrazoic acid ($HN_3$) by millimeter-wave Spectroscopy," J. Chem. Phys. **143**, 104310 (2015).
[88]B. J. Esselman, B. K. Amberger, J. D. Shutter, M. A. Daane, J. F. Stanton, R. C. Woods, and R. J. McMahon, "Rotational spectroscopy of pyridazine and its isotopologs from 235–360 GHz: Equilibrium structure and vibrational satellites," J. Chem. Phys. **139**, 224304 (2013).
[89]M. A. Zdanovskaia, B. J. Esselman, R. C. Woods, and R. J. McMahon, "The 130–370 GHz rotational spectrum of phenyl isocyanide ($C_6H_5NC$)," J. Chem. Phys. **151**, 024301 (2019).
[90]H. M. Pickett, "Determination of collisional linewidths and shifts by a convolution method," Appl. Opt. **19**, 2745–2749 (1980).
[91]Z. Kisiel, L. Pszczółkowski, B. J. Drouin, C. S. Brauer, S. Yu, J. C. Pearson, I. R. Medvedev, S. Fortman, and C. Neese, "Broadband rotational spectroscopy of acrylonitrile: Vibrational energies from perturbations," J. Mol. Spectrosc. **280**, 134–144 (2012).
[92]Z. Kisiel, L. Pszczółkowski, I. R. Medvedev, M. Winnewisser, F. C. De Lucia, and E. Herbst, "Rotational spectrum of *trans–trans* diethyl ether in the ground and three excited vibrational states," J. Mol. Spectrosc. **233**, 231–243 (2005).
[93]H. M. Pickett, "The fitting and prediction of vibration-rotation spectra with spin interactions," J. Mol. Spectrosc. **148**, 371–377 (1991).
[94]Z. Kisiel, "Assignment and analysis of complex rotational spectra," in *Spectroscopy from Space*, edited by J. Demaison, K. Sarka, and E. A. Cohen, 1st ed. (Springer Netherlands, Dordrecht, 2001), pp 91–106.
[95]See http://info.ifpan.edu.pl/~kisiel/prospe.htm for PROSPE—Programs for ROtational SPEctroscopy.
[96]J. F. Stanton, J. Gauss, M. E. Harding, and P. G. Szalay, with contributions from A. A. Auer, R. J. Bartlett, U. Benedikt, C. Berger, D. E. Bernholdt, Y. J. Bomble, L. Cheng, O. Christiansen, M. Heckert, O. Heun, C. Huber, T.-C. Jagau, D. Jonsson, J. Jusélius, K. Klein, W. J. Lauderdale, D. A. Matthews, T. Metzroth, L. A. Mück, D. P. O'Neill, D. R. Price, E. Prochnow, C. Puzzarini, K. Ruud, F. Schiffmann, W. Schwalbach, S. Stopkowicz, A. Tajti, J. Vázquez, F. Wang, J. D. Watts, and the integral packages MOLECULE (J. Almlöf and P. R. Taylor), PROPS (P. R. Taylor), ABACUS (T. Helgaker, H. J. Aa. Jensen, P. Jørgensen, and J. Olsen), and ECP routines by A. V. Mitin and C. van Wüllen, CFOUR, Coupled-Cluster techniques for Computational Chemistry, a quantum-chemical program package. For the current version, see http://www.cfour.de.
[97]J. F. Stanton, C. L. Lopreore, and J. Gauss, "The equilibrium structure and fundamental vibrational frequencies of dioxirane," J. Chem. Phys. **108**, 7190–7196 (1998).
[98]W. Schneider and W. Thiel, "Anharmonic force fields from analytic second derivatives: Method and application to methyl bromide," Chem. Phys. Lett. **157**, 367–373 (1989).
[99]I. M. Mills, "Vibration-rotation structure in asymmetric- and symmetric-top molecules," in *Molecular Spectroscopy: Modern Research*, edited by K. N. Rao and C. W. Mathews (Academic Press, New York, 1972), Vol. 1, pp 115–140.
[100]C. Puzzarini, J. Bloino, N. Tasinato, and V. Barone, "Accuracy and interpretability: The devil and the holy grail. New routes across old boundaries in computational spectroscopy," Chem. Rev. **119**, 8131–8191 (2019).
[101]J. W. Williams and C. D. Hurd, "An improved apparatus for the laboratory preparation of ketene and butadiene," J. Org. Chem. **5**, 122–125 (1940).
[102]P. J. Paulsen and W. D. Cooke, "Preparation of deuterated solvents for nuclear magnetic resonance spectrometry," Anal. Chem. **35**, 1560 (1963).
[103]J. K. G. Watson, "Determination of centrifugal distortion coefficients of asymmetric-top molecules," J. Chem. Phys. **46**, 1935–1949 (1967).
[104]G. Winnewisser, "Millimeter wave rotational spectrum of HSSH and DSSD. II. Anomalous $K$ doubling caused by centrifugal distortion in DSSD," J. Chem. Phys. **56**, 2944–2954 (1972).
[105]B. P. van Eijck, "Reformulation of quartic centrifugal distortion Hamiltonian," J. Mol. Spectrosc. **53**, 246–249 (1974).
[106]V. Typke, "Centrifugal distortion analysis including $P^6$-terms," J. Mol. Spectrosc. **63**, 170–179 (1976).
[107]L. Margulès, A. Perrin, J. Demaison, I. Merke, H. Willner, M. Rotger, and V. Boudon, "Breakdown of the reduction of the rovibrational Hamiltonian: The case of $S^{18}O_2F_2$," J. Mol. Spectrosc. **256**, 232–237 (2009).
[108]R. A. Motiyenko, L. Margulès, E. A. Alekseev, J.-C. Guillemin, and J. Demaison, "Centrifugal distortion analysis of the rotational spectrum of aziridine: Comparison of different Hamiltonians," J. Mol. Spectrosc. **264**, 94–99 (2010).
[109]J. Doose, A. Guarnieri, W. Neustock, R. Schwarz, F. Winther, and F. Hegelund, "Application of a PC-controlled MW-spectrometer for the analysis of ketene-$D_2$. Simultaneous analysis of vibrational excited states using microwave and infrared spectra," Z. Naturforsch., A: Phys. Sci. **44**, 538–550 (1989).
[110]K. Vávra, P. Kania, J. Koucký, Z. Kisiel, and Š. Urban, "Rotational spectra of hydrazoic acid," J. Mol. Spectrosc. **337**, 27–31 (2017).
[111]A. G. Császár, J. Demaison, and H. D. Rudolph, "Equilibrium structures of three-, four-, five-, six-, and seven-membered unsaturated $N$-containing heterocycles," J. Phys. Chem. A **119**, 1731–1746 (2015).
[112]R. K. Bohn, J. A. Montgomery, Jr., H. H. Michels, and J. A. Fournier, "Second moments and rotational spectroscopy," J. Mol. Spectrosc. **325**, 42–49 (2016).